Aerosols-plasma interaction in Titan's ionosphere

Audrey Chatain

Aerosols-plasma interaction in Titan's ionosphere

Thèse de doctorat de l'université Paris-Saclay

Thèse présentée et soutenue à Guyancourt, le 29 juin 2020, par

Audrey CHATAIN

Composition du Jury

Francois LEBLANC Directeur de recherche, LATMOS	Président & examinateur
Gilles CARTRY Professeur, Université d'Aix Marseille	Rapporteur & examinateur
Ella SCIAMMA O'BRIEN Research Scientist, NASA Ames	Rapporteur & examinatrice
Andrew COATES Professor, University College London	Examinateur
Sandrine VINATIER Chargée de recherche, LESIA	Examinatrice
Nathalie CARRASCO Professeure, UVSQ	Directrice de thèse
Olivier GUAITELLA Ingénieur de recherche de l'Ecole polytechnique, HDR, LPP	Co-Directeur de thèse
Jan-Erik WAHLUND Associate Professor, Swedish Institute of Space Physics (IRF)	Invité
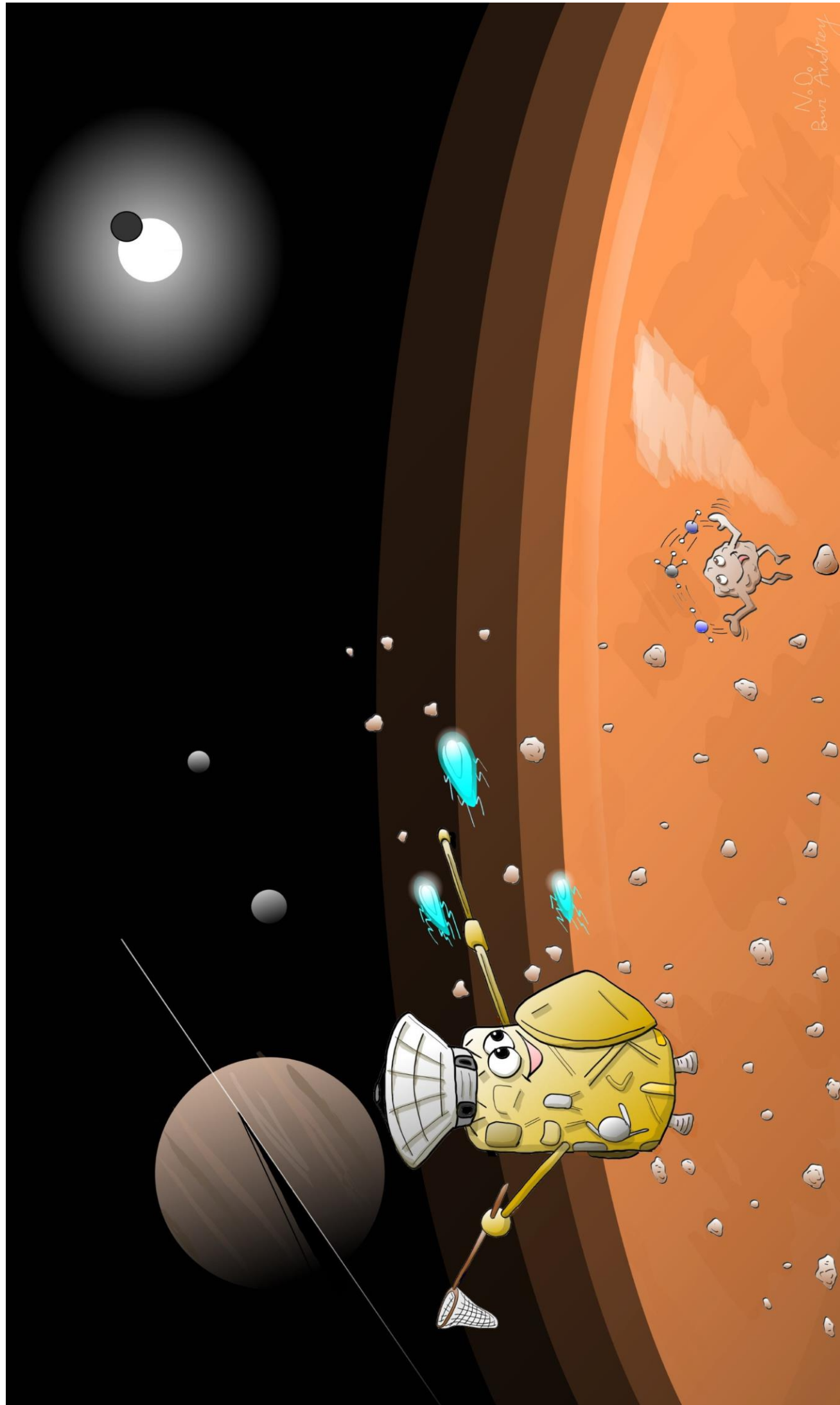
Remerciements

Les expériences et études réalisées dans cette thèse n'auraient pas eu lieu (ou ne se seraient pas si bien passées) sans l'aide de nombreux collègues, merci à vous !

Tout d'abord, un grand merci à Nathalie de m'avoir prise en thèse sur mon sujet favori : Titan ! Tu m'as aussi appris une chose très précieuse : voir toujours les choses du bon côté ☺. Merci à Olivier, pour m'avoir appris à maniper dans un laboratoire de recherche et pour ses intarissables bonnes (et intrépides ?) idées de manips. Merci Ludo, Ô grand maître de la Ludo-thèque et dompteur de spectro de masse, les manips n'auraient pas aussi bien marché sans toi ! Merci aussi à Guy, mon référent plasmas, monitorat et Shadocks malgré ses week-ends de 6 jours.

Je souhaite remercier également tous les autres membres de l'équipe ATMOSIM – Pierre, David D., Laura, Lisseth, Julien, Lora, Thomas, Maryse, Zoé, Nicolas J. – pour les bons moments passés en équipe, les conseils de guerre pour comprendre les caprices du spectro de masse, les secrets des tholins, et le meilleur emplacement pour faire une pause thé-café-chocolat ! Merci aussi aux collègues du LATMOS – Yann, Antoine, Léa, Aurélien, Elisabeth, Loïc, Christophe, Ashwin, Margaux, Caro, Cyril, Emmanuel… - pour les discussions entre deux couloirs, au réfectoire et en réunion planéto !

On the LPP side, thanks all for warmly welcoming me home at LPP a few days per month, it was a real pleasure to work in close collaboration with you. In particular, thank you Ana-Sofia, Abhyuday, Florian, Marlous, Thomas and Marine for the banana breaks, the treks and excursions in Paris and abroad, and the movie-sushi parties!

During my PhD I had the opportunity to stay a few weeks in Uppsala. It was a wonderful experience! First, thanks Ronan for showing me the way! I would like to thank all the Uppsala IRF team for being very welcoming, and in particular Jan-Erik and Michiko, for taking time for me, accepting my crazy idea of electron populations, but also for the telescope night and the Swedish dinner ☺. Thanks Lina for the ambitious bike tour, the un-finished expedition to Kiruna, the chocolate breaks, the smoothies in Boulder and all your motivating advices! Thank you Oleg for your always quick, very good and inspiring comments, I drew a lot of inspiration from your thesis and papers!

De retour en France, merci aux planétos du LMD, toujours chaleureux et avides de prendre des nouvelles, vous avez été mon 3e labo parisien ! Merci à Nicolas V. pour avoir été un excellent responsable d'enseignements à Orsay alors que je débutais dans l'enseignement des TPs/TDs à l'université. Merci à l'équipe Portugaise (Miguel, Luis et Luis) pour les discussions et pour m'avoir donné une bonne entrevue du monde de la modélisation des décharges plasma. Merci à Nathalie R. pour les longues sympathiques heures passées à l'analyse des tholins au microscope électronique. Merci à Sébastien R et Rosario pour les discussions sur les indices optiques, on parviendra peut-être un jour à finir ce projet ! Merci Jean-Pierre, grand-père Cassini, pour les discussions en conférences et séminaires, notamment sur la sonde de Langmuir et sur comment trouver un postdoc sur Titan. Merci également aux jeunes Titaniens

Julie, Maélie et Benoît pour nos discussions titaniennes en conférences, et à Daniel, Sébastien L., Sandrine, Alice et Aymeric pour m'aider à poursuivre mes études sur Titan en post-doc.

Je souhaite également remercier l'ENS Paris-Saclay pour le financement de mon projet de thèse. Merci à mon jury d'avoir pu relire ma thèse et assister à ma soutenance malgré les fortes incertitudes et contraintes sanitaires en cette période de Covid19. Un grand merci à Danielle de l'OVSQ, David C. et les informaticiens du LATMOS pour m'avoir permis de soutenir 'en vrai' malgré les fortes contraintes sanitaires. Et enfin, merci à Nicolas, artiste spécialisé en tholins et cuisto aux petits soins en période de rédaction confinée !
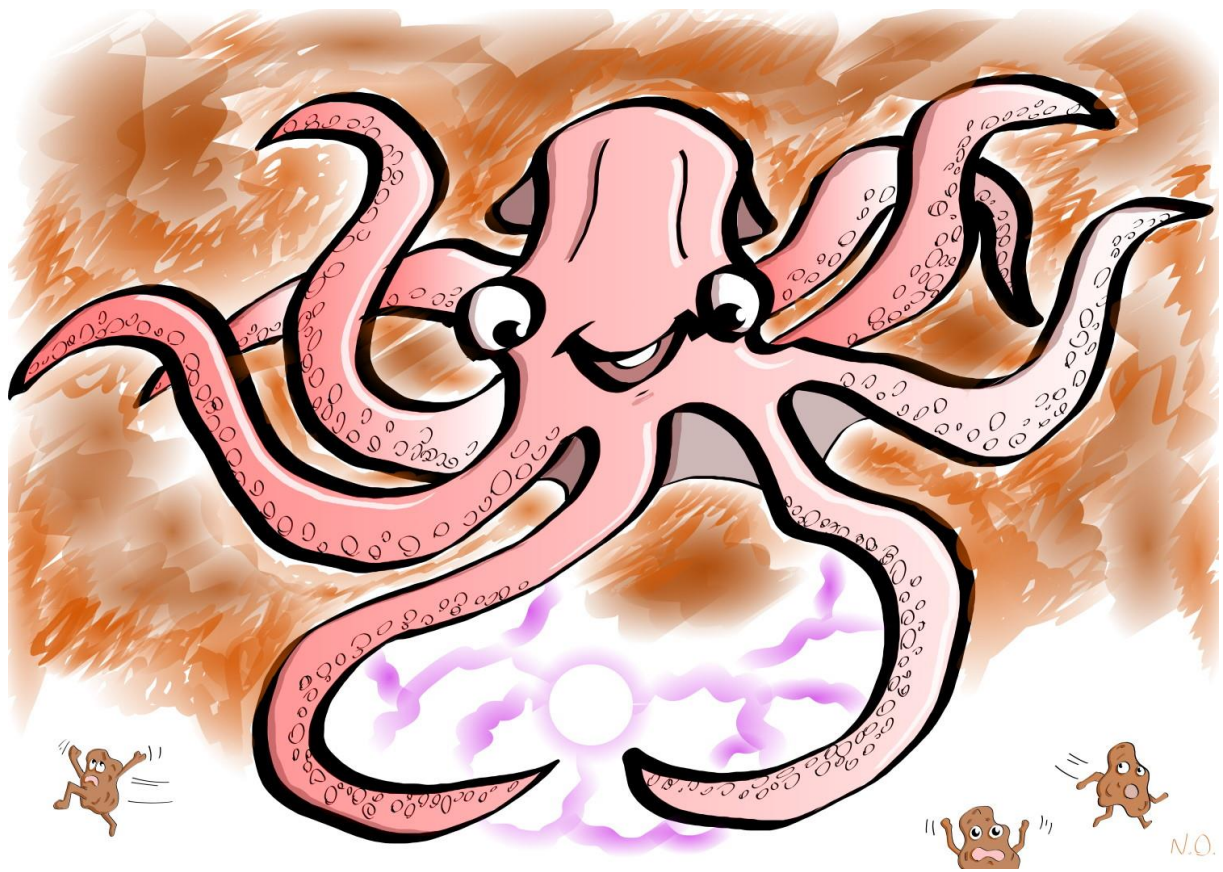
Vue d'artiste de mon expérience THETIS s'attaquant à des tholins.

Peter : Allons Wendy en route !

Michel : Où est-ce qu'on va ?

Wendy : Au pays imaginaire

Michel : Au pays imaginaire !

Wendy : Mais Peter comment est-ce qu'on va là-bas ?

Peter : En volant bien sûr !

Wendy : En volant !!

Peter : C'est facile, pour voler il vous suffit de rêver d'aventure.

(…)

Oh mais j'ai oublié quelque chose, la poussière !

Wendy, Jean et Michel : La poussière ?

Peter : Et hop ! Juste un peu de **poussière d'atmosphère**…

Peter Pan, Walt Disney, 1953

TABLE OF CONTENTS

Chapter III: Erosion of organic aerosols in a N_2-H_2 plasma environment

1- Introduction: experimental simulation of the interaction between aerosols and a N_2-H_2 plasma

2- Morphological and chemical evolution of the aerosols

3- Evolution of the plasma in contact with tholins

Chapter IV: Re-analysis of the Cassini Langmuir Probe data: are the electrons disturbed by the aerosols in the ionosphere?

1- Introduction: the RPWS/LP on-board Cassini

1.1.a. The Radio and Plasma Wave Science (RPWS) instrument
1.1.b. Bases of the Langmuir Probe
1.1.c. Theory of the Langmuir Probe
1.1.d. Measurements with the Cassini Langmuir Probe

1.2.a. Electron density
1.2.b. Electron temperature
1.2.c. Modeling of Titan's ionosphere
1.2.d. Objective of Chapter IV

2- Re-analysis of the LP data: method

2.1.a. Extraction of the electron current from the LP raw data
2.1.b. Examples of sweeps from Titan's ionosphere: several electron populations
2.1.c. The second derivative of the current: a quick way to spot electron populations
2.1.d. A complex case: how many populations?

2.2.a. The Druyvesteyn method
2.2.b. EEDF in the case of one population
2.2.c. Maxwellian EEDF for each population

2.3.a. d^2I from data points as a function of altitude: simple diagnostics of the electron population evolution
2.3.b. d^2I from data points as a function of altitude: strong correlation with the Solar Zenith Angle
2.3.c. A different evolution of the populations with altitude on nightside and on dayside

2.4.a. Typical profile for the family F1: nightside far from the terminator
2.4.b. Typical profile for the family F2: nightside close to the terminator
2.4.c. Typical profile for the family F3: dayside
2.4.d. Summary: typical profiles for the three flyby families
2.4.e. Discussion on the origin of the electron populations

3- Statistics with the complete Cassini dataset

3.1.a. Study of all the Cassini flybys in Titan's ionosphere
3.1.b. Electron densities and temperatures for the electron populations
3.1.c. Strong dependence with Solar Zenith Angle (SZA)
3.1.d. Relation between electron density and temperature measurements

3.2.a. Correlation with the extreme UV fluxes?
3.2.b. Impact of seasons?
3.2.c. Correlation with ion density?

Related publications

The work presented in this PhD dissertation led to the redaction of 7 journal articles, which will be referred to as '**Paper #**' in the following sections.

Paper 1: Chatain A., Jiménez-Redondo M., Vettier L., Guaitella O., Carrasco N., Alves L.L., Marques L. and Cernogora G., *N_2-H_2 capacitively coupled radio-frequency discharges at low pressure. Part I. Experimental results: effect of the H_2 amount on electrons, positive ions and ammonia formation,* accepted in Plasma Sources Science and Technology (2020).

Paper 2: Jiménez-Redondo M., **Chatain A.**, Vettier L., Guaitella O., Cernogora G., Carrasco N., Alves L.L. and Marques L., *N_2-H_2 capacitively coupled radio-frequency discharges at low pressure. Part II. Modelling results: the relevance of plasma-surface interaction,* accepted in Plasma Sources Science and Technology (2020).

Paper 3: Chatain A., Carrasco N., Ruscassier N., Gautier T., Vettier L. and Guaitella O., *Interaction dust – plasma in Titan's ionosphere: an experimental simulation of aerosols erosion*, Icarus 345 (2020) 113741.

Paper 4: Maillard J., Rüger C., **Chatain A.**, Schmitz-Afonso I., Weisbrod C., Bailly L., Petit E., Gautier T., McKenna A., Carrasco N. and Afonso C., *Dark-ageing of aerosols in the atmosphere of the early Earth,* to be submitted.

Paper 5: Chatain A., Vettier L., Carrasco N. and Guaitella O., *Interaction dust – plasma in Titan's ionosphere: experimental investigation of the gas phase modifications*. To be submitted to Icarus.

Paper 6: Chatain A., Wahlund J.-E., Morooka M., Shebanits O., Hadid L., Eriksson A., Carrasco N. and Guaitella O., *Re-analysis of the Cassini RPWS/LP data in Titan's ionosphere. Part 1. Detection of several electron populations*. Submitted to the Journal of Geophysical Research, Space Physics.

Paper 7: Chatain A., Wahlund J.-E., Morooka M., Shebanits O., Hadid L., Eriksson A., Carrasco N. and Guaitella O., *Re-analysis of the Cassini RPWS/LP data in Titan's ionosphere. Part 2. Electron densities and temperatures*. Submitted to the Journal of Geophysical Research, Space Physics.

My **PhD defense** is also available here: https://youtu.be/vamF9aU3LYQ

INTRODUCTION: TITAN'S IONOSPHERE, A COLD DUSTY PLASMA

in which aerosols and plasma species interact
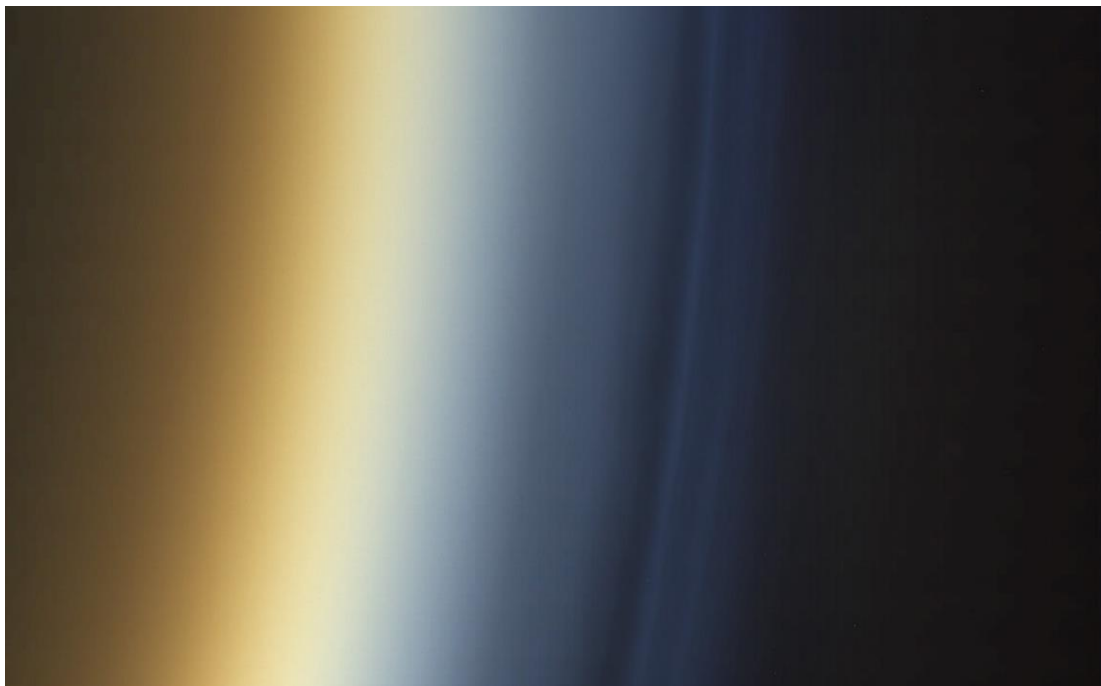
Contents

1- Titan

Titan is an amazing place, which presents a lot of similarities the Earth: in particular, a hydrological cycle at its surface and a thick atmosphere mainly composed of nitrogen. But what makes Titan exceptional is that it is a place governed by organic materials. These pre-biotic materials fill the entire atmosphere in the form of aerosols and deposit at the surface, forming dunes.

1.1- Titan, the biggest moon of Saturn

Titan is a **moon of Saturn** (see **Figure I.1-1**). It has a synchronous rotation of ~16 days around the planet. Consequently, a day on Titan is equivalent to **16 days** on Earth. Titan has also seasons. Together with Saturn, Titan orbits around the Sun in **~29 years**, with a perihelion at 9 AU and an aphelion at 10 AU. Their inclination is ~2.5° to the ecliptic.

Figure I.1-1: Titan and Saturn in the plane of the rings. Picture by the Cassini spacecraft on May 6, 2012. Credit: NASA/JPL - Caltech/Space Science Institute.
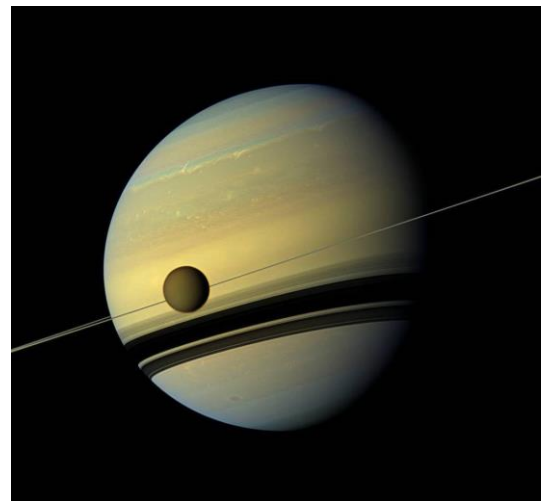
With a radius of 2 575 km, Titan is the **biggest moon of Saturn** (see **Figure I.1-2**), and the second biggest moon in the Solar System, just behind Ganymede (r = 2 634 km). Titan is even 6% bigger than the planet Mercury (r = 2 440 km), and 50% larger than our moon (r = 1 737 km). In the Saturnian system, it is located at ~20.3 Saturn radius away from Saturn.
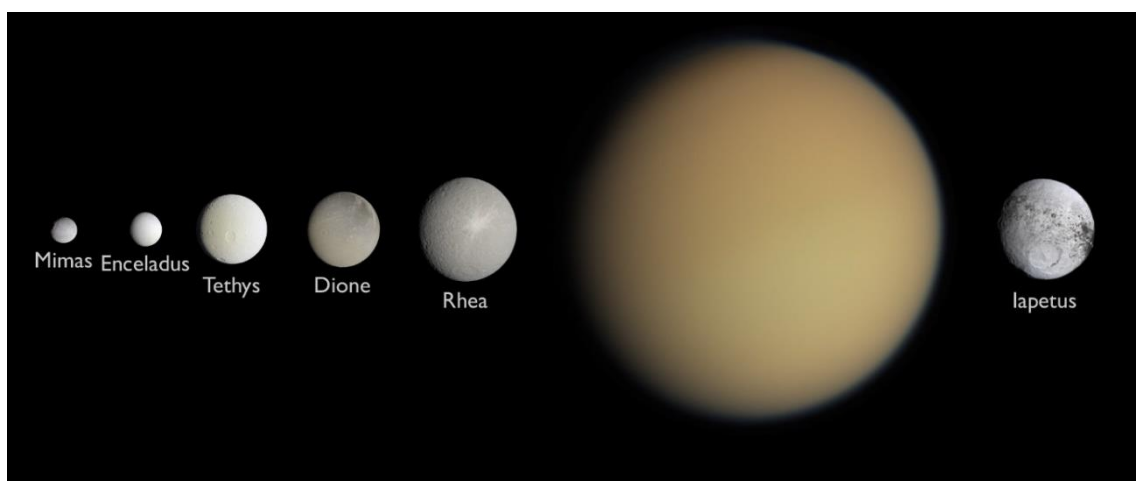
Figure I.1-2: Pictures of Saturn's biggest moons, at comparative real size scale. They are positioned with increasing distance to Saturn from left to right. Credit: NASA/JPL/Cassini.

1.2- Discovery and exploration

Today, we can easily observe Titan with a small telescope from our garden (see **Figure I.1-3**).
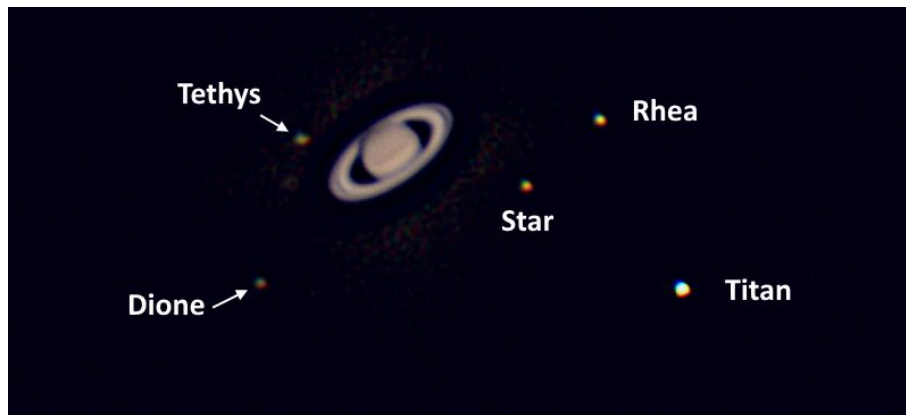
Figure I.1-3: The Saturn system observed with a small telescope on August 21st, 2018 20:47 UTC (France). Iapetus was out of range and Mimas and Enceladus too faint and close to Saturn to be resolved by the acquisition.

However, during the XVII century, telescopes had just been invented and were not as resolved as today. The first to associate a tiny little moving point to a satellite of Saturn was the Dutch astronomer **Christiaan Huygens in 1655**. He registered 68 cycles of Titan around Saturn to be sure of its orbital period around Saturn.

Titan is relatively far from Earth (~9.5 AU), and before the recent areas of the international large telescopes, few information could be deduced from Earth-based Titan observations. Only **in 1944**, the Dutch-American astronomer **Gerard Kuiper** recorded a spectrum of Titan in visible and in the infrared, and deduced the **presence of an atmosphere** from the observation of **methane** bands.

The first spacecraft mission to enter Saturn's system was the NASA probe **Pioneer 11** in September 1979. Pictures were of low quality. Nevertheless, the study of Saturn's magnetosphere brought up a fundamental conclusion: the Titan moon should be **too cold to host life at its surface**.

The **Voyager I** spacecraft reached Titan in November 1980. It confirmed the presence of methane, but also observed that it is not the main component of the atmosphere as previously thought: there is only a few percents of methane in a **bulk of molecular nitrogen** (Strobel and Shemansky, 1982).

The first close pictures of Titan taken by Pioneer 11, Voyager 1 and Voyager 2 shown in **Figure I.1-4** suggest that **the surface of Titan is hidden by orange hazes or clouds**.
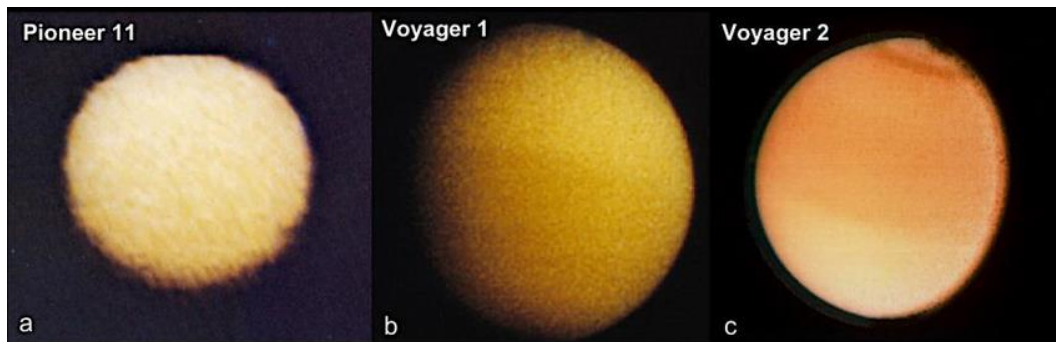
Figure I.1-4: First close up images of Titan as seen by (a) Pioneer 11 (1979) at a distance of 360 000 km, (b) Voyager 1 (1980) at 4 000 km and (c) Voyager 2 (1981) at 2 300 000 km. Image credit: NASA. Image configuration by A. Solomonidou.

The Cassini-Huygens mission was the first to be completely **dedicated to the study of Saturn's system**. It was a joint mission of NASA, ESA and ASI (the Italian Space Agency). It was a large spacecraft of the size of a bus: 6.8 m in length and 4 m in diameter, for 5.82 tons (with only 49 kg for the scientific instruments). The mission was launched in 1997, and arrived in Saturn's system in **2004**. The Cassini NASA spacecraft initially carried an ESA module, Huygens, that detached from Cassini to land on Titan in January 2005. Huygens had 6 scientific instruments onboard dedicated to the study of Titan's atmosphere during the descent and the landing of the probe. The Cassini mission arrived just after Saturn's winter solstice (see **Figure I.1-5**). It was extended through the equinox and until the summer solstice. The mission finally ended in **September 2017**, plunging into Saturn, at the occasion of 'The Grand Finale'.

One of the main objectives of the Cassini spacecraft was **to closely overfly Titan several times** (126), to analyze from distance Titan's lower atmosphere and surface, but also to study *in situ* the upper atmosphere of Titan and its plasma environment.
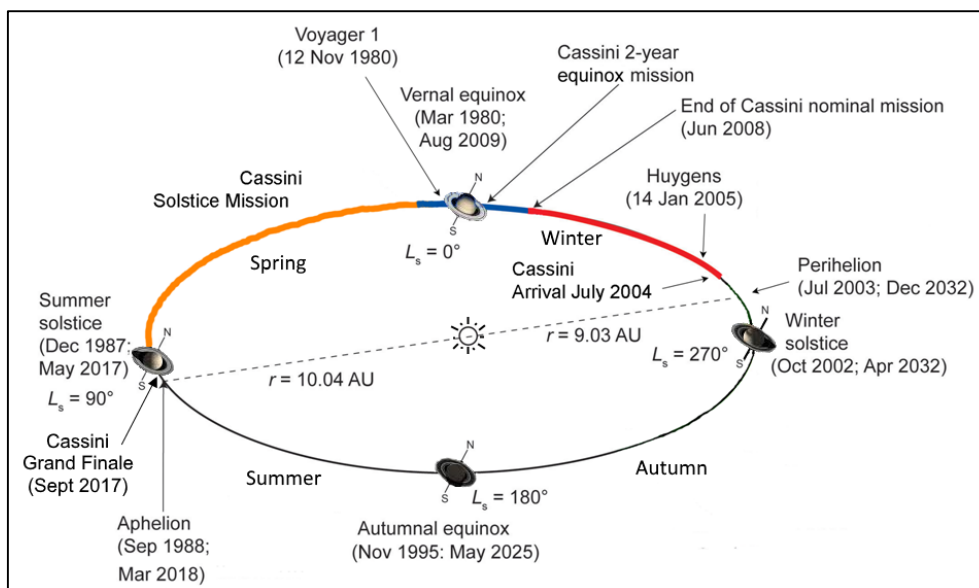
Figure I.1-5: Saturn's seasons from Cassini point of view. Adapted from Tokano et al. (1999).

The Cassini mission left us with 13 years of cumulated data to analyze. Many wonderful discoveries have been found out, like the presence of dunes and lakes at the surface or the complex organic chemistry happening in the upper atmosphere. In addition, there is still a lot to work out from the Cassini data! Nevertheless, the community already looks forward to come back. Besides, Titan is far from Earth and the inter-planetary travel takes 7 to 8 years. Therefore, efforts should be started now for the design and the construction of Cassini's successor.

In June 2019, the **Dragonfly** project was selected by NASA to be the next mission to Titan (Lorenz et al., 2018). The mission will use a **rotorcraft lander**, provided with 4 double rotors of 1 m in diameter (see **Figure I.1-6**). The aircraft will be able to travel at 36 km/h and to go up to 4 km in altitude. The objective of the mission is to investigate Titan's surface. It will jump to several places and analyze them thanks to 4 science packages. DraMS (Dragonfly Mass Spectrometer) will analyze the **chemical components** in surface and atmospheric samples. DraGNS (Dragonfly Gamma-ray and Neutron Spectrometer) will identify the **composition of the subsurface**. DraGMET (Dragonfly Geophysics and Meteorology Package) will have **meteorological sensors and a seismometer**. Finally, DragonCam (Dragonfly Camera Suite) will **take panoramic and microscopic images** at the landing sites. The mission is planned to be **launched in 2026** and to land on Titan in 2034.
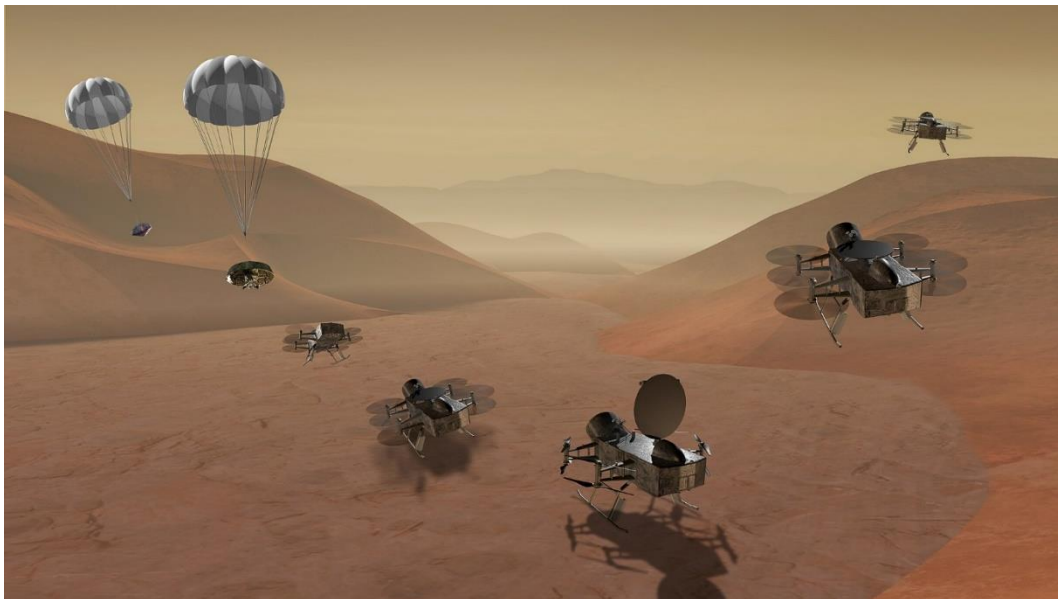
Figure I.1-6: Artist view of the Dragonfly mission arriving at the surface of Titan and flying in its atmosphere. Credit: NASA.

1.3- Titan's specificities

1.3.a. Liquid methane and dunes at the surface

Titan's surface is surprisingly similar to Earth's. As we knew that Titan was covered by an orange haze optically thick in most of the visible wavelengths, the Cassini mission was given adapted instruments to probe down to Titan's surface: cameras in specific wavelengths at which the atmosphere does not absorb, a radar / radiometer and the landing probe Huygens.

Some previous hypotheses suggested that Titan would be covered by a methane ocean (Lunine, 1993). Consequently, **Huygens** was designed to float. But in fact it landed on an arid place where only **brown-orange sandy grains and small rounded rocks** could be seen (see **Figure I.1-7**).

Figure I.1-7: Titan's surface as seen by the Huygens lander in January 2005. Credit: ESA/NASA/JPL/University of Arizona.
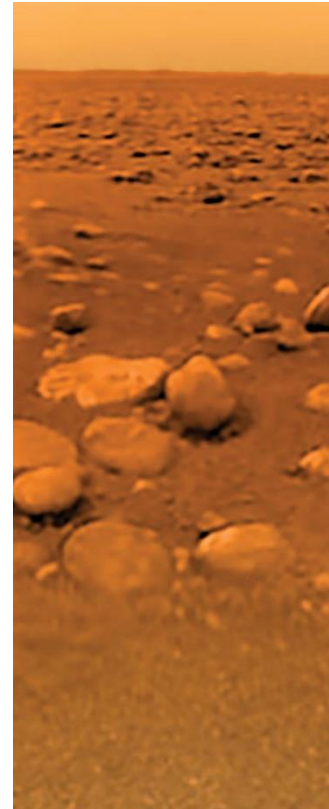
From above, landscapes look like Earth with an orange filter (see **Figure I.1-8**). DISR (the Descent Imager / Spectral Radiometer) images show some **mountains and valleys**, with two very different compositions. The white zones are due to the **water ice bedrock** while the brown-orange surfaces are **deposits of organic aerosols**. Some thin twisted lines resemble **riverbeds and their affluents** on Earth (Soderblom et al., 2007). They have certainly been created by methane rainfalls.

Indeed, Titan's surface temperature is very cold, in average ~94 K (-179 °C). The surface pressure is ~1.5 bar. Consequently, Titan's surface conditions are near the methane triple point (91 K and 0.12 bar). It results in a **methane cycle** similar to the Earth water cycle (evaporation, condensation, precipitation) (Hayes et al., 2018). It leads to many landscape structure similar to those on Earth, but with a completely different chemistry.
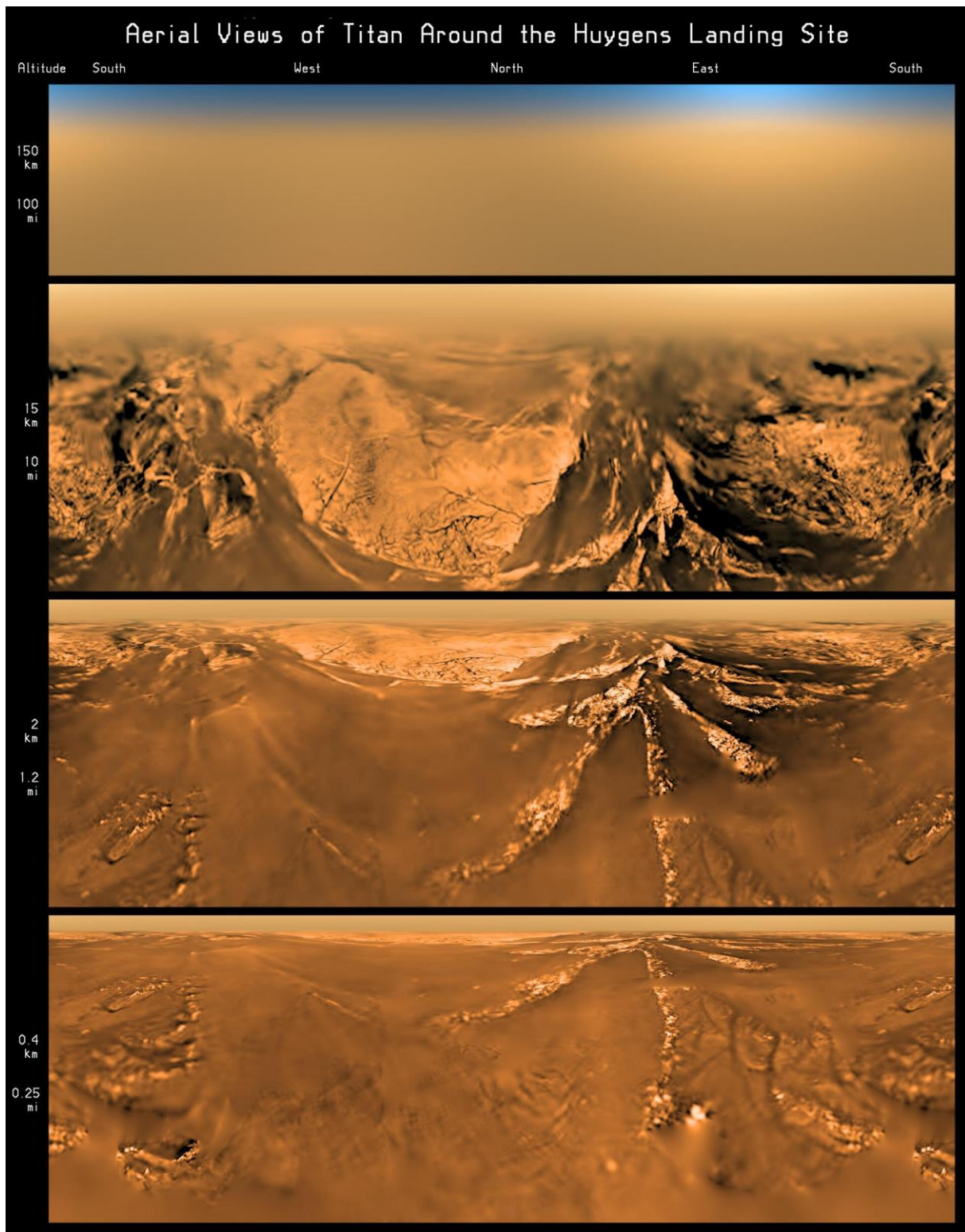
Figure I.1-8: Projections of Huygens's view of Titan at different altitudes. Credit: ESA/NASA/JPL/University of Arizona.

In particular, the instruments SAR (the Synthetic Aperture Radar), VIMS (the Visual and Infrared Mapping Spectrometer) and ISS (the Imaging Science Subsystem) observed and mapped many **lakes and seas** in the region of the north pole (see **Figure I.1-9**) (Hayes, 2016).

The analysis of the lakes and seas by **VIMS** spectra suggests a composition of methane, ethane, and maybe others hydrocarbons and dissolved nitrogen (Brown et al., 2008). Cordier and Carrasco (2019), Glein and Shock (2013) and Tan et al. (2015) **estimated the chemical composition** of the lakes from Huygens composition measurements at the surface, completed by photochemical and cryogenic models: certainly **methane**, **ethane**, with propane and other hydrocarbon/nitrile compounds are present.

The **radar** soundings gave information on the **depth profile** of Titan's lakes and seas (down to 100 – 150 m). The low attenuation through the lakes demonstrate that the liquid is a **nearly pure methane-ethane composition**. More than 0.1% of impurities as microwave absorbing hydrocarbons, nitriles and suspended particles would lead to a higher attenuation of the signal (Le Gall et al., 2016; Mastrogiuseppe et al., 2019, 2014).

One interesting question addressed recently by Cordier and Carrasco (2019) is the floatability of the orange dust deposited at the surface of Titan. Does it float or sink? Depending on its wettability properties, the dust could transiently float and create a slick in agreement with the smoothness of the seas as detected by Cassini radar observations.
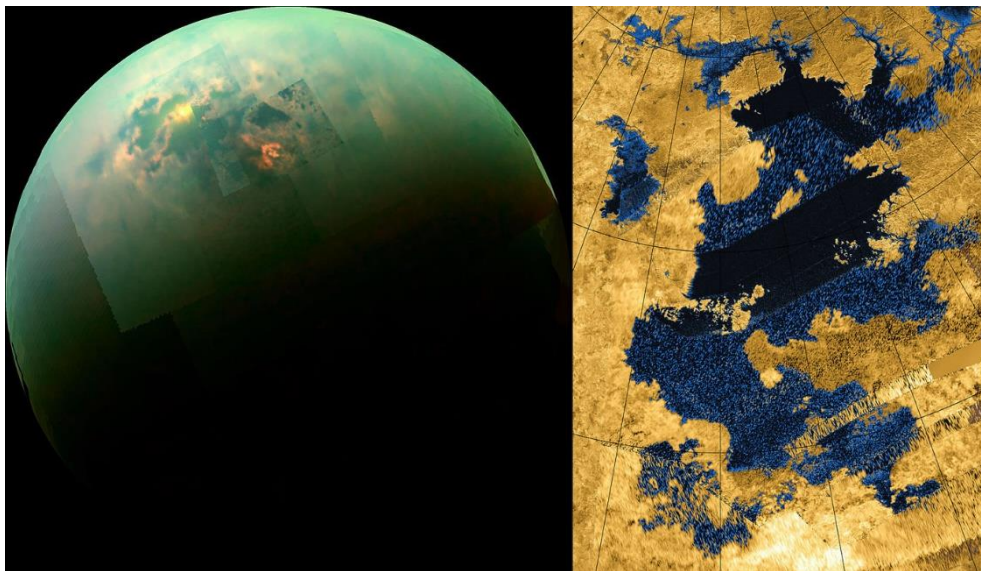
Figure I.1-9: Observation of Titan's northern lakes by Cassini's instruments. (a) In near infrared light by VIMS. Sunlight glints on lakes are visible. (b) Radar image of Kraken mare. Credit: NASA/JPL.

SAR, ISS and VIMS mapped nearly all the surface of Titan. It gave a global view of Titan's surface (Le Mouélic et al., 2019), and enabled to define **geological units** (Lopes et al., 2019, 2010). Among them are **plains (65%), dunes (17%), hummocky terrains (14%), labyrinth zones (1.5%), lakes (1.5%) and craters (0.4%)**. Their distribution is mapped in **Figure I.1-10**.
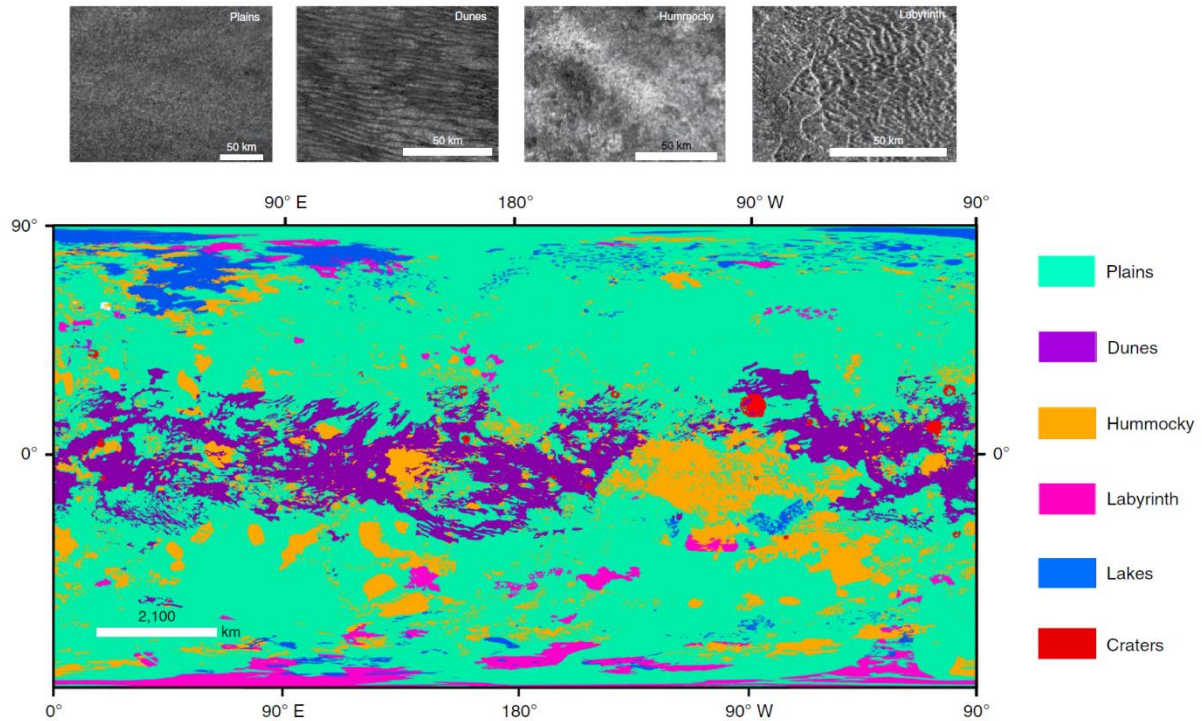
Figure I.1-10: Global map of Titan's major geomorphological units and SAR images showing examples of the main units. From Lopes et al. (2019).

One can observe that these different terrains are latitude dependent. In particular, dunes are found only at the equator. Regarding their composition, plains (Lopes et al., 2016) and dunes (Barnes et al., 2008; Rodriguez et al., 2014) have been found to be **dominated by organic material**.

1.3.b. A thick atmosphere obscured by an orange haze

A THICK ATMOSPHERE

Titan is the only moon with a fully developed **dense atmosphere** (Flasar et al., 2005; Fulchignoni et al., 2005). Besides, its atmosphere is very similar to the Earth's. In particular, the surface pressure is 1.5 bar and the main component of the atmosphere is **nitrogen** (~97%). The other molecules are **methane** (a few %, see **Figure I.1-11**) and trace amounts (< 0.01 %) of **various hydrocarbons** (ethane C_2H_6, acetylene C_2H_2, hydrogen cyanide HCN, cyanogen C_2N_2, propane C_3H_8, ethylene C_2H_4, diacetylene C_4H_2, methylacetylene CH_3C_2H, cyanoacetylene HC_3N, benzene C_6H_6), and CO_2 (with a mixing ratio of ~10^{-8}) (Niemann et al., 2010; Vinatier et al., 2015). The **origin of the methane** on Titan has not been elucidated yet. A common explanation is that methane is degassed from Titan's interior or sub-surface via **cryovolcanism** (Tobie et al., 2006).
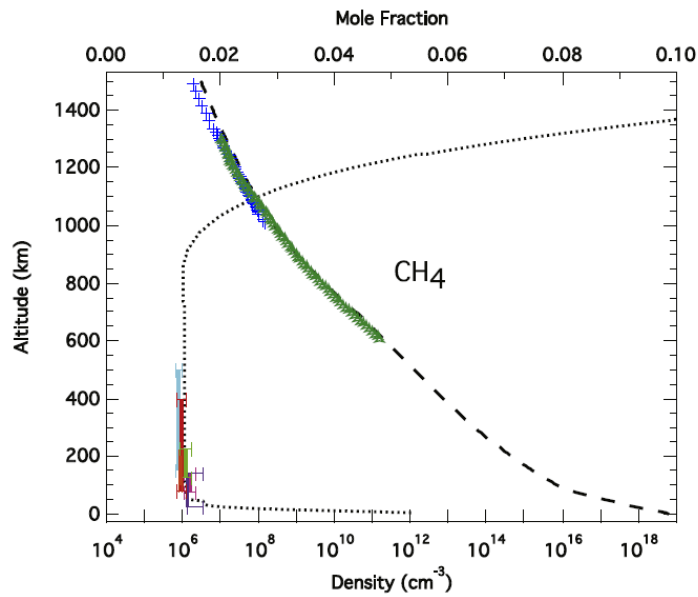
Figure I.1-11: Density (dashed line) and mole fraction (dotted line) of CH_4. The data points are combined observations from Cassini instruments UVIS, VIMS and CIRS, Huygens instruments GCMS and DISR, and observations with Herschel. Picture from Vuitton et al. (2019).

The Huygens probe recorded the pressure and temperature profiles with altitude during its descent (see **Figure I.1-12**). Several sharp changes in the temperature variation can be observed. They define the **different layers** of Titan's atmosphere. The lower layer, the **troposphere**, extends up to 40 km (~0.1 bar). It hosts a lot of weather phenomena, as clouds and rain. The main circulation of the atmosphere happens in the **stratosphere**, from ~40 to ~300 km (~0.1 mbar). It includes a large haze layer at about 100-210 km, which tends to heat up the layer. In the layer just above, the **mesosphere**, extending from ~300 to 500-600 km (10^{-3} mbar), a second thinner haze layer can be observed, at around 450-500 km. The upper layer is the **thermosphere**, at very low pressure (< 10^{-3} mbar).
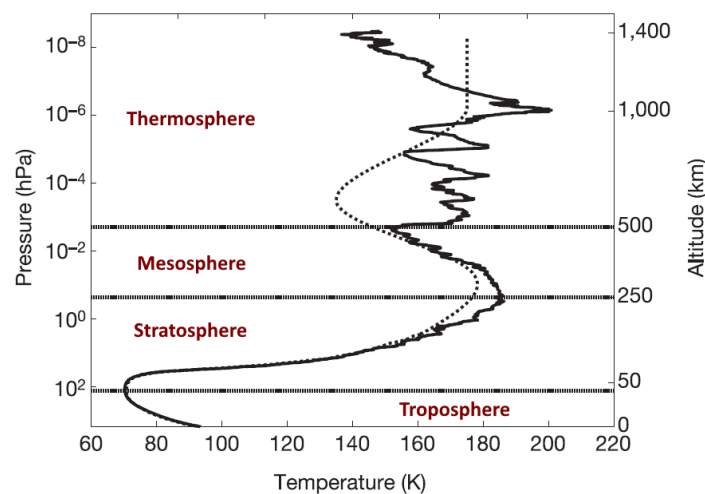
Figure I.1-12: The atmospheric temperature profile measured by HASI (the Huygens Atmospheric Structure Instrument). The prediction by the engineering model is shown with the dashed line. From Fulchignoni et al. (2005).

The main feature of Titan's atmosphere is its orange haze (see **Figure I.1-13**). There are two principal haze layers, separated of ~100 km, and merging at high northern latitudes.

The upper one, the **detached haze layer** is usually observed at **500 km**. The analysis of the UV observations with the ISS (for Imaging Science Subsystem) Narrow Angle Camera compared to fractal aggregate scattering models gave information on the physical properties of the aerosols forming the haze. Seignovert et al. (2017) concluded on the presence of **aggregates of at least ten monomers of 60 nm radius**. The detached haze layer **evolves with seasons**. West et al. (2018) observed its descent in altitude at the vernal equinox, its disappearance, and its reappearance before the summer solstice.

On the other side, the **main haze layer** is **thicker** (from ~100 to 300 km in altitude), and always present. It has been investigated by many instruments of the mission Cassini-Huygens. CIRS gave access to the optical depths of the haze at various altitudes and latitudes, observing an enrichment of the haze around the equator at 0.1 mbar (Vinatier et al., 2010). DISR (the Descent Imager / Spectra Radiometer) on the Huygens probe gathered *in situ* information on the size, shape, optical properties and vertical distribution of the haze aerosols (Tomasko et al., 2009, 2008). In this layer, **aggregates could have more than 4000 monomers**. Further discussion on the formation of haze aerosols is given later, in **Section I.3.3.d**.
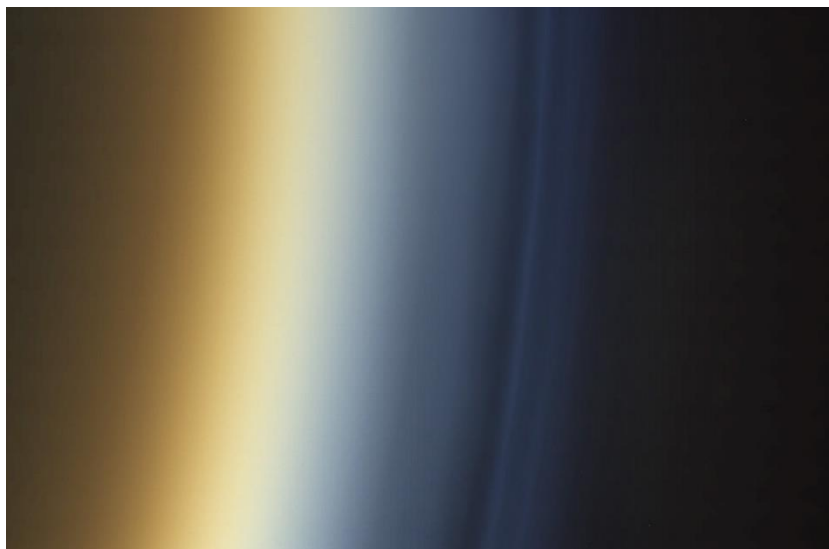
Figure I.1-13: Composite image of Titan's nightside limb (UV3 338 nm, BLU1 451 nm, GRN 568 nm and RED 650 nm filters). It shows the main and the detached haze layers. Taken on 13 December 2004. Credits: NASA/JPL-Caltech/SSI/B. Seignovert.

AEROSOLS: A STRONG CLIMATIC EFFECT

Atmospheric aerosols have important impacts on a planet's climate. They are **efficient scatterers of light** and **nucleation sites for clouds**. Consequently, they can modify strongly the **radiative budget** and impact the atmospheric dynamics in a way hard to predict. These particles also play a major role in atmospheric chemistry, especially as they favor **surface-catalyzed processes**.

While it is difficult to understand and quantify their effects, **atmospheric aerosols are found in all planetary atmospheres**, and this strengthens the necessity to study them. In the various planetary atmospheres of the solar system, aerosols come from very different origins, such as volcanism, oceans or human actions on Earth (Jacobson et al., 2000; Pöschl, 2005), dust on Mars (Madeleine et al., 2011) or atmospheric chemistry on Jupiter and Saturn (Courtin, 2005; Guerlet et al., 2015; Zhang et al., 2015).

Titan is an extreme case in the Solar system where aerosols are present in huge quantity (see **Figure I.1-13**). The characterization and the understanding of the haze processes are therefore fundamental to study the climate of Titan. **Numerical climate models** are a useful tool to study the impact of aerosols, including radiative transfer, microphysics and dynamics (Larson et al., 2015; Lebonnois et al., 2012; Rannou et al., 2004).

AN ATMOSPHERE SIMILAR TO THE EARLY-EARTH'S?

On the Earth today, the second main component after nitrogen is oxygen. However, it has not always been the case. 2.3 Ga ago, before the Great Oxidation Event (GOE), **methane was at higher concentration on Earth** than today (Kasting, 2005). Among others, it was responsible for an enhanced greenhouse effect that kept the early climate warm despite the fact that the young Sun was less bright than nowadays (Charnay et al., 2013; Haqq-Misra et al., 2008).

Before the apparition of life, hypotheses for the formation of methane include **outgassing from mid-ocean ridges** (initially formed by serpentinization beneath the ocean floor, ~7 ppmv) and **meteoritic impacts** at 3.8 Ga (~1 ppmv). Kasting (2005) supposes that this value for the concentration of methane (8 ppmv in total) is certainly greatly underestimated and would be time dependent. The presence of methane in the atmosphere before the apparition of life and during its development until the GOE is fundamental. Indeed, like what happens on Titan, the presence of methane and nitrogen in an atmosphere can lead to the formation of other organics and nitrile-compounds (Tian et al., 2005). Especially **HCN is very important for prebiotic synthesis** (Tian et al., 2011). It is suspected to be a precursor to form amino-acids (Strecker synthesis). As on Titan, the atmosphere of the early Earth was expected to have an organic haze, but certainly thinner. **Could a Titan like organic chemistry have happened on Earth 3.5 Ga ago and led to the formation of complex organics that sustained the emergence of life?**

In any case, the apparition of life at the Archean induced a strong increase in the methane concentration in the atmosphere. **Methanogens** metabolize CO_2 and H_2 from the atmosphere into CH_4. It should have led to 0.01 to 3.5 % of CH_4 (Kharecha et al., 2005). Consequently, it was Titan-like conditions, with higher temperatures, and more CO_2.

The early Earth was covered by an **organic haze** as Titan today (Arney et al., 2016; Zerkle et al., 2012). It would have provided an ultraviolet shield for greenhouse gases required to warm the planet. **Studying Titan and its hazy atmosphere is therefore a way to study Earth at the origin of life.**

2- Ionospheres

One of the main discoveries of the Cassini mission concerns the birthplace of the organic aerosols forming the hazes: the grains start to form in the ionosphere, above 1200 km altitude!

2.1- The ionospheres of planets

The ionosphere is the part of an atmosphere ionized by solar radiations or other energetic particles. On Earth, it spreads from 60 km to the top of the atmosphere.

When entering the upper atmosphere at low density, energetic photons and particles collide with neutral molecules in the atmosphere, starting **ionization and dissociation** reactions. This leads to the formation of **electrons, ions and radicals**. Ionospheres are very reactive environments; they are natural **plasmas**.

Ionospheres are usually present in **upper atmospheres**, at low gas density. It is the case on Earth as shows **Figure I.2-1**, where the ionosphere mainly covers the thermosphere and the mesosphere. As they are usually triggered by strong UV solar rays, the ionospheres get thinner and **weaker** on **nightsides**. They are then the place of **electron-ion recombinations**, sometimes luminescent. Ionosphere are dependent on the above magnetosphere and the solar enlightment. **Figure I.2-2 (a)** shows how it **varies with latitude** on Saturn. On **Titan**, the ionosphere has moreover a **part at very low altitude**, detected by Huygens at nearly 0.1 bar (see **Figure I.2-2 (b)**).
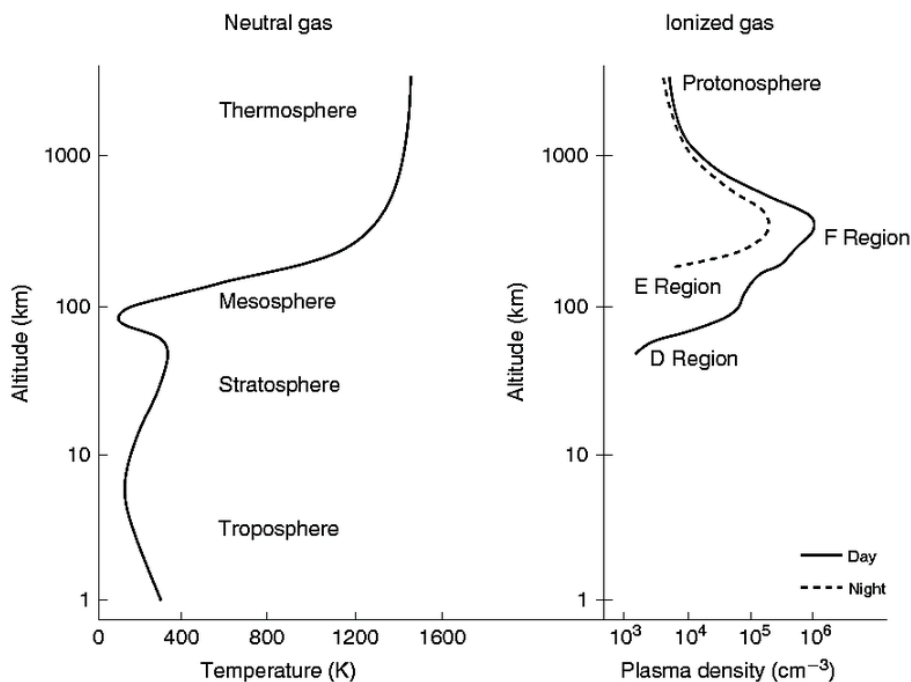
Figure I.2-1: Atmosphere and ionosphere structures on Earth. From Hadavandkhani et al. (2016).
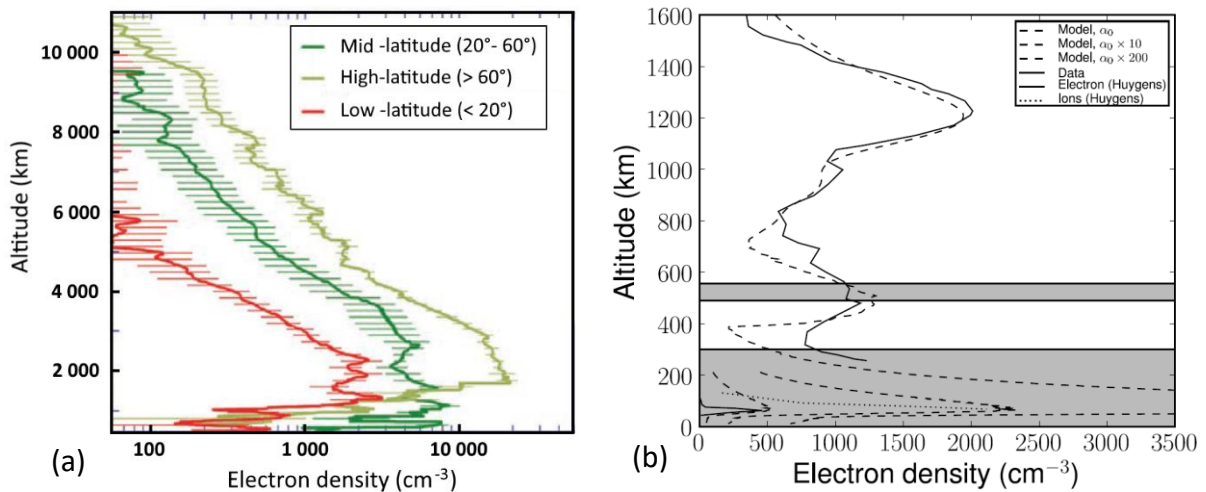
Figure I.2-2: Structures of different ionospheres. (a) Saturn, measured by Cassini radio occultations, 11 observations in 2005. From Nagy et al. (2006, 2009). (b) Titan, electron density data above 300 km comes from Kliore et al. (2008), ion and electron densities below 100 km come from López-Moreno et al. (2008). The position of the haze layers is highlighted in grey. Figure from Gronoff et al. (2009a).

Aside from electrons and positive ions, some ionospheres also host specific species. On Earth, **negative ions** have been detected in the D-region, where they are primarily formed by **electron attachment** to electronegative species such as oxygen atoms (Hargreaves, 1992). Negative ions were also found in the coma of comet Halley (Chaizy et al., 1991) and in the Enceladus plumes (Coates et al., 2010a, 2010b). Other detected species in some ionospheric plasmas are **dust particles**. On Earth, particles have been detected in the polar mesosphere and at the origin of noctilucent clouds (Havnes et al., 1996). They are suspected to interact strongly with the surrounding plasma by being **a sink of free electrons**, which tend to attach on dust grains. In the Solar System, dusty plasmas have also been observed in cometary comas, Enceladus plumes (Shafiq et al., 2011), on Saturn and its rings (Morooka et al., 2019; Wahlund et al., 2009a), and in the ionosphere of Titan.

2.2- The particular case of Titan's ionosphere

2.2.a. A complex electromagnetic environment

Titan has a complex electromagnetic environment. Titan has no intrinsic magnetic field but the interaction of Titan's ionosphere with the Saturn's magnetic field creates a complete **magnetosphere** around Titan (Backes et al., 2005; Ness et al., 1982). It is similar to the magnetospheres of Mars or Venus in the solar wind (Bertucci et al., 2011), except that on Titan, the incoming plasma flow is not always aligned in the direction of the Sun. Therefore, depending on the localization of Titan according to **Saturn and the Sun** (see **Figure I.2-3**), Titan magnetospheric conditions can be very different, and can **influence the ionosphere** below (Coates, 2009).

Saturn and its magnetosphere have a ~11-hour rotation period (Gurnett et al., 2005). This creates a magnetospheric plasma flow of a few 100s km/s that interacts with the upper atmosphere of Titan. Especially, energetic particles from Saturn's magnetosphere participate to its ionization (Wahlund et al., 2005).
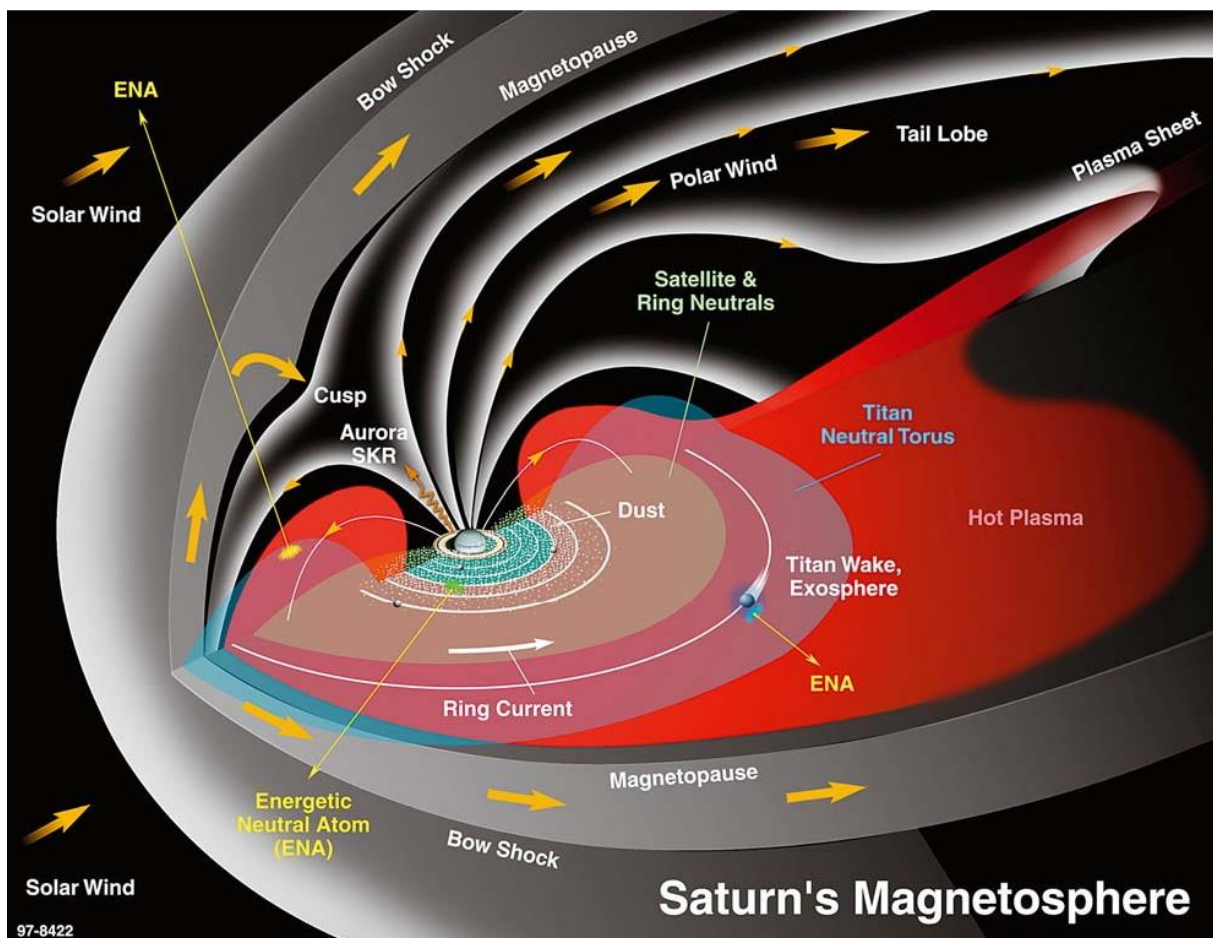
Figure I.2-3: Place of Titan in Saturn's magnetosphere. From Krimigis et al. (2004).

2.2.b. The ionization sources

The upper atmosphere of Titan is mainly ionized by the solar EUV on the dayside, which leads to remnants on the nightside (Cravens et al., 2004; Cui et al., 2009a; Shebanits et al., 2017). Therefore, plasma densities **vary significantly with the solar illumination**, i.e. with Solar Zenith Angle (SZA) (500 to 3000 cm^{-3} at the ionospheric peak) and altitude. Variations across the solar cycle can be observed on Titan, with densities at the ionospheric peak that could double (Edberg et al., 2013). The orbital phase of Saturn (~29.5 years) also induces seasonal variations due to the eccentricity of Saturn's orbit.

To this superimpose other ionization sources, on both day and night sides (Gronoff et al., 2009a), as presented in **Figure I.2-4**. Most of them trigger ionization above 600 km. They are energetic sources such as electrons coming from the magnetosphere of Saturn (Edberg et al., 2015), > 10 keV electrons (Coates et al., 2007b; Cravens et al., 2009; Gronoff et al., 2009b; Lavvas et al., 2011a), micro-meteorites (Molina-Cuberos et al., 2001), solar hard X-rays, energetic ions and MeV proton events (Cravens et al., 2008).

The Huygens probe also detected an ionosphere far lower, around 65 km altitude, with the measurement of the electrical conductivity by PWA (Permittivity, Wave and Altimetry) (Fulchignoni et al., 2005; Grard et al., 2006; Hamelin et al., 2007; López-Moreno et al., 2008). It corresponds to the location of ionization by the Galactic Cosmic Rays, the most penetrating kind of radiation, already predicted in 1976 by Capone et al. (1976), and then by Molina-Cuberos et al. (1999), and Gronoff et al. (2011) with new insights from the Huygens probe. Such an energy deposit leads to high electron (~450 cm^{-3}) and positive ion (~2000 cm^{-3}) densities. Molina-Cuberos et al. (2018) explains the large difference between electrons and positive ions by the attachment of free electrons on aerosols.
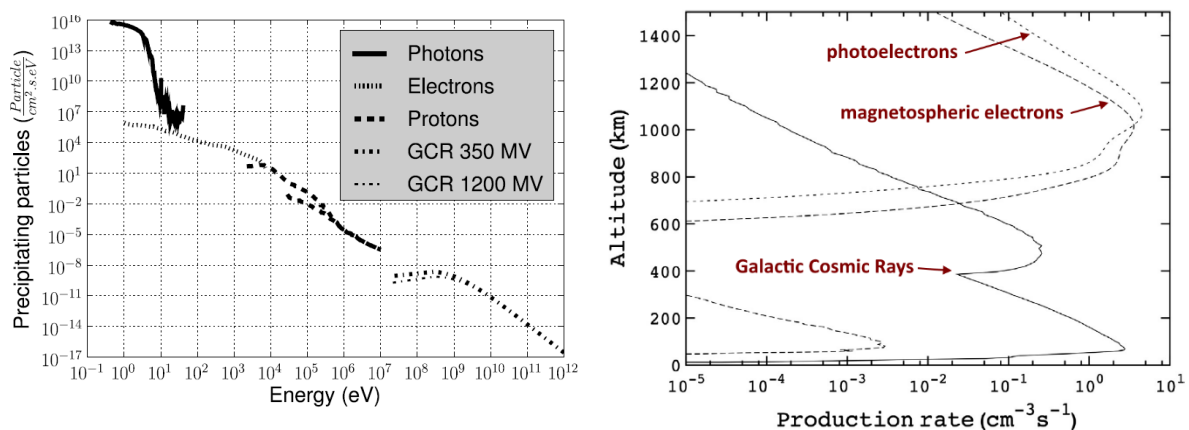
Figure I.2-4: Energetic inputs in Titan's atmosphere. (a) From Gronoff, Lilensten, Desorgher, et al. (2009). (b) From Dobrijevic et al. (2016).

3- Investigation of Titan's ionosphere

Titan's ionosphere is unique in the Solar System, and from far the one hosting the most complex ion chemistry. The Cassini spacecraft crossed the upper ionosphere of Titan a hundred times and each time took *in situ* measurements that led to unexpected observations.

3.1- Dedicated instruments onboard the Cassini mission

The Cassini spacecraft was equipped with 12 instruments. Some took measurements of the inner atmospheric layers and the surface by remote sensing thanks to light analysis in various wavelengths and a radar. **Three of them were dedicated to the study of the ionospheric plasma surrounding Titan.**

3.1.a. The Ion and Neutral Mass Spectrometer (INMS)

INMS was a fundamental instrument in the search for organic species in Titan's ionosphere. It aimed at measuring positive ion and neutral species composition and structure in the upper atmosphere (Kasprzak et al., 1996; Waite et al., 2004).

INMS is a quadrupole mass spectrometer. It counts how many ions reach its detector at a given mass / charge ratio and a given energy. The energy chosen result from a precise calibration, tested on Earth and optimized in-flight (Mandt et al., 2012). INMS therefore gives **mass / charge spectra**. Its mass / charge range goes up to 99 u/q, with a resolution of 1 u/q. In the neutral mode (closed source), the detection limit is 10^4 cm^{-3}. In positive ion mode (open source), the detection threshold is ~10^{-2} cm^{-3}.

The instrument was produced at NASA's Goddard Space Flight Center (Planetary Environments Laboratory) and at the University of Michigan (Space Physics Research Laboratory). **Figure I.3-1** shows the different **parts of the instrument**: the two possible entrances for the species ('closed source' for neutrals, 'open source' for reactive species), the focusing lenses, the quadrupole mass analyzer and the detector.

During the Cassini mission, INMS has revealed to be essential to constrain photochemical models in Titan's ionosphere (see **Section I.3.2.b**).
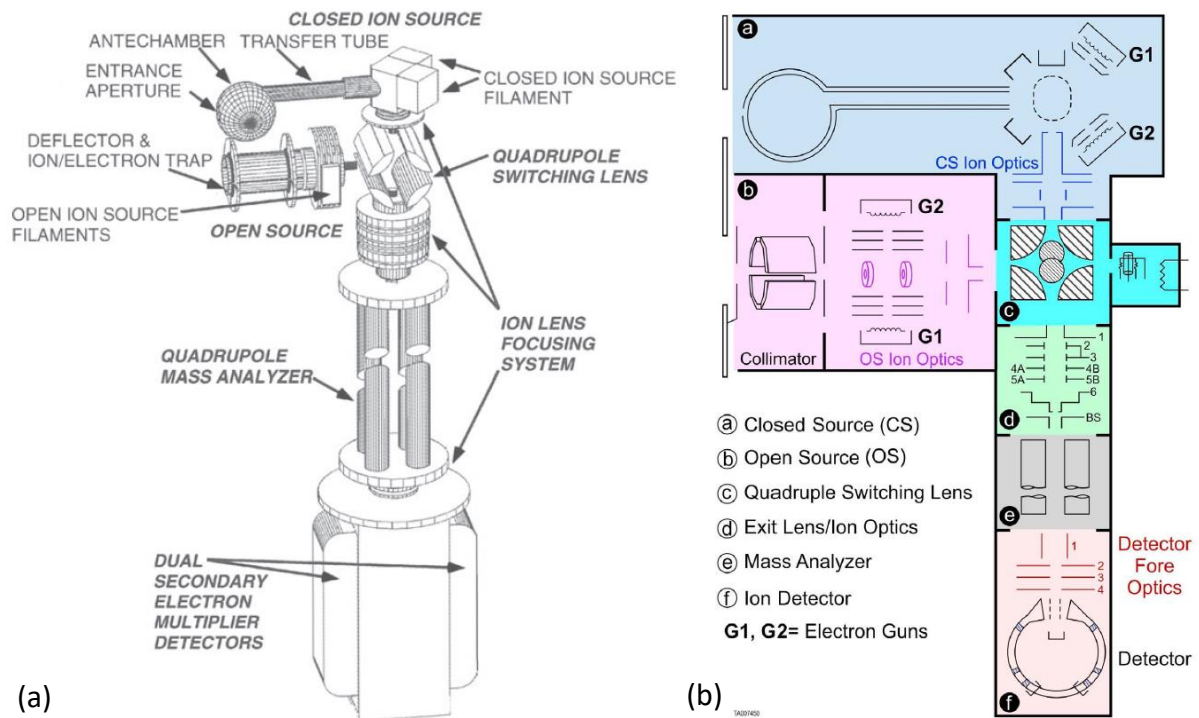
Figure I.3-1: Schemes of INMS showing the different parts of the instrument (a) from the outside (Waite et al., 2004), and (b) from the inside (Mandt et al., 2012).

3.1.b. The Cassini Plasma Spectrometer (CAPS)

CAPS was initially designed to analyze Saturn's magnetosphere. It contains three instruments (see **Figure I.3-2**): the Electron Spectrometer (ELS), the Ion Beam Spectrometer (IBS), and the Ion Mass Spectrometer (IMS) (Young et al., 2004). IMS was designed to measure low-concentration of ion species and was saturating in Titan's ionosphere. On the contrary, **IBS and ELS revealed to be essential in the characterization of Titan's ionospheric plasma.**

ION BEAM SPECTROMETER (IBS)

The IBS was an electrostatic analyzer, designed to measure positive ion velocity distributions with very high angular and energy resolution from 1 eV to 50 keV. **It was initially designed to measure ion beams expected in the solar wind.** It was designed and produced by the SouthWest Research Institute (SWRI).

However, the ion thermal velocities being small in the ionosphere (120-250 K between ~950 and ~1600 km respectively), the ions were far slower than the supersonic velocities of Cassini (~6 km/s). Thanks to this point, Waite et al. (2007) and Crary et al. (2009) have been able to use the energy / charge spectra of IBS to infer **ion mass / charge spectra**. It can then provide the positive ion mass / charge distribution up to **~370 u/q**. However, the mass resolution is far lower than the one of INMS (effective mass resolution of 30 at 28 Da).

ELECTRON SPECTROMETER (ELS)

The ELS was created at the Mullar Space Science Laboratory (MSSL). It was an electrostatic analyzer measuring the energy / charge ratio of **species charged negatively**. It was originally designed only for energetic electrons (Linder et al., 1998). However, similarly to IBS, in the end it succeeded in measuring negative ions (Coates et al., 2009, 2007a). The Cassini spacecraft moving at supersonic velocities in the cold ionosphere, negative ions are collected by the instrument only when it points in the ram direction (i.e. the direction of the spacecraft movement). Therefore, negative ion populations appear as a sharply defined beam in ELS data. It enables to deduce **mass / charge spectra** of the negative ions from the energy spectra.

The mass resolution is nevertheless strongly limited, to ~5 at ~16 u/q, and drops at higher masses. It is sensitive up to 150 000 u/q in theory.
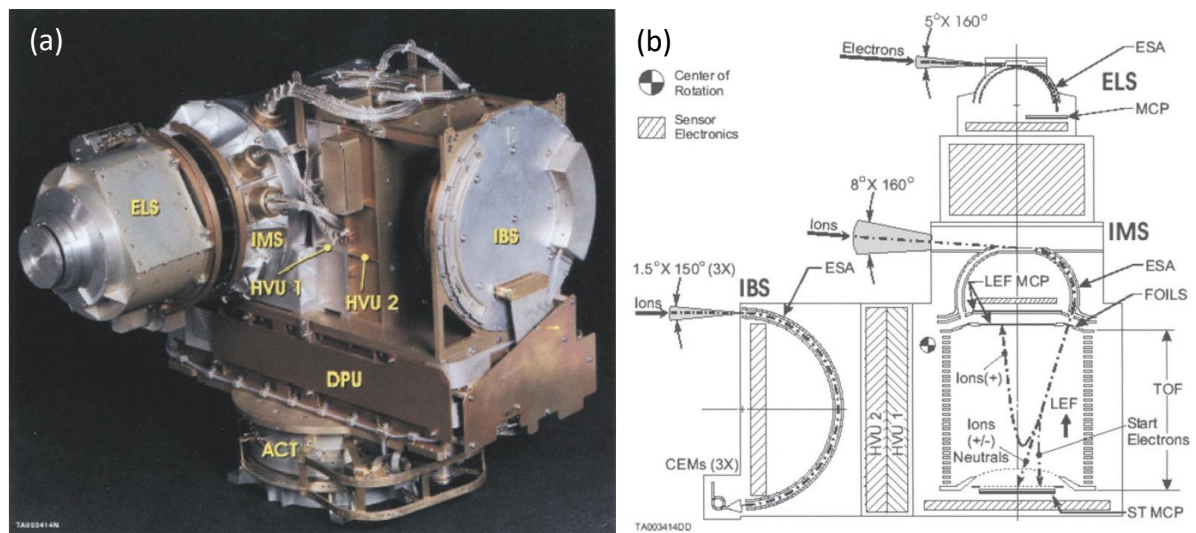
Figure I.3-2: (a) Photograph of the CAPS flight model prior to delivery to the Cassini spacecraft. (b) Scheme showing the optical layout, fields-of-view, and key sensor elements of CAPS. Heavy dashed lines suggest the general shape of particle trajectories. From Young et al. (2004).

3.1.c. The Langmuir Probe (LP)

The LP is part of the Radio and Plasma Wave Science (RPWS) instrument. It **measures electron density and temperature** (Gurnett et al., 2004), but **information on ions** can also be deduced from its data (Shebanits et al., 2016, 2013; Wahlund et al., 2009b).

The instrument has been designed and built by the Swedish Institute of Space Physics in Uppsala. It consists mainly in a sensor, a preamplifier and associated control electronics. The Langmuir probe sensor is a 5 cm diameter sphere positioned at the end of a long thin rod. As LP data is analyzed in **Chapter IV**, more information is given on the instrument in **Section IV.1.1**.

3.2- Observation of a complex organic chemistry

Prior to the Cassini mission, model expected the **complex chemistry leading to the aerosols** to take place below ~750 km. As the Cassini spacecraft took measurements above ~950 km, no complex species were expected to be detected… But it was not the case!
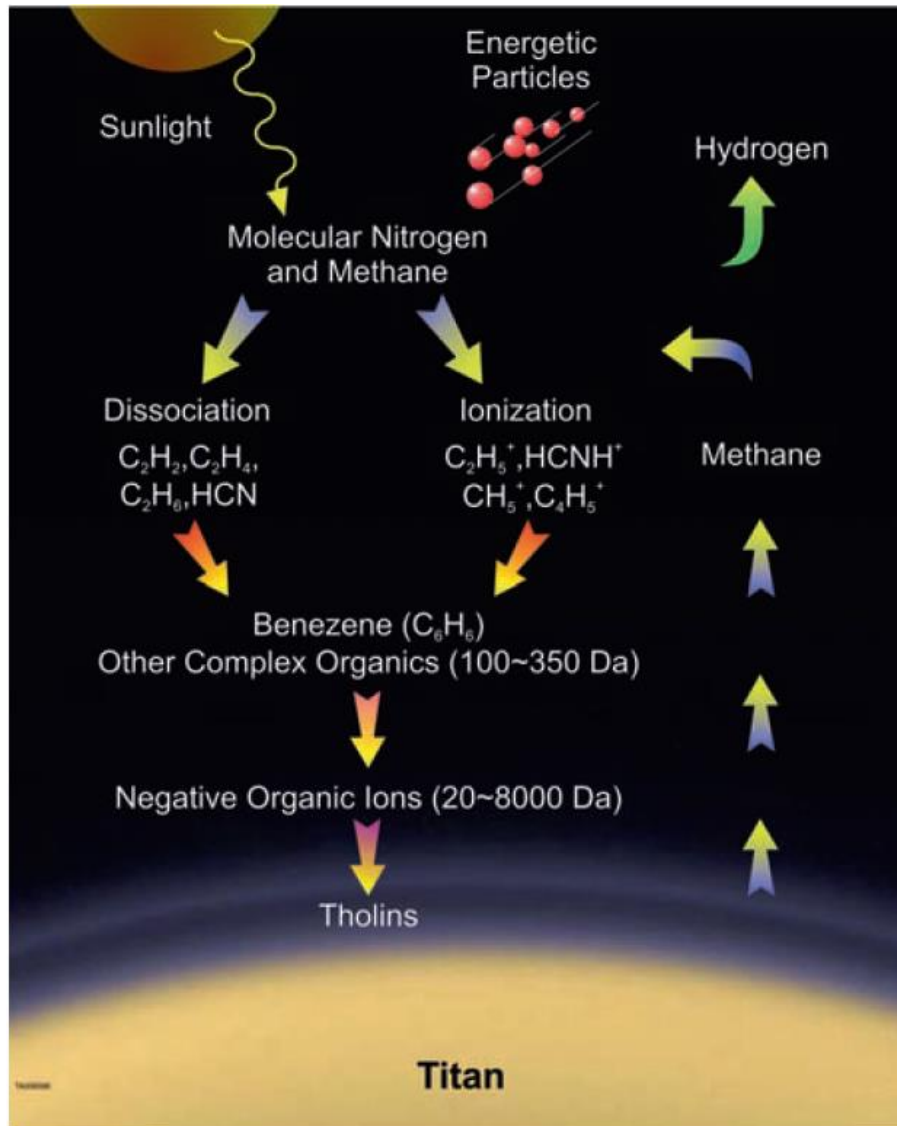
Figure I.3-3: Cartoon illustrating the aerosol formation as result of high-altitude ion-neutral chemistry. Over tens of millions of years methane is, with the loss of hydrogen to space, irreversibly converted to the complex hydrocarbon-nitrile compounds that are the precursors of the aerosols (Waite et al., 2010, 2007).

3.2.a. Photo-ionization at the top of the atmosphere

Most of the solar radiation is deposited above 600 km, and is at the origin of Titan's upper ionosphere (see **Section I.2.2.b**). **Solar radiations**, along with **energetic particles** from Saturn's magnetosphere, collide with the **main constituents of the atmosphere**: N_2 and CH_4. It results in their **ionization** or **dissociation**, forming ions and radicals. It consequently forms a reactive environment, as well as the C, N and H atoms required for the synthesis of complex organic molecules.

The first ions formed come from the interaction of N_2 and CH_4 with solar photons and suprathermal photo- and secondary electrons. **The major primary ions are N_2^+, N^+ and CH_4^+.**

Then, these ions react efficiently with the surrounding neutral molecules (N_2, CH_4, H_2) to **form new ions**, namely CH_3^+, CH_2^+, N_2H^+, $HCNH^+$, HCN^+, NH^+, CH_5^+… which started a complex ion chemistry. All chemical reactions known to date and relevant for Titan's ionosphere are detailed in Vuitton et al. (2019) and references therein.

3.2.b. Complex ion chemistry in the ionosphere

Insights on the complex chemistry occurring in Titan's ionosphere have been **given by the spacecraft Cassini** at the occasion of Titan flybys with trajectories inside the ionosphere.

PRECISE DETECTION OF NEUTRALS AND POSITIVE IONS UP TO 100 U

The Ion and Neutral Mass Spectrometer (INMS) onboard Cassini aimed at characterizing the neutral and positively charged species in Titan's ionosphere.

The first Cassini flyby of Titan (T_A) went down to 1174 km, where INMS measured N_2, CH_4, H_2 and Ar. However, it also detected as minor species **various hydrocarbons and nitrile-compounds** (Waite et al., 2005). They already suggested the presence of C_2H_2, C_2H_4, C_2H_6, C_3H_4, C_3H_8, C_4H_2, C_6H_6, C_3HN, C_2N_2 and HCN.

Cravens et al. (2006) reported the first INMS measurements obtained on **nightside** (during the flyby T5). They observed a substantial ionosphere even on the nightside, and a **complex ion chemistry**. Between 1000 and 1200 km, the ion and neutral channels detected masses up to 100 u, the detection limit of INMS.

After the acquisition of several flybys, Waite et al. (2007) compared results of ion and neutral mass spectra (see **Figure I.3-4**). They observed a very good **correspondence between the neutral and ion species**. In particular, the 7 observed clusters of species with the same number of heavy atoms (C, N or O; thus spaced of ~12 u) are similar in neutral and ion spectra. **This suggests a strong coupling in the ion-neutral chemistry**.
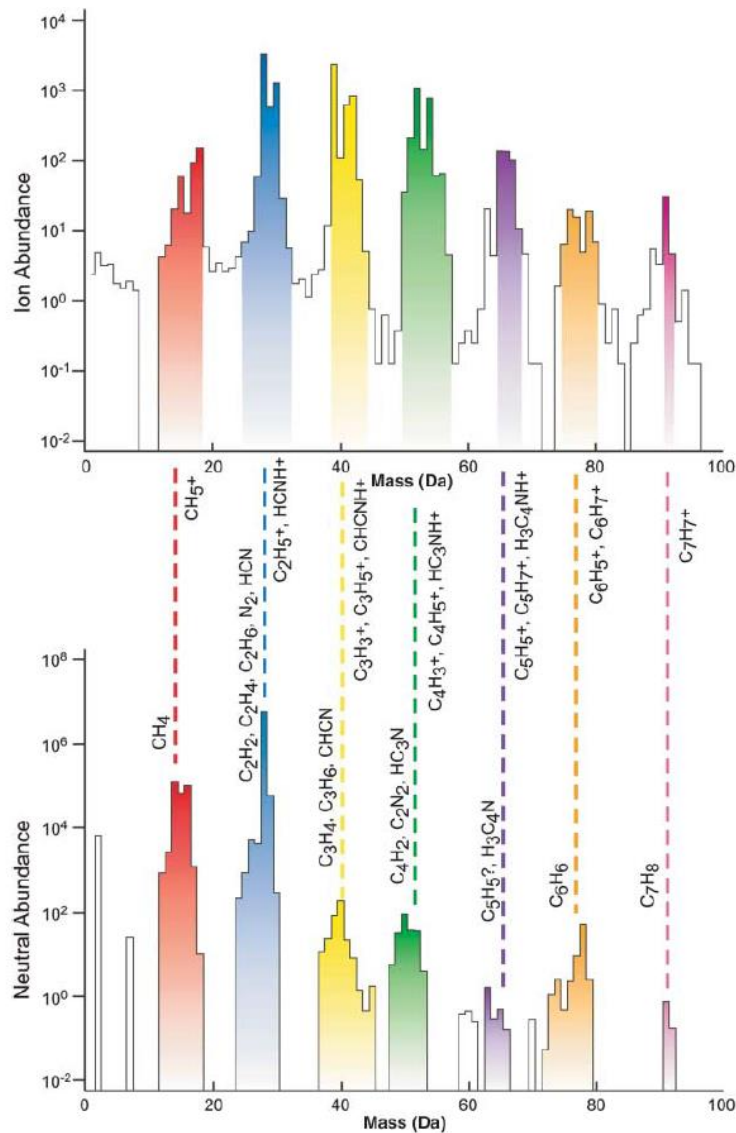
Figure I.3-4: Correspondence of ion (upper) and neutral (lower) mass spectra measured by INMS during the flyby T19 between 950 and 1000 km. From Waite et al. (2007).

In the case of neutral species, Cui et al. (2009b) and Magee et al. (2009) proposed independently improvements in the analysis, to remove impurities, correct instrumental effects and deconvolve spectra. Cui et al. (2009b) focused on 15 close flybys and confirmed the detection of C_2H_2, C_2H_4, C_2H_6, CH_3C_2H, C_4H_2, C_6H_6, CH_3CN, HC_3N, C_2N_2, NH_3. They observed that minor species are essentially found at lower altitudes, below 1200 km. Magee et al. (2009) analyzed 20 flybys to infer the average neutral composition between 1000 and 1100 km. They detected also HCN, C_3H_6 and C_2H_5CN.

In the case of positive ions, Mandt et al. (2012) investigated the INMS ion results of 14 flybys. They identified 48 ions, and observed that more positive ions are present on dayside, with a maximum density around 1100 km.

In conclusion, INMS spectra enabled to identify many neutral and positive ions in Titan's ionosphere. Nevertheless, its detection limit has been quickly reached with the detection of neutrals and ions up to 100 u. This suggests that heavier species are also present.

Crary et al. (2009) extended the analysis of CAPS/IBS data to quantify the abundance of ions above 100 u, and to statistically estimate their composition. They compared their results for masses < 100 u with INMS data, which gave consistent results (see **Figure I.3-5**). In the ionosphere, heavy positive ions are detected by IBS, up to 350 u. Ions > 100 u even become a major constituent of the positive ion population below ~1200 km, and they increase with depth in the atmosphere, becoming > 50% of the total at 950 km. The resolution of IBS is not high enough to identify species. However, the authors suppose that such heavy ions are most likely aromatic hydrocarbons (in particular PAH, as benzene has been detected by INMS (Waite et al., 2007)). Acetylene and nitrile polymers could be also relatively common. In particular, Westlake et al. (2014) suggest the abundance of building blocks such as C_2H_2 and C_2H_4 in the structure of Titan's aerosols.
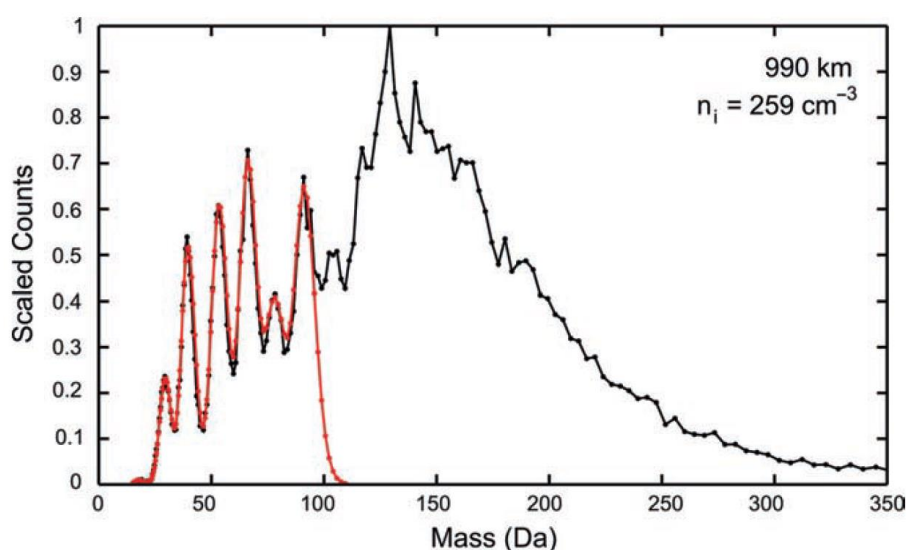
Figure I.3-5: IBS spectrum from flyby T26. The match to the Cassini INMS ion spectrum below 100 u is marked in red (Crary et al., 2009).

The complex ion chemistry happening in Titan's ionosphere finally leads to the **formation of heavy negative ions**. Negative ions are produced by dissociative and radiative **electron attachment on neutral molecules**. Dissociative electron attachment depends on energetic electrons, while radiative electron attachment is linked to the thermal electron distribution. Negative ions also grow through reactions with neutrals (Vuitton et al., 2009). Before the arrival of Cassini, negative ions were not expected in Titan's ionosphere.

Coates et al. (2007a) relate the discovery of negative ions in Titan's ionosphere. They used **CAPS/ELS** energy / charge spectra to retrieve negative ion mass / charge spectra in the ionosphere (see **Section I.3.1.b** and **Figure I.3-6**). Using a data set obtained with 16 flybys, they observe that the **higher densities of negative ions are found at lower altitudes**, the lower limit of the observations being the lower altitude reachable by Cassini (~900 km).
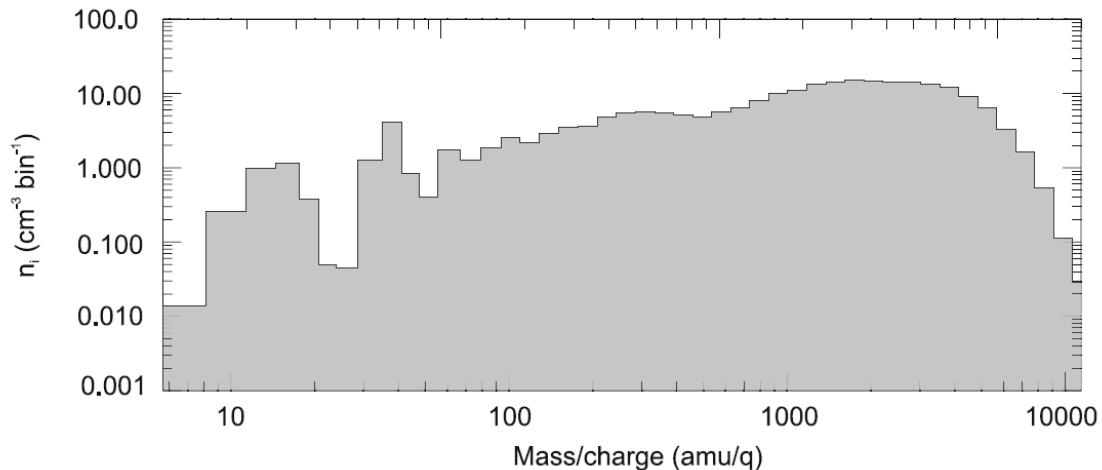
Figure I.3-6: Negative ion mass / charge spectra deduced from ELS data, at an altitude of 953 km during the T16 flyby (Coates et al., 2007a).

The effect of altitude is validated by Coates et al. (2009). The analysis of 23 flybys showed that **heavier ions are also found at lower altitudes.** In these regions, the electron density of 1-10 eV electrons is significant and coincident with the ionospheric thermal electron peak. This favors the **electron attachment** on already heavy molecules. The authors suggest that the ions grow even further below the altitudes reachable by Cassini. They also observed **heavier ions at higher latitudes and on the terminator.** The fainter sun irradiation at these places can be part of the explanation, by **attenuating the photo-dissociation processes**.

Wellbrock et al. (2013) confirmed these trends with the study of 34 Titan flybys. They observed negative **ions up to 13 800 u/q**. Depending on the density supposed for the heavy negative ions, an estimated radius for the particles at 13 000 u/q for a charge q = 1 is in the range **3.8 to 38 nm, the size of small aerosols**. However, only the mass / charge ratio can be inferred from ELS measurements. If the ion charge is q > 1 electron, then the ion mass and size would be proportionally larger. The resolution of the instrument is not high enough to identify the ions. However, some candidates can be suggested for the smaller ions (Vuitton et al., 2009) thanks to their high electron affinity: **CN^-, C_3N^-/C_4H^- and C_5N^-**.

Ågren et al. (2012) and Shebanits et al. (2013) used a different method to study the negative ions. The **RPWS/LP** data can be used to infer negative and positive mean densities as well as the electron density. Their results are consistent with Wellbrock et al. (2013). Besides, they observed that on the nightside, very few free electrons are detected in the deepest regions (< 1050 km), contrary to ions. **On the nightside, the ionosphere is dominated by negatively and positively charged heavy (> 100 u) organic ions.**

As soon as the first INMS spectra became available, several groups started to **model the complex chemistry happening in Titan's ionosphere**. On the dayside, the first step was to model the **photochemical processes**, leading to the formation of the first primary ions. On the nightside, energy rather comes from **energetic particles** from Saturn's magnetosphere. Empirical models try to understand the **ion-neutral reactions** from the detailed analysis of INMS spectra. Mandt et al. (2012) synthesizes the advantages and drawback of each model.

Based on the first INMS spectra, Vuitton et al. (2006) tried to **associate the observations of neutral and ions with simple chemical models**, without any ion-neutral coupled processes. They found that nitrogen chemistry on Titan is more extensive than previously thought (Keller et al., 1992).

Waite et al. (2007) compared neutral, positive and negative ion data from INMS, CAPS/IBS and CAPS/ELS. They discuss the possible **pathways to form benzene**, a molecule necessary to form PAH-nitrile compounds. Comparisons are made with models forming soot on Earth. They suspect then that an **aggregation of the PAH-nitrile compounds** could lead to the heavy negative ions. A strong indication is that PAHs and cyano-aromatics have high electron affinities.

The chemical models need to be very complex. Nevertheless, one should know the limits and the **sensitivity of the models**. For this purpose, Carrasco et al. (2008) studied the sensitivity of a model to the ion-molecule reaction parameters, such as temperatures and density distributions. In particular, they identified **35 key ion molecule reactions**, including: 32 growth reactions, 5 protonations and 5 charge transfer reactions.

De La Haye et al. (2008) developed a 1D model coupling 36 neutral species and 47 ions. The model uses energy inputs from the Sun and from the magnetosphere of Saturn. In particular, it allows them to study the **diurnal variations** induced on the chemistry by the variations of the energy inputs into the upper atmosphere. One of their main conclusions, supported by Plessis et al. (2012), is that a complete understanding of the coupled ion – neutral chemistry is required, because these reactions make significant contributions to the production of important neutral species.

Vuitton et al. (2009) proposed the first model including **negative ions**. They studied the production and loss processes for 11 negative ions, including CN^-, C_3N^-, C_5N^-, C_4H^-, C_6H^-. They identified three pathways to form negative ions: negative ion chemistry, electron attachment on already heavy particles and reactions with radicals.

Models tended to separate day and nightside, that deal with very different energy inputs. Among the **dayside models**, Westlake et al. (2012) present a 1D photochemical model, with which they focused on the **major ions** CH_5^+, $C_2H_5^+$ and $HCNH^+$. They also developed an empirical model calculating ion densities from INMS results to compare the results with the photochemical model. Lavvas et al. (2011) and Mandt et al. (2012) discuss about the importance of **high-resolution photo-absorption cross-sections** for proper calculation of the primary products by photo-dissociation and photo-ionization. Later, Richard et al. (2015a)

focused their attention on the variations observed with **altitude and solar illumination** on the photochemical products.

The nightside ionosphere is not ionized by photo-ionization, but by **energetic particles** from Saturn's magnetosphere. Cravens et al. (2009) and Richard et al. (2015b) modelled this different chemistry. They also suggested that Titan nightside should also host **long-lived ions** coming from the dayside. Based on nightside CAPS/IBS data that detected positive ions with up to 13 carbons, Westlake et al. (2014) analyzed the **production of large positive ions** by electron-impact ionization of ambient neutrals, proton exchange reactions of ambient neutrals and production via **ion-molecule growth processes**. They selected the third solution as the most probable in light of the neutral densities measured by INMS. The ion-molecule growth mechanisms are likely to use **hydrocarbon building blocks** such as C_2H_2 and C_2H_4.

Recently, Vuitton et al. (2019) developed a 1D model based on the results obtained with the various previous models. They included positive ions up to 116 u, negative ions up to 74 u and multiple hydrocarbon and nitrile-bearing neutrals and radicals. The reactions taken into account include photo-ionizations, photo-dissociations and photo-detachments, electron ionizations and electron dissociations, neutral-neutral and ion-neutral reactions, recombination and attachment reactions. The model simulates Titan's atmospheric chemistry from the surface to 1500 km. **It reproduces the densities and/or trends observed for many species (see Figure I.3-7). They observed that the chemistry depends strongly on the deposited energy, which varies with the altitude and the solar cycle.**
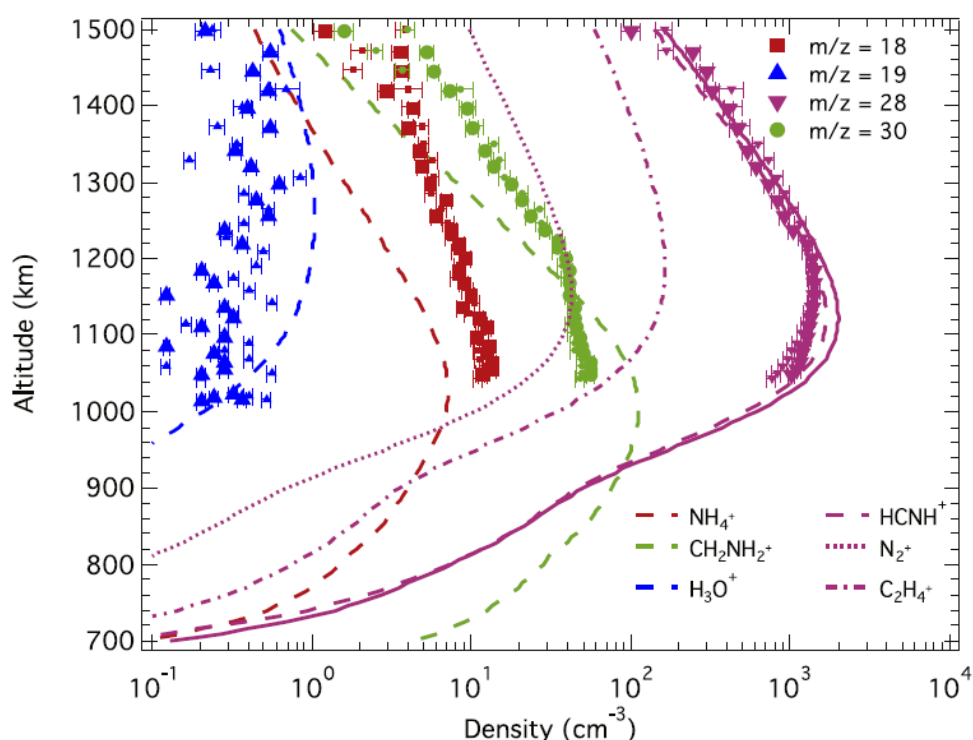
Figure I.3-7: Model results for the density of NH_4^+, H_3O^+, $HCNH^+$ / N_2^+ / $C_2H_4^+$ and $CH_2NH_2^+$, and comparison with the T40 INMS ion density measurements at m/z = 18, 19, 28, 30 (Vuitton et al., 2019).

3.2.c. Formation of nanoparticles in the ionosphere

Danielson et al. (1973) was the first to suggest that the **photo-chemistry** occurring in the upper atmosphere was a possible **source of the aerosols** forming the haze below.

Then, the Cassini mission brought insights on the **presence of aerosols at high altitude**, in the mesosphere, suggesting that the aerosols are formed there.

In particular, the aerosol profile with altitude has been retrieved by (Liang et al., 2007). They used **UVIS** (Cassini Ultraviolet Imaging Spectrograph) data obtained during stellar and solar occultations of Titan. The **altitude distribution and size** of the haze grains were deduced from the scattering the incident solar flux (see **Figure I.3-8**). It suggests a formation of macromolecules above 1000 km, with sizes of ~10-20 nm.
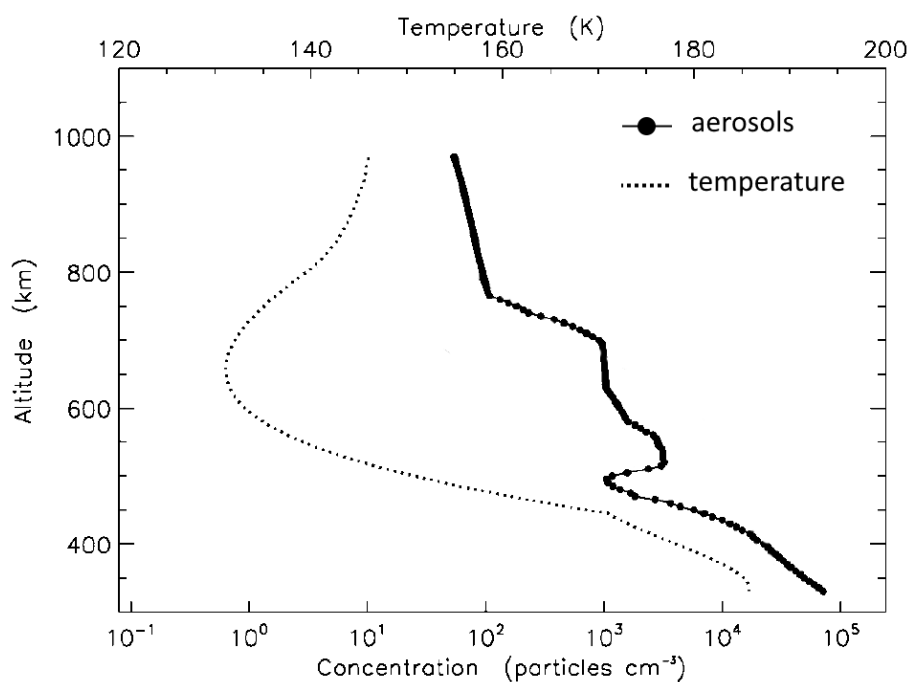
Figure I.3-8: Aerosol density and temperature profile derived from UVIS data (Liang et al., 2007).

Wahlund et al. (2009b) compared the results of different instruments that took *in situ* measurements in the ionosphere of Titan: RPWS/LP, RPWS/E, INMS, CAPS/ELS and CAPS/IBS. They concluded that the ion population of the ionosphere of Titan **below 1150 km** is at 50 to 70% composed of **heavy positive ions** (> 100 u). The ion density is relatively large: 100-2000 cm^{-3}. These ions could be a sizable source for the aerosol formation.

The **CAPS/ELS** instrument measured **heavy negative ions** in Titan's ionosphere, that are suggested to be the precursors of the aerosols. The instrument made in situ measurements in the ionosphere down to ~950 km. It always observed negative ions below 1400 km, the heavy negative ion production being more efficient at lower altitudes (Coates et al., 2010b).

These discoveries suggest that nanoparticles in Titan's ionosphere are formed by **ion-neutral chemistry**, forming ions always larger and more complex, until producing small particles.

Recently, Lindgren et al. (2017) suggested a new formation pathway, that could happen in parallel to ion-neutral chemistry in the ionosphere. Particles in the upper atmosphere are negatively charged and thus should repel each other. Nevertheless, nitrated hydrocarbon particles have a dielectric constant that enables them to overcome the electrostatic barrier that separates them from another particle. The particles can then grow through **physical aggregation with other particles**.

Aerosols are strongly present around and below 1100 km altitude, well mixed among plasma species. The ionosphere below this altitude is consequently a '**dusty plasma**', which cannot be studied or modelled without considering the aerosols (Lavvas et al., 2013; Shebanits et al., 2016). This point is detailed in **Section IV.1.2**.

3.2.d. Aerosol growth in the mesosphere and the stratosphere

The first models before the Cassini mission did not predict any complex chemistry above 750 km. Two models studied growth pathways for the aerosols, both expected a **production zone around 200 km**. (Lebonnois et al., 2002) proposed polymerization mechanisms, transforming simple molecules in macromolecules, as polymers of acetylene and cyano-acetylene, polycyclic aromatics and polymers of HCN and other nitriles, and polyynes. Wilson and Atreya (2003) performed a similar study and concluded on the dominance of pathways considering polycyclic aromatic hydrocarbons (PAH).

During the Cassini era, the Cassini spacecraft discovered the complex chemistry happening in the thermosphere, and the Huygens descent provided *in situ* observations of aerosols in the stratosphere and troposphere. In particular, the Descent Imager / Spectral Radiometer (DISR) instrument measured the brightness of sunlight from 150 km to the surface. Tomasko et al. (2008) inferred properties of the aerosols from these measurements and computations of scattering from fractal aggregates. They suggested **aggregates formed of monomers of ~0.1 µm**, with a number of monomers of ~3000 above 60 km.

These results enabled a strong improvement in the models of formation and growth through the atmosphere. They include polymerization, but also condensation and particle aggregation.

Lavvas et al. (2008a, 2008b) developed a 1D radiative-convective / photochemical / microphysical model to study Titan's atmospheric properties leading to the haze formation. They included pathways based on pure hydrocarbons and pure nitriles polymers, and hydrocarbon / nitrile copolymers. The stronger contributions come from the **nitrile polymer and copolymer pathways**. Such results are in agreement with the observations of the ACP (Aerosol Collector and Pyrolyser) instrument onboard Huygens that detected nitrogen in pyrolyzed haze. Results of the model indicate **two formation zones**: at ~800 km and at ~200 km. The high altitude production zone was not expected from pre-Cassini models.

Supposing initial conditions for the aerosol formation, Lavvas et al. (2010) computed **the evolution in size and density** of the aerosols through the atmosphere (see **Figure I.3-9**). Based

on heavy negative ions detected by Coates et al. (2007a), they estimated a radius of 3 nm at 1000 km and a mass density of 1 g.cm^{-3}. Particles aggregate rapidly in the upper haze layer at ~500 km. Below 200 km their size is constant, ~1 μm. Lavvas et al. (2011b) added heterogeneous processes to the model, allowing a spherical growth by deposition of aromatic structures on the surface of the particles. It resulted in a **competition between surface growth, coagulation and sedimentation**, as shown in **Figure I.3-10**.
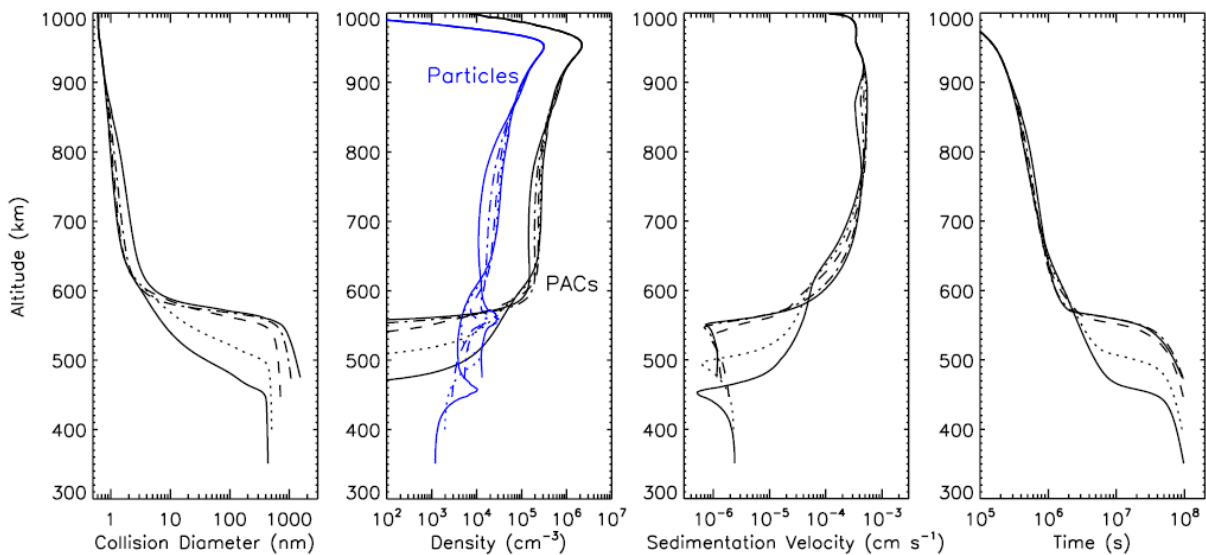
Figure I.3-9: Some results of the aerosols formation model by Lavvas et al. (2011b). The different curves show the sensitivity of the model.
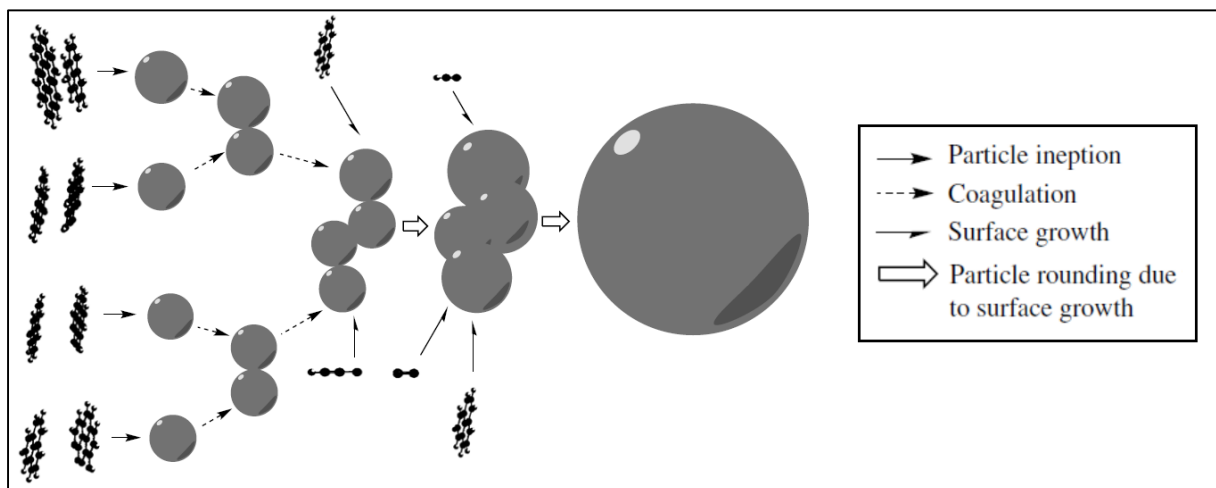
Figure I.3-10: Processes included in the model described by Lavvas et al. (2011b). In this example, the PACs provide primary particles which then coagulate to form an aggregate. Eventually the surface chemistry acting on the aggregate provides a new, larger primary particle. Figure from Lavvas et al. (2011b).

The model by Vuitton et al. (2019), described just above in **Section I.3.2.b**, also included some parameterization for the aerosols, in particular to use aerosol opacity and compute Rayleigh scattering on the grains. The processes that could lead to the formation of aerosols are numerous and complex. The authors of the paper **suggest some mechanisms that could lead to the growth of aerosols on Titan**. They considered pathways with radical-radical, radical-molecule and ion-electron reactions. As found by Lavvas et al. (2008b), all mechanisms studied show two specific production zones: around 900-1000 km, and at ~200 km (see **Figure I.3-11**). Logically, these locations correspond to two layers of the atmosphere with strong energy deposition (see **Section I.2.2.b**).
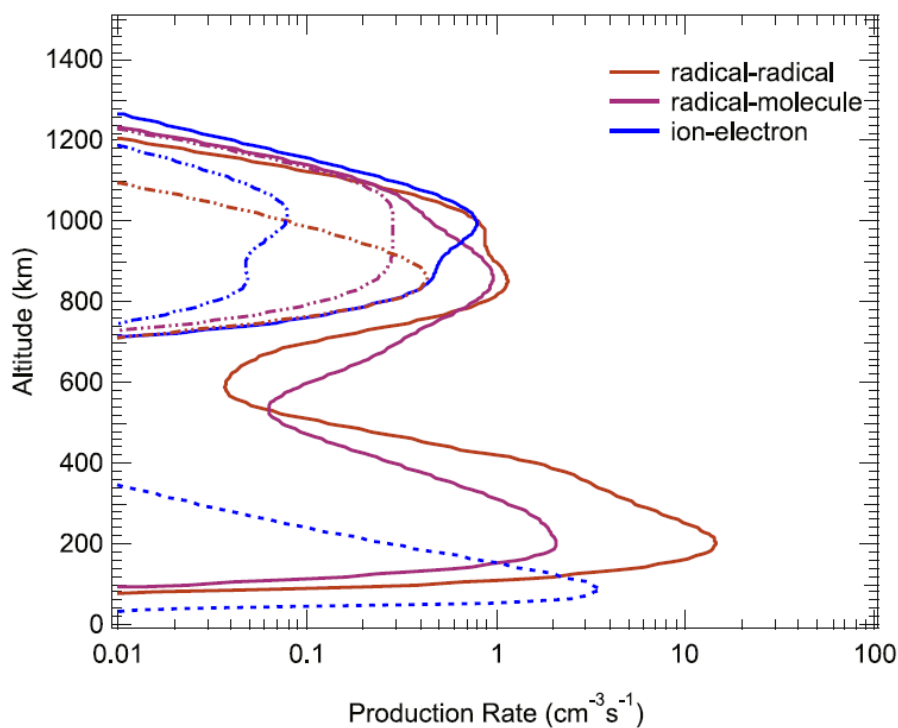
Figure I.3-11: Calculated production rate of species that are considered as aerosol seeds. Dot-dashed lines represent the production rate of nitrogen-bearing species. The dotted line shows the production rate from the electron recombination of cluster ions resulting from galactic cosmic ray impact; they all contain nitrogen. From Vuitton et al. (2019).

CONCLUSION OF CHAPTER I.1-2-3: RESULTS FROM TITAN

The Cassini-Huygens mission increased drastically our understanding of Titan, from its underground to the top of its atmosphere. Here is a brief summary of the major discoveries that triggered my PhD subject.

(1) The aerosols covering Titan's atmosphere and surface **start forming in the upper atmosphere** in ionized conditions.

(2) The presence of the aerosols in the ionosphere disturbs the plasma. Plasma models have to take the aerosols into account. The ionosphere of Titan is called a '**dusty plasma**'.

(3) Aerosols form and evolve over several hundreds of kilometers. They **interact with very different environments**, over a large range of pressure, temperature, ionization conditions and gas composition.

Figure I.3-12 gathers the vertical profiles of important parameters and species in Titan's atmosphere. They show that the 1000-1200 km zone is a place where aerosols form in quantity. At this altitude, grains are of a few nanometers and generally negatively charged. A strong correlation is observed between the production zone of the aerosols and the altitudes where the **radical and heavy ions** are present in quantity. Radicals and heavy ions are therefore suspected to play a major role in the production of the aerosols. Besides, they certainly interact strongly with them during their slow sedimentation through the ionosphere.

Next page: Figure I.3-12: Summary of the vertical profiles of various species on Titan. (a) Pressure and temperature from Cassini-Huygens data (Fulchignoni et al., 2005). (b) CH_4 and H_2 mixing ratios. Combination of data and model results (Vuitton et al., 2019). The red dots are measurements of H_2 not consistent with the model trend. (c) Radical mixing ratios predicted by photochemical models (Lavvas et al., 2011a; Vuitton et al., 2019). (d) The average mass of positively and negatively charged particles measured by CAPS (Lavvas et al., 2011a). (e) Densities of charged particles. Combination of observations above 1000 km and model results (Lavvas et al., 2013). (f) Aerosols properties from a model of aerosols growth (Lavvas et al., 2011b; Vuitton et al., 2019).
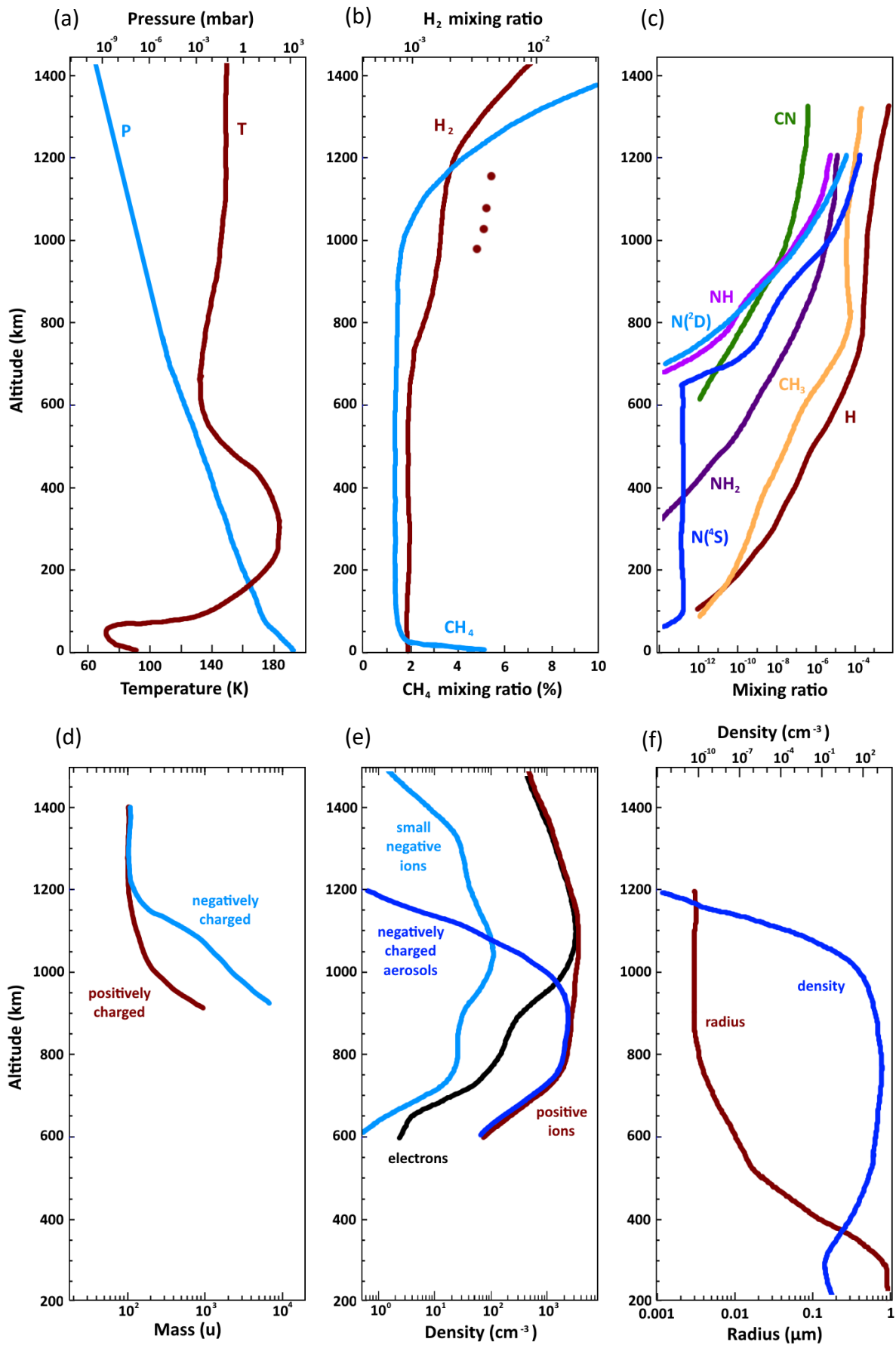
4- Laboratory simulations of Titan's ionosphere

A very complex chemistry happens in Titan's atmosphere, eventually leading to the formation of organic aerosols. Such a complex system is difficult to investigate in details from Earth, even with data taken by a well-instrumented spacecraft such as Cassini. A fundamental strategy in this investigation is the experimental simulation. The chemical processes happening on Titan can be simulated in the laboratory. Then, the variations of the experimental parameters as well as the use of high-resolution instruments enable the detailed study of the chemical processes going on. Here is presented a brief record of the experimental simulations performed since 1953.

4.1- Historical and actual experiments

4.1.a. Experiments prior to the Voyager encounters

The first simulation of atmospheric organic chemistry in the laboratory has been performed by Miller and Urey (Miller, 1953). The main objective was at the moment focused on the early Earth: **could organic compounds needed for life have been formed in the atmosphere?** Miller and Urey guessed that the primitive atmosphere of the Earth was composed of **methane, ammonia, water and hydrogen**. The energy required for the gas phase chemistry in the atmosphere could have come from ultraviolet solar irradiation and/or electrical discharges. For technical reasons, as their quartz reactor absorbed UV light, Miller and Urey used an **electrical discharge** to observe its effects on a mixture of CH_4, NH_3, H_2O and H_2. This atmosphere was also in contact with boiling water. After a few days, the water had become red and they observed the **formation of several amino-acids.**

Experiments with Titan's atmosphere started a little later. **Before the Voyager missions**, the composition of Titan's atmosphere was just approximate. **CH_4 and C_2H_6** had been detected with certitude and there was evidence for **C_2H_2 and C_2H_4** (Gillett, 1975). Nevertheless, the presence of **N_2 remained unclear**. It was predicted by Hunten (1978) and Atreya et al. (1978), but very hard to detected from Earth. According to Scattergood and Owen (1977), the reddish-brown albedo of Titan's atmosphere could suggest the presence of **species containing nitrogen or sulfur**.

Sagan and Khare extended the work of Miller and Urey to reducing atmospheres of planets, like Jupiter, Saturn and Titan, where they had observed the predominance of red clouds. They **irradiated** a **mixture of CH_4, NH_3, H_2S**, with sometimes H_2O and C_2H_4, at 254 nm (in the UV spectrum). They characterized the formation of amino-acids (Sagan and Khare, 1971), and analyzed the **solid powdery orange-brown polymer** that coated the interior of the chamber (Khare and Sagan, 1973). In the next years, they investigated different gas mixtures and electrical discharges. They usually formed a solid brown and sometimes sticky residue that they called '**tholins**' (Sagan and Khare, 1979). The analysis of tholins formed in different conditions showed that are always **complex organic materials**.

At this time, Titan was suspected to be covered by a photochemical smog (Strobel, 1974). Then, several groups **tented to form Titan-like dust particles** with laboratory experiments (Chang et al., 1979). One strategy of the **polymerization of simple compounds** (i.e. CH_4, C_2H_2, NH_3) by photolysis (Bar-nun and Podolak, 1979; Podolak et al., 1979; Scattergood and Owen, 1977). A second strategy is to **start from Titan's main atmospheric components, CH_4 and certainly N_2**. Their exposure to an electric discharge produces many different saturated and unsaturated hydrocarbons and nitriles (Toupance et al., 1975).

4.1.b. Experiments between Voyager and Cassini

THE CONTEXT

The Voyager missions identified more precisely the composition of the atmosphere of Titan, mainly thanks to the instrument IRIS (for InfraRed Interferometer Spectrometer) (Hanel et al., 1982, 1981; Kunde et al., 1981; Maguire et al., 1981). They observed **predominantly N_2** (> 80%), **some CH_4**, and other **minor contributions of hydrocarbons** (C_2H_2, C_2H_4, C_3H_8) **and nitriles** (HCN, HC_3N, C_2N_2). Earth-based observations also improved and brought up some insights on the composition of the atmosphere, in particular with the detection of benzene with ISO (the Infrared Space Observatory) (Coustenis et al., 2003).

Based on Titan data and helped by previous experimental measurements**, photo-chemical models** started to develop. Their objective was to describe how were produced the hydrocarbons and nitriles observed, starting from the dissociation of N_2 and CH_4 (Toublanc et al., 1995; Wilson and Atreya, 2004; Yung et al., 1984).

The experimental studies at that time were focusing on two strategies: (1) to understand the formation processes by photo-polymerization, and (2) to simulate the complete neutral chemistry in a N_2-CH_4 gas mixture (Cabane and Chassefière, 1995; McKay et al., 2001).

STRATEGY 1: CREATION OF PHOTO-POLYMERS

The point of this strategy is to start from mixtures already produced from the N_2-CH_4 photochemistry. It enables to focus on only a few reactions, and greatly simplifies the interpretations.

(Bar-Nun et al., 1988) and Scattergood et al. (1992) focused on the photolysis of C_2H_2, of C_2H_4 and HCN. Scanning Electron Microscopy (SEM) observations showed **spherical particles** < 1 µm and **aggregates** of a few spherical monomers. Khare et al. (1994) observed that **poly-HCN** do not have optical constants representative of Titan's haze, to the contrary of tholins.

Clarke and Ferris (1997) started from a mixture more complex: **HC_3N/C_2H_2**. They observed the formation of **co-polymers**, with morphological structures even more complex (see **Figure I.4-1**), and IR signatures closer to those of tholins.
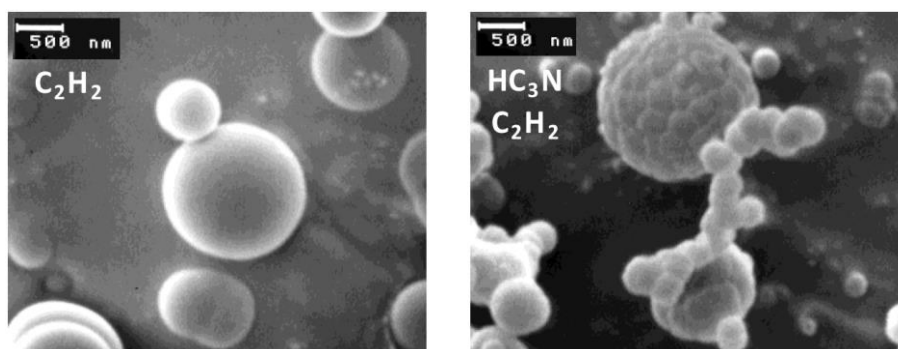
Figure I.4-1: C_2H_2 and C_2H_2/HC_3N polymers observed by scanning electron microscopy (Clarke and Ferris, 1997).

STRATEGY 2: SIMULATION OF TITAN N_2-CH_4 ATMOSPHERE TO FORM THOLINS

This strategy aimed at realizing a simulation of the complete Titan chemical system, starting from N_2 and CH_4. Indeed, photon irradiation experiments described above are done at one precise wavelength, and are not representative of the total solar energy spectrum arriving on Titan. On the opposite to photon irradiations, plasma discharges excite the gas with a continuum energy spectrum. They lead to the ionization of the gas inside the reactor, similarly to the plasmas found in the upper atmospheres of planets, northern lights or lightning. Different configurations of plasma sources exist (Bogaerts et al., 2002) and have different characteristics (homogeneity, energy, electron density...). **N_2-CH_4 plasma discharges are therefore an interesting way to simulate the upper atmosphere of Titan** (see **Figure I.4-3**).

A group at LISA (Laboratoire Interuniversitaire des Systèmes Atmosphériques in Créteil, France) focused on **DC discharges** (working with a high potential between two electrodes) at low pressure (~1 mbar) and **low temperature** (100-150 K), the temperature and pressure range of Titan's stratosphere. A gas mixture of N_2-CH_4 is injected in a chamber immersed in a cryogenic fluid. Thanks to this setup, de Vanssay et al. (1995) analyzed the formation of **organic compounds thermally unstable** and requiring an analysis at low temperature. They detected polyynes C_6H_2, and maybe HC_5N, clue that a complex chemistry including nitrogen is at work. These molecules were previously used in photochemical models but had never been observed in laboratory experiments. Coll et al. (1999) observed that methane was totally consumed, used to form many **new hydrocarbon and nitrogen-bearing compounds**. A solid phase was also synthesized: **tholins**. MEB observations of tholins formed at ambient temperature show particles of a few micrometers that are aggregates of ~300 nm spheres (see **Figure I.4-2**).
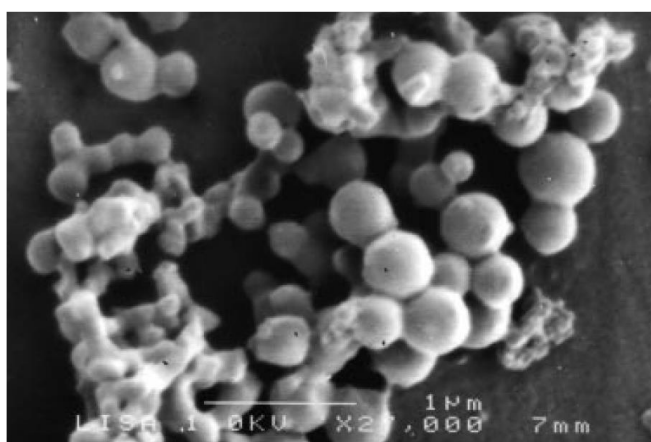
Figure I.4-2: Electron microscopy observation of tholins dissolved in nitriles (Coll et al., 1999).

C. Sagan, B.N. Khare and W. Reid Thompson also led several experiments **at Cornell University** to investigate the chemical processes happening in Titan's upper atmosphere. (Khare et al., 1984) used a **DC discharge** in N_2-CH_4 (90:10) at 0.2 mbar to form tholin thin films. They analyzed the solid sample by IR spectrometry and the volatile components by gas chromatography combined to mass spectroscopy (GC/MS). The experiments were performed **at room temperature**. Indeed, the effective temperature of the energy source required for molecular dissociation is very large compared to the room temperature. They conclude that working at ambient temperature instead of Titan temperature may not affect the results significantly. Reid Thompson et al. (1991) rather studied an **inductively coupled plasma (ICP) discharge** in a continuous flow of N_2-CH_4 at low pressure (0.24 - 17 mbar). The precise analysis of the evolution of the gas phase by GC/MS showed the formation of gaseous hydrocarbons and nitriles. Such measurements then help to model the minor constituents in Titan's atmosphere. These two experiments also led to the formation of tholins, that were analyzed and compared in Sagan et al. (1993, 1992).
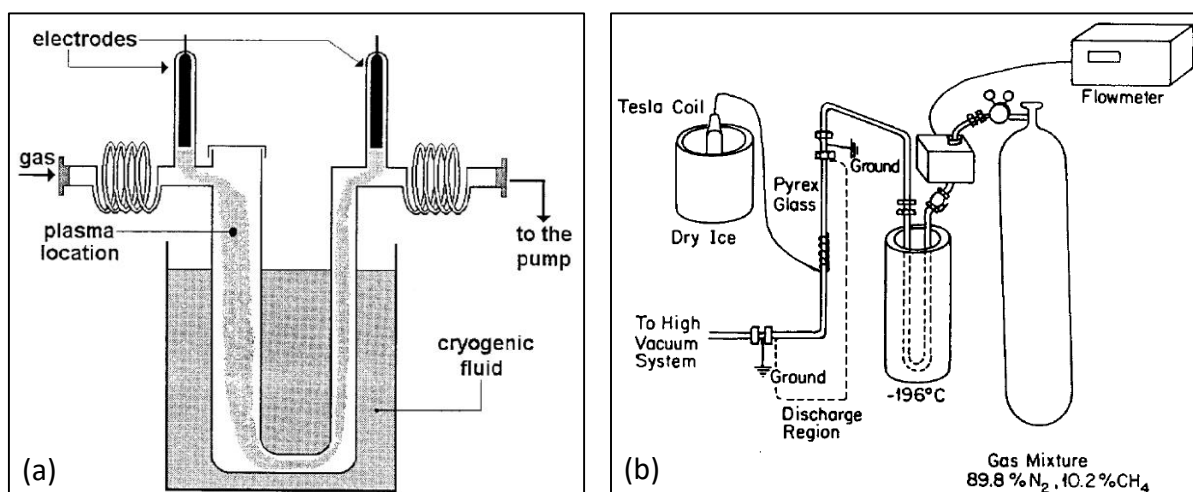
Figure I.4-3: Two different plasma discharges to study Titan's upper atmosphere. (a) DC glow discharge (Coll et al., 1999). (b) ICP discharge (Reid Thompson et al., 1991).

Later, Khare et al. (2002) used an ICP discharge in N_2-CH_4 (90:10) to measure *in situ* the time **variation of the IR spectrum** of a tholin film during its development. They made important observations: **at the ignition of the plasma, aromatic rings form quickly, then the nitrile and amine compounds appear later**. They also saw that **exposure to air immediately oxidizes and destroys the aromatic rings**.

At **NASA Ames**, McKay (1996) investigated the formation of tholins for **various percentages of CH_4** in N_2, from 3 to 100%. He used a ICP discharge at 1.15 bar and room temperature. The tholins formed revealed to be very different. Then, Imanaka et al. (2004) studied the effect of pressure on the chemical composition and the optical properties of tholins. They ignited ICP discharges in N_2-CH_4 (90:10) at room temperature and at various pressures from 0.1 to 23 mbar. They observed a **strong effect of pressure**. Comparisons with Titan data match better at low pressure, forming nitrogen-containing polycyclic aromatic compounds. In any case,

these results indicate that **aerosols formed at different altitudes on Titan should have different properties**.

Experiments simulating the atmospheric chemistry of Titan with N₂-CH₄ plasma discharges form tholins. In all cases, they were diagnosed as a material with low C/N (~2-4), and IR analyses revealed a complex organic mix of alkanes, aromatic compounds, heteropolymers and amino acid precursors.

4.1.c. Post-Cassini experiments

The Cassini mission revealed that aerosols form in the ionosphere, as products of a complex ion chemistry. Post-Cassini experiments mimic the ionized environment of the ionosphere to study the complex ion chemistry happening there. There are mainly two ways of experimental investigation: by analyzing directly the ionizing effects induced by photon irradiations, or by mimicking the ionospheric plasma with plasma discharges. Many works are performed using one or the other, or both techniques (Hörst et al., 2018).

STRATEGY 1: PHOTO-IRRADIATIONS

The main ionization source on Titan are solar photons (Ågren et al., 2009). **The most efficient to ionize the neutral molecules in Titan's upper atmosphere are extreme UV rays**.

Many experiments use **mercury lamps** at 253.7 nm (Clarke and Ferris, 1997; Vuitton et al., 2006a) or **hydrogen lamps** at 121.6 nm (Dodonova, 1966) to mimic the solar UV irradiation of Titan. Es-Sebbar et al. (2015) and Hong et al. (2018) used a **H₂/He microwave plasma discharge** in different conditions to obtain an emission varying between 115 and 170 nm. Several studies rather used a **deuterium lamp** (115-400 nm) to irradiate a volume of gas at high pressure and form aerosols (Gautier et al., 2017; Sebree et al., 2014; Trainer et al., 2013; Yoon et al., 2014). They studied the effect of the addition of trace aromatics in the gas phase on the aerosols formed. In particular, they studied the irradiation of a N₂-CH₄ gas mixture with ppm-levels of **benzene** and showed that the addition of C₆H₆ increase the mass of the aerosols, but decrease their nitrogen incorporation. As radiations above 110 nm get through MgF₂ windows, such photo-irradiations can be done in close cells.

However, such radiations cannot directly photo-dissociate N₂, which requires wavelengths shorter than 100 nm (see **Figure I.4-4**). One solution to obtain vacuum UV (VUV) is to couple the gas chamber to a **VUV synchrotron beamline**. The exposure of Titan like N₂-CH₄ gas mixtures to synchrotron beamlines have been studied by a few groups (Carrasco et al., 2013; Imanaka and Smith, 2010, 2007; Peng et al., 2013; Thissen et al., 2009). Their results are fundamental for the improvement of photochemical models.
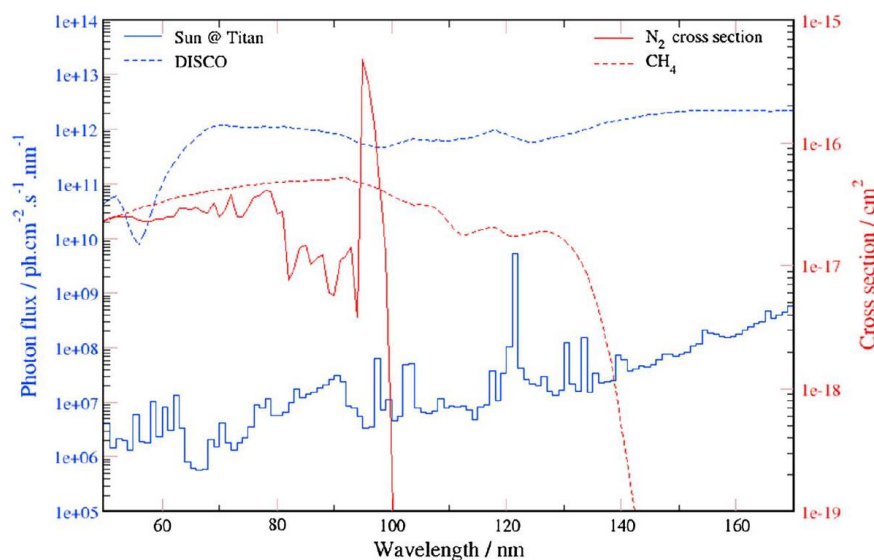
Figure I.4-4: N_2 and CH_4 ionization cross-sections, superposed to the photon flux from the Sun at Titan, and from the DISCO synchrotron beamline at SOLEIL (France). From Peng et al. (2013).

Bourgalais et al. (2019a) used an alternative source of extreme UV photons: the high harmonic generation (HHG) of **a femtosecond laser**. They also observed the formation of hydrocarbons and nitrogen-bearing species after the exposure of the beam to a N_2-CH_4 gas mixture (0.95:0.05).

For more flexibility than synchrotron and femtosecond laser, Tigrine et al. (2016) developed a **small VUV laboratory source**. **Noble gas microwave plasma discharges** are used to provide VUV photons. Argon emits at 104.8 nm and does not dissociate N_2, but neon (73.6 and 74.4 nm) and helium (58.4 and 53.7 nm) do. Bourgalais et al. (2019b) analyzed the neutral and positive ion species formed in a N_2-CH_4 gas mixture (0.9:0.1) irradiated at 73.6 nm. In particular, they detected **methanimine** $H_2C=NH$, which could be key compound to explain the N-enrichment of aerosols in Titan's atmosphere.

In parallel, experimental and ab initio studies tend to characterize specific reactions. For instance, Bourgalais et al. (2016) experimentally showed that C_3N^- + HC_3N, cannot contribute to the growth of molecular anions, and Mouzay et al. (2019) numerically investigated a new route of formation for HC_3N.

Photo-irradiation experiments have the advantage to directly reproduce the effects of photons on the molecules in Titan's ionosphere. Nevertheless, such experiments are limited by the available UV sources, usually discrete and not strong enough to form aerosols in quantity. The development of new VUV sources in the near future promises to go further in the understanding of Titan's photo-chemistry.

Contrarily to photo-irradiation experiments discussed above, cold plasma discharges do not enable to focus on the study of the photo-ionization and photo-detachment reactions observed on Titan. However, these experiments **mimic the ionospheric plasma**. The **electron energy distribution function** (EEDF) of a cold plasma discharge is relatively similar to the energy deposited by the solar photons on Titan Szopa et al. (2006) (see **Figure I.4-8**). Plasma discharges give an **ionization degree** (i.e. the ratio electron density / total density) similar to Titan's ionosphere, and lead to an **efficient production of tholins**.

The studies started before the Cassini era using **spark DC discharges** go on with several works (Hörst et al., 2018; Hörst and Tolbert, 2013; Trainer et al., 2004). They study the gas and aerosols formed at 0.8 mbar by mass spectrometry. The advantage of their setup is to analyze directly the aerosols **without exposing them to ambient air**, that would oxidize them.

Radio-frequency capacitively coupled plasma (RF CCP) discharges are well-known to form dusty plasmas at low pressure under particular conditions. Thanks to this technique, tholins are no longer formed on the walls of the reactor, which could induce a surface catalysis bias, but in **suspension** in the plasma. Such an experiment has been built in LATMOS to study Titan's atmospheric chemistry (Szopa et al., 2006). It is described further in the next section.

Experiments studying Titan's atmospheric chemistry are usually led at ambient temperature, as **cold Titan temperatures** would make the neutral molecules condense on the walls of the chambers. Sciamma-O'Brien et al. (2014) designed a new setup to solve both the temperature and the condensation problems, igniting a **plasma in the stream of a pulsed supersonic jet-cooled expansion**. This experiment has also a unique advantage: as the gas species only stay a few instants in the plasma, the chemistry is reduced to a few reactions. The injection of a N_2-CH_4 gas mixture leads to the study of the **first step of the chemistry**, leading to the first simple ions formed. However, if more complex mixtures including various hydrocarbons (i.e. C_2H_2 or C_6H_6) are injected, the experiment gives insights on the **next steps of the chemistry**. Precise reactions can also be studied by the injection of the needed reagent gases. This kind of discharge also leads to the **formation of aerosols**, with shapes and IR spectra similar to other studies (Sciamma-O'Brien et al., 2017).

4.2- The PAMPRE experiment

The PAMPRE experiment is located at LATMOS. It is one of the experiments I used during my PhD to study analogues of Titan's aerosols in a plasma environment. The present sub-section describes the experiment as well as the main studies realized with it.

4.2.a. Production of tholins with PAMPRE

The PAMPRE experiment (French acronym for Production d'Aérosols en Microgravité par Plasma REactifs – Aerosols Production in Microgravity by REactive Plasma) is especially suited to provide analogues of Titan aerosols (Szopa et al., 2006). Its specificity is to **create analogues in suspension** in the chamber using a **radiofrequency (RF) capacitively coupled plasma (CCP) discharge**. The organic aerosols are formed in the middle of the plasma and sediment once they reach a limit size. Indeed, dust particles in a plasma tend to charge electrically and they are maintained in levitation by the electric field between the electrodes. Their **retention time** in the plasma can be modified by parameters of the experiment, usually estimated to ~1-2 min (Alcouffe et al., 2010; Hadamcik et al., 2009).

The chamber is a stainless steel cylinder of 40 cm in height and 30 cm in diameter (see **Figures I.4-5** and **I.4-6**). The upper electrode is a stainless steel disk grid of 12.6 cm in diameter. An aluminium alloy cylindrical **box** is adjusted to the upper electrode to confine the plasma. This configuration is in agreement with the 'GEC RF Reference cell' (Hargis et al., 1994). Both the upper electrode and the bottom of the box are pierced with small holes to let the gas go through. An RF potential (at 13.56 MHz) is applied to the upper electrode, leading to the lightning of the plasma discharge in the box.
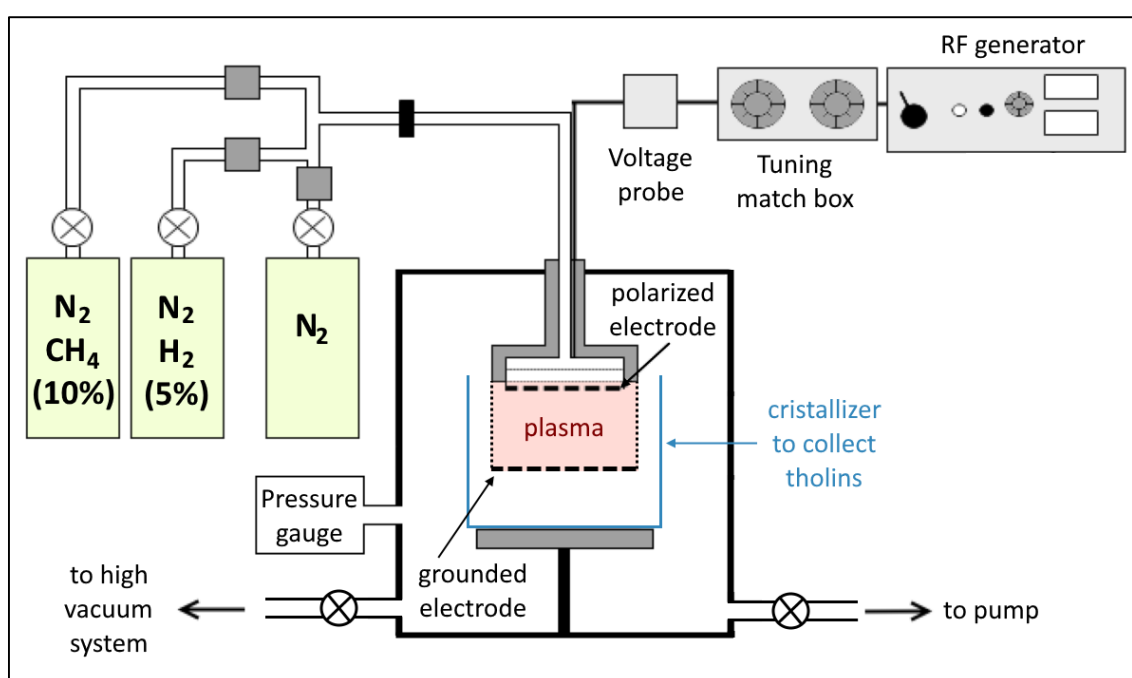
Figure I.4-5: Scheme of the PAMPRE setup to produce analogues of Titan's aerosols.

A N$_2$-CH$_4$ gas mixture is continuously injected in the chamber. We use a pre-mixed gas bottle with 10% methane in nitrogen (Air Liquide – CRYSTAL mixture), and can dilute it with pure nitrogen (Air Liquide – alphagaz 2). They are high purity gases (> 99.999%).
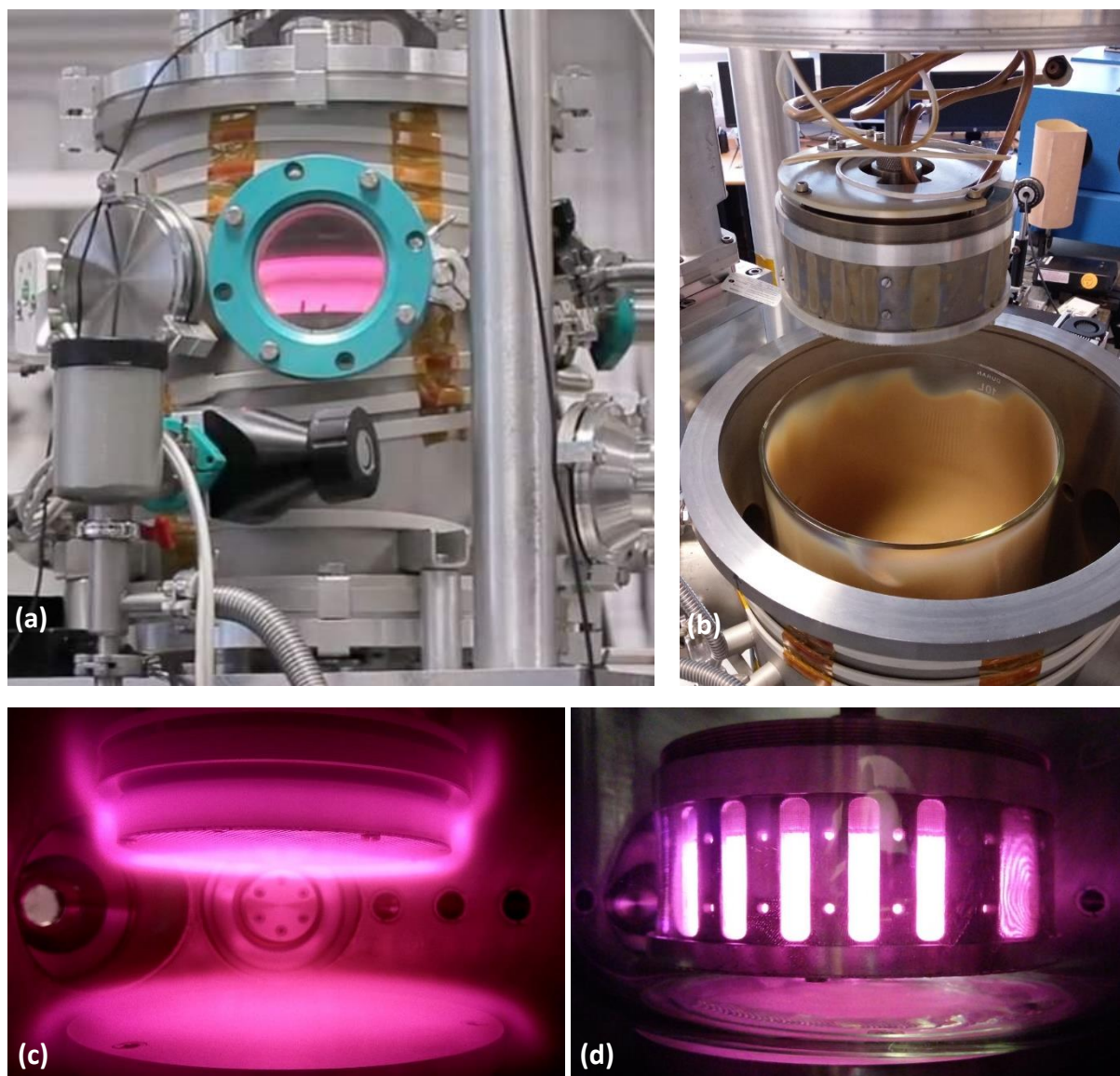
Figure I.4-6: Pictures of the production of tholins with the PAMPRE setup. (a) External view of the chamber. (b) Opening of the chamber after a tholin production. The aerosols are collected in a glass vessel (crystallizer). (c) Discharge inside the chamber, without the plasma confining box. (d) Discharge in the chamber with the confining box and the crystallizer.

The varying parameters of the experiment are the gas mixture, the gas flux (and the pressure) and the discharge incident power. The **working conditions** in PAMPRE to form the analogues are discussed in Sciamma-O'Brien et al. (2010): usually 0.90 mbar of a N$_2$-CH$_4$ mixture at 5% in CH$_4$ injected at 55 sccm (standard cubic centimeters per minute), with a 30 W incident power (i.e. ~12 W coupled power to the plasma, see **Section II.2.1.b**). The discharge is ignited during several hours to produce tholin aerosols. The temperature of the polarized electrode reaches maximum 60-80°C after several hours of production. Then the

chamber is opened and tholins are collected. This strategy has the inconvenient to expose the samples to air and oxidize their surface (see **Section III.2.4**). **Before a new production, the chamber is cleaned** with ethanol, and vinegar if necessary, exterior walls are heated at ~110 °C to desorb water and a N_2 (+H_2) plasma is ignited to desorb impurities on the interior confining box. Finally, the chamber is pumped down to 2.10^{-6} mbar for > 15h with a turbo-molecular pump.

4.2.b. Previous studies of the plasma in PAMPRE

To understand the processes leading to the formation of the aerosols, several studies have been performed to characterize the plasma in PAMPRE.

ELECTRIC PARAMETERS AND ELECTRON DENSITY AND ENERGY

Electron density has been measured by Alcouffe et al. (2010) and Wattieaux et al. (2015), using the confining box as **a resonant cavity**. Indeed, the resonant frequencies are depending on the electron density. More details on this method are given in **Section II.2.1.c**. The electron density measured is **~10^9 cm^{-3}**, and decreases with the addition of CH_4 to N_2. The authors explain it by the attachment of free electrons on the dust particles. In N_2-CH_4 discharges, the decrease in electron density is observed during the first 30-40s of the discharge (see **Figure I.4-7 (a)**).

The plasma discharge emits light that can be analyzed by optical emission spectroscopy (OES). Emission lines come from the de-excitation of atoms, molecules or ions previously excited by inelastic collision with an electron. The analysis of these lines give information of the electrons, atoms, molecules, ions and radicals present. In particular, Szopa et al. (2006) could study lines emitted by N_2, N_2^+, CN and H. Alcouffe et al. (2010) deduced from EOS measurements the **temperature of the neutral gas phase, ~325 K** for an injected power of 30 W and 5% CH_4. The gas is not heated much by the plasma discharge. They also studied the evolution of the **electron energy** with the injection of CH_4 in N_2. They observed an increase in the electron energy in N_2-CH_4 compared to pure N_2. This is explained by the lower electron density in N_2-CH_4. To maintain the plasma discharge with less electrons their energy has to increase. Then, they more efficiently ionize molecules during collisions. Wattieaux et al. (2015) investigated the evolution of the electron energy at the ignition of the discharge. They observe an increase of the energy during the first ~30-90 s, depending on the methane amount. This stabilization time is linked to the stabilization of the methane amount in the chamber, which decreases strongly from the injected amount.

Alcouffe et al. (2010) and Wattieaux et al. (2015) also observed that the **self-bias voltage** (V_{DC}) between the electrodes is strongly disturbed at the **apparition of dust** in the discharge. Therefore, they used it to study the apparition time of the aerosols in the plasma for different conditions. They observed that an increase in pressure reduces the apparition time, at the opposite to an increase in CH_4 amount that increases the formation time (see **Figure I.4-7 (b)**).
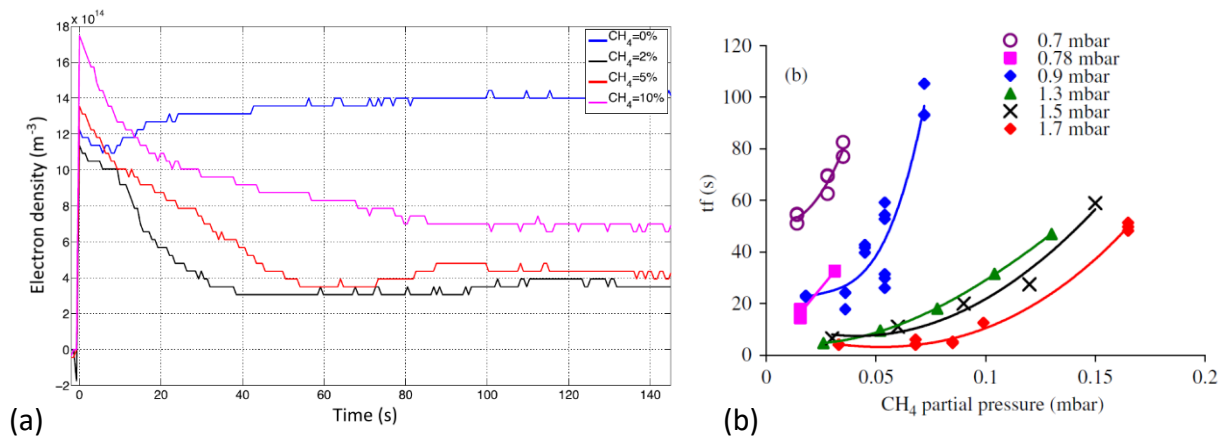
Figure I.4-7: Diagnosis of the plasma produced in PAMPRE. (a) Electron density at the ignition of the discharge (Wattieaux et al., 2015). (b) Formation time of the aerosols as function of the injected methane amount (Alcouffe et al., 2010).

To understand further the behavior of the plasma, a collaboration between LATMOS and the Instituto de Plasmas e Fusão Nuclear (Portugal) started with the objective to **model the plasma discharge**. RF CCP plasma discharges are complex to model, requiring a 2D simulation. As a N_2-CH_4 plasma mixture induces a very complex chemistry in the gas phase, the strategy has been to **first model the discharge in pure N_2**. The simulation is a hybrid code that couples a 2D time-dependent fluid module (dynamics of the charged particles), and a 0D kinetic module (chemistry). It is described in Alves et al. (2012). **This model gives access to parameters that cannot be measured**. In particular, it gives the **2D distribution of the electron and ion densities**, as well as the **electron energy distribution function** (EEDF) at different places in the discharge. This confirms a similitude between the solar spectrum and the energy given to the electrons in PAMPRE (see **Figure I.4-8**).
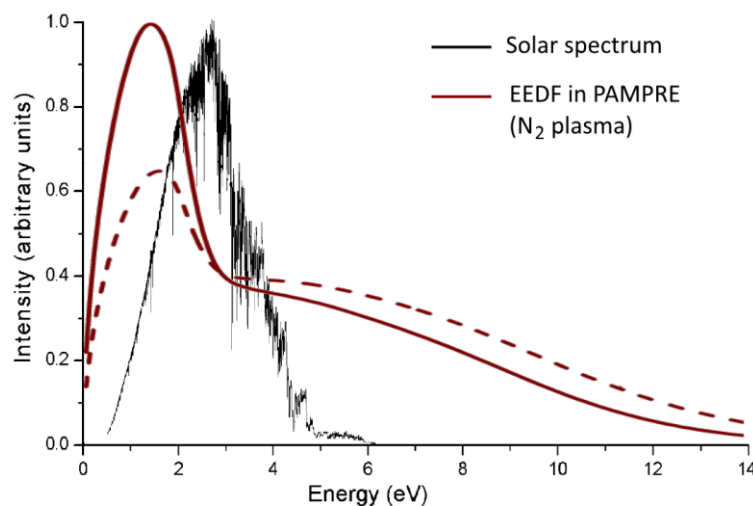
Figure I.4-8: Comparison of the solar spectrum to the modelled Electron Energy Distribution Function (EEDF) of a pure N_2 discharge in PAMPRE at 1 mbar (solid line) and 0.5 mbar (dashed line). From Alves et al. (2012) and Szopa et al. (2006).

Sciamma-O'Brien et al. (2010) recorded the **evolution of the methane amount** at the ignition of the discharge. It is chemically consumed and stabilizes after 1-2 minutes. To obtain a stabilized methane concentration similar to Titan's upper atmosphere (1.3-2.4%), the injected methane amount should be **4-6%.**

Tholins collected in the crystallizer can be weighted, and then the **production rate** can be deduced. Sciamma-O'Brien et al. (2010) observed a maximum in the production rate with CH_4 amount (see **Figure I.4-9**). The maximum varies between 4 and 6% depending on the pressure in the chamber. Titan's conditions are therefore consistent with an optimized tholins production in our experiment. The presence of a maximum suggests that **two processes are in competition**. For low amounts of methane, the production rate is proportional to the methane amount (i.e. the methane consumption). Then, for higher methane amounts, an inhibiting process dominates. This limitation could be linked to the increase of atomic hydrogen, which increases with the CH_4 amount, as showed in N. Carrasco et al. (2012).
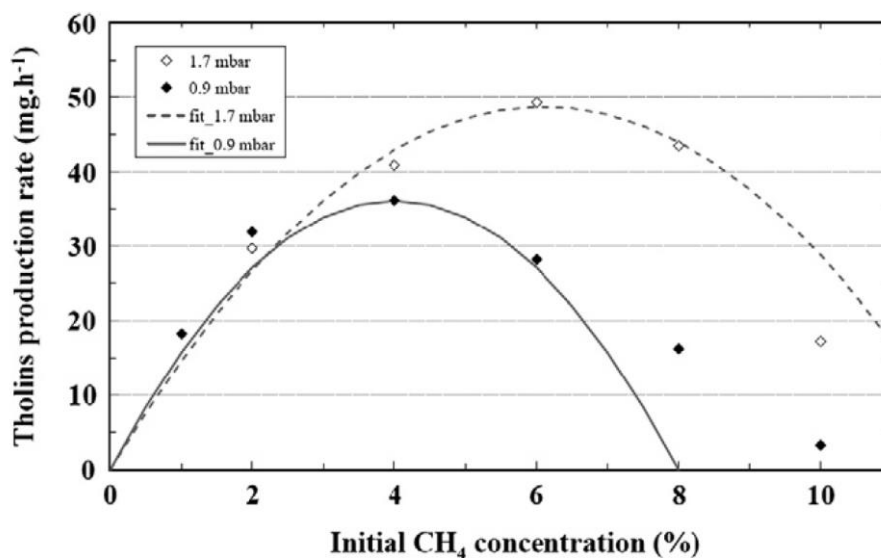
Figure I.4-9: Tholins production rate as function of the injected CH_4 % (Sciamma-O'Brien et al., 2010).

The neutral composition of the gas phase has been investigated by **mass spectrometry** in different studies (Carrasco et al., 2012; Dubois et al., 2019b; Wattieaux et al., 2015). They observe the **formation of many organic molecules and N-bearing species**. HCN is the main product and increases with the amount of CH_4 injected. Many heavy species appear, up to more than 70 u (see **Figure I.4-10**, to compare to INMS spectrum on Titan in **Figure I.3-4**).
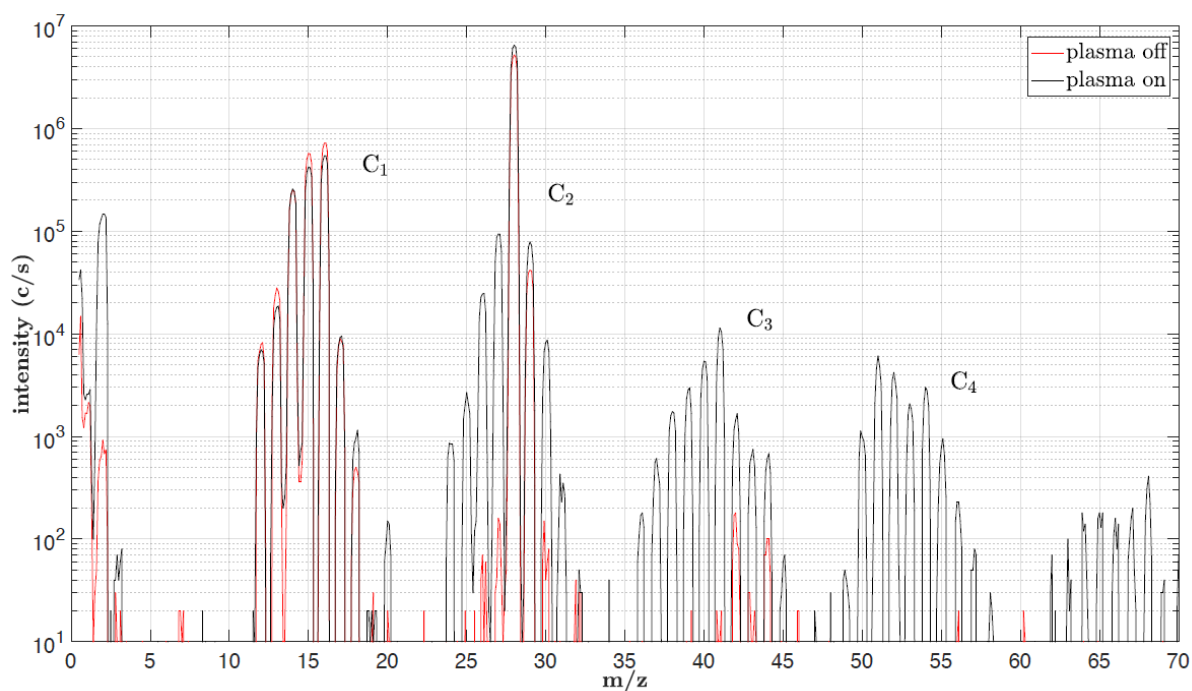
Figure I.4-10: Neutral mass spectra in PAMPRE in a N_2-CH_4 (0.9:0.1) mixture with plasma off (red) and plasma on (black). The consumption of methane at m/z 16 and its fragments m/z 15, 13, 12 is visible after the plasma is switched on. (Dubois et al., 2019b)

To help the attributions, **IR absorption spectroscopy** has also been performed on the gas phase. During the plasma, the gas pressure in the reactor is low (~1 mbar), which does not permit direct IR analysis. Dubois et al. (2019b) and Gautier et al. (2014) used cold traps to collect the species formed during several hours. Then, when the trap is heated and releases the molecules, the pressure is high enough to perform IR absorption spectroscopy. They especially studied ammonia (NH_3), acetylene (C_2H_2), hydrogen cyanide (HCN) and ethylene (C_2H_4).

The content of the cold trap has also been analyzed by **gas chromatography coupled to mass spectrometry** (Gautier et al., 2011). They identified more than 30 reaction products, most of them being nitrile species, along with aliphatic hydrocarbons and a few aromatic compounds. This work showed the importance of the nitrogen-bearing species in Titan's chemistry.

Recently, the ion populations have been investigated in the plasma by mass spectrometry. Dubois et al. (2020) discussed results on **positive ions** (see **Figure I.4-11**). They observed a higher abundance of amine ions such as NH_4^+ at lower methane concentration. On the opposite, aliphatic ion compounds dominate at higher CH_4 amounts. Dubois et al. (2019a) obtained the first measurements of **negative ions** in PAMPRE, detecting among others CN^-, C_2H^- and C_3N^-, in agreement with *in situ* CAPS measurements on Titan. This work enabled to identify new negative ions (e.g. CNN^- and $CHNN^-$) thanks to the higher resolution of the laboratory instrument.
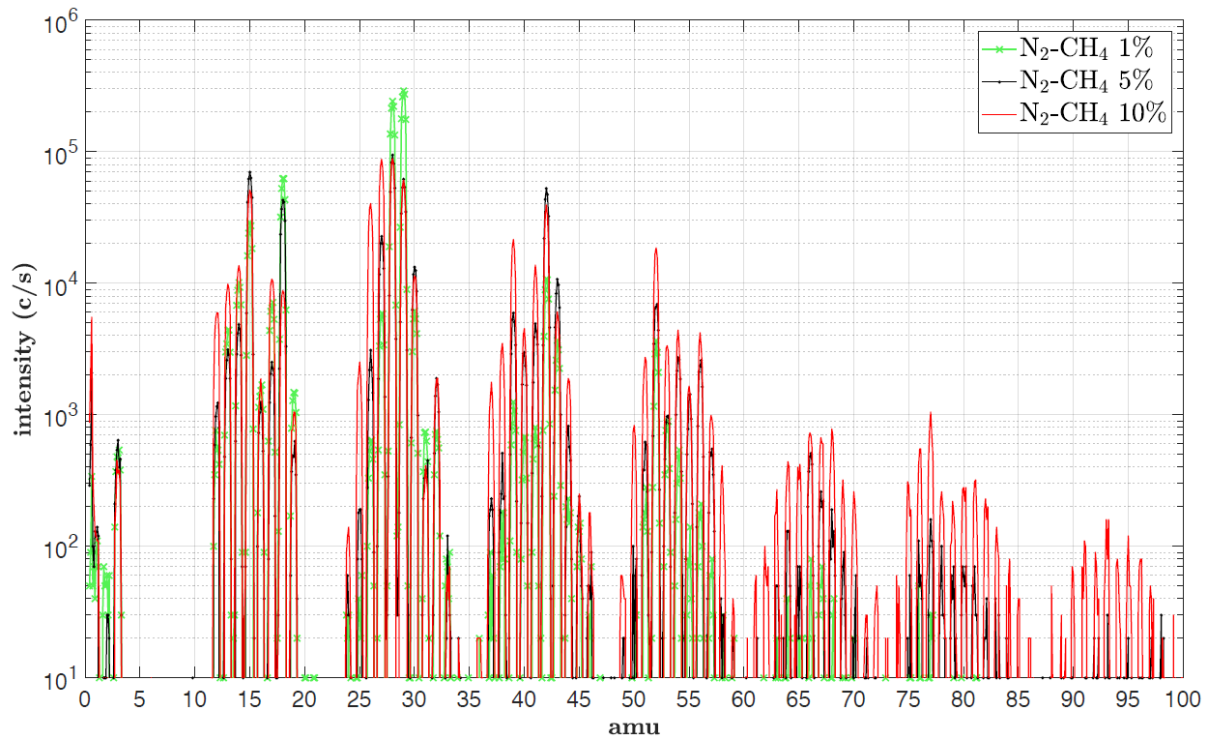
Figure I.4-11: Positive ion mass spectra in PAMPRE in a N_2-CH_4 plasma. (Dubois et al., 2020)

5- Analogues of Titan's aerosols

It is very interesting to study the plasma and the gas phase chemistry in which the aerosols form. The aerosol grains as such are also an important source of information. What do they look like? How to they interact with light? What is their chemical composition? They are the focus of many studies. Analyzing their characteristics gives insights on their history: what are their formation mechanisms? Does their plasma environment affect them during their growth?

5.1- Physical properties of the aerosols

5.1.a. Morphology observed by Scanning Electron Microscopy (SEM)

Tholin grains formed in PAMPRE are spherical with a slightly rough surface. They sometimes gather in aggregates, with bonded grains. The distribution in size depends on the plasma parameters: the gas flux, the plasma power and the gas composition (see **Figure I.5-1**).
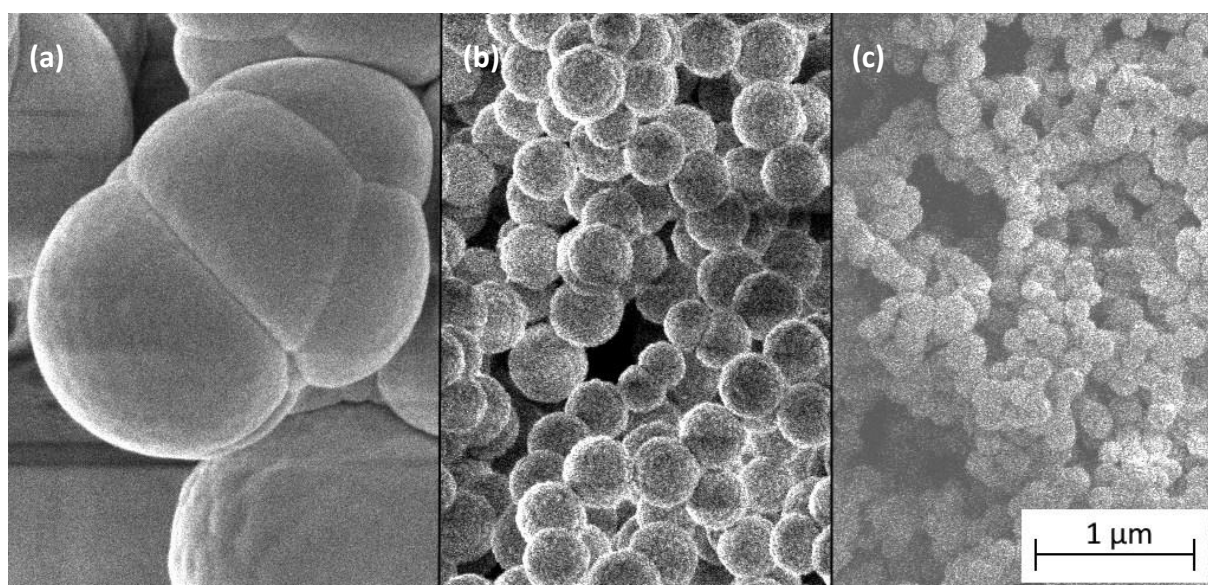
Figure I.5-1: Scanning Electron Microscopy pictures of tholins formed in PAMPRE in a N_2-CH_4 (0.95:0.05) gas mixture at 0.9 mbar. (a) Continuous discharge at 10 sccm. (b) Continuous discharge at 55 sccm. (c) Pulsed discharge (40s on / 60s off) at 55 sccm. Pictures acquired by N. Ruscassier at Centrale-Supélec/LPGM. (Perrin et al., 2019)

Hadamcik et al. (2009) studied grains formed in different conditions. The longer the grains stay in the plasma, the bigger they grow: smaller grains are obtained with higher gas flows and shorter plasma durations. The effect of the discharge power is less important; grains are slightly larger at higher power. The gas composition mainly changes the width of the size distribution: thin for 5% CH_4 (+/- 100 nm) and large for 10% CH_4 (+/- 400 nm). During **pulsed**

discharges, the plasma is ignited only a few 10s of seconds and is then stopped to eject the particles from the confining box. This technique enables to stop the growth of the particles before they reach the limit size that makes them leave the plasma. Different pulse durations have been tested in a N_2-CH_4 (0.98:0.02) gas mixture, from 10 to 110 s. Grains formed with durations > 100-150 s are of the same size as the grains formed in a continuous plasma discharge. This shows that the grains formed in a continuous discharge reach the limit size after 100-150 s and are ejected from the plasma. **Their residence time is then estimated to 100-150 s** in these conditions.

The round grains and aggregates formed in PAMPRE are similar in size and morphology to the photo-chemically produced aerosols of poly-acetylene, poly-ethylene and poly-HCN in various works (Bar-Nun et al., 1988; Clarke and Ferris, 1997; Scattergood et al., 1992) (see **Figure I.4-1**). Coll et al. (1999) also observed similar structures in a DC discharge, (see **Figure I.4-2**).

The aerosol grains formed in these experiments are in a size range **consistent with Cassini data** collected on Titan at ~ 500 km altitude or below. Liang et al. (2007) suspect smaller grains at 1000 km, with sizes ~10-20 nm. As discussed in **Section I.3.2.d**, grains rapidly grow in the upper haze layer at ~500 km, up to grains of 1 μm in average. The coagulation of monomers to form aggregates (as observed in **Figure I.5-1 (a)**) is investigated in most of the growth models. A Scanning Electron Microscope (SEM) picture taken on a cut grain indicates a **radial growth** of the grains in the plasma (see **Figure I.5-2**).
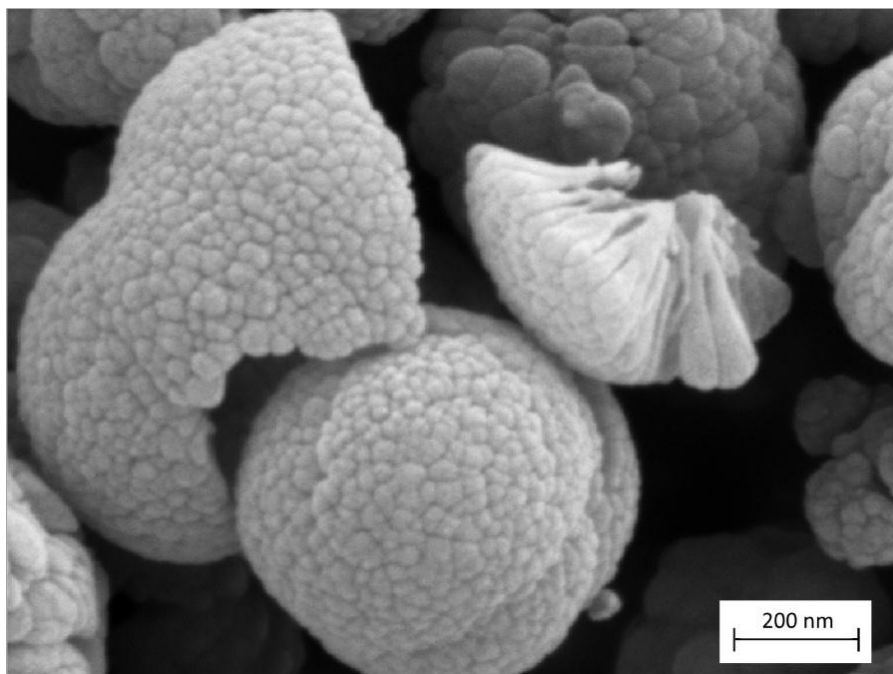
Figure I.5-2: Scanning Electron Microscopy pictures of tholins formed in PAMPRE in a N_2-CH_4 (0.95:0.05) gas mixture at 0.9 mbar (55 sccm). Zoom on a cut grain showing the radical growth of the aerosols (Stephane Borensztajn LISE/CNRS/Sorbonne Univ.).

5.1.b. Light-scattering by the aerosols

Aerosols in suspension in PAMPRE can also be analyzed by light-scattering. A green laser (532 nm) is directed through the PAMPRE chamber during the production of tholins. The confining box and the crystallizer have been removed for the experiment. A photodiode is positioned perpendicularly to the laser beam and measures the reflection of light on the aerosols. Alcouffe et al. (2010) computed the **polarization degree** from these measurements and deduced the particle size based on the **Mie scattering** theory. They found that particles are detectable only if they are larger than 150 nm. **This method cannot study the first steps of the production of the particles**. However, they recorded the evolution of the particle size in time during the later growth (see **Figure I.5-3**).
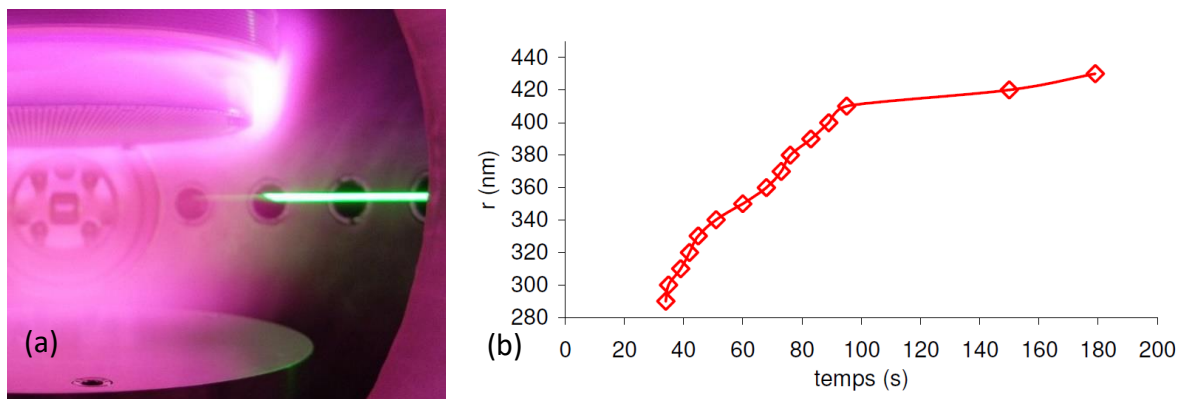
Figure I.5-3: (a) Picture of the reflection of the green laser beam by the aerosols inside PAMPRE. In these conditions, an electrical force expulses the grains form the center. (b) Evolution of the average aerosol radius at the ignition of the discharge (4% CH_4, 1.1 mbar). Estimated from polarization measurements. (Alcouffe PhD thesis, 2010)

Hadamcik et al. (2013, 2009) studied the light-scattering of the PAMPRE tholins thanks to the **PROGRA2** (PROpriétés Optiques des Grains Atmosphériques et Astronomiques) setup, at LPC2E in Orléans (France). Tholin aerosols are lifted with a gas flow (or under micro-gravity during a 0G flight) and are enlightened by lasers at 632.8 nm and 543.5 nm. In the case of 70 nm grains, the measured **phase curve is similar to the ones obtained in Titan's haze** by Pioneer 11 and Voyager 2. Hadamcik et al. (2013, 2009) obtain **agglomerates of hundreds of thousands of grains**, of 40-100 μm. The inconvenient of this technique is that they took the aerosols from a vial, in which the individual grains or small aggregates have certainly gathered into artificially formed bigger agglomerates.

5.1.c. Other physical properties

Growth models, Titan's data analysis and SEM pictures of analogues indicate that Titan's aerosols are certainly fractal particles, aggregates and thus hollow structures. Their mass density is therefore not easily deduced from their mass. Nevertheless, the knowledge of their mass density is fundamental to compute several others physical properties of the aerosols.

Brouet et al. (2016) measured the mass density of tholins formed in PAMPRE with a helium pycnometer. The **solid density was found equal to 1.44** +/- 0.01. The **porosity estimated was 73% and 95%** for compacted and non-compacted samples. Lethuillier et al. (2018) studied the variation of the solid density with the CH_4 amount: they obtained 1.45 at 2% CH_4, 1.44 at 5% and 1.34 at 8%. Imanaka et al. (2012) observed a similar density (1.31) for tholin films formed in a ICP discharge at 1.6 mbar, with 10% CH_4. On Titan, Michael et al. (2011) estimated a bulk density of 1-10 $kg.m^{-3}$, slightly lower than the bulk density obtained on analogues of aerosols in PAMPRE by Brouet et al. (2016), ~70 $kg.m^{-3}$. Experiments by photo-irradiation seem to form tholins at lower density, 0.5-1.15 (Hörst and Tolbert, 2013; Trainer et al., 2006).

Lethuillier et al. (2018) developed an experimental bench to measure the **dielectric permittivity** of tholins. This property is fundamental to interpret the Huygens Mutual Impedance Probe results, to estimate the composition of Titan's surface at the Huygens landing site. They found the permittivity to be strongly varying with temperature (see **Figure I.5-4**). They deduced from this measurement that there should be at most 50-60% of organic dust in the first meter below the surface at the Huygens landing site, with at least 10% of water ice and 15% of porosity.
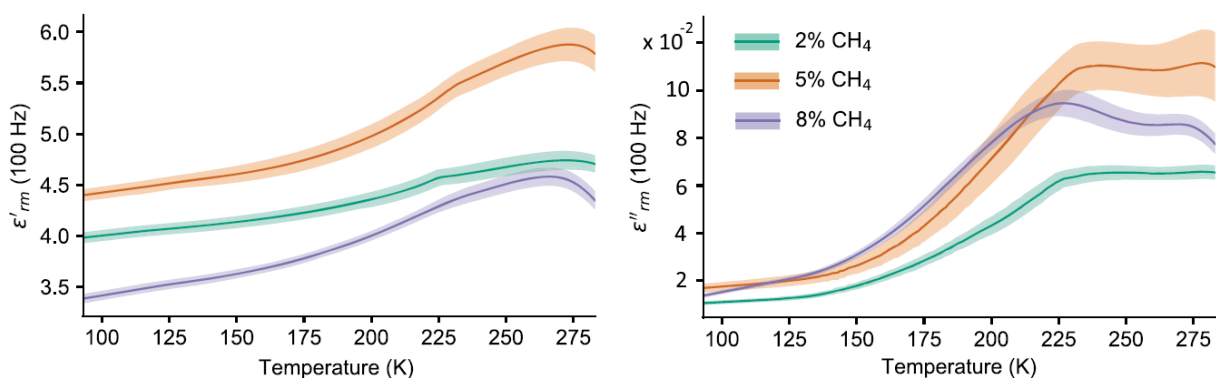
Figure I.5-4: Temperature dependence of the real and imaginary parts of the complex permittivity of bulk tholins obtained for three gas mixture compositions. (Lethuillier et al., 2018)

5.2- Optical constants

Another fundamental characteristic of the aerosols is their optical indexes, which show how they diffuse and absorb the incoming light in all wavelengths. Optical indexes are very useful to analyze Cassini measurements in various wavelengths, to take into account the effects of the aerosols. They are also fundamental for radiative models of the atmosphere of Titan.

In the visible wavelengths, a difference in color is already observed for tholins produced at different methane percentages (see **Figure I.5-5**). Mahjoub et al. (2012) and Sciamma-O'Brien et al. (2012) measured the real and imaginary parts of the **refractive indices by spectroscopic ellipsometry** on thin tholin films. Films are produced on substrates exposed to the N_2-CH_4 plasma. Their characteristics are certainly different from aerosol powders produced in the gas phase (Carrasco et al., 2016). Nevertheless, precise methods used to obtain the refractive

indices cannot be done on powders yet. Results on films are coherent with previous laboratory works and Cassini data for the **real part (n) of the refractive index: a decrease from 1.62-1.68 at 370 nm to 1.49-1.60 at 1000 nm**. They observe a strong variability with the initial methane concentration: n is higher for higher percentages. **The imaginary part (k) decreases more sharply. At 370 nm, k ≈ 0.04-0.15. They observe an exponential decay from 370 to 500 nm, and a plateau at 0.003-0.03 from 500 to 1000 nm**. Again, a variability is observed with the methane concentration. Tholins formed at higher CH_4 amounts have a lower k. These results are consistent with the fact that tholins formed at lower CH_4 percentages are darker. Mahjoub et al. (2014) observed that optical indices of tholins formed at low temperature (~100 K) are slightly lower than indices of tholins formed at 300 K.
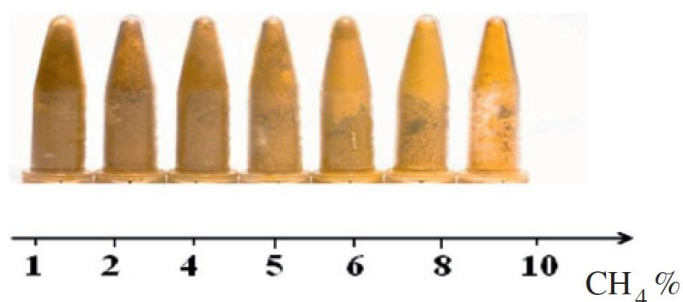
Figure I.5-5: Colors of powder tholins produced at different CH_4 %. (Mahjoub et al., 2012)

In the infrared range, parts of the spectrum of the aerosols on Titan can be deduced from observations (Anderson and Samuelson, 2011; Kim et al., 2011; Vinatier et al., 2012). **Figure I.5-6** compares the spectra obtained on Titan with two laboratory experiments forming tholins. Imanaka et al. (2012) deduced the real and imaginary parts of the refractive index in the mid-infrared (2.5 – 25 μm; 4000 – 400 cm^{-1}).
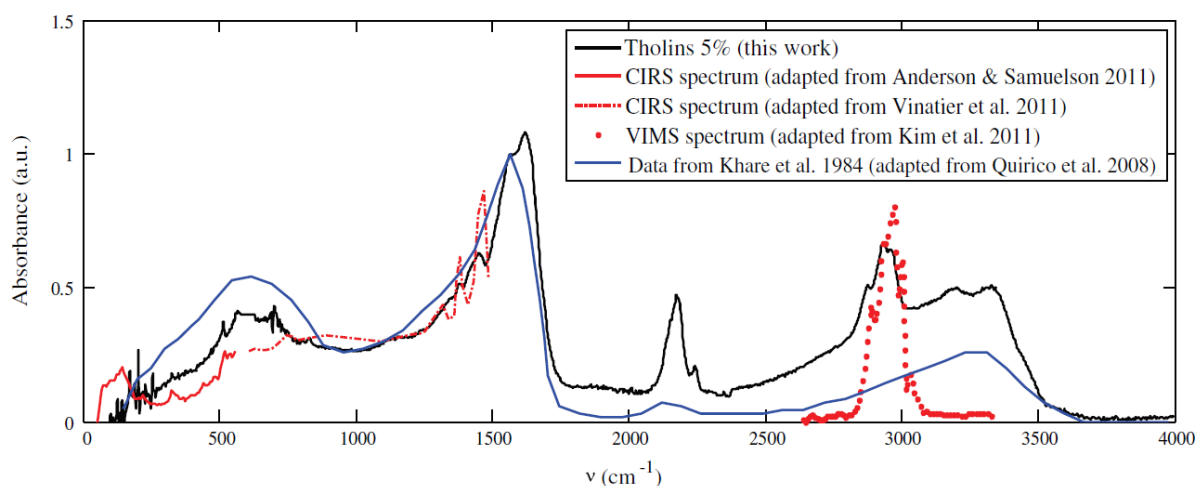
Figure I.5-6: Absorbance spectrum from far-IR to mid-IR of PAMPRE tholins made with 5% of CH_4 (black), compared to another laboratory tholins spectrum (blue), and to Cassini measurements. (Gautier et al., 2012)

In the part of the spectrum between ~1500 and 4000 cm^{-1} (6.7 to 2.5 μm), **absorption bands can easily be attributed to chemical functions**. Attributions are explained and discussed in previous works (Imanaka et al., 2004; Khare et al., 2002; Quirico et al., 2008) and in **Section III.2.2**. Gautier et al. (2012) and Quirico et al. (2008) observe a strong influence of the methane percentage used to produce the tholins on their IR spectrum. In particular, CH bands (around 2900 cm^{-1}) are stronger at high CH$_4$ amounts and nearly inexistent at low CH$_4$ values. Quirico et al. (2008) compared spectra obtained on tholin powder and films. They are some differences, especially concerning the CH bands: films develop stronger CH bands. Mahjoub et al. (2014) studied the effect of temperature on the formation of tholins and observed that tholins formed at low temperature (~100 K) have a lower optical absorption. This absorption decrease is explained by the depletion of nitrogen-containing products in both the gas phase and the tholins. Mathé et al. (2018) investigated the region at 1890-2400 cm^{-1} (5.3-4.1 μm), associated to nitriles and overtones of aromatic CH vibrations. They compared spectra of tholins formed in different mixtures with N_2-CH_4-C_5H_5N (pyridine) and revealed the possibility to detect aromatic signatures on Titan through their overtones in the 1890-2400 cm^{-1} spectral range.

5.3- Chemical analysis

5.3.a. Elementary analysis

A common observation in the elemental analyses of tholins is their high concentration in nitrogen (Imanaka et al., 2004; Szopa et al., 2006). Sciamma-O'Brien et al. (2010) studied the evolution of the molar **percentage of H, C, N and O in the tholins** with the injected CH$_4$ amount. They found that the carbon proportion stays at ~32%. The **hydrogen percentage increases** from 35% (at 1% CH$_4$) to 47% (at 10% CH$_4$), to the opposite of **nitrogen that decreases** from 27% to 15%. It gives a C/N = 1.5 for 4% CH$_4$ injected. Stable ~6% of oxygen are also detected, coming from the superficial oxidation of tholins exposed to air, or the adsorption of water. The composition of tholins varies with the methane concentration. **This certainly induces differences in the aerosols composition at different altitudes in Titan's atmosphere.**

Carrasco et al. (2016) studied tholin films. They showed that films are homogeneous, except for the first 20 nm that are more abundant in oxygen, sign of a surface oxidation or H_2O adsorption. **Films are less nitrogenated and hydrogenated than powders**, with a C/N of 2.8-10 depending on the methane amount. Films stay in the discharge during several hours contrary to aerosol grains that are ejected out of the plasma after 1-2 minutes. The differences observed between films and powders could be partly explained by the **different residence time** of the film and powder tholins in the plasma. Supplementary etching processes could occur on the films.

5.3.b. Pyrolysis – Gas Chromatography / Mass Spectrometry (GCMS)

Pyrolysis coupled to Gas Chromatography / Mass Spectrometry (GCMS) has been performed on Titan. The **Aerosol Collector and Pyrolyser (ACP) onboard Huygens** collected aerosols at two different altitudes during the descent of the probe (130-35 km and 25-20 km). The samples were heated up to 600 °C and gas products were analyzed by GCMS. The two main products were **ammonia (NH_3) and hydrogen cyanide (HCN)**, showing that carbon and nitrogen are present in the core of the aerosols (Israël et al., 2005).

Szopa et al. (2006) analyzed PAMPRE tholins with the same technique. However, in the laboratory they could increase the temperature slowly to observe the degassing of molecules step by step. They could **identify many hydrocarbons and nitrile-bearing species**, and their relative abundances. In particular, they detected aromatic species and aliphatic molecules mostly unsaturated. Their results are coherent with pyrolysis – GCMS done on other tholins formed in plasma discharges (Coll et al., 1999; Khare et al., 1984). Morisson et al. (2016) summarized all the experiments performed on tholins by pyrolysis-GCMS. They investigated in details the results of this technique on PAMPRE tholins, in particular for samples produced at different CH_4 amounts. They observed a larger nitrile amount (in number and abundance) compared to hydrocarbons at lower CH_4 percentage.

5.3.c. High resolution mass spectrometry

High resolution mass spectrometry (HR-MS) gives directly the formula of the compounds analyzed. Tholins are very complex compounds. To analyze them by this technique, a sample of tholins is first gently ionized (by electrospray or Laser Induced Ionization), and the produced ions are measured. High resolution mass spectrometry is in particular used to study petroleum compounds. The analysis of tholins was adapted for nitrogen-rich compounds. By identifying the formula of many molecules of tholins, Pernot et al. (2010) could **observe repetition patterns between the compounds: CH_2, HCN and C_2H_3N are possible growth units**. Gautier et al. (2014) investigated the possibility of a HCN (or CH_3CN) / C_2H_4 based copolymer. HR-MS cannot resolve isomers. To unveil the isomeric ambiguity, Gautier et al. (2016) coupled HR-MS to high performance liquid chromatography (HPLC). With this improvement they could identify seven new molecules, in particular cyanoguanidine (H_2N-NH-NH-CN) and cyclic molecules including at least two nitrogen atoms in the ring.

The studies cited above worked with the soluble fraction of tholins in solvents (mainly methanol). However, only ~35% in mass of the tholin samples are soluble in methanol. Carrasco et al. (2009) observed that pictures by Scanning Electron Microscopy and IR absorption of samples of the total and insoluble fractions were rather similar. Maillard et al. (2018) investigated the differences in their chemical structure thanks to an ionization source that does not require the sample to be liquid. They used a laser desorption / ionization source. They confirmed that the soluble fraction of tholins was a set of polymers with an average formula $(C_2H_3N)_n$. **Concerning the insoluble fraction, they observed a significantly different**

set of polymers, with an average formula of ($C_4H_3N_2$)$_n$ (see **Figure I.5-7**). The insoluble part is consequently less hydrogenated, and is based on different repetition patterns (as C_2H_2).
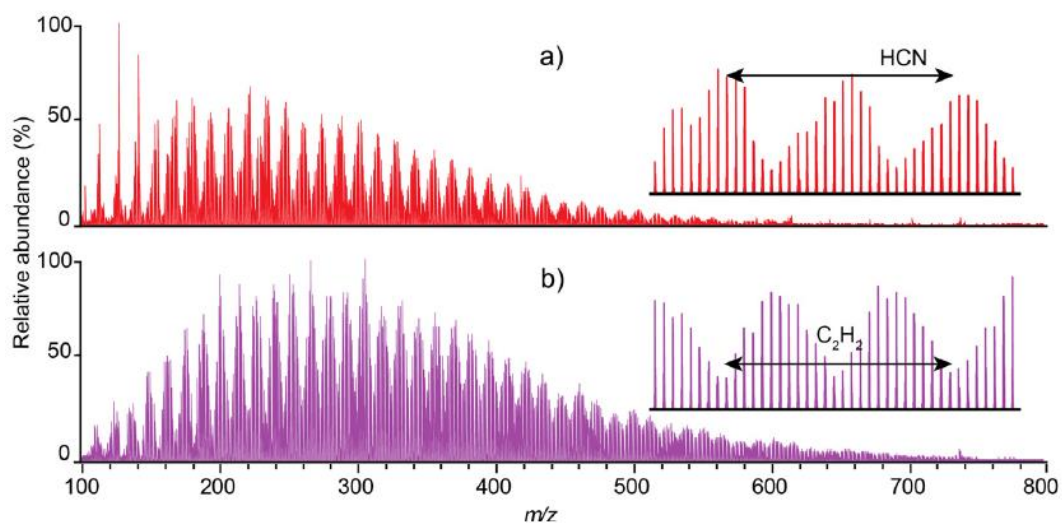
Figure I.5-7: Laser desorption/ionization FTICR MS spectra of (a) the soluble fraction and (b) the non-soluble fraction. (Maillard et al., 2018)

Maillard et al. (2020) used **ion mobility spectrometry** coupled to MS to obtain information on the **size and 3D structures of the detected species**. By comparison with standard molecules, they excluded structures such as pure poly-HCN and pure poly-cyclic aromatic hydrocarbons. **They observed structures containing small aromatics cores connected by short chains.**

6- Evolution of the aerosols in the ionosphere

In conclusion to the introduction section, we can summary that **Titan is a world where the atmosphere and surface are governed by organic aerosols.** Almost all studies concerning Titan imply aerosols. It is then fundamental to know their physical properties and their chemical composition. **A strategy to study these aerosols is to reconstruct their formation pathway**, from the first steps of their formation to their travel through the atmosphere and their sedimentation at the surface. The Cassini mission discovered that the aerosols start forming in the ionosphere of Titan, at ~ 1200 – 1000 km altitude. **The ionosphere of Titan is a plasma**: the neutral molecules N_2, CH_4 and H_2 are ionized by the solar extreme UV photons from the Sun and the energetic particles coming from the magnetosphere of Saturn. It is a highly reactive environment with a complex ion chemistry, **leading to the formation of the organic aerosols.** Laboratory studies can reproduce such a complex ion chemistry in cold plasma reactors, also leading to the formation of orange organic aerosols. Such experiments help to understand the first steps of the complex ion chemistry leading to the formation of the aerosols.

Once they have started to form, the aerosols stay a few weeks in the ionosphere, from about 1200 km to 850 km altitude, before falling to the lower layers of the atmosphere. Aerosols are then likely to evolve during their stay, by exposure to the UV rays, but also by the plasma itself. The study of the evolution of tholins in the ionosphere is only a few years old question and is at the center of the ERC-PRIMCHEM project at LATMOS (2015-2021). Some effects have already been investigated and are presented below.

6.1- Previous works on the erosion of tholins

6.1.a. Thermal degradation

The degradation of tholins by high temperature is not likely to happen on Titan. However, the study of the evolution of tholins with temperature is fundamental to know the impact of the temperature in laboratory conditions.

Several works studied the **thermal degradation of tholins** (Bonnet et al., 2015; He et al., 2015; Nna-Mvondo et al., 2013). They observed no change in the tholins properties below ~150 °C except the desorption of water, sign that the tholins are highly hydrophilic. **At higher temperatures**, other **small molecules are released**, showing that tholins are undergoing an endothermic **decomposition**, breaking some chemical bonds. The main molecules observed are NH_3, HCN, H_3C_2N, CH_4, with a few other hydrocarbons (C_2H_4, C_3H_8), but no cyclic molecules. Finally, for temperatures **above 575°C**, the tholin are structurally changed toward a non-crystalline graphitic residue (the carbon contain increases compared to nitrogen and hydrogen). This last step is called **carbonization**.

In conclusion, no alteration of the tholins are observed below 150°C. This allows the experimental measurements to be performed at ambient temperature. A slight heating can even be performed before a diagnostic to remove the adsorbed water.

6.1.b. UV degradation

Solar UV radiations, and especially far UV (FUV) radiations can affect the organic aerosols in suspension in Titan's atmosphere. In particular, radiations with wavelengths below 100 nm (> 12.4 eV) goes down to 900 km, those between 100 and 150 nm (8.3-12.4 eV) reaches 400 km and those between 150 and 200 nm (6.2-8.3 eV) can penetrate down to < 100 km.

The FUV irradiation is likely to chemically erode the tholins. To investigate this possible erosion, Carrasco et al. (2018) **exposed tholin films to synchrotron irradiations** at 95 nm (~13 eV) and 121.6 nm (Lyman-α, 10.2 eV). They observe a general decrease of the IR absorption bands, sign that the material is eroded during the exposure. **Small modifications** have also been detected on the C-H and N-H bonds, indicating a hydrogen loss of the organic material during the exposure.

Another work focused on the **formation of photo-electrons** from the irradiation of analogues of Titan's aerosols to FUV photons (Tigrine et al., 2018). They observed an **ionization threshold of 6 eV** (207 nm). The kinetic energy of the electrons formed were also analyzed (see **Figure I.5-8**). For an incident photon at 9 eV, they collected photo-electrons at 0.6 eV. This experiment showed that aerosols can be a source of secondary electrons by photo-detachment. It is a lead to investigate the aerosols effects on the ionospheric plasma.
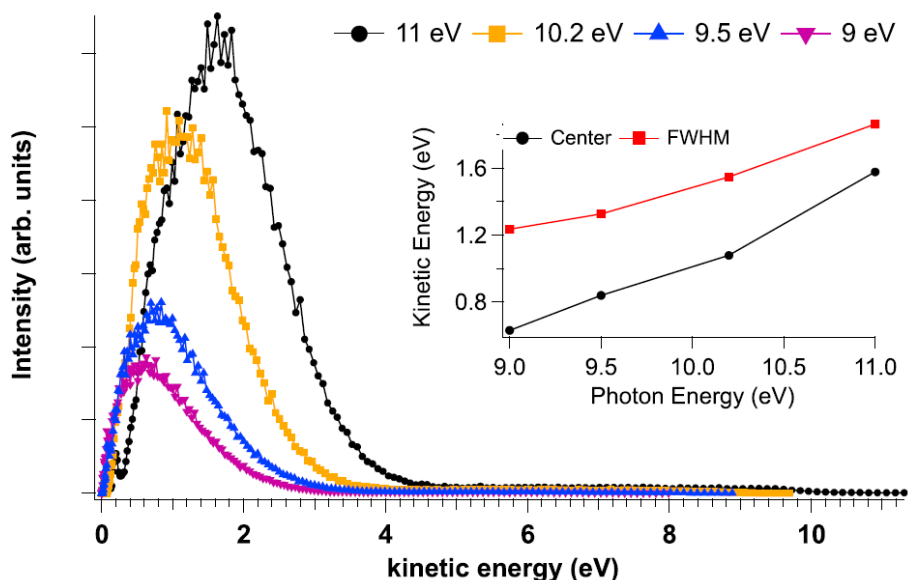
Figure I.5-8: Kinetic energy distributions of the electrons coming from the photoionization of tholins at different photon energies. The area of the curves has been normalized to the total cross sections. The inset shows the evolution of the position of the most probable kinetic energy (center) and full width at half maximum (FWHM) as a function of the photon energy. (Tigrine et al., 2018)

6.2- My thesis question: how do aerosols interact with Titan's ionospheric plasma?

The understanding of the chemical and physical processes happening in the upper atmosphere of Titan and leading to the formation of the aerosols drastically improved since the arrival of the Cassini-Huygens mission. There are today very detailed models reproducing rather well the gas phase chemistry. Microphysical models also investigated the growth of aerosols through the atmosphere. Nevertheless, there is still a step to overcome: what are the chemical processes describing the growth of nanometer-sized aerosols from the heaviest ions formed in the gas phase chemical models? How do the grains interact with their plasma environment? Do they favor interactions with specific species? Which ones? The charged ones? The most reactive ones? How do these interactions process the surface of the grains? Are new species adsorbed? Are some chemical bonds modified? Could the grains give back new species into the gas phase?

Among all these questions, I chose to address two main issues:

(1) Do the plasma species alter the organic aerosols? Recent studies investigated the role of VUV irradiations. But what can be the effect of the various plasma species: electrons, ions, radicals, excited species?

(2) What are the retroactive effects of the organic aerosols on the plasma? Recent studies with VUV showed the possibility of the production of photo-detached electrons from the aerosol grains. Similarly, I expect some possible effects of the aerosols erosion on the surrounding ionospheric plasma.

In this context, my thesis has the objective to study the interaction between the aerosols and the plasma in the ionosphere of Titan.

The processes are complex, and a strategic approach in the laboratory would be to isolate some specific mechanisms. Plasma discharges emits VUV radiations. Therefore, the separate study of the effect of VUV irradiation has been a first important point. Another strategy was to focus on short reaction times, to observe step by step the grains formation and growth (Sciamma-O'Brien et al., 2014). In this PhD work, my strategy has been to simplify the gas composition and prevent the aerosol chemical growth in the presence of methane. I analyzed the effects of the plasma species on tholins using first a pure N_2 plasma and then N_2-H_2 gas mixtures.

Data from Cassini can also bring insights on the interactions between the aerosols and the plasma on Titan. In particular, many instruments were dedicated to the detailed investigation of the ionospheric plasma.

Therefore, to investigate this issue, I had two complementary strategies: (1) the simulation in the laboratory of the dust-plasma interaction, and (2) the analysis of Cassini data to get clues on the disturbance of the ionospheric plasma by the presence of the aerosols.

The results I obtained with laboratory simulation are detailed in the two following chapters. **Chapter II** studies the species present in the plasma and likely able to erode the aerosols, and **Chapter III** analyses the evolution of both the solid and the gas phase by exposure of tholins to the erosive plasma. **Chapter IV** focuses on the analysis of the Langmuir Probe data acquired by Cassini in the ionosphere of Titan, to investigate the interesting variations observed below 1200 km, at the apparition of the aerosols.

HOW DO AEROSOLS INTERACT WITH TITAN'S IONOSPHERIC PLASMA?
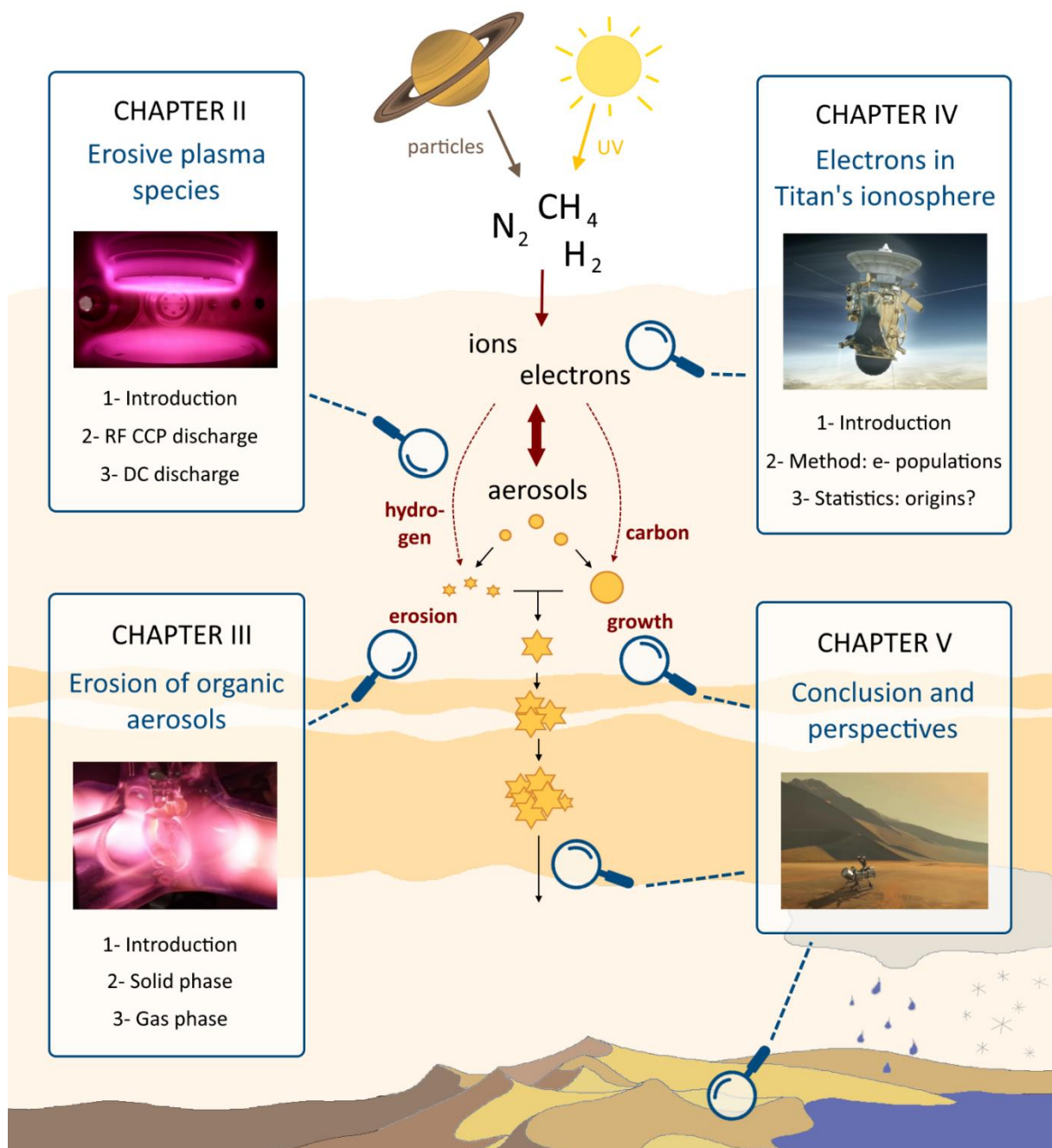
References for Chapter I

Ågren, K., Edberg, N.J.T., Wahlund, J.E., 2012. Detection of negative ions in the deep ionosphere of Titan during the Cassini T70 flyby. Geophys. Res. Lett. 39, L10201. https://doi.org/10.1029/2012GL051714

Ågren, K., Wahlund, J.-E., Garnier, P., Modolo, R., Cui, J., Galand, M., Müller-Wodarg, I., 2009. On the ionospheric structure of Titan. Planet. Space Sci. 57, 1821–1827. https://doi.org/10.1016/J.PSS.2009.04.012

Alcouffe, G., 2010. Production d'equivalents d'aerosols de l'atmosphere de Titan par plasma radio-frequence. PhD thesis, Univ. Versailles Saint Quentin en Yvelines, Fr.

Alcouffe, G., Cavarroc, M., Cernogora, G., Ouni, F., Jolly, A., Boufendi, L., Szopa, C., 2010. Capacitively coupled plasma used to simulate Titan's atmospheric chemistry. Plasma Sources Sci. Technol. 19, 015008. https://doi.org/10.1088/0963-0252/19/1/015008

Alves, L.L., Marques, L., Pintassilgo, C.D., Wattieaux, G., Es-Sebbar, E., Berndt, J., Kovacević, E., Carrasco, N., Boufendi, L., Cernogora, G., 2012. Capacitively coupled radio-frequency discharges in nitrogen at low pressures. Plasma Sources Sci. Technol. 21, 045008. https://doi.org/10.1088/0963-0252/21/4/045008

Anderson, C.M., Samuelson, R.E., 2011. Titan's aerosol and stratospheric ice opacities between 18 and 500 μm: Vertical and spectral characteristics from Cassini CIRS. Icarus 212, 762–778. https://doi.org/10.1016/j.icarus.2011.01.024

Arney, G., Domagal-Goldman, S.D., Meadows, V.S., Wolf, E.T., Schwieterman, E., Charnay, B., Claire, M., Hébrard, E., Trainer, M.G., 2016. The Pale Orange Dot: The Spectrum and Habitability of Hazy Archean Earth. Astrobiology 16, 873–899. https://doi.org/10.1089/ast.2015.1422

Atreya, S.K., Donahue, T.M., Kuhn, W.R., 1978. Evolution of a nitrogen atmosphere on Titan. Science 201, 611–613. https://doi.org/10.1126/science.201.4356.611

Backes, H., Neubauer, F.M., Dougherty, M.K., Achilleos, N., André, N., Arridge, C.S., Bertucci, C., Jones, G.H., Khurana, K.K., Russell, C.T., Wennmacher, A., 2005. Titan's magnetic field signature during the first Cassini encounter. Science 308, 992–995. https://doi.org/10.1126/science.1109763

Bar-Nun, A., Kleinfeld, I., Ganor, E., 1988. Shape and optical properties of aerosols formed by photolysis of acetylene, ethylene, and hydrogen cyanide. J. Geophys. Res. 93, 8383. https://doi.org/10.1029/jd093id07p08383

Bar-nun, A., Podolak, M., 1979. The photochemistry of hydrocarbons in Titan's atmosphere. Icarus 38, 115–122. https://doi.org/10.1016/0019-1035(79)90091-5

Barnes, J.W., Brown, R.H., Soderblom, L., Sotin, C., Le Mouèlic, S., Rodriguez, S., Jaumann, R., Beyer, R.A., Buratti, B.J., Pitman, K., Baines, K.H., Clark, R., Nicholson, P., 2008. Spectroscopy, morphometry, and photoclinometry of Titan's dunefields from Cassini/VIMS. Icarus 195, 400–414. https://doi.org/10.1016/j.icarus.2007.12.006

Bertucci, C., Duru, F., Edberg, N., Fraenz, M., Martinecz, C., Szego, K., Vaisberg, O., 2011. The induced magnetospheres of mars, venus, and titan. Space Sci. Rev. 162, 113–171. https://doi.org/10.1007/s11214-011-9845-1

Bogaerts, A., Neyts, E., Gijbels, R., Van der Mullen, J., 2002. Gas Discharge Plasmas and Their Applications. Spectrochim. Acta Part B 57, 609–658.

Bonnet, J.Y., Quirico, E., Buch, A., Thissen, R., Szopa, C., Carrasco, N., Cernogora, G., Fray, N., Cottin, H., Roy, L. Le, Montagnac, G., Dartois, E., Brunetto, R., Engrand, C., Duprat, J., 2015. Formation of analogs of cometary nitrogen-rich refractory organics from thermal degradation of tholin and HCN polymer. Icarus 250, 53–63. https://doi.org/10.1016/j.icarus.2014.11.006

Bourgalais, J., Carrasco, N., Vettier, L., Gautier, T., Blanchet, V., Petit, S., Fedorov, D.D.N., Delos, R., Gaudin, J., 2019a. An EUV Non-Linear Optics Based Approach to Study the Photochemical Processes of Titan's Atmosphere.

Bourgalais, J., Carrasco, N., Vettier, L., Pernot, P., 2019b. Low-Pressure EUV Photochemical Experiments: Insight on the Ion Chemistry Occurring in Titan's Atmosphere. J. Geophys. Res. Sp. Phys. 124, 9214–9228. https://doi.org/10.1029/2019JA026953

Bourgalais, J., Jamal-Eddine, N., Joalland, B., Capron, M., Balaganesh, M., Guillemin, J.C., Le Picard, S.D., Faure, A., Carles, S., Biennier, L., 2016. Elusive anion growth in Titan's atmosphere: Low temperature kinetics of the C3N- + HC3N reaction. Icarus 271, 194–201. https://doi.org/10.1016/j.icarus.2016.02.003

Brouet, Y., Levasseur-Regourd, A.C., Sabouroux, P., Neves, L., Encrenaz, P., Poch, O., Pommerol, A., Thomas, N., Kofman, W., Le Gall, A., Ciarletti, V., Hérique, A., Lethuillier, A., Carrasco, N., Szopa, C., 2016. A porosity gradient in 67P/C-G nucleus suggested from CONSERT and SESAME-PP results: An interpretation based on new laboratory permittivity measurements of porous icy analogues. Mon. Not. R. Astron. Soc. 462, S89–S98. https://doi.org/10.1093/mnras/stw2151

Brown, R.H., Soderblom, L.A., Soderblom, J.M., Clark, R.N., Jaumann, R., Barnes, J.W., Sotin, C., Buratti, B., Baines, K.H., Nicholson, P.D., 2008. The identification of liquid ethane in Titan's Ontario Lacus. Nature 454, 607–610. https://doi.org/10.1038/nature07100

Cabane, M., Chassefière, E., 1995. Laboratory simulations of Titan's atmosphere: organic gases and aerosols. Planet. Space Sci. 43, 47–65. https://doi.org/10.1016/0032-0633(94)00131-A

Capone, L.A., Whitten, R.C., Dubach, J., Prasad, S.S., Huntress, W.T., 1976. The lower ionosphere of Titan. Icarus 28, 367–378. https://doi.org/10.1016/0019-1035(76)90150-0

Carrasco, N., Alcaraz, C., Dutuit, O., Plessis, S., Thissen, R., Vuitton, V., Yelle, R., Pernot, P., 2008. Sensitivity of a Titan ionospheric model to the ion-molecule reaction parameters. Planet. Space Sci. 56, 1644–1657. https://doi.org/10.1016/j.pss.2008.04.007

Carrasco, N., Gautier, T., Es-sebbar, E. touhami, Pernot, P., Cernogora, G., 2012. Volatile products controlling Titan's tholins production. Icarus 219, 230–240. https://doi.org/10.1016/j.icarus.2012.02.034

Carrasco, N., Giuliani, A., Correia, J.J., Cernogora, G., 2013. VUV photochemistry simulation of planetary upper atmosphere using synchrotron radiation. J. Synchrotron Radiat. 20, 587–589. https://doi.org/10.1107/S0909049513013538

Carrasco, N., Jomard, F., Vigneron, J., Etcheberry, A., Cernogora, G., 2016. Laboratory analogues simulating Titan's atmospheric aerosols: Compared chemical compositions of grains and thin films. Planet. Space Sci. 128, 52–57. https://doi.org/10.1016/j.pss.2016.05.006

Carrasco, N., Schmitz-Afonso, I., Bonnet, J.Y., Quirico, E., Thissen, R., Dutuit, O., Bagag, A., Laprévote, O., Buch, A., Giulani, A., Adandé, G., Ouni, F., Hadamcik, E., Szopa, C., Cernogora, G., 2009. Chemical characterization of titan's tholins: Solubility, morphology and molecular structure revisited. J. Phys. Chem. A 113, 11195–11203. https://doi.org/10.1021/jp904735q

Carrasco, N., Tigrine, S., Gavilan, L., Nahon, L., Gudipati, M.S., 2018. The evolution of Titan's high-altitude aerosols under ultraviolet irradiation. Nat. Astron. 2, 1. https://doi.org/10.1038/s41550-018-0439-7

Chaizy, P., Rème, H., Sauvaud, J.A., D'Uston, C., Lin, R.P., Larson, D.E., Mitchell, D.L., Anderson, K.A., Carlson, C.W., Korth, A., Mendis, D.A., 1991. Negative ions in the coma of comet Halley. Nature 349, 393–396. https://doi.org/10.1038/349393a0

Chang, S., Scattergood, T., Aronowitz, S., Flores, J., 1979. Organic chemistry on Titan. Rev. Geophys. 17, 1923. https://doi.org/10.1029/RG017i008p01923

Charnay, B., Forget, F., Wordsworth, R., Leconte, J., Millour, E., Codron, F., Spiga, A., 2013. Exploring the faint young Sun problem and the possible climates of the Archean Earth with a 3-D GCM. J. Geophys. Res. Atmos. 118, 10,414-10,431. https://doi.org/10.1002/jgrd.50808

Clarke, D.W., Ferris, J.P., 1997. Titan haze: Structure and properties of cyanoacetylene and cyanoacetylene-acetylene photopolymers. Icarus 127, 158–172. https://doi.org/10.1006/icar.1996.5667

Coates, A.J., 2009. Interaction of Titan's ionosphere with Saturn's magnetosphere. Philos. Trans. R. Soc. A Math.

Phys. Eng. Sci. 367, 773–788. https://doi.org/10.1098/rsta.2008.0248

Coates, A.J., Crary, F.J., Lewis, G.R., Young, D.T., Waite, J.J.H., Sittler, J.E.C., 2007a. Discovery of heavy negative ions in Titan's ionosphere. Geophys. Res. Lett. 34, L22103. https://doi.org/10.1029/2007GL030978

Coates, A.J., Crary, F.J., Young, D.T., Szego, K., Arridge, C.S., Bebesi, Z., Sittler, J.C., Hartle, R.E., Hill, T.W., 2007b. Ionospheric electrons in Titan's tail: Plasma structure during the Cassini T9 encounter. Geophys. Res. Lett. 34, L24S05. https://doi.org/10.1029/2007GL030919

Coates, A.J., Jones, G.H., Lewis, G.R., Wellbrock, A., Young, D.T., Crary, F.J., Johnson, R.E., Cassidy, T.A., Hill, T.W., 2010a. Negative ions in the Enceladus plume. Icarus 206, 618–622. https://doi.org/10.1016/j.icarus.2009.07.013

Coates, A.J., Wellbrock, A., Lewis, G.R., Jones, G.H., Young, D.T., Crary, F.J., Waite, J.H., 2009. Heavy negative ions in Titan's ionosphere: Altitude and latitude dependence. Planet. Space Sci. 57, 1866–1871. https://doi.org/10.1016/j.pss.2009.05.009

Coates, A.J., Wellbrock, A., Lewis, G.R., Jones, G.H., Young, D.T., Crary, F.J., Waite, J.H., Johnson, R.E., Hill, T.W., Sittler, E.C., 2010b. Negative ions at Titan and Enceladus: Recent results. Faraday Discuss. 147, 293–305. https://doi.org/10.1039/c004700g

Coll, P., Coscia, D., Smith, N., Gazeau, M.C., Ramírez, S.I., Cernogora, G., Israël, G., Raulin, F., 1999. Experimental laboratory simulation of Titan's atmosphere: Aerosols and gas phase. Planet. Space Sci. 47, 1331–1340. https://doi.org/10.1016/s0032-0633(99)00054-9

Cordier, D., Carrasco, N., 2019. The floatability of aerosols and wave damping on Titan's seas. Nat. Geosci. 12, 315–320. https://doi.org/10.1038/s41561-019-0344-4

Courtin, R., 2005. Aerosols on the Giant Planets and Titan. Space Sci. Rev. 116, 185–199. https://doi.org/10.1007/s11214-005-1955-1

Coustenis, A., Salama, A., Schulz, B., Ott, S., Lellouch, E., Encrenaz, T., Gautier, D., Feuchtgruber, H., 2003. Titan's atmosphere from ISO mid-infrared spectroscopy. Icarus 161, 383–403. https://doi.org/10.1016/S0019-1035(02)00028-3

Crary, F.J., Magee, B.A., Mandt, K., Waite, J.H., Westlake, J., Young, D.T., 2009. Heavy ions, temperatures and winds in Titan's ionosphere: Combined Cassini CAPS and INMS observations. Planet. Space Sci. 57, 1847–1856. https://doi.org/10.1016/j.pss.2009.09.006

Cravens, T.E., Robertson, I.P., Ledvina, S.A., Mitchell, D., Krimigis, S.M., Waite, J.H., 2008. Energetic ion precipitation at Titan. Geophys. Res. Lett. 35, L03103. https://doi.org/10.1029/2007GL032451

Cravens, T.E., Robertson, I.P., Waite, J.H., Yelle, R. V., Kasprzak, W.T., Keller, C.N., Ledvina, S.A., Niemann, H.B., Luhmann, J.G., McNutt, R.L., Ip, W.H., De La Haye, V., Mueller-Wodarg, I., Wahlund, J.E., Anicich, V.G., Vuitton, V., 2006. Composition of Titan's ionosphere. Geophys. Res. Lett. 33, L07105. https://doi.org/10.1029/2005GL025575

Cravens, T.E., Robertson, I.P., Waite, J.H., Yelle, R. V., Vuitton, V., Coates, A.J., Wahlund, J.E., Ågren, K., Richard, M.S., De La Haye, V., Wellbrock, A., Neubauer, F.M., 2009. Model-data comparisons for Titan's nightside ionosphere. Icarus 199, 174–188. https://doi.org/10.1016/j.icarus.2008.09.005

Cravens, T.E., Vann, J., Clark, J., Yu, J., Keller, C.N., Brull, C., 2004. The ionosphere of Titan: An updated theoretical model. Adv. Sp. Res. 33, 212–215. https://doi.org/10.1016/j.asr.2003.02.012

Cui, J., Galand, M., Yelle, R. V., Vuitton, V., Wahlund, J.E., Lawas, P.P., Müller-Wodarg, I.C.F., Cravens, T.E., Kasprzak, W.T., Waite, J.H., 2009a. Diurnal variations of Titan's ionosphere. J. Geophys. Res. Sp. Phys. 114, A06310. https://doi.org/10.1029/2009JA014228

Cui, J., Yelle, R. V., Vuitton, V., Waite, J.H., Kasprzak, W.T., Gell, D.A., Niemann, H.B., Müller-Wodarg, I.C.F., Borggren, N., Fletcher, G.G., Patrick, E.L., Raaen, E., Magee, B.A., 2009b. Analysis of Titan's neutral upper atmosphere from Cassini Ion Neutral Mass Spectrometer measurements. Icarus 200, 581–615. https://doi.org/10.1016/j.icarus.2008.12.005

Danielson, R.E., Caldwell, J.J., Larach, D.R., 1973. An inversion in the atmosphere of Titan. Icarus 20, 437–443. https://doi.org/10.1016/0019-1035(73)90016-X

De La Haye, V., Waite, J.H., Cravens, T.E., Robertson, I.P., Lebonnois, S., 2008. Coupled ion and neutral rotating model of Titan's upper atmosphere. Icarus 197, 110–136. https://doi.org/10.1016/j.icarus.2008.03.022

de Vanssay, E., Gazeau, M.C., Guillemin, J.C., Raulin, F., 1995. Experimental simulation of Titan's organic chemistry at low temperature. Planet. Space Sci. 43, 25–31. https://doi.org/10.1016/0032-0633(94)00146-I

Dobrijevic, M., Loison, J.C., Hickson, K.M., Gronoff, G., 2016. 1D-coupled photochemical model of neutrals, cations and anions in the atmosphere of Titan. Icarus 268, 313–339. https://doi.org/10.1016/j.icarus.2015.12.045

Dodonova, N.Y., 1966. Activation of nitrogen by vacuum ultraviolet radiation. Russ. J. Phys. Chem. 40, 523.

Dubois, D., Carrasco, N., Bourgalais, J., Vettier, L., Desai, R.T., Wellbrock, A., Coates, A.J., 2019a. Nitrogen-containing Anions and Tholin Growth in Titan's Ionosphere: Implications for Cassini CAPS-ELS Observations. Astrophys. J. 872, L31. https://doi.org/10.3847/2041-8213/ab05e5

Dubois, D., Carrasco, N., Jovanovic, L., Vettier, L., Gautier, T., Westlake, J., 2020. Positive ion chemistry in an N_2-CH_4 plasma discharge: Key precursors to the growth of Titan tholins. Icarus 338. https://doi.org/10.1016/j.icarus.2019.113437

Dubois, D., Carrasco, N., Petrucciani, M., Vettier, L., Tigrine, S., Pernot, P., 2019b. In situ investigation of neutrals involved in the formation of Titan tholins. Icarus 317, 182–196. https://doi.org/10.1016/j.icarus.2018.07.006

Edberg, N.J.T., Andrews, D.J., Bertucci, C., Gurnett, D.A., Holmberg, M.K.G., Jackman, C.M., Kurth, W.S., Menietti, J.D., Opgenoorth, H.J., Shebanits, O., Vigren, E., Wahlund, J.-E., 2015. Effects of Saturn's magnetospheric dynamics on Titan's ionosphere. J. Geophys. Res. Sp. Phys. 120, 8884–8898. https://doi.org/10.1002/2015JA021373

Edberg, N.J.T., Andrews, D.J., Shebanits, O., Ågren, K., Wahlund, J.E., Opgenoorth, H.J., Cravens, T.E., Girazian, Z., 2013. Solar cycle modulation of Titan's ionosphere. J. Geophys. Res. Sp. Phys. 118, 5255–5264. https://doi.org/10.1002/jgra.50463

Es-Sebbar, E.T., Bénilan, Y., Fray, N., Cottin, H., Jolly, A., Gazeau, M.C., 2015. Optimization of a solar simulator for planetary-photochemical studies. Astrophys. Journal, Suppl. Ser. 218, 19. https://doi.org/10.1088/0067-0049/218/2/19

Flasar, F.M., Achterberg, R.K., Conrath, B.J., Gierasch, P.J., Kunde, V.G., Nixon, C.A., Bjoraker, G.L., Jennings, D.E., Romani, P.N., Simon-Miller, A.A., Bézard, B., Coustenis, A., Irwin, P.G.J., Teanby, N.A., Brasunas, J., Pearl, J.C., Segura, M.E., Carlson, R.C., Mamoutkine, A., Schinder, P.J., Barucci, A., Courtin, R., Fouchet, T., Gautier, D., Lellouch, E., Marten, A., Prangé, R., Vinatier, S., Strobel, D.F., Calcutt, S.B., Read, P.L., Taylor, F.W., Bowles, N., Samuelson, R.E., Orton, G.S., Spilker, L.J., Owen, T.C., Spencer, J.R., Showalter, M.R., Ferrari, C., Abbas, M.M., Raulin, F., Edgington, S., Ade, P., Wishnow, E.H., 2005. Titan's atmospheric temperatures, winds, and composition. Science 308, 975–978. https://doi.org/10.1126/science.1111150

Fulchignoni, M., Ferri, F., Angrilli, F., Ball, A.J., Bar-Nun, A., Barucci, M.A., Bettanini, C., Bianchini, G., Borucki, W., Colombatti, G., Coradini, M., Coustenis, A., Debei, S., Falkner, P., Fanti, G., Flamini, E., Gaborit, V., Grard, R., Hamelin, M., Harri, A.M., Hathi, B., Jernej, I., Leese, M.R., Lehto, A., Lion Stoppato, P.F., López-Moreno, J.J., Mäkinen, T., McDonnell, J.A.M., McKay, C.P., Molina-Cuberos, G., Neubauer, F.M., Pirronello, V., Rodrigo, R., Saggin, B., Schwingenschuh, K., Seiff, A., Simões, F., Svedhem, H., Tokano, T., Towner, M.C., Trautner, R., Withers, P., Zarnecki, J.C., 2005. In situ measurements of the physical characteristics of Titan's environment. Nature 438, 785–791. https://doi.org/10.1038/nature04314

Gautier, T., Carrasco, N., Buch, A., Szopa, C., Sciamma-O'brien, E., Cernogora, G., 2011. Nitrile gas chemistry in Titan atmosphere. Icarus 213, 625. https://doi.org/10.1016/j.icarus.2011.04.005ï

Gautier, T., Carrasco, N., Mahjoub, A., Vinatier, S., Giuliani, A., Szopa, C., Anderson, C.M., Correia, J.J., Dumas, P., Cernogora, G., 2012. Mid- and far-infrared absorption spectroscopy of Titan's aerosols analogues. Icarus

221, 320–327. https://doi.org/10.1016/j.icarus.2012.07.025

Gautier, T., Carrasco, N., Stefanovic, I., Sikimic, B., Cernogora, G., Winter, J., 2014. Methane conversion in a N2-CH4 radiofrequency discharge. Plasma Process. Polym. 11, 472–481. https://doi.org/10.1002/ppap.201300158

Gautier, T., Schmitz-Afonso, I., Touboul, D., Szopa, C., Buch, A., Carrasco, N., 2016. Development of HPLC-Orbitrap method for identification of N-bearing molecules in complex organic material relevant to planetary environments. Icarus 275, 259–266. https://doi.org/10.1016/j.icarus.2016.03.007

Gautier, T., Sebree, J.A., Li, X., Pinnick, V.T., Grubisic, A., Loeffler, M.J., Getty, S.A., Trainer, M.G., Brinckerhoff, W.B., 2017. Influence of trace aromatics on the chemical growth mechanisms of Titan aerosol analogues. Planet. Space Sci. 140, 27–34. https://doi.org/10.1016/j.pss.2017.03.012

Gillett, F.C., 1975. Further observations of the 8-13 micron spectrum of Titan. Astrophys. J. 201, L41. https://doi.org/10.1086/181937

Glein, C.R., Shock, E.L., 2013. A geochemical model of non-ideal solutions in the methane-ethane-propane-nitrogen-acetylene system on Titan. Geochim. Cosmochim. Acta 115, 217–240. https://doi.org/10.1016/j.gca.2013.03.030

Grard, R., Hamelin, M., López-Moreno, J.J., Schwingenschuh, K., Jernej, I., Molina-Cuberos, G.J., Simões, F., Trautner, R., Falkner, P., Ferri, F., Fulchignoni, M., Rodrigo, R., Svedhem, H., Béghin, C., Berthelier, J.J., Brown, V.J.G., Chabassière, M., Jeronimo, J.M., Lara, L.M., Tokano, T., 2006. Electric properties and related physical characteristics of the atmosphere and surface of Titan. Planet. Space Sci. 54, 1124–1136. https://doi.org/10.1016/j.pss.2006.05.036

Gronoff, G., Lilensten, J., Desorgher, L., Flückiger, E., 2009a. Ionization processes in the atmosphere of Titan - I. Ionization in the whole atmosphere. Astron. Astrophys. 506, 955–964. https://doi.org/10.1051/0004-6361/200912371

Gronoff, G., Lilensten, J., Modolo, R., 2009b. Ionization processes in the atmosphere of Titan II. Electron precipitation along magnetic field lines. Astron. Astrophys. 506, 965–970. https://doi.org/10.1051/0004-6361/200912125

Gronoff, G., Mertens, C., Lilensten, J., Desorgher, L., Flückiger, E., Velinov, P., 2011. Ionization processes in the atmosphere of Titan-III. Ionization by high-Z nuclei cosmic rays. Astron. Astrophys. 529, A143. https://doi.org/10.1051/0004-6361/201015675

Guerlet, S., Fouchet, T., Vinatier, S., Simon, A.A., Dartois, E., Spiga, A., 2015. Stratospheric benzene and hydrocarbon aerosols detected in Saturn's auroral regions. Astron. Astrophys. 580, A89. https://doi.org/10.1051/0004-6361/201424745

Gurnett, D.A., Kurth, W.S., Hospodarsky, C.B., Persoon, A.M., Averkamp, T.F., Cecconi, B., Lecacheux, A., Zarka, P., Canu, P., Cornilleau-Wehrlin, N., Galopeau, P., Roux, A., Harvey, C., Louarn, P., Bostrom, U., Gustafsson, G., Wahlund, J.E., Desch, M.D., Farrell, W.M., Kaiser, M.L., Goetz, K., Kellogg, P.J., Fischer, G., Ladreiter, H.P., Rucker, H., Alleyne, H., Pedersen, A., 2005. Radio and plasma wave obervations at Saturn from Cassini's approach and first orbit. Science 307, 1255–1259. https://doi.org/10.1126/science.1105356

Gurnett, D.A., Kurth, W.S., Kirchner, D.L., Hospodarsky, G.B., Averkamp, T.F., Zarka, P., Lecacheux, A., Manning, R., Roux, A., Canu, P., Cornilleau-Wehrlin, N., Galopeau, P., Meyer, A., Boström, R., Gustafsson, G., Wahlund, J.-E., Åhlen, L., Rucker, H.O., Ladreiter, H.P., Macher, W., Woolliscroft, L.J.C., Alleyne, H., Kaiser, M.L., Desch, M.D., Farrell, W.M., Harvey, C.C., Louarn, P., Kellogg, P.J., Goetz, K., Pedersen, A., 2004. The Cassini Radio and Plasma Wave Investigation, in: The Cassini-Huygens Mission. Springer Netherlands, pp. 395–463. https://doi.org/10.1007/978-1-4020-2774-1_6

Hadamcik, E., Renard, J.B., Alcouffe, G., Cernogora, G., Levasseur-Regourd, A.C., Szopa, C., 2009. Laboratory light-scattering measurements with Titan's aerosols analogues produced by a dusty plasma. Planet. Space Sci. 57, 1631–1641. https://doi.org/10.1016/j.pss.2009.06.013

Hadamcik, E., Renard, J.B., Mahjoub, A., Gautier, T., Carrasco, N., Cemogora, G., Szopa, C., 2013. Optical properties of analogs of Titan's aerosols produced by dusty plasma. Earth, Planets Sp. 65, 1175–1184.

https://doi.org/10.5047/eps.2013.05.019

Hadavandkhani, S., Nikouravan, B., Ghazimaghrebi, F., 2016. Artificial aurora and ionospheric heating by HAARP. Adv. Appl. Phys. 4, 23–30. https://doi.org/10.12988/aap.2016.667

Hamelin, M., Béghin, C., Grard, R., López-Moreno, J.J., Schwingenschuh, K., Simões, F., Trautner, R., Berthelier, J.J., Brown, V.J.G., Chabassière, M., Falkner, P., Ferri, F., Fulchignoni, M., Jernej, I., Jeronimo, J.M., Molina-Cuberos, G.J., Rodrigo, R., Tokano, T., 2007. Electron conductivity and density profiles derived from the mutual impedance probe measurements performed during the descent of Huygens through the atmosphere of Titan. Planet. Space Sci. 55, 1964–1977. https://doi.org/10.1016/j.pss.2007.04.008

Hanel, R., Conrath, B., Flasar, F.M., Kunde, V., Maguire, W., Pearl, J., Pirraglia, J., Samuelson, R., Herath, L., Allison, M., Cruikshank, D., Gautier, D., Gierasch, P., Horn, L., Koppany, R., Ponnamperuma, C., 1981. Infrared observations of the Saturnian system from voyager 1. Science 212, 192–200. https://doi.org/10.1126/science.212.4491.192

Hanel, R., Conrath, B., Plasar, F.M., Kunde, V., Maguire, W., Pearl, J., Pirraglia, J., Samuelson, R., Cruikshank, D., Gautier, D., Gierasch, P., Horn, L., Ponnamperuma, C., 1982. Infrared observations of the Saturnian system from Voyager 2. Science 215, 544–548. https://doi.org/10.1126/science.215.4532.544

Haqq-Misra, J.D., Domagal-Goldman, S.D., Kasting, P.J., Kasting, J.F., 2008. A revised, hazy methane greenhouse for the Archean Earth. Astrobiology 8, 1127–1137. https://doi.org/10.1089/ast.2007.0197

Hargis, P.J., Greenberg, K.E., Miller, P.A., Gerardo, J.B., Torczynski, J.R., Riley, M.E., Hebner, G.A., Roberts, J.R., Olthoff, J.K., Whetstone, J.R., Van Brunt, R.J., Sobolewski, M.A., Anderson, H.M., Splichal, M.P., Mock, J.L., Bletzinger, P., Garscadden, A., Gottscho, R.A., Selwyn, G., Dalvie, M., Heidenreich, J.E., Butterbaugh, J.W., Brake, M.L., Passow, M.L., Pender, J., Lujan, A., Elta, M.E., Graves, D.B., Sawin, H.H., Kushner, M.J., Verdeyen, J.T., Horwath, R., Turner, T.R., 1994. The Gaseous Electronics Conference radio-frequency reference cell: A defined parallel-plate radio-frequency system for experimental and theoretical studies of plasma-processing discharges. Rev. Sci. Instrum. 65, 140–154. https://doi.org/10.1063/1.1144770

Hargreaves, J., 1992. The solar-terrestrial environment: an introduction to geospaceSthe science of the terrestrial upper atmosphere, ionosphere and magnetosphere, Cambridge university press. https://doi.org/10.5860/choice.31-0283

Havnes, O., Trøim, J., Blix, T., Mortensen, W., Naesheim, L.I., Thrane, E., Tønnesen, T., 1996. First detection of charged dust particles in the Earth's mesosphere. J. Geophys. Res. Sp. Phys. 101, 10839–10847. https://doi.org/10.1029/96ja00003

Hayes, A.G., 2016. The Lakes and Seas of Titan. Annu. Rev. Earth Planet. Sci. 44, 57–83. https://doi.org/10.1146/annurev-earth-060115-012247

Hayes, A.G., Lorenz, R.D., Lunine, J.I., 2018. A post-Cassini view of Titan's methane-based hydrologic cycle. Nat. Geosci. https://doi.org/10.1038/s41561-018-0103-y

He, J., Buch, A., Carrasco, N., Szopa, C., 2015. Thermal degradation of organics for pyrolysis in space: Titan's atmospheric aerosol case study. Icarus 248, 205–212. https://doi.org/10.1016/j.icarus.2014.10.010

Hong, P., Sekine, Y., Sasamori, T., Sugita, S., 2018. Experimental study of heterogeneous organic chemistry induced by far ultraviolet light: Implications for growth of organic aerosols by CH_3 addition in the atmospheres of Titan and early Earth. Icarus 307, 25–39. https://doi.org/10.1016/j.icarus.2018.02.019

Hörst, S.M., Tolbert, M.A., 2013. In situ measurements of the size and density of titan aerosol analogs. Astrophys. J. Lett. 770. https://doi.org/10.1088/2041-8205/770/1/L10

Hörst, S.M., Yoon, Y.H., Ugelow, M.S., Parker, A.H., Li, R., de Gouw, J.A., Tolbert, M.A., 2018. Laboratory investigations of Titan haze formation: In situ measurement of gas and particle composition. Icarus 301, 136–151. https://doi.org/10.1016/j.icarus.2017.09.039

Hunten, D.M., 1978. A Titan atmosphere with a surface temperature of 200K. JPL Saturn Syst. 127–140.

Imanaka, H., Cruikshank, D.P., Khare, B.N., McKay, C.P., 2012. Optical constants of Titan tholins at mid-infrared

wavelengths (2.5-25 μm) and the possible chemical nature of Titan's haze particles. Icarus 218, 247–261. https://doi.org/10.1016/j.icarus.2011.11.018

Imanaka, H., Khare, B.N., Elsila, J.E., Bakes, E.L.O., McKay, C.P., Cruikshank, D.P., Sugita, S., Matsui, T., Zare, R.N., 2004. Laboratory experiments of Titan tholin formed in cold plasma at various pressures: Implications for nitrogen-containing polycyclic aromatic compounds in Titan haze. Icarus 168, 344–366. https://doi.org/10.1016/j.icarus.2003.12.014

Imanaka, H., Smith, M.A., 2010. Formation of nitrogenated organic aerosols in the Titan upper atmosphere. Proc. Natl. Acad. Sci. U. S. A. 107, 12423–12428. https://doi.org/10.1073/pnas.0913353107

Imanaka, H., Smith, M.A., 2007. Role of photoionization in the formation of complex organic molecules in Titan's upper atmosphere. Geophys. Res. Lett. 34, L02204. https://doi.org/10.1029/2006GL028317

Israël, G., Szopa, C., Raulin, F., Cabane, M., Niemann, H.B., Atreya, S.K., Bauer, S.J., Brun, J.F., Chassefière, E., Coll, P., Condé, E., Coscia, D., Hauchecorne, A., Millian, P., Nguyen, M.J., Owen, T., Riedler, W., Samuelson, R.E., Siguier, J.M., Steller, M., Sternberg, R., Vidal-Madjar, C., 2005. Complex organic matter in Titan's atmospheric aerosols from in situ pyrolysis and analysis. Nature 438, 796–799. https://doi.org/10.1038/nature04349

Jacobson, M.C., Hansson, H.-C., Noone, K.J., Charlson, R.J., 2000. Organic atmospheric aerosols: Review and state of the science. Rev. Geophys. 38, 267–294. https://doi.org/10.1029/1998RG000045

Kasprzak, W., Niemann, H., Harpold, D., Richards, J., Manning, H.L., Patrick, E., Mahaffy, P., 1996. Cassini orbiter ion and neutral mass spectrometer instrument, in: Cassini/Huygens: A Mission to the Saturnian Systems. International Society for Optics and Photonics., pp. 129–140.

Kasting, J.F., 2005. Methane and climate during the Precambrian era. Precambrian Res. 137, 119–129. https://doi.org/10.1016/j.precamres.2005.03.002

Keller, C.N., Cravens, T.E., Gan, L., 1992. A model of the ionosphere of Titan. J. Geophys. Res. 97, 12117. https://doi.org/10.1029/92ja00231

Khare, B.N., Bakes, E.L.O., Imanaka, H., McKay, C.P., Cruikshank, D.P., Arakawa, E.T., 2002. Analysis of the time-dependent chemical evolution of Titan Haze tholin. Icarus 160, 172–182. https://doi.org/10.1006/icar.2002.6899

Khare, B.N., Sagan, C., 1973. Red clouds in reducing atmospheres. Icarus 20, 311–321. https://doi.org/10.1016/0019-1035(73)90008-0

Khare, B.N., Sagan, C., Thompson, W.R., Arakawa, E.T., Meisse, C., Tuminello, P.S., 1994. Optical properties of poly-HCN and their astronomical applications. Can. J. Chem. 72, 678–694. https://doi.org/10.1139/v94-093

Khare, B.N., Sagan, C., Thompson, W.R., Arakawa, E.T., Suits, F., Callcott, T.A., Williams, M.W., Shrader, S., Ogino, H., Willingham, T.O., Nagy, B., 1984. The organic aerosols of Titan. Adv. Sp. Res. 4, 59–68. https://doi.org/10.1016/0273-1177(84)90545-3

Kharecha, P., Kasting, J., Siefert, J., 2005. A coupled atmosphere-ecosystem model of the early Archean earth. Geobiology 3, 53–76. https://doi.org/10.1111/j.1472-4669.2005.00049.x

Kim, S.J., Jung, A., Sim, C.K., Courtin, R., Bellucci, A., Sicardy, B., Song, I.O., Minh, Y.C., 2011. Retrieval and tentative indentification of the 3 μm spectral feature in Titans haze. Planet. Space Sci. 59, 699–704. https://doi.org/10.1016/j.pss.2011.02.002

Kliore, A.J., Nagy, A.F., Marouf, E.A., French, R.G., Flasar, F.M., Rappaport, N.J., Anabttawi, A., Asmar, S.W., Kahann, D.S., Barbinis, E., Goltz, G.L., Fleischman, D.U., Rochblatt, D.J., 2008. First results from the Cassini radio occultations of the Titan ionosphere. J. Geophys. Res. Sp. Phys. 113, n/a-n/a. https://doi.org/10.1029/2007JA012965

Krimigis, S.M., Mitchell, D.G., Hamilton, D.C., Livi, S., Dandouras, J., Jaskulek, S., Armstrong, T.P., Boldt, J.D., Cheng, A.F., Gloeckler, G., Hayes, J.R., Hsieh, K.C., Ip, W.-H., Keath, E.P., Kirsch, E., Krupp, N., Lanzerotti, L.J., Lundgren, R., Mauk, B.H., McEntire, R.W., Roelof, E.C., Schlemm, C.E., Tossman, B.E., Wilken, B.,

Williams, D.J., 2004. Magnetosphere Imaging Instrument (MIMI) on the Cassini Mission to Saturn/Titan, in: The Cassini-Huygens Mission. Springer Netherlands, pp. 233–329. https://doi.org/10.1007/978-1-4020-2774-1_3

Kunde, V.G., Aikin, A.C., Hanel, R.A., Jennings, D.E., Maguire, W.C., Samuelson, R.E., 1981. C4H2, HC3N and C2N2 in Titan's atmosphere. Nature 292, 686–688. https://doi.org/10.1038/292686a0

Larson, E.J., Toon, O.B., West, R.A., Friedson, A.J., 2015. Microphysical modeling of Titan's detached haze layer in a 3D GCM. Icarus 254, 122–134.

Lavvas, P., Galand, M., Yelle, R. V., Heays, A.N., Lewis, B.R., Lewis, G.R., Coates, A.J., 2011a. Energy deposition and primary chemical products in Titan's upper atmosphere. Icarus 213, 233–251. https://doi.org/10.1016/j.icarus.2011.03.001

Lavvas, P., Sander, M., Kraft, M., Imanaka, H., 2011b. Surface chemistry and particle shape: Processes for the evolution of aerosols in Titan's atmosphere. Astrophys. J. 728. https://doi.org/10.1088/0004-637X/728/2/80

Lavvas, P., Yelle, R. V., Griffith, C.A., 2010. Titan's vertical aerosol structure at the Huygens landing site: Constraints on particle size, density, charge, and refractive index. Icarus 210, 832–842. https://doi.org/10.1016/j.icarus.2010.07.025

Lavvas, P., Yelle, R. V., Koskinen, T., Bazin, A., Vuitton, V., Vigren, E., Galand, M., Wellbrock, A., Coates, A.J., Wahlund, J.E., Crary, F.J., Snowden, D., 2013. Aerosol growth in Titan's ionosphere. Proc. Natl. Acad. Sci. U. S. A. 110, 2729–2734. https://doi.org/10.1073/pnas.1217059110

Lavvas, P.P., Coustenis, A., Vardavas, I.M., 2008a. Coupling photochemistry with haze formation in Titan's atmosphere, Part I: Model description. Planet. Space Sci. 56, 27–66. https://doi.org/10.1016/j.pss.2007.05.026

Lavvas, P.P., Coustenis, A., Vardavas, I.M., 2008b. Coupling photochemistry with haze formation in Titan's atmosphere, Part II: Results and validation with Cassini/Huygens data. Planet. Space Sci. 56, 67–99. https://doi.org/10.1016/j.pss.2007.05.027

Le Gall, A., Malaska, M.J., Lorenz, R.D., Janssen, M.A., Tokano, T., Hayes, A.G., Mastrogiuseppe, M., Lunine, J.I., Veyssière, G., Encrenaz, P., Karatekin, O., 2016. Composition, seasonal change, and bathymetry of Ligeia Mare, Titan, derived from its microwave thermal emission. J. Geophys. Res. Planets 121, 233–251. https://doi.org/10.1002/2015JE004920

Le Mouélic, S., Cornet, T., Rodriguez, S., Sotin, C., Seignovert, B., Barnes, J.W., Brown, R.H., Baines, K.H., Buratti, B.J., Clark, R.N., Nicholson, P.D., Lasue, J., Pasek, V., Soderblom, J.M., 2019. The Cassini VIMS archive of Titan: From browse products to global infrared color maps. Icarus 319, 121–132. https://doi.org/10.1016/j.icarus.2018.09.017

Lebonnois, S., Bakes, E.L.O., McKay, C.P., 2002. Transition from gaseous compounds to aerosols in titan's atmosphere. Icarus 159, 505–517. https://doi.org/10.1006/icar.2002.6943

Lebonnois, S., Burgalat, J., Rannou, P., Charnay, B., 2012. Titan global climate model: A new 3-dimensional version of the IPSL Titan GCM. Icarus 218, 707–722. https://doi.org/10.1016/j.icarus.2011.11.032

Lethuillier, A., Le Gall, A., Hamelin, M., Caujolle-Bert, S., Schreiber, F., Carrasco, N., Cernogora, G., Szopa, C., Brouet, Y., Simões, F., Correia, J.J., Ruffié, G., 2018. Electrical Properties of Tholins and Derived Constraints on the Huygens Landing Site Composition at the Surface of Titan. J. Geophys. Res. Planets 123, 807–822. https://doi.org/10.1002/2017JE005416

Liang, M.-C., Yung, Y.L., Shemansky, D.E., 2007. Photolytically Generated Aerosols in the Mesosphere and Thermosphere of Titan. Astrophys. J. 661, L199–L202. https://doi.org/10.1086/518785

Linder, D.R., Coates, A.J., Woodliffe, R.D., Alsop, C., Johnstone, A.D., Grande, M., Preece, A., Narheim, B., Young, D.T., 1998. The Cassini CAPS Electron Spectrometer. Geophys. Monogr. - Am. Geophys. Union 102, 257–262.

Lindgren, E.B., Stamm, B., Chan, H.K., Maday, Y., Stace, A.J., Besley, E., 2017. The effect of like-charge attraction on aerosol growth in the atmosphere of Titan. Icarus 291, 245–253. https://doi.org/10.1016/j.icarus.2016.12.013

Lopes, R.M.C., Malaska, M.J., Schoenfeld, A.M., Solomonidou, A., Birch, S.P.D., Florence, M., Hayes, A.G., Williams, D.A., Radebaugh, J., Verlander, T., Turtle, E.P., Le Gall, A., Wall, S.D., 2019. A global geomorphologic map of Saturn's moon Titan. Nat. Astron. https://doi.org/10.1038/s41550-019-0917-6

Lopes, R.M.C., Malaska, M.J., Solomonidou, A., Le Gall, A., Janssen, M.A., Neish, C.D., Turtle, E.P., Birch, S.P.D., Hayes, A.G., Radebaugh, J., Coustenis, A., Schoenfeld, A., Stiles, B.W., Kirk, R.L., Mitchell, K.L., Stofan, E.R., Lawrence, K.J., 2016. Nature, distribution, and origin of Titan's Undifferentiated Plains. Icarus 270, 162–182. https://doi.org/10.1016/j.icarus.2015.11.034

Lopes, R.M.C., Stofan, E.R., Peckyno, R., Radebaugh, J., Mitchell, K.L., Mitri, G., Wood, C.A., Kirk, R.L., Wall, S.D., Lunine, J.I., Hayes, A., Lorenz, R., Farr, T., Wye, L., Craig, J., Ollerenshaw, R.J., Janssen, M., LeGall, A., Paganelli, F., West, R., Stiles, B., Callahan, P., Anderson, Y., Valora, P., Soderblom, L., 2010. Distribution and interplay of geologic processes on Titan from Cassini radar data. Icarus 205, 540–558. https://doi.org/10.1016/j.icarus.2009.08.010

López-Moreno, J.J., Molina-Cuberos, G.J., Hamelin, M., Grard, R., Simões, F., Godard, R., Schwingenschuh, K., Béghin, C., Berthelier, J.J., Brown, V.J.G., Falkner, P., Ferri, F., Fulchignoni, M., Jernej, I., Jerónimo, J.M., Rodrigo, R., Trautner, R., 2008. Structure of Titan's low altitude ionized layer from the Relaxation Probe onboard HUYGENS. Geophys. Res. Lett. 35, L22104. https://doi.org/10.1029/2008GL035338

Lorenz, R.D., Turtle, E.P., Barnes, J.W., Trainer, M.G., Adams, D.S., Hibbard, K.E., Sheldon, C.Z., Zacny, K., Peplowski, P.N., Lawrence, D.J., Ravine, M.A., McGee, T.G., Sotzen, K.S., MacKenzie, S.M., Langelaan, J.W., Schmitz, S., Wolfarth, L.S., Bedini, P.D., 2018. Dragonfly: A rotorcraft lander concept for scientific exploration at titan. Johns Hopkins APL Tech. Dig. 34, 374–387.

Lunine, J.I., 1993. Does Titan have an ocean? A review of current understanding of Titan's surface. Rev. Geophys. 31, 133–149. https://doi.org/10.1029/92RG02794

Madeleine, J.-B., Forget, F., Millour, E., Montabone, L., Wolff, M.J., 2011. Revisiting the radiative impact of dust on Mars using the LMD Global Climate Model. J. Geophys. Res. 116, E11010. https://doi.org/10.1029/2011JE003855

Magee, B.A., Waite, J.H., Mandt, K.E., Westlake, J., Bell, J., Gell, D.A., 2009. INMS-derived composition of Titan's upper atmosphere: Analysis methods and model comparison. Planet. Space Sci. 57, 1895–1916. https://doi.org/10.1016/j.pss.2009.06.016

Maguire, W.C., Hanel, R.A., Jennings, D.E., Kunde, V.G., Samuelson, R.E., 1981. C_3H_8 and C_3H_4 in Titan's atmosphere. Nature 292, 683–686. https://doi.org/10.1038/292683a0

Mahjoub, A., Carrasco, N., Dahoo, P.R., Fleury, B., Gautier, T., Cernogora, G., 2014. Effect of the synthesis temperature on the optical indices of organic materials produced by N_2-CH_4 RF plasma. Plasma Process. Polym. 11, 409–417. https://doi.org/10.1002/ppap.201300150

Mahjoub, A., Carrasco, N., Dahoo, P.R., Gautier, T., Szopa, C., Cernogora, G., 2012. Influence of methane concentration on the optical indices of titan's aerosols analogues. Icarus 221, 670–677. https://doi.org/10.1016/j.icarus.2012.08.015

Maillard, J., Carrasco, N., Schmitz-Afonso, I., Gautier, T., Afonso, C., 2018. Comparison of soluble and insoluble organic matter in analogues of Titan's aerosols. Earth Planet. Sci. Lett. 495, 185–191. https://doi.org/10.1016/J.EPSL.2018.05.014

Maillard, J., Hupin, S., Carrasco, N., Schmitz-Afonso, I., Gautier, T., Afonso, C., 2020. Structural elucidation of soluble organic matter: Application to Titan's haze. Icarus 340, 113627. https://doi.org/10.1016/j.icarus.2020.113627

Mandt, K.E., Gell, D.A., Perry, M., Hunter Waite, J., Crary, F.A., Young, D., Magee, B.A., Westlake, J.H., Cravens, T., Kasprzak, W., Miller, G., Wahlund, J.E., Gren, K., Edberg, N.J.T., Heays, A.N., Lewis, B.R., Gibson, S.T., De La Haye, V., Liang, M.C., 2012. Ion densities and composition of Titan's upper atmosphere derived from the

Cassini Ion Neutral Mass Spectrometer: Analysis methods and comparison of measured ion densities to photochemical model simulations. J. Geophys. Res. E Planets 117. https://doi.org/10.1029/2012JE004139

Mastrogiuseppe, M., Poggiali, V., Hayes, A., Lorenz, R., Lunine, J., Picardi, G., Seu, R., Flamini, E., Mitri, G., Notarnicola, C., Paillou, P., Zebker, H., 2014. The bathymetry of a Titan sea. Geophys. Res. Lett. 41, 1432–1437. https://doi.org/10.1002/2013GL058618

Mastrogiuseppe, M., Poggiali, V., Hayes, A.G., Lunine, J.I., Seu, R., Mitri, G., Lorenz, R.D., 2019. Deep and methane-rich lakes on Titan. Nat. Astron. 3, 535–542. https://doi.org/10.1038/s41550-019-0714-2

Mathé, C., Gautier, T., Trainer, M.G., Carrasco, N., 2018. Detection Opportunity for Aromatic Signature in Titan's Aerosols in the 4.1 – 5.3 μm Range. Astrophys. J. Lett. 861, L25. https://doi.org/10.3847/2041-8213/aacf88

McKay, C.P., 1996. Elemental composition, solubility, and optical properties of Titan's organic haze. Planet. Space Sci. 44, 741–747. https://doi.org/10.1016/0032-0633(96)00009-8

McKay, C.P., Coustenis, A., Samuelson, R.E., Lemmon, M.T., Lorenz, R.D., Cabane, M., Rannou, P., Drossart, P., 2001. Physical properties of the organic aerosols and clouds on Titan. Planet. Space Sci. 49, 79–99. https://doi.org/10.1016/S0032-0633(00)00051-9

Michael, M., Tripathi, S.N., Arya, P., Coates, A., Wellbrock, A., Young, D.T., 2011. High-altitude charged aerosols in the atmosphere of Titan. Planet. Space Sci. 59, 880–885. https://doi.org/10.1016/j.pss.2011.03.010

Miller, S.L., 1953. A production of amino acids under possible primitive earth conditions. Science 117, 528–529. https://doi.org/10.1126/science.117.3046.528

Molina-Cuberos, G.J., Cardnell, S., García-Collado, A.J., Witasse, O., López-Moreno, J.J., 2018. Aerosols: The key to understanding Titan's lower ionosphere. Planet. Space Sci. 153, 157–162. https://doi.org/10.1016/j.pss.2018.02.007

Molina-Cuberos, G.J., Lammer, H., Stumptner, W., Schwingenschuh, K., Rucker, H.O., López-Moreno, J.J., Rodrigo, R., Tokano, T., 2001. Ionospheric layer induced by meteoric ionization in Titan's atmosphere. Planet. Space Sci. 49, 143–153. https://doi.org/10.1016/S0032-0633(00)00133-1

Molina-Cuberos, G.J., López-Moreno, J.J., Rodrigo, R., Lara, L.M., O'Brien, K., 1999. Ionization by cosmic rays of the atmosphere of Titan. Planet. Space Sci. 47, 1347–1354. https://doi.org/10.1016/S0032-0633(99)00056-2

Morisson, M., Szopa, C., Carrasco, N., Buch, A., Gautier, T., 2016. Titan's organic aerosols: Molecular composition and structure of laboratory analogues inferred from pyrolysis gas chromatography mass spectrometry analysis. Icarus 277, 442–454. https://doi.org/10.1016/j.icarus.2016.05.038

Morooka, M.W., Wahlund, J. -E., Hadid, L.Z., Eriksson, A.I., Edberg, N.J.T., Vigren, E., Andrews, D.J., Persoon, A.M., Kurth, W.S., Gurnett, D.A., Farrell, W.M., Waite, J.H., Perryman, R.S., Perry, M., 2019. Saturn's Dusty Ionosphere. J. Geophys. Res. Sp. Phys. 124, 1679–1697. https://doi.org/10.1029/2018JA026154

Mouzay, J., Assadourian, C., Piétri, N., Chiavassa, T., Couturier-Tamburelli, I., 2019. New possible route of HC_3N formation in Titan's atmosphere. Low Temp. Phys. 45, 701–709. https://doi.org/10.1063/1.5103251

Nagy, A.F., Kliore, A.J., Marouf, E., French, R., Flasar, M., Rappaport, N.J., Anabtawi, A., Asmar, S.W., Johnston, D., Barbinis, E., Goltz, G., Fleischman, D., 2006. First results from the ionospheric radio occultations of Saturn by the Cassini spacecraft. J. Geophys. Res. Sp. Phys. 111, A06310. https://doi.org/10.1029/2005JA011519

Nagy, A.F., Kliore, A.J., Mendillo, M., Miller, S., Moore, L., Moses, J.I., Müller-Wodarg, I., Shemansky, D.E., 2009. Upper atmosphere and ionosphere of Saturn, in: Saturn from Cassini-Huygens. Springer, Dordrecht, pp. 181–201. https://doi.org/10.1007/978-1-4020-9217-6

Ness, N.F., Acuna, M.H., Behannon, K.W., Neubauer, F.M., 1982. The induced magnetosphere of Titan. J. Geophys. Res. Sp. Phys. 87, 1369–1381. https://doi.org/10.1029/ja087ia03p01369

Niemann, H.B., Atreya, S.K., Demick, J.E., Gautier, D., Haberman, J.A., Harpold, D.N., Kasprzak, W.T., Lunine, J.I., Owen, T.C., Raulin, F., 2010. Composition of Titan's lower atmosphere and simple surface volatiles as

measured by the Cassini-Huygens probe gas chromatograph mass spectrometer experiment. J. Geophys. Res. E Planets 115, 1–22. https://doi.org/10.1029/2010JE003659

Nna-Mvondo, D., De La Fuente, J.L., Ruiz-Bermejo, M., Khare, B., McKay, C.P., 2013. Thermal characterization of Titan's tholins by simultaneous TG-MS, DTA, DSC analysis. Planet. Space Sci. 85, 279–288. https://doi.org/10.1016/j.pss.2013.06.025

Peng, Z., Gautier, T., Carrasco, N., Pernot, P., Giuliani, A., Mahjoub, A., Correia, J., Buch, A., Bénilan, Y., Szopa, C., Cernogora, G., 2013. Titan's atmosphere simulation experiment using continuum UV-VUV synchrotron radiation. J. Geophys. Res. Planets 118, 778–788. https://doi.org/10.1002/jgre.20064

Pernot, P., Carrasco, N., Thissen, R., Schmitz-Afonso, I., 2010. Tholinomics—Chemical Analysis of Nitrogen-Rich Polymers. Anal. Chem. 82, 1371–1380. https://doi.org/10.1021/ac902458q

Perrin, Z., Chatain, A., Ruscassier, N., Vettier, L., Perrin, Z., Chatain, A., Ruscassier, N., Vettier, L., 2019. Analogues of Titan's aerosols: the different steps of formation in a N2-CH4 plasma., in: EPSC-DPS Joint Meeting 2019. Geneva, Switzerland, p. pp.EPSC-DPS2019-2035.

Plessis, S., Carrasco, N., Dobrijevic, M., Pernot, P., 2012. Production of neutral species in Titan's ionosphere through dissociative recombination of ions. Icarus 219, 254–266. https://doi.org/10.1016/j.icarus.2012.02.032

Podolak, M., Noy, N., Bar-Nun, A., 1979. Photochemical aerosols in Titan's atmosphere. Icarus 40, 193–198. https://doi.org/10.1016/0019-1035(79)90065-4

Pöschl, U., 2005. Atmospheric aerosols: Composition, transformation, climate and health effects. Angew. Chemie - Int. Ed. https://doi.org/10.1002/anie.200501122

Quirico, E., Montagnac, G., Lees, V., McMillan, P.F., Szopa, C., Cernogora, G., Rouzaud, J.N., Simon, P., Bernard, J.M., Coll, P., Fray, N., Minard, R.D., Raulin, F., Reynard, B., Schmitt, B., 2008. New experimental constraints on the composition and structure of tholins. Icarus 198, 218–231. https://doi.org/10.1016/j.icarus.2008.07.012

Rannou, P., Hourdin, F., McKay, C.P., Luz, D., 2004. A coupled dynamics-microphysics model of Titan's atmosphere. Icarus 170, 443–462. https://doi.org/10.1016/j.icarus.2004.03.007

Reid Thompson, W., Henry, T.J., Schwartz, J.M., Khare, B.N., Sagan, C., 1991. Plasma discharge in N2 + CH4 at low pressures: Experimental results and applications to Titan. Icarus 90, 57–73. https://doi.org/10.1016/0019-1035(91)90068-5

Richard, M.S., Cravens, T.E., Wylie, C., Webb, D., Chediak, Q., Mandt, K., Waite, J.H.J., Rymer, A., Bertucci, C., Wellbrock, A., Windsor, A., Coates, A.J., 2015a. An empirical approach to modeling ion production rates in Titan's ionosphere II: Ion production rates on the nightside. J. Geophys. Res. Sp. Phys. 120, 1281–1298. https://doi.org/10.1029/2006JA011892

Richard, M.S., Cravens, T.E., Wylie, C., Webb, D., Chediak, Q., Perryman, R., Mandt, K., Westlake, J., Waite, J.H., Robertson, I., Magee, B.A., Edberg, N.J.T., 2015b. An empirical approach to modeling ion production rates in Titan's ionosphere I: Ion production rates on the dayside and globally. J. Geophys. Res. Sp. Phys. 120, 1264–1280. https://doi.org/10.1002/2013JA019706

Rodriguez, S., Garcia, A., Lucas, A., Appéré, T., Le Gall, A., Reffet, E., Le Corre, L., Le Mouélic, S., Cornet, T., Courrech du Pont, S., Narteau, C., Bourgeois, O., Radebaugh, J., Arnold, K., Barnes, J.W., Stephan, K., Jaumann, R., Sotin, C., Brown, R.H., Lorenz, R.D., Turtle, E.P., 2014. Global mapping and characterization of Titan's dune fields with Cassini: Correlation between RADAR and VIMS observations. Icarus 230, 168–179. https://doi.org/10.1016/j.icarus.2013.11.017

Sagan, C., Khare, B.N., 1979. Tholins: Organic chemistry of interstellar grains and gas. Nature 277, 102–107. https://doi.org/10.1038/277102a0

Sagan, C., Khare, B.N., 1971. Long-Wavelength Ultraviolet Photoproduction of Amino Acids on the Primitive Earth. Science 173, 417–420. https://doi.org/10.1126/science.173.3995.417

Sagan, C., Khare, B.N., Thompson, W.R., McDonald, G.D., Wing, M.R., Bada, J.L., Vo-Dinh, T., Arakawa, E.T., 1993. Polycyclic aromatic hydrocarbons in the atmospheres of Titan and Jupiter. Astrophys. J. 414, 399–405. https://doi.org/10.1086/173086

Sagan, C., Thompson, W.R., Khare, B.N., 1992. Titan: A Laboratory for Prebiological Organic Chemistry. Acc. Chem. Res. 25, 286–292. https://doi.org/10.1021/ar00019a003

Scattergood, T., Owen, T., 1977. On the sources of ultraviolet absorption in spectra of Titan and the outer planets. Icarus 30, 780–788. https://doi.org/10.1016/0019-1035(77)90095-1

Scattergood, T.W., Lau, E.Y., Stone, B.M., 1992. Titan's aerosols I. Laboratory investigations of shapes, size distributions, and aggregation of particles produced by UV photolysis of model Titan atmospheres. Icarus 99, 98–105. https://doi.org/10.1016/0019-1035(92)90174-6

Sciamma-O'Brien, E., Carrasco, N., Szopa, C., Buch, A., Cernogora, G., 2010. Titan's atmosphere: An optimal gas mixture for aerosol production? Icarus 209, 704–714. https://doi.org/10.1016/j.icarus.2010.04.009

Sciamma-O'Brien, E., Dahoo, P.R., Hadamcik, E., Carrasco, N., Quirico, E., Szopa, C., Cernogora, G., 2012. Optical constants from 370nm to 900nm of Titan tholins produced in a low pressure RF plasma discharge. Icarus 218, 356–363. https://doi.org/10.1016/j.icarus.2011.12.014

Sciamma-O'Brien, E., Ricketts, C.L., Salama, F., Sciamma-O'Brien, E., 2014. The titan haze simulation experiment on cOsmic: Probing titan's atmospheric chemistry at low temperature. Icarus 243, 325–336. https://doi.org/10.1016/j.icarus.2014.08.004

Sciamma-O'Brien, E., Upton, K.T., Salama, F., 2017. The Titan Haze Simulation (THS) experiment on COSmIC. Part II. Ex-situ analysis of aerosols produced at low temperature. Icarus 289, 214–226. https://doi.org/10.1016/j.icarus.2017.02.004

Sebree, J.A., Trainer, M.G., Loeffler, M.J., Anderson, C.M., 2014. Titan aerosol analog absorption features produced from aromatics in the far infrared. Icarus 236, 146–152. https://doi.org/10.1016/j.icarus.2014.03.039

Seignovert, B., Rannou, P., Lavvas, P., Cours, T., West, R.A., 2017. Aerosols optical properties in Titan's detached haze layer before the equinox. Icarus 292, 13–21. https://doi.org/10.1016/j.icarus.2017.03.026

Shafiq, M., Wahlund, J.E., Morooka, M.W., Kurth, W.S., Farrell, W.M., 2011. Characteristics of the dustplasma interaction near Enceladus' South Pole. Planet. Space Sci. 59, 17–25. https://doi.org/10.1016/j.pss.2010.10.006

Shebanits, O., Vigren, E., Wahlund, J.E., Holmberg, M.K.G., Morooka, M., Edberg, N.J.T., Mandt, K.E., Waite, J.H., 2017. Titan's ionosphere: A survey of solar EUV influences. J. Geophys. Res. Sp. Phys. 122, 7491–7503. https://doi.org/10.1002/2017JA023987

Shebanits, O., Wahlund, J.-E., Edberg, N.J.T., Crary, F.J., Wellbrock, A., Andrews, D.J., Vigren, E., Desai, R.T., Coates, A.J., Mandt, K.E., Waite, J.H., 2016. Ion and aerosol precursor densities in Titan's ionosphere: A multi-instrument case study. J. Geophys. Res. Sp. Phys. 121, 10,075-10,090. https://doi.org/10.1002/2016JA022980

Shebanits, O., Wahlund, J.E., Mandt, K., Ågren, K., Edberg, N.J.T., Waite, J.H., 2013. Negative ion densities in the ionosphere of Titan-Cassini RPWS/LP results. Planet. Space Sci. 84, 153–162. https://doi.org/10.1016/j.pss.2013.05.021

Soderblom, L.A., Tomasko, M.G., Archinal, B.A., Becker, T.L., Bushroe, M.W., Cook, D.A., Doose, L.R., Galuszka, D.M., Hare, T.M., Howington-Kraus, E., Karkoschka, E., Kirk, R.L., Lunine, J.I., McFarlane, E.A., Redding, B.L., Rizk, B., Rosiek, M.R., See, C., Smith, P.H., 2007. Topography and geomorphology of the Huygens landing site on Titan. Planet. Space Sci. 55, 2015–2024. https://doi.org/10.1016/j.pss.2007.04.015

Strobel, D.F., 1974. The photochemistry of hydrocarbons in the atmosphere of Titan. Icarus 21, 466–470. https://doi.org/10.1016/0019-1035(74)90149-3

Strobel, D.F., Shemansky, D.E., 1982. EUV emission from Titan's upper atmosphere: Voyager 1 encounter. J.

Geophys. Res. Sp. Phys. 87, 1361–1368. https://doi.org/10.1029/ja087ia03p01361

Szopa, C., Cernogora, G., Boufendi, L., Correia, J.J., Coll, P., 2006. PAMPRE: A dusty plasma experiment for Titan's tholins production and study. Planet. Space Sci. 54, 394–404. https://doi.org/10.1016/J.PSS.2005.12.012

Tan, S.P., Kargel, J.S., Jennings, D.E., Mastrogiuseppe, M., Adidharma, H., Marion, G.M., 2015. Titan's liquids: Exotic behavior and its implications on global fluid circulation. Icarus 250, 64–75. https://doi.org/10.1016/j.icarus.2014.11.029

Thissen, R., Vuitton, V., Lavvas, P., Lemaire, J., Dehon, C., Dutuit, O., Smith, M.A., Turchini, S., Catone, D., Yelle, R. V., Pernot, P., Somogyi, A., Coreno, M., 2009. Laboratory studies of molecular growth in the titan ionosphere. J. Phys. Chem. A 113, 11211–11220. https://doi.org/10.1021/jp9050353

Tian, F., Kasting, J.F., Zahnle, K., 2011. Revisiting HCN formation in Earth's early atmosphere. Earth Planet. Sci. Lett. 308, 417–423. https://doi.org/10.1016/j.epsl.2011.06.011

Tian, F., Toon, O.B., Pavlov, A.A., De Sterck, H., 2005. A hydrogen-rich early Earth atmosphere. Science 308, 1014–1017. https://doi.org/10.1126/science.1106983

Tigrine, S., Carrasco, N., Bozanic, D.K., Garcia, G.A., Nahon, L., 2018. FUV Photoionization of Titan Atmospheric Aerosols. Astrophys. J. 867, 164. https://doi.org/10.3847/1538-4357/aae4d8

Tigrine, S., Carrasco, N., Vettier, L., Cernogora, G., 2016. A microwave plasma source for VUV atmospheric photochemistry. J. Phys. D. Appl. Phys. 49. https://doi.org/10.1088/0022-3727/49/39/395202

Tobie, G., Lunine, J.I., Sotin, C., 2006. Episodic outgassing as the origin of atmospheric methane on Titan. Nature 440, 61–64. https://doi.org/10.1038/nature04497

Tokano, T., Neubauer, P.M., Laube, M., McKay, C.P., 1999. Seasonal variation of Titan's atmospheric structure simulated by a general circulation model. Planet. Space Sci. 47, 493–520. https://doi.org/10.1016/S0032-0633(99)00011-2

Tomasko, M.G., Doose, L., Engel, S., Dafoe, L.E., West, R., Lemmon, M., Karkoschka, E., See, C., 2008. A model of Titan's aerosols based on measurements made inside the atmosphere. Planet. Space Sci. 56, 669–707. https://doi.org/10.1016/j.pss.2007.11.019

Tomasko, M.G., Doose, L.R., Dafoe, L.E., See, C., 2009. Limits on the size of aerosols from measurements of linear polarization in Titan's atmosphere. Icarus 204, 271–283. https://doi.org/10.1016/j.icarus.2009.05.034

Toublanc, D., Parisot, J.P., Brillet, J., Gautier, D., Raulin, F., McKay, C.P., 1995. Photochemical Modeling of Titan's Atmosphere. Icarus 113, 2–26. https://doi.org/10.1006/icar.1995.1002

Toupance, G., Raulin, F., Buvet, R., 1975. Formation of prebiochemical compounds in models of the primitive Earth's atmosphere - I: CH4-NH3 and CH4-N2 Atmospheres. Orig. Life 6, 83–90. https://doi.org/10.1007/BF01372392

Trainer, M.G., Pavlov, A.A., DeWitt, H.L., Jimenez, J.L., McKay, C.P., Toon, O.B., Tolbert, M.A., 2006. Organic haze on Titan and the early Earth. Proc. Natl. Acad. Sci. U. S. A. 103, 18035–42. https://doi.org/10.1073/pnas.0608561103

Trainer, M.G., Pavlov, A.A., Jimenez, J.L., McKay, C.P., Worsnop, D.R., Toon, O.B., Tolbert, M.A., 2004. Chemical composition of Titan's haze: Are PAHs present? Geophys. Res. Lett. 31. https://doi.org/10.1029/2004GL019859

Trainer, M.G., Sebree, J.A., Yoon, Y.H., Tolbert, M.A., 2013. The influence of benzene as a trace reactant in titan aerosol analogs. Astron. J. Lett. 766:L4. https://doi.org/10.1088/2041-8205/766/1/L4

Vinatier, S., Bézard, B., de Kok, R., Anderson, C.M., Samuelson, R.E., Nixon, C.A., Mamoutkine, A., Carlson, R.C., Jennings, D.E., Guandique, E.A., Bjoraker, G.L., Michael Flasar, F., Kunde, V.G., 2010. Analysis of Cassini/CIRS limb spectra of Titan acquired during the nominal mission II: Aerosol extinction profiles in the 600-1420cm-1 spectral range. Icarus 210, 852–866. https://doi.org/10.1016/j.icarus.2010.06.024

Vinatier, S., Bézard, B., Lebonnois, S., Teanby, N.A., Achterberg, R.K., Gorius, N., Mamoutkine, A., Guandique, E.,

Jolly, A., Jennings, D.E., Flasar, F.M., 2015. Seasonal variations in Titan's middle atmosphere during the northern spring derived from Cassini/CIRS observations. Icarus 250, 95–115. https://doi.org/10.1016/j.icarus.2014.11.019

Vinatier, S., Rannou, P., Anderson, C.M., Bézard, B., Kok, R. De, Samuelson, R.E., 2012. Optical constants of Titan's stratospheric aerosols in the 70 – 1500 cm-1 spectral range constrained by Cassini / CIRS observations. Icarus 219, 5–12. https://doi.org/10.1016/j.icarus.2012.02.009

Vuitton, V., Doussin, J.F., Bénilan, Y., Raulin, F., Gazeau, M.C., 2006a. Experimental and theoretical study of hydrocarbon photochemistry applied to Titan stratosphere. Icarus 185, 287–300. https://doi.org/10.1016/j.icarus.2006.06.002

Vuitton, V., Lavvas, P., Yelle, R. V., Galand, M., Wellbrock, A., Lewis, G.R., Coates, A.J., Wahlund, J.E., 2009. Negative ion chemistry in Titan's upper atmosphere. Planet. Space Sci. 57, 1558–1572. https://doi.org/10.1016/j.pss.2009.04.004

Vuitton, V., Yelle, R. V., Anicich, V.G., 2006b. The Nitrogen Chemistry of Titan's Upper Atmosphere Revealed. Astrophys. J. 647, L175–L178. https://doi.org/10.1086/507467

Vuitton, V., Yelle, R. V., Klippenstein, S.J., Hörst, S.M., Lavvas, P., 2019. Simulating the density of organic species in the atmosphere of Titan with a coupled ion-neutral photochemical model. Icarus 324, 120–197. https://doi.org/10.1016/j.icarus.2018.06.013

Wahlund, J.E., André, M., Eriksson, A.I.E., Lundberg, M., Morooka, M.W., Shafiq, M., Averkamp, T.F., Gurnett, D.A., Hospodarsky, G.B., Kurth, W.S., Jacobsen, K.S., Pedersen, A., Farrell, W., Ratynskaia, S., Piskunov, N., 2009a. Detection of dusty plasma near the E-ring of Saturn. Planet. Space Sci. 57, 1795–1806. https://doi.org/10.1016/j.pss.2009.03.011

Wahlund, J.E., Boström, R., Gustafsson, G., Gurnett, D.A., Kurth, W.S., Pedersen, A., Averkamp, T.F., Hospodarsky, G.B., Persoon, A.M., Canu, P., Neubauer, F.M., Dougherty, M.K., Eriksson, A.I., Morooka, M.W., Gill, R., André, M., Eliasson, L., Müller-Wodarg, I., 2005. Cassini measurements of cold plasma in the ionosphere of Titan. Science 308, 986–989. https://doi.org/10.1126/science.1109807

Wahlund, J.E., Galand, M., Müller-Wodarg, I., Cui, J., Yelle, R. V., Crary, F.J., Mandt, K., Magee, B., Waite, J.H., Young, D.T., Coates, A.J., Garnier, P., Ågren, K., André, M., Eriksson, A.I., Cravens, T.E., Vuitton, V., Gurnett, D.A., Kurth, W.S., 2009b. On the amount of heavy molecular ions in Titan's ionosphere. Planet. Space Sci. 57, 1857–1865. https://doi.org/10.1016/j.pss.2009.07.014

Waite, J.H., Lewis, W.S., Kasprzak, W.T., Anicich, V.G., Block, B.P., Cravens, T.E., Fletcher, G.G., Ip, W.-H., Luhmann, J.G., McNutt, R.L., Niemann, H.B., Parejko, J.K., Richards, J.E., Thorpe, R.L., Walter, E.M., Yelle, R. V., 2004. The Cassini Ion and Neutral Mass Spectrometer (INMS) Investigation, in: The Cassini-Huygens Mission. Springer Netherlands, pp. 113–231. https://doi.org/10.1007/978-1-4020-2774-1_2

Waite, J.H., Niemann, H., Yelle, R. V., Kasprzak, W.T., Cravens, T.E., Luhmann, J.G., McNutt, R.L., Ip, W.H., Gell, D., De La Haye, V., Müller-Wordag, I., Magee, B., Borggren, N., Ledvina, S., Fletcher, G., Walter, E., Miller, R., Scherer, S., Thorpe, R., Xu, J., Block, B., Arnett, K., 2005. Ion Neutral Mass Spectrometer results from the first flyby of Titan. Science 308, 982–986. https://doi.org/10.1126/science.1110652

Waite, J.H., Young, D.T., Cravens, T.E., Coates, A.J., Crary, F.J., Magee, B., Westlake, J., 2007. Planetary science: The process of tholin formation in Titan's upper atmosphere. Science 316, 870–875. https://doi.org/10.1126/science.1139727

Waite, J.H., Young, D.T., Westlake, J.H., Lunine, J.I., McKay, C.P., Lewis, W.S., 2010. High-altitude production of titan's aerosols, in: Titan from Cassini-Huygens. Springer Netherlands, pp. 201–214. https://doi.org/10.1007/978-1-4020-9215-2_8

Wattieaux, G., Carrasco, N., Henault, M., Boufendi, L., Cernogora, G., 2015. Transient phenomena during dust formation in a N_2-CH_4 capacitively coupled plasma. Plasma Sources Sci. Technol. 24, 015028. https://doi.org/10.1088/0963-0252/24/1/015028

Wellbrock, A., Coates, A.J., Jones, G.H., Lewis, G.R., Waite, J.H., 2013. Cassini CAPS-ELS observations of negative ions in Titan's ionosphere: Trends of density with altitude. Geophys. Res. Lett. 40, 4481–4485.

https://doi.org/10.1002/grl.50751

West, R.A., Seignovert, B., Rannou, P., Dumont, P., Turtle, E.P., Perry, J., Roy, M., Ovanessian, A., 2018. The seasonal cycle of Titan's detached haze. Nat. Astron. 2, 495–500. https://doi.org/10.1038/s41550-018-0434-z

Westlake, J.H., Waite, J.H., Carrasco, N., Richard, M., Cravens, T., 2014. The role of ion-molecule reactions in the growth of heavy ions in Titan's ionosphere. J. Geophys. Res. Sp. Phys. 119, 5951–5963. https://doi.org/10.1002/2014JA020208

Westlake, J.H., Waite Jr, J.H., Mandt, K.E., Carrasco, N., Bell, J.M., Magee, B.A., Wahlund, J.-E., 2012. Titan's ionospheric composition and structure: Photochemical modeling of Cassini INMS data. J. Geophys. Res. Sp. PhysicsGR Sp. Phys. 117, 1–21. https://doi.org/10.1029/2011JE003883

Wilson, E.H., Atreya, S.K., 2004. Current state of modeling the photochemistry of Titan's mutually dependent atmosphere and ionosphere. J. Geophys. Res. E Planets 109, E06002. https://doi.org/10.1029/2003JE002181

Wilson, E.H., Atreya, S.K., 2003. Chemical sources of haze formation in Titan's atmosphere, in: Planetary and Space Science. Pergamon, pp. 1017–1033. https://doi.org/10.1016/j.pss.2003.06.003

Yoon, Y.H., Hörst, S.M., Hicks, R.K., Li, R., de Gouw, J.A., Tolbert, M.A., 2014. The role of benzene photolysis in Titan haze formation. Icarus 233, 233–241. https://doi.org/10.1016/j.icarus.2014.02.006

Young, D.T., Berthelier, J.J., Blanc, M., Burch, J.L., Coates, A.J., Goldstein, R., …, McComas, D.J., 2004. Cassini Plasma Spectrometer Investigation, in: The Cassini-Huygens Mission. Springer, Dordrecht, pp. 1–112. https://doi.org/10.1007/978-1-4020-2774-1_1

Yung, Y.L., Allen, M., Pinto, J.P., 1984. Photochemistry of the atmosphere of Titan - Comparison between model and observations. Astrophys. J. Suppl. Ser. 55, 465. https://doi.org/10.1086/190963

Zerkle, A.L., Claire, M.W., Domagal-Goldman, S.D., Farquhar, J., Poulton, S.W., 2012. A bistable organic-rich atmosphere on the Neoarchaean Earth. Nat. Geosci. 5, 359–363. https://doi.org/10.1038/ngeo1425

Zhang, X., West, R.A., Irwin, P.G.J., Nixon, C.A., Yung, Y.L., 2015. Aerosol influence on energy balance of the middle atmosphere of Jupiter. Nat. Commun. 6, 10231. https://doi.org/10.1038/ncomms10231

Erosive species in Titan's ionosphere: simulations with N_2-H_2 cold plasmas
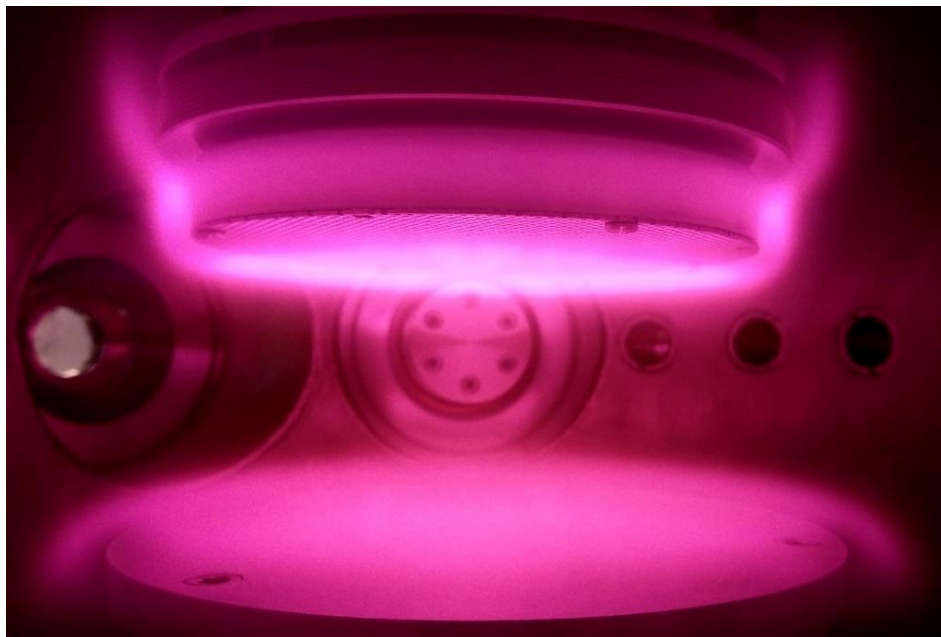
Contents

1- Introduction: laboratory plasmas to study the erosive species of Titan's ionosphere

Titan's ionosphere can be simulated by a N₂-CH₄ plasma discharge. From plasma studies, species formed with nitrogen and hydrogen are likely to erode the organic aerosols. Which are these species? In this chapter, plasma discharges in N₂-H₂, mimicking the erosive part of Titan's ionospheric plasma, are characterized.

1.1- N₂-H₂ discharges to simulate the erosive part of Titan's ionospheric plasma

1.1.a. N₂-H₂: A simplification of N₂-CH₄

As presented in **Chapter I**, Titan's ionosphere is a complex environment. The photo-ionization and dissociation of N_2, CH_4 and H_2 molecules in the upper atmosphere lead to a coupled ion-neutral chemistry. Heavy ions and neutral molecules are formed, growing up to the apparition of organic grains. Thousands of reactions are already implemented in the chemical models, but still a lot of processes are not well-known.

In the objective to investigate the effect of erosive plasma species on aerosols, the first necessary step is to characterize the erosive species in the plasma. Carbon chemistry in methane plasmas is well-known to lead to carbon chain growth. This characteristic is used to form films and membranes with specific properties: for example, composite membranes for gas separation (Inagaki and Ohkubo, 1986), transparent super-hydrophobic surfaces on glass (Han and Moon, 2015), diamond-like quality films (Cicala et al., 2004; Gottardi et al., 2008). **Hydrogen plasmas on the other side are very erosive**. Plasmas in hydrogen are known to erode graphite (Goebel et al., 1988; Roth and Garcia-Rosales, 1996) and –C:H films (Fox-Lyon et al., 2011; Nagai et al., 2002). **In the objective to study only erosive plasma processes and avoid the growth mechanisms, we remove carbon from the gas mixture and use a N₂-H₂ plasma**.

Besides, a N₂-CH₄ plasma discharge is complex and hard to model. Therefore, the investigation of N₂-H₂ plasma discharges will also be a **first step in the understanding of N₂-CH₄ plasma discharges**. Indeed, the chemistry of N₂-H₂ is included in the one of N₂-CH₄.

N₂-H₂ plasma discharges have also an interesting property: they form ammonia (NH₃). Ammonia is present in Titan's atmosphere (Cui et al., 2009; Yelle et al., 2010), but the value of its concentration is under debate. Indeed, NH_3 and NH_4^+ are both present but current models deriving NH_3 amounts from NH_4^+ measurements underestimate NH_3 production by a factor of 10-100 (Dobrijevic et al., 2016; Lavvas et al., 2008). Several processes could explain this difference. First, ammonia tends to stick on metallic surfaces, and could stay adsorbed on

INMS antechamber. The production of NH_3 on surfaces (like on the metallic walls of INMS or on solid aerosols) is also to be investigated (Cui et al., 2009). Finally, ammonia could be formed by the Cassini spacecraft thrusters fueled with hydrazine (N_2H_4) (Magee et al., 2009). Nevertheless, the pyrolysis of Titan aerosols by ACP on Huygens (see **Section I.5.3.b**) released ammonia. **Therefore, ammonia seems to be part of the complex chemistry leading to the formation of Titan's aerosols. Its precise role is still to be investigated**. NH_3 is also present in Saturn and Jupiter atmospheres, and plays an important role in the photo-chemistry (Atreya et al., 2005; Burgdorf et al., 2004). For instance, it could form chromophores explaining the color of Jupiter Great Red Spot (Carlson et al., 2016; Keane, 2017).

1.1.b. What we already know about N_2-H_2 plasmas

Nitrogen and hydrogen are usual gases, and a lot of studies have been conducted with the objective to understand pure N_2 (Cernogora et al., 1981; Guerra et al., 2004) and pure H_2 (Amorim et al., 2001; Shirley and Hall, 1977) plasmas. However, as soon as the two gases are mixed, plasmas become different, and much harder to understand. **Today important issues deal with the chemical mechanisms happening in the gas phase and on the surfaces in contact, and especially with the processes leading to the formation of ammonia (NH_3).**

Nowadays many technological applications use N_2-H_2 plasmas, as the plasma species formed with both hydrogen and nitrogen have interesting properties. A major application is the industry of thin film growth, among which are the silicon (SiN) films fundamental for the semiconductor and the photovoltaic industries. These films are formed by plasma-enhanced chemical vapor deposition (PECVD), with gas mixtures containing Si, N_2 and H_2 (Aberle, 2001; Sekine et al., 1999; Watanabe et al., 1986; Wróbel et al., 2003). Another major industrial application of N_2-H_2 plasmas is nitriding, used to harden metal surfaces (Bouanis et al., 2010; Hudis, 1973). In nuclear fusion, N_2 is added to hydrogen plasma to inhibit organic film deposition on walls (Body et al., 2018; Oberkofler et al., 2015; Tabarés et al., 2002). The formation of ammonia has a strong industrial interest as ammonia is already produced in huge quantities to be used as a basic precursor for the synthesis of chemicals such as fertilizers. The current technique known as the Haber-Bosch process has a yield of 15-20% and research is on-going to exceed this yield using plasmas (Hong et al., 2017). In aerospace applications, N_2-H_2 plasmas are used for propulsion through arcjet thrusters (Wang et al., 2010). In all these applications, the understanding of N_2-H_2 plasma is fundamental to optimize the protocols and designs of technologies.

T**he understanding of N_2-H_2 plasmas is not only considered for the industrial world, but also in astrophysics and planetary sciences.** In the interstellar medium for instance, nitrogen and hydrogen excited species and ions are present in large quantity. A current issue is to understand the formation processes of ammonia which abundance is not explained by current models. E. Carrasco et al. (2012, 2013) and Herbst (2001) explain that it could be due to an additional surface chemistry on ice and dust particles. Another issue is about the detection of N_2 in radio astronomy. N_2 has no dipolar moment and is therefore not detectable by

absorption measurements. However, N_2H^+ can be detected. To deduce the density of N_2 from measurements on N_2H^+ requires a complete understanding of the sources and sinks of N_2H^+ in this environment (Petrie and Bohme, 2007; Womack et al., 1992). Finally, the study of the ionospheres of planets also often deals with N_2-H_2 plasmas, in particular concerning Jupiter, Saturn and Titan (see above in **Section II.1.1.a**).

Plasma understanding requires intertwined experimental and numerical simulation studies. Diagnostics and modeling of N_2-H_2 discharges started with the works of Garscadden and Nagpal (1995) and Loureiro and Ricard (1993) on DC glow discharges. Gordiets et al. (1998a, 1998b) continued this work with the complexification of the chemical model, especially with the introduction of surface kinetics. Ammonia density among other species could not be explained by bulk processes, and led Gordiets et al. (1998b) to discover the fundamental role of surface reactions on the global discharge kinetics. They also showed that surface kinetics is highly dependent on the surface state: the surface material, but also the way it has been processed before the measurements. The complex ion processes are studied in E. Carrasco et al. (2011, 2012, 2013) working at low pressure (0.8-8 Pa), while details on the mechanism at the surface are described at atmospheric pressure in Hong et al. (2017, 2018).

Plasma characteristics depend on the geometry and on the nature of the discharge. All the studies cited in the above paragraph have been performed in DC glow discharges, which are very homogeneous and can be modelled in 0D. However, N_2-H_2 plasma applications do not all work in DC glow discharges. In particular, material processing or functionalization are often performed with radiofrequency capacitively coupled (RF CCP) discharges (Bouanis et al., 2010; Leyland et al., 1990), as well as the study of Titan's ionosphere (Szopa et al., 2006). Some first studies on the characterization of N_2-H_2 plasma discharges different from DC glow discharges addressed microwave discharges (Tatarova et al., 2005) and radiofrequency inductively coupled plasmas (Kumar et al., 2000; Sode et al., 2015). I this work we use an RF CCP discharge, which is the type of discharge of our experiment PAMPRE (see **Section I.4.2**).

RF CCP discharges are more complex to diagnose and to model than DC plasmas. Indeed, charged species are not homogeneously distributed in the plasma. For that purpose, Marques et al. (2007 and Salabas et al. (2004) implemented a two-dimensional model to describe pure H_2 RF CCP discharges. It is a hybrid model in which the dynamics of charged species are described by a 2D, time-dependent fluid module, while a zero-dimensional kinetic module solves the chemistry. This work has been extended to a pure nitrogen discharge by Alves et al. (2012).

Experiments and models in glow DC discharges show the strong modifications of pure N_2 (and pure H_2) plasmas with the small addition of H_2 (resp. N_2), and the major effect of surface processes on the plasma global kinetics. Similar effects are then expected in an RF CCP discharge.

1.1.c. Objective of Chapter II

My objective here is to analyze modifications due to the addition of hydrogen in nitrogen plasmas in the discharges used during my PhD work. Section II.2 focuses on a **capacitively coupled radio-frequency plasma discharge** (the case of PAMPRE). It gives experimental and modeling results obtained with the addition of small amounts of H_2 (up to 5%) in an initially pure N_2 plasma, at low pressure (0.3 – 1 mbar) and low coupled power (3 – 13 W) conditions. Section II.3 compares the results obtained in Section II.2 with similar measurements done on a **DC plasma discharge** (THETIS), which is used in Chapter III.

I performed different measurements, probing electric parameters, electron density, ammonia density and positive ion evolutions. These measurements have then been used to improve the model previously developed for pure N_2 discharges (Alves et al., 2012), the main additions being the new N_xH_y species, their gas-phase reactions and the surface processes. To investigate these species, I used a **neutral and ion mass spectrometer**, which is introduced in Section II.1.2.
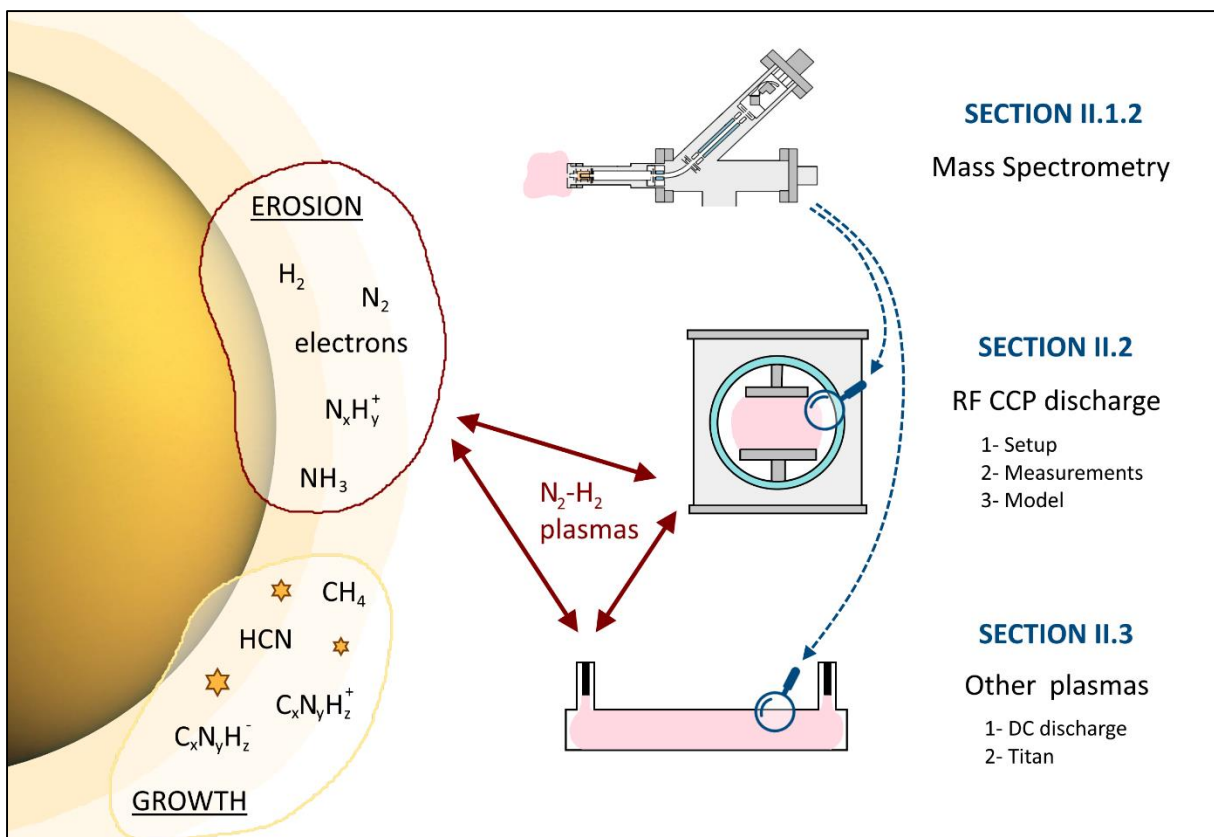
1.2- Neutral and ion analysis by mass spectrometry

During various experiments performed in this PhD work, **neutral and ion species have been measured by mass spectrometry** (MS). The MS used is a quadrupole mass spectrometer from Hiden Analytical, EQP (Electrostatic Quadrupole Probe) series. It is a mass/energy analyzer adapted for plasma diagnostics. **This part presents how the MS measures neutrals and ions, and how to deduce neutral densities, and ion relative fluxes from these measurements.**

1.2.a. Global functioning of the mass spectrometer

The Hiden EQP system has two operating modes: the Residual Gas Analysis (RGA) mode for the study of neutral species, and the Secondary Ion Mass Spectrometry (SIMS) mode for positive and negative ions.

In any case, gas species (neutrals and ions) are first **sampled by a collector head** positioned next to or inside the plasma. This collector head is situated on the left of the scheme presented in **Figure II.1-1**. The gas species enter through a 100 µm diameter orifice, which keeps the inside of the MS at low pressure (< 5x10^{-6} mbar). The collector head can be moved inside the vacuum chamber thanks to a 300 mm movable arm.
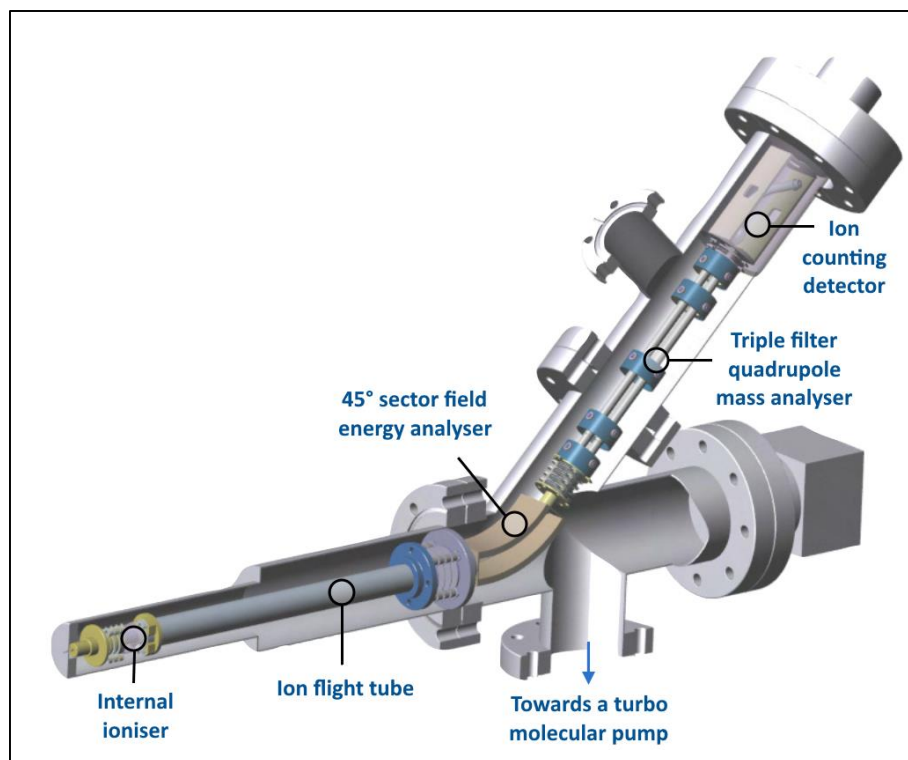
Figure II.1-1: 3D scheme of the Hiden EQP mass spectrometer. Adapted from Hiden Analytical documentation.

Positive ions are attracted inside by a negative voltage of ~-40 V, the '**extractor**'. They can directly be analyzed after being sampled. On the other side, **the study of neutrals requires the use of an internal ionizer**. Two oxide coated iridium filaments are positioned close to the

plasma sampling orifice. They serve as an electron impact ion source, working at low pressure (10^{-5} mbar). The source operating parameters can be controlled from the EQP software: the filament emission (10 µA), the source cage voltage (3 V) and the ionizing electron energy (70 eV). **Figure II.1-2** indicates the positions of the main adjustable parameters.

Ions are then filtered by their energy thanks to a 45° electrostatic parallel plate energy analyzer. The energy is usually tuned to maximize the signal for each ion. Energy pass band is 0.5 eV. Examples of energy spectra for different ions are shown in **Figures II.1-15** and **II.1-16.**

All along the trajectory of the ions, the ion flux is focused by electromagnetic lenses that are named: lens 1 (for ions only), flight-focus, lens 2, vert, horiz, DC quad and focus 2.

Thereafter, ions enter a triple filter mass analyzer. A quadrupole mass filter is formed by four parallel cylindrical conducting rods, on which are applied DC and/or radiofrequency (RF) potentials. The main filter is RF and DC. The pre and post filters (RF only) are present to minimize the effects from fringe fields. Masses from m/z 0.4 to 200 can be detected, with a mass resolution of 1 u.

Finally, the journey of the ions ends with an ion counting detector. A secondary electron multiplier (SEM) detector was used, with a seven-decade continuous dynamic range. It is an off axis mounted continuous dynode electron multiplier. Detection is controlled by three variables: the first dynode voltage (-3500 V), the multiplier (varied with the aging of the detector from 1800 to 2400 V) and the discriminator (-10 %) working as a counting threshold. A signal gating input can be used for time resolved plasma studies.

More details on each element of the MS can be found in Godet (2006).
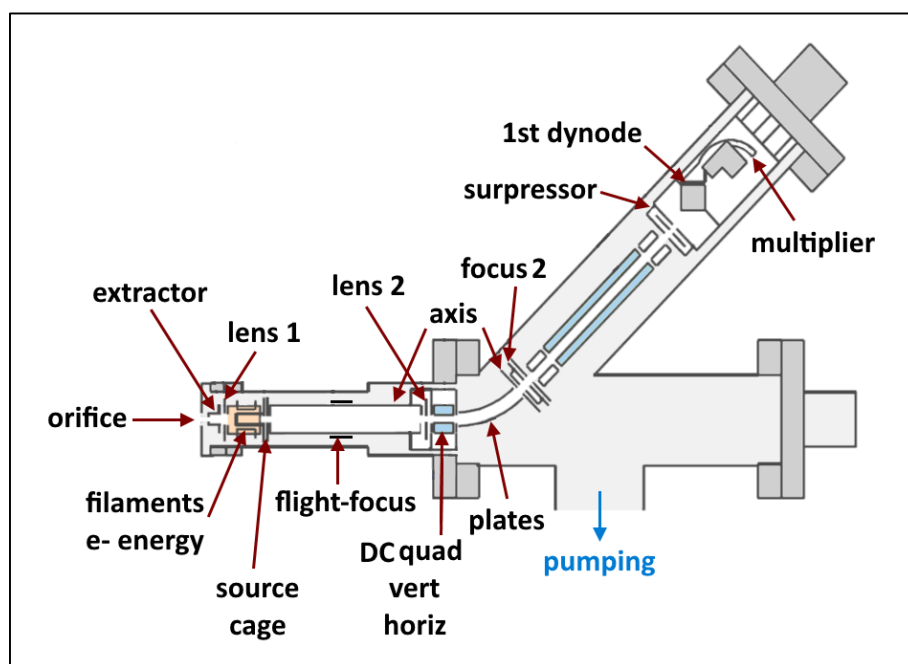
Figure II.1-2: 2D scheme of the MS showing the position of the main parameters. Adapted from Hiden Analytical documentation and Godet (2006).

1.2.b. Calibration of RGA measurements

BASIC PRINCIPLE

Mass spectrometers do not give directly absolute measurements of the species density. Usually, it is even not possible to compare the intensities of two different peaks to deduce the density ratio of the corresponding molecules. **Indeed, the ionization, the flight in the MS and through the quadrupole and the detection depend on the mass and the intrinsic properties of the species. Nevertheless, a transmission curve can be obtained with neutral atoms and molecules.** The idea is to inject a gas (or gas mixture if we know the proportions) with a well-known pressure in a cell and take a mass spectrum. The density in the cell is deduced from the pressure, and from the MS measurement we can deduce the transmission of the MS for the mass of the injected gas. The transmission curve as a function of mass is obtained once the measurement is done with different gases at various masses. Methods similar to the one described below has been previously used: with EQP MS from Hiden equipped with SEM (Kechkar et al., 2014; Kondo et al., 2018; Lopaev et al., 2017); or with other MS (Godet, 2006; Pulpytel et al., 2005; Sode et al., 2015, 2013). They always use several gases among H_2, He, Ne, N_2, O_2, Ar, Kr and Xe. As a transmission curve depends strongly on the MS configuration set, the curves obtained in the literature vary from one to another.

CHOICE OF A SET OF PARAMETERS FOR THE MS

The MS ion lenses can be tuned to optimize the detection of a chosen mass. A tuning on mass 28 (in N_2) gives a good signal for masses > 10. However, for lower masses, a tuning on mass 2 (in H_2) is a better option. Depending on the experiment, we will choose between the two tunings, or do both. **To perform the calibration, we will therefore use two sets of parameters, one tuned on mass 28 (N_2) and one tuned on mass 2 (H_2).** This optimization step is performed using a gas bottle of 95% N_2- 5% H_2. A gas flow of 60 standard cubic centimeters per minute of gas is continuously injected in the chamber, leading to a constant pressure of 0.90 mbar.

All available parameters were tested and optimized (see above, **Section II.1.2.a**). Some have the same optimized value in all conditions. We selected only those having varying optimized values for our customized tuning (see **Table II.1-1** below). We observed a few differences on the tuning optimization results when we used different filaments, especially for the lower masses. When both filaments are activated on MASsoft, only the first one is working. These differences are certainly due to the different ageing of the filaments. **Table II.1-1** and **Figure II.1-3** present typical results of tuning.

Most parameters are stable in time, except the distribution of the parameter 'energy' which can vary a lot (up to 1.5V) between two different days. **Therefore, we only run our customized tuning in N_2-H_2 on mass 2 and mass 28 at the beginning of a measurement campaign. But it is necessary to adjust the value of the parameter 'energy' at the beginning of each measurement session (day or half-day if there is a break).**
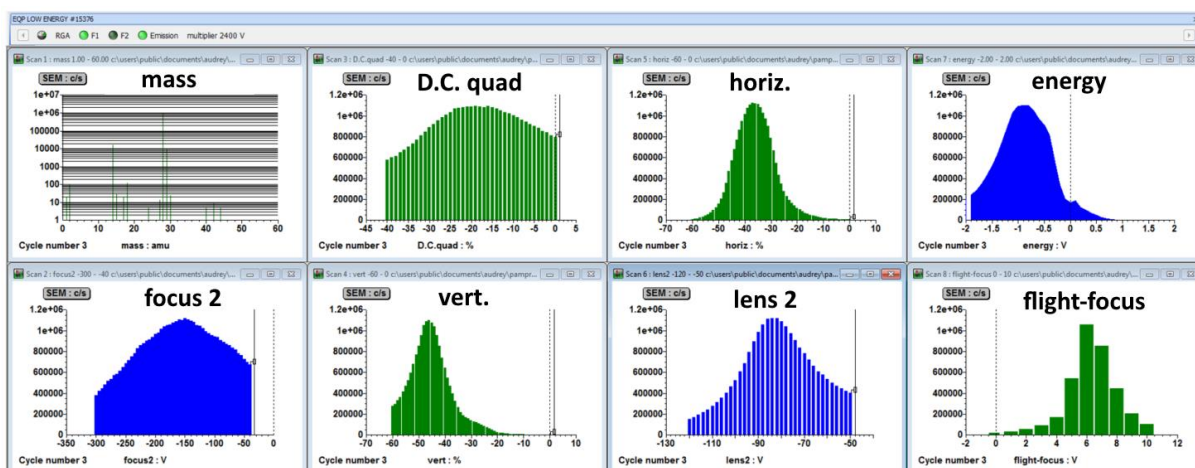
Figure II.1-3: Result of a tuning on m/z 28, in 95% N_2 – 5% H_2, at 0.9 mbar, with filament 1. MASsoft interface.

Parameter	Tuning range	Unit	filament 1		filament 2	
			m 2	m 28	m 2	m 28
focus 2	-300 / -40	V	-185	-150	-170	-165
D.C. quad	-40 / 0	%	-17	-19	-13	-18
vert.	-60 / 0	%	-42	-46	-34	-44
horiz.	-60 / 0	%	-10	-36	-32	-42
lens 2	-120 / -50	V	-74	-82	-78	-82
energy	-3 / 2	V	**0.1**	**-0.9**	**0**	**-0.9**

Table II.1-1: Typical tuning of the MS to optimize the detection of m/z 2 and 28.

MS SIGNATURE FOR A GIVEN NEUTRAL: ISOTOPES

To obtain the evolution of the MS transmission with mass, the calibration has to be performed with several gases of different masses. For this work we used 5 different bottles with high purity gases (> 99.999%). The gases are listed in **Table II.1-2**.

Mass spectrometry differentiates isotopes, for example $^{14}N^{14}N^+$ at m/z 28, $^{14}N^{15}N^+$ at m/z 29 and $^{15}N^{15}N^+$ at m/z 30. Especially for high mass atoms, a lot of isotopes are expected (and observed). All should be included for the calibration, therefore we first measured the intensity ratio between the isotopes of a same molecule. It fits well the ratio given by the NIST* database for natural abundances, as shows **Figure II.1-4**.

Afterwards, only the major peak is measured, and a corrective coefficient (K_{iso}) is applied to take into account the quantity of isotopes.
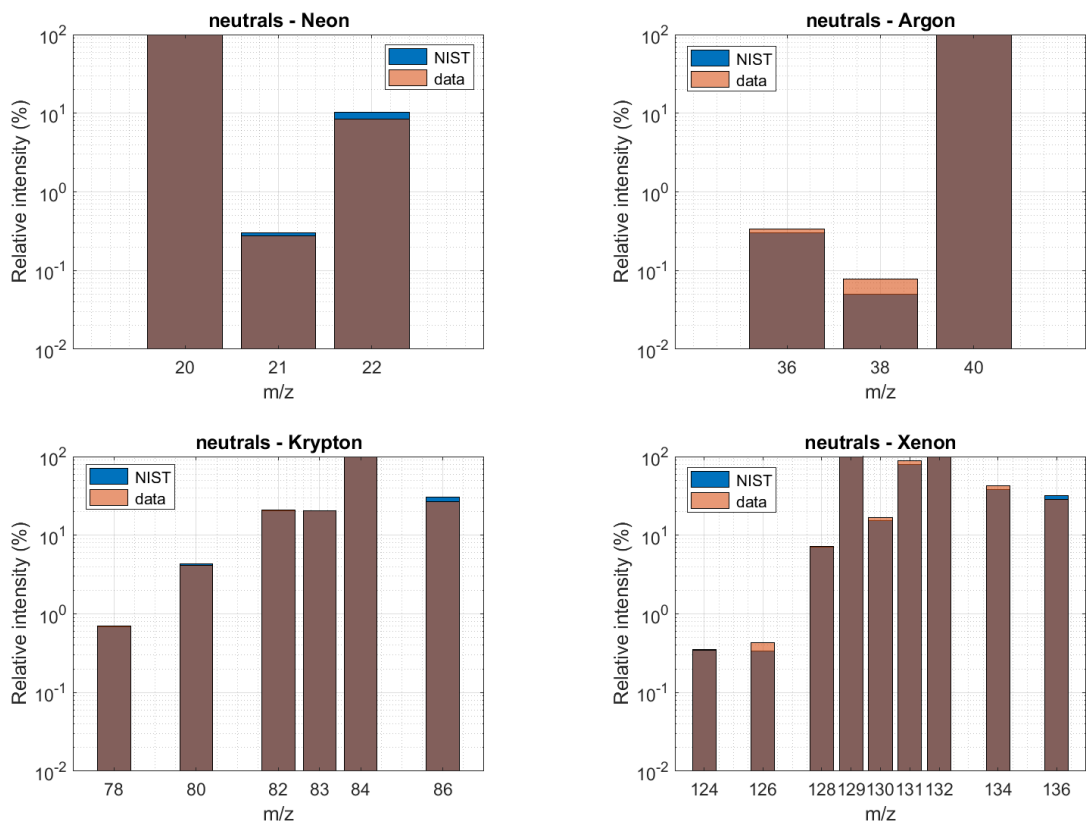
Figure II.1-4: Measured mass spectra (orange area) of isotopes of noble gases compared to the NIST* database (blue area) for natural abundances. The brown area corresponds to the superposition of orange (data) and blue (NIST*).

MS SIGNATURE FOR A GIVEN NEUTRAL: FRAGMENTATION PATTERN

The ionization source used is based on electronic impact with electrons accelerated at 70 eV. The ionization of species by such an ionization source also leads to the formation of double charged species, and **fragments** (if there are several atom). Some fragments or double ionized species can be an important percentage of the total ionized species formed (see values given by the NIST* database in **Table II.1-2**). However, it depends strongly on the ionization source used, its tuning and its ageing. Therefore, we avoid to take them into account. We measure only the main peak and **we consider the simple ionization process** on the atom/molecule X:

$$X + e^- \rightarrow X^+ + e^- + e^-$$
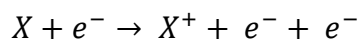
Nevertheless, ionization cross sections are hard to measure and model: their values have large uncertainties which affect the calibration. It is especially the case for molecular gases that fragment. Values given for simple ionization coefficients by different sources are compared in **Table II.1-2**: results of computations with the databases of Biagi* (program Magboltz) and IST*, and measurements with the Phelps* database. For consistency, we always used Phelps*'s values when they exist.

Therefore, we use the simple ionization cross section at 70 eV (σ_X). It links the flux of ions X^+ ($j_{X+,MS}$) formed in the ionization chamber to n_X the density of the atom/molecule X in the reaction chamber.

Bottle	Gas	Mass of major peak (atomic unit)	Isotopes (NIST*, and *SIS* if different)	Isotopes corrective coefficient K_{iso}	Fragmentation and double ionization (NIST*)	Simple ionization cross section σ (Å² = 10^{-20} m²)	Estimated uncertainty on σ (+/- %)
95% N₂ 5% H₂	H₂	2	/	1.000	1 (2.1%)	0.935 (Biagi*) 0.967 (IST*) **0.967 (Phelps*)**	10
pure N₂	N₂	28	29 (0.7%)	1.007	14 (13.8%)	2.33 (Biagi*) 1.92 + 0.23 (IST*) **2.15 + 0.17** (Phelps*)	20
90% N₂ 10% CH₄	CH₄	16	17 (1.6% – *1.1%*)	1.016	12 (3.8%) 13 (10.7%) 14 (20.4%) 15 (88.8%)	**1.95** (IST*) (strong variations in other databases)	30
Noble gases: 75% He 15% Ne 5% Ar 3% Kr 2% Xe	He	4	/	1.000	/	0.313 (Biagi*) 0.322 (IST*) **0.313 (Phelps*)**	10
	Ne	20	21 (*0.3%*) 22 (*10.2%*)	1.105	/	0.490 (Biagi*) **0.514 (Phelps*)**	10
	Ar	40	36 (0.3%) 38 (0.05%)	1.0035	20 (14.6%)	2.77 (Biagi*) 2.77 (IST*) **2.7 (Phelps*)**	10
	Kr	84	78 (0.7% - *0.6%*) 80 (4.3% - *3.9%*) 82 (20.6% - *20.4%*) 83 (20.5% - *20.2%*) 86 (30.6% - *30.4%*)	1.767	41 (3.47%) 42 (15.9%) 43 (5.0%)	**4.21** (Biagi*)	10
	Xe	132	124 (0.4%) 126 (0.3%) 128 (7.1%) 129 (98.4% - *98.1%*) 130 (15.2%) 131 (79.4% - *78.8%*) 134 (37.8% - *38.7%*) 136 (32.0% - *33.1%*)	3.706	64 (1.3%) 65 (2.9%) 66 (17.8%) 67 (6.9%) 68 (6.1%)	**5.3** (Biagi*)	10
pure O₂	O₂	32	33 (*0.1%*) 34 (*0.4%*)	1.005	16 (21.8%)	2.38 (Biagi*) 2.8 (IST*) **2.36** (Phelps*)	20

Table II.1-2: Gases used for calibration and their properties.

Databases used for this work:

- **NIST***: https://webbook.nist.gov/chemistry/
- **Isotope Distribution Calculator by SIS***: https://www.sisweb.com/mstools/isotope.htm
- **Biagi***: www.lxcat.net/Biagi. Computed cross-sections of rare gases and simple molecules – With fortran program MAGBOLTZ by SF Biagi.
- **IST***: www.lxcat.net/IST-Lisbon. Computed cross sections: Alves (2014); CH_4: based on Chatham et al. (1984).
- **Phelps***: www.lxcat.net/Phelps. Measurements. General: Rapp and Englander-Golden (1965); N_2: Isola et al (2010); Ne: Tachibana and Phelps (1987); Ar: Yamabe et al (1983); O_2: Lawton and Phelps (1978).

CALIBRATION FOR EACH NEUTRAL (AT A GIVEN TUNING)

We therefore use the intensity I_{MS}, corresponding to the main isotope and the main fragment of the gas injected.

To obtain the total transmission curve through the MS, we measure the I_{MS} of gases of different masses m_X for a known pressure P_X (cf **Figure II.1-5**). To remove the effect of isotopes and ionization, the **total transmission** is defined as in Sode et al. (2013):

$$T_{tot}(m_X) = \frac{I_{MS}(m_X) \times K_{iso,X}}{\sigma_X \times P_X} \quad with \quad n_X = \frac{P_X}{k_B T} \qquad (II.1-1)$$

with σ_X the simple ionization cross section of X, P_X the partial pressure of X and $K_{iso,X}$ the coefficient to take all its isotopes into account.
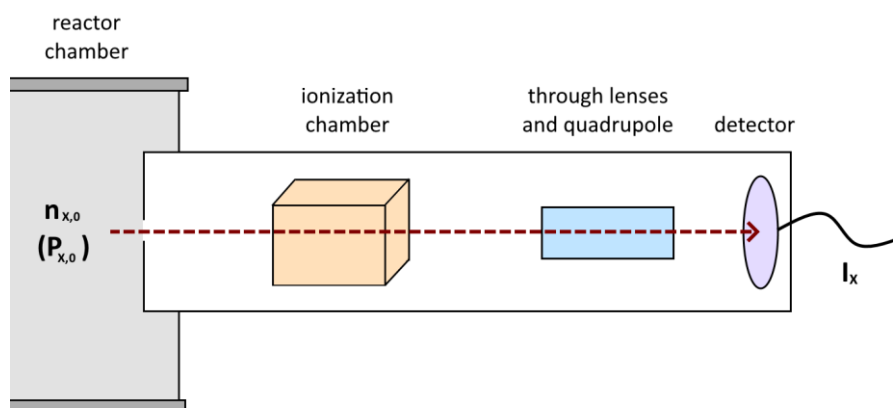
Figure II.1-5: The total transmission links the gas density $n_{x,0}$ (or pressure $P_{x,0}$) in the chamber to its intensity I_x detected by the MS detector. It takes into account the passage through the entrance pin hole, the ionization chamber, the lenses and the quadrupole.

For this measurement, the MS is used in Multiple Ion Detection (MID) mode on the major peak(s) of the injected gas(es). Their intensity is continuously measured during 90s. This method enables to check the stability of the signal, and to reduce measurement uncertainties by doing an average on more than 130 measurements, obtained during an acquisition of 90s.

For more precise measurements, and to generalize at different pressures representative of our usual experiments, measurements on each gas are done at several pressures varying between 0.5 and 1.3 mbar as shown on **Figure II.1-6**. **The final variable used in the following is then the slope of the curve of I$_{MS}$ as function of partial pressure P$_X$ of the gas studied**. To check repeatability, each case is done at least twice on two different days. Results for N$_2$ obtained on three different bottles (pure N$_2$, N$_2$ - 5% H$_2$ and N$_2$ - 10% CH$_4$) are compared, and give similar values. We observed that intensity values tend to saturate above 10^6 counts/second (c/s), as shown in **Figure II.1-6 (a)**. The saturated points are not taken into account for the transmission curves.

Such calibration curves are obtained for many gases: H$_2$, He, CH$_4$, Ne, N$_2$, O$_2$, Ar, Kr and Xe.
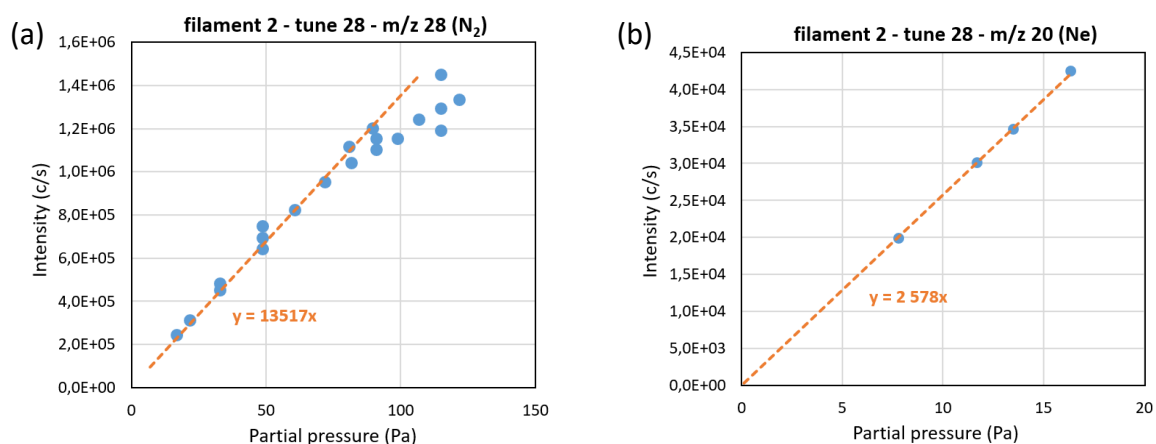
Figure II.1-6: Example of measurement in (a) N$_2$, on m/z 28 and in (b) Ne, on m/z 20, with a reference tuning on m/z 28, using filament 2. A saturation is observed above 10^6 c/s.

THE TRANSMISSION CURVE (AT A GIVEN TUNING)

With the calibration curves obtained for different gases, we can deduce the transmission curve of the mass spectrometer, defined by **Equation II.1-1**.

We observe that it can reasonably be fitted by a **log-normal law** (see **Figure II.1-7**):

$$f(\mathrm{x}; G, \mu, s) = \frac{G}{x.\ s.\ \sqrt{2\pi}} . \exp\left(-\frac{(\ln(x) - \mu)^2}{2s^2}\right) \qquad (II.1-2)$$

with x the variable (here m/z), G, μ and s the coefficients adapted for the fit.

The simple ionization cross sections for atomic gases is better constrained than the one for molecular gases (except in the case of H$_2$). To obtain a better fitting, we preferred to **only fit the data points from the noble gases**, and from H$_2$. Nevertheless, the data points obtained with molecular gases are shown on **Figure II.1-7** for information. It seems simple ionization cross sections used for molecular gases are underestimated in the case of our MS.
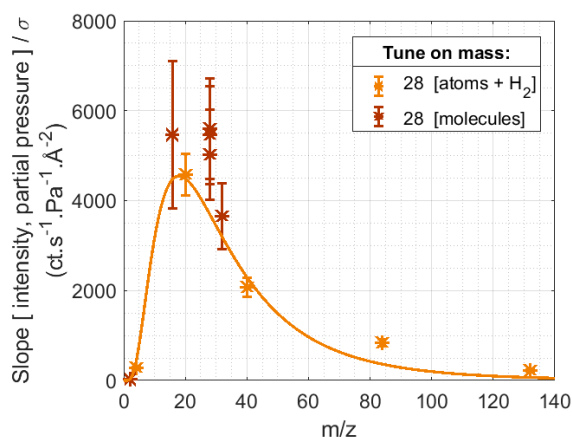
Figure II.1-7: Transmission curve obtained for a tuning on mass 28. Fit with a log-normal law.

MODIFICATION OF THE TRANSMISSION CURVE WITH THE TUNING OF THE MS

The transmission curve depends strongly on the tuning used. Figure II.1-8 (a) shows the result for the tuning on mass 2 and the tuning on mass 28. **Figure II.1-8 (b)** gives the transmission curve obtained for tuning done on mass 4, 20, 40, 84 and 132, with noble gases.

Therefore, one should take the transmission curve associated with the chosen tuning. Nevertheless, Figure II.1-8 shows that only tunings done on low masses like 2 (H_2) or 4 (He) have a very different transmission curve than the others.
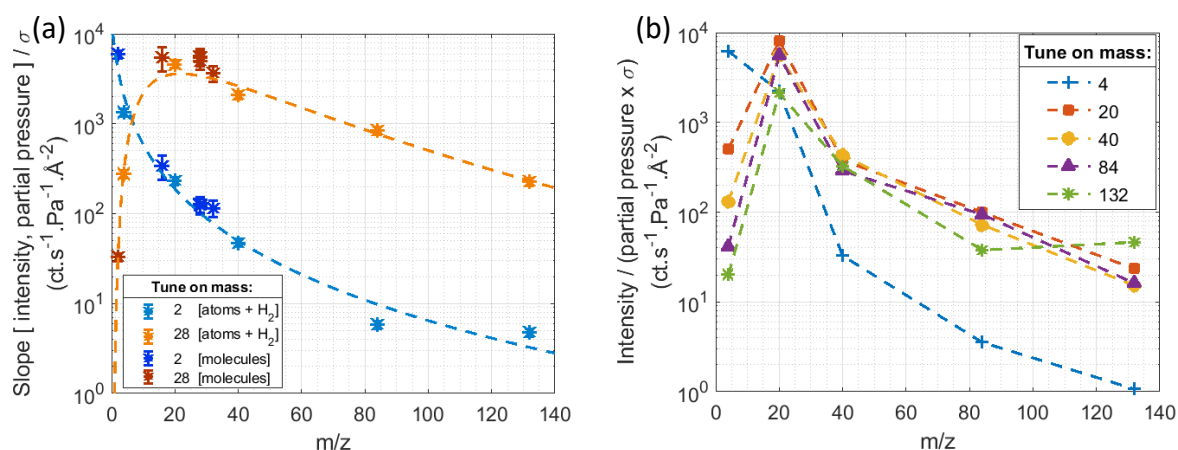
Figure II.1-8: Transmission curves for different MS tunings. (a) Tunings done on masses 2 (H_2) and 28 (N_2). (b) Tunings done on masses 4 (He), 20 (Ne), 40 (Ar), 84 (Kr) and 132 (Xe).

We also detected a slight variation in the transmission curve while using one or the other filament of the ionization source, as shown in **Figure II.1-9**. Filament 1 is the one usually used to acquire spectra, it should be more aged than filament 2. Therefore, we can guess that ageing of the filaments change their ionizing properties. Here, the use of filament 1 leads to a weaker signal at lower m/z.
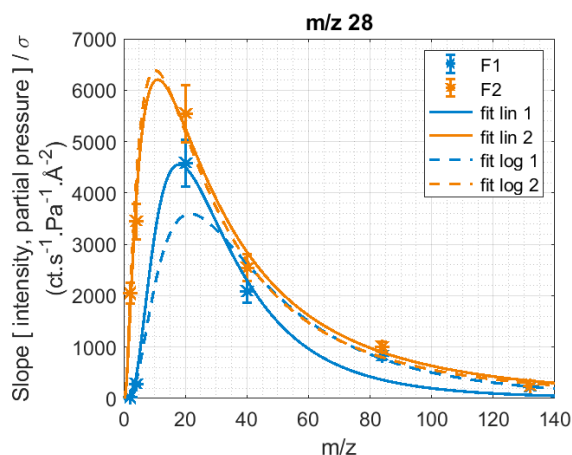
Figure II.1-9: Transmission curves for MS parameters tuned on mass 28, with either filament 1 or filament 2 on, linear and logarithmic fitting.

TRANSMISSION CURVE WITH THE ERROR BARS

The final parameters retained for the log-normal fit of T_{tot} for the tuning on m/z 28 are: G = 290 000, µ = 3.42 and s = 1. Figure II.1-10 plot a +/- 10% and a +/- 25% uncertainty area around the transmission curve. All the data points in noble gases with filament 2 are within the +/- 10% area. All the others are within the +/- 25% area, except for m/z 2 and 4 with filament 1, and for m/z 28. This could indicate an underestimation of the simple ionization cross section for N_2 in the case of our mass spectrometer. As the slope is very steep for m/z < 10, one should be very careful when interpreting the measurements of the low masses.
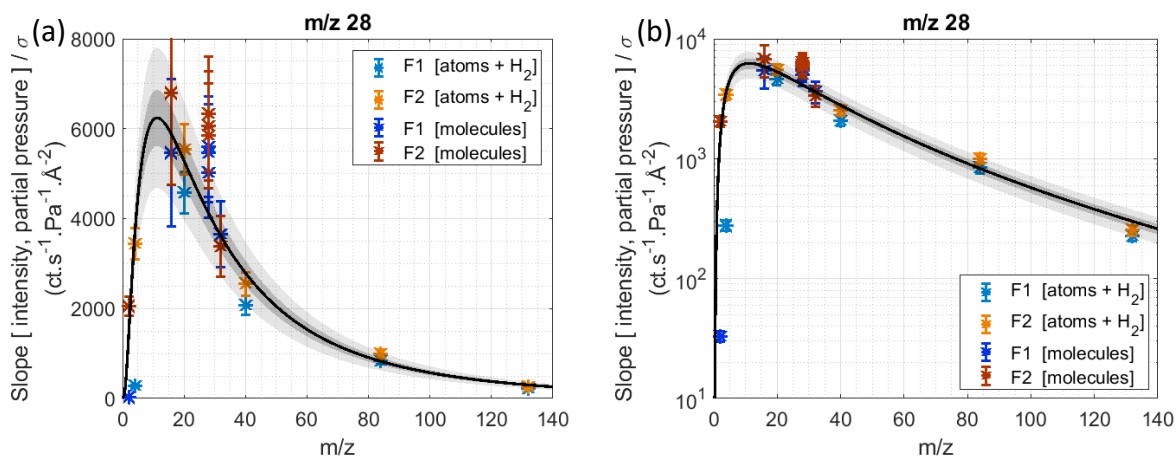
Figure II.1-10: Transmission curve for MS parameters tuned on mass 28 (with +/- 10% uncertainty), superposed with all the data points, from filament 1 and 2, from molecular and noble gases, (a) in linear scale and (b) in logarithmic scale.

The ionization of argon lead to the formation of double ionized argon Ar^{2+}, which has a m/z of 20, the same as Ne^+. Afterwards, we can have an idea of the error made on this point from the MS transmission measured and the argon double ionization ratio given by the NIST* (see

Table II.1-2). $I_{Ne^+} = I_{m/z20} - 0.146 \times \frac{T_{Ne}}{T_{Ar}} \times I_{m/z40}$. The ratio of transmission measured is $\frac{T_{Ne}}{T_{Ar}} \approx 2$. Therefore, we think the intensity of Ne used for the transmission above are overestimated of ~13%, which stays within the error bars of the transmission curve.

The above transmission curves can directly be used to obtain neutral densities from MS intensity measurements with the Equation II.1-1. The measurement should be taken with the same set of parameters than the ones used for the transmission. The low masses region is extremely sensitive to these parameters. Therefore, we do not recommend to deduce densities from MS measurements on low masses (m/z < ~10) if a precise transmission curve has not been done just before.

DETAILS OF THE TRANSMISSIONS INSIDE THE MS

The total transmission through the MS is due to three main mass-selective steps, shown in Figure II.1-11. The knowledge of their individual effect is not required for the analysis of neutral species. Nevertheless, their study is necessary to extend the calibration to the analysis of ions. Indeed, steps (1) and (2) are not applicable in the case of ions (see Section II.1.2.c).
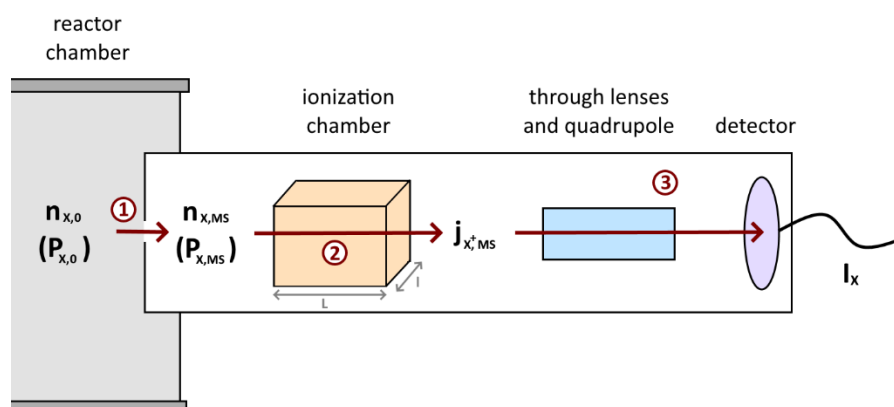
Figure II.1-11: Scheme of the detection of neutrals through the MS. The intensity collected by the detector for the atom / molecule X (I_X) is related to its density in the chamber ($n_{X,0}$) by three steps: (1) the transmission through a 100 μm aperture (T_{ap}), (2) the transmission through the ionization chamber (T_{ioni}) and (3) the transmission through the lenses, the quadrupole and the detector (T_{MS}).

With individual transmissions for the passage of the aperture, the ionization chamber and the quadrupole, the intensity measured by the MS (I_{MS}, in count/s) at the m/z of an atom/molecule X is linked to its neutral density in the chamber ($n_{X,0}$, in m^{-3}) by the following equation (Godet, 2006; Singh et al., 1999):

$$I_{MS}(m_X) = n_{X,0} \times T_{ap}(m_X) \times T_{ioni,X} \times T_{MS}(m_X) \times \frac{1}{K_{iso,X}} \qquad (II.1-3)$$

with T_{ap} the transmission through the pin hole aperture of the MS and T_{MS} the transmission through the MS (lenses, quadrupole, detector) at the main mass of X. $T_{ioni,X}$ is the transmission through the ionization chamber and $K_{iso,X}$ the coefficient to take all the isotopes of X into

account. The definitions of these transmissions are given just below. The computations to obtain their expressions is detailed further.

(1) The transmission through the pin hole aperture of the MS depends on the mass of the atom / molecule X (m_X) and the average mass of the carrier gas (m_{avg}).

$$T_{ap}(m_X) \equiv \frac{n_{X,MS}}{n_{x,0}} = \frac{P_{X,MS}}{P_{X,0}} \propto \frac{C_2}{\sqrt{m_{avg}}} + \frac{0.38}{\sqrt{m_X}} \qquad (II.1-4)$$

with C_2 = 0.46 for atoms and C_2 = 0.49 for diatomic molecules and methane.

(2) The transmission through the ionization chamber links the X neutral density at the entrance of the MS ($n_{X,MS}$) and the ion flux of X^+ inside the MS (j_{X+}).

$$T_{ioni}(X) \equiv \frac{j_{X^+,MS}}{n_{X,MS}} = \sigma_X \times cst1 \qquad [m.s^{-1}] \qquad (II.1-5)$$

(3) The transmission through the lenses, the quadrupole and the detector depends strongly on the MS parameters chosen. It relates the ion flux in the MS and the intensity detected.

$$T_{MS}(m_X) \equiv \frac{I_{MS}(m_X)}{j_{X^+,MS}} \qquad [ct.m^2] \qquad (II.1-6)$$

Finally, the total transmission is given by:

$$T_{tot}(m_X) = \frac{cst1}{k_B.T} \times T_{ap}(m_X) \times T_{MS}(m_X) \qquad [ct.s^{-1}.m^{-2}.Pa^{-1}] \qquad (II.1-7)$$

HOW TO DEDUCE THE ION FLUX INSIDE THE MS

It is also possible to get information on the ion flux inside the MS with a model for T_{ap} and $T_{ioni} = \sigma.cst1$. Indeed, Equations II.1-6 and II.1-7 lead to:

$$j_{Y^+,MS} = \frac{I_{MS}(m_Y)}{T_{MS}(m_Y)} \quad with \quad T_{MS}(m) = \frac{k_B T}{cst1} \times \frac{T_{tot}(m)}{T_{ap}(m)} \qquad (II.1-8)$$

T_{ap} and T_{ioni} depend on several constant parameters not always well known. Therefore, it is more convenient to **study the relative ion flux of Y^+, compared to the total ion flux inside the MS**. Therefore, we introduce $\tilde{T}_{MS}(m)$, the mass-dependent part of $T_{MS}(m)$ such as: $T_{MS}(m) = \tilde{T}_{MS}(m) \times cst$.

$$\frac{j_{Y^+,MS}}{j_{tot^+,MS}} = \frac{I_{MS}(m_Y)}{\tilde{T}_{MS}(m_Y)} \times \frac{1}{\sum_i \frac{I_{MS}(m_i)}{\tilde{T}_{MS}(m_i)}} \qquad (II.1-9)$$

At the entrance of the MS, the gas goes through a 100 µm hole. The main function of this hole is to reduce the pressure inside the MS, from ~1 mbar to ~5x10^{-6} mbar. **The passage of the hole can induce a differential transmission of the atoms and molecules depending on their mass.** It is governed by the flow regime, represented by the Knudsen number, ratio of the Debye length to the characteristic length of the system:

$$Kn = \frac{\lambda_D}{D} = \frac{k_B T}{\sqrt{2}.\pi.d^2.P.D} \qquad (II.1-10)$$

with D the diameter of the hole (100 µm), d the diameter of the particles (~300-400 pm for simple molecules), P the pressure and T the temperature of the gas. **Table II.1-3** gives the values of Kn for different configurations in our experiment.

Configuration	Pressure (mbar)	Characteristic dimensions	Kn	regime
inside PAMPRE	$P_0 \approx 0.5 - 1$	~10 cm	~10^{-3}	viscous
inside MS	$P_{MS} \approx 10^{-5}$	~1 cm	~10^3	molecular
at orifice, side of PAMPRE	P_0	100 µm	0.6 - 2	transitional
at orifice, side of MS	P_{MS}	100 µm	~10^5	molecular
inside orifice	**~(P$_0$+P$_{MS}$)/2**	**100 µm**	**1 - 4**	**transitional**

Table II.1-3: Knudsen number computed for different configurations of the experiment. The last line (in bold) is our case of interest.

The flux of a molecule (Q_X) through the pin hole depends on the (partial) pressures on both sides ($P_{X,0}$ and $P_{X,MS}$), and is expressed differently depending on the flow regime (O'Hanlon, 2003).

● **In the case of Kn > 10, the regime is a free molecular flow.** The mean free path is large compared to the aperture size, so the flow is determined by gas-wall collisions. Molecules have different fluxes depending on their mass (m_x) and their partial pressure ($P_{X,0} = R_X. P_0$):

$$Q_{molecular,X} = A.\frac{v_X}{4}.\left(P_{X,0} - P_{X,MS}\right)$$

$$with \ v_X = \sqrt{\frac{8.k_B T}{\pi.m_X}} \quad and \quad A = \pi.\left(\frac{D}{2}\right)^2 \qquad (II.1-11)$$

And for $P_{X,0} \gg P_{X,MS}$:

$$Q_{molecular,X} \approx A.P_{X,0}.\sqrt{k_B T}.C_1 \times \frac{1}{\sqrt{m_X}} \qquad with \ C_1 = \frac{1}{\sqrt{2\pi}} \qquad (II.1-12)$$

● **In the case of Kn < 0.01, the gas is considered viscous.** Molecules interact with each other. When the pressure on one side of the hole is much lower than the pressure on the other side, the flow reaches a maximum value as the gas is travelling at the speed of sound. In these conditions, the total flow depends on the average particle mass of the gas mixture injected (m_{avg}):

$$Q_{viscous} = A.P_0.\sqrt{k_B T}.C_2 \times \frac{1}{\sqrt{m_{avg}}}$$

$$with \; C_2 = C' \times \sqrt{\frac{2\gamma}{\gamma+1}} \times \left(\frac{2}{\gamma+1}\right)^{\frac{\gamma}{\gamma-1}} \qquad (II.1-13)$$

$$with \; the \; condition: \; \sim 10^{-5} = \frac{P_{MS}}{P_0} \leq \left(\frac{2}{\gamma+1}\right)^{\frac{\gamma}{\gamma-1}} \approx 0.5$$

C' is a factor taking into account that high-speed gas stream continues to decrease in diameter after passing through the orifice. For thin circular orifices, C' is equal to ~0.85. γ is the specific heat ratio, equals to ~1.4 for diatomic gases, 1.667 for monoatomic gases and 1,32 for methane. No selection in mass is done at the passage of the orifice. Therefore, in the case of a gas mixture, the individual flux of one molecule is $Q_{viscous,X} = R_X.Q_{viscous}$.

● **Nevertheless, in the case of interest here, 0.1 < Kn < 10: it is a transitional flow regime.** Collisions between molecules and with the walls are similarly important as the mean free paths is about the size of the hole. The theory of this regime is complex to define. However, O'Hanlon (2003) and Livesey (2001) consider a linear combination of $Q_{molecular,X}$ and $Q_{viscous,X}$, with a coefficient depending on the Knudsen number:

$$Q_{transition,X} = Q_{viscous,X} + Z \times Q_{molecular,X}$$

$$with \; Z \approx \frac{1}{1 + \frac{3\pi}{128}.\frac{1}{Kn}} \qquad (II.1-14)$$

The total gas flow can be also expressed as a function of the pumping speed (S_p) and the MS pressure (Godet, 2006):

$$Q_X = P_{MS,X} \times S_p \qquad (II.1-15)$$

From **Equations II.1-4, II.1-12, II.1-13, II.1-14** and **II.1-15**, we deduce **the transmission through the 100 μm aperture:**

$$T_{ap}(m_X) \equiv \frac{P_{X,MS}}{P_{X,0}} \approx \frac{A}{S_p}.\sqrt{k_B T} \times \left(\frac{C_2}{\sqrt{m_{avg}}} + \frac{Z.C_1}{\sqrt{m_X}}\right) \quad \propto \quad \frac{C_2}{\sqrt{m_{avg}}} + \frac{0.38}{\sqrt{m_X}} \qquad (II.1-16)$$

with C_2 = 0.46 for atoms and C_2 = 0.49 for diatomic molecules and methane.

The transmission through the ionization chamber links the neutral density of the atom / molecule X entering the chamber (n$_{X,MS}$) to the ion flux inside the MS (j$_{X+,MS}$). They are linked by the simple ionization cross section (σ$_X$).

$$\frac{dn_X}{dt} = -\sigma_X \, n_X \, n_e v_e$$

$$=> \quad n_X(t) = n_{X,MS} \times \exp(-\sigma_X \, n_e v_e t) \quad with \quad t = \frac{L}{v_X}$$

$$(II.1-17)$$

for t corresponding to the crossing of the ionization chamber by X. L is the length of the ionization chamber, n$_X$ (resp. n$_e$) the density of X (resp. electrons) in the ionization chamber, v$_X$ (resp. v$_e$) the velocity of X (resp. electrons). As $\frac{\sigma_X \, n_e v_e \, L}{v_X} \sim 10^{-7} \ll 1$, the Taylor expansion gives:

$$n_{X,L} \approx n_{X,MS} \times \left(1 - \frac{\sigma_X \, n_e v_e \, L}{v_X}\right) \qquad (II.1-18)$$

The evolution of X density is directly linked to the formation of the ion X$^+$.

$$n_{X^+,L} = n_{X,MS} - n_{X,L} = \; n_{X,MS} \times \left(\frac{\sigma_X \, n_e v_e \, L}{v_X}\right) \qquad (II.1-19)$$

Ion flux (j$_{X+,MS}$, in s^{-1}.m^{-2}) and electron current (I$_e$, in A) are more convenient to use than ion and electron densities in the ionization chamber. We therefore use:

$$j_{X^+,MS} = \frac{1}{4} \, n_{X^+,L} \times v_{X^+} \qquad (II.1-20)$$

$$I_e = \; \frac{1}{4} \, n_e \times v_e \times e \times l \times L \qquad (II.1-21)$$

with v$_{X+}$ the velocity of the ion X$^+$, supposed equal to v$_X$ in the ionization chamber, e the elementary charge, l the width and L the length of the ionization chamber.

The relation between j$_{X+}$ and n$_{X,MS}$ is obtained by combining Equations II.1-19, II.1-20 and II.1-21:

$$j_{X^+} = n_{X,MS} \times \sigma_X \times \frac{I_e}{l.e} = n_{X,MS} \times T_{ioni}(X)$$

$$(II.1-22)$$

$$with \quad T_{ioni}(X) \equiv \sigma_X \times \frac{I_e}{l.e} = \sigma_X \times cst1$$

The only dependence in the atom / molecule X chosen is the simple ionization cross section (σ$_X$). T$_{ioni}$ has *a priori* no dependence in mass.

EMPIRICAL ESTIMATION OF T_{MS}

The transmission through the lenses, the quadrupole and the detector (T_{MS}) can be deduced from the measured T_{tot} (m) and models for T_{ap} (m) and T_{ioni}. Especially, if one is interested only in the mass-dependent part, $\tilde{T}_{MS}(m)$, the computation is simplified in:

$$\tilde{T}_{MS}(m_X) = \frac{T_{tot}(m_X)}{\dfrac{C_2}{\sqrt{m_{avg}}} + \dfrac{0.38}{\sqrt{m_X}}} \qquad (II.1-23)$$

Figure II.1-12 shows that **T_{MS}(m) is not very different from T_{tot}(m)**. Both can be fitted by a log-normal law. For transmissions normalized on m/z 20, the parameters for the fits are: G_{tot} = 52, G_{MS} = 55, μ_{tot} = 3.4, μ_{MS} = 3.6 and s_{tot} = s_{MS} = 1.
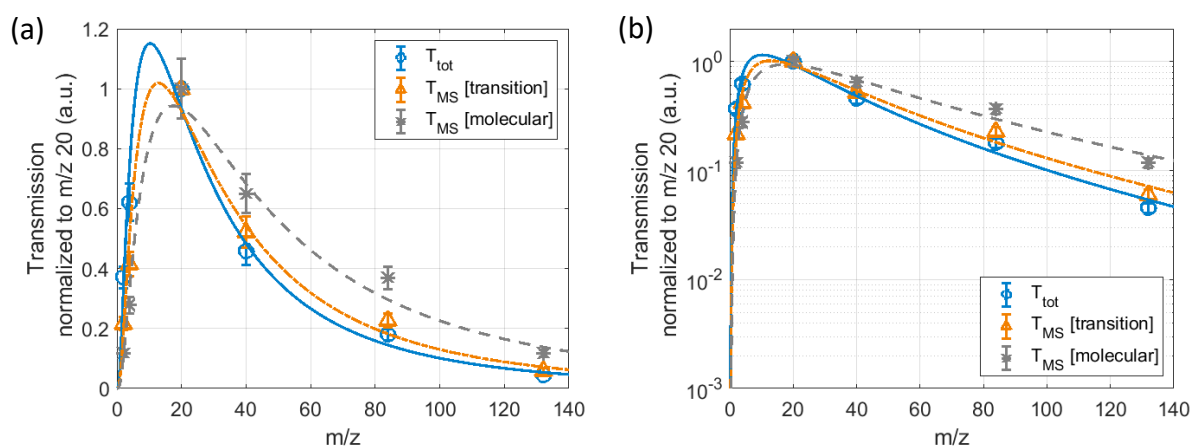
Figure II.1-12: Transmissions normalized to m/z 20: total transmission (line), and transmission only through the lenses, quadrupole and detector, deduced from T_{tot}, supposing a transition regime (dotted-dashed line) and a free molecular regime (dashed line). (a) With linear scale for the transmissions. (b) With logarithmic scale.

1.2.c. Possibility to use the transmission curve with ion measurements?

DIFFERENCES BETWEEN NEUTRAL AND ION MEASUREMENTS

In the case of ions, there is no ionization source, but the addition of a high voltage just after the entrance of the MS (the 'extractor') and an associated lens ('lens 1') to focus the incoming ions towards the inside of the MS (see **Figure II.1-13**). It is difficult to directly obtain a transmission curve for ions as one would need another instrument able to measure ions entering the MS. Therefore, **the MS transmission curve obtained in RGA mode is also used for ions, after some verifications.**
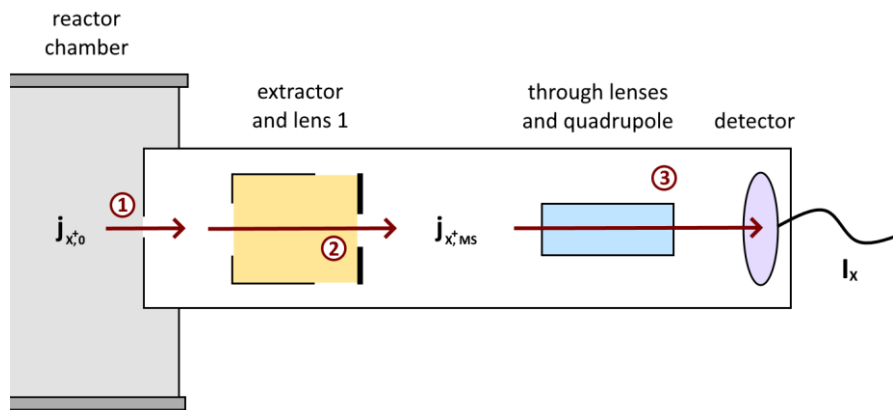
Figure II.1-13: Scheme of the detection of ions through the MS. The intensity collected by the detector for the ion X^+ (I_X) is related to its flux in the chamber ($j_{X+,0}$) by three steps: (1) the transmission through a 100 µm aperture, (2) the transmission through the extractor and lens 1 (T_{extr}) and (3) the transmission through the lenses, the quadrupole and the detector (T_{MS}).

(1) As we work with ion fluxes, **no change is expected from the passage of the 100 µm aperture** (Achkasov, 2015). A sheath forms on the surface of the collector head and accelerates ions perpendicularly to the surface. Due to this, ions become highly energetic (non-thermal) and mono-directional. Therefore, the ion beam goes through the orifice without changes in ion fluxes.

(3) The transmission of ions through the lenses (except lens 1), the quadrupole and the detector is the same as in RGA mode: **T_{MS} is the same as the one calibrated above.**

(2) **The only part to study is the travel of ions through the extractor and lens 1**: do they induce a mass-dependent transmission of ions (T_{extr})? To have an idea, we studied the passage of ions of different masses through the extractor and lens 1.

$$T_{extr} \equiv \frac{j_{X^+,MS}}{j_{X^+,0}} \qquad (II.1-24)$$

with $j_{X+,0}$ the ion flux at the entrance of the MS, and $j_{X+,MS}$, the ion flux after lens 1.

Measurements in ion mode are not stable in time due to charging effects in the MS [see **Figure SII.2-8** in **Section II.2.1**]. Therefore, with ions, we always work with relative intensities.

Figure II.1-14 shows that **the tuning of the MS parameters for the positive ions gives values very similar to the tuning in RGA mode**, with the addition of lens 1. This point is fundamental to possibly use the neutral calibration work with ions.
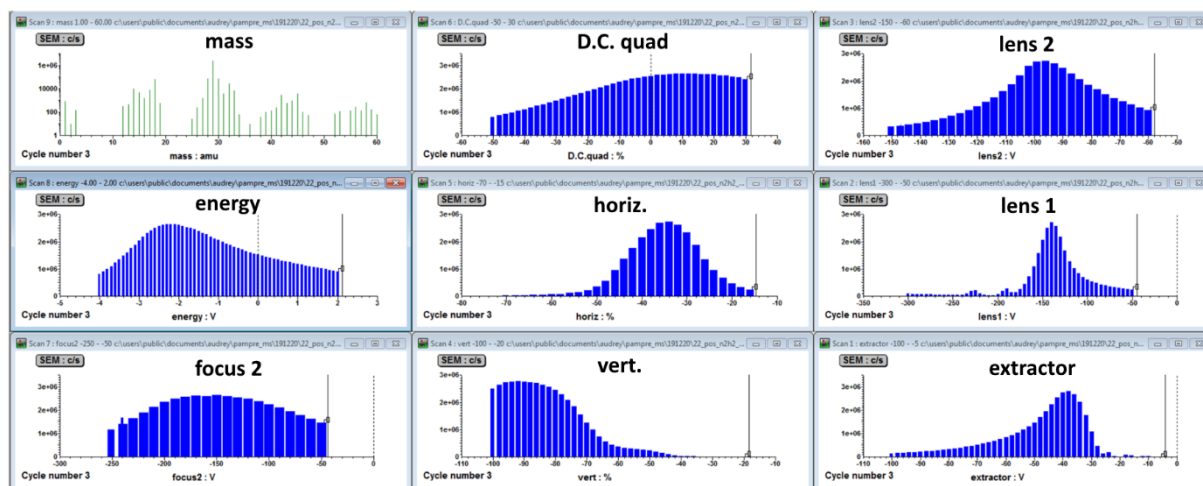
Figure II.1-14: Tuning of MS parameters in positive ion mode, on m/z 29, in $N_2 - 5\%$ H_2 plasma at 0.80 mbar and at an incident power of 30 W. The MS collecting head is positioned at 23 mm from the electrodes. Configuration without the confining box.

Lens 1 should be adapted to the value of the extractor chosen. Therefore, the parameter lens 1 was scanned and tuned for different values of the extractor. The 'energy' parameter was also scanned and tuned at the same time.

ENERGY DISTRIBUTION OF DIFFERENT IONS AS A FUNCTION OF THE EXTRACTOR POTENTIAL

As for neutrals, the 'energy' parameter is likely to change with the conditions and the ion nature. It is necessary to know its variations with the ions and the other MS parameters to find/validate the mass-dependence of the MS transmission with ions.

Energy scans give an idea of the distribution in energy of the ions measured. The values of energy in volts should be calibrated to get them in electron volts. In particular, the lowest energy should be equal to zero (here at ~-5/-6V). Indeed, ions that elastically collide just at the entrance of the MS enter with no energy.

Figure II.1-15 shows that the energy scans have similar shapes for all the ions in a N_2-H_2 plasma at 0.80 mbar. It is not the case for noble gas ions, that have very different energy distributions (see **Figure II.1-16**). The energy distributions change depending on the value applied to the extractor, and usually shift to higher values of the energy for a higher extractor. The extractor tends to accelerate the ions.

To compare the measured intensities of ions within a same spectrum, one should check that they have similar energy distributions, with the same maximum at a given value of the extractor potential (Barton et al., 2000; Walton et al., 2007). **Figure II.1-17** shows there is no

problem with ions in N_2-H_2 (it is also valid in N_2-CH_4), except for H_3^+. However, it is not the case for noble gas ions.
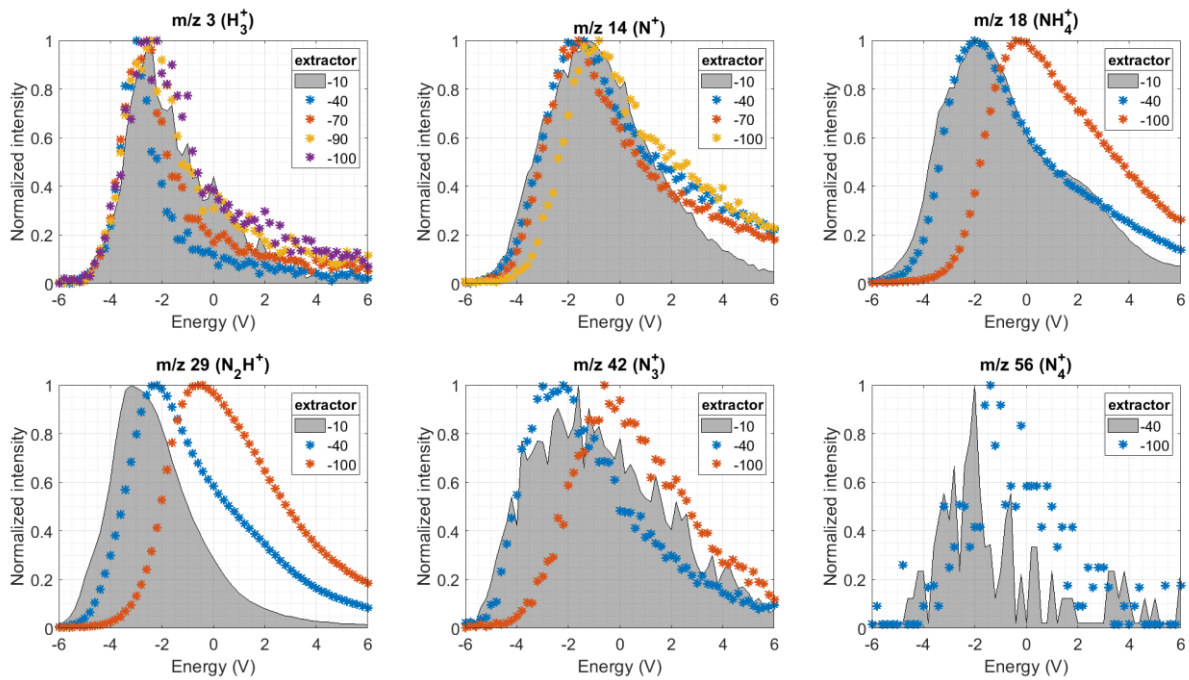
Figure II.1-15: Energy scans for different ions of a N_2-H_2 plasma (same conditions as **Figure II.1-14**) for different values of the extractor potential.
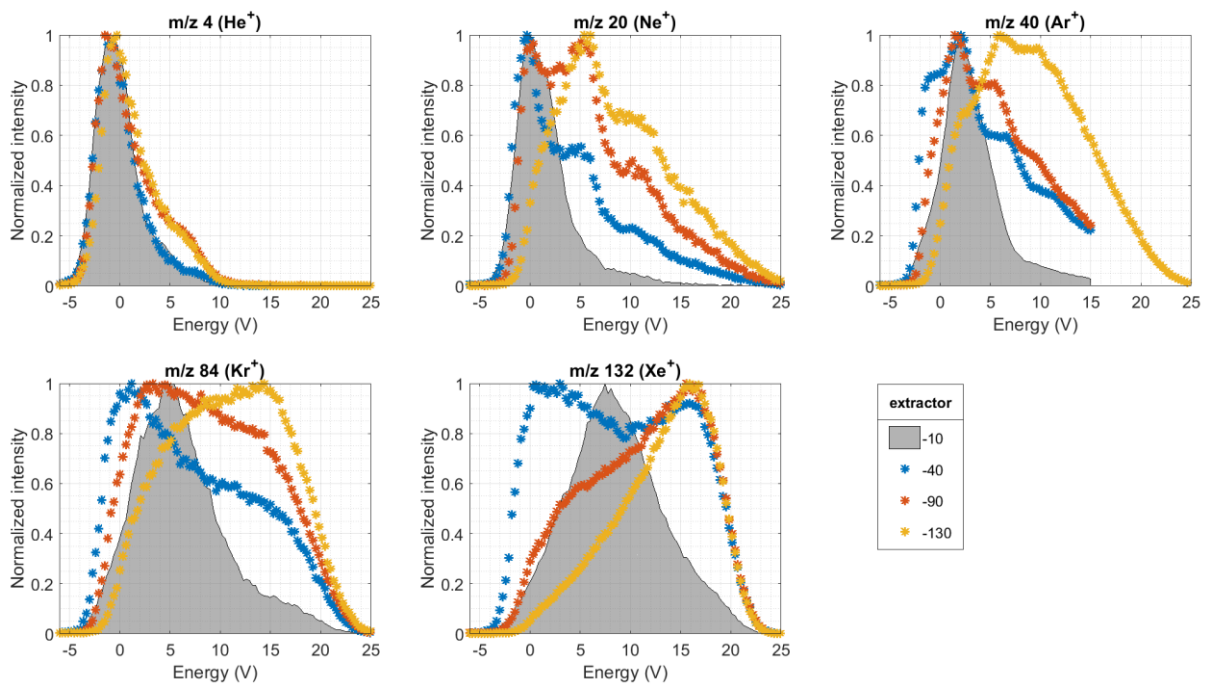
Figure II.1-16: Energy scans for different ions of a plasma in He-Ne-Ar-Kr-Xe (0.84 mbar, incident 30 W) for different values of the extractor potential. The plasma was not confined and the collector head was positioned at 23 mm from the electrodes. Configuration without the confining box.
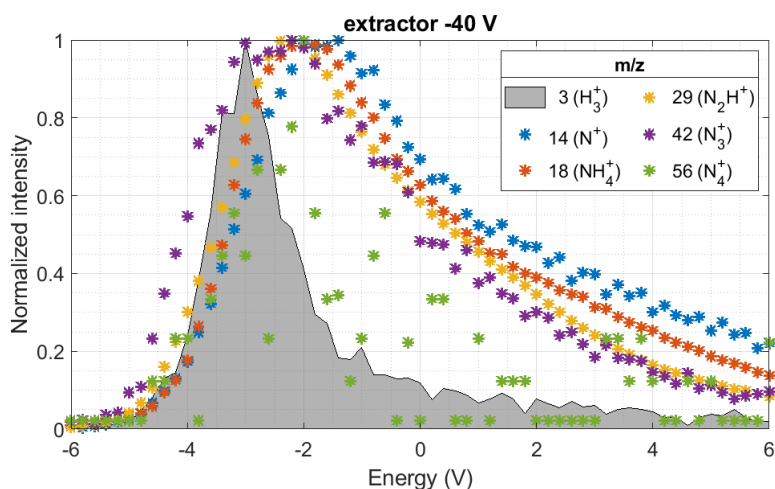
Figure II.1-17: Energy scans for different ions of a N_2-H_2 plasma (same conditions as **Figure II.1-14**). The value of the extractor potential was fixed at -40 V.

LENS 1 SCANS FOR DIFFERENT IONS AS A FUNCTION OF THE EXTRACTOR POTENTIAL

The other MS parameter to investigate to find if it has a mass-dependent transmission is lens 1. The extractor accelerates ions, which are focused back in the MS by lens 1. Therefore, **lens 1 should be adapted for each value of the extractor** (see **Figure II.1-18 (a)**). **Figure II.1-18 (b)** shows a linear dependence between lens 1 and the extractor for values of the extractor between 0 and -60 V. Below, the value for lens 1 is optimized at ~ -250 V, and can vary of 50V.
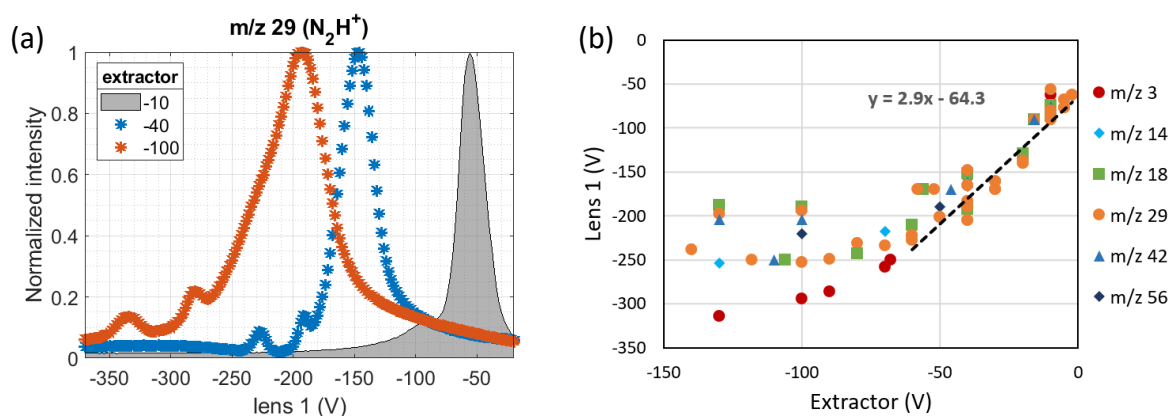
Figure II.1-18: Evolution of Lens 1 tunings with the value of the extractor in a N_2-H_2 plasma (same conditions as **Figure II.1-14**). (a) Lens 1 scans at m/z 29. (b) Maximum of Lens 1 for different ions.

Figure II.1-19 shows that for small values of the extractor, scans of lens 1 for different ions are very similar. At -40 V, H_3^+ has a distribution shifted toward larger absolute values of the extractor. This enhances the fact that MS measurements for small masses should not be directly compared to the measurements at higher m/z. For higher absolute values of the extractor, the shape and the central value of lens 1 scans start to change from one ion to another. Besides, the modifications are not linear with the mass of the ions, and seem more due to the nature of the ions. **In conclusion, for absolute values of the extractor below 40-60, one should reasonably say that lens 1 focuses similarly all the ions (< 20-30% error) except the ions with small masses (below m/z ~ 5-10).**
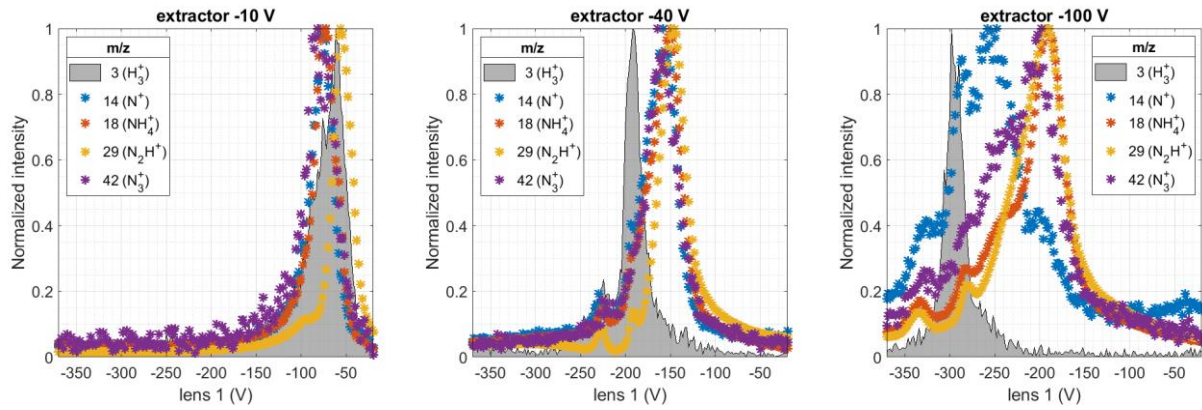
Figure II.1-19: Lens 1 scans for different values of the extractor. N_2-H_2 plasma, in the same conditions as for **Figure II.1-14**.

CONCLUSION: A TRANSMISSION CURVE FOR THE IONS?

Ions in the MS undergo a supplementary process in ion mode than in RGA mode: the passage through the extractor and lens 1. At high potential of the extractor, ion energy is likely to change. As lens 1 focuses similarly all the ions (except very low masses) for absolute values of the extractor below 40-60 V, we can expect that **the group formed by the extractor and lens 1 has a transmission (T_{extr}) non mass dependent** in these conditions (at least < 20-30% modifications).

Therefore, to compare ions measured on a same mass spectrum, with similar energies, we can use the above transmission curve T_{MS}, obtained in RGA mode. For an ion X^+ present in the chamber, leading to an intensity of $I_{MS}(m_X)$ [ct/s] detected by the MS, the relative ion flux in the chamber can be deduced by:

$$\frac{j_{X^+,0}}{j_{tot^+,0}} = \frac{j_{X^+,MS}}{j_{tot^+,MS}} = \frac{I_{MS}(m_X)}{\tilde{T}_{MS}(m_X)} \times \frac{1}{\sum_i \frac{I_{MS}(m_i)}{\tilde{T}_{MS}(m_i)}} \qquad (II.1-25)$$

The results obtained are then valid in order of magnitude, with a possible 20-30% modification. They are not valid for ions of low masses (ex: H_3^+) or for ions with very different energy distributions (ex: Kr, Xe).

The ion flux computed in this way is the ion flux at the entrance of the MS. A sheath forms on the MS collector head, the ion flux measured is therefore not equal to the ion flux in the bulk of the plasma discharge. Sode et al. (2013) developed a simple model to take the sheath effect into account, to deduce the ion flux in the bulk, as well as the ion densities from the electron density. In the case of PAMPRE, the ion 3D distribution is studied by a more complex model, created in collaboration with the Centro de Física das Universidades do Minho e do Porto, and described in **Section II.2.3**. By using this model we will be able to relate the ion fluxes determined at the entrance of the MS as described above with the bulk properties of the ions in the plasma.

CONCLUSION ON THE MS CALIBRATION

The MS intensity measurement has been calibrated with the injection of different gases in known quantity. This calibration enables afterwards to obtain the absolute density of neutral species, and to relatively compare the ion densities at different m/z.

For neutrals: the total transmission curves have been computed in two cases: for MS parameters tuned on m/z 2, and on m/z 28, respectively for low masses (< 4 u) and heavier masses. In both cases the 'energy' parameter should be adjusted before the acquisition.

The total transmission T_{tot} enables to retrieve the partial pressure P_x of a gas species X from the intensity $I_{MS}(m_X)$ of the peak corresponding to its major isotope and its major fragment:

$$T_{tot}(m_X) = \frac{I_{MS}(m_X) \times K_{iso,X}}{\sigma_X \times P_X}$$

with σ_X the simple ionization cross section of the atom/molecule X and $K_{iso,x}$ the coefficient to take all its isotopes into account.

The total transmission curves are well fitted by a log-normal law:

$$f(m_X; G, \mu, s) = \frac{G}{x.\ s.\ \sqrt{2\pi}} . \exp\left(-\frac{(\ln(m_X) - \mu)^2}{2s^2}\right)$$

with G = 37 100, μ = 1 and s = 1.57 for the tuning on m/z 2 and G = 290 000, μ = 3.42 and s = 1 for the tuning on m/z 28.

For positive ions: the transmission curve has been deduced from the one in the neutral mode. In the case of ions, this correction is only relative because the MS ion intensities are not quantitative. The value for the extractor should be selected below 60-40 V. The parameters lens 1 and 'energy' should be tuned before the acquisition.

The relative flux j/j_{tot} of the ion X^+ entering the MS collecting head can be deduced from:

$$\frac{j_{X^+,0}}{j_{tot^+,0}} = \frac{I_{MS}(m_X)}{\tilde{T}_{MS}(m_X)} \times \frac{1}{\sum_i \frac{I_{MS}(m_i)}{\tilde{T}_{MS}(m_i)}}$$

with $\tilde{T}_{MS}$ the transmission through the MS and Σ_i the sum on all the ions. $\tilde{T}_{MS}$ is well fitted by a log-normal law with: μ = 3.6 and s = 1 (in the case of an acquisition with parameters tuned on m/z 28).

2- Case of an RF CCP discharge with the PAMPRE experiment

The PAMPRE experiment (see Section I.4.2) can ignite radiofrequency capacitively coupled plasma (RF CCP) discharges. As part of the strategy developed in Section II.1.1.a, we extensively studied discharges in N₂-H₂. The aim is to understand the N₂-H₂ plasma is this configuration and build a 2D model of the discharge.

This work was done in collaboration with a team from the Instituto de Plasmas e Fusão Nuclear (Portugal), and led to two papers (**Paper 1** and **Paper 2**: *N₂-H₂ capacitively coupled radiofrequency discharges at low pressure* part I and II), combining experimental data and modeling of the discharge. Their content is reproduced below, and some supplementary information is added with grey boxes.

2.1- The experimental setup

2.1.a. PAMPRE: an RF CCP discharge in N₂-H₂
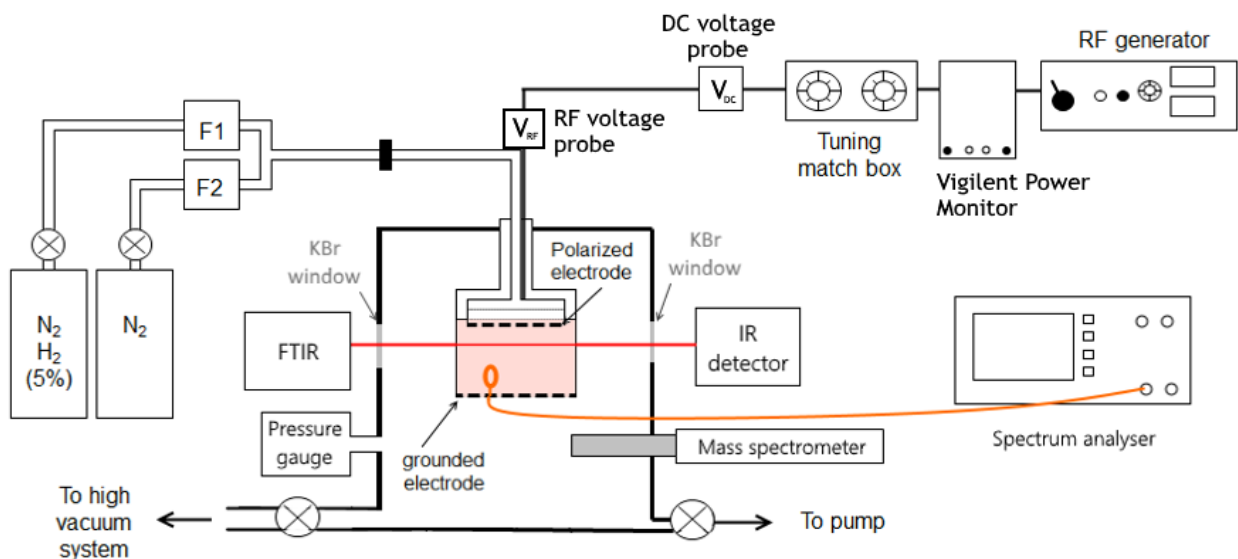
Figure II.2-1: Experimental set up.

The experiment is a radiofrequency capacitively coupled plasma discharge (RF CCP) set up presented in **Figure II.2-1** (Alcouffe et al., 2010; Szopa et al., 2006). It is a wide stainless steel cylindrical chamber, with a diameter of 30 cm and a height of 40 cm. Two KBr windows are disposed for IR absorption measurements. In the middle of the chamber, the RF voltage is applied to the upper electrode which is a stainless steel disk grid of 12.6 cm in diameter. Through this grid the gas is injected as a homogeneous flow. **The plasma is confined in a grounded aluminum alloy cylindrical box** surrounding the upper electrode. The bottom of the

box at 3.4 cm from the upper electrode is also a grid to let the gas go through. Four 2 cm-large and 4 cm-high slits are pierced in the sides of the box for the instruments to access the plasma. They are covered by thin metallic grids when unused in order to maintain the plasma in the box.

Some parameters are varied for this study: the percentage of H_2, the total pressure and the injected RF power. Before each experiment the chamber is heated and pumped to high vacuum (down to 10^{-6} mbar) with a turbo-molecular pump in order to clean the chamber. At the beginning of each experiment, the selected gas mixture is injected in continuous flow. The gas flow stabilizes after ~3 min and only then the plasma is ignited.

High purity gases (Air Liquide N60 Alphagaz 2, purity > 99.999%) are used. The amount of H_2 from 0 to 5% is obtained by mixing pure N_2 and a 95% N_2 - 5% H_2 mixture. The mixing is obtained by two mass flow controllers (MKS 100 Standard Cubic Centimeter per Minute (sccm), full scale accuracy 1%) injecting gas with individual flow varying from 2 to 70 sccm, and giving a global gas flow from 10 to 70 sccm. Pressure, measured by a capacitance gauge (MKS baratron 100 mbar full scale accuracy 0.15%), can therefore be adjusted from 0.3 to 1 mbar. The RF power generator delivers an incident power of 5 to 30 W at 13.56 MHz (SAIREM GRP01KE – 100 W maximum power). A matchbox is connected between the generator and the plasma for impedance adaptation.

2.1.b. Electrical measurements

The RF peak-to-peak voltage ($V_{RF,pp}$) is one of the key reference parameters used to describe the experimental conditions. It is measured by a high-voltage probe connected to the driven electrode by a stainless steel tube of 30 cm in length, which induces almost no potential drop. It is positioned under vacuum to avoid electrical breakdown. **A DC voltage probe situated between the polarized electrode and the match box gives the self-bias potential V_{DC}** with a precision of 0.3V. The self-bias potential appears when both electrodes differ in size and when a coupling capacitor is present between the RF power supply and the electrode (the match box in **Figure II.2-1**). In these conditions, the asymmetry of currents collected on the two electrodes creates the self-bias potential (Bogaerts et al., 2002). It is related to the electron density and the electron temperature.

RF power measurements are performed by a digital V-I probe (Vigilent Power Monitor Solayl) positioned between the generator and the match box. It gives the transmitted power with an accuracy of 2%. The incident and reflected power and the RF current (± 0.01A) are measured. The transmitted power measured with plasma ON is subtracted by the transmitted power with plasma OFF for the same RF peak-to-peak voltage to obtain the power absorbed by the plasma.

2.1.c. Electron density measured by a resonant cavity method

One of the most relevant parameter of the plasma is the electron density. It is determined in various sets of parameters thanks to a resonant cavity method, as similarly done in Alcouffe et al. (2010), Alves et al. (2012) and Wattieaux et al. (2015).

The metallic confining box is used as a microwave resonance cavity. Microwaves are emitted and measured by an antenna loop of 0.8 cm in diameter. The antenna is positioned perpendicularly to a box radius to enhance the transversal modes (TM). A second loop can be positioned symmetrically to measure the transmitted signal. Measurements done in transmission with two antennas and in reflexion with only one antenna have been compared (see **Supplement SII.2-1**). We found that reflexion measurements are more precise, so this mode was chosen in the following. Microwaves from 1 to 4 GHz are delivered and detected with a spectrum analyzer (Rohde & Schwarz ZVL Accuracy of reflection measurements: < 0.4 dB for 0 dB to -15 dB and < 1dB for -15 dB to -25 dB).

Microwaves emitted in a metallic cylindrical box (R_c = 6.9 cm, L_c = 3.5 cm) theoretically lead to **resonant $TM_{l,m,p}$ modes** described by:

$$f_{lmp} = \frac{c}{2\pi\sqrt{\varepsilon_r}} \sqrt{\frac{\lambda_{lm}^2}{R_c^2} + \frac{p^2\pi^2}{L_c^2}} \qquad l, p = 0,1,2 \dots \qquad m = 1,2 \dots \qquad (II.2-1)$$

where λ_{lm} is the mth zero of the equation $J_l(\lambda)$=0, where J_l is the lth Bessel function. In air or vacuum, the theoretical resonant frequencies lower than 4 GHz are the transversal modes TM_{010} (1.66 GHz), TM_{110} (2.65 GHz) and TM_{210} (3.55 GHz).

The dielectric constant ε_r of the plasma is a function of the electron density. It induces a shift in the resonance frequency with and without plasma, which gives the relation: (Haverlag et al., 1991)

$$n_e = A \times \frac{8\,\pi^2 m_e \epsilon_0}{e^2} \times \frac{f^2}{f_0} \times (f - f_0) \qquad (II.2-2)$$

where n_e, m_e and e are respectively the electron density, mass and charge, f and f_0 the resonant frequencies respectively with and without plasma. Finally, A is a factor depending on the cavity geometry and the chosen mode (Alves et al., 2012). It was calculated for pure N_2 plasmas taking into account n_e profiles in our conditions: 1.03 for TM_{010}, 1.09 for TM_{110} and 1.14 for TM_{210} (G. Wattieaux – private communication).

Improvements have been done on the technique since Alcouffe et al. (2010), Alves et al. (2012) and Wattieaux et al. (2015). Microwave resonance spectra directly acquired in the confining box show parasitic absorption. These absorptions are attributed to the gap between the polarized electrode and the grounded box. We added a thin copper crown in between the polarized electrode and the box sides in order to create a more ideal cylindrical cavity (see **Supplement II.2-2**). Parasitic absorption peaks disappear with this method (see **Supplement SII.2-1**). **Figure II.2-2** shows a schematic of the addition of the copper crown in the experiment, and the resonance shifts obtained for a N_2-H_2 (95-5) mixture at 0.9 mbar.
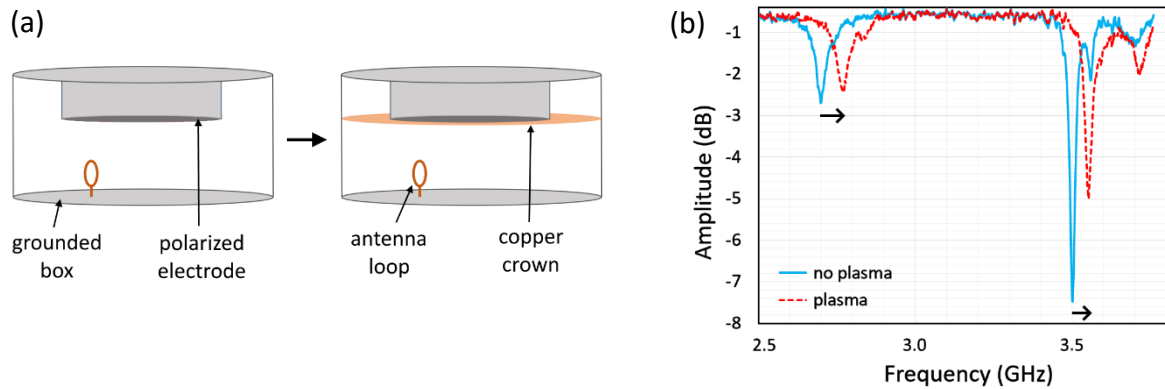
Figure II.2-2: Electron density measurement.   (a) Scheme of the installation of a copper crown between the polarized electrode and the confining grounded box to improve the signal.   (b) Spectra showing the resonant frequencies in the box, before and after plasma ignition (0.91 mbar – N_2-H_2 5% - 13.5 W)

Two peaks are especially visible at 2.70 and 3.50 GHz, attributed to the modes TM_{110} and TM_{210}. Measurements with both frequencies give similar results for the electron density, with differences of only 2%. Therefore, **we then focused only on the TM_{210} mode because it had a greater intensity.** The resolution of frequency measurements is ~0.5 MHz, which gives a resolution of ~6.10^7 cm^{-3} for electron density.

We observe a slow shift of the resonance when the plasma is turned OFF due to the box cooling, changing slightly its dimensions and therefore the resonance frequency (see **Supplement SII.2-3**). Consequently, f_0 is measured just after plasma extinction for all the experimental conditions. Each measurement was done at least 2 to 3 times on different days to ensure the repeatability. **For measurements with identical H_2 amount, pressure and RF peak-to-peak voltage, the mean standard deviations are ~8% for the electron density, ~5% for the transmitted power and ~2% for the DC voltage.**

Figure SII.2-1 presents the resonant TM modes acquired without and with the crown. These spectra are obtained in the configuration with two antennas (transmission mode). Especially, the TM_{110} and TM_{210} are more clearly identified with the crown.
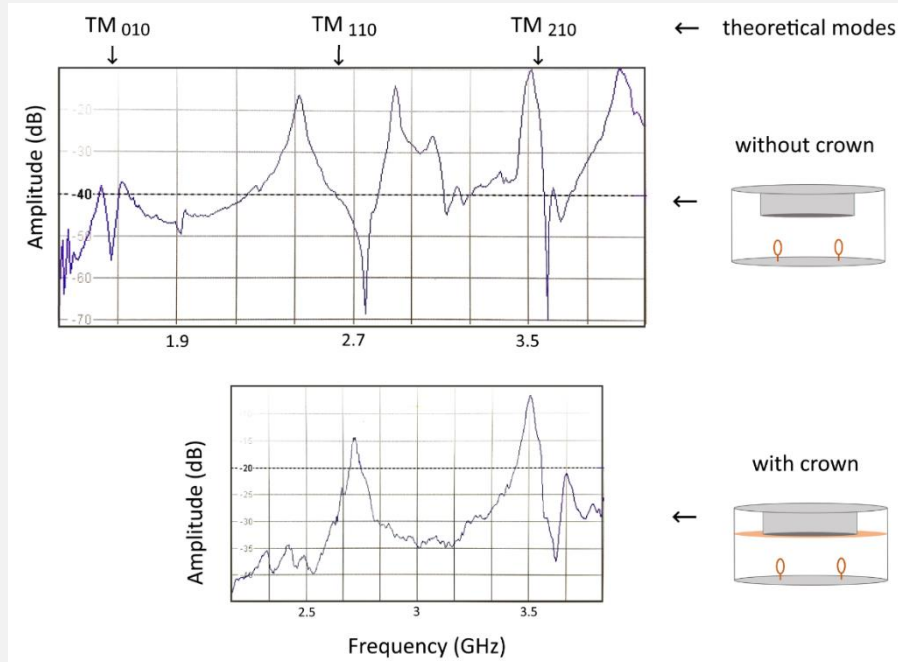
Figure SII.2-1: Spectra showing resonant TM modes in the box, without and with the copper crown.

The resonance is also detected by the reflection on the emitting antenna. **Spectra acquired in transmission (with two antennas) and in reflection (with one antenna) are presented in Figure SII.2-2.** The signal in reflection has a more stable baseline and thinner peaks. As the signal for the TM_{210} mode is the most intense, measurements of resonance shifts are done in reflection, and with this mode.
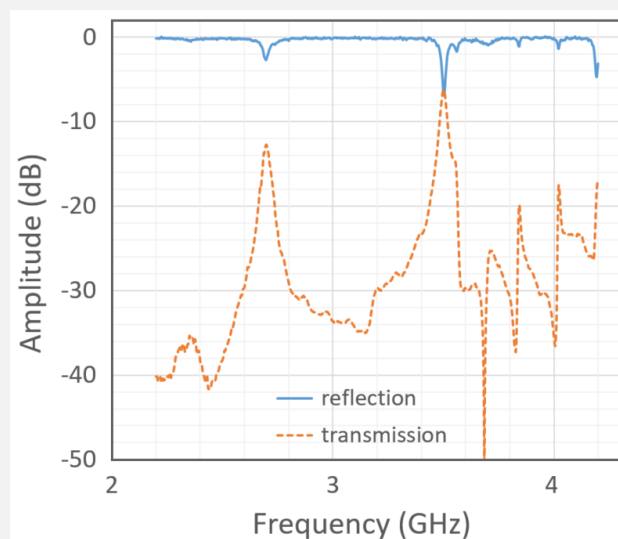
Figure SII.2-2: Resonances of the TM_{110} TM_{210} frequencies in the box, in reflection and in transmission.

(a)

(b)

Figure SII.2-3: Pictures of the resonant cavity. (a) Top part, with a copper crown and its insulating tape. (b) Lower part, in the case of 2 loop antennas.

SUPPLEMENT SII.2-3: DRIFT OF THE RESONANT FREQUENCY DUE TO TEMPERATURE EFFECT

The resonant frequencies in the cavity depends on the cavity dimensions (see **Equation II.2-1**). These dimensions are likely to change slightly due to the heating of the aluminum box by the plasma during the measurement (a few minutes). **Here we investigate the impact of a change in temperature (T) on the radius of the box (R_c) and on the resonant frequencies (f).**

From **Equation II.2-1** we can deduce for a small change of the radius:

$$\frac{\Delta f}{f} = \frac{\Delta R_C}{R_C} \qquad (SII.2-1)$$

The dilatation of a length L of aluminum is obtained by:

$$\frac{\Delta L}{L} = \alpha.\Delta T \qquad with \ \alpha = 23 \times 10^{-6} \ K^{-1} \qquad (SII.2-2)$$

Concerning the cavity, L corresponds to the perimeter. Consequently:

$$\frac{\Delta L}{L} = \frac{\Delta R_C}{R_C} \qquad\qquad (SII.2-3)$$

Therefore, we obtain the relation between the change induced by temperature on the resonant frequency:

$$\frac{\Delta f}{f} = \alpha . \Delta T \qquad\qquad (SII.2-4)$$

The resonant frequency without plasma f_0 measured just after the plasma is usually < 0.6 MHz smaller than the resonant frequency measured before the plasma (3.505 GHz).

From the previous equations we deduce the variations on R_c and on T required to obtain a shift of 0.6 MHz for f_0. We obtain $\Delta R \approx 0.1\ mm$ and $\Delta T \approx 7°C$, which are realistic values. **This confirms that the shift observed for f_0 measured before and after plasma is due to a temperature effect.**

2.1.d. Ammonia measurements by IR transmission spectroscopy and neutral mass spectrometry

Note: the calibration of the MS presented in **Section II.1.2** has been performed after this study on ammonia. Neutral MS measurements in this section have not been acquired with the same setup parameters than for the calibration. Therefore, the transmission curve obtained in **Section II.1.2** is not applicable there. Ammonia cannot directly be deduced from the MS spectra. To quantify ammonia in this study we rather used IR absorption spectroscopy.

QUANTIFICATION OF AMMONIA DENSITY BY IR TRANSMISSION SPECTROSCOPY

Simple gaseous molecules have previously been studied in PAMPRE using IR spectroscopy. The plasma was ignited during hours and molecules accumulated in an external (Gautier et al., 2011) or internal (Dubois et al., 2019) cold trap. Thereafter, the content of the trap was released in the chamber for the IR analysis. The main objective was to obtain densities high enough for an accurate IR measurement. This method was tested for **ammonia** but without a good accuracy because ammonia adsorbs easily on metallic surfaces. Therefore, direct measurements during the plasma are necessary. Even if ammonia is homogeneously distributed in the chamber (see **Supplement SII.2-6**), its density is low and the absorption length between the two KBr windows (50.8 cm) is not long enough to easily measure the absorption. **The parameters of the FTIR spectrometer have to be finely adjusted to maximize the signal.** We focused on a short wavelength range centered on the two most intense NH_3 IR absorption bands (between 850 and 1050 cm^{-1}).

Spectra are taken by a Fourier Transform IR spectrometer (FTIR – Nicolet 6700 from Thermo Fisher), with a MCT detector and a Michelson speed of 0.63 cm/s. 3000 to 6000 scans are accumulated, at resolutions between 1 and 4 cm^{-1}. A single final spectrum takes 2 to 3 hours to be obtained. The IR analysis is used for calibration of the MS (see **Supplement SII.2-7**).

Final spectra are analyzed with a **program** developed by Klarenaar et al. (2017). It **deduces the ammonia amount from the IR absorption spectrum**, the experimental conditions (mainly total pressure) and the molecular data from the HITRAN database. The main uncertainty on the deduced value of ammonia density is the neutral gas temperature which requires a higher resolution to be deduced from the IR spectra. A Resistance Temperature Detector (RTD, PT 100) measures the polarized electrode temperature. This temperature increases from 25 to 60°C during the 3-hours plasma duration. **Such gas temperature variations lead to 15-20% uncertainty on the ammonia density calculation.** **Figure II.2-3** presents a typical IR absorption spectra recorded for a plasma of 3% of H_2 at 0.53 mbar.
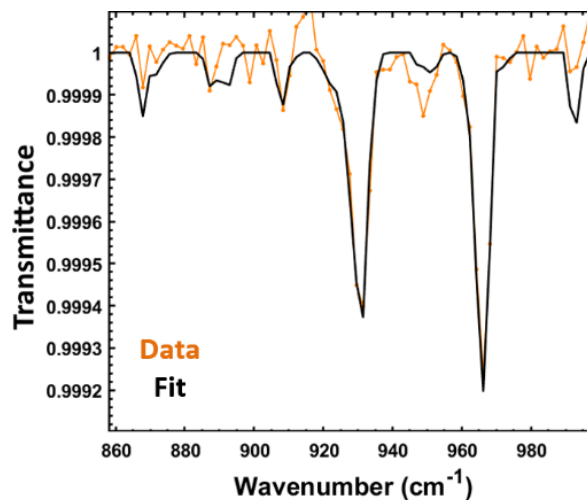
Figure II.2-3: IR spectra of ammonia detected in the experiment (N_2-H_2 3% - 0.53 mbar – 8.4 W) and fitted to deduce ammonia density. Spectra integrated over 1h45 at 4 cm^{-1} resolution.

Eight spectra were acquired for different conditions: for amounts of H_2 of 1, 3 and 5% and at two different pressures, 0.53 mbar and 0.91 mbar. Results are given in **Section II.2.2.b**.

CALIBRATION OF THE MASS SPECTROMETER WITH SIMULTANEOUS INFRARED SPECTROSCOPY MEASUREMENTS

The ammonia amount is measured in the chamber by the quadrupole mass spectrometer introduced in **Section II.1.2**. The movable grounded sampling stick is positioned at a few centimeters from the confining box, with a sampling orifice of 100 µm. Ammonia is detected with the residual gas analyzer mode (RGA), with an electron energy of 70 V and a filament intensity of 5 µA. The detector is a Secondary Electron Multiplier (SEM). Spectra were acquired with m/z ratio from 2 to 60, averaged on 3 to 10 scans, with a total acquisition time of 1-2 minutes, and a dynamic range of 10^6 c/s.

Ammonia fragmentation main ion peaks in RGA are at m/z 17 and 16. Traces of water are detected at m/z 18. We deduced from the peak at m/z 18 and the NIST database the minor contributions of water to the peaks at m/z 17 and 16 and removed it to obtain the contribution of ammonia (5-20% correction) (see **Supplement II.2-4**). **Figure II.2-4** presents mass spectra recorded for 3 gas mixture conditions.
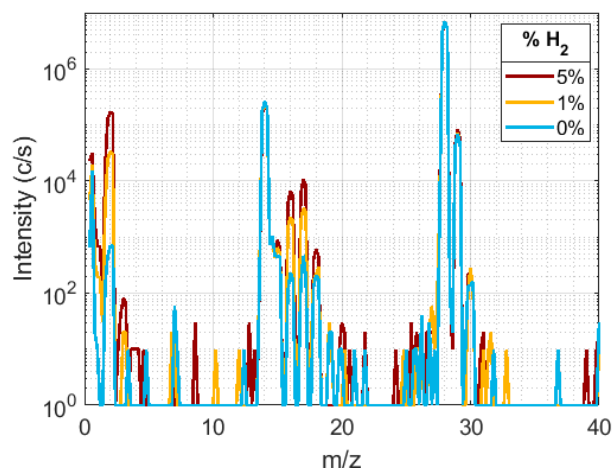
Figure II.2-4: MS spectra during plasma (0.91 mbar, ~11 W) in N_2 and N_2-H_2 at different percentages of H_2. N_2 has fragments at m/z 7, 14, 15, 28, 29, 30. H_2 is visible at m/z 2. m/z 16 and 17 are mainly associated to ammonia. Traces of water are detected at m/z 18. The lower detection limit is at ~30 c/s.

MS are highly sensitive to their electrical environment and measured intensities can drift up to 25% (see **Supplement II.2-5**). It is especially the case when acquisitions are done during a long time, without adjusting the 'energy' parameter of the MS (see **Section II.1.2**). To avoid any changes in the global intensity due to charging effects by the plasma, **intensities where divided by a reference peak in the spectra.** We chose m/z 14, a dissociation peak of N_2 which is closer to the m/z 17 peak of NH_3 than m/z 28.

At the ignition of the discharge, close to the confining box, the ammonia amount roughly stabilizes in 2-3 minutes (see **Supplement II.2-8**). However, ammonia tends to adsorb on the metallic walls of the chamber and the homogenization of ammonia in the chamber takes several tens of minutes to hours, depending on the surface state of the walls and the plasma parameters (see **Supplement II.2-6**). **Simultaneous measurements of ammonia by IR spectroscopy and MS spectrometry are therefore both started 30 min after the ignition of plasma, and integrated over 1.5 to 3 hours** (depending on the parameters for the IR spectrum acquisition).

We performed two calibrations at two different pressures (see **Supplement SII.2-7**). The precision is limited by the IR measurement (+/- 10%). The evolution of the calibration coefficient between NH_3 density and m/z ratio 17/14 is linear with pressure.

Sᴜᴘᴘʟᴇᴍᴇɴᴛ SII.2-4: Wᴀᴛᴇʀ ɪɴ ᴛʜᴇ ᴇxᴘᴇʀɪᴍᴇɴᴛ?

In mass spectrometry, water induces a main peak at 18 u, but also smaller peaks at 17 u and 16 u. However, the signal of ammonia is mainly observed at 17 u and 16 u (see **Figure SII.2-4**).
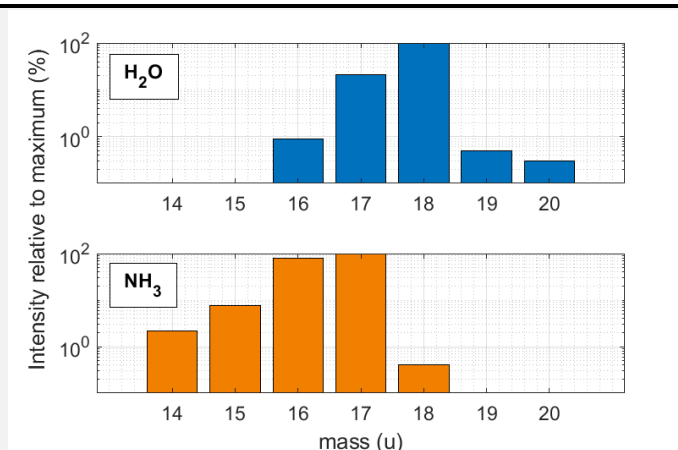
Figure SII.2-4: Water and ammonia signatures in MS, from the NIST database.

Nevertheless, **the contribution of water in the peaks at 16 and 17 u can be easily removed** thanks to the measurement on mass 18 and the known ratios between peaks due to water given by the NIST database. **Figures SII.2-5 (a)** and **(b)** show the effect of the removal of the water contribution on the intensities at 16 and 17 u. The 'experiment 1' is a case with a lot of water at the beginning of the plasma because it happened just after a complete cleaning of the chamber, that required to open it to ambient air. Even after heating and pumping at high vacuum for a night, a lot of H_2O molecules are still adsorbed on the walls. However, it is progressively removed by the N_2-H_2 plasma. The 'experiment 2' presented on **Figure SII.2-5 (c)** happens only a few hours after another experiment forming ammonia, without any opening of the chamber to ambient air. We observe a far lower level of water (at 18 u) than in the case of 'experiment 1'.
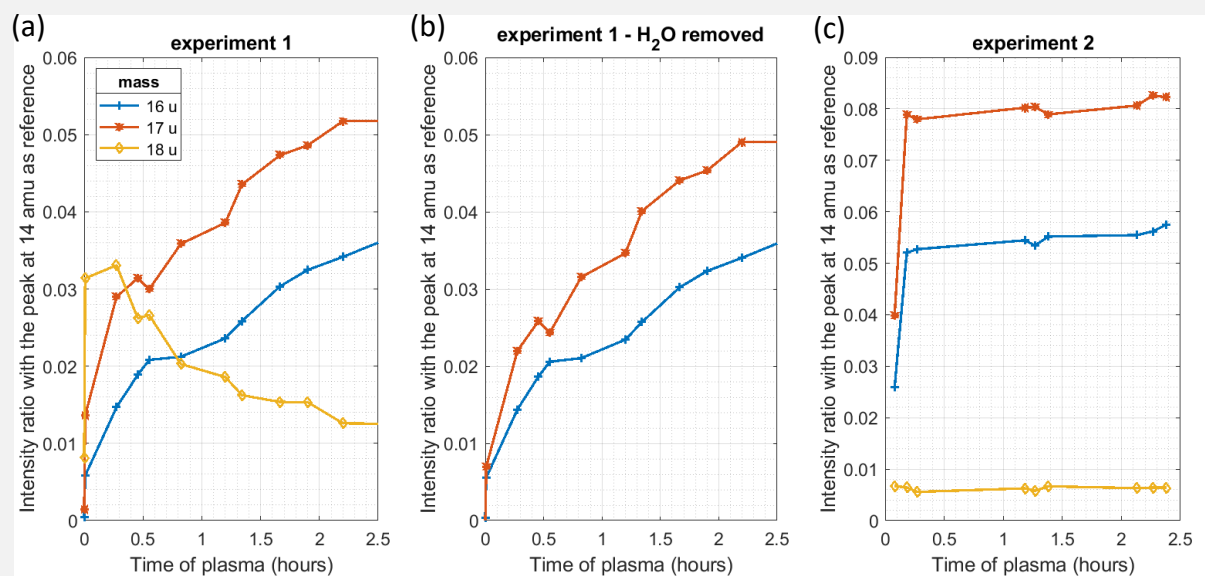
Figure SII.2-5: Relative intensities at 16, 17 and 18 u as function of time after the ignition of a N_2-H_2 plasma (0.53 mbar – 3% H_2 – 8.4 W). Experiment 1 started after the wall surfaces being manually cleaned, while experiment 2 is started only a few hours after a previous experiment forming NH_3. (a), (c) Direct measurements at 16, 17 and 18 u, relative to 14 u. (b) After removal of the water contribution on intensities at 16 and 17 u.

The measured intensities in RGA mode can drift for long acquisition times. It is due to a drift in the maximum of the 'energy' parameter (see **Section II.1.2**), that cannot be adjusted during long acquisitions. **Figure SII.2-6** illustrates a case where the intensities where strongly modified during the acquisition, while the pressure in the experiment stayed constant. The effect is observed at all distances from the plasma, which proves that it is an instrumental bias. **To avoid this effect on long acquisitions, we work only with relative intensities.**

However, the sharp decrease observed on **Figure SII.2-6 (a)** just after the ignition of the plasma is real. It corresponds to a strong consumption of H_2 molecules.
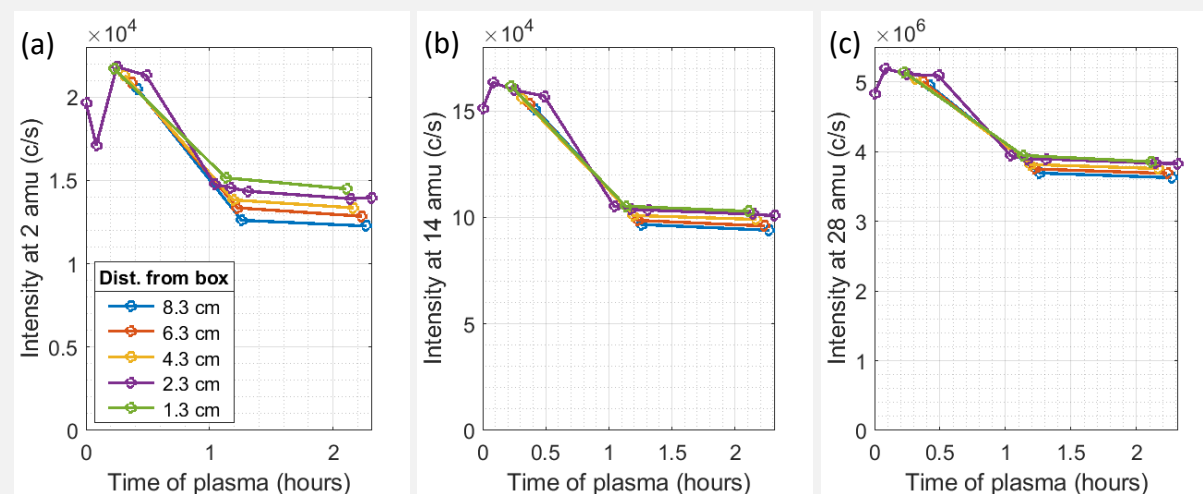
Figure SII.2-6: Raw MS measurements after the ignition of a N_2-H_2 plasma (0.53 mbar – 1% H_2 – 8.8 W), at different distances from the box. At the mass (a) 2 [H_2], (b) 14 [N_2 fragment] and (c) 28 [N_2].

Due to the very low signal, IR absorption measurements have to be integrated over several hours. On the opposite, mass spectrometry measurements have a very good signal to noise ratio. Nevertheless, they give only relative values if not calibrated.

Ammonia is created in the confined plasma at the center of the chamber; it diffuses through the grids of the metallic box, fills all the volume of the chamber and adsorbs on the chamber's walls. Depending on the plasma conditions, it can take several hours to reach the steady state of ammonia flux, and therefore a homogeneous ammonia spatial distribution in the chamber.

The spatial homogeneity and the reaching of the steady state of ammonia density in the chamber are studied with the mass spectrometer. Its collecting head can be radially moved from the metallic box to the wall of the chamber for measurements at different locations. **Figure SII.2-7 shows that the spatial distribution of NH₃ is homogeneous.** However, we observe a **strong dependence of the total stabilization time with the surface state of the walls**. An experiment starting with perfectly cleaned walls can take a few hours to reach the steady state (depending on the conditions). To avoid any influence of the stabilization time

for calibration measurements, the IR spectrum is integrated over ~2h, and we integrate the mass spectrum over the same acquisition period.
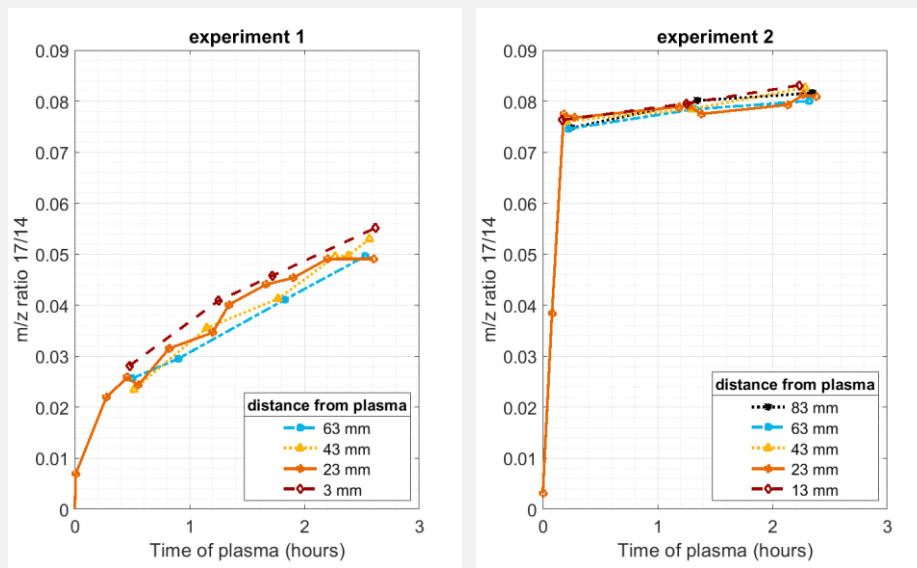
Figure SII.2-7: Variation of m/z ratio 17/14 (representative of ammonia) in time and distance from plasma (0.53 mbar – 3% H_2 – 8.4 W). Experiment 1 started with wall surfaces perfectly cleaned of ammonia, while experiment 2 is started only a few hours after a previous experiment forming NH_3.

The plasma confining box plays an important role in the homogenization of ammonia inside the chamber. Measurements without the confining box show that the plasma expands and processes are different, leading to a strong heterogeneity of ammonia in the chamber even after 10 min of plasma. **In the case without box, the homogenization in the chamber takes more time. Figure SII.2-8** illustrates this point, showing that measurements at 2 and 14 u (related to the injected H_2 and N_2) are constant with distance to plasma, on the opposite to the intensity of 17 u (ammonia) that is higher closer to the plasma, where ammonia forms.
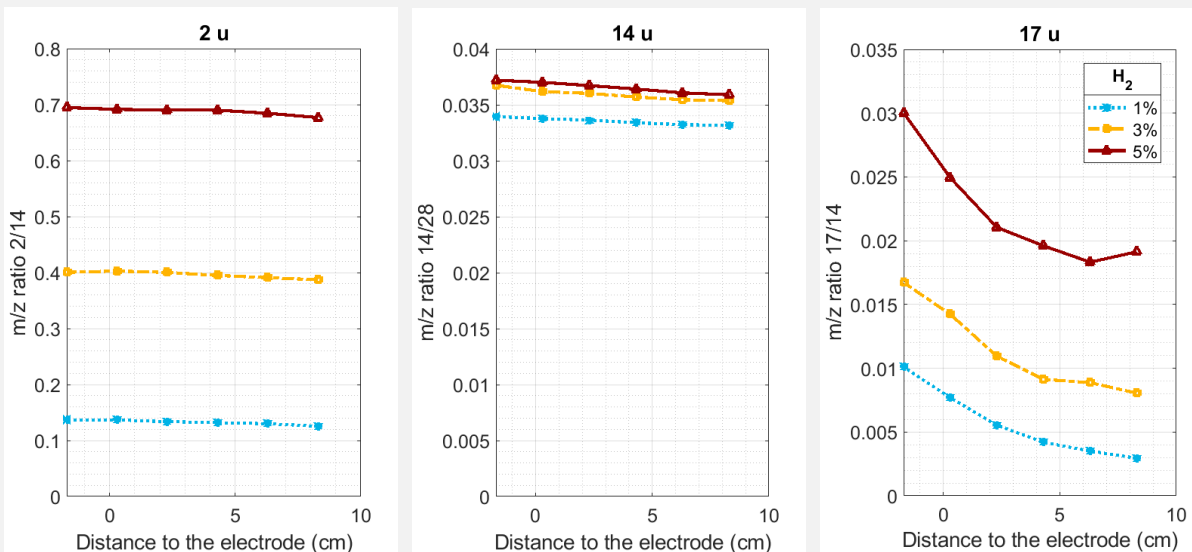
Figure SII.2-8: Variation of 2, 14 and 17 u intensities with the distance to the edge of the upper electrode. Measurements taken 10 min after plasma ignition in a configuration without confining box. Conditions with 1, 3 or 5 % of H_2 in N_2, 0.86 mbar and 360 V_{RF}.

As NH₃ is homogeneous along a chamber diameter, the density can directly be deduced from the IR absorption. For a given experimental conditions, this density is compared with the ratio 17/14 of the mass spectrometer m/z intensities as presented **Figure SII.2-9**.
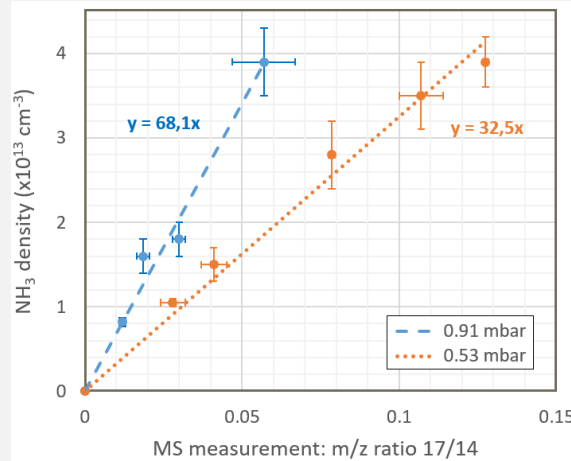
Figure SII.2-9: Calibration of MS measurements of NH₃ with IR data. Experiments done at 2 different pressures (0.91 and 0.53 mbar) in a N₂-H₂ plasma discharge, for a same RF peak-to-peak voltage of 480 V (at resp. 14 and 8.5 W).

The calibrations curves lead to the following calibration formula:

$$[NH_3] \approx \frac{I(17)}{I(14)} * 70 * P \ (.10^{13} cm^{-3}) \qquad\qquad (SII.2-1)$$

with [NH₃] the average ammonia density in the chamber, $\frac{I(17)}{I(14)}$ the ratio of intensities measured at m/z 17 and m/z 14 by the mass spectrometer, corrected of any water contribution, and P the pressure in mbar.

MEASUREMENTS OF AMMONIA DENSITY BY MASS SPECTROMETRY

Once the MS is calibrated at m/z 17 thanks to IR spectroscopy, it is useful to measure fast and local modifications of ammonia density in the chamber. The influence of H₂ percentage, RF plasma voltage and pressure are studied.

As ammonia tends to adsorb on the reactor walls, a great care was taken to have a clean wall surface state before each experiment. After a long exposure to plasma, walls are heated for several hours to eliminate residual ammonia. However, we observed that for short plasma durations (11 min), the use of a high vacuum pump between two experiments is sufficient. The MS took continuous measurements on a few selected masses (at m/z 14, 16, 17, 18, 28), starting 30 s before the ignition of the plasma and continuing during the 10 following minutes of the discharge. Ammonia intensity is roughly stable after a few minutes (see **Supplement SII.2-8**). The intensity was integrated over the last few minutes when the signal is stable to get the final value for the deduction of the NH₃ density.

2.1.e. Positive ions measured by mass spectrometry

The positive ion mode of the MS is used to detect positive ions formed in the discharge. A small hole is pierced in the confining box and the collecting head of the MS is positioned in front, in contact with the box to keep the plasma confined inside (see **Supplement SII.2-9**). **Consequently, the MS measures ions present next to the walls inside the confining box, at ~1 cm from the upper polarized electrode.** The collecting hole of the mass spectrometer and the confining box are both at the ground. **Figure II.2.5** shows typical MS spectra taken in ion mode in N_2 and N_2-H_2 plasmas.
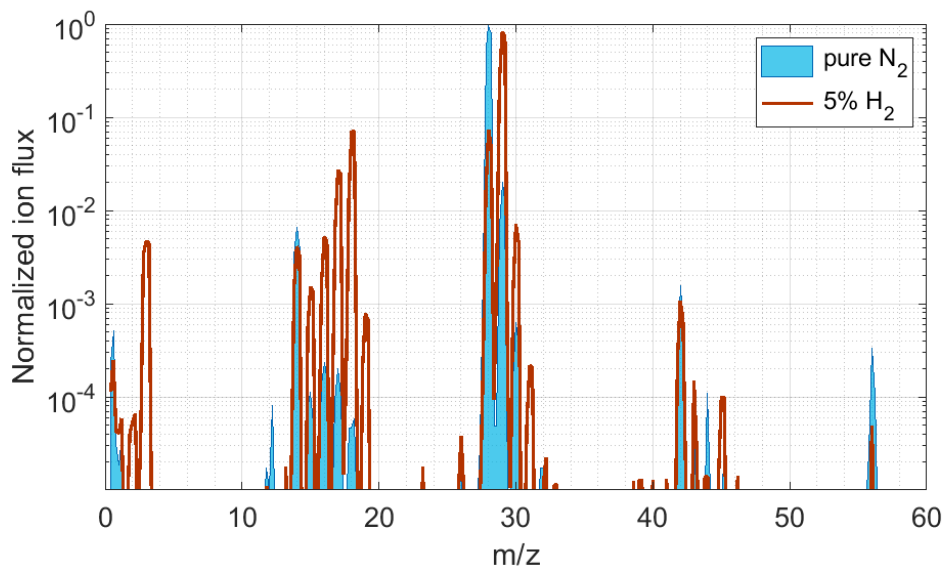
Figure II.2-5: MS normalized spectra of ions in N_2 and $N_2 - 5\%$ H_2 discharges, at 0.86 mbar (55 sccm) and for an absorbed power of ~11 W (406 $V_{RF,pp}$)

m/z	corresponding ion	m/z	corresponding ion
2	H_2^+	28	N_2^+
3	H_3^+	29	N_2H^+ / isotope N_2^+
14	N^+	30	$N_2H_2^+$/ isotope N_2H^+
15	NH^+ / isotope N^+	42	N_3^+
16	NH_2^+	43	N_3H^+
17	NH_3^+	44	$N_3H_2^+$
18	NH_4^+	45	$N_3H_3^+$
19	isotope NH_4^+ / H_3O^+	56	N_4^+

Table II.2-1: Selected ions for the study

MS acquisition parameters tuned for each mass are the same for m/z from 14 to 56, but are different for m/z 2 and 3. Therefore, for optimized measurements for all m/z, we used two different sets of parameters: one optimized for m/z 2 and 3, and one optimized for the others m/z. At such low power conditions, only ions with a charge z=1 are expected to be detected. Selected ion peaks at given m/z values (see **Figure II.2-5** and **Table II.2-1**) are measured in continuous acquisition by the MS in ion mode from the ignition of the plasma and until stabilization of the signal. The intensity of each ion is then averaged over few minutes after stabilization of the signal (from ~8 to 10 min, see **Supplement SII.2-8**).

MS does not give reliable absolute values for ions. Indeed, the absolute intensities measured depend on MS selected parameters and sometimes vary during the acquisition due to charging effects. Therefore, we provide only relative intensity values. **In the following, ion intensities**

(or fluxes) are normalized by the total intensity (or flux) measured for ions, which is approximated by the sum of the intensities measured for m/z 28, 29, 17, 18 and 14 (see **Figure II.2-5**).

The ^{15}N isotope of nitrogen is usually 0.36% of nitrogen atoms, and can therefore be detected by the MS, especially in pure N_2 at m/z 15 ($^{15}N^+$), 29 ($^{14}N^{15}N^+$) and 30 ($^{15}N^{15}N^+$) (see table 1). In N_2-H_2 discharges, it can also influence intensity measurements at m/z 19 ($^{15}NH_4^+$) and 30 ($^{14}N^{15}NH^+$**). Isotopes are therefore taken into account to study the intensities of other ions at m/z 15, 19, 29 and 30**. Water has a strong proton affinity and H_2O adsorbed in small quantities on the walls in the reactor easily forms H_3O^+, which contributes at m/z 19. As H_2O^+ (m/z 18) should be present in far lower quantities than H_3O^+, the strong signal at m/z 18 can be entirely attributed to NH_4^+. **Impurities** from air should be seen at m/z 32 (O_2^+) and m/z 44 (CO_2^+) in both pure N_2 and N_2-H_2 plasmas. **Figure II.2-5** confirms that they **can be neglected** in this study.

Intensities measured by the MS at different m/z cannot be directly compared as the ionization, the flight in the MS through the quadrupole and the detection depend on the mass and the intrinsic properties of the species. **We use the transmission curve obtained in Section II.1.2 to correct the ion measurements** for m/z > ~10, and work with ion fluxes. As the transmission curve at low m/z has large uncertainties, we prefer not to correct the data and work with raw intensities in these cases.

SUPPLEMENT SII.2-9: PICTURE OF THE MS POSITION TO COLLECT IONS

Contrarily to neutral species, ions cannot escape from the plasma confining box. To measure them with the MS, a hole is open in the box, and the collecting head is positioned in front of it (see **Figure SII.2-11**). The head is in contact with the box, both are grounded. The junction between them is close: no plasma can escape on the sides.
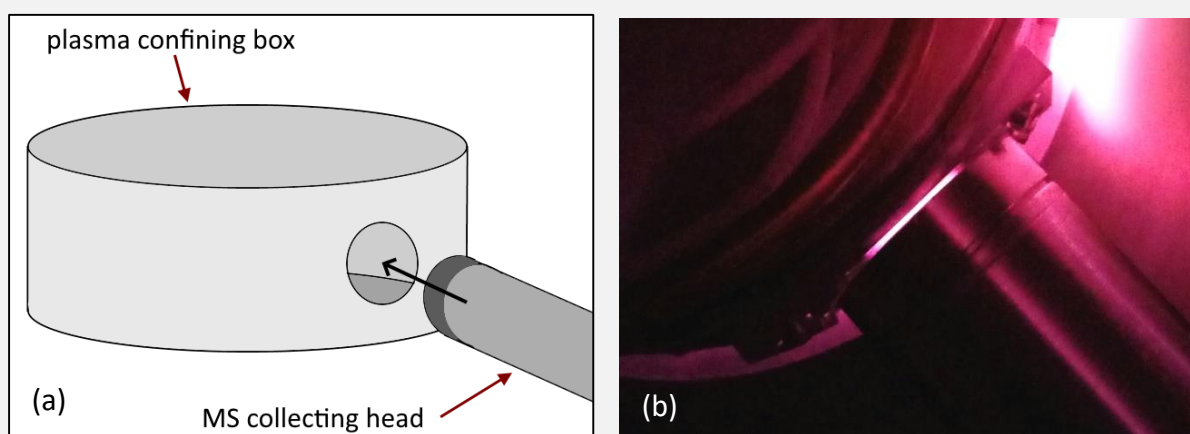
Figure SII.2-11: Scheme (a) and picture (b) to illustrate the position of the collecting head of the MS to measure ions in the plasma. Ions collected are ions present next to the walls of the box.

2.2- Experimental results

Essentially three **experimental parameters** are varied to test their effect on the measurements. The **H₂ percentage** in the N₂-H₂ gas mixture varies from 0 to 5%. **Pressure** is varied from 0.33 to 0.91 mbar by changing the gas flow (from 10 to 70 sccm). RF peak-to-peak **voltage** is varied between 254 and 483 V.

2.2.a. Electrical measurements and electron density

In the following figures, **error bars take into account the accuracy and the measurements repeatability.** Measurements are done at several selected peak-to-peak RF voltages ($V_{RF,pp}$: 254, 326, 367, 406 and 483 V). However, as mentioned in Alves et al. (2012) the most relevant plasma parameter for the comparison between experiment and model is the RF power absorbed by the plasma (W_{eff}). The RF power measurements with the digital V-I probe (Solayl, placed between the generator and the matchbox) (± 0.5 W) are much more accurate than measurements done in Alves et al. (2012) (±2W). The measured absorbed power is given for all the conditions studied and plotted according to the RF peak-to-peak voltage in **Figure II.2-6 (a)**.
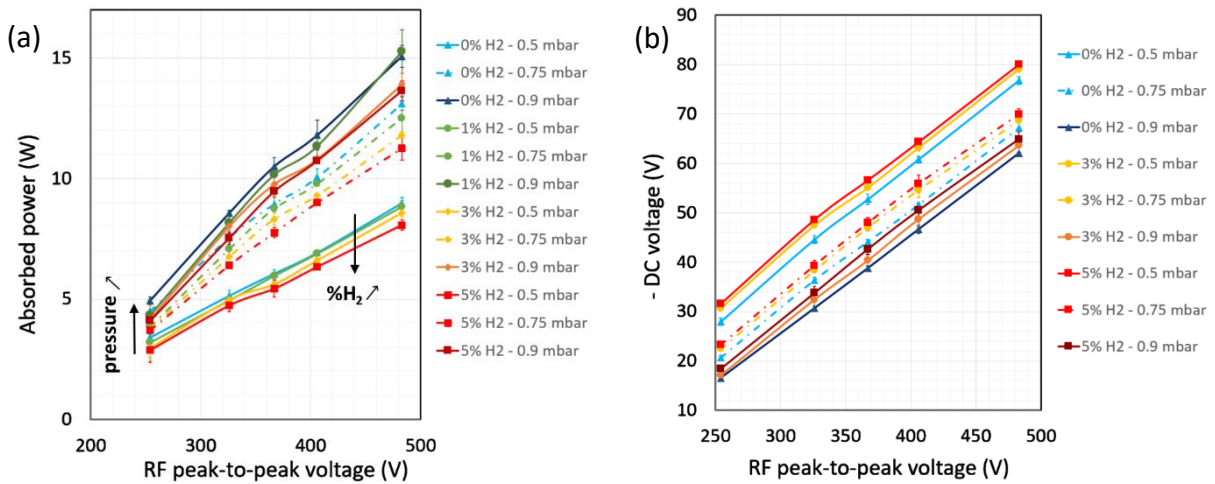
Figure II.2-6: (a) RF power absorbed by the plasma and (b) self-bias potential V_{DC} as function of $V_{RF,pp}$ in all the conditions studied here (various $V_{RF,pp}$, % of H₂ and pressure).

Absorbed power increases systematically with the RF peak-to-peak voltage. However, **H₂ amount and pressure also have an effect on its value**. At a given percentage of H₂ and a given $V_{RF,pp}$, the absorbed power increases strongly with pressure. At a given $V_{RF,pp}$ and pressure, the absorbed power decreases slightly with the amount of H₂.

Figure II.2-6 (b) presents the self-bias potential ($V_{DC} < 0$ in this configuration) for all the experimental conditions. These measurements are fundamental to validate the model described in **Section II.2.3**. The experiments show a **linear dependence of $|V_{DC}|$ against $V_{RF,pp}$**, with a constant slope of 0.2 in all conditions of pressure and hydrogen content. The variation of $|V_{DC}|$ with the discharge parameters relates to changes in the ion current (Lieberman and Lichtenberg, 2005). In an asymmetric reactor, a higher ion current increases the asymmetry in

the collection of charges at the electrodes, leading to a higher $|V_{DC}|$. At high $V_{RF,pp}$ the absorbed power increases, inducing an increase in the electron density, the ion current and thus $|V_{DC}|$. On the other hand, an increase in the pressure leads to the reduction of the sheath thickness (Lieberman and Lichtenberg, 2005), implying a decrease in the ion current and $|V_{DC}|$, consistent with previous observations in pure N_2 (Alves et al., 2012).

Figure II.2-7 (a) presents electron density results as a function of absorbed RF power. The experiments show that **the electron density increases exponentially with W_{eff}**. At a given W_{eff}, an increase in the pressure leads to lower electron densities, but the exponential behavior is maintained. For pure N_2 the n_e values are globally in agreement with published values in Alves et al. (2012). According to the model detailed in **Section II.2.3**, **the exponential increase is due to plasma interaction with surfaces, leading to the production of secondary electrons.**

The percentage of H_2 in the mixture does not have any effect on the electron density, except for the higher W_{eff} cases. For high W_{eff}, despite large error bars, it seems that the increase of hydrogen content leads to an increase of the electron density at a given pressure. **The ionization degree is obtained from the electron density by dividing by the total neutral density**. **Figure II.2-7 (b)** shows that trends are the same as for electron density.
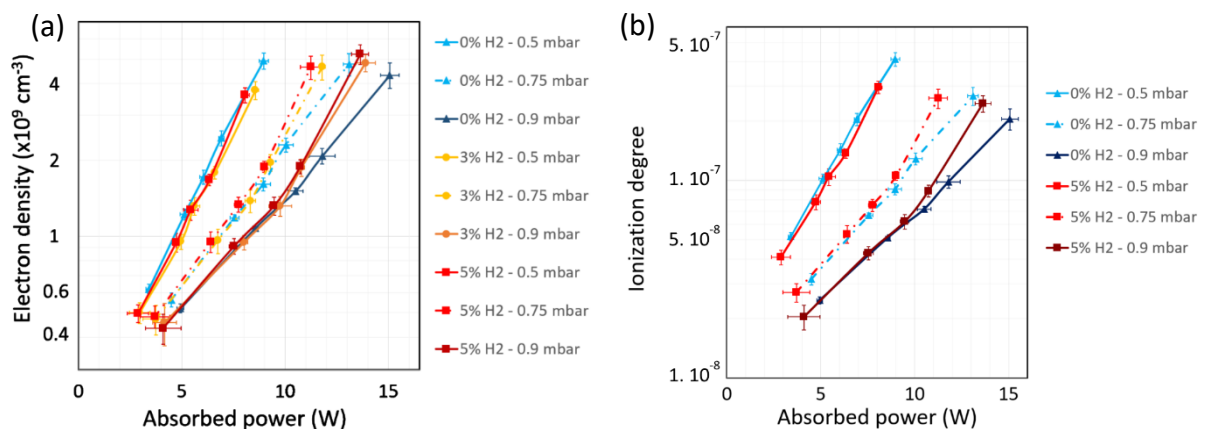
Figure II.2-7: (a) Electron density and (b) ionization degree measured for several experimental conditions.

2.2.b. Ammonia density

Ammonia is the most stable molecule formed in a N_2-H_2 plasma. The abundance of ammonia is a major constraint in the chemistry of the plasma. A study of the formation of NH_3 depending on the different discharge conditions is shown in **Figure II.2-8**. For each condition NH_3 density is given in absolute values. An uncertainty of 20% is indicated on the graphs, evaluated from the uncertainty on the calibration coefficient and the MS measurements.
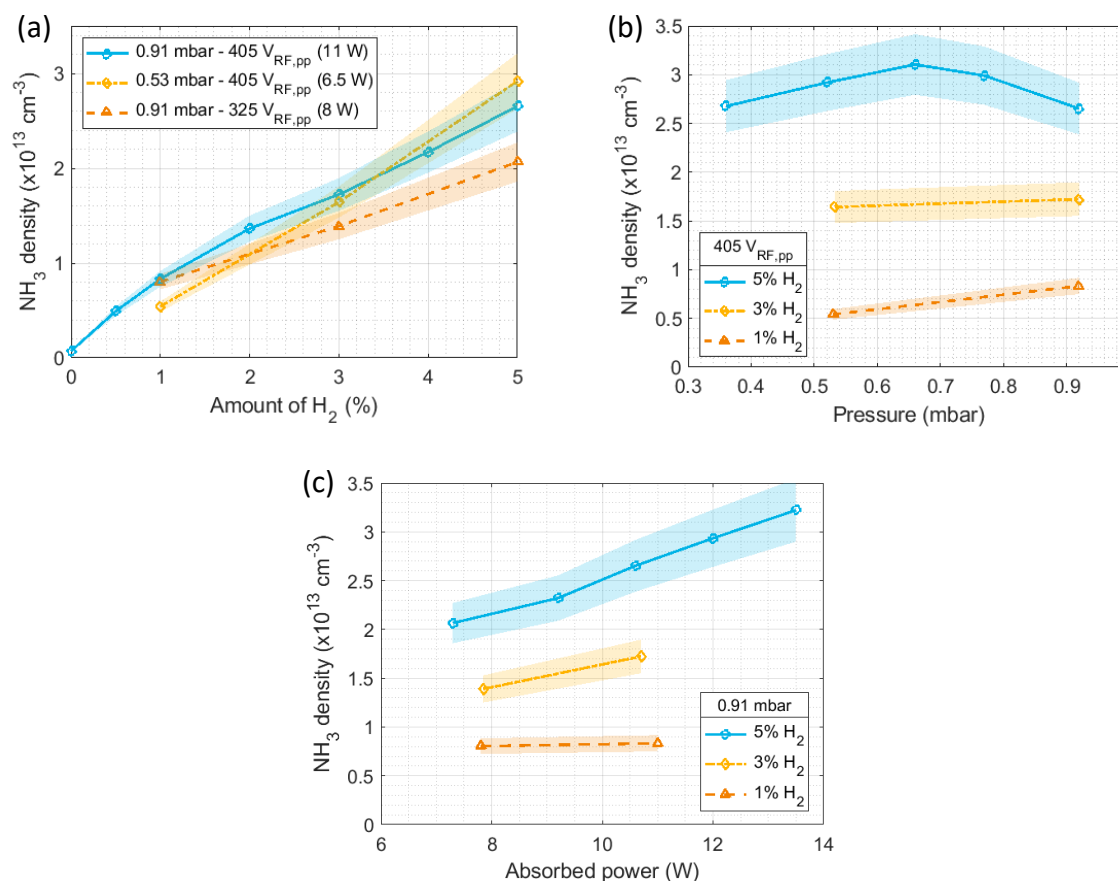
Figure II.2-8: NH_3 amount as function of injected H_2 (a), pressure (b) and absorbed power (c).

Ammonia density increases linearly with the percentage of H_2 in N_2. It also **increases slightly with the absorbed power**. However, the absolute density of NH_3 is **constant with pressure** from 0.35 to 0.9 mbar. This suggests that ammonia density is controlled by surface processes, as discussed in E. Carrasco et al. (2011), Gordiets et al. (1998) and in **Section II.2.3**.

2.2.c. Positive ions

The positive ions give important indications on the gas phase chemistry happening in the plasma and on nearby surfaces. They have been measured two to four times for each of the selected experimental conditions. Following figures present the average data points for each condition. Error bars are estimated from the reproducibility of the measurements and an uncertainty on the MS calibration estimated to +/- 20% (see **Section II.1.2**). These error bars take into account the instrumental (charging effects) and plasma effects (stabilization of the ion fluxes in the plasma as presented in **Supplement SII.2-3**, variations of the impurities quantity…). The following figures present the evolution of ion fluxes with the parameters of the experiment (H_2 amount, pressure and absorbed power). These are the **ion fluxes at the entrance of the MS**. The 2D ion densities inside the reactor chamber are retrieved by the model presented in **Section II.2.3**.

Figure II.2-9 shows the evolution of relative ion fluxes with the percentage of H_2 in the plasma. As explained in **Section II.1.2**, the analysis of m/z 2 and 3 is separated from the others. No calibration is applied to correct these measurements at low m/z, therefore no quantitative comparison can be done with the other m/z. For reproducibility (see **Section II.2.1.e**), the ion measurements are normalized to the sum of all ion fluxes (or to the sum of all intensities in the case of m/z 2 and 3).
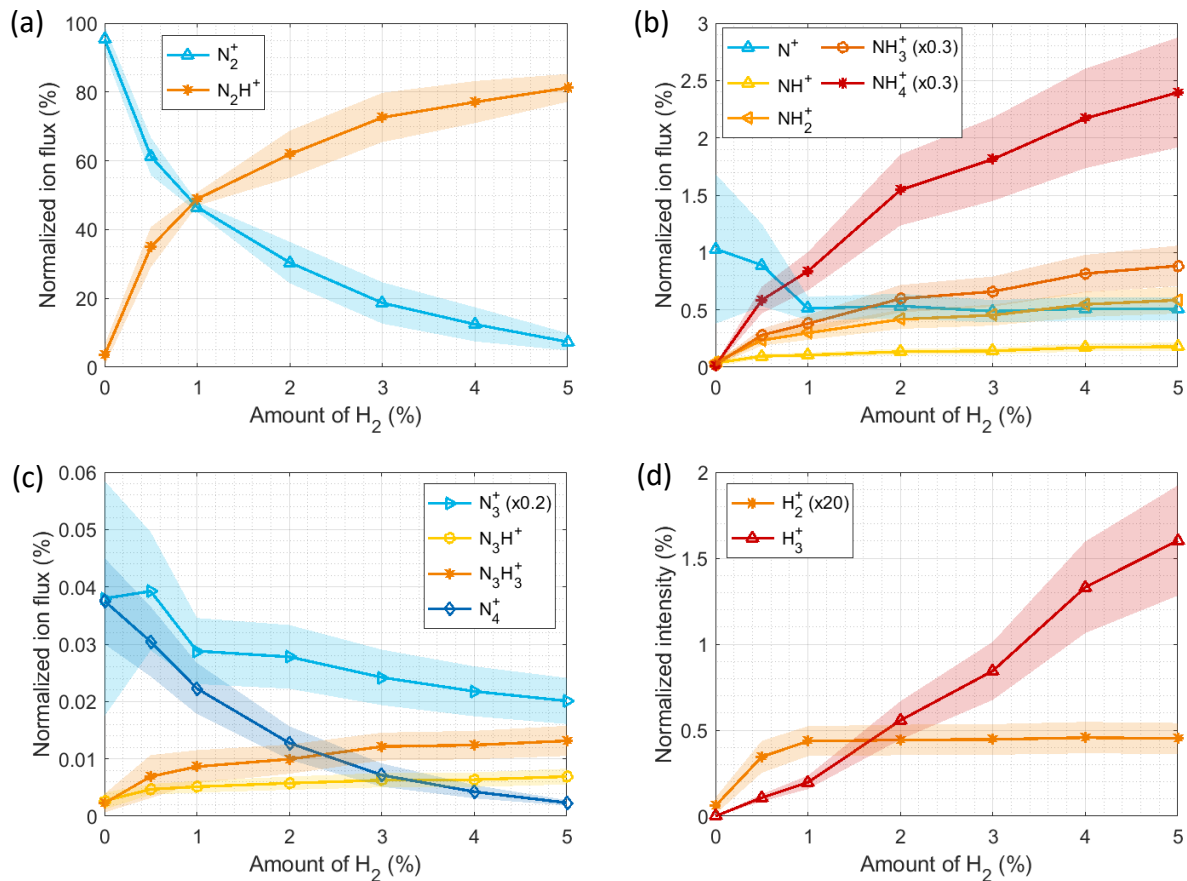
Figure II.2-9: Normalized positive ion fluxes (a,b,c) or intensities (d) as function of the percentage of H_2 injected in the experiment. Conditions with 0.9 mbar (55 sccm) and ~10 W absorbed power (405 $V_{RF,pp}$).

The amount of H_2 injected in the plasma has a strong impact on the ions produced. In pure N_2 plasma, N^+, N_2^+, N_3^+ and N_4^+ are detected. These **ions formed with only nitrogen decrease** as soon as a small quantity of H_2 is injected in the plasma. N_2^+ and N_4^+ have nearly disappeared with 4-5% of H_2. N^+ and N_3^+ on one side, and N_2^+ and N_4^+ on the other side, have similar trends. Their formation and/or stabilization processes are linked.

On the other hand, **new species containing hydrogen appear**: nitrogen ions become protonated thanks to the injection of hydrogen. The H_3^+ ion increases linearly with the injected H_2%, no saturation effect is seen for values of hydrogen inferior to 5%. On the contrary, H_2^+ stabilizes as soon as 1% of H_2 is injected in the experiment. $N_xH_y^+$ ions form in the presence of hydrogen, but their growth is not linear with the amount of H_2: their formation is limited by another variable than the quantity of hydrogen, contrarily to H_3^+. Especially, N_2H^+ tends

toward saturation at ~5% of H_2. Its evolution is anti-correlated with the one of N_2^+: its formation is limited by the available quantity of ionized nitrogen. At 5% H_2 (at 0.9 mbar and ~10 W), N_2^+ decreases at 7.3% and the major ions after N_2H^+ (78%) are the ions NH_4^+ (10%) and NH_3^+ (3.7%) leading to the formation (or formed thanks to) ammonia. This is consistent with observations by Sode et al. (2015) in an ICP discharge, where N_2H^+ is predicted to be dominant for percentages of H_2 lower than 60%, NH_4^+ and NH_3^+ being dominant for H_2 amounts above this value.

Ion populations are modified by the variation of pressure (induced by the variation of the gas flow from 10 to 70 sccm). Results are presented in **Figure II.2-10**.
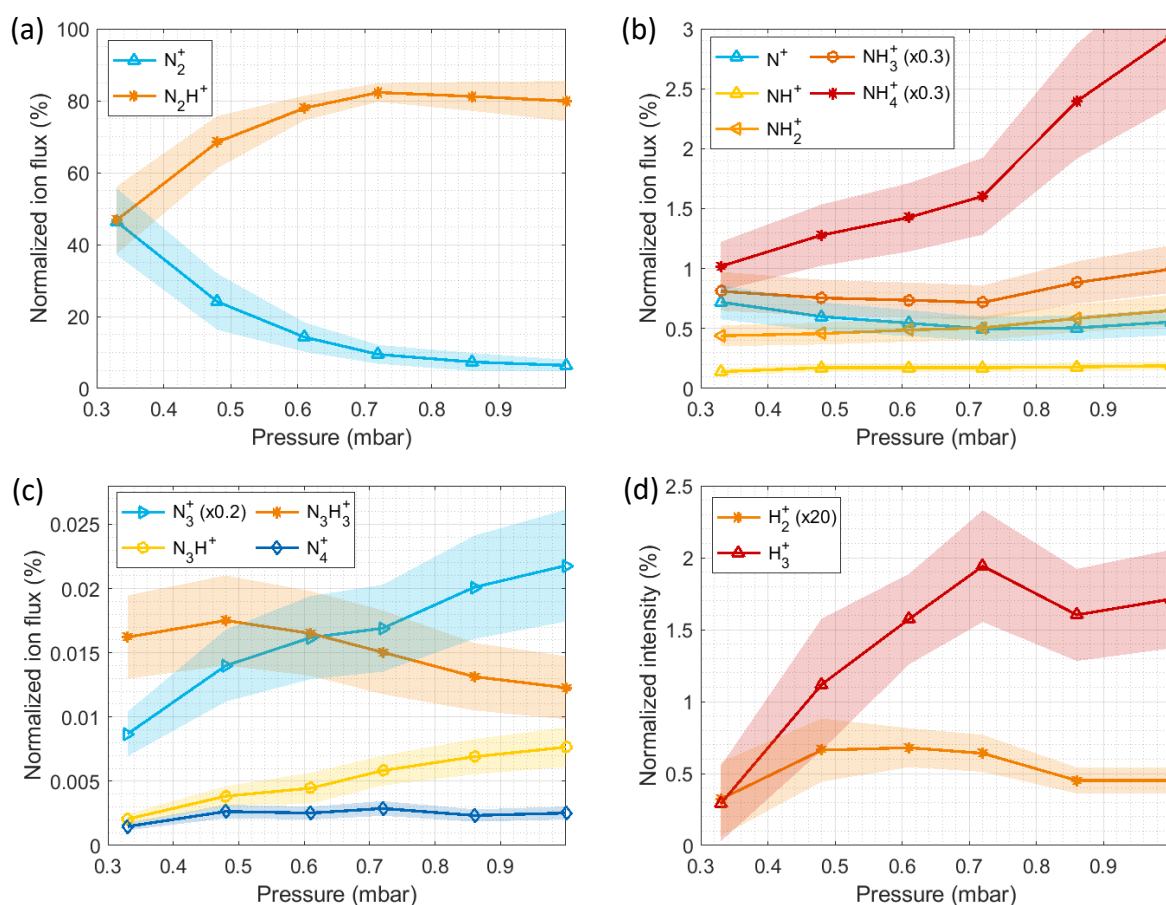
Figure II.2-10: Normalized positive ion fluxes (a,b,c) or intensities (d) as function of pressure. Conditions with 5% H_2 and 6-11 W absorbed power (405 $V_{RF,pp}$).

The increase of the gas flow (and therefore the pressure) **leads to an increase of nearly all the ions, except N_2^+ and N^+**. Especially, at 0.33 mbar, N_2^+ and N_2H^+ have equal fluxes. It seems that **at higher pressures, more complex and/or protonated ions are formed and/or transported in higher quantities to the walls** of the confining box where the measurement is done. N_2H^+, NH_4^+, H_3^+, and in smaller proportions N_3^+, N_4^+ and N_3H^+ increase clearly with pressure, while H_2^+, NH^+, NH_2^+ and NH_3^+ stay rather constant. This can be easily explained by the fact that N_2H^+, NH_4^+, H_3^+, N_3^+, N_4^+ and N_3H^+ require a reaction between an ion (or radical)

and a neutral gas phase molecule to form, whereas H_2^+, N_2^+, N^+, NH^+, NH_2^+ and NH_3^+ can be simply formed by direct ionization of neutrals H_2, N_2 and NH_3. With the increase of pressure, ion – neutral collisions increase and consequently ions formed from such collisions are formed in higher proportions compared to ions formed by direct ionization (see **Figure II.2-12**). Similar observations are discussed in E. Carrasco et al. (2011).

Ions are also influenced by the power absorbed by the plasma (see **Figure II.2-11**).
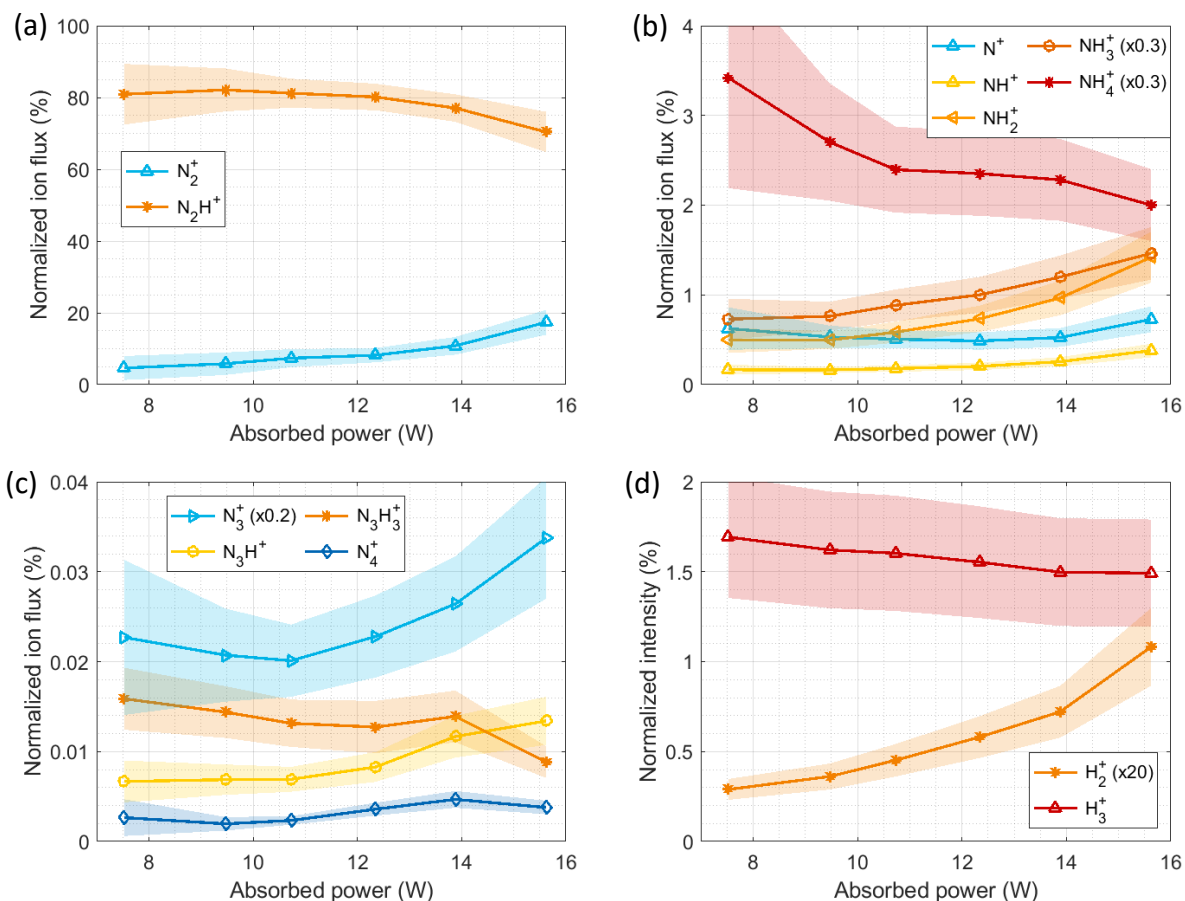
Figure II.2-11: Normalized positive ion fluxes (a,b,c) or intensities (d) as function of the power aborbed by the plasma. Conditions with 5% H_2 and 0.9 mbar (55 sccm).

The increase of absorbed power moderately impacts the positive ion relative fluxes. However, the electron density increases, consequently the total ion density should increase similarly. A decrease of the relative intensities is observed for some species formed by ion (or radical) – neutral processes: of 10% for H_3^+, N_2H^+, $N_3H_3^+$ and 40% for NH_4^+. On the contrary, species formed by direct ionization increase: H_2^+, NH^+, NH_2^+, NH_3^+, N_2^+. Contrarily to the increase of pressure, **an increase of power favors the formation of species by direct ionization** (see **Figure II.2-12**). A small relative increase of N_3^+, N_3H^+ and N_4^+ can also be noted.

2.2.d. Conclusion on experimental results

In this work, an RF CCP discharge in nitrogen with small amounts of hydrogen (up to 5%), at low coupled power (3 to 13 W) and low pressure (0.3 to 1 mbar) is experimentally characterized. Electrical parameters, electron density, ammonia density and positive ions are measured in various different plasma conditions. One of the objectives is to form a complete dataset for the implementation of hydrogen-linked processes in the model of pure N_2 RF CPP discharge described in Alves et al. (2012). The model is described in the next section.

A complete study of the MS transmission curve has been performed to deduce relative ion fluxes from MS measurements. The main conclusion is that **transmission curves depend on the set of MS parameters**. In particular, sets of parameters obtained for a tuning on small m/z (like 2) lead to MS transmissions very different than if tuned on larger m/z (as 28).

The addition of hydrogen in an initially pure N_2 discharge induces some **electrical changes**. A 10-15% decrease of the coupled power for a same peak-to-peak RF potential is observed. However, the electron density stays rather constant with the H_2 amount, except for the higher pressure and power cases, where it could increase up to 25% with the addition of 5% hydrogen.

Concerning the molecular plasma species, the addition of H_2 has the expected effect to **hydrogenate nitrogen ions**, and lead to the **formation of NH_3**. N_2H^+ is the major ion in the discharge for H_2 amounts above 1% (~78% for 5% injected H_2), while NH_3^+ and NH_4^+ are the following dominant protonated ions (at respectively ~10% and ~3.5% for 5% injected H_2). The improvements to the model in pure N_2 thus focus on the addition of new protonated species and reactions using them as reactants or products. A particular attention is given to ammonia and surface processes.

The variation of pressure from 0.3 to 1 mbar and **coupled power** from 3 to 13 W also leads to **plasma modifications**. An exponential increase of the electron density is observed with the increase of coupled power. It is due to the production of secondary electrons on surfaces. On the opposite, electron density decreases with the increase of pressure.

Ammonia quantity always increases similarly to NH_2^+ and NH_3^+, which suggests a strong dependence between these species, NH_2^+ and NH_3^+ being easily formed by direct ionization of NH_3. Ammonia absolute density stays constant with a pressure variation. Therefore, it suggests that ammonia formation is not governed only by bulk processes but mainly by surface processes. This point is discussed further in the next section. On the other hand, ions are formed in the bulk and disappear at the contact of surfaces. Their quantities are more sensitive to pressure variations. In particular, NH_4^+, N_2H^+, H_3^+, N_3^+, N_4^+ and N_3H^+, which require ion-neutral gas phase reactions to form, increase at higher pressure compared to other ions formed by direct ionization (especially N_2^+ and N^+). The increase of coupled power seems to have an opposite effect by enhancing the formation of ions by direct ionization, with the

increase of N_2^+, NH^+, NH_2^+, NH_3^+, H_2^+ and the decrease of NH_4^+, N_2H^+ and $N_2H_2^+$. **Figure II.2-12** synthesizes these points.
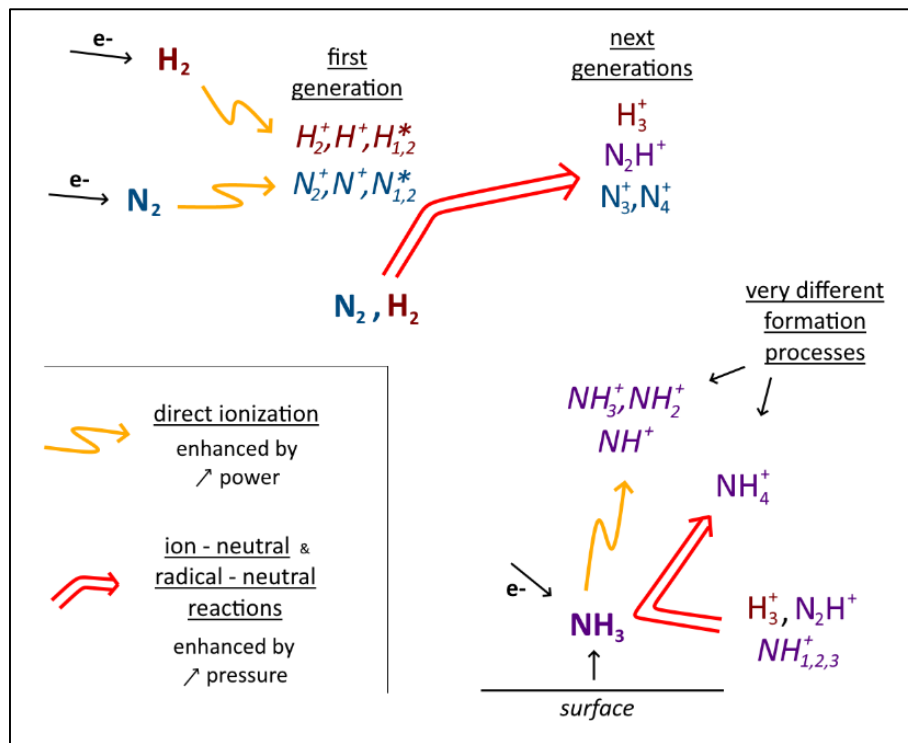
Figure II.2-12: How coupled power and pressure affect ion formation: the main reactions.

On the present work we analyzed new plasma conditions, different from the studies by E. Carrasco et al. (2011, 2012, 2013) and Sode et al. (2015). Experiments were performed with only a few percent of H_2 (< 5% here, compared to > 40% in the studies cited above), at lower powers (~10 W compared to > 50 W) and higher pressures (~1 mbar compared to < 0.08 mbar). All these changes lead to a lower relative production of ammonia (0.15% compared to > 3%).

2.3- Modeling of the discharge and discussion

The results presented above were motivated by a collaboration with the Instituto de Plasmas e Fusão Nuclear (Portugal). In the **objective to model the plasma** in the reactor PAMPRE, we worked with a team in Portugal used to self-consistent kinetic plasma modeling. Results of the model and the implications on the plasma produced in PAMPRE are detailed in **Paper 3**.

We started from a model developed in 2012, focusing on pure N_2 plasma in PAMPRE (Alves et al., 2012). The addition of H_2 changes strongly the description of the discharge, as discussed in **Section II.2.2**. **The main improvements to the model are the complexification of the chemical reaction list, and new parameterizations to take into account some specificities of N_2-H_2 discharges compared to a pure N_2 plasma**.

2.3.a. Description of the model

The model is a **hybrid code** that couples a 2D (r,z) time-dependent fluid module characterizing the dynamics of charged particles with a very complete 0D kinetic module, on the model of Alves et al. (2012).

The fluid module solves the continuity and the momentum transfer equations for electrons, positive ions N^+, N_2^+, N_3^+, N_4^+, H^+, H_2^+, H_3^+, N_2H^+, NH^+, NH_2^+, NH_3^+ and NH_4^+, and negative ions H^- and NH_2^-, the electron mean energy transport equations, and Poisson's equation for the radiofrequency electric potential. Details are given in **Paper 3**.

One of the interesting novelty compared to Alves et al. (2012) is the **addition of fast electrons**. They are parametrized as a single-beam model, generated by secondary emission at the walls. The fast electrons are assumed to be created at the surfaces in contact with the plasma (both electrodes and the surrounding cage) by impingent positive ions, and their initial energy is set to 1 eV. After they enter the plasma bulk, they are thermalized to the ambient electron temperature by inelastic collisions (from ionizations and excitations). **The secondary electron yield in the model is adjusted to fit the experimental trends of the electron density as function of coupled power** (see **Section II.2.2.a**).

The 0D kinetic module supervises the main plasma species N_2, H_2, NH_3, N, H, including many vibrational states (61), electronic excited states (8), adsorbed species (5) and radicals.

A surface chemistry model is also added to describe the multi-step formation of ammonia at the reactor walls (E. Carrasco et al. 2013). **The reaction coefficient used is adjusted to fit with ammonia measurements** (see **Section II.2.2.b**).

2.3.b. Results on plasma parameters and electron density

Figure II.2-13 compare the model results to the experimental measurements of the electron density. If it does not take into account the fast electrons (dotted-line), the model prediction for electron density is far lower than the experimental measurements. **Electrons produced by secondary emission play a fundamental role in the plasma to create more electrons by collisions and reach the total electron density. Similarly to the experimental data points, the increase in electron density with coupled power is exponential if fast electrons are taken into account.** At higher pressure the curve n_e (W_{eff}) is displaced towards higher powers. This can be explained by the fact that at higher pressure, heavy particles reach the wall with lower energy, and therefore form secondary electrons in smaller quantities and/or with lower energies. However, the slight changes in electron density with H_2 amount observed in the experimental data (**Figure II.2-7**) cannot be interpreted by the model. The model for fast electrons being rather simplified, fine changes at high W_{eff} cannot be reproduced.
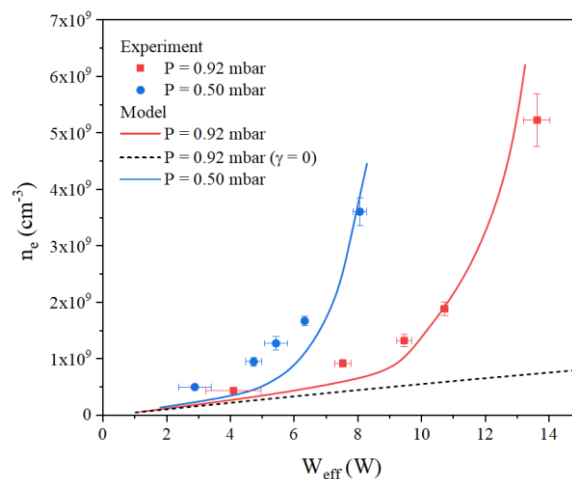
Figure II.2-13: Simulations (curves) and measurements (points) for the electron density, as a function of the power coupled to the plasma, for a mixture with 5% H_2 at the following pressures (in mbar): 0.5 (blue circles and line); 0.92 (red squares and line). The dotted curve was obtained at 0.92 mbar, neglecting the electron production by secondary emission.

The model results give access to the electron energy distribution function for the slow electrons (EEDF, $f(u)\sqrt{u}$, normalized so that $\int_0^\infty f(u)\sqrt{u}du = 1$). Under low power conditions, slow electrons are responsible for most of the ionization processes and fast electrons are less relevant. In this case, **Figure II.2-14** shows an observable difference between the distributions in the bulk and in the sheath (near the walls). In the sheath, there is a significantly populated tail up to 12 eV, while bulk electrons EEDF drop more abruptly. These differences reveal a significant difference in the efficiency of electron-impact excitations and ionization in both regions.
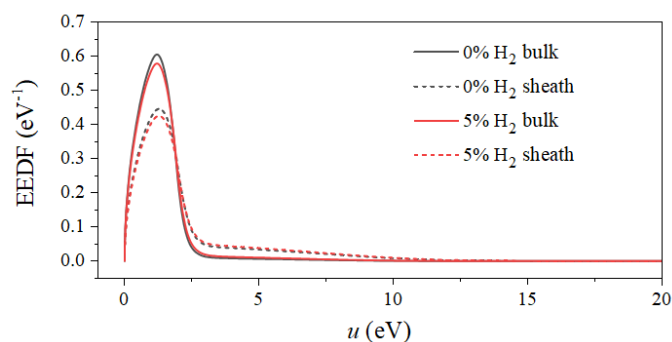
Figure II.2-14: Calculated EEDF of the plasma (slow) electrons, at 0.92 mbar and 5 W and for two different positions along the discharge axis, corresponding to the plasma bulk (solid lines) and within the sheath near the walls (dashed). Curves for pure N_2 (black) and 5% H_2 mixtures (red).

The influence of the fast electrons in the plasma can be visualized by comparing the time-averaged densities, mean energies and ionization rates for both slow/fast electrons (see **Figure II.2-15**).

The results in density show that both slow and fast electrons are mainly present in the bulk of the plasma. Slow electrons exhibit a maximum density closer to the powered electrode (*z/d* =1) and fast electrons are distributed rather homogeneously, with density values ~4 orders of magnitude lower.

The results for the energy are opposite to the density results. Slow electrons typically reach mean energies of ~10 eV due to collisional heating near the walls. In parallel, the fast electron beam can be accelerated up to ~60–80 eV by the electric field, within the sheath close to the powered electrode, and easily sustain 20–40 eV elsewhere, well above the ionization threshold.

Both density and energy have fundamental implications on the ionization rate. For the comparison, the lower panels of **Figure II.2-15** show the contribution of both groups of electrons to the N_2 ionization rate. As expected, the main ionization region is in the sheaths. Similar intensities are found in the sheath for both cases. However, a difference is observed in the bulk. While for the slow electrons the ionization in the center of the plasma is negligible, for the **fast electrons** it becomes a **relevant source of charged particles**. It results in a **significant increase in the volume-averaged electron density**, as shown previously in **Figure II.2-13**, and a **substantial change in the plasma ion chemistry**.

In pure N_2 discharges, the model predicts a lower electron density and a lower ionization rate. This can be explained by a reduction in the ionization threshold for hydrogenated gas mixtures: it is set at 10.2 eV (corresponding to NH_3) in a N_2-H_2 plasma, compared to 15.4 eV (for N_2) required to ionize pure nitrogen discharges.
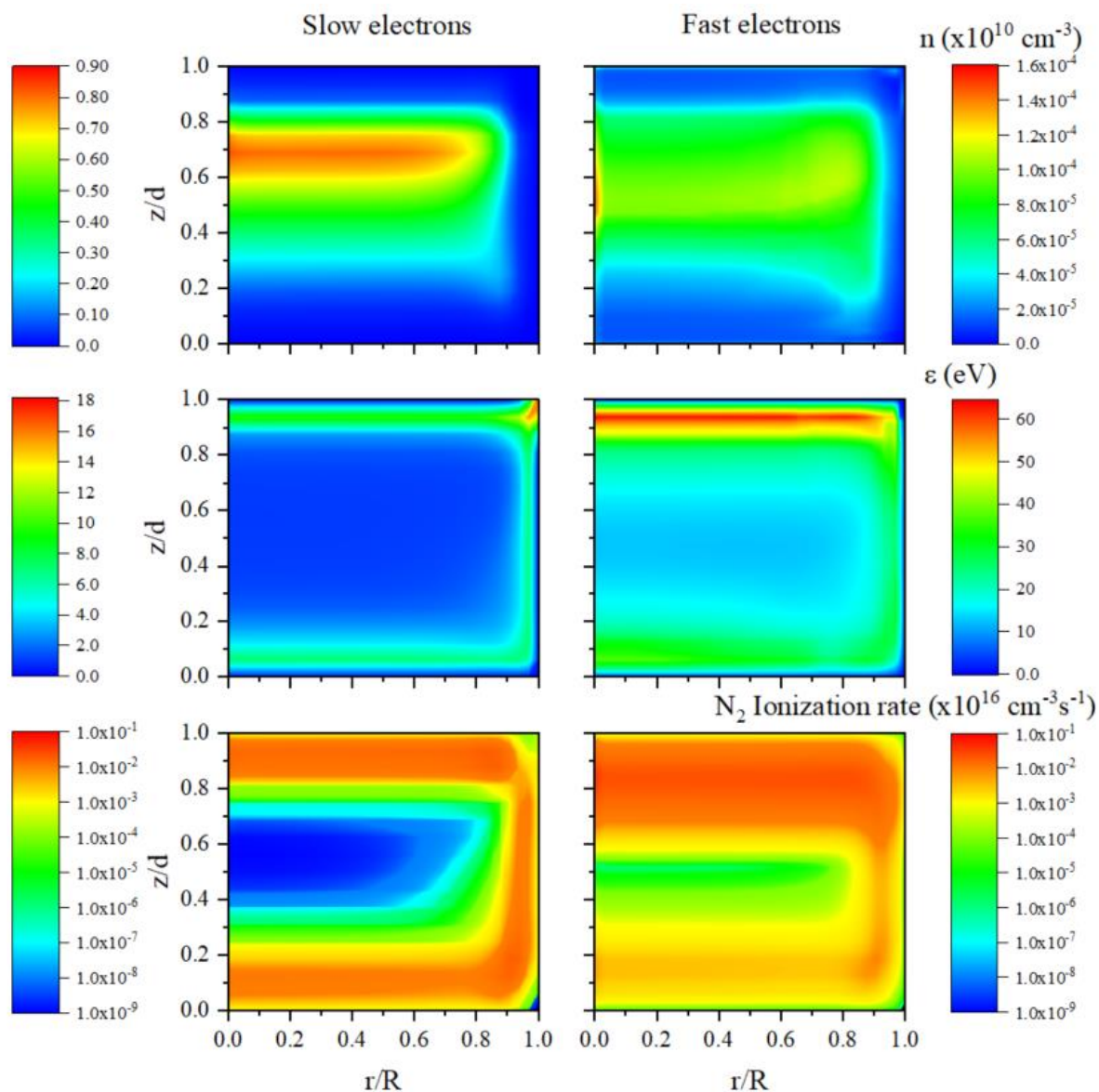
Figure II.2-15: Calculated contour plots of time-averaged densities, mean energies and N_2 ionization rate contributions for slow (left) and fast (right) electrons, for a 5% H_2 mixture at 0.92 mbar and 11.5 W. The spatial scales are normalized to the discharge radius R and the inter-electrode distance d. Note the different color scales in the slow and fast electron plots.

2.3.c. Results on ion and neutral composition

The model reproduces well the main ion fluxes and their variations with H_2 amount (see **Figure II.2-16**) and pressure. Some discrepancies happen with minor ions, more sensible to the fine description of the chemical reactions and the ionization conditions.
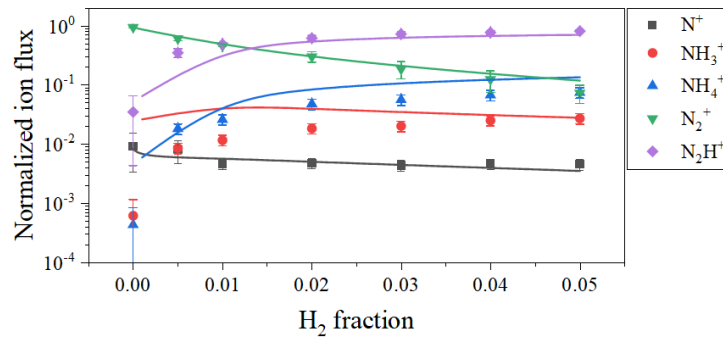
Figure II.2-16: Calculated normalized ion fluxes to the wall as a function of the H_2 content in the mixture for a discharge at 0.92 mbar and 10 W (lines), and comparison with the experimental measurements (dots).

Measurements can only be done at the wall of the confining box. However, **the model gives access to the ion densities inside the box**. **Figure II.2-17** shows the variation of the main ions N_2^+, N_2H^+ and NH_4^+ inside the box. One can observe that **N_2^+ and N_2H^+ are denser near the walls while NH_4^+ dominates at the center of the discharge.**
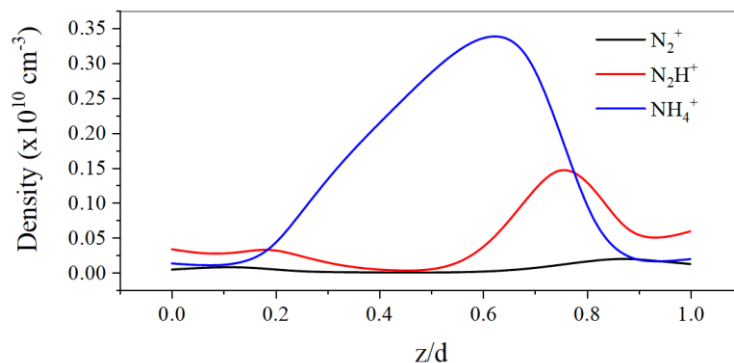
Figure II.2-17: Calculated ion densities for the same conditions as in **Figure II.2-16**. Absolute densities for the three most abundant ionic species, at the axis of the discharge (r = 0) as a function of the distance to the grounded electrode (same color codes as in **Figure II.2-16**).

These differences in the ion composition close to the reactor walls and in the discharge bulk can be justified by recalling that the sheaths are the regions with the **higher ionization rates**, and especially the one near the RF-driven electrode (see lower panel in **Figure II.2-15**). This is due to a strong variation of the electric field in these regions and the presence of energetic secondary-electrons coming from the surfaces.

The three main ions are especially linked by the three following relations:

$$e + N_2 \rightarrow N_2^+ + 2e \qquad (1)$$

$$N_2^+ + H_2 \rightarrow N_2H^+ + H \qquad (2)$$

$$N_2H^+ + NH_3 \rightarrow NH_4^+ + N_2 \qquad (3)$$
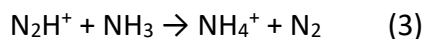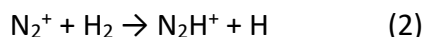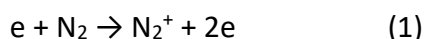
Both ion-molecule reactions are very efficient. Therefore, the relative abundance of the three main ions is controlled by the efficiency of the ionization reaction (1). In **high ionization** regions, the equilibrium is displaced towards the formation of N_2^+. It results in **N_2H^+ being the major ion**. Nevertheless, in the **center of the discharge**, where less ionization occurs, most of these ions are **converted into NH_4^+**, if NH_3 is present in sufficient amounts.

The abundance of ammonia plays a key role in the ion plasma chemistry, and is primarily dependent on the balance between electron impact dissociation of the precursors and the subsequent surface recombination. The density of ammonia and its increase with the H_2 amount is rather well reproduced by the model (see **Figure II.2-18**). The model predicts also a decrease with increasing pressure and an increase with increasing power, however, the changes in density are usually underestimated.
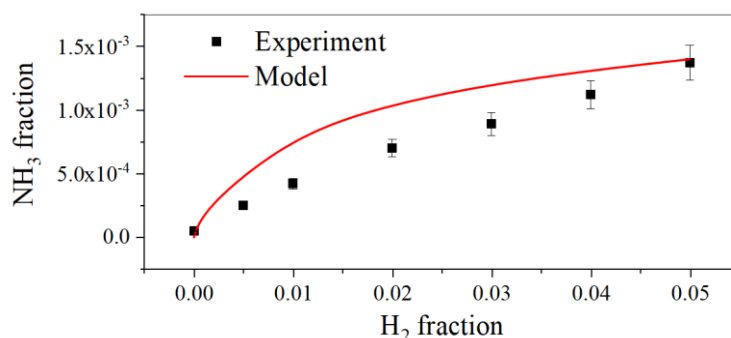
Figure II.2-18: Simulation (curve) and measurement (points) of the NH_3 fraction, as a function of the H_2 fraction in the mixture. Working conditions are 360 V voltage and 0.92 mbar pressure.

The main reactions leading to the formation of ammonia imply surfaces (see **Figure II.1-19**). The only reaction in the gas phase is strongly enhanced with the discharge power, in which case the ion neutralization by electron capture becomes as relevant as its recombination at the surfaces. Consequently, **the surface coverage is the most important factor in the formation of NH_3**. It is particularly sensitive to changes in the mixture composition: H(s) dominates at high H_2 fractions, at the expanse of N(s) and free surface sites. One can note that the high H(s) abundance for mixtures with > 1% H_2 hinders the production of NH_3, as a higher N(s) abundance would make NH_3 formation more efficient. NH(s) and NH_2(s) are also present in lower quantities, at respectively 3 and 4 order of magnitude below H(s). It shows that they are quickly used for subsequent reactions.
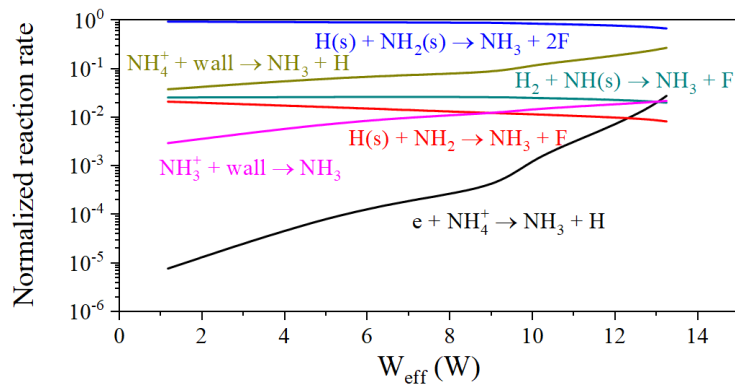
Figure II.2-19: Normalized reaction rates for the main sources of ammonia, at 5% H_2 and 0.92 mbar pressure. F stands for free surface sites.

CONCLUSION OF SECTION II.2

This work done in close collaboration between experiments and models led to an **advanced characterization of the CCP RF N_2-H_2 discharges** at low pressure, with small amounts of H_2.

We observed that the addition of small amounts of H_2 in a N_2 discharge changes strongly the plasma, in particular with the formation of new species such as ammonia, and the ions N_2H^+, NH_4^+ and H_3^+.

Another main result of this project is the **fundamental influence of surfaces on the plasma**.

(1) They are surrounded by a sheath that accelerates positive ions towards the surfaces. This leads to the production of **fast electrons by secondary emission**, which subsequently increases the global electron density in the bulk of the discharge.

(2) The increased energy of electrons in the sheath favors a stronger ionization of neutral molecules, leading to N_2^+ and N_2H^+. The **ion chemistry is different** in the bulk of the discharge where NH_4^+ dominates.

(3) Surfaces are also the place of an intense **formation of ammonia**. Besides, ammonia is a key precursor for many reactions in the gas phase. The ion chemistry in the plasma bulk is therefore also strongly influenced by the surfaces.

3- Comparison of different plasma discharges in N_2-H_2: what can we expect on Titan?

3.1- Case of a glow discharge with the THETIS experiment

The experiments studied in **Chapter III** required the use of a second plasma discharge, different from PAMPRE. THETIS, for THolins Evolution in Titan's Ionosphere Simulation, is a DC plasma reactor. N_2-H_2 plasmas have been previously studied by the community in DC discharges (see **Section II.1.1.b**). However, none has been performed in our experimental conditions.

The following work aimed to study the THETIS DC discharge with similar tools than the ones used for the previous section. We analyzed the electric field, the electron density, the ions and ammonia formation in the reactor.

3.1.a. The plasma reactor

DC plasma discharges are one of the simplest to create and study. **Figure II.3-1** shows a simplified scheme of the setup.

The reactor is a Pyrex tube 23 cm-long and with a 2 cm inner diameter. A **gas mixture of N_2-H_2 at low density** (0.5 to 5 mbar) is injected in the tube in **continuous flow.** We used high purity gases (> 99.999%). The gas from a 95% N_2 – 5% H_2 gas bottle (Air Liquide – CRYSTAL mixture) was diluted in pure N_2. The flow is fixed at 5 sccm (Standard Cubic Centimeters per Minute) by flowmeters from Brooks Instrument (range up to 5 sccm). The pressure is measured downstream of the reactor with two pressure gauges, one adapted for the mbar range (a capacitance gauge CMR 363 11mbar from Pfeiffer) and one for the ultra-high vacuum (a full range PKR250 from Pfeiffer). The gauges are situated downstream of the reactor to avoid any ignition of the plasma discharge on them. They were previously calibrated in different gases thanks to a third capacitance pressure gauge connected to a direct opening in the Pyrex tube.

Two cylindrical iron **electrodes** are positioned on both sides of the tube. They are coated with nickel with a small quantity of barium fluoride (BaF_2), an 'activator' whose role is to facilitate the extraction of electrons by ionic impact. A high voltage DC generator (maximum 3kV, 100 mA, regulated in current) creates a high voltage (1 to 3 KV) between the electrodes, leading to the ignition of the discharge inside the tube. Currents studied are **10-40 mA**. The generator is coupled to a ceramic power resistor (10 kΩ) to stabilize the ignition of the discharge.

DC discharges, also called **glow discharges**, are self-sustained discharges in which secondary electron emission from the cathode under ion bombardment compensates the loss of charges in the plasma. They have the advantage of developing with a peculiar structure well described in many text books (Raizer, 1991), including a large volume homogeneous zone with relatively

low and constant electric field called the positive column. This homogeneous positive column is filling the main part of the glass tube, which is a fundamental asset in the study of complex processes. The Pyrex **walls** confine closely the plasma, and could be a source of impurities. To limit such an influence, a great care is taken in **cleaning** the inside of the reactor between two experiments, especially in the case where they involve organic compounds. First, the inside of the glass tube is manually cleaned with ethanol – and sometimes diluted acetic acid if an organic deposit resists -, then the tube is closed and pumped to high vacuum (~10^{-6} mbar) with a turbo-molecular pump. To remove compounds – especially water – adsorbed on the walls, the tube is heated to ~80°C thanks to a heating cord and aluminum foil for 50 min. Finally, the tube is let under vacuum during > 30 min, until the MS detects very few impurities.
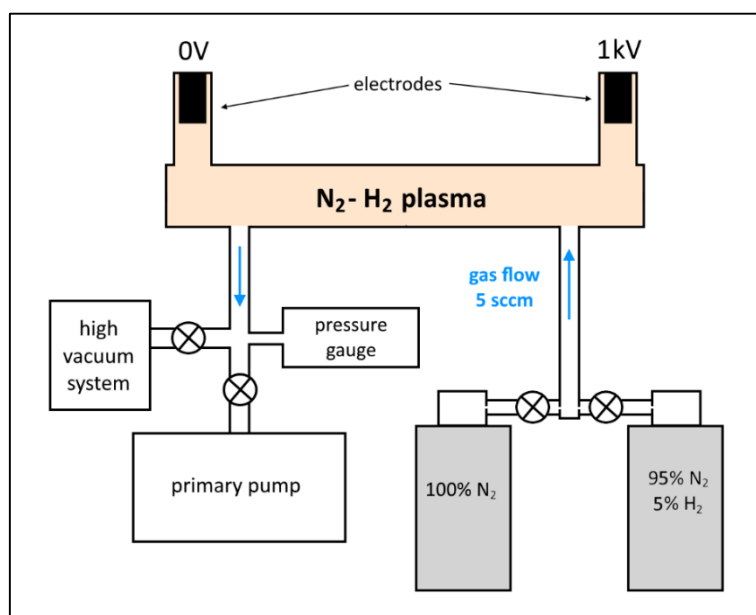
Figure II.3-1: Simplified scheme of the THETIS setup. DC plasma reactor, and gas circuit.

3.1.b. Electrical measurements and electron density

THE INSTRUMENTAL SETUP

The electric field and the electron density are measured in a reactor similar to the one presented above (2 cm diameter), but equipped with electrical probes (**see Figure II.3-2**). It is longer (55 cm), but this does not change the properties of the positive column in terms of electric field and electron density.

The electric field of a glow discharge is constant in the positive column (i.e. the central tube). Consequently, a simple measurement of the potential U_E between two probes separated by d = 20 cm in the plasma gives the electric field: $E = \frac{U_E}{d}$ (V.m^{-1}). In the literature, the reduced electric field E/N is often used, defined as the ratio of the electric field over the total density. It is usually given in Townsend (1 Td = 10^{-21} V.m^2).
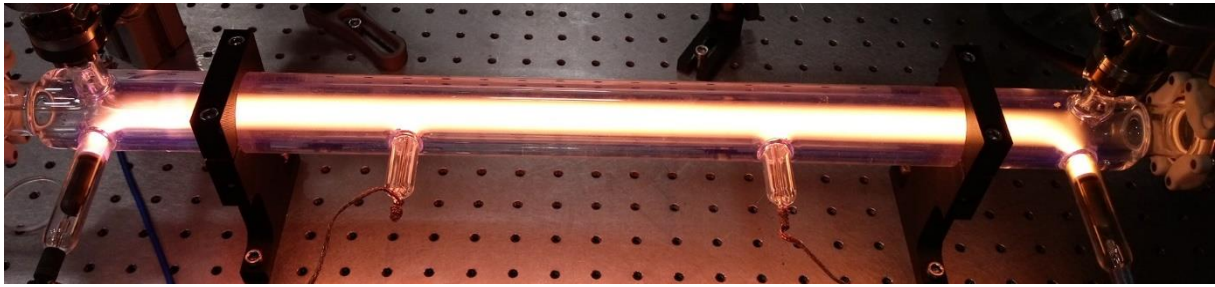
Figure II.3-2: Plasma reactor used for the measurement of the electric field and the electron density. The two probes for the measurement of the electric field are in the middle of the picture. The hairpin probe for the electron density measurements is on the left.
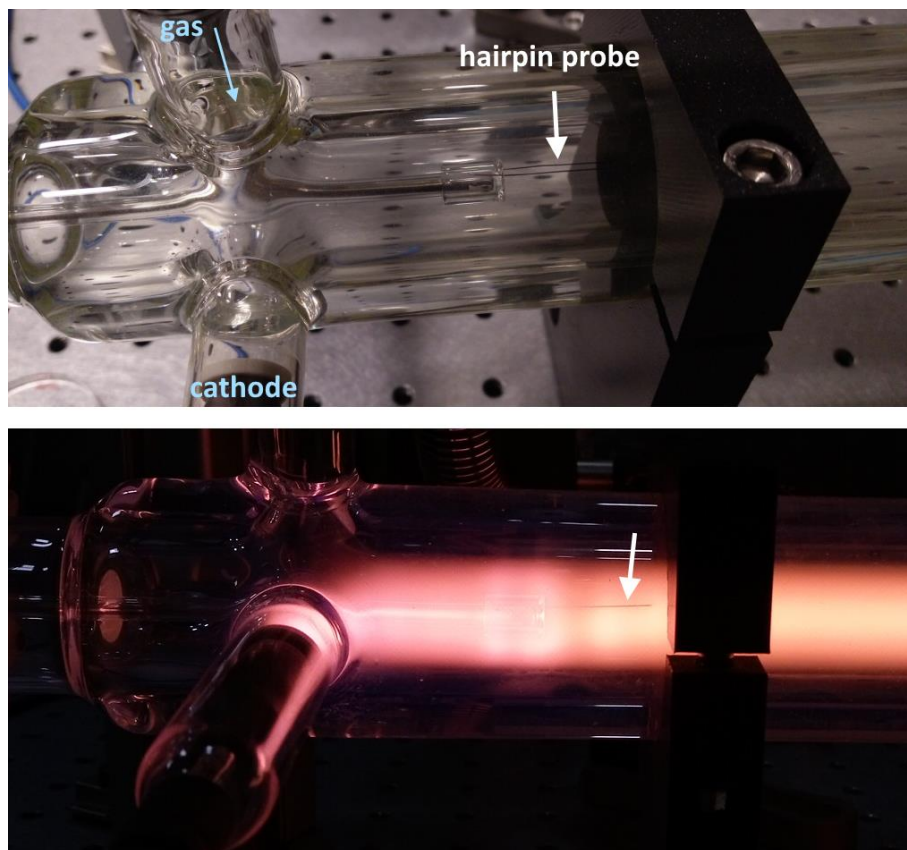
Figure II.3-3: Hairpin resonator introduced in the plasma tube.

The electron density is measured by a hairpin resonator. This technique is described in Piejak et al. (2004). A tungsten wire shaped like the letter U (0.1 mm radius, tines 25 mm long, separated by 1.8 mm) is introduced in the plasma (**see Figure II.3-3**). It is attached to a glass tube containing a rigid coaxial cable terminated in a loop that inductively couples a small amplitude microwave signal to the probe. A microwave sweep oscillator (HP, 8350B) provides the microwave signal, repetitively swept over a small frequency range. The reflected amplitude is measured using a Shottky diode, and recorded with an oscilloscope (LeCroy, Waverunner LT584M). The resonant frequency is related to the electron density by the following equation:

$$n_e = \frac{\pi . m_e}{e^2} \times \frac{f_r^2 - f_0^2}{\zeta} \qquad (II.3-1)$$

where f_r is the resonant frequency with plasma, f_0 the resonant frequency without plasma, m_e and e the mass and charge of an electron. ζ is a correction factor to take into account the sheath forming around the probe, and the collision in the gas phase induced at higher pressures (Sands et al., 2007).

EXPERIMENTAL RESULTS
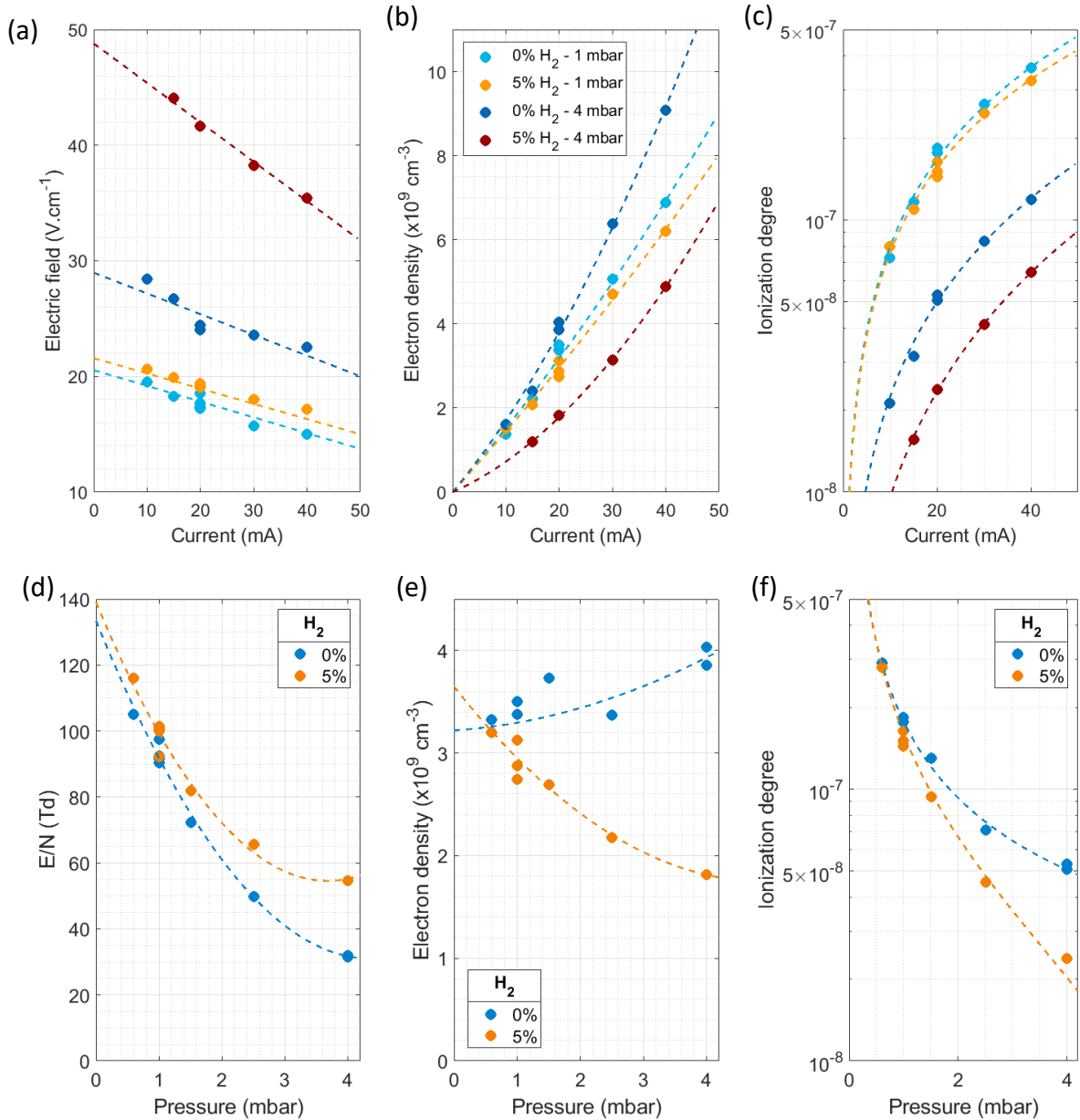
Figure II.3-4: (a) Electric field, (b) electron density and (c) ionization degree as function of the current. (d) E/N, (e) electron density and (f) ionization degree as function of the pressure at 20 mA.

Figure II.3-4 shows the experimental results for varying experimental conditions. We observe that **the electric field E decreases with the electric current** (the increase of temperature expands the gas and decreases the collision frequency). **It increases with pressure** because the collision frequency increases. Nevertheless, E increases less relatively to the pressure and **the reduced electric E/N field decreases with pressure. Both E and E/N increase with the addition of hydrogen to the gas mixture.**

The electron density, and therefore the ionization degree, increase strongly with the electric current. In the case of pure N_2, at 1 mbar, the electron density increases from $1.5x10^9$ cm^{-3} at 10 mA to $7x10^9$ cm^{-3} at 40 mA. In these conditions, the ionization degree varies from $7x10^{-8}$ to $4x10^{-7}$.

The electron density and the ionization degree decrease with the addition of hydrogen. The difference induced by the hydrogen increases with pressure. In pure N_2 the electron density increases from $3.3 \ 10^9$ cm^{-3} at 0.6 mbar to $3.9 \ 10^9$ cm^{-3} at 4 mbar. On the opposite, with 5% H_2 the electron density decreases from $3.2 \ 10^9$ cm^{-3} at 0.6 mbar to $1.8 \ 10^9$ cm^{-3} at 4 mbar. We recommend to stay careful with the values at higher pressure (especially at 4 mbar) because the correction factor ζ to take into account the hairpin sheath and the collisions is more difficult to estimate after a few millibars.

Discussion of the results

The value for the electron density can be estimated from the value of the electric field E by the following equation, deduced from the definition of the current density j:

$$ j = \frac{I}{\pi R^2} = q n_e \, \mu_e E \quad => \quad \boldsymbol{n_e = \frac{I}{q \, \mu_e E \pi R^2}} \qquad (II.3-2) $$

where R is the radius of the discharge tube, q, n_e and μ_e the charge, the density and the mobility of the electrons. μ_e depends on the E/N ratio in the discharge, with N being the total density. Brovikova and Galiaskarov (2001) measured a gas temperature of 340 K in a similar discharge, validated by a model by Pintassilgo and Guerra (2017). This gives a total density N = $2.1x10^{16}$ cm^{-3} at 1 mbar and 20 mA, and therefore E/N ≈ 80 Td. The electron mobility in these conditions is μ_e ≈ $5.2x10^5$ cm^2.V^{-1}.s^{-1} (Laplace database on LXCat - Fletcher and Reid 1980). Finally, the estimation of the electron density in the pure N_2 plasma discharge (1 mbar, 20 mA) is n_e ≈ $4.5x10^9$ cm^{-3}, which is in the same order of magnitude than our measurement ($3.4x10^9$ cm^{-3}).

Besides, our observations are consistent with the measurements in the same conditions in a pure N_2 plasma by Cernogora et al. (1981). Their value for the electric field at 1 mbar and 20 mA is 17 V/cm, and the trends with pressure and current are the same as the ones observed in **Figure II.3-4 (a)**. They measured the electron density by resonant cavity and found a value lower than in our work: $6x10^8$ cm^{-3} at 1 mbar and 20 mA. Nevertheless, the authors have doubts on this value, suspecting a mistake in the selection of the resonant mode (G. Cernogora, *private communication*). In any case, the trend with current and pressure is similar to the work presented here.

The increase of the electric field and the decrease of the electron density with the current between pure N₂ and N₂-H₂ (0.95:0.05) is also observed by Thomaz, Amorim, and Souza (1999). The increase in the E field strength with the addition of small percentages of H_2 is an indirect effect already described in the literature (de Souza et al., 1999; Gordiets et al., 1998a; Loureiro and Ricard, 1993). It would be the consequence of the quenching on the one hand of the metastable states N₂(a'), N₂(A) and on the other hand of the upper vibrational states N₂(v) which contribute significantly to the ionization in N_2 plasmas by associative ionization processes producing N_4^+ then N_2^+. By removing these processes, the electric field must increase to compensate the ionization when adding H_2. Then, the increase in the electric fields leads to an increase of the electron drift velocity, that has to be compensated by a decrease of the electron density to keep the current constant.

Conclusions on the evolution of the N₂ discharge with the addition of H₂

Electric field and electron density measurements in our discharge are consistent with the glow discharge literature. We can therefore legitimately suppose that processes described in the literature also apply in our case (de Souza et al., 1999; Garscadden and Nagpal, 1995; Gordiets et al., 1998a, 1998b; López-Moreno et al., 2008; Loureiro and Ricard, 1993). Here are the main points.

The addition of a few percents of H_2 leads to the **quenching of the (higher) vibrational levels of N₂,** as well as its energetic metastable states N₂(a') and N₂(A). In particular, these play a role in the ionization processes in a pure N_2 discharge. Consequently, **E and E/N increase** with the amount of H_2 to increase the ionization efficiency.

Contrarily to E and E/N, **the electron density decreases** with the H_2 amount. This leads to electrons less numerous, but **more energetic** that could possibly enable dissociation.

At low H_2 percentages, the dissociation of H_2 can be supposed globally similar to the dissociation of N_2 (Gordiets et al., 1998b; Guerra and Loureiro, 1997). The increase of the electron energy could possibly **increase slightly the dissociation of both N₂ and H₂.** An important pathway to the **formation of atomic H** is *a priori* the quenching of N₂(a'): $N_2(a') + H_2 \rightarrow N_2 + 2\,H$. The dissociation rate in a pure N_2 discharge is ~1%.

The **vibrationally excited N₂(v) and metastable states** are also present in the discharge (>0.005%). The quenching induced by H atoms with the addition of H_2 takes down the most energetic excited and metastable species. Nevertheless, the increase in the electron energy leads to an increase in the density of the lower energy excited states.

In conclusion, the chemical reactivity of the plasma increases with the addition of H₂. The main vector is the apparition of atomic H. But there is also an increase of atomic N and of the lower energy vibrationally excited and metastable species. Ions are also expected to evolve with the addition of H₂ (see further).

3.1.c. Neutrals and positive ions by mass spectrometry

Neutral and positive ion spectra are taken in the plasma with the mass spectrometer previously introduced in **Section II.1.2** and used in **Section II.2**. For the ion measurements, the collecting head of the MS required to be a few centimeters from the plasma, next to the grounded electrode (see **Figure III.3-5**). However, to measure the perturbations that the collecting head could induce on the plasma by being close to it, neutral measurements have been performed in two configurations: close to the plasma (a few cm as for the ions) and far from the plasma (~30 cm, see **Figure III.1-3**).

NEUTRAL SPECTRUM AND QUANTIFICATION OF AMMONIA

Similarly to the N$_2$-H$_2$ plasma in PAMPRE, the discharge in N$_2$-H$_2$ in the THETIS reactor leads to the formation of ammonia. **Figure II.3-5 (a)** shows the quick apparition of ammonia at the ignition of the discharge. m/z 17 can be due to NH$_3$, or to a fragment of H$_2$O, whose main peak is at m/z 18. According to the NIST database, the intensity of the fragment of H$_2$O at m/z 17, $I_{17}(H_2O)$, should be $\approx 0.21 \times I_{18}(H_2O)$. With $I_{17} \gg I_{18}$, the intensity I_{17} after t = 19 min is mainly due to ammonia. An increase of water is also observed at the ignition of the plasma as water is desorbed from the reactor walls. However, this contribution decreases strongly after a few minutes. Measurements presented in the following are done in the stabilized region, after the desorption of water.
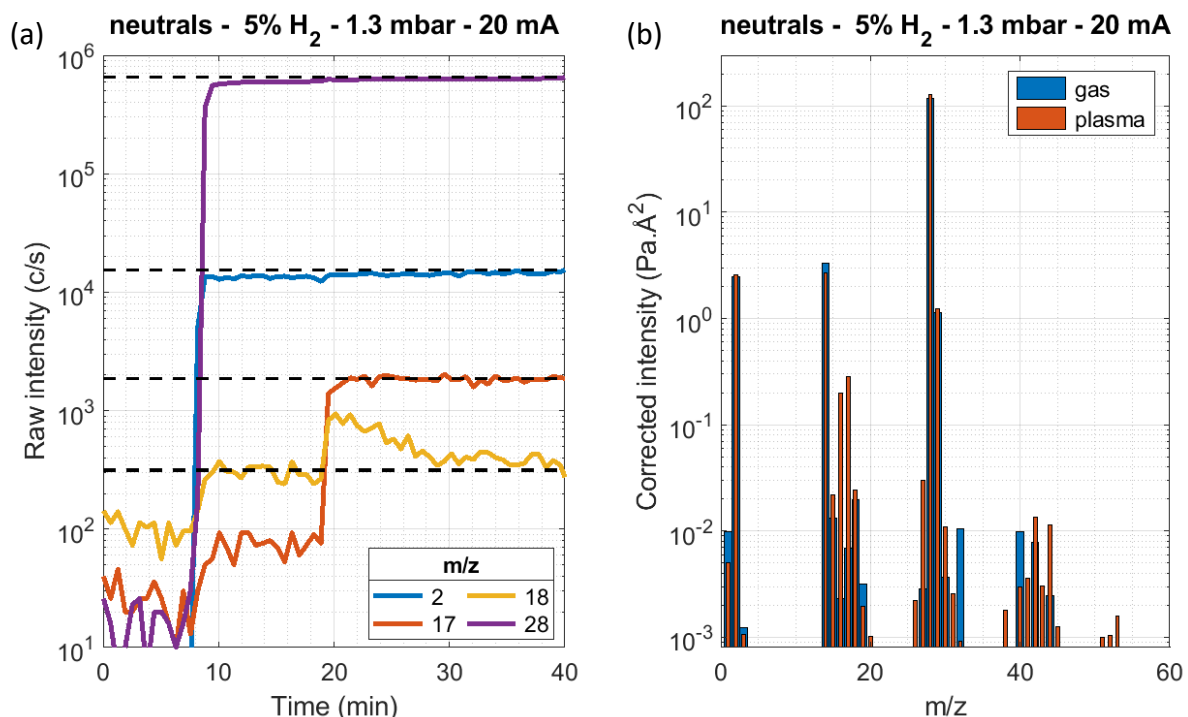
Figure II.3-5: MS measurements at the ignition of a N$_2$-H$_2$ plasma discharge (5% H$_2$, 1.3 mbar, 20 mA). (a) Evolution in time of m/z 2 (H$_2$), 17 (NH$_3$ + H$_2$O), 18 (H$_2$O) and 28 (N$_2$). Gases are injected at t = 8 min, and the plasma is ignited at t = 19 min. (b) Total spectrum with only the gases, and after the ignition of the discharge.

Figure II.3-5 (b) gives the complete spectra before and after the ignition of the plasma. The apparition of ammonia is visible at m/z 16 and 17. No other major species are formed. One can notice that m/z 27 and 44 increase slightly; they are attributed to HCN and CO_2 formed by the carbon and water residues in the reactor. This spectrum will serve as reference in **Section III.3.1** that studies the evolution of the gas phase with the addition of a tholin sample.

To compare mass peak intensities in **Figure II.3-5 (b)**, the intensity measured by the MS has been **corrected by the MS transmission**, which is mass-dependent. Details on the calibration are given in **Section II.1.2**. However, as the calibration has not been done just before the measurement, a correction in amplitude is required to deduce the quantity of ammonia produced. For this purpose, we used the known partial pressure of N_2, P_{N_2}.

$$P_{NH_3} = \frac{I_{NH_3}}{\sigma_{NH_3}} \times \frac{\sigma_{N_2}}{I_{N_2}} \times P_{N_2} \qquad (II.3-3)$$

σ_{NH_3} and σ_{N_2} are the simple ionization cross sections of NH_3 and N_2. σ_{N_2} is extracted from the **Table II.1-2**. σ_{NH_3} is taken from the Hayashi database (= 2.43 Å², www.lxcat.net/Hayashi). I_{NH_3} and I_{N_2} are the MS intensities at m/z 17 and 28 corrected from the MS transmission. The intensity at m/z 17 has also been corrected of the H_2O contribution. In the reference plasma conditions shown in **Figure II.3-5**, we obtain a **partial pressure of ammonia at 0.23 ± 0.02 Pa, which gives a density of 5.0 ± 0.7 x10^{13} cm^{-3}, and a percentage of 0.18 ± 0.01 %.**
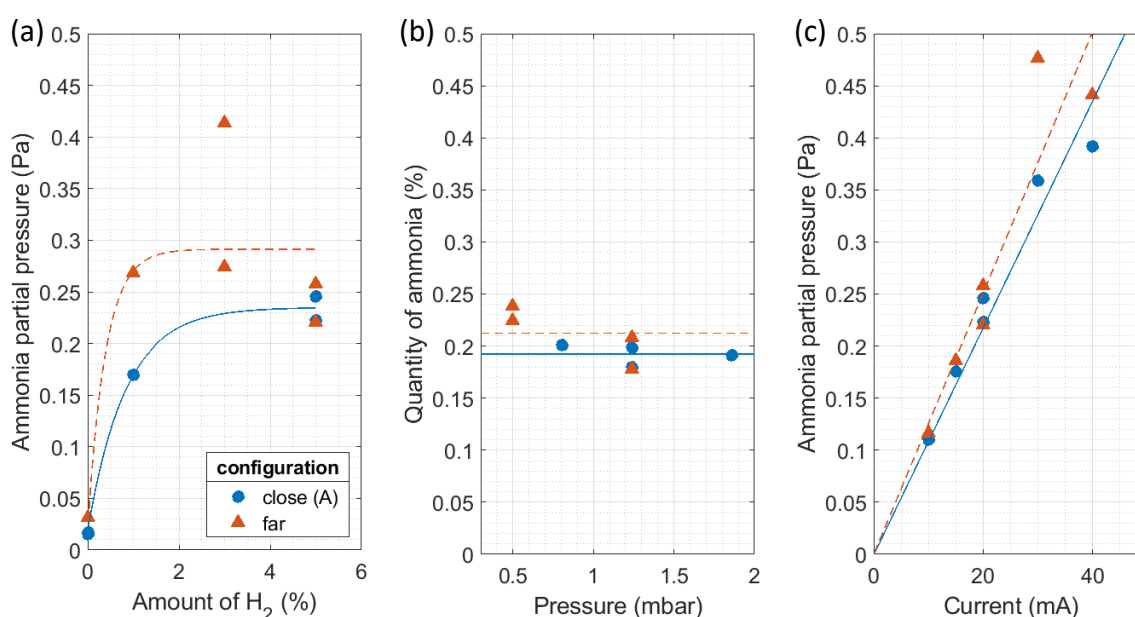
Figure II.3-6: Evolution of the ammonia quantity in the experiment for varying plasma parameters. The reference parameters are 5% H_2, 1.3 mbar and 20 mA. (a) Effect of the H_2 percentage on the ammonia partial pressure. (b) Effect of the pressure on the ammonia percentage in the gas phase. (c) Effect of the current on the ammonia partial pressure.

The ammonia detected in the reactor is sensitive to the plasma parameters. Figure II.3-6 shows the influence of the H_2 amount, the pressure and the current values on the production of ammonia. Ammonia appears as soon as a small amount of hydrogen is injected in the discharge. However, **no significant variation in the ammonia partial pressure is observed from 1 to 5% of H_2**. We observe large variability on the data points for 3% H_2. The partial pressure of ammonia increases with the total pressure, but **the mixing ratio of ammonia stays ~0.2% at all pressures**. The current as a strong impact on the production of ammonia. **The partial pressure of ammonia produced is linear to the current value, with a slope of ~0.011 Pa/mA**.

Similar results are obtained for the experiments with the MS being close or far from the plasma. This shows that the metallic head of the MS does not have a strong influence on the N_2-H_2 plasma if positioned at a few centimeters from it. **This validates the ion measurements performed in the 'close' configuration.**

The measured ammonia density is consistent with previous works. However, none have been performed in exactly the same conditions. Studies at 5% H_2, 2.7 mbar, 50 mA and 200 sccm measured an ammonia density of ~1.10^{12} cm^{-3} (Amorin et al., 1996; Gordiets et al., 1998b). It is about one order of magnitude lower than in our experiment, which could be explained by their higher gas flow velocity (200 sccm compared to 5 sccm). Experiments at 90% H_2, 0.08 mbar, 150 mA in a tube of 10 cm in diameter give an ammonia production of ~1% (E. Carrasco et al. 2011). This is about one order of magnitude higher than in our experiment, which can mainly be explained by the higher electric current used.

DETECTION OF POSITIVE IONS
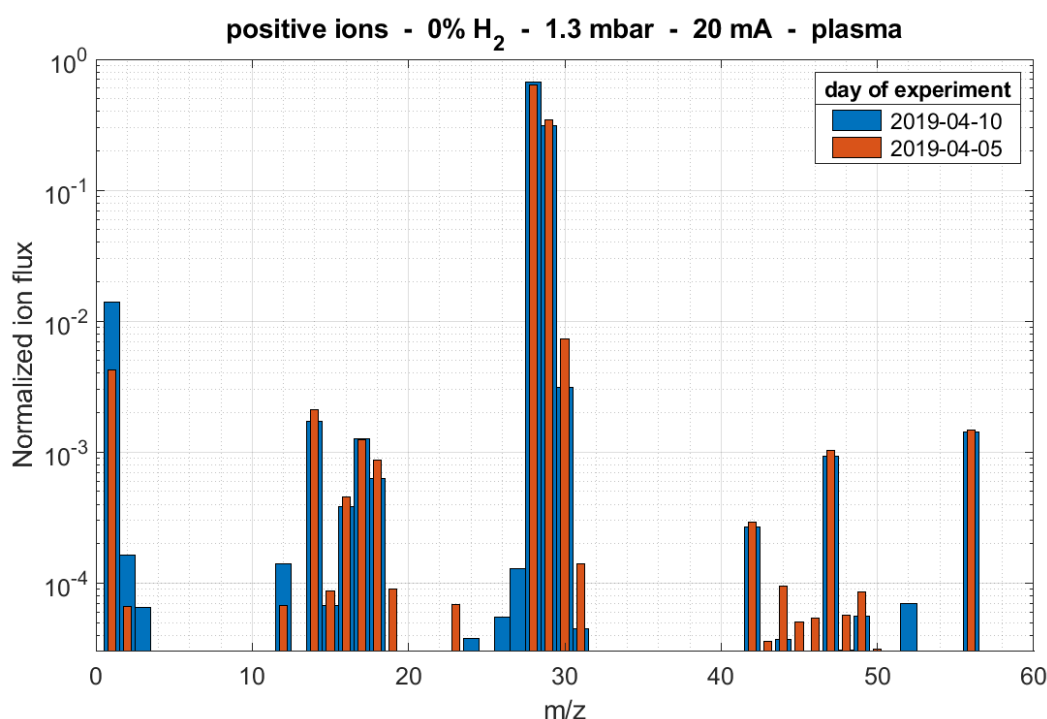
Figure II.3-7: Reproducibility of a positive ion mass spectrum in a pure N_2 plasma.

Ions are measured by the MS in the 'close' position. Spectra present the ion populations at a few centimeters from the plasma glow, which can be slightly different from the ion populations in the glow. First, 'background' measurements are acquired in a pure N_2 plasma. **Figure II.3-7** shows the repeatability of the measurement, and **Figure II.3-8** presents the evolution of the spectrum with the addition of 5% hydrogen.

With the addition of H_2 in the plasma, the ion species change. The main ion N_2^+ becomes N_2H^+ and ammonia ions NH_x^+ are formed in high quantities. One can also notice the appearance of H_3^+ and the increase of H_3O^+. The variations of the detected ions are presented in **Table II.3-1**.
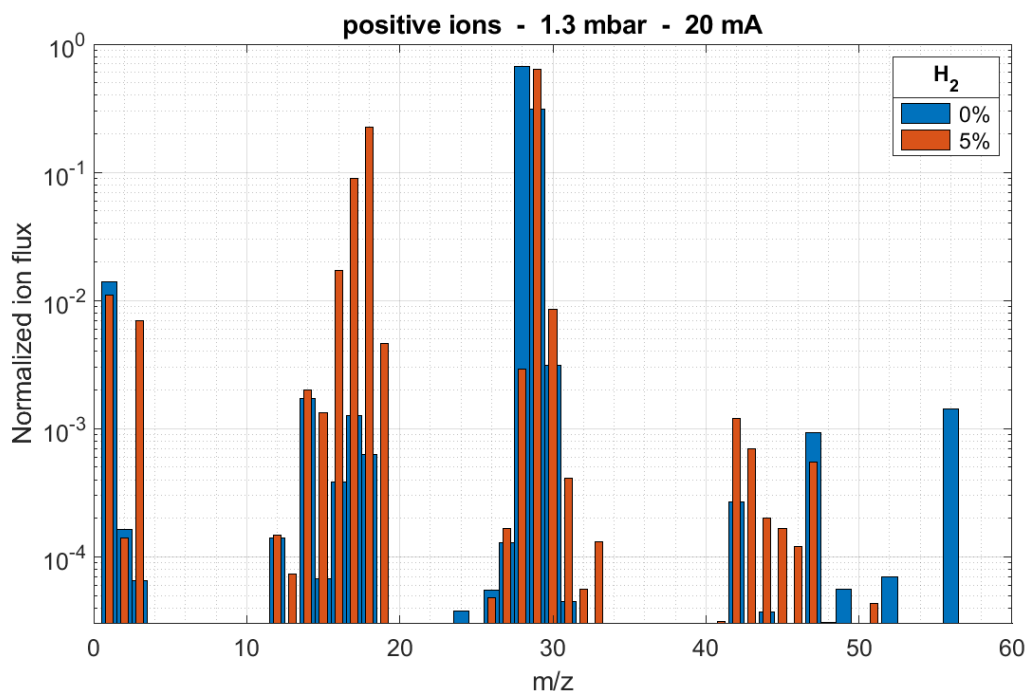
Figure II.3-8: Comparison of the positive ion mass spectrum in pure N_2 plasma and N_2-H_2 plasma.

m/z	in N_2 plasma	in N_2-H_2 plasma	N_2-H_2 case compared to pure N_2	attribution
3	-	++	↗↗↗	H_3^+
14	+	+	-	N^+
15	-	+	↗↗	NH^+
16	+	++	↗↗	NH_2^+
17	+	+++	↗↗	NH_3^+ / HO^+
18	+	+++	↗↗↗	NH_4^+ / H_2O^+
19	-	++	↗↗↗	H_3O^+ / F^+ (see **Section III.3.2.c**)
28	+++	++	↘↘↘	N_2^+
29	+++	+++	↗	N_2H^+
30	++	++	↗	isotope N_2H^+ / $N_2H_2^+$
31	-	+	↗	$N_2H_3^+$ / NOH^+
42	+	+	↗	N_3^+
43	-	+	↗↗	N_3H^+
47	+	+	↘	N_2F^+ (see **Section III.3.2.c**)
56	+	-	↘↘	N_4^+

Table II.3-1: Positive ions peaks detected in N_2 and N_2-H_2 plasmas, and their suggested attributions. '+++' is for an ion flux > 3%, '++' for [0.3 ; 3]%, '+' for [0.03 ; 0.3]% and '-' for < 0.03%.
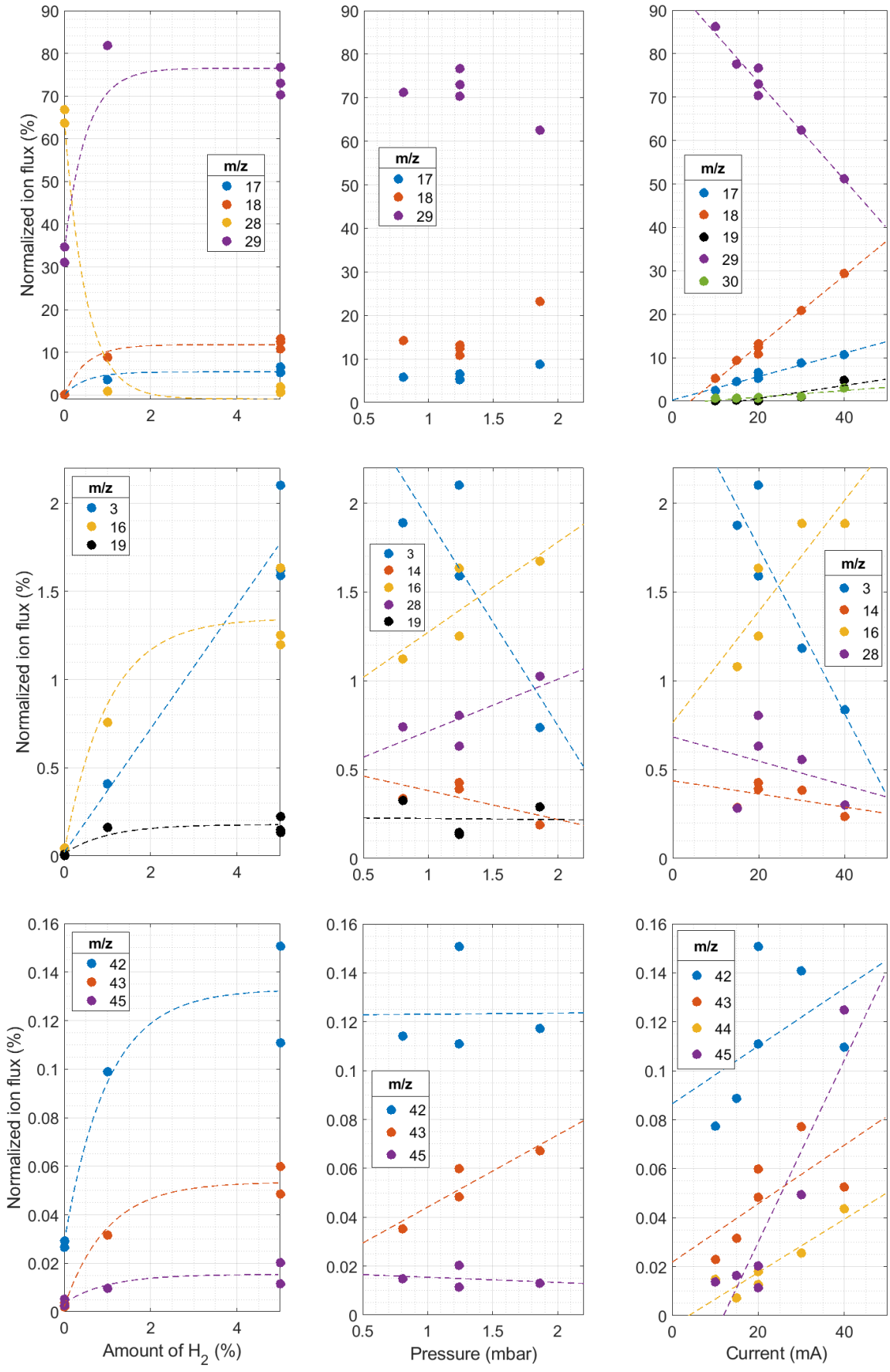
Figure II.3-9: Evolution of normalized ion fluxes with the injected amount of H$_2$, pressure and current.

The variation of the ion fluxes with the injected amount of H_2, pressure and electric current are shown in **Figure II.3-9**. **With these variations in the plasma parameters, the balance between the four main ions changes strongly**. **N_2^+ (m/z 28) which is the main ion in pure N_2** plasma is **hydrogenated to N_2H^+ (m/z 29)** as soon as some hydrogen is added in the reactor. Hydrogen also induces the formation of NH_3^+ (m/z 17) and NH_4^+ (m/z 18), respectively up to 8% and 12% at 1.3 mbar and 20 mA. A variation in pressure between 0.8 and 1.9 does not change greatly the ratios between the main ions. However, an **increase of the electric current leads to a strong increase in the production of NH_x^+ ions, to the expense of N_2H^+**. N_2H^+ decreases from 85% at 10 mA to 50% at 40 mA. On the opposite, NH_4^+ (resp. NH_3^+) increase from 5% (resp. 2%) to 30% (resp. 10%). This can be explained by the different dissociation cross sections of H_2 and N_2. H_2 is dissociated at lower energy than N_2, then N_2H^+ can be formed in the lower energy conditions. With increasing current, N_2 is more dissociated, increasing the formation of NH_x^+ ions to the expense of N_2H^+.

H_3^+ ratio increases linearly with the injected amount of H_2, but decreases strongly with an increasing pressure or current. H_3O^+ also increases with the injection of H_2 as it favors the desorption of water on the walls by protonation. On the opposite to H_3^+, its production is strongly enhanced by an increasing electric current. m/z 42 to 45 also increase with the amount of H_2 and the electric current. The H_2 percentage has as greater effect on m/z 42 and 43 (N_3^+, N_3H^+), whereas the current has a stronger effect on m/z 44 and 45 ($N_3H_2^+/CO_2H^+$ and $N_3H_3^+$).

All the experiments presented in **Figure II.3-9** have been conducted in the context of experiments for **Section III.3.2**. For this purpose, a tholin sample was positioned at ~30 cm from the plasma, to be inserted later in the plasma. Even if positioned far from the plasma, we suspect that the presence of the tholins sample could change slightly the ion results. An experiment in the reference conditions (5% H_2, 1.3 mbar, 20 mA) was conducted without tholins in the vacuum chamber (presented in **Figure II.3-8**). Results are globally similar, with only a small increase in the ammonia ions NH_x^+ (x 2) and a decrease of H_3^+ (÷ 1.5) and of the trace carbon-containing ions at m/z 12 and 26-27-28 (÷ 4). So we can conclude that the presence of tholins at a long distance from the plasma did not disturb significantly the plasma. The introduction of the sample inside the experiment but at long distance from the plasma does not bias the results.

3.2- Lessons from PAMPRE and THETIS: and on Titan?

3.2.a. Electron density and the ionization ratio

The electron density measured in PAMPRE (see **Figure II.2-7 (a)**) and in the DC glow discharge (see **Figure II.3-4 (b)**) are similar, mostly between **1 x10⁹ and 5x10⁹ cm⁻³**. Conditions tested can reach lower values on PAMPRE and higher values in the glow discharge because of the difference in power density (~0.03 W.cm⁻³ in PAMPRE compared to ~0.1 W.cm⁻³ in THETIS, see **Figure II.3-11**).

The comparison of the **ionization degree** obtained in the glow discharge and PAMPRE (see **Figure II.2-7 (b)** and **Figure II.3-4 (c)**) gives very similar exploration ranges: **between 2x10⁻⁸ and 4x10⁻⁷**. For the two experiments, the ionization degree decreases with an increasing pressure.

Laboratory experiments are conducted at higher pressure than on Titan's ionosphere for several reasons. The very low pressures in Titan's ionosphere (10^{-8} to 10^{-6} mbar) would require a huge reactor to limit the wall effects. Besides, in such a dilute environment, collisions are rare, and the chemical evolution of the environment is slow. To increase the pressure is therefore also a way to accelerate the processes to perform an experiment in hours or days instead of months or more. This point is further discussed in **Section III.1.2.b**.

However, a fundamental quantity to reproduce to enable a similar chemistry is the **ionization degree**. The values reachable by our two experiments enable to probe the ionosphere of Titan between 900 and 1200 km (see **Figure II.3-10**), exactly at the altitude range interesting in our objective to study the evolution of the aerosols in the ionosphere.
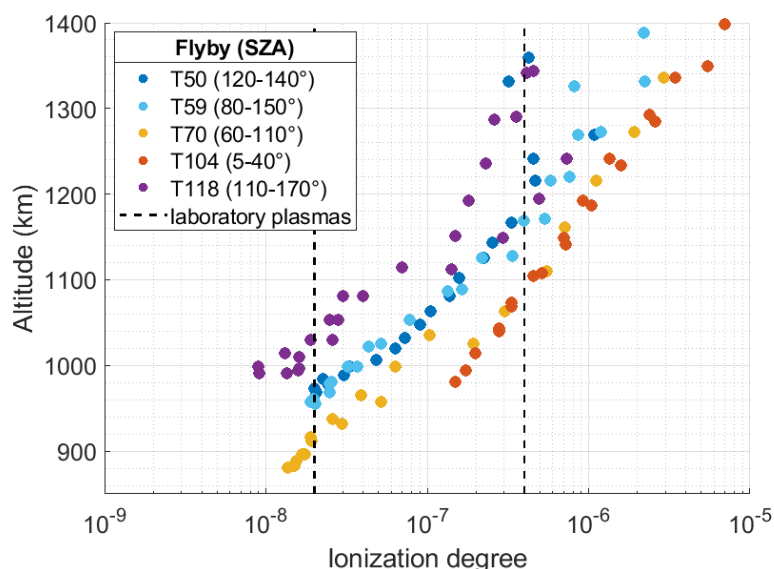
Figure II.3-10: Ionization degree (i.e. the electron density over total density ratio) as function of altitude on Titan for flybys at different Solar Zenith Angles (SZA). Data from Edberg et al. (2013). The ionization degrees reached in the laboratory are between the two dashed lines.

3.2.b. Ammonia density

Ammonia is produced in the two experiments, PAMPRE and THETIS, as soon as some hydrogen is injected in the gas phase and the plasma ignited. The reference conditions in PAMPRE and THETIS are globally similar: (5% H_2, 0.91 mbar, 6 W, 55 cm^3) for PAMPRE and (5% H_2, 1.3 mbar, 18 W, 425 cm^3) for THETIS. To compare the evolution of ammonia with different parameters in the two experiments, **Figure II.3-11** compares the ammonia proportion. This enables to correct from the effect of pressure, which is a bit different in the two experiments. Indeed, as shown in **Figure II.3-11 (b)**, the **ammonia proportion is globally constant (~0.15-0.2%) with pressure in THETIS, and decreases in PAMPRE**. This difference is certainly due to the difference of geometry and material of the two reactors, that modifies the production of ammonia on the walls.

Figure II.3-11 (c) shows that in both cases, **ammonia is very sensitive to the power density given to the plasma and increases linearly with it**. On THETIS, the power density in the positive column is computed from the electric field (E) measurement with:

$$\frac{Pw}{V} = \frac{E\left(\frac{V}{cm}\right) \times d(cm) \times I(A)}{\pi \times r^2 \times d \ (cm^3)} \qquad (II.3-4)$$

with r = 1 cm and d = 17 cm, the radius and the length of the positive column of the discharge in THETIS. The power density is higher in THETIS in all the conditions studied because of the difference in volume $V_{PAMPRE} \gg V_{THETIS}$. However, regarding the linear trends, for a given power density, more ammonia is formed in PAMPRE compared to THETIS. This can be explained by the materials composing the walls of the two discharges: the metallic walls in PAMPRE are more efficient to synthesize ammonia than the Pyrex walls of THETIS tube.
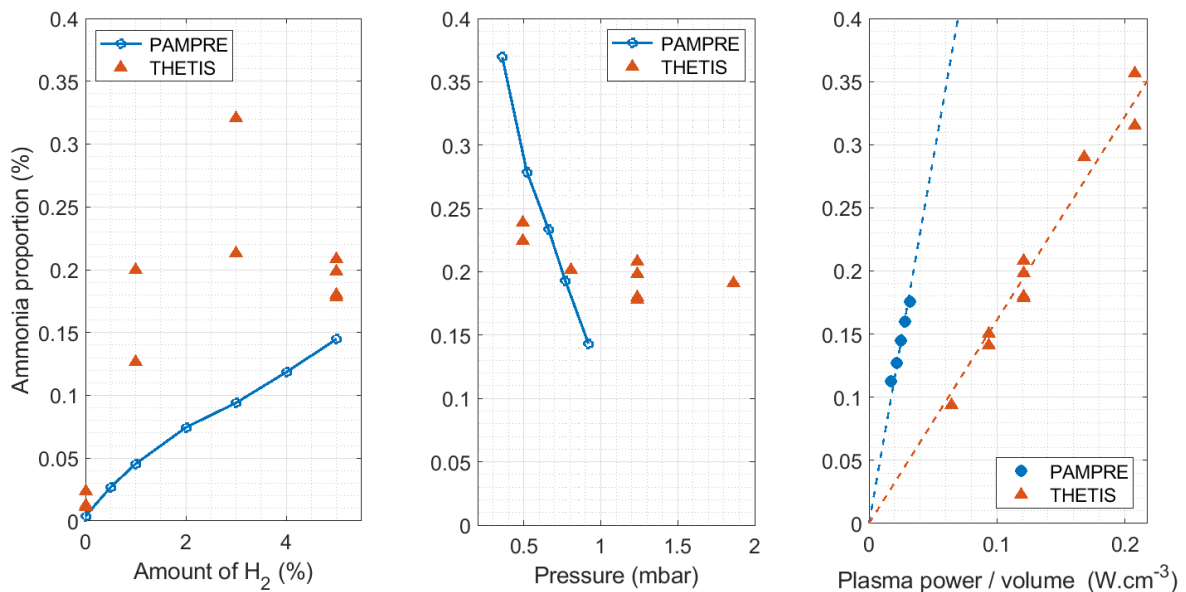
Figure II.3-11: Comparison of ammonia proportion detected in the N_2-H_2 plasma discharges in PAMPRE and THETIS, for different plasma conditions. The reference condition for the PAMPRE experiment is (5% H_2, 0.91 mbar, 11 W) and for the THETIS experiment (5% H_2, 1.3 mbar, 20 mA).

A different trend between the two experiments is observed with the injected H₂ amount. A linear increase is observed in the case of PAMPRE, at the difference of a sharp increase and a plateau for THETIS. This also could be explained by the walls materials. Indeed, the formation of ammonia on metallic surfaces is quicker than on Pyrex (Hong et al., 2017; Shah et al., 2018; Touvelle et al., 1987). In the case of THETIS, the surface is possibly saturated in NH_3 adsorbed precursors. Therefore, the limiting parameter in the production of ammonia is the available surface. In the case of PAMPRE, the metallic surface does not saturate and the limiting parameter is the available H_2 amount.

In conclusion, in a N₂-H₂ plasma discharge, ammonia formation is enhanced by the addition of hydrogen and an increasing power delivered to the plasma. The production of ammonia depends on the surface material.

These observations are difficult to extrapolate directly to Titan, especially because of the presence of walls, strongly catalyzing the production of ammonia, as shown in **Section II.2.3.c**. Besides, the surface of organic aerosols could also have an influence, as well as the carbon-containing plasma species. This point is studied in **Section III.3**.

3.2.c. Positive ions

Positive ions play a fundamental part in the plasma chemistry, either in THETIS, PAMPRE or on Titan.

H^+, H_2^+, H_3^+ (M/Z 1 TO 3)

The hydrogen ions were found in the N₂-H₂ plasma discharges in both THETIS and PAMPRE experiments. The MS measurements at m/z 1 (H^+) are not reliable. However, we observed in both cases that **H_3^+ was dominant** over H_2^+. This can be explained by the quick conversion of H_2^+ into H_3^+ which is more stable. This result has been previously observed in laboratory plasmas and discussed in Méndez et al. (2006) and Tanarro et al. (2007).

As hydrogen is the major molecular species in the universe, its derived ions H_x^+ are found in many places at low density, such as the **interstellar medium** (McCall and Oka, 2000; Oka, 2006) and the **upper atmospheres of giant planets** (Majeed et al., 2004; Migliorini et al., 2019). Hydrogen is the third major species in Titan's ionosphere, after N_2 and CH_4 (Cui et al., 2009, 2008). Therefore, its ions should be present and play a role in the ionospheric chemistry.

Hydrogen ions **increase with increasing H₂** injected amount in both the THETIS and PAMPRE experiments, reaching ~1.5 to 2% of the total ion fluxes for 5% of H_2 injected. Similarly, as the percentage of H_2 increases with altitude, more hydrogen ions should be proportionally present at higher altitudes in the ionosphere of Titan. While the percentage of hydrogen ions is rather constant with pressure and power in PAMPRE, it decreases in both cases in THETIS. This could be due to the certainly different electron energy distribution functions in the two discharges.

In particular, **H₃⁺** is relatively stable and is a strong **protonating agent**. Indeed, H_2 has a low proton affinity, and H_3^+ has high cross-sections relative to ion-molecule collisions. Milligan et al. (2002) showed that in contact with species containing C, N and O, H_3^+ leads to the **formation of new unsaturated molecules and ions** in these low pressure environments. In the case of a N_2-H_2 plasma discharge, E. Carrasco et al. (2013) observed that H_3^+ is a protonating agent leading to the formation of N_2H^+ from N_2, NH_4^+ from NH_3 and NH^+ and NH_2^+ from N.

N^+, NH^+, NH_2^+, NH_3^+, NH_4^+ (M/Z 14 TO 18)

In pure N_2 plasmas, only N^+ is present from the electron ionization of N_2 between m/z 14 and 18. Nevertheless, **with the addition of hydrogen in the gas phase, the NH_x^+ ions are formed in quantity**, in both PAMPRE and THETIS. For 5% injected H_2, at ~1 mbar and respectively 11W and 15 mA, the proportions of NH_4^+ and NH_3^+ in the two experiments are very similar, at **~8% for NH_4^+ and ~3% for NH_3^+**. The evolution of the NH^+, NH_2^+ and NH_3^+ ions are exactly correlated with the variations of NH_3, with the H_2 injected amount, pressure and discharge power, for both PAMPRE and THETIS. Only NH_4^+ has a slightly different behavior in the case of PAMPRE: its proportion increases with pressure instead of staying constant and it decreases with power instead of increasing. This point could be related to the fact that the CCP discharge in PAMPRE is highly not homogeneous, as previously discussed in **Section II.2.3.c**.

The NH_x^+ ions are therefore strongly correlated to the quantity of ammonia produced in the discharge. Previous models of the chemistry in N_2-H_2 plasmas in DC glow discharges explain this correlation, as **the ions are mainly directly formed from ammonia** (E. Carrasco et al., 2013; Tanarro et al., 2007). Indeed, NH_4^+ is produced by the protonation of ammonia by a protonating agent such as H_3^+ or N_2H^+. NH_3^+ is formed partly by direct electron ionization and by reaction with H^+ or H_2^+. Similar reactions can also lead to the production of NH_2^+ and NH^+ in smaller quantities.

On Titan, the detection of the NH_x^+ ions by mass spectrometry with INMS is difficult as the ions have masses superposed to the CH_x^+ numerous ions. In addition to the processes presented above in a N_2-H_2 plasma discharge, on Titan their production pathways can also include CH_4 (Yelle et al., 2010). NH^+, NH_2^+ and NH_3^+ are *a priori* quickly used to form other more stable molecules, as in $NH^+ + N_2 \rightarrow N_2H^+ + N$ (Vuitton et al., 2019). Nevertheless, NH_4^+ stays strongly related to NH_3 density because the proton addition to NH_3 and the recombination of NH_4^+ are quick reactions. Therefore, **on Titan NH_4^+ is often used as an indicator of the NH_3 density** (Cravens et al., 2006).

N_2^+, N_2H^+ (M/Z 28 TO 31)

In all the experiments except in pure N_2 plasma, N_2H^+ is the main ion, at 70-80%. Its variations with the hydrogen content and the pressure are the same for the two experimental setups. We observe a sharp increase with the addition of ~1% hydrogen in the gas phase and then a stabilization of its value. Concerning the pressure, the N_2H^+ proportion stays constant at least between 0.6 and 1.5 mbar. Nevertheless, **in the case of a varying**

discharge power the results in THETIS and PAMPRE are different. In THETIS, an increasing current leads to a large production of NH_4^+ (30% at 40 mA), which proportionally induces a decrease in the N_2H^+ percentage. As discussed in the above paragraph, it is not the case in PAMPRE at the location of the measurement. Consequently, the N_2H^+ ratio stays relatively constant with an increasing plasma power in PAMPRE. In PAMPRE, N_2H^+ variations are always balanced by N_2^+, mainly because NH_4^+ is underestimated by the measurement in this non-homogeneous discharge. On the other hand, in THETIS, except in pure N_2 plasmas, the variations of N_2H^+ are balanced by NH_4^+ and NH_3^+.

In both PAMPRE and THETIS, the peak at m/z 30 is partly due to the $^{15}N^{14}NH^+$ isotope of $^{14}N_2H^+$, and maybe also to $N_2H_2^+$. The small peak appearing at m/z 31 in N_2-H_2 can be attributed to the diazenium ion ($N_2H_3^+$).

N_2H^+ is a common ion in ionized low pressure environments with nitrogen and hydrogen. It is mainly formed by the protonation of N_2 by H_2^+ or H_3^+ or by the reaction of N_2^+ with H_2 (Tanarro et al., 2007). It does not react with N_2 or H_2. Then, it is found in the interstellar clouds (Petrie and Bohme, 2007; Womack et al., 1992).

On the opposite, N_2H^+ reacts easily with CH_4, as a protonating agent (Tanarro et al., 2007). Besides, the detection of N_2H^+ on Titan INMS mass spectra is difficult as the major ion $C_2H_5^+$ also has a mass of 29 u. In any case, **N_2H^+ plays an important role in Titan's complex chemistry** (Vuitton et al., 2019).

N_3^+, N_4^+ (M/Z 42+ AND 56)

In both PAMPRE and THETIS experiments, peaks at 42 and 56 u are observed in pure N_2 plasma. They are attributed to the N_3^+ and N_4^+ ions. According to Alves et al. (2012) and Anicich et al. (2000), N_3^+ and N_4^+ are formed by the reaction of N^+ and N_2^+ with N_2. In any case, their peaks at 42 and 56 u would be hidden by other carbon-containing species in the ionosphere.

In the two experiments, N_4^+ disappears with the addition of H_2 to the gas mixture. It is consistent with the decrease of N_2^+, which is needed to form N_4^+. Nevertheless, N_3^+ stays present (as N^+), and other ions appear at m/z 43 to 46. The main one, at a mass of 43 u is certainly N_3H^+ (Shahin, 1966; Sinha et al., 2013, 2004). 44 and 45 u could be due to $N_3H_x^+$ ions, but also to CO_2^+ and CO_2H^+ ions, formed from residues of CO_2 or O_2 in the reactor.

CONCLUSION OF CHAPTER II

The addition of small amounts of H_2 has been investigated in two different N_2 plasma discharges: PAMPRE, an RF CCP discharge, and THETIS, a DC glow discharge. The plasma conditions are at low pressure (~1 mbar) and low power (0.02 to 0.2 W.cm^{-3}). The two experiments led to very similar observations.

The addition of less than 1% H_2 has a strong effect on the N_2 plasma discharges. Hydrogen quenches the (higher) vibrational levels of N_2 and some of its energetic metastable states. This leads to the increase of the discharge electric field and consequently of the electron energy. As a result, higher quantities of radical and excited species are suspected to be produced.

The addition of hydrogen leads to the formation of new species. In particular, it is the case of H and NH_x radicals that start the formation of ammonia on the walls surrounding the discharges. The apparition of many new ions have also been observed: N_2H^+ and NH_4^+ being the major ones, and also H_3^+, NH^+, NH_2^+, NH_3^+, N_3H^+ and $N_3H_3^+$.

To go further in the experimental investigation:

In the case of THETIS, most of the conclusions have been made by analogy with the literature. Nevertheless, there is no perfect reference studying the precise parameters of the experiment. Therefore, it would still be interesting to investigate further some species in the experiment. In particular, the understanding of the radical and excited species seems of importance in the analysis of the plasma chemistry. Experimentally, these could be analyzed by actinometry or TALIF (two photon absorption laser induced fluorescence). A 0D model based on the chemistry used in E. Carrasco et al. (2011) in the working conditions of THETIS would also be a fundamental tool to understand precisely the radical-induced plasma chemistry.

In the case of PAMPRE, the next step to understand the N_2-CH_4 complex chemistry happening during the production of tholins is the modeling of the carbon chemistry!

The objective of this section was to understand the differences between a pure N_2 and a N_2-H_2 plasma discharge with a few percents of hydrogen. On Titan, both N_2 and H_2 are present in the ionosphere. Hydrogen species are especially likely to erode organic material. We saw that the radical species H and NH are present in quantity in the discharge, as well as N_2H^+, NH_4^+, H_3^+ and other protonated ions. These are very reactive species. How do they interact with organic aerosols on Titan?
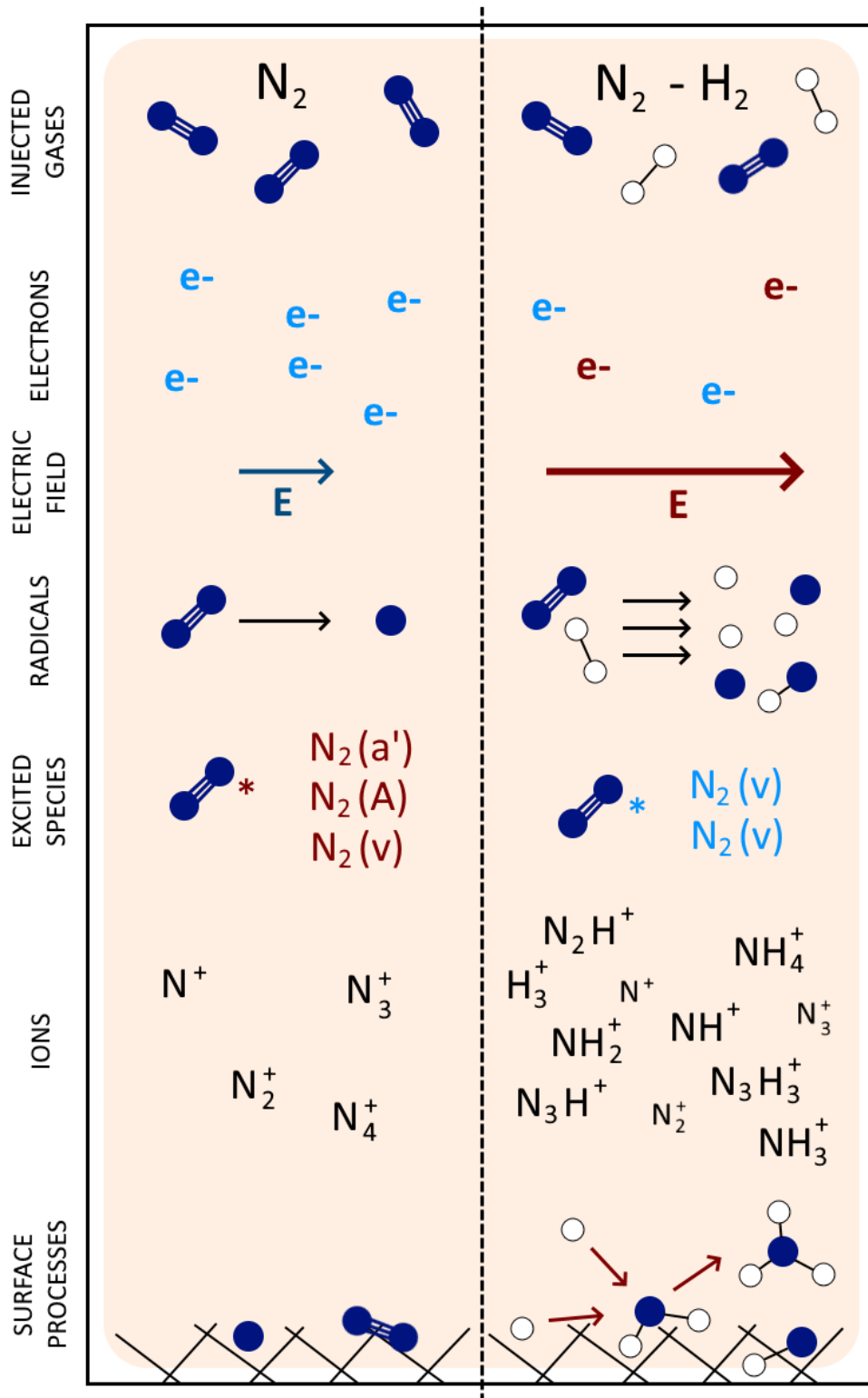
Figure II.3-12: Summary scheme of the differences between N_2 and N_2-H_2 plasma discharges. The most energetic electrons and excited species are represented in red, by opposition to the blue ones.

References for Chapter II

Aberle, A.G., 2001. Overview on SiN surface passivation of crystalline silicon solar cells. Sol. Energy Mater. Sol. Cells 65, 239–248. https://doi.org/10.1016/S0927-0248(00)00099-4

Achkasov, K., 2015. Study of negative ion surface production in cesium-free H_2 and D_2 plasmas: application to neutral beam injectors for ITER and DEMO. PhD thesis, Univ. d'Aix-Marseille, Fr.

Alcouffe, G., Cavarroc, M., Cernogora, G., Ouni, F., Jolly, A., Boufendi, L., Szopa, C., 2010. Capacitively coupled plasma used to simulate Titan's atmospheric chemistry. Plasma Sources Sci. Technol. 19, 015008. https://doi.org/10.1088/0963-0252/19/1/015008

Alves, L.L., 2014. The IST-LISBON database on LXCat, in: Journal of Physics: Conference Series. IOP Publishing, p. 012007. https://doi.org/10.1088/1742-6596/565/1/012007

Alves, L.L., Marques, L., Pintassilgo, C.D., Wattieaux, G., Es-Sebbar, E., Berndt, J., Kovacević, E., Carrasco, N., Boufendi, L., Cernogora, G., 2012. Capacitively coupled radio-frequency discharges in nitrogen at low pressures. Plasma Sources Sci. Technol. 21, 045008. https://doi.org/10.1088/0963-0252/21/4/045008

Amorim, J., Loureiro, J., Schram, D., 2001. Formation of H^- ions via vibrational excited molecules produced from recombinative wall desorption of H atoms in a low-pressure H_2 positive column. Chem. Phys. Lett. 346, 443–448. https://doi.org/10.1016/S0009-2614(01)00977-0

Amorin, J., Baravian, G., Bockel, S., Ricard, A., Sultan, G., 1996. Laser and Emission Spectroscopy in H2 and H2-N2 dc Discharges. J. Phys. III Fr. EDP Sci. 6, 1147–1155.

Anicich, V.G., Milligan, D.B., Fairley, D.A., McEwan, M.J., 2000. Termolecular Ion-Molecule Reactions in Titan's Atmosphere, I: Principal Ions with Principal Neutrals. Icarus 146, 118–124. https://doi.org/10.1006/icar.2000.6353

Atreya, S.K., Wong, A.S., Baines, K.H., Wong, M.H., Owen, T.C., 2005. Jupiter's ammonia clouds - Localized or ubiquitous?, in: Planetary and Space Science. Pergamon, pp. 498–507. https://doi.org/10.1016/j.pss.2004.04.002

Barton, D., Heason, D.J., Short, R.D., Bradley, J.W., 2000. The measurement and control of the ion energy distribution function at a surface in an RF plasma. Meas. Sci. Technol. 11, 1726–1731. https://doi.org/10.1088/0957-0233/11/12/312

Body, T., Cousens, S., Kirby, J., Corr, C., 2018. A volume-averaged model of nitrogen-hydrogen plasma chemistry to investigate ammonia production in a plasma-surface-interaction device. Plasma Phys. Control. Fusion 60, 075011. https://doi.org/10.1088/1361-6587/aab740

Bogaerts, A., Neyts, E., Gijbels, R., Van der Mullen, J., 2002. Gas Discharge Plasmas and Their Applications. Spectrochim. Acta Part B 57, 609–658.

Bouanis, F.Z., Jama, C., Traisnel, M., Bentiss, F., 2010. Study of corrosion resistance properties of nitrided carbon steel using radiofrequency N_2/H_2 cold plasma process. Corros. Sci. 52, 3180–3190. https://doi.org/10.1016/j.corsci.2010.05.021

Brovikova, I.N., Galiaskarov, E.G., 2001. Kinetic characteristics of production and loss of nitrogen atoms in N2 plasma. High Temp. 39, 809–814. https://doi.org/10.1023/A:1013174518832

Burgdorf, M.J., Orton, G.S., Encrenaz, T., Davis, G.R., Lellouch, E., Sidher, S.D., Swinyard, B.M., 2004. Far-infrared spectroscopy of the giant planets: Measurements of ammonia and phosphine at Jupiter and Saturn and the continuum of Neptune, in: Advances in Space Research. Elsevier Ltd, pp. 2247–2250. https://doi.org/10.1016/j.asr.2004.04.004

Carlson, R.W., Baines, K.H., Anderson, M.S., Filacchione, G., Simon, A.A., 2016. Chromophores from photolyzed ammonia reacting with acetylene: Application to Jupiter's Great Red Spot. Icarus 274, 106–115. https://doi.org/10.1016/j.icarus.2016.03.008

Carrasco, E., Jiménez-Redondo, M., Tanarro, I., Herrero, V.J., 2012. Chemistry in low-pressure cold plasmas: Ions of astrophysical interest. Plasma Phys. Control. Fusion 54, 124019. https://doi.org/10.1088/0741-3335/54/12/124019

Carrasco, E., Jiménez-Redondo, M., Tanarro, I., Herrero, V.J., 2011. Neutral and ion chemistry in low pressure dc plasmas of H_2/N_2 mixtures: Routes for the efficient production of NH_3 and NH_4^+. Phys. Chem. Chem. Phys. 13, 19561–19572. https://doi.org/10.1039/c1cp22284h

Carrasco, E., Tanarro, I., Herrero, V.J., Cernicharo, J., 2013. Proton transfer chains in cold plasmas of H_2 with small amounts of N_2. The prevalence of NH_4^+. Phys. Chem. Chem. Phys. 15, 1699–1706. https://doi.org/10.1039/c2cp43438e

Cernogora, G., Hochard, L., Touzeau, M., Matos Ferreira, C., 1981. Population of $N_2(A\ ^3\Sigma_u^+)$ metastable states in a pure nitrogen glow discharge. J. Phys. B At. Mol. Phys. 14, 2977–2987. https://doi.org/10.1088/0022-3700/14/16/025

Chatham, H., Hils, D., Robertson, R., Gallagher, A., 1984. Total and partial electron collisional ionization cross sections for CH4, C2H6, SiH4, and Si 2H6. J. Chem. Phys. 81, 1770–1777. https://doi.org/10.1063/1.447848

Cicala, G., Bruno, P., Losacco, A.M., Mattei, G., 2004. Plasma deposition of hydrogenated diamond-like carbon films from CH4-Ar mixtures. Surf. Coatings Technol. 180–181, 222–226. https://doi.org/10.1016/j.surfcoat.2003.10.044

Cravens, T.E., Robertson, I.P., Waite, J.H., Yelle, R. V., Kasprzak, W.T., Keller, C.N., Ledvina, S.A., Niemann, H.B., Luhmann, J.G., McNutt, R.L., Ip, W.H., De La Haye, V., Mueller-Wodarg, I., Wahlund, J.E., Anicich, V.G., Vuitton, V., 2006. Composition of Titan's ionosphere. Geophys. Res. Lett. 33, L07105. https://doi.org/10.1029/2005GL025575

Cui, J., Yelle, R. V., Vuitton, V., Waite, J.H., Kasprzak, W.T., Gell, D.A., Niemann, H.B., Müller-Wodarg, I.C.F., Borggren, N., Fletcher, G.G., Patrick, E.L., Raaen, E., Magee, B.A., 2009. Analysis of Titan's neutral upper atmosphere from Cassini Ion Neutral Mass Spectrometer measurements. Icarus 200, 581–615. https://doi.org/10.1016/j.icarus.2008.12.005

Cui, J., Yelle, R. V, Volk, K., 2008. Distribution and escape of molecular hydrogen in Titan's thermosphere and exosphere. J. Geophys. Res. 113, E10004. https://doi.org/10.1029/2007JE003032

de Souza, A.R., Digiacomo, M., Muzart, J.L.R., Nahorny, J., Ricard, A., 1999. Dissociation of N2 in flowing glow discharge: Influence of H2*. Eur. Phys. J. Appl. Phys. 5, 185–189.

Dobrijevic, M., Loison, J.C., Hickson, K.M., Gronoff, G., 2016. 1D-coupled photochemical model of neutrals, cations and anions in the atmosphere of Titan. Icarus 268, 313–339. https://doi.org/10.1016/j.icarus.2015.12.045

Dubois, D., Carrasco, N., Petrucciani, M., Vettier, L., Tigrine, S., Pernot, P., 2019. In situ investigation of neutrals involved in the formation of Titan tholins. Icarus 317, 182–196. https://doi.org/10.1016/j.icarus.2018.07.006

Edberg, N.J.T., Andrews, D.J., Shebanits, O., Ågren, K., Wahlund, J.E., Opgenoorth, H.J., Cravens, T.E., Girazian, Z., 2013. Solar cycle modulation of Titan's ionosphere. J. Geophys. Res. Sp. Phys. 118, 5255–5264. https://doi.org/10.1002/jgra.50463

Fletcher, J., Reid, I.D., 1980. The transport parameters of an electron swarm in nitrogen at elevated E/N. J. Phys. D. Appl. Phys. 13, 2275–2283. https://doi.org/10.1088/0022-3727/13/12/013

Fox-Lyon, N., Oehrlein, G.S., Ning, N., Graves, D.B., 2011. Hydrogenation and surface density changes in hydrocarbon films during erosion using Ar/H2 plasmas, in: Journal of Applied Physics. American Institute of Physics, p. 104314. https://doi.org/10.1063/1.3662953

Garscadden, A., Nagpal, R., 1995. Non-equilibrium electronic and vibrational kinetics in H2-N 2 and H2 discharges. Plasma Sources Sci. Technol. 4, 268–280. https://doi.org/10.1088/0963-0252/4/2/011

Gautier, T., Carrasco, N., Buch, A., Szopa, C., Sciamma-O'brien, E., Cernogora, G., 2011. Nitrile gas chemistry in

Titan atmosphere. Icarus 213, 625. https://doi.org/10.1016/j.icarus.2011.04.005ï

Godet, L., 2006. Development of pulsed plasma doping system for semiconductor processing : characterization of the plasma and its interaction with the materials. PhD thesis, Univ. Nantes, Fr.

Goebel, D.M., Bohdansky, J., Conn, R.W., Hirooka, Y., LaBombard, B., Leung, W.K., Nygren, R.E., Roth, J., Tynan, G.R., 1988. Erosion of graphite by high flux hydrogen plasma bombardment. Nucl. Fusion 28, 1041. https://doi.org/10.1088/0029-5515/28/6/007

Gordiets, B., Ferreira, C.M., Pinheiro, M.J., Ricard, A., 1998a. Self-consistent kinetic model of low-pressure N_2-H_2 flowing discharges: I. Volume processes. Plasma Sources Sci. Technol. 7, 363–378. https://doi.org/10.1088/0963-0252/7/3/015

Gordiets, B., Ferreira, C.M., Pinheiro, M.J., Ricard, A., 1998b. Self-consistent kinetic model of low-pressure N_2-H_2 flowing discharges: II. Surface processes and densities of N, H, NH_3 species. Plasma Sources Sci. Technol. 7, 379–388. https://doi.org/10.1088/0963-0252/7/3/016

Gottardi, G., Laidani, N., Bartali, R., Micheli, V., Anderle, M., 2008. Plasma enhanced chemical vapor deposition of a-C:H films in CH4-CO2 plasma: Gas composition and substrate biasing effects on the film structure and growth process. Thin Solid Films 516, 3910–3918. https://doi.org/10.1016/j.tsf.2007.07.179

Guerra, V., Loureiro, J., 1997. Electron and heavy particle kinetics in a low-pressure nitrogen glow discharge. Plasma Sources Sci. Technol. 6, 361–372. https://doi.org/10.1088/0963-0252/6/3/013

Guerra, V., Sá, P.A., Loureiro, J., 2004. Kinetic modeling of low-pressure nitrogen discharges and post-discharges. EPJ Appl. Phys. 28, 125–152. https://doi.org/10.1051/epjap:2004188

Han, D., Moon, S.Y., 2015. Rapid formation of transparent superhydrophobic film on glasses by He/CH4/C4F8 plasma deposition at atmospheric pressure. Plasma Process. Polym. 12, 172–179. https://doi.org/10.1002/ppap.201400145

Haverlag, M., Kroesen, G.M.W., Bisschops, T.H.J., de Hoog, F.J., 1991. Measurement of electron densities by a microwave cavity method in 13.56-MHz RF plasmas of Ar, CF_4, C_2F_6, and CHF_3. Plasma Chem. Plasma Process. 11, 357–370. https://doi.org/10.1007/BF01458916

Herbst, E., 2001. The chemistry of interstellar space. Chem. Soc. Rev. 30, 168–176. https://doi.org/10.1039/a909040a

Hong, J., Pancheshnyi, S., Tam, E., Lowke, J.J., Prawer, S., Murphy, A.B., 2018. Corrigendum: Kinetic modelling of NH_3 production in N_2-H_2 non-equilibrium atmospheric-pressure plasma catalysis (2017 J. Phys. D: Appl. Phys. 50 154005). J. Phys. D. Appl. Phys. https://doi.org/10.1088/1361-6463/aaa988

Hong, J., Pancheshnyi, S., Tam, E., Lowke, J.J., Prawer, S., Murphy, A.B., 2017. Kinetic modelling of NH_3 production in N_2-H_2 non-equilibrium atmospheric-pressure plasma catalysis. J. Phys. D. Appl. Phys. 50, 154005. https://doi.org/10.1088/1361-6463/aa6229

Hudis, M., 1973. Study of ion-nitriding. J. Appl. Phys. 44, 1489–1496. https://doi.org/10.1063/1.1662398

Inagaki, N., Ohkubo, J., 1986. Plasma polymerization of hexafluoropropene/methane mixtures and composite membranes for gas separations. J. Memb. Sci. 27, 63–75. https://doi.org/10.1016/S0376-7388(00)81382-4

Isola, L.M., Gómez, B.J., Guerra, V., 2010. Determination of the electron temperature and density in the negative glow of a nitrogen pulsed discharge using optical emission spectroscopy. J. Phys. D. Appl. Phys. 43, 015202. https://doi.org/10.1088/0022-3727/43/1/015202

Keane, T.C., 2017. Mechanism for the Coupled Photochemistry of Ammonia and Acetylene: Implications for Giant Planets, Comets and Interstellar Organic Synthesis. Orig. Life Evol. Biosph. 47, 223–248. https://doi.org/10.1007/s11084-017-9545-2

Kechkar, S., Babu, S.K., Swift, P., Gaman, C., Daniels, S., Turner, M., 2014. Investigation of absolute atomic fluorine density in a capacitively coupled SF6/O2/Ar and SF6/Ar discharge. Plasma Sources Sci. Technol. 23, 065029. https://doi.org/10.1088/0963-0252/23/6/065029

Klarenaar, B.L.M., Engeln, R., Van Den Bekerom, D.C.M., Van De Sanden, M.C.M., Morillo-Candas, A.S., Guaitella, O., 2017. Time evolution of vibrational temperatures in a CO_2 glow discharge measured with infrared absorption spectroscopy. Plasma Sources Sci. Technol. 26, 115008. https://doi.org/10.1088/1361-6595/aa902e

Kondo, Y., Ishikawa, K., Hayashi, T., Sekine, M., Hori, M., 2018. Electron impact ionization of perfluoro-methyl-vinyl-ether C_3F_6O. Plasma Sources Sci. Technol. 27, 015009. https://doi.org/10.1088/1361-6595/aaa22e

Kumar, S., Baldwin, M.J., Fewell, M.P., Haydon, S.C., Short, K.T., Collins, G.A., Tendys, J., 2000. The effect of hydrogen on the growth of the nitrided layer in r.f.-plasma-nitrided austenitic stainless steel AISI 316. Surf. Coatings Technol. 123, 29–35. https://doi.org/10.1016/S0257-8972(99)00393-X

Lavvas, P.P., Coustenis, A., Vardavas, I.M., 2008. Coupling photochemistry with haze formation in Titan's atmosphere, Part II: Results and validation with Cassini/Huygens data. Planet. Space Sci. 56, 67–99. https://doi.org/10.1016/j.pss.2007.05.027

Lawton, S.A., Phelps, A. V., 1978. Excitation of the b $^1\Sigma^+_g$ state of O_2 by low energy electrons. J. Chem. Phys. 69, 1055. https://doi.org/10.1063/1.436700

Leyland, A., Fancey, K.S., James, A.S., Matthews, A., 1990. Enhanced plasma nitriding at low pressures: A comparative study of d.c. and r.f. techniques. Surf. Coatings Technol. 41, 295–304. https://doi.org/10.1016/0257-8972(90)90140-8

Lieberman, M.A., Lichtenberg, A.J., 2005. Principles of Plasma Discharges and Materials Processing: Second Edition, Principles of Plasma Discharges and Materials Processing: Second Edition. https://doi.org/10.1002/0471724254

Livesey, R.G., 2001. Method for calculation of gas flow in the whole pressure regime through ducts of any length. J. Vac. Sci. Technol. A Vacuum, Surfaces, Film. 19, 1674–1678. https://doi.org/10.1116/1.1345895

Lopaev, D. V, Volynets, A. V, Zyryanov, S.M., Zotovich, A.I., Rakhimov, A.T., 2017. Actinometry of O, N and F atoms. J. Phys. D. Appl. Phys. 50, 075202. https://doi.org/10.1088/1361-6463/50/7/075202

López-Moreno, J.J., Molina-Cuberos, G.J., Hamelin, M., Grard, R., Simões, F., Godard, R., Schwingenschuh, K., Béghin, C., Berthelier, J.J., Brown, V.J.G., Falkner, P., Ferri, F., Fulchignoni, M., Jernej, I., Jerónimo, J.M., Rodrigo, R., Trautner, R., 2008. Structure of Titan's low altitude ionized layer from the Relaxation Probe onboard HUYGENS. Geophys. Res. Lett. 35, L22104. https://doi.org/10.1029/2008GL035338

Loureiro, J., Ricard, A., 1993. Electron and vibrational kinetics in an N_2-H_2 glow discharge with application to surface processes. J. Phys. D. Appl. Phys. 26, 163–176. https://doi.org/10.1088/0022-3727/26/2/001

Magee, B.A., Waite, J.H., Mandt, K.E., Westlake, J., Bell, J., Gell, D.A., 2009. INMS-derived composition of Titan's upper atmosphere: Analysis methods and model comparison. Planet. Space Sci. 57, 1895–1916. https://doi.org/10.1016/j.pss.2009.06.016

Majeed, T., Waite, J.H., Bougher, S.W., Yelle, R. V., Gladstone, G.R., McConnell, z. J.C., Bhardwaj, A., 2004. The ionospheres-thermospheres of the giant planets. Adv. Sp. Res. 33, 197–211. https://doi.org/10.1016/j.asr.2003.05.009

Marques, L., Jolly, J., Alves, L.L., 2007. Capacitively coupled radio-frequency hydrogen discharges: The role of kinetics. J. Appl. Phys. 102, 063305. https://doi.org/10.1063/1.2779268

McCall, B.J., Oka, T., 2000. H3+, An ion with many talents. Science 287, 1941–1942. https://doi.org/10.1126/science.287.5460.1941

Méndez, I., Gordillo-Vázquez, F.J., Herrero, V.J., Tanarro, I., 2006. Atom and Ion Chemistry in Low Pressure Hydrogen DC Plasmas. J. Phys. Chem. A 110, 6060–6066. https://doi.org/10.1021/JP057182+

Migliorini, A., Dinelli, B.M., Moriconi, M.L., Altieri, F., Adriani, A., Mura, A., Connerney, J.E.P., Atreya, S.K., Piccioni, G., Tosi, F., Sindoni, G., Grassi, D., Bolton, S.J., Levin, S.M., Gérard, J.C., Noschese, R., Cicchetti, A., Sordini, R., Olivieri, A., Plainaki, C., 2019. H 3+ characteristics in the Jupiter atmosphere as observed at limb with Juno/JIRAM. Icarus 329, 132–139. https://doi.org/10.1016/j.icarus.2019.04.003

Milligan, D.B., Wilson, P.F., Freeman, C.G., Meot-Ner (Mautner), M., McEwan, M.J., 2002. Dissociative proton transfer reactions of H3+, N2H+, and H3O+ with acyclic, cyclic, and aromatic hydrocarbons and nitrogen compounds, and astrochemical implications. J. Phys. Chem. A 106, 9745–9755. https://doi.org/10.1021/jp014659i

Nagai, H., Takashima, S., Hiramatsu, M., Hori, M., Goto, T., 2002. Behavior of atomic radicals and their effects on organic low dielectric constant film etching in high density N2/H2and N2/NH3plasmas. J. Appl. Phys. 91, 2615–2621. https://doi.org/10.1063/1.1435825

O'Hanlon, J., 2003. A User's Guide to Vacuum Technology. Wiley, New Jersey.

Oberkofler, M., Alegre, D., Aumayr, F., Brezinsek, S., Dittmar, T., Dobes, K., Douai, D., Drenik, A., Köppen, M., Kruezi, U., Linsmeier, C., Lungu, C.P.P., Meisl, G., Mozetic, M., Porosnicu, C., Rohde, V., Romanelli, S.G.G., 2015. Plasma–wall interactions with nitrogen seeding in all-metal fusion devices: Formation of nitrides and ammonia. Fusion Eng. Des. 98–99, 1371–1374.

Oka, T., 2006. Interstellar H3+. Proc. Natl. Acad. Sci. U. S. A. 103, 12235–12242. https://doi.org/10.1073/pnas.0601242103

Petrie, S., Bohme, D.K., 2007. Ions in space. Mass Spectrom. Rev. https://doi.org/10.1002/mas.20114

Piejak, R.B., Godyak, V.A., Garner, R., Alexandrovich, B.M., Sternberg, N., 2004. The hairpin resonator: A plasma density measuring technique revisited. J. Appl. Phys. 95, 3785–3791. https://doi.org/10.1063/1.1652247

Pintassilgo, C.D., Guerra, V., 2017. Modelling of the temporal evolution of the gas temperature in N2 discharges. Plasma Sources Sci. Technol. 26. https://doi.org/10.1088/1361-6595/aa5db2

Pulpytel, J., Arefi-Khonsari, F., Morscheidt, W., 2005. Threshold ionization mass spectrometry study of singlet molecular oxygen in the deposition of SnO_2 by PACVD. J. Phys. D. Appl. Phys. 38, 1390–1395. https://doi.org/10.1088/0022-3727/38/9/010

Raizer, Y.P., 1991. Gas Discharge Physics. Springer-Verlag.

Rapp, D., Englander-Golden, P., 1965. Total cross sections for Ionization and attachment in gases by electron impact. I. Positive ionization. J. Chem. Phys. 43, 1464–1479. https://doi.org/10.1063/1.1696957

Roth, J., Garcia-Rosales, C., 1996. Analytic description of the chemical erosion of graphite by hydrogen ions. Nucl. Fusion 36, 1647. https://doi.org/10.1088/0029-5515/36/12/I05

Salabas, A., Marques, L., Jolly, J., Gousset, G., Alves, L.L., 2004. Systematic characterization of low-pressure capacitively coupled hydrogen discharges. J. Appl. Phys. 95, 4605–4620. https://doi.org/10.1063/1.1690488

Sands, B.L., Siefert, N.S., Ganguly, B.N., 2007. Design and measurement considerations of hairpin resonator probes for determining electron number density in collisional plasmas. Plasma Sources Sci. Technol. 16, 716. https://doi.org/10.1088/0963-0252/16/4/005

Sekine, K., Saito, Y., Hirayama, M., Ohmi, T., 1999. Silicon nitride film growth for advanced gate dielectric at low temperature employing high-density and low-energy ion bombardment. J. Vac. Sci. Technol. A Vacuum, Surfaces, Film. 17, 3129–3133. https://doi.org/10.1116/1.582016

Shah, J., Wang, W., Bogaerts, A., Carreon, M.L., 2018. Ammonia Synthesis by Radio Frequency Plasma Catalysis: Revealing the Underlying Mechanisms. ACS Appl. Energy Mater. 1, 4824–4839. https://doi.org/10.1021/acsaem.8b00898

Shahin, M.M., 1966. Mass-spectrometric studies of corona discharges in air at atmospheric pressures. J. Chem. Phys. 45, 2600–2605. https://doi.org/10.1063/1.1727980

Shirley, J.A., Hall, R.J., 1977. Vibrational excitation in H2 and D2 electric discharges. J. Chem. Phys. 67, 2419–2421. https://doi.org/10.1063/1.435213

Singh, H., Coburn, J.W., Graves, D.B., 1999. Mass spectrometric detection of reactive neutral species: Beam-to-background ratio. J. Vac. Sci. Technol. A Vacuum, Surfaces, Film. 17, 2447–2455.

https://doi.org/10.1116/1.581981

Sinha, H.S.S., Oyama, K.I., Watanabe, S., 2013. Detection of long-living neutral hydrated clusters in laboratory simulation of ionospheric D region plasma. J. Geophys. Res. Sp. Phys. 118, 583–589. https://doi.org/10.1029/2012JA017945

Sinha, H.S.S., Tokuyama, Y., Oyama, K.I., Watanabe, S., 2004. Production and detection of hydrated cluster ions in laboratory plasma mimicking ionospheric D region. Geophys. Res. Lett. 31, n/a-n/a. https://doi.org/10.1029/2004GL019985

Sode, M., Jacob, W., Schwarz-Selinger, T., Kersten, H., 2015. Measurement and modeling of neutral, radical, and ion densities in H_2-N_2-Ar plasmas. J. Appl. Phys. 117, 083303. https://doi.org/10.1063/1.4913623

Sode, M., Schwarz-Selinger, T., Jacob, W., 2013. Quantitative determination of mass-resolved ion densities in H_2-Ar inductively coupled radio frequency plasmas. J. Appl. Phys. 113, 093304. https://doi.org/10.1063/1.4794165

Szopa, C., Cernogora, G., Boufendi, L., Correia, J.J., Coll, P., 2006. PAMPRE: A dusty plasma experiment for Titan's tholins production and study. Planet. Space Sci. 54, 394–404. https://doi.org/10.1016/J.PSS.2005.12.012

Tabarés, F.L., Tafalla, D., Tanarro, I., Herrero, V.J., Islyaikin, A., Maffiotte, C., Tabar s, F.L., Tafalla, D., Tanarro, I., Herrero, V.J., Islyaikin, A., Maffiotte, C., 2002. Suppression of hydrogenated carbon film deposition by scavenger techniques and their application to the tritium inventory control of fusion devices. Plasma Phys. Control. Fusion 44, L37–L42. https://doi.org/10.1088/0741-3335/44/8/101

Tachibana, K., Phelps, A. V., 1987. Excitation of the $1s_5$ and $1s_4$ levels of neon by low-energy electrons. Phys. Rev. A 36, 999–1007. https://doi.org/10.1103/PhysRevA.36.999

Tanarro, I., Herrero, V.J., Islyaikin, A.M., Méndez, I., Tabare, F.L., Tafalla, D., 2007. Ion chemistry in cold plasmas of H_2 with CH_4 and N_2. J. Phys. Chem. A 111, 9003–9012. https://doi.org/10.1021/jp073569w

Tatarova, E., Dias, F.M., Gordiets, B., Ferreira, C.M., 2005. Molecular dissociation in N_2-H_2 microwave discharges. Plasma Sources Sci. Technol. https://doi.org/10.1088/0963-0252/14/1/003

Thomaz, J.C., Amorim, J., Souza, C.F., 1999. Validity of actinometry to measure N and H atom concentration in N2-H2 direct current glow discharges. J. Phys. D. Appl. Phys. 32, 3208–3214. https://doi.org/10.1088/0022-3727/32/24/317

Touvelle, M., Licea, J.L.M., Venugopalan, M., 1987. Plasma chemical synthesis. II. Effect of wall surface on the synthesis of ammonia. Plasma Chem. Plasma Process. 7, 101–108. https://doi.org/10.1007/BF01016001

Vuitton, V., Yelle, R. V., Klippenstein, S.J., Hörst, S.M., Lavvas, P., 2019. Simulating the density of organic species in the atmosphere of Titan with a coupled ion-neutral photochemical model. Icarus 324, 120–197. https://doi.org/10.1016/j.icarus.2018.06.013

Walton, S.G., Fernsler, R.F., Leonhardt, D., 2007. Measurement of ion energy distributions using a combined energy and mass analyzer. Rev. Sci. Instrum. 78, 083503. https://doi.org/10.1063/1.2769352

Wang, H.-X., Geng, J.-Y., Chen, X., Pan, W.X., Murphy, A.B., 2010. Modeling Study on the Flow, Heat Transfer and Energy Conversion Characteristics of Low-Power Arc-Heated Hydrogen/Nitrogen Thrusters. Plasma Chem. Plasma Process. 30, 707–731. https://doi.org/10.1007/s11090-010-9257-0

Watanabe, H., Katoh, K., Imagi, S.-I., 1986. Properties of silicon nitride films prepared by plasma-enhanced chemical vapour deposition of SiH_4-N_2 mixtures. Thin Solid Films 136, 77–83. https://doi.org/10.1016/0040-6090(86)90110-0

Wattieaux, G., Carrasco, N., Henault, M., Boufendi, L., Cernogora, G., 2015. Transient phenomena during dust formation in a N_2-CH_4 capacitively coupled plasma. Plasma Sources Sci. Technol. 24, 015028. https://doi.org/10.1088/0963-0252/24/1/015028

Womack, M., Ziurys, L.M., Wyckoff, S., 1992. A survey of N_2H^+ in dense clouds - Implications for interstellar nitrogen and ion-molecule chemistry. Astrophys. J. 387, 417. https://doi.org/10.1086/171094

Wróbel, A.M., Błaszczyk, I., Walkiewicz-Pietrzykowska, A., Tracz, A., Klemberg-Sapieha, J.E., Aoki, T., Hatanaka, Y., 2003. Remote hydrogen-nitrogen plasma chemical vapor deposition from a tetramethyldisilazane source. Part 1. Mechanism of the process, structure and surface morphology of deposited amorphous hydrogenated silicon carbonitride films. J. Mater. Chem. 13, 731–737. https://doi.org/10.1039/b211415c

Yamabe, C., Buckman, S.J., Phelps, A. V., 1983. Measurement of free-free emission from low-energy-electron collisions with Ar. Phys. Rev. A 27, 1345–1352. https://doi.org/10.1103/PhysRevA.27.1345

Yelle, R. V., Vuitton, V., Lavvas, P., Klippenstein, S.J., Smith, M.A., Hörst, S.M., Cui, J., 2010. Formation of NH_3 and CH_2NH in Titan's upper atmosphere. Faraday Discuss. 147, 31–49. https://doi.org/10.1039/c004787m

EROSION OF ORGANIC AEROSOLS

IN A N_2-H_2 PLASMA ENVIRONMENT

Contents

1- Introduction: experimental simulation of the interaction between aerosols and a N$_2$-H$_2$ plasma

Titan's organic aerosols stay several days or more in the ionospheric plasma: do they evolve in this highly reactive environment? And the other way around, is the plasma disturbed by the presence of the aerosols? In this chapter, we simulate this interaction between aerosols and plasma in the laboratory, with the THETIS experiment, built for this specific purpose.
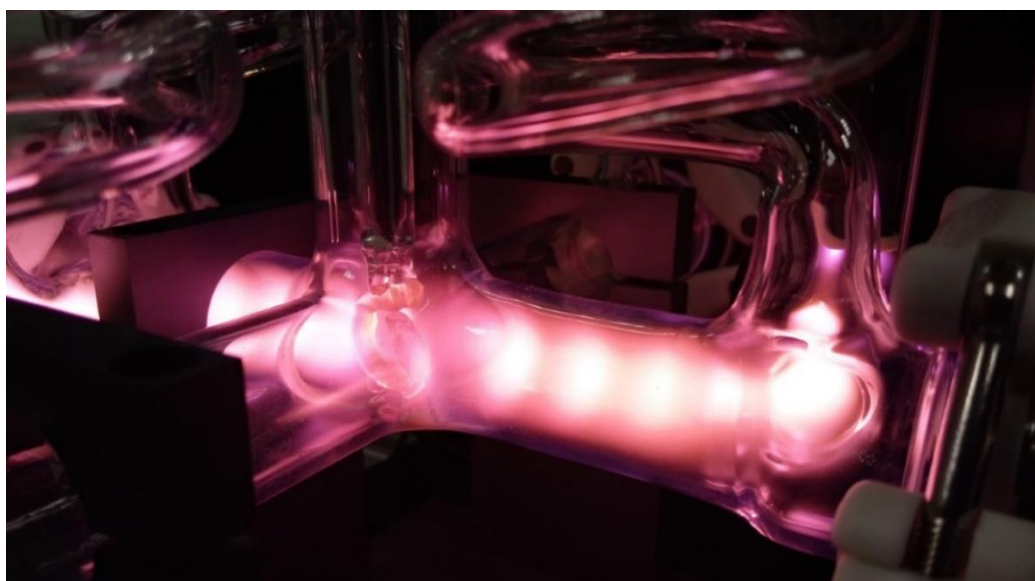
1.1- State of the art: evolution of organic matter in contact with a plasma

1.1.a. Aged organic matter in astrophysics

There are several examples of organic matter in astrophysics being transformed by exposure to various irradiations. Organic ices present in protoplanetary discs are exposed to extreme conditions (radiations, temperature, energetic particles…) and evolve into complex organic matter. This matter can still be present in the interplanetary or interstellar medium, as individual grains, asteroids or comets. Depending on its localization and especially its distance to a star, organic matter in space continues to evolve. The analysis of evolved organic matter found in interstellar grains or comets gives information on the irradiation and temperature conditions they have undergone (Fray et al., 2016; Herd et al., 2011). This gives clues on the conditions in our Solar System through billions of years.

Laboratory studies have already been performed to mimic a possible evolution of organic matter in protoplanetary discs, in the interstellar medium and on comets. Depending on the energy deposited, the exposure of an organic material to ion, electron and photon (X rays and UV) irradiation lead to changes in morphology and/or in chemical composition (Öberg, 2016). For example, laboratory experiments observed that the UV irradiation of organic ices leads to the formation of solid organic residues that remains after heating to ambient temperature (Danger et al., 2013; de Marcellus et al., 2017; Henderson and Gudipati, 2015; Kuga et al., 2015; Nuevo et al., 2011). To go further, Moroz et al. (2004) simulated an energetic ion irradiation on organics and observed a change in the optical properties of the sample. The effect of energetic electrons has been instigated by Laurent et al. (2014). It induces an amorphization of the sample through chain scissions and an increase of the CH_2/CH_3 ratio.

The combined **effects of ion, electron and photon irradiations** are processes similar to what would occur in a plasma and could happen in Titan's ionosphere. A first work has been done to study the evolution of laboratory analogues (tholins) **exposed to VUV radiations** (Carrasco et al., 2018). Under exposure, the nitrile infrared bands of tholins shift and their intensities are modified. The impact of **atomic hydrogen** on tholins has also been studied in Sekine et al. (2008). They observed a hydrogenation of the tholins (these points are discussed further in

Sections III.2.3.b-c). **Therefore, the next logical step, which is investigated here, is the complementary effect of electrons, ions and other plasma species on tholins.**

1.1.b. Organic matter: often eroded or transformed by exposure to a plasma

Organic matter is highly sensitive to plasma. There is a lot of examples in the industry where organics are eroded and/or transformed by plasma exposure (Bogaerts et al., 2002). Cold plasma discharges are used to change the properties of surfaces: coating for protection or strength, surface sterilization or modification of properties such as the wettability, printability, bio-compatibility, the thermal and electrical conductivities... They can also induce etching on specific surfaces, especially used in the microelectronics and semiconductor fields. These properties of the plasma to induce surface processing make them essential in many sectors: biomedical, energy research, environmental…

Plasmas containing carbon generally lead to carbon chain growth, forming films and/or particles**. On the opposite, N_2-H_2 plasmas are often used to remove organic matter**. On Titan, we expect both processes being in competition. As discussed previously in **Section II.1.1.a**, we focus here on the erosion processes, induced by N_2-H_2 plasma species.

A first example is the cleaning of organic films deposited on walls of fusion devices (Voitsenya et al., 2006). They observe that a higher etching rate is obtained a heavy element is added to H_2, N_2 being more efficient than Ne, Kr or Xe because it has two atoms. Indeed, during a collision with the C-C bonds of the organic films, the **ion N_2H^+** transfers more energy and efficiently breaks the bonds.

Plasmas in N_2 and/or H_2 and/or Ar are also widely used for organic film etching. Studies are especially focused on diverse polymers, and on low-dielectric constant films used in integrated circuits. Both physical and chemical modifications are observed (Kurihara et al., 2005).

Depending on the plasma conditions, one should expect mainly three processes: the sputtering of energetic ions, the high chemical reactivity of short life excited species (radicals, ions, vibrationally and electronically excited molecules) and the emission of VUV photons by the hydrogen plasma (Moon et al., 2010; Uchida et al., 2008). Nagai et al. (2002) studied the importance of **H radicals** for the etching. They observed that on the opposite, N radicals tend to form a protection layer against the etching. N radicals and N_2 interact with the organic film to form CN. The addition of N_2 in H_2 plasmas forms erosive N_2H^+ ions, but also protective N radicals. They found a maximum etching rate for 30% N_2 in H_2. Jacob et al. (2006) suggest that atomic hydrogen and ions could have a combined effect. Moon et al. (2010) also include the ammonium ions NH_3^+ and NH_4^+ in the etching process. Wertheimer et al. (1999) performed different experiments to irradiate various polymers to VUV photons produced by plasma. They observed some evolutions, but far less efficient than the direct effect of ions and radicals in a plasma.

The etching of the organic films leads to the formation of new gaseous species. Hong et al. (2002), Hong and Turban (1999), Ishikawa et al. (2006) and Kurihara et al. (2006) observed the decomposition of the films exposed to a N_2 or N_2-H_2 plasma into **HCN, CN and C_2N_2**. Van Laer

et al. (2013) modelled the processes at work in the erosion of a (C:H) organic film by a N_2-H_2 plasma. They predict the formation of many neutral species (from highest to lowest density: N, H, N*, NH, NH_3, HCN, CH_4, NH_2, CH_3, CN, CH, C, CH_2) and ions (N_2H^+, N_2^+, H_2^+, NH^+, N^+, H^+, NH_2^+, NH_3^+, H_3^+, NH_4^+, CH_3^+, CH_4^+, HCN^+, CH_2^+, CH^+, C^+).

The organic films are not just physically eroded. The chemical composition and structure at their surface change in the presence of a hydrogen plasma. Fox-Lyon et al. (2011) observed the hydrogenation and the saturation of H in a film exposed to a Ar-H_2 plasma. Kral et al. (2007) noticed modifications in the chemical bonds of a polymer exposed to a N_2-H_2 plasma.

In conclusion, N_2 and/or H_2 plasmas can strongly erode organic films and polymers both physically and chemically. Studies have been performed in very different gas mixtures, pressure and temperature conditions, and on various organic substrates. What can we expect for the organic aerosols in Titan's conditions?

1.1.c. Objective of Chapter III: tholins in a N_2-H_2 plasma

Titan's organic aerosols stay several days in the ionospheric layer ionized by VUV radiations and magnetospheric electrons from 1200 to 900 km (Lavvas et al., 2013). **The effect of plasma exposure on such time scale on Titan is still unknown**. **The objective of this work is to experimentally study the possible erosion of the aerosols by exposure to the species of a N_2-H_2 plasma** (see discussion in **Section II.1.1**). Carrasco et al. (2016) previously observed that aerosol particles and films formed simultaneously in the plasma reactor PAMPRE have different chemical signatures. Especially, films contain less hydrogen and nitrogen than grains. The difference could be explained partly by the difference of residence time of the two samples in the plasma: aerosol grains stay only 1-2 minutes, compared to films that are exposed during several hours. Other processes can enhance this difference: the catalytic effect of the surface on which films are deposited, the difference in the sheath properties between small grains and large surfaces, and the difference of composition in the plasma which is non-homogeneous between the center of the discharge and the sides. In any case, this strongly encourages the study of the effect of the plasma on tholins.

This chapter presents the results of a new experiment that I developed at LATMOS during my PhD: THETIS, for Tholin Evolution in Titan's Ionosphere Simulation. Section III.1.2 presents the setup, which enables to expose tholins to a N_2-H_2 plasma and perform *in situ* diagnostics. **Section III.2** shows the modifications induced on the tholins, and **Section III.3** discusses the evolution of the gas phase.

SECTION III.1.2	SECTION III.2	SECTION III.3
Development of THETIS	Evolution of the tholins	Evolution of the gas phase
	1- Protocol 2- Results 3- Discussions 4- Oxidation in air?	1- Neutrals 2- Ions 3- Processes
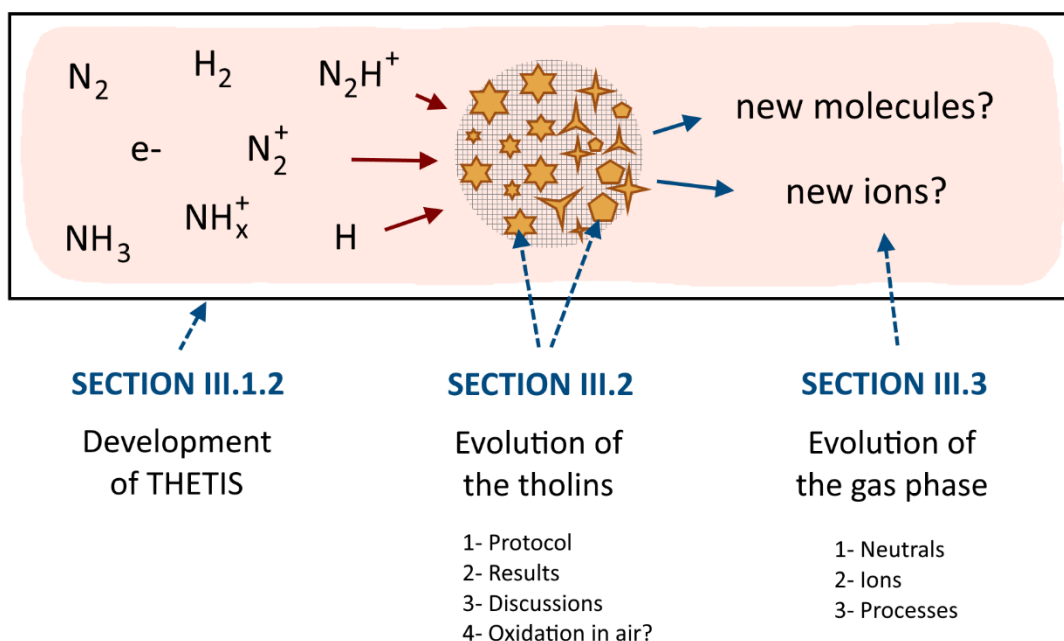
1.2- Development of the THETIS experiment

This chapter is focused on the development of a new experimental setup for this PhD work, to analyze the interaction between aerosols and plasma in the ionosphere of Titan: THETIS – for Tholin Evolution in Titan's Ionosphere Simulation. The objective is to expose analogues of Titan's aerosols to a plasma representative of the ionosphere, and analyze the evolution of both the aerosols and the gas phase. On the basis of the strategy exposed in Section II.1.1.a., this setup is dedicated to the study of the exposure to N$_2$ and N$_2$-H$_2$ plasmas.

1.2.a. Sample synthesis with the PAMPRE reactor

The first step of this experiment is to produce analogues of Titan aerosols. The PAMPRE experiment located in LATMOS is well suited to synthesize such samples. As this work intends to test the reactivity of tholins exposed to plasma conditions without any further constraints, we used standard working conditions in PAMPRE to form the analogues (Sciamma-O'Brien et al., 2010). The production of tholins with the PAMPRE experiment is detailed in Section I.4.2.a.

After the production, tholins are temporarily exposed to **ambient air** during their collection and the making of pellets. The fabrication of pellets is described in Section III.2.1.b, two techniques are investigated: the production of pressed pellets of tholins mixed with KBr, and the simple spreading of tholins on thin metallic grids. When exposed to air, **water adsorption and oxidation** appear on the first nanometers of the grains, as measured in Carrasco et al. (2016). The effect of water adsorption and oxidation on tholins is the subject of a dedicated study, presented in Section III.2.4 and Paper 4. Before each experiment, samples are **exposed to vacuum and heated at 80-100°C to desorb water** (see Section III.2.1.b).

1.2.b. Exposure in a DC plasma reactor

Once analogues of Titan's aerosols are produced, we aim at exposing them to a laboratory plasma, simulating the interaction between aerosols and plasma in Titan's ionosphere. We exposed the samples in the positive column of a **DC glow discharge**. It is a kind of discharge often used for the analysis of plasma-surface interactions (Azzolina-Jury and Thibault-Starzyk, 2017). The main reason is its high **homogeneity** which enables to attribute sample modifications to precise characteristics of the plasma. We try to avoid conditions with apparent striations as shown in **Figure III.1-2**. The plasma reactor is presented in **Section II.3.1.a**. The sample is deposited on a movable glass support. The reference study used a current of 20 mA, which gave an electron density in the tube of about 3.10^9 cm^{-3} and a gas temperature that did not exceed 340 K (see **Section II.3.1.b**). As shown in **Section II.3**, these conditions are very similar to the ones in PAMPRE.

In order to approach ionospheric environmental conditions in the laboratory, a great care is given to compensate effects to **be as representative to Titan as possible** (see **Table III.1-1**). Especially, in the plasma discharge the pressure cannot be as low as on Titan's ionosphere (10^{-8} to 10^{-6} mbar). However, if the electron density is also increased in the experiment, the ionization degree can be the same as on Titan. Nevertheless, as the electron density is 10^7 times higher in the experiment, erosion processes should be ~10^7 times faster (days become seconds). Therefore, the exposure time is reduced in the laboratory compared to Titan's case. Finally, Titan ionospheric aerosols are smaller than tholins formed in PAMPRE. As the erosion of bigger grains takes more time, the exposure time should be adapted to compensate this difference. **We therefore expose grains during minutes to hours in the laboratory**.

	on Titan	in the experiment
pressure (mbar)	10^{-8} to 10^{-6}	$0.5 - 4$
electron density n_e (cm^{-3})	[700 ; 3000] varying with the altitude (Ågren et al., 2009)	$10^9 - 10^{10}$
ionization degree $\alpha = \dfrac{n_e}{n_{tot}}$	[10^{-8} ; 10^{-6}] varying with the altitude	$10^{-8} - 4\times10^{-7}$
grain size (nm)	1 to a few 10s (Lavvas et al., 2013)	a few 100s (Hadamcik et al., 2009)
exposure time	a few days (Lavvas et al., 2013)	a few minutes to hours
hydrogen amount	~0.5% H_2 and 1.4% CH_4	0-5% H_2

Table III.1-1: Comparison of physical variables fundamental to the study of aerosol evolution by plasma in the ionosphere of Titan and in the experiment described here.

1.2.c. Specificities of the THETIS setup

The geometry of the THETIS reactor is not conventional. It has been specifically designed for the experiment. **The reactor is formed with two perpendicular Pyrex tubes**, with inner diameters of 2 cm and openings at the end of each tube. One tube has hollow cylindrical electrodes positioned perpendicularly at each extremity and is dedicated to the plasma discharge. The second axis is used to couple the instruments. Pictures of the THETIS reactor are illustrated in **Figures III.1-1-2-3-4**. The descriptions of the gas and electrical inputs are given in **Section II.3.1.a**.

Windows transparent in IR (KBr, CaF_2 or BaF_2) can be positioned at the extremities of a tube to perform IR transmission spectroscopy. A **mass spectrometer** can be coupled either at an extremity of the plasma or of the second axis to make measurements at different distances from the plasma. In particular, ion measurements require the MS to be on the plasma axis. When unused, openings at the extremities of the tubes are closed. At each extremity a thinner Pyrex tube enables the **gas circulation**. These tubes are long and curled to prevent the discharge to arc with the metallic junctions on the other extremity of the glass tubes. To preserve the IR transparent windows from an eventual organic deposit, the gas influx comes from the small tubes near the windows, and leave the reactor at the ends of the other axis.

Finally, a last vertical entrance is positioned at the center of the reactor for the sample. This entrance is coupled to a long glass tube closed at its other extremity that contains a thin long glass rod which has a strong magnet at one extremity, and a sample holder at the other end. This tool enables to move the sample in and out of the plasma reactor under vacuum. It serves for background measurements, and enables the stabilization and the analysis of the plasma just before the insertion of the sample. In addition, it is easier to ignite the plasma without the sample in the middle of the reactor.
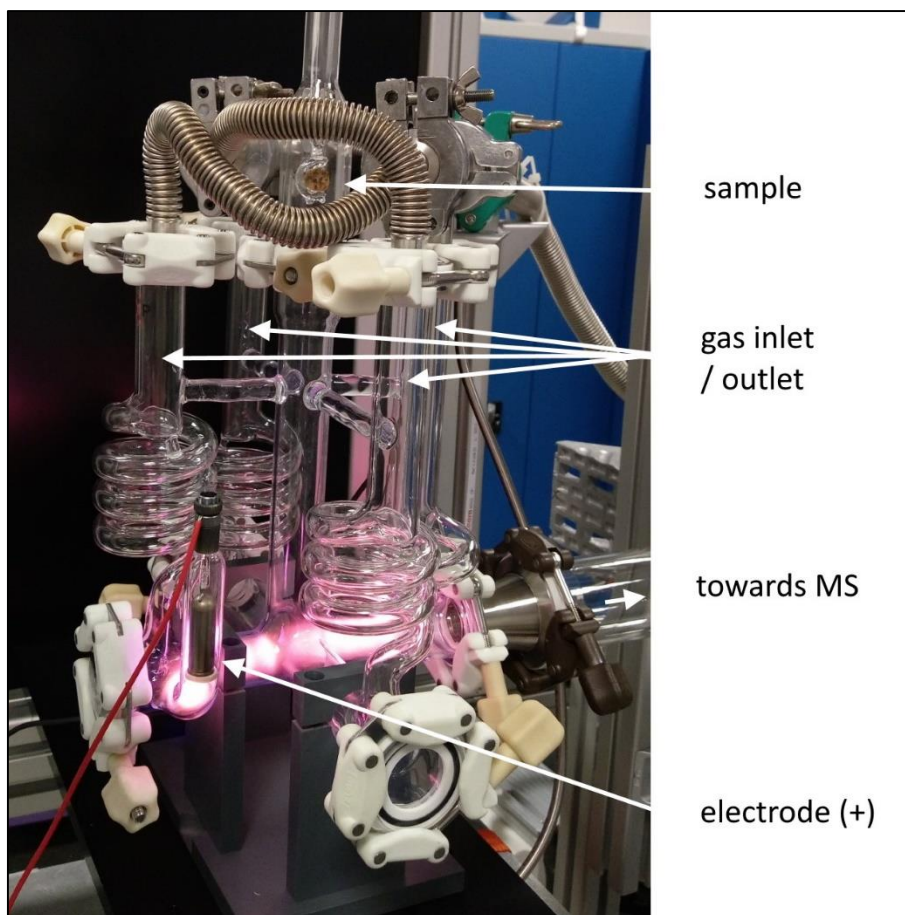
Figure III.1-1: Picture of the THETIS reactor. Setup for an ion analysis by mass spectrometry.
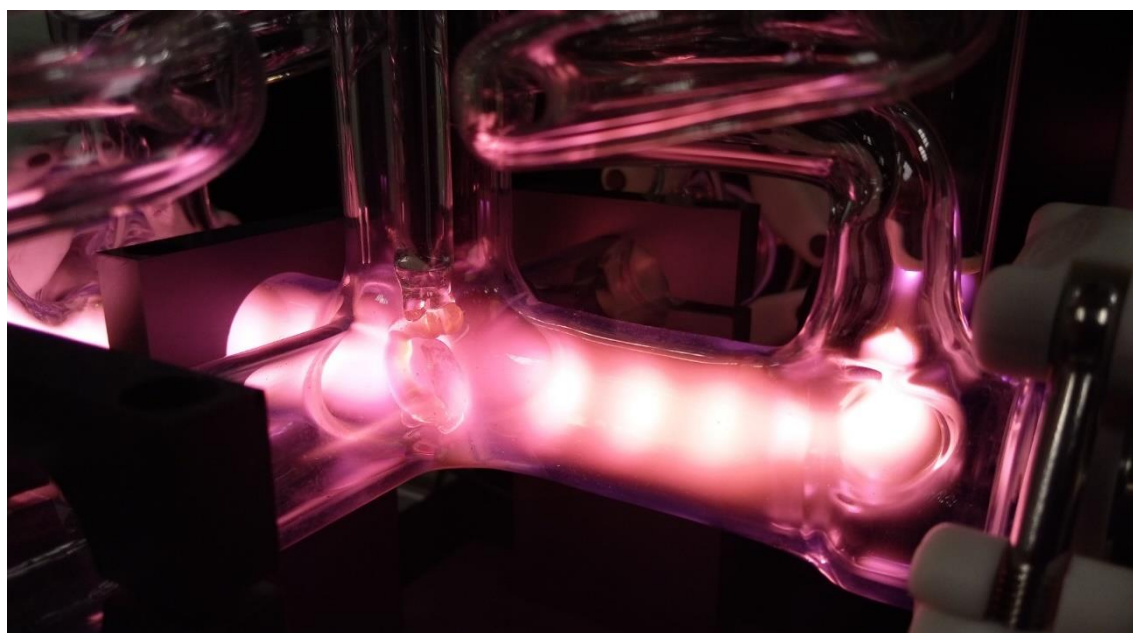
Figure III.1-2: Picture of the THETIS reactor. Zoom on the sample exposed at the center of the discharge.
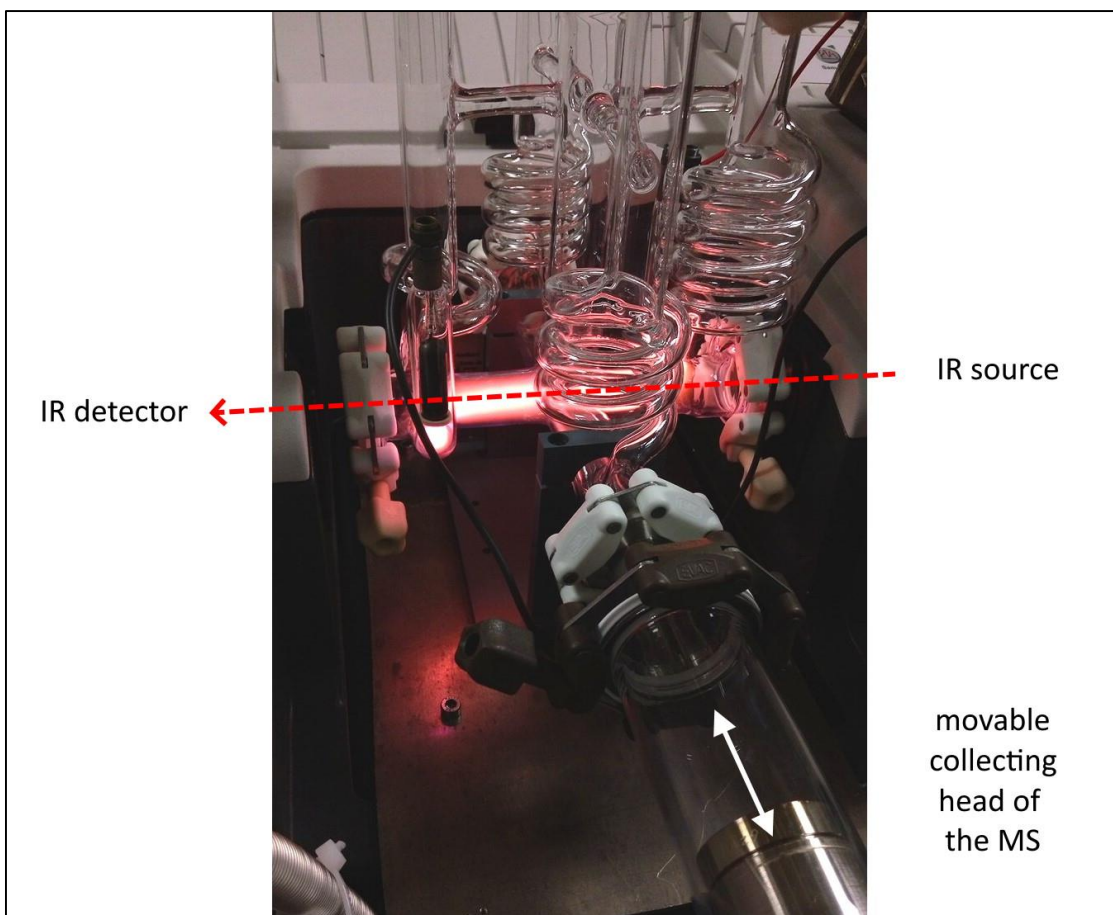
Figure III.1-3: Picture of the THETIS reactor. Setup for a neutral analysis by mass spectrometry simultaneous with IR transmission spectroscopy through the sample.
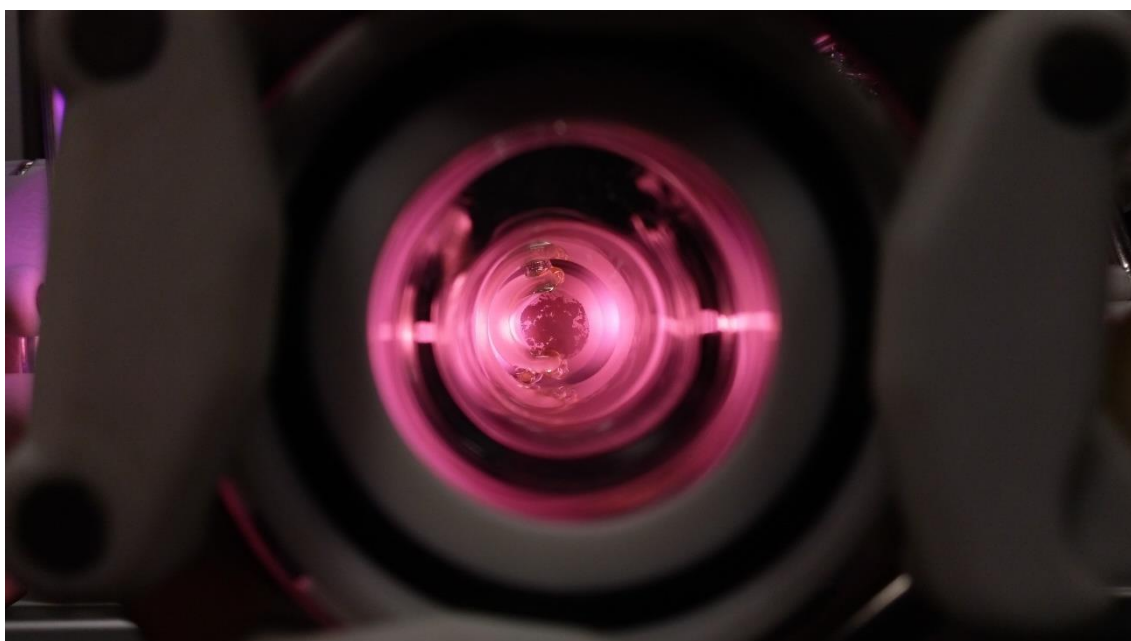
Figure III.1-4: Picture of the THETIS reactor. Zoom on the sample exposed at the center of the discharge. Axis for IR transmission spectroscopy.

2- Morphological and chemical evolution of the aerosols

This work investigates for the first time the effect of plasma exposure on Titan aerosols analogues, thanks to the THETIS experimental setup. Both morphology and chemical properties are analyzed by the mean of electron microscopy and *in situ* infrared spectroscopy.

The presented results are published in Icarus (**Paper 3**: *Interaction dust – plasma in Titan's ionosphere: an experimental simulation of aerosols erosion*). An additional study focuses on the oxidation of tholins exposed to ambient air and is the subject of **Paper 4** (*Dark-ageing of aerosols in the atmosphere of the early Earth*).

2.1- Experimental protocol

2.1.a. Pellet analysis with SEM and IR spectroscopy

This first work focuses on the evolution of the solid phase during its exposure to the plasma, in a reference case at a pressure of 4 mbar, with 1% H_2 in N_2 and at a current of 20 mA. The morphology of the grains is analyzed by Scanning Electron Microscopy (SEM) and their chemical structure by IR transmission spectroscopy (see **Figure III.2-1**).

SURFACE EVOLUTION BY SEM

The surfaces of different samples were compared before and after plasma exposure by means of Scanning Electron Microscopy (SEM). The instruments used were an environment SEM Quanta 200 from FEI (with a LFD detector, a high voltage of 12.5kV and at 0.5 mbar) and a Field Emission Gun SEM LEO1530 (with a high voltage of 2kV), both at Centrale-Supélec (Gif sur Yvette, France). Scanning electron microscopy gives information on the topography of sample surfaces. An EDS (Energy Dispersive X-ray Spectroscopy) probe coupled to the environment SEM also determined the elementary composition at different locations on the surface.

ABSORPTION BANDS MODIFICATIONS BY IR SPECTROSCOPY

Infrared transmission spectroscopy was used to get information on the chemical evolution of the pellets, with a similar technique as in Jia and Rousseau (2016) and in Mohammad Gholipour et al. (2017). The reactor was put inside the sample compartment of a Nicolet 6700 FTIR from Thermo so that the evolution of the transmitted light could be monitored before, during and after the exposure. The spectra were acquired by a DTGS detector between 900 and 4000 cm^{-1}, this range being limited by the KBr and CaF_2 windows used respectively on the

FTIR and the reactor. We chose a spectral resolution of 1 cm^{-1}, a Michelson speed of 0.63 cm/s and averaged each spectrum from 5 scans. With these parameters, spectra were acquired in ~30s. We aimed such a short acquisition time to have also a short time step resolution during the evolution of the sample. The width of the IR beam at the focal point is a few millimeters.

2.1.b. Production of two different kinds of pellets

Tholins formed in PAMPRE are grains of few hundred nanometers, likely to be dragged by the gas flow and/or the electrostatic force when exposed to a DC plasma. Here we compare two different techniques to keep them in the plasma during the exposure (see **Table III.2-1**). A major constraint is that the final sample should not be opaque in IR wavelengths.

The first technique is the most common (Abdu et al., 2018). We made **pressed pellets with tholins and a KBr matrix**. A pressure of 5 tons was applied to form pellets of 0.13 g, 1.3 cm in diameter and about 0.5 mm in thickness. A mass mixing ratio of 1.5% tholins - 98.5% KBr thin grains has been found optimal for both mechanical solidity and IR transmission. KBr is totally transparent in IR wavelengths. However, the KBr grains of the pellet are suspected to protect tholins from the plasma species. Besides, KBr is known to be strongly hydrophilic. Samples have to be heated under vacuum before the beginning of the experiments to outgas adsorbed water.

To be certain that KBr grains do not affect our results, we compared them to those obtained with another technique. 1 mg of tholin grains are **spread on a thin stainless steel grid** of 1.3 cm in diameter. Threads are 25 μm-large and meshes are of 38 μm. This leads to a transmission of 20% in IR wavelengths [cf **Supplement SIII.2-1**].

To remove adsorbed water, before each experiment (for both KBr and grid pellets) samples are put inside the glass reactor under secondary pumping for a few hours, reaching a pressure of ~2.10^{-6} mbar. At the beginning of the pumping, the glass, and the sample in contact with the glass, are heated for 45 min at 80 to 100°C to desorb water. The **effect of temperature** on tholins is discussed in **Section III.2.2.d**. The IR spectra of tholins during heating show the disappearance of adsorbed water, but no evolution is seen on the other absorption bands. Spectra are given in **Supplement SIII.2-6** and are discussed with the analysis of each band (see **Section III.2.2.c**).

Pellet	Characteristics
P$_{th}$	KBr pellet with 1.5% tholins (1.6 mg of tholins), 110 mg, pressed under 5 tons
P$_{kbr}$	pure KBr, 115 mg, pressed under 5 tons
P$_{gr}$	1 mg of tholins spread on a thin metallic grid. Experiment done twice for reproducibility.

Table III.2-1: Studied samples
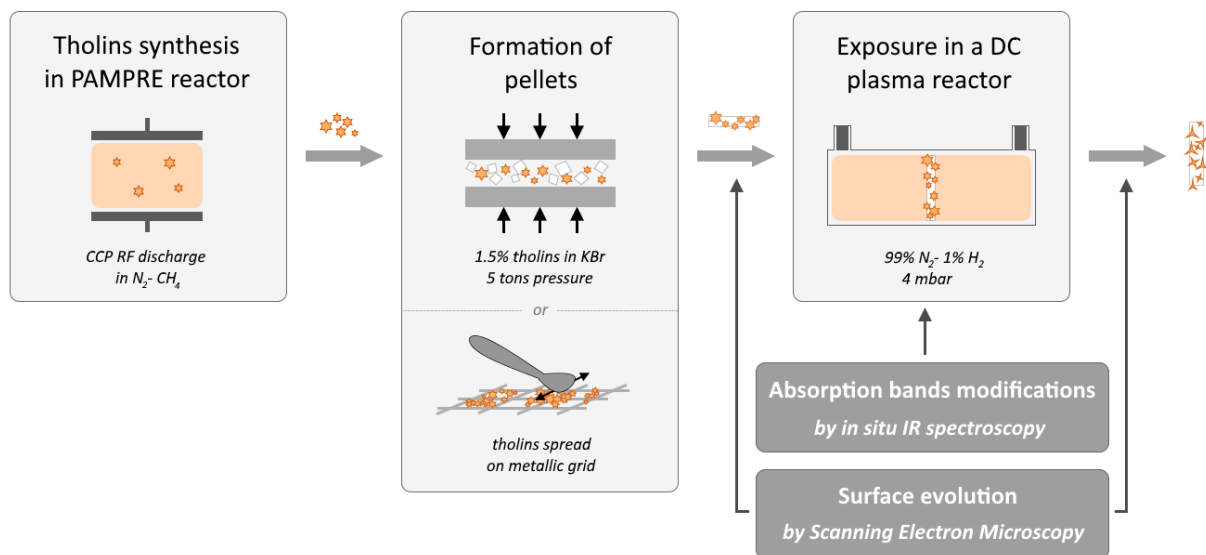
Figure III.2-1: Experimental protocol

2.2- Results

2.2.a. Characterization of the samples before exposure

IR ABSORPTION SPECTRUM OF THOLINS

Two different forms of tholins grow in the PAMPRE reactor: powders in suspension in the gas phase and films deposited on surfaces. Mainly tholin films have been previously studied by IR transmission spectroscopy (Gautier et al., 2012). Even if formed at the same time in the reactor PAMPRE, powders and films follow different production pathways. This leads to different elementary composition. In particular, powders have a higher nitrogen content than films (Carrasco et al., 2016).

The IR signature of tholins shows three major absorption bands: from 2700 to 3600 cm^{-1} due to amine and C-H stretching bonds, around 2200 cm^{-1} due to nitriles and isonitriles stretching modes and from 1100 to 1800 cm^{-1} due to many different stretching and bending bonds (Imanaka et al., 2004).

The comparison of powders and film spectra (see Figure III.2-2) shows a few differences: nitriles (C≡N) and C-H bonds (~2950 cm^{-1}) have lower contributions in powders than in films, which is consistent with the work cited above (Carrasco et al., 2016). One study has already compared IR spectra of powders and films (Quirico et al., 2008). It was done with a different percentage of methane than in the present work but the observations were similar.

Normalized IR spectra of the same tholin sample, but obtained by the two different methods on powders (with KBr *vs* on grids) are only slightly different (see Figure III.2-2). **The powders spectra in Figure III.2-2 will serve as references for the following study of powder evolution under plasma exposure.**
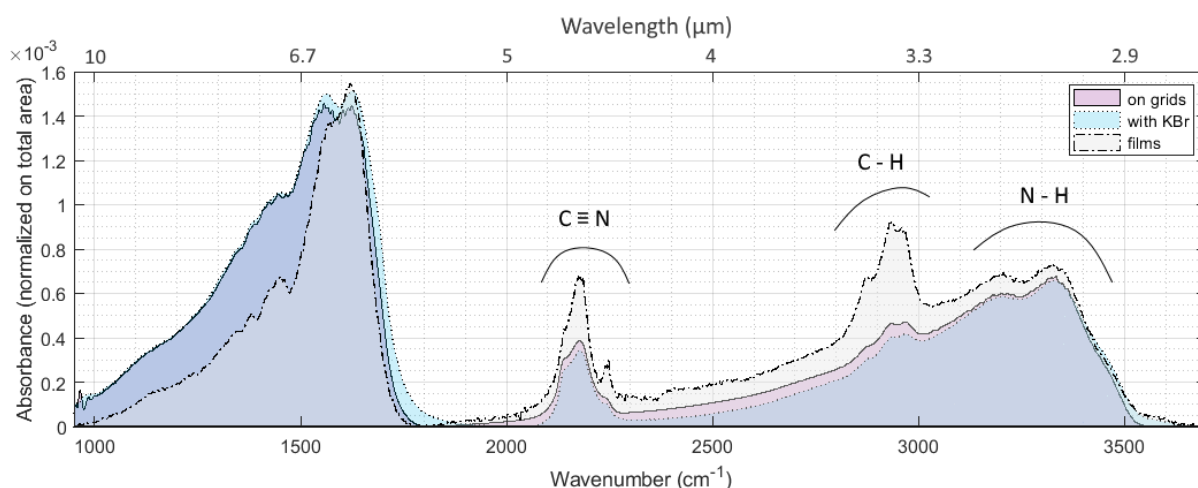
Figure III.2-2: IR spectra of tholins formed in PAMPRE in 95% N_2 - 5% CH_4. Absorbance is normalized on the total area of the spectra from 950 to 3700 cm^{-1}. Superimposition of the IR signature of powders and films from Gautier et al. (2012) (dotted-dashed line). Spectra with the two techniques presented here: pellets with grids (plain line) and pellets with KBr (dotted line).

SEM pictures of the surfaces of pellets were taken for tholins-KBr and pure KBr pellets at different scales (from 500 µm to 10 µm – see **Figure III.2-5**). All the surfaces of samples were analyzed and the pictures presented here are representative of the whole samples.

An EDS probe was used to obtain composition maps of the surface (cf **Figure III.2-3**). Pictures clearly show two different materials. White grains are made of potassium and bromine as expected, and the black material contains carbon, nitrogen and some oxygen. Oxygen is not present in the gas injected to form tholins in PAMPRE, but previous studies showed that they oxidize as soon as they are in contact with air (Carrasco et al., 2016). KBr is highly hydrophilic and its mixture with tholins could also enhance the oxidation of tholins.

The mixing of tholins and KBr is not homogeneous at the micrometric scale. KBr grains are ~200 µm large. Tholins are small spheres of ~500 nm in diameter, but they tend to aggregate in clusters of 10 to 100 µm at the surface of KBr grains or in between grains. KBr has been flattened by the tableting. Individual tholin grains are still round, but clusters are spread out and their flat surfaces are cracked.
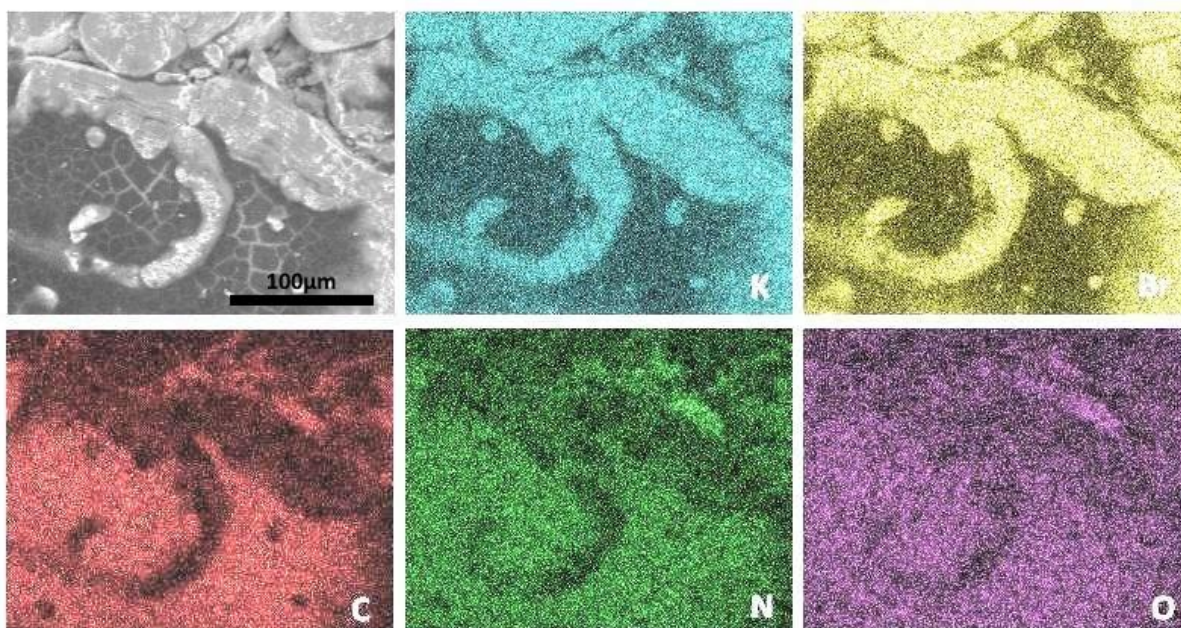
Figure III.2-3: Elementary analysis with an EDS probe of the surface of a pellet with KBr and tholins (P_{th}). Potassium, bromine, carbon, nitrogen and oxygen have been detected. Hydrogen cannot be seen by this method. The 100 µm scale is similar for all six images.

Tholins gather inside the meshes. They form round grains of 450-500 nm in diameter with a rather smooth surface, as seen in Hadamcik et al. (2009). SEM pictures are given in **Figure III.2-6**.

2.2.b. Physical erosion of the pellets

EVOLUTION OF THE SURFACES

Naked eyes are enough to see that the sample changes during exposure (see **Figure III.2-4**). Initial brown samples in KBr (P_{th}) turn into white, become rougher and eroded on the sides. Tholins are also removed from the grids (P_{gr}). ~1 mg of tholins is used in P_{th} and P_{gr}. Tholins are still present in P_{th} after 4h plasma while all tholins are removed from P_{gr} in less than 1h. KBr grains protect tholins from erosion.

	1.5% tholins in KBr (P_{th})	pure KBr (P_{kbr})	tholins spread on grid (P_{gr})
Before exposure			
After exposure	5h	3h	1h
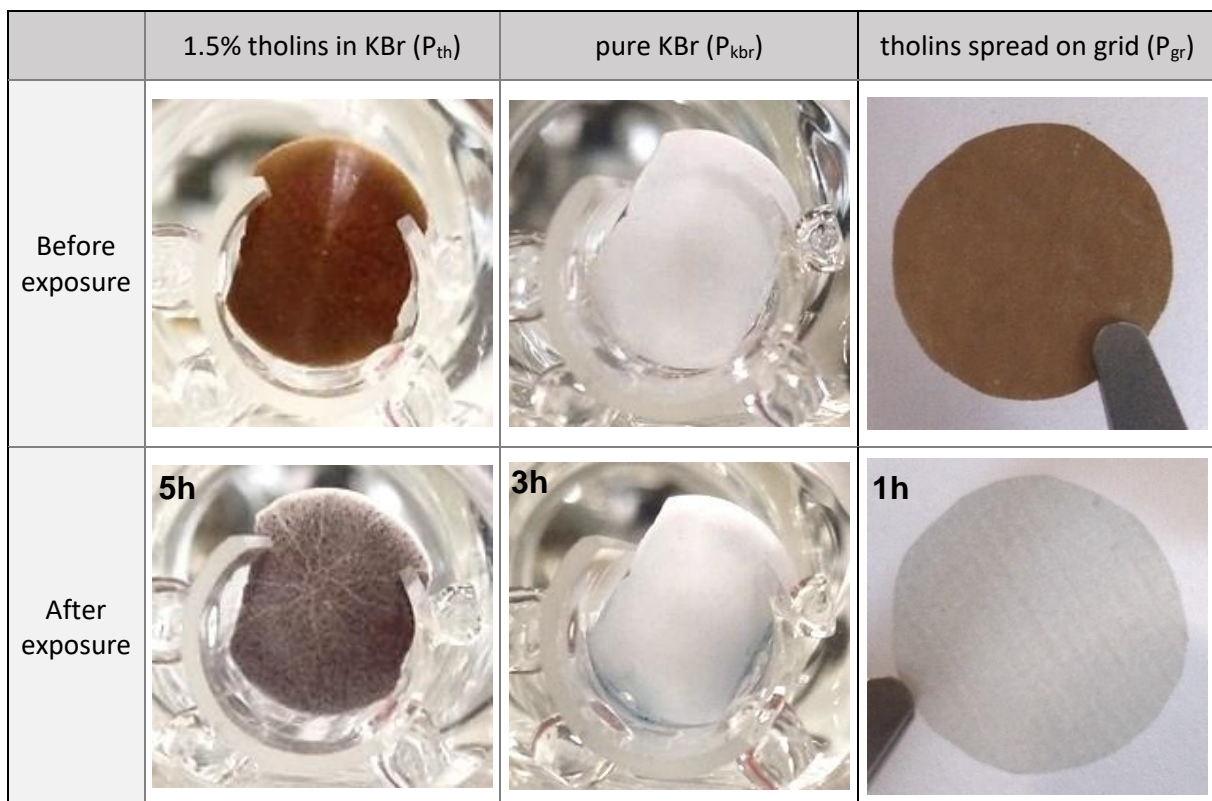
Figure III.2-4: Pictures of the samples inside their holder before and after being exposed to plasma. Samples with 1.5% of tholins in KBr (P_{th}), with pure KBr (P_{kbr}) and tholins spread on a metallic grid (P_{gr}).

Concerning the KBr(-tholins) pellets, **SEM pictures of the pellets surfaces after exposure show a strong physical erosion** (see **Figure III.2-5**). Sputtering indentations appear on KBr grains. Tholins are totally removed from the surface after a few hours of exposure to the plasma. However, while only KBr can be seen at the surface, the pellets appear still brown. Tholins are still present inside, but KBr grains protect them from a fast full erosion. **Therefore, the use of KBr to form pellets slows down the erosion of tholins by forming a protecting layer at the surface of the pellet.**
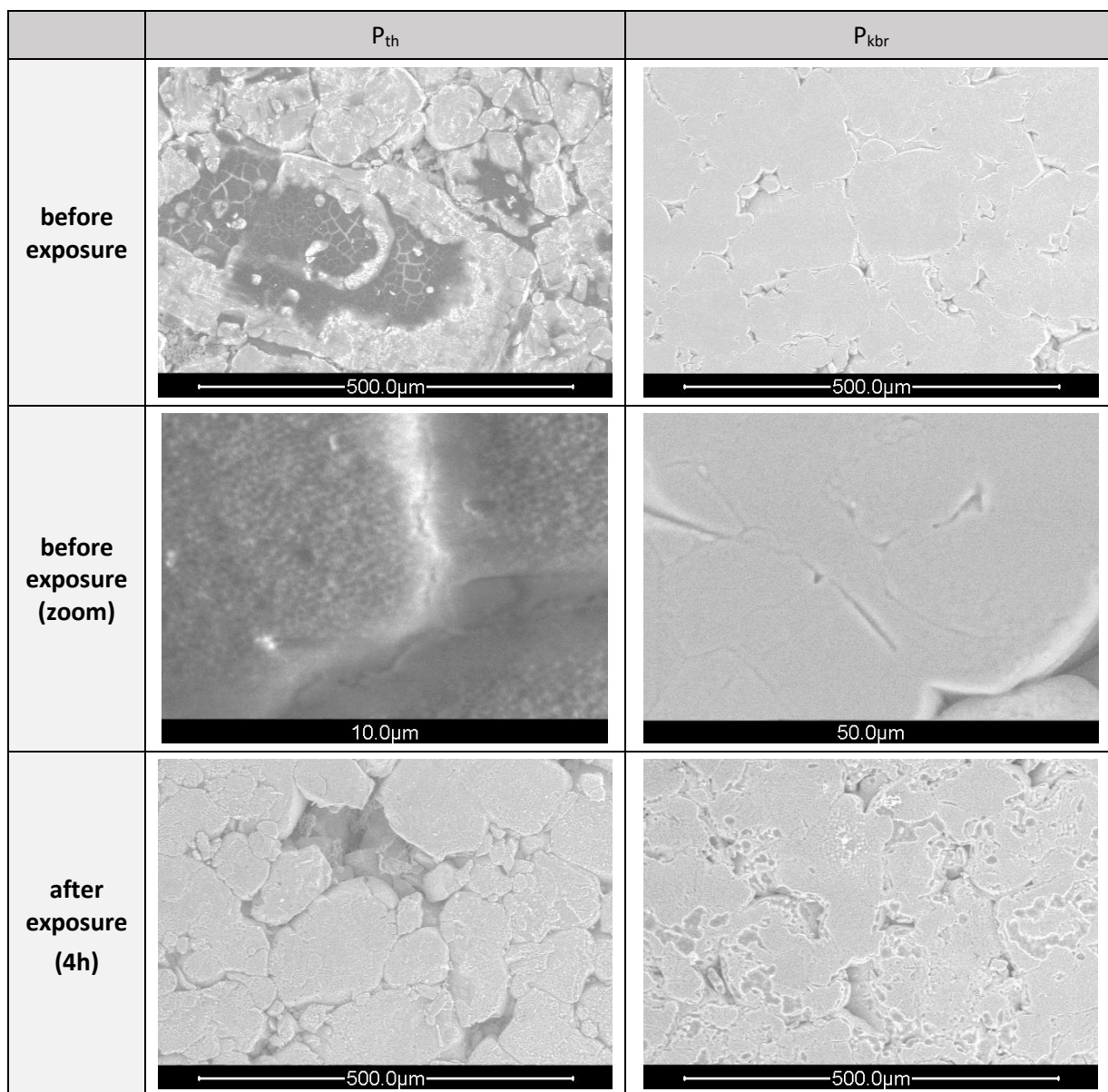
Figure III.2-5: Surface of P_{th} and P_{kbr} before and after exposure seen by secondary electron detection with an environment SEM.

Tholins spread on grids are more quickly altered by the exposure to the plasma. The grid was cleared from tholins in less than 1h. SEM pictures were taken on pellet grids exposed during one hour to a N_2-H_2 plasma with 5% H_2 and at 1 mbar (see **Figure III.2-6**). Under plasma exposure, grains are eroded and become more porous. Holes of ~10 nm form inside the grains. After the main grains are totally eroded, only the small structures formed by particles of less than 100 nm remain. The sheath formed by the plasma in these conditions is ~100 μm. Therefore, erosion due to sputtering by ions should *a priori* lead to surface modifications with spatial resolution larger than the sheath size. **Effects seen here are smaller than 100 μm, suggesting that they should be due to chemical processes.**

- 173 -

This second technique has the advantage of exposing only tholins and not KBr grains to the plasma. However, when tholins are eroded, the structure is weakened. Packs of tholins are quickly removed from the mesh and the grid is cleared from tholins.

before exposure		
after exposure (1h)		
after exposure (1h)		
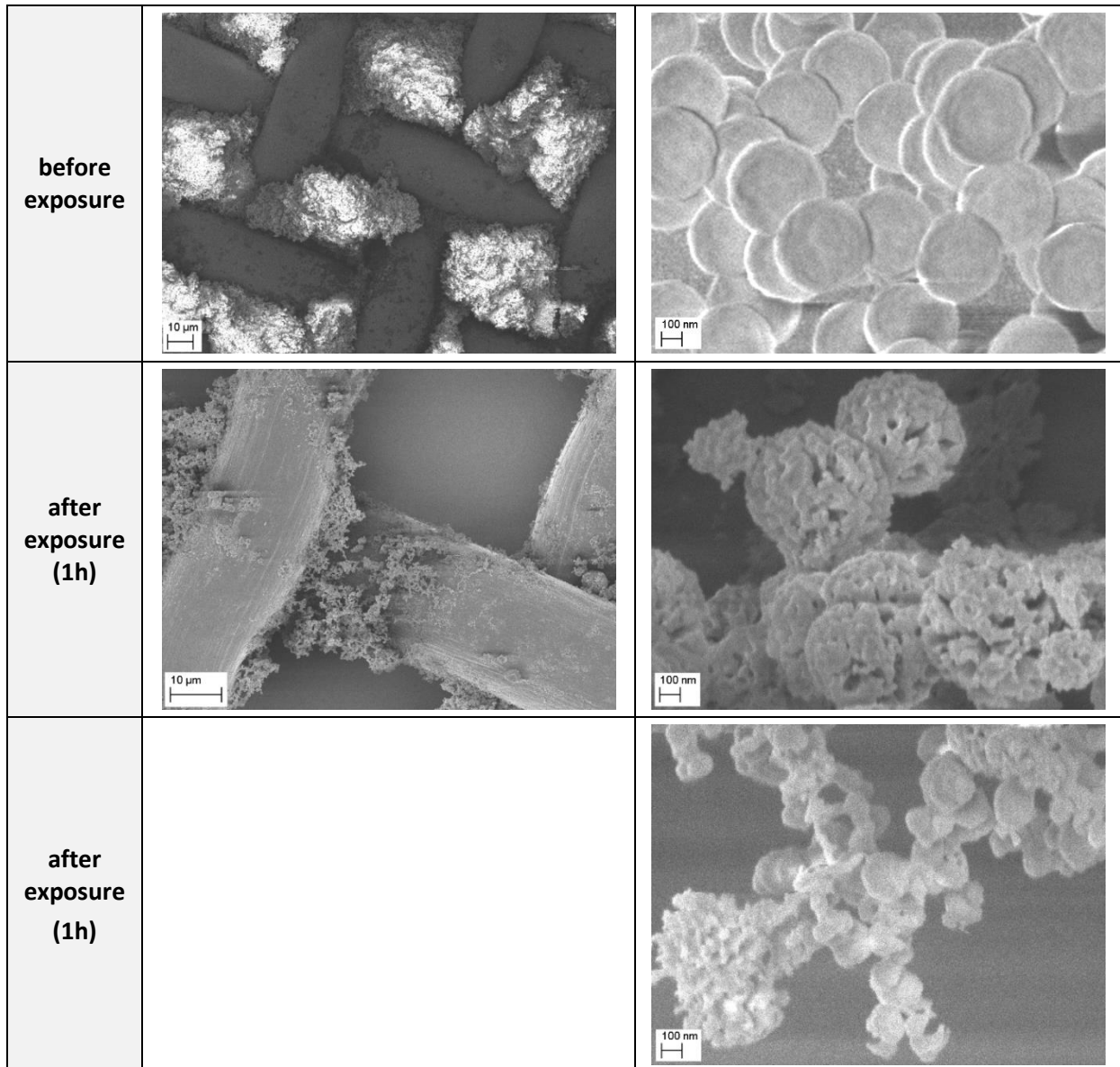
Figure III.2-6: Surface of P_{gr} before and after exposure with a FEG SEM.

From the comparison of the SEM pictures for the two techniques of pellets, we conclude that in KBr-tholins pellets, KBr grains protect the tholins and slow down their evolution under plasma exposure. On the other side, grid pellets expose directly tholins to plasma, and meshes are quickly cleared by the plasma.

The IR spectrum of pellets changes during exposure to plasma. Raw data gives the extinction, which is the combined effect of absorbance and diffusion:

$$extinction = -\log\left(\frac{I_{sample}}{I_0}\right)$$

I_{sample} is the IR beam intensity collected after the tholins sample and I_0 is the intensity collected after a reference sample: pure KBr pellet non exposed to plasma or empty grid. Reflection is also generally included in extinction. However, here samples are positioned perpendicularly to the IR beam and they are not moved during the exposure. Therefore, the effect of reflection is supposed negligible for this study.

Grids decrease the transmission by a factor of 5, due to the physical obstacle of the threads and the enhanced diffusion through the meshes. Indeed, threads are ~38 µm large, which is close to the IR wavelengths (10 µm / 1000 cm^{-1}) [see **Supplement SIII.2-1** showing the IR intensity transmitted through pure KBr pellet and empty grid]. However, these effects are compensated by the division by I_0 in the computation of the absorbance. KBr pellets become rougher during the exposure to plasma (see above), and this increases the scattering of IR light and therefore adds an offset to the extinction spectra during the experiment. To deduce the absorption spectra, the baseline is corrected by an adjusted polynomial [see raw data and polynomial fit in **Supplements SIII.2-2** and **SIII.2-3**].
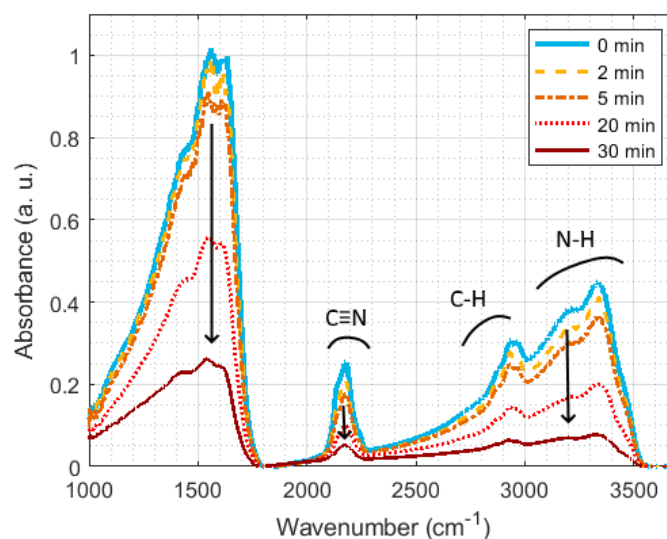
Figure III.2-7: Evolution of IR spectrum of tholins on grids (P$_{gr}$) during exposure to plasma.

In both cases, the main effect is the global decrease of the absorbance (see **Figure III.2-7**). It is consistent with the SEM observations described just above: some absorbent material is lost during the exposure to plasma.
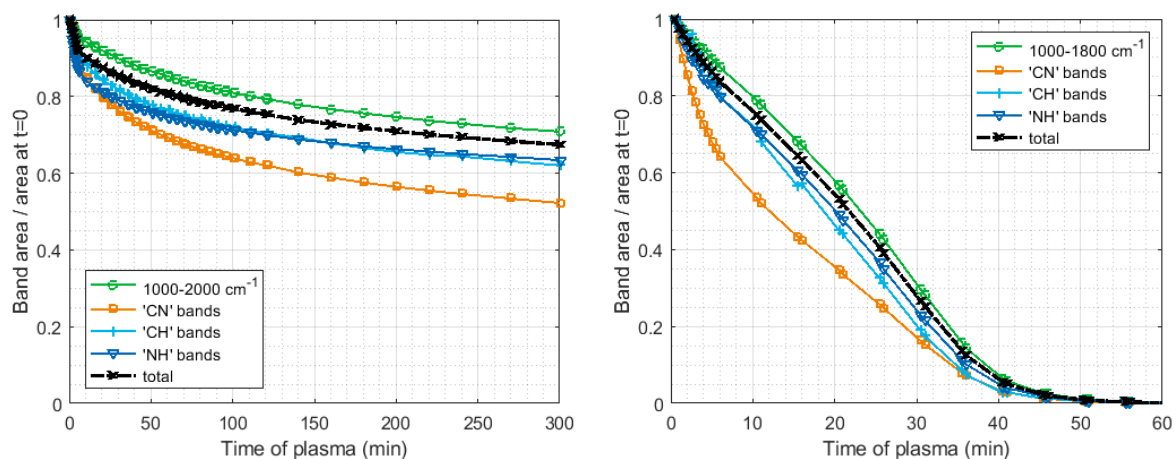
Figure III.2-8: Relative evolution of the three main absorption bands area during exposure to plasma: P_{th} (left) et P_{gr} (right). 'CN' (resp. 'CH') bands area is the area between 2020 and 2300 cm^{-1} (resp. 2500 and 3100 cm^{-1}) once the underlying 'NH' band is removed. 'NH' bands area for P_{th} (resp. P_{gr}) is taken between 2000 and 3700 cm^{-1} (resp. 1800 and 3700 cm^{-1}) once the 'CN' and 'CH' bands are removed [see **Supplement SIII.2-4**]. The total area is taken between 1000 and 3700 cm^{-1}.

The decrease of the band area of spectra in time gives an idea of the loss time scale (see **Figure III.2-8**). Results are different for the two pellets. The pellet with KBr loses 5% of its absorption in 5 minutes, but the decrease slows down after a few minutes and 70% of the absorbent material is still present after 3 hours. On the contrary, the decrease is linear for pellets with grids and all the absorbent material is gone after 45 min. This confirms the conclusions made from the SEM observations above: **KBr grains protect tholins from plasma erosion.**

The areas of the major bands decrease slightly differently in time. In particular, CN bands disappear more quickly than the others. This suggests a different evolution of the chemical bonds and therefore the action of chemical processes during the erosion.

	KBr pellet (P_{th})	Grid (P_{gr})
Advantages	**Best method for IR analysis** - very good transmission in IR	**Best method to expose aerosols to plasma** - direct exposure of tholins to plasma seen on SEM pictures
Drawbacks	**Exposure aerosols/plasma hampered by KBr grains** - surface passivated by KBr grains (SEM pictures) - slower decrease of IR absorbance during exposure to plasma **Increased chemical pollution** - KBr is highly hydrophilic, it contains some water, which can interact / absorb on tholins during the preparation of the pellet. - presence of an -OH band at 3500 cm^{-1} and a C=O band at 1700 cm^{-1}, due to absorption of water and oxidation of the surface of tholins. Trapped in the KBr matrix, they are not entirely removed by heating. - possible chemical interaction between Br$^-$ and positive ions formed in the discharge or derived from tholins.	**IR transmitted intensity 80% lower than with KBr pellets: lower signal to noise ratio.** - 75% absorption / reflection by threads - diffusion through meshes of 38 μm and threads of 25 μm, close to IR wavelengths. Enhanced by the apparition of empty meshes after exposure to plasma.

Table III.2-2: Comparison of KBr and grid pellets: advantages and drawbacks.

Both methods can be used to obtain IR spectra of tholins. However, each of them has its drawbacks (see Table III.2-2): KBr pellets give the best IR spectra, but slow down the interaction of tholins with plasma and induce unwanted chemical effects. Therefore, it is fundamental to compare both techniques to conclude on the IR absorption of tholins.

SUPPLEMENT SIII.2-1: IR INTENSITY THROUGH KBR PELLET AND GRID
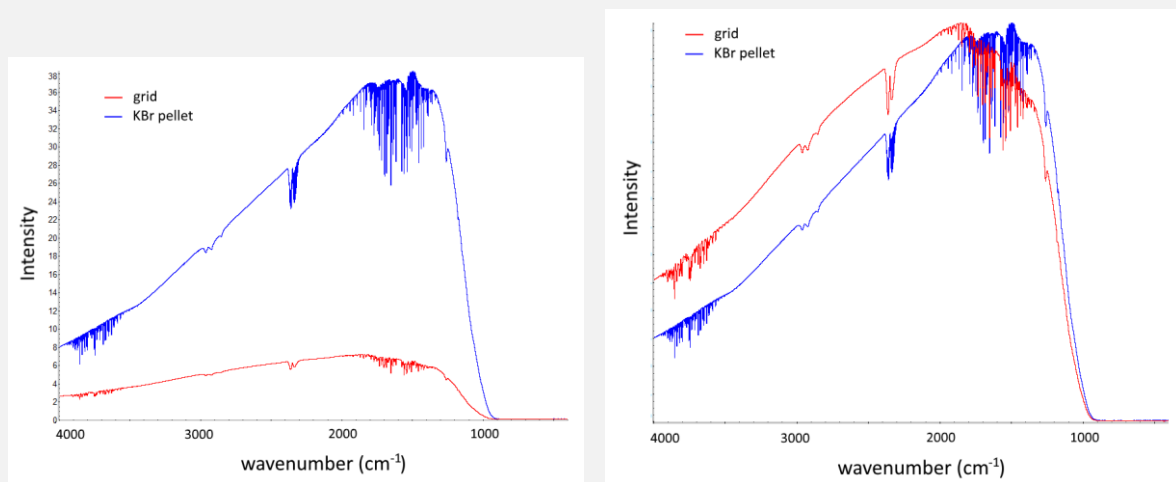
Figure SIII.2-1: IR intensity through reference pellets (without tholins). Normalized on the right panel.

KBr is transparent in IR wavelengths. It is often used to make pellets mixed with a material to study. On the other hand, grids of 38 μm absorb 80% of IR light and give noisier spectra. Grids also deform the IR lamp emission spectrum by diffraction through the meshes.

SUPPLEMENT SIII.2-2: EVOLUTION OF THE BASELINE DURING THE EXPOSURE
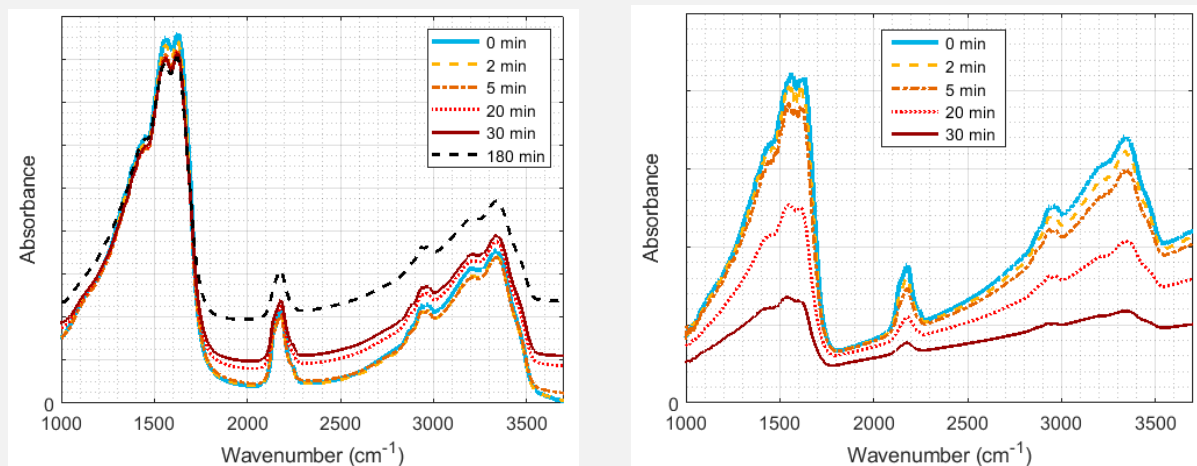
Figure SIII.2-2: Evolution of IR spectra of samples during exposure to plasma, raw absorbance. Left: on a KBr pellet (P_{th}). Right: on a grid pellet (P_{gr}).

Spectra evolve during exposure to plasma. Concerning the KBr pellet, the mean value of the baseline increases and can be explained by the enhancement of diffusion through pellets as they become rougher. In parallel, for both KBr and grid pellets, the total amplitude of the extinction decreases, which mainly means a loss of absorbing particles. Both phenomena are consistent with the visual and SEM observations, detailed in **Section III.2.2.b**.

Figure SIII.2-3: Polynomial correction of the baseline of absorbance spectra of tholins. Left: on a KBr pellet (P_{th}). Right: on a grid pellet (P_{gr}).

The baseline can be corrected to remove the major effect of diffusion. Here a polynomial is subtracted to the original baseline. It is defined by two reference wavelength ranges where tholins do not absorb (from 1790 to 1830 cm^{-1} and from 3600 to 4000 cm^{-1} in the case of grids; from 1990 to 2030 cm^{-1} and from 3700 to 4000 cm^{-1} in the case of KBr pellets). The polynomial fit is computed for each spectrum.

SUPPLEMENT SIII.2-4: AREAS OF 'CN', 'CH' AND 'NH' BANDS
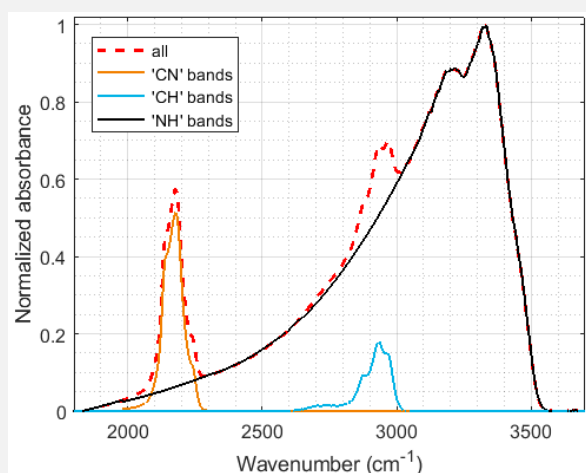
Figure SIII.2-4: 'CN' and 'CH' bands are dissociated from the 'NH' bands thanks to polynomial fits. IR spectrum of P_{gr} before exposure to plasma.

NH (and OH) bands (1800-3600 cm^{-1}) are superimposed with CN (2000-2300 cm^{-1}) and CH bands (2500-3100 cm^{-1}). We removed the CN and CH bands thanks to polynomial fits on the left wing of the NH bands.

Evolution of the spectra

The relative evolution of bands on Figure III.2-8 shows that nitriles and isonitriles bands are the most eroded by plasma. On the other hand, the NH and CH bands decrease at exactly the same speed. On **Figure III.2-2**, films of tholins have an increase of CH bands compared to amines similarly to what is seen with powders. Films are produced during a longer exposure to N_2-CH_4 plasma than powders. As no change is seen regarding relative evolution of CH and NH here, we conclude that the differences between films and powders are not due to long exposure to N_2-H_2 plasma species. Methane should play a fundamental role.

To study more closely the evolution of chemical functions of samples, each of the main broad bands is renormalized to its maximum. Interpretations on the evolution of the shapes of bands are therefore relative to these reference points.

Interesting modifications are observed on the nitrile and isonitrile bands (C≡N). The decrease of unsaturated structures such as C=C and C=N is observed thanks to the disappearance of a band at 1665 cm^{-1}, and the decrease of specific C-H bands at 2950 cm^{-1}.

Excluding erosion, the amine band does not show any strong modification, but only a small decrease (< 4% in intensity compared to the maximum at 3340 cm^{-1}) of the left part of the band, below 3200 cm^{-1} [presented in **Supplement SIII.2-5**]. This large band can be attributed to ammoniums or carboxylic acids. This loss also happens during heating. It can therefore be due to the loss of ammoniums which are highly unstable, or to the desorption of volatiles organic compounds (VOCs) formed at the surface of tholins by oxidation when they are exposed to air. The increase of diffusion with grids (from 1800 to 3300 cm^{-1}) and the loss of –OH bands (~3550 cm^{-1}) from water desorption on KBr pellets modify also this broad band. Nevertheless, we can conclude that amine bands do not evolve much during plasma exposure.

Bands showing modifications are discussed in the following parts. The baseline of each band is adjusted with a polynomial fit [explained in **Supplement SIII.2-4**] and bands are normalized at their maximum or at a selected reference point. Each plot of IR spectrum evolving in time goes along with a plot subtracting all spectra to the spectrum taken at t = 0. These plots enhance changes seen, and enable a clear view of the appearance and disappearance of bands. However, one should keep in mind that those curves depend on the reference normalizing point chosen.

Evolution of the nitrile and isonitrile bands

Bands between 2040 and 2260 cm^{-1} are the most modified by the exposure to plasma. They are usually associated with nitriles and isonitriles functional groups which have strong stretching absorption modes in this wavenumber range. On the sample before exposure, the major band at 2177 cm^{-1} is therefore usually associated with conjugated nitriles. At 2135 cm^{-1} one can see the signature of isonitriles (R-N≡C), or maybe carbodiimines (R-N=C=N-R). The band at 2245 cm^{-1} is due to saturated aliphatic nitriles (see **Table III.2-3**).
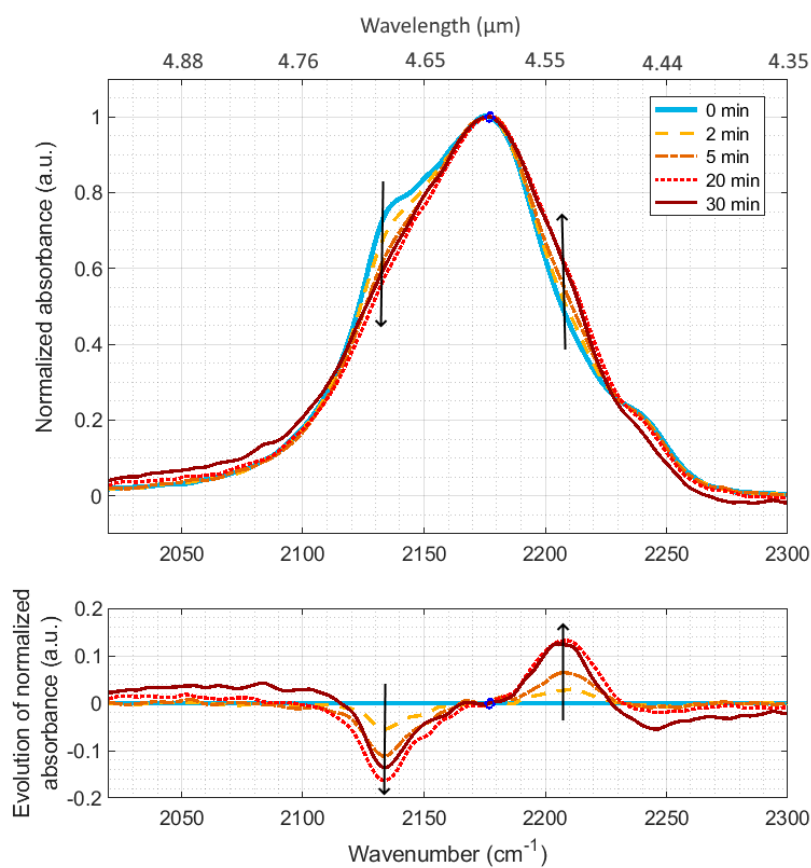
Figure III.2-9: Evolution of the IR nitrile band during exposure to plasma. Measurements with P_{gr}.

cm^{-1}	bond	evolution	reference
2135	isonitriles (R-N≡C) and/or carbo-diimides (-N=C=N-)	quicker loss than the other bands	S04, I04
2177	conjugated nitriles (R-C≡N) and/or isonitriles with short 'R'	*reference point of the study*	S04, I04 T08, M99
2210	β-unsaturated nitriles, aryl nitriles and/or cyanamides (>N-C≡N)	increase compared to the other bands	S04, I04
2245	saturated aliphatic nitriles	none	S04, I04

Table III.2-3: Band attributions in the range 2040-2260 cm^{-1}. All are stretching vibrations. S04 refers to Socrates (2004), I04 to Imanaka et al. (2004), T08 to Truica-Marasescu and Wertheimer (2008) and M99 to Mutsukura and Akita (1999)

When exposed to plasma we see similar evolutions for both pellets P_{th} and P_{gr}. **The isonitrile group at 2135 cm^{-1} disappears more quickly than the other bands** (cf **Figure III.2-9**). In isonitriles, the N≡C bond is a terminal unsaturated and reactive function, which can easily be hydrogenated by H_2 and H in the plasma, explaining its rapid decay. This band can also be due to carbodiimides (-N=C=N-) functions.

On the other side a new band of unsaturated nitriles grows around 2210 cm^{-1}. It could be associated to β-unsaturated nitriles and/or cyanamides (>N-C≡N), which have previously been detected in MS/MS measurements in the fragment $C_2N_3^-$ (Carrasco et al., 2009). There could be two explanations to this evolution: either this band resists more to plasma than the other nitriles, or it comes from the formation of additional functions, which could be linked to the transformation of isonitriles and/or carbodi-imides. Indeed, with grid pellets, bands at 2135 and 2210 cm^{-1} evolve with similar timescales and intensities (~15% of the main band).

Alkynes (C≡C) absorb also at these wavelengths, at 2100-2150 cm^{-1} if mono-substituted, and at 2190-2260 cm^{-1} if di-substituted. However, these absorptions should have weak absorption bands compared to nitriles (Socrates, 2004), and previous GC-MS measurements on these tholins do not identify alkynes (Morisson et al., 2016). With KBr pellets the variations are slower and the band at 2210 cm^{-1} is less intense.

Samples have also been analyzed during heating at 80°C, at 10^{-6} mbar or under gas flux of N_2-H_2 at 4 mbar. In both cases, nitrile bands shift slightly during heating (with changes in intensity < 5% of the main band) but come back to their initial position at the end [spectra are presented in **Supplement SIII.2-6**]. The pellet temperature during heating is similar to its temperature during plasma exposure. Therefore, observations discussed above on the experiment under plasma exposure are not due to a heating effect, but rather to reactions with plasma species.

MODIFICATIONS OF UNSATURATED STRUCTURES AT 1665 CM^{-1}

Absorption bands from 1000 to 1750 cm^{-1} show also some modifications under plasma exposure. Both on grids and KBr pellets, a large band around 1665 cm^{-1} decreases strongly. We therefore present only results on P_{gr} here (see **Figure III.2-10**).

Attributions in the wavenumber range 1000-1700 cm^{-1} are ambiguous because several bonds have close absorption bands (see **Table III.2-4**). In particular, bands at 1550 and 1620 cm^{-1} can be due to secondary and primary amine (N-H) deformation vibrations, but also to unsaturated bonds such as C=C, C=N or N=N. The band at 1665 cm^{-1} can be due to C=N stretching vibrations in R-CH=N-R' or to C=C stretching vibrations if tri- or tetra-substituted or in the >C=C-N< structure. The relative decrease of this band compared to the others shows that unsaturated bonds such as C=C and C=N are more easily modified by the N_2-H_2 plasma that the N-H and C-H bonds. This result is consistent as reactive H_2 and H species in the plasma will affect mainly unsaturations through hydrogenation reactions.

Figure III.2-10: Evolution of the IR band from 1000 to 1750 cm^{-1} during exposure to plasma. Measurements with P$_{gr}$. The reference point for normalization was chosen at 1167 cm^{-1} to give a clearer illustration of the evolution of the band. Indeed, the main peak at 1550 cm^{-1} seems to evolve in time with reference to the rest of the band.

cm^{-1}	bond	evolution	reference
1000-1450	various possibilities, especially bending vibrations of C-H bonds and stretching vibrations of C-N.	none	S04, I04
1550	**N-H** (secondary or in C=N-H) **N=N** **C=N** (conjugated) *pirimidine (C=C and C=N)*	small decrease at the end of the exposure	S04
1620	**N-H** (primary) **C=N** (unsaturated) **C=C** (aromatic)		S04, I04
1665	R-**C**H=**N**-R' **C=C** (especially tri- or tetra- substituted, or from >C=C-N<)	decrease under plasma	S04
1690	**C=O** (from α,β-unsaturated or aryl aldehydes / ketones) **C=C** (from α,β-unsaturated amines: CH$_2$=C-N<)	small decrease under heating	S04

Table III.2-4: Band attributions in the range 1000-1750 cm^{-1}: stretching vibrations of C=O, C=C, C=N and N=N, and deformation vibrations of C-H and N-H. S04 refers to Socrates (2004) and I04 to Imanaka et al. (2004).

Before the exposure, **during heating**, only a thin band around 1690 cm^{-1} decreases by 5% in intensity with reference to the maximum at 1550 cm^{-1} [spectra are presented in **Supplement SIII.2-6**]. Heating at ~100°C does not affect tholins formed in PAMPRE (He et al., 2015). Therefore, the loss of the band at 1690 cm^{-1} could be attributed to the desorption of Volatile Organic Compounds (VOCs) during the heating phase. Indeed, this band at 1690 cm^{-1} could be attributed to stretching vibrations of C=O, or C=C in unsaturated amines (see **Table III.2-4**). These VOCs should be mainly formed by oxidation processes at the surface of tholins when they are exposed to air (Pernot et al., 2010). On KBr grains, this band continues to decrease during plasma exposure: it seems all VOCs have not desorbed after the heating phase, especially the ones trapped inside the KBr grains pellet. However, thanks to experiments on grids, we are sure that modifications seen under plasma exposure at 1665 cm^{-1} are not due to heating, but to plasma species.

MODIFICATION OF UNSATURATED STRUCTURES SEEN ON CH BANDS

Bands from 2700 to 3050 cm^{-1} are due to C-H bonds. CH_2 and CH_3 structures have at least 2 different absorption bands, from symmetric and asymmetric stretching vibrations. Symmetric vibrations of acyclic CH_2 and CH, and of aliphatic CH_3 absorb at wavelengths inferior to 2900 cm^{-1}. Between 2900 and 3000 cm^{-1}, different bands superimpose: symmetric vibrations of acyclic CH_2 and CH, and aliphatic CH_3, plus symmetric and asymmetric vibrations from CH_3 bonded to unsaturated functions or >CHCN. Details are given in **Table III.2-5**. No absorption band is observed at wavelengths superior to 3010 cm^{-1}, which discards the presence of C-H bonds on aromatic structures (Abdu et al., 2018; Socrates, 2004).

Exposure to plasma leads to the loss of a large band from ~2910 to ~3020 cm^{-1} with reference to the rest of the bands (see **Figure III.2-11**). As symmetric and asymmetric absorption bands should evolve similarly, the disappearance of this band should be due to the loss of structures with methyl bonded to unsaturated structures or to >CHCN. This agrees with the previous conclusions showing that C=C, C=N, and C≡N tend to disappear more quickly than saturated structures when exposed to a N_2-H_2 plasma.

On grids, no evolution is observed during heating, which confirms that the observations are due to plasma species interaction [see **Supplement SIII.2-6**].

However, **on KBr pellets**, other side effects are seen: it seems CH bonded to aldehydes are observed at 2700 and 2775 cm^{-1} and decrease during exposure to plasma. This point is consistent with the decrease of C=O bands during exposure of KBr pellets discussed just above. Besides, some changes are also seen during heating of pure KBr pellets, they could be due to water or VOCs still trapped between KBr grains. Anyway, as these effects are not seen on grid pellets, they are not due to tholins and we will not further analyze them.
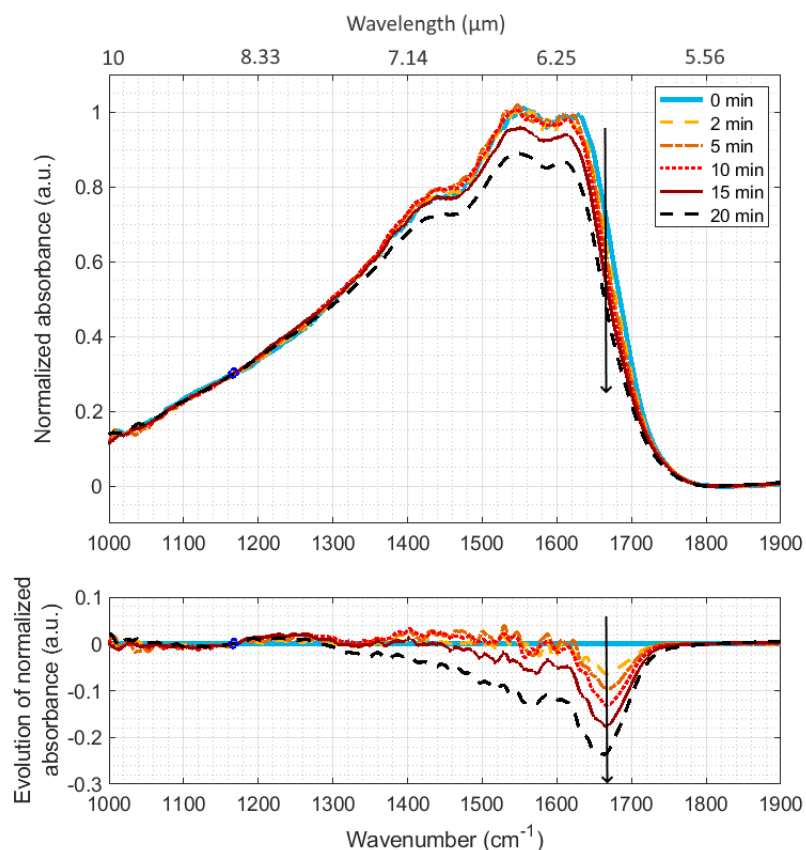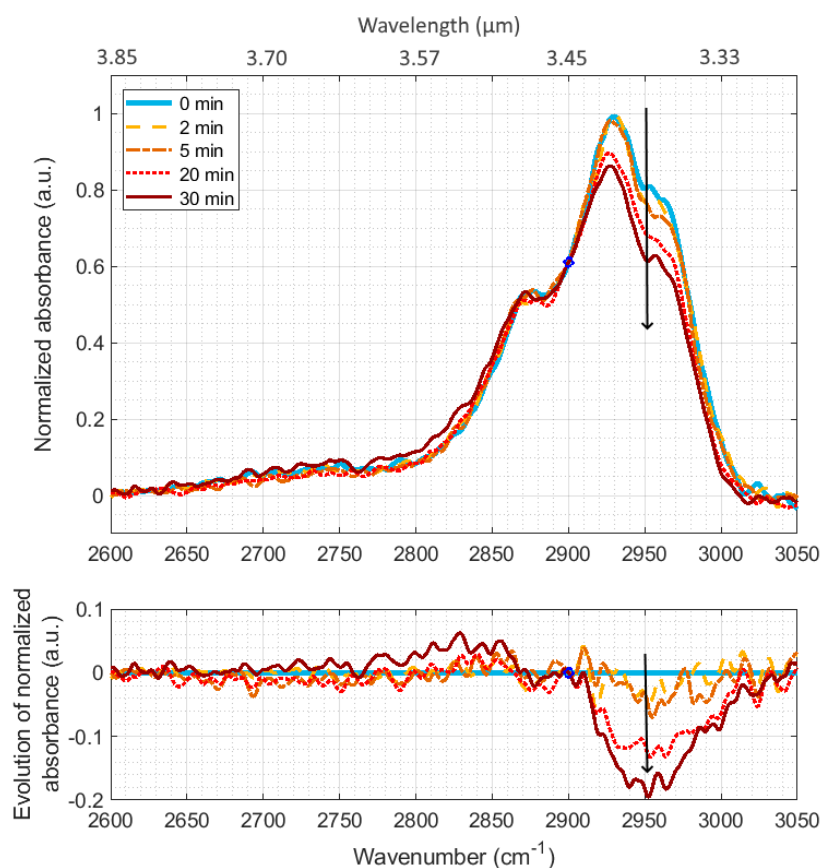
Figure III.2-11: Evolution of the IR band from 2600 to 3050 cm^{-1} during exposure to plasma. Measurements with P$_{gr}$. The reference point for normalization was chosen at 2900 cm^{-1} to give a clearer illustration of the evolution of the band. Indeed, the main peak at 2930 cm^{-1} seems to evolve in time with reference to the rest of the band.

cm^{-1}	bond	evolution	reference
2650-2800	-N-CH$_3$ or –N-CH$_2$-(?) (sym)	none	S04, I04
2850	acyclic CH$_2$ (sym)	none	S04, D18, A18
2875	aliphatic CH$_3$ (sym)	none	S04, I04, D18
2880-2890	acyclic CH (weak)	none	S04, G12
2880-3010	unsaturated –CH$_3$, 3 bands in this range	loss during plasma	S04
2900-2910	aliphatic CH$_2$ (Fermi resonance)		D05, D18
2930	acyclic CH$_2$ (asym)		S04, I04, G12, D18, A18
2935-3035	-CH$_3$ linked to >CH-C≡N or –C(sat group)$_3$, 2 bands		S04
2960-2970	CH$_3$ (asym)		S04, I04, G12, D18, A18

Table III.2-5: Band attributions in the range 2600-3050 cm^{-1}: stretching vibrations of C-H. S04 refers to Socrates (2004), I04 to Imanaka et al. (2004), G12 to Gautier et al. (2012), D05 to Dartois et al. (2005), D18 to Dionnet et al. (2018) and A18 to Abdu et al. (2018).
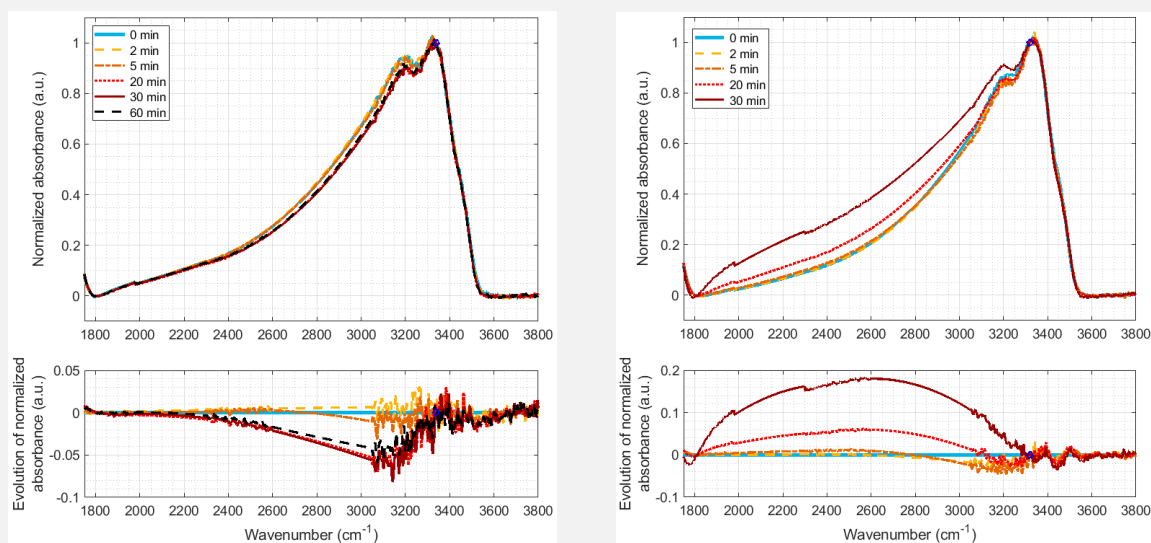
Figure SIII.2-51: Evolution of the IR band from 1800 to 3600 cm^{-1} during exposure to plasma, after the removal of 'CN' and 'CH' bands. Measurements with P$_{gr}$. The reference point for normalization was chosen on the main peak at 3338 cm^{-1}. Left: evolution during heating. Right: evolution under plasma exposure.

No strong modification happens in the amine band concerning tholins. A small decrease of a large band around 3200 cm^{-1} could be due to the loss of ammoniums under heating. The large band from 1800 to 3200 cm^{-1} appears at the end of plasma exposure, but only on grid samples. It should be due to diffusion through the emptying meshes. KBr pellets show a strong loss at 3550 cm^{-1} (-OH bonds) due to the desorption of water.

Figure SIII.2-6: Evolution of IR bands during heating of the sample P$_{gr}$ at 80-100°C at 4 mbar. Spectra of the three bands presented above, 'CN' bands on **Figure III.2-9**, 'CH' bands on **Figure III.2-10**, and **Figure III.2-11**.

Only small evolutions are seen on IR spectra during sample heating: the shift of nitriles and the loss of a band around 1690 cm^{-1} due to VOCs desorption.

2.2.d. Experimental conclusions

COMPARISON OF KBR AND GRID PELLETS

In the present study we used two different kinds of pellets. The comparison of both gave us insights on their advantages and drawbacks. It also gave us confidence that the presented effects are related to tholin evolution under plasma exposure, as they can be discriminated from possible artifacts induced by KBr or metal grids. Indeed, all evolutions presented above are seen using both techniques. The ones seen only with one technique were immediately discarded and attributed to the influence of the technique used to make the pellet (KBr grains or metallic thin grids).

Concerning the comparison of the two methods, it turned out that grid pellets were more appropriate for our application. KBr pellets are often used for FTIR study of solids (Abdu et al., 2018), because it gives spectra with a really good signal to noise ratio, contrarily to grid pellets that transmit only 20% of the incoming light because of absorption, reflexion and scattering [the transmitted intensity is presented in **Supplement SIII.2-1**]. However, in our case, the exposure of tholins to plasma is hampered by the presence of KBr. KBr grains physically protect tholins inside the pellet from the plasma. They also trap water and VOCs inside the pellet and hinder them from desorbing during the cleaning heating before the exposure to plasma (see results in **Section III.2.2.b**). This last point is enhanced by the fact that KBr is highly hydrophilic.

In conclusion, to avoid physical or chemical actions of KBr that could modify IR spectra, we recommend the use of grid pellets in this experimental configuration.

EFFECT OF TEMPERATURE IN THE PLASMA DISCHARGE

A difference between our experiment and Titan's atmosphere is the gas temperature which is not controlled at 170K in our experiment. To work at ambient temperature can affect the reaction rates, the products and their stability in the plasma. It should mainly **accelerate processes**. However, no further study on this subject can be done with this setup as condensation appears on the walls at low temperature. Nevertheless, it is necessary to check that a higher temperature does not induce by itself new chemical evolutions of the sample. Previous works (Bonnet et al., 2015; He et al., 2015; Morisson et al., 2016) studied the degradation of tholins under heating. Effects are seen only above 300°C, where tholins start to carbonize and create polyaromatic structures.

During our experiment here, the lightning of the discharge at 20 mA **increases the gas temperature to about 60-80°C** (Loureiro and Ricard, 1993; Pintassilgo and Guerra, 2017). According to the works cited in the previous paragraph, the temperature rise here should not degrade by itself the tholin chemical structure.

Measurements during heating are consistent with this hypothesis. They are described in **Supplement SIII.2-6**. Measurements of the temperature of the glass in contact with the pellet gives a temperature of ~80°C. **No interesting evolution** has been detected in IR analysis, just the desorption of water and VOCs, especially in the case of KBr pellets.

In conclusion, the physical and chemical modifications seen on the pellets are not due to a degradation by the rise of temperature but to the physical and chemical erosion by the N_2-H_2 plasma.

2.3- Discussions

2.3.a. Evolution processes in the plasma

Several evolution processes can be deduced from the results obtained here. First ion sputtering should be one physical process leading to the global erosion of the sample. Ions from N_2-H_2 plasma, and in particular hydrogenated ions, should be energetic enough to erode surfaces exposed to the plasma (Sharma et al., 2006; Tanarro et al., 2007).

Besides, we observed that the nanometric erosion of individual grains, under the dimensions of the plasma sheath linked to sputtering, and the evolution of IR bands reflect also chemical evolution processes (see **Section III.2.2.c**). The accelerated decrease of nitrile and isonitrile bands compared to the others shows a preferential erosion of these highly unsaturated bonds. On the other side, N-H and C-H bands evolve similarly and cannot explain the differences seen between powder and film spectra (see **Figure III.2-2**). The study of bands around 1665 and 2950 cm^{-1} seems to indicate a preferential erosion of unsaturated centers

like C=N and C=C compared to simple bonds as N-H and C-H. In conclusion, we observed that unsaturations are more affected by plasma exposure. This is consistent with the fact that hydrogenated species in the N_2-H_2 plasma react with unsaturated sites.

The evolution of the nitrile and isonitrile band is simple enough to infer the chemical process at stake. The quasi-simultaneous evolution of two bands at 2135 and 2210 cm^{-1} suggests that isonitriles (-N≡C) are converted into nitriles (-C≡N). These evolutions can also be explained by the transformation of carbo-diimides (-N=C=N-) into cyanamides (>N-C≡N). In both cases, more stable bonds are formed.

2.3.b. Modifications due to photon irradiation

On Titan, the upper atmosphere is ionized by energetic electrons coming from Saturn's magnetosphere, but also by solar photons. Especially, UV irradiation has a major impact in the upper layers (Gronoff et al., 2009; Lavvas et al., 2011a), and among them VUV photons ionize easily nitrogen and methane in the atmosphere.

Laboratory plasmas also emit VUV photons, thanks to excited species. Consequently, surfaces exposed to plasma undergo combined effects of plasma particles and VUV photons. In particular, excited hydrogen and nitrogen emit strongly in the region 170-120 nm (Wertheimer et al., 1999). A study on the plasma VUV photons impact on polymer surfaces showed they can photochemically ablate the polymers and create volatile fragments (Hong et al., 2002). Therefore, this effect could appear in the experiment described here. However, further studies are required to quantify it. Besides, we expect VUV photon fluxes in the plasma to be weak compared to fluxes on Titan because of strong self-re-absorption in the gas phase in the plasma reactor.

A recent study focused on the only effect of VUV photons on tholin films (Carrasco et al., 2018). To be consistent with the UV irradiation dose received by aerosols on Titan, samples were exposed during 24h to strong fluxes, using synchrotron light. It showed the de-hydrogenation of the chemical functions.

Results here do not include de-hydrogenation but other chemical modifications. Consequently, modifications observed in this work cannot be attributed to VUV photons (especially on the short time scales used). In our plasma discharge photons are therefore less efficient to alter tholins than ions, electrons or radicals.

Consequently, at least two erosive agents could be at work on Titan's aerosols: VUV photons for de-hydrogenation and N_2-H_2 plasma particles that modify the unsaturated functions. In the ionosphere, carbon growth and hydrogenation processes should be in competition, from the influence of carbon and hydrogen of plasma species derived from CH_4. However, just below the ionosphere, ion processes should stop and modifications should be dominated by VUV irradiation, leading to the de-hydrogenation of the organic grains.

2.3.c. Modifications due to atomic hydrogen irradiation

Similarly to VUV photons, atomic hydrogen counts among the reactive species present in Titan's upper atmosphere and likely to affect aerosols through heterogeneous reactions. Atomic hydrogen is mainly formed around 800 km on Titan due to direct photo-dissociation of methane and CH_3, and reaction of CH with methane (Lebonnois et al., 2003; Vuitton et al., 2019). It can reach a density up to 10^8 cm^{-3}. Another source of atomic hydrogen is present lower, in the stratosphere, where unsaturated hydrocarbons undergo photo-dissociation.

The effect of atomic hydrogen on Titan's aerosols has been studied in the conditions of Titan's stratosphere and mesosphere (below 600 km) by Sekine et al. (2008a). They observed a strong loss of H by hydrogenation at the surface of tholins and by recombination in H_2. No significant chemical evolution of the tholins has been noted, the main conclusion being the strong consumption (~60%) of atomic hydrogen by heterogeneous reactions at these altitudes (Sekine et al., 2008b; Vuitton et al., 2019).

Atomic hydrogen is also present in large quantities (~0.1%) in both the ionosphere of Titan (Vuitton et al., 2019) **and in N_2-H_2 laboratory plasmas** (Carrasco et al., 2013; Sode et al., 2015). **Therefore, hydrogenation of tholins and recombination due to atomic hydrogen could also appear**, both in the experiment presented here and in the ionosphere of Titan. Hydrogen atoms can also have synergetic effects combined with nitrogen atoms and other species.

2.3.d. Evolution expected on Titan

As the experiment described here aims to mimic phenomena happening on Titan, one should expect that physical and chemical modifications seen in the laboratory should also appear on Titan's aerosols. The experimental simulation simplifies the conditions in Titan's ionosphere. Only N_2-H_2 plasma species are present in the experiment while at least methane and VUV photons also play simultaneously a great role in Titan's ionospheric chemistry. **Therefore, the processes studied here will be concomitant with other evolution processes on Titan.**

Few information is known about aerosols in Titan's ionosphere, making it difficult to compare with experimental results. In the whole infrared range studied here, only the small part around CH bands can be compared to Cassini data. In addition, the ionosphere is not dense enough for infrared measurement and these spectra have been taken around 200 km, in the stratosphere (Kim et al., 2011).

VIMS spectra show a complex CH band group, with CH_2 and CH_3 signatures, in agreement with tholins here (see **Section III.2.2.c**). However, the main difference is the presence of absorption peaks above 3000 cm^{-1} in VIMS data that are not seen with PAMPRE tholins. These bands are attributed to CH linked to aromatic structures (Socrates, 2004). Therefore, we showed that aromatic structures are *a priori* not formed by N_2-H_2 plasma processes. However, as VIMS spectra are taken far **below the ionosphere**, many **other processes** could be thought of to explain this formation, with for instance a large abundance of polycyclic aromatic

hydrocarbons (PAHs) in the atmosphere (López-Puertas et al., 2013) or the condensation of ice on aerosols (Kim et al., 2011).
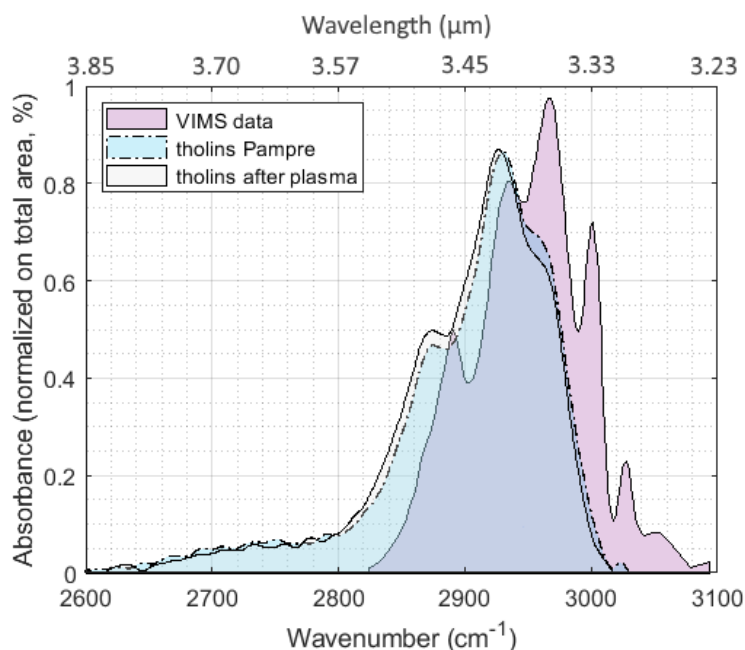
Figure III.2-122: Comparison of infrared CH absorption bands in our experiment partially mimicking Titan's ionosphere and VIMS data in the stratosphere (Kim et al., 2011).

We showed that the exposure of grains to N_2-H_2 plasma species leads to the formation of 10-nm erosion structures on grains (see **Section III.2.2.b**). This effect is certainly enhanced by the absence of methane in the mixture that would tend to form new carbon chains around. However, it shows that nanostructures could be formed and **increase the sticking coefficient** of grains that would tend to adsorb smaller molecules or form **agglomerates of grains**, as suggested by Lavvas et al. (2011b). This enhanced granularity should also influence the efficiency of organic aerosols to act as **condensation nucleus** lower in the atmosphere of Titan.

2.4- Complement: oxidation of tholins exposed to air

Comparing IR signatures from tholins freshly produced to older ones, we observed some strong modifications of the IR bands. Tholins used in the previous study were all freshly produced. Nevertheless, we performed a small study to **quantify the evolution of tholins under air exposure**. The objective is to know precisely the ageing of the tholins exposed to air to **avoid false detections** in our various experiments using tholins. In addition, the exposure of tholins to air, containing O_2 and H_2O to the contrary of Titan, can mimic the **Great Oxidation Event on Earth**, at a period when Titan-like aerosol formation in the atmosphere of the Earth is suspected (cf **Section I.1.3.b**). This study has been realized in collaboration with the COBRA (Chimie Organique et Bioorganique – Réactivité et Analyse) laboratory in Rouen (France) specialized on analytical chemistry. It is the focus of **Paper 4**.

2.4.a. Tholins exposed to air during several years

The PAMPRE experiment has been working for several years, and surplus samples are stocked in **small vials in dark conditions**. We studied samples formed in the **reference conditions**: with 5% CH_4 in N_2, at 0.9 mbar and at an injected power of 30 W.

Production date	Time exposed to air (months)
08/2019	0
03/2019	4
03/2018	17
07/2017	25
05/2014	63

Table III.2-6: Tholins samples studied.

The tholins samples listed in **Table III.2-6** are spread on thin **metallic grids**, positioned in a vacuum chamber in the sample compartment of the FTIR and left under vacuum for ~30 min. Even if the tholin mass spread on the pellets is controlled, the spreading is not perfectly homogeneous. Therefore, the IR spectra from different samples, or from one sample at different locations can have different total absorption. To avoid this bias, **we compare only the normalized intensities**, on the total spectrum or on specific bands.

In particular, **Figure III.2-13** shows that **proportionally the 'NH-OH' bands between 2300 and 3800 cm^{-1} increases in time** compared to the other bands. In the context of exposure to air, one can suggest that this increase is mainly due to OH bonds, that can be due to water adsorption or the formation of alcohols or carboxylic acids.
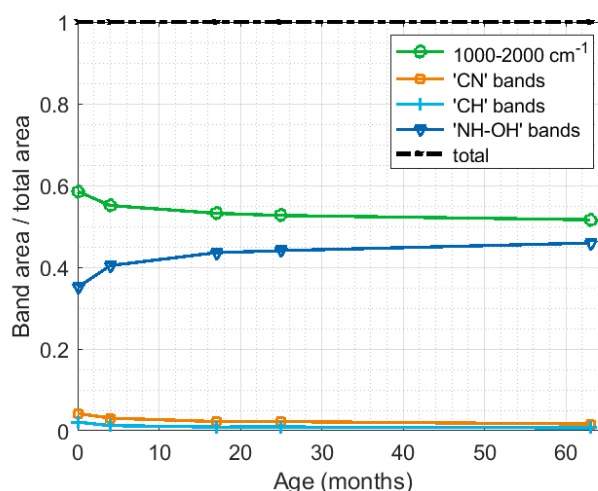
Figure III.2-13: Evolution of the ratio of the areas of the main bands with the age of tholins.

We observed strong evolutions specifically on two bands: the bands around 1600 cm^{-1}, and the CH bands. The evolution of their spectra is plotted in **Figure III.2-14**. The main feature is the apparition of a thin band at **1700 cm^{-1}**, attributed to **C=O bonds**. In parallel, CH bands shift towards a strong increase of the bands around **2650 and 2800 cm^{-1}**, that are attributed to **CH bonds linked to aldehydes**.
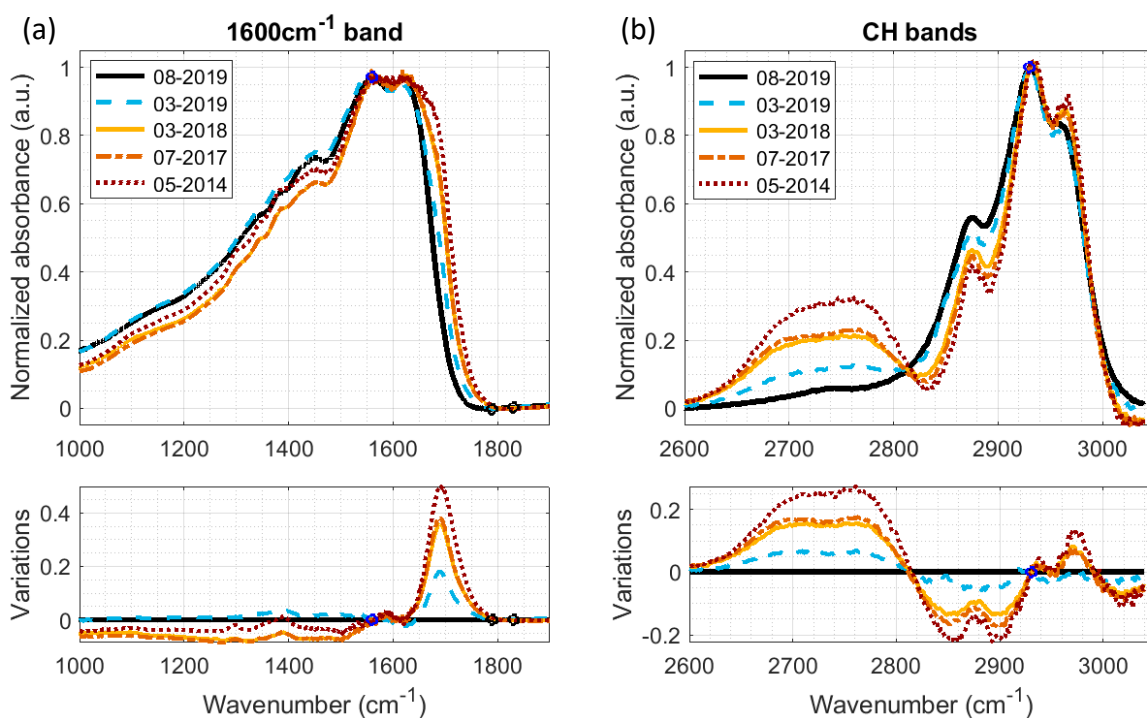
Figure III.2-14: Evolution of the normalized absorbance of bands (a) around 1600 cm^{-1} and (b) around 2900 cm^{-1}, during the ageing of tholins exposed to air.

In conclusion, we observe that if exposed to air (with H$_2$O and O$_2$), tholins chemical functions change. We notice the increase of **OH bonds**, from water adsorption or the formation of OH-containing functions, as well as the increase of the **C=O bonds and the proximity of CH with C=O bonds**, that could come from the formation of aldehydes. Similar changes on tholins exposed to air have previously been observed by Sciamma-O'Brien et al. (2017).

This increase of the oxygen content in the aged tholins has also been investigated by **high resolution mass spectrometry**. The samples were analyzed with a FTICR (Fourier Transform Ion Cyclotron Resonance) mass spectrometer equipped with a 21 Tesla superconducting magnet at the National High Magnetic Field Laboratory in Florida. It shows a **strong increase in the oxygen-containing fragments, and also an increase in the number of O atoms in these fragments.**

2.4.b. The evolution of tholins in a few minutes and days

To go further in the investigation of the oxidation of tholins when exposed to air, we performed another experiment, this time focused on the **ageing of a given sample during several days**. In this objective, a grid covered with fresh tholins is inserted in the vacuum chamber in the sample compartment of the FTIR. After the acquisition of a reference IR absorption spectrum, the chamber is opened to ambient air for several days. Once every 3 to 4 days, the chamber is put under vacuum for 30-50 min and IR spectra are acquired regularly during the pumping. We expect smaller changes in the spectrum than in the previous section because exposure times are shorter. However, the sample is fixed during the whole

experiment, and therefore spectra can be directly compared, without any baseline correction and normalization.

The first observation, is the evolution of the sample at the beginning of its exposure to vacuum (~10^{-4} mbar). The raw absorbance in **Figure III.2-15 (a)** shows a strong decrease from 3000 to 3600 cm^{-1}. **Figure III.2-15 (b)** shows that this decrease of the NH-OH band stabilizes after ~30 min. On the other hand, at the re-exposure to air, the band reappears in ~10 min.
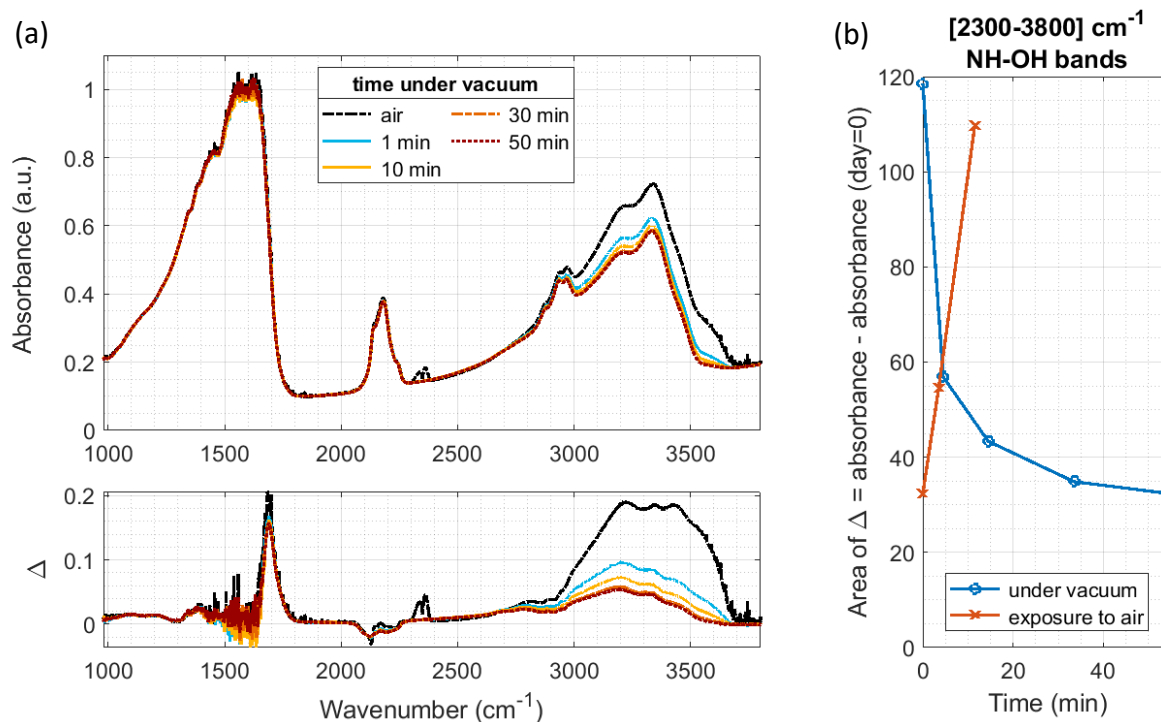
Figure III.2-15: (a) Evolution of the tholin spectrum exposed to vacuum. The tholins sample used is the one after 17 days exposure to air. (b) Evolution of the area of Δ, representing the difference between the absorbance at t, and the reference absorbance of fresh tholins (taken on day = 0). Evolution during the exposure to vacuum, and at the opening of the chamber to ambient air.

We attribute this band to the adsorption of water on the tholin samples. Therefore, at the exposure of tholins to air, **water quickly adsorbs in quantity** on them. An exposure to vacuum removes the major part of the adsorbed water in ~30 min. **To avoid the signature of water on the measurement of tholins IR spectra it is thus necessary to let them under vacuum for at least 30 min.**

THE SLOW OXIDATION OF THOLINS

Figure III.2-16 (a) shows **the evolution of the tholin sample IR spectrum after being exposed for several days to ambient air**. The spectra are taken after 30-50 min of vacuum to avoid the absorption due to adsorbed water. The evolution of Δ, representing the difference between the absorbance on the day of the measurement, and the reference absorbance of fresh tholins

(taken on day = 0), shows the apparition of **two main bands**: one thin band **at 1700 cm^{-1}** and one large band **between 2500 and 3500 cm^{-1}**.

(a)　　　　　　　　　　　　　　　　　　　　　　　　　(b)
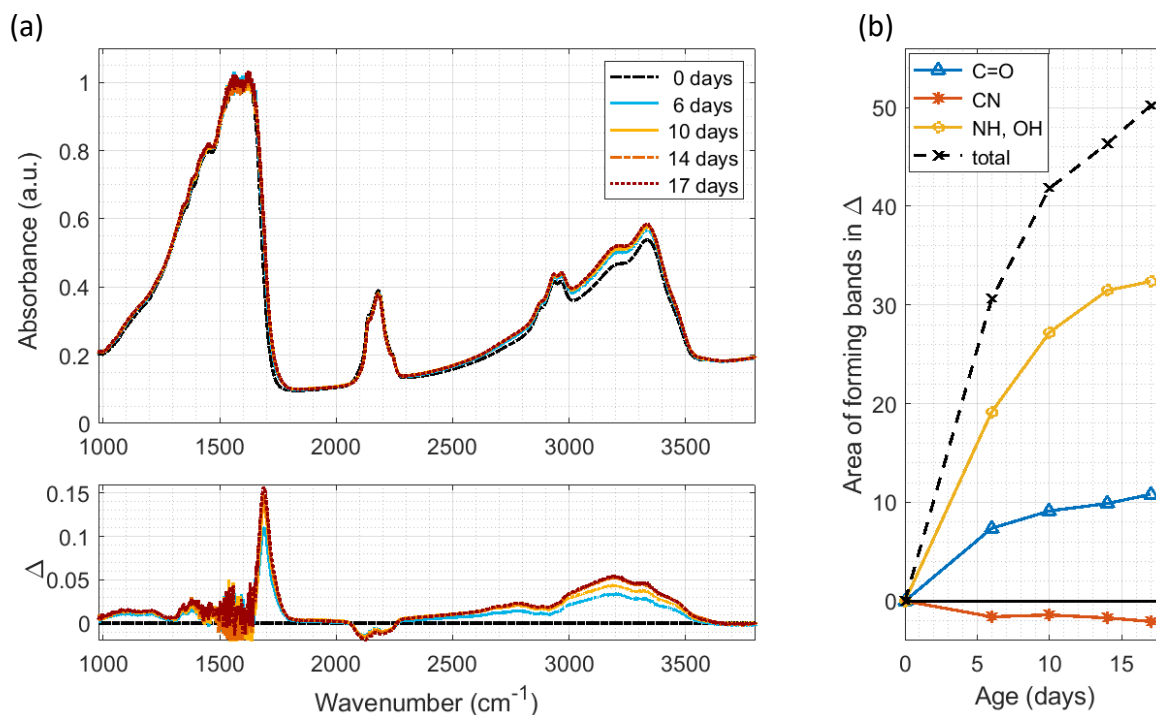
Figure III.2-16: (a) Evolution of the tholins spectrum exposed to air during several days after 30-50 min under vacuum. (b) Evolution of the area of Δ, representing the difference between the absorbance at t, and the reference absorbance of fresh tholins (taken on day = 0). Evolution of several bands: 'C=O' is taken between 1633 and 1850 cm^{-1}, 'CN' between 2000 and 2300 cm^{-1}, 'NH-OH' between 2300 and 3800 cm^{-1} and 'total' between 1000 and 3800 cm^{-1}.
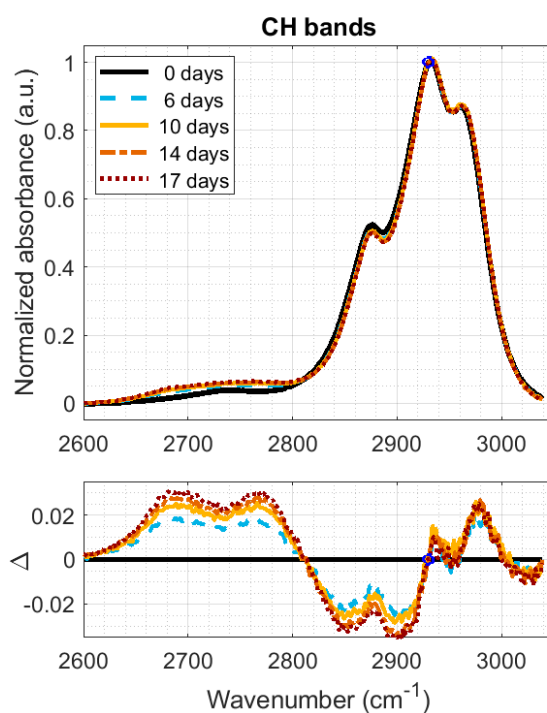
Figure III.2-17: Evolution of the CH bands of the tholins spectrum exposed to air during several days.

We studied in more details the evolution of three main bands in **Figure III.2-16 (b)**. Similarly to the previous study on 1-5 years old tholins, we observe the strong apparition of the **C=O band at 1700 cm^{-1}**. The fact that spectra can be compared without normalization shows the **increase of the large NH/OH band**. It can be attributed to **OH bonds in carboxylic acids**. Finally, one can also observe a small **decrease of the CN band**. This can be due to the oxidation of the C≡N bond, rather fragile in oxygenated environments. In particular, nitriles are well-known to react slowly with water to give carboxylic acids.

Figure III.2-17 shows the evolution of the CH bands, similarly to the **Figure III.2-14 (b)** in the case of 1-5-year-old tholins. One can observe exactly the same evolution, with an amplitude 10 times smaller due to the difference in exposure durations. **The environment of CH bonds becomes more oxidized**, in particular forming aldehydes.

In conclusion, the oxidation of tholins observed in the study of 1-5 years old tholins is also found in the more precise study of 6-17 days old tholins. The second study gives access to finer evolutions like the small decrease of CN bonds. It also gives an idea on the kinetics of the oxidizing processes in the range of a few days: the evolution is sharp during the first days and slows down after 10-15 days. Nevertheless, observations of the 1-5 years old tholins shows that oxidation continues for years. Tholins are not entirely passivated by a protective oxidized layer. We observe the formation of C=O bonds, and certainly aldehydes and carboxylic acids.

In addition to this long-term oxidation, a quick and quantitative adsorption of water is observed on the tholins as soon as they are exposed to air. To protect tholins from ageing, we therefore recommend to keep them in dry air conditions (no water), and if possible under nitrogen air or vacuum (no O$_2$).

A future work on going in the team is to collect tholins in PAMPRE without ever exposing them to ambient air. Indeed, functions sensitive to oxidation could disappear instantaneously during the opening of the reactor.

CONCLUSION OF SECTION III.2

The experimental simulation presented here aims to **mimic the evolution of Titan's aerosols in its ionosphere**. Thanks to analogues of these aerosols and to a plasma discharge in nitrogen with 1% hydrogen, we showed that **organic matter typical to Titan's ionosphere is sensitive to its plasma environment**. In particular, originally **round smooth grains are eroded** by N_2-H_2 plasma species, leading to nanostructures at their surface. **Chemical functions are also modified**. Isonitriles and/or carbo-diimides decrease strongly, contrarily to more stable functions as nitriles and/or cyanamides which grow compared to the global nitrile band. Double bonds as C=C and C=N are more affected by the plasma exposure than amines and C-H bonds. On the contrary, N-H and C-H absorption bands keep a similar ratio in intensity and their shape does not vary. **VIMS spectra** in Titan's stratosphere show new aromatic CH bands compared to laboratory aerosols mimicking ionospheric particles, which are not explained by the plasma erosion studied there. This suggests that other processes also modify aerosols in Titan's atmosphere.

Concerning the erosion due to N_2-H_2 plasma, the **next steps are to understand individually the role of each of the plasma species**. Indeed, the gas phase interacting with the aerosols is composed by neutral, electrons, ions and excited species. Besides, the influence of hydrogen can especially arouse interest as protons H^+ and small protonated ions are mobile and very reactive.

3- Evolution of the plasma in contact with tholins

In this section, I investigate the effect on the gas phase of tholins placed in a N$_2$-H$_2$ plasma, mimicking the effect of Titan's aerosols on the N$_2$-H$_2$ erosive species of the ionosphere. Neutral species and positive ions are measured by mass spectrometry in different plasma conditions.

The presented results are the subject of **Paper 5** (*Interaction dust – plasma in Titan's ionosphere: experimental investigation of the gas phase modifications*).

3.1- Disappearance and formation of neutral species

3.1.a. General observations

THE EXPERIMENTAL SETUP

Tholin samples are exposed to a N$_2$-H$_2$ plasma in the THETIS experimental setup. The samples are thin metallic grids on which tholins formed in PAMPRE are spread. Details on the setup and the formation of the samples are given in **Section III.1.2**. For the measurement of neutral species, the **Mass Spectrometer** (MS) presented in **Section II.1.2** is coupled to a branch of the reactor (see **Figure III.3-1**). To maximize the collection of newly formed species, the pumping system is positioned in the same branch as the MS.
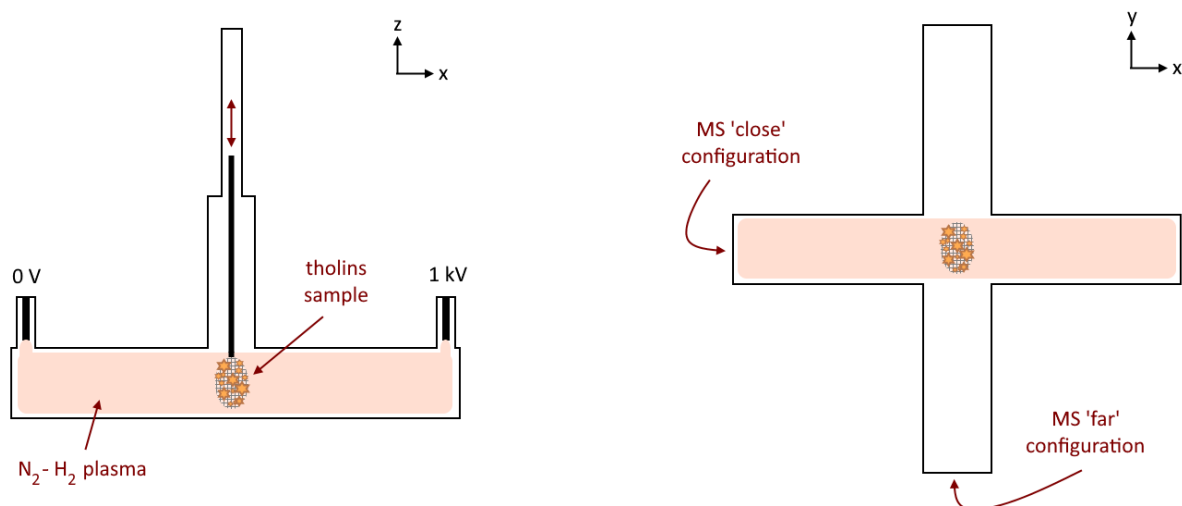
Figure III.3-1: Scheme of the experimental setup THETIS for the analysis of the gas phase.

The MS continuously takes spectra during the experiment. Each spectrum is from 1 to 100 u with a resolution of 1 u, and its acquisition takes ~30 s. **Figure III.3-2 shows the evolution of m/z 2, 17, 18, 27, 28 and 41** in the case of an experiment in which tholins are exposed to a **plasma in N_2-H_2 with 5% H_2, at 1.3 mbar and with a current of 20 mA**. These conditions will be referred to as the **reference conditions** in the following parts.

In this case, **the gases N_2 (at 28 u) and H_2 (at 2 u) are injected** in the experiment at t = 6 min. As the pressure increases, water that desorbs from the reactor walls can be detected at 18 and 17 u. Once the pressure is stabilized, **the plasma is ignited** in the reactor (at t = 13 min). As discussed in **Section II.3.1**, plasma discharges in N_2-H_2 mixtures lead to the formation of ammonia (at 17 u). The ignition of the plasma also helps to desorb impurities inside the reactor: H_2O at 18 u, HCN at 27 u and a heavy organic compound at 41 u, possibly CH_3CN. During this phase, the tholin sample is positioned ~30 cm away from the plasma. Nevertheless, we suspect that some plasma species could interact with the tholins at this distance, participating in the formation of the traces of HCN and other carbon-containing compounds detected. However, we showed that this contribution is minor (see **Section II.3.1.c**).
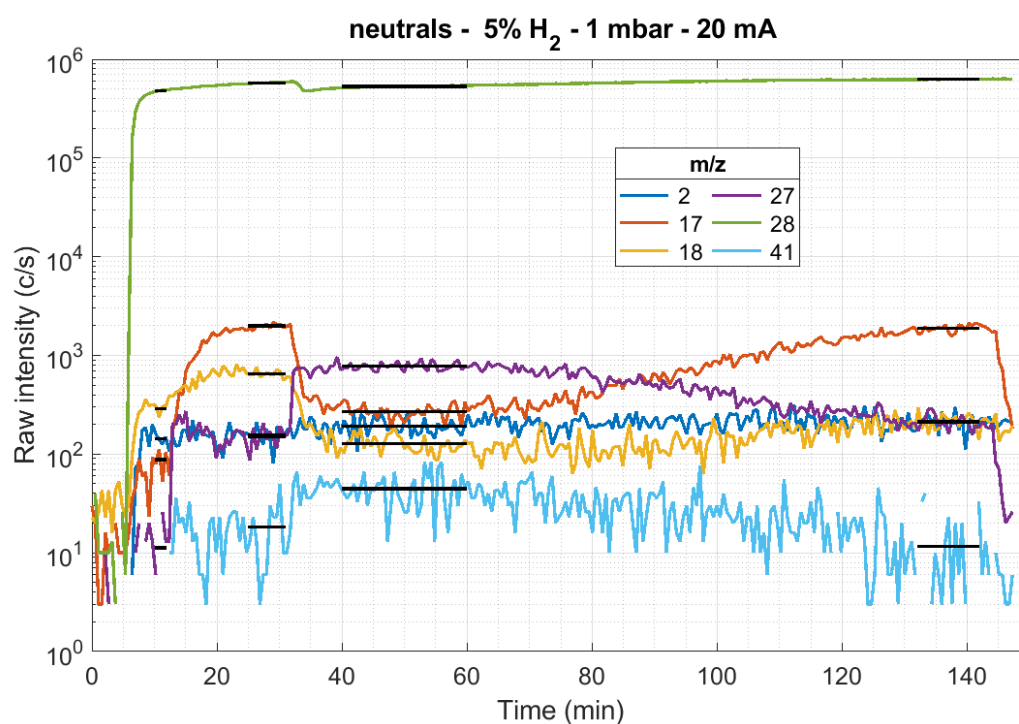
Figure III.3-2: MS measurement of a few masses during a complete experiment of tholin exposure to a N_2-H_2 plasma (5% H_2, 1.3 mbar and 20 mA). The gas mixture is injected at t = 6 min, the plasma is ignited at t = 13 min, the sample is added at t = 32 min and the plasma is stopped at t = 145 min. The black lines represent the stabilized values for each mass on the different sections.

The formation of ammonia takes a few minutes to stabilize, then **the sample is introduced in the plasma** (at t = 32 min). At this point, an **important modification of the gas phase composition** is observed. The **ammonia** formed in the N_2-H_2 plasma alone **suddenly drops** (divided by 10 in the conditions of **Figure III.3-2**). On the opposite, new carbon-containing

species are formed (as 41 u). The **main neutral species, aside from N$_2$ and H$_2$, becomes HCN**. **After 130 min**, the neutral gas composition is identical to the N$_2$-H$_2$ plasma conditions without tholins. Indeed, the tholins on the grid have all been eroded and nothing remains on the metallic grid. The exposure time needed to 'clean' the grid from tholins depends on the plasma parameters chosen and on the exact spreading of tholins on the pellet. In the conditions tested, it varied from 40 min (at 40 mA) up to more than 3h (time limit after which the experiment is stopped). This also shows that the presence of the sole metallic grid in the plasma does not affect the neutral species. The only difference is the detection of water at 18 u that has decreased. Indeed, most of the water adsorbed previously on the walls has been removed by the plasma.

Average and calibration of the signal

Figure III.3-2 shows directly the intensity measured by the MS. Noisy variations are observed, especially for species at low intensity. In the following we therefore consider **average values taken on 4 specific zones**: (1) the gas mixture before plasma ignition, (2) the plasma without sample and (3)-(4) the plasma with sample at the beginning and at the end of the experiment. The average values chosen in the case of **Figure III.3-2** are plotted in black lines. Except for (4), these zones are globally at the same time periods in the different experiments performed.

As discussed in **Section II.1.2, the raw intensity measured by the MS has to be corrected by a mass-dependent transmission function**. Then, the deduced intensity is in Pa.Å^2. To obtain the partial pressure (or the number density) of the species in the gas phase, the fragmentation pattern, the isotopes and the ionization cross section (Å²) of the different species have also to be taken into account. The MS transmission of low masses (m/z <= 4) is very different from the transmission of the other masses. To maximize the signal, low masses have usually been acquired with MS parameters tuned on m/z 2, while the other masses have been measured with MS parameters tuned on m/z 28. The transmission curves used to correct both are therefore different (see **Figure II.1-8 (a)**). In both cases, the transmission curve is a log-normal law (see **Equation II.1-2**). For the tuning focused on m/z 2, the coefficients are: $G = 37\,100\,; \mu = 1\,; s = 1.57$. And for the tuning focused on m/z 28, we used: $G = 290\,000\,; \mu = 3.42\,; s = 1$.

Evolution of the spectrum in reference conditions

Figure III.3-3 shows the spectra obtained in the reference conditions for the 3 first zones defined above: (1) gas mixture before the plasma ignition, (2) plasma without sample and (3) plasma with sample. The evolution of the main gas species is the same as observed on **Figure III.3-2**. Nevertheless, the complete spectra presented in **Figure III.3-3** show all the **new organic species formed by exposure of the tholins to the N$_2$-H$_2$ plasma**. A summary of the observations is given in **Table III.3-1**.
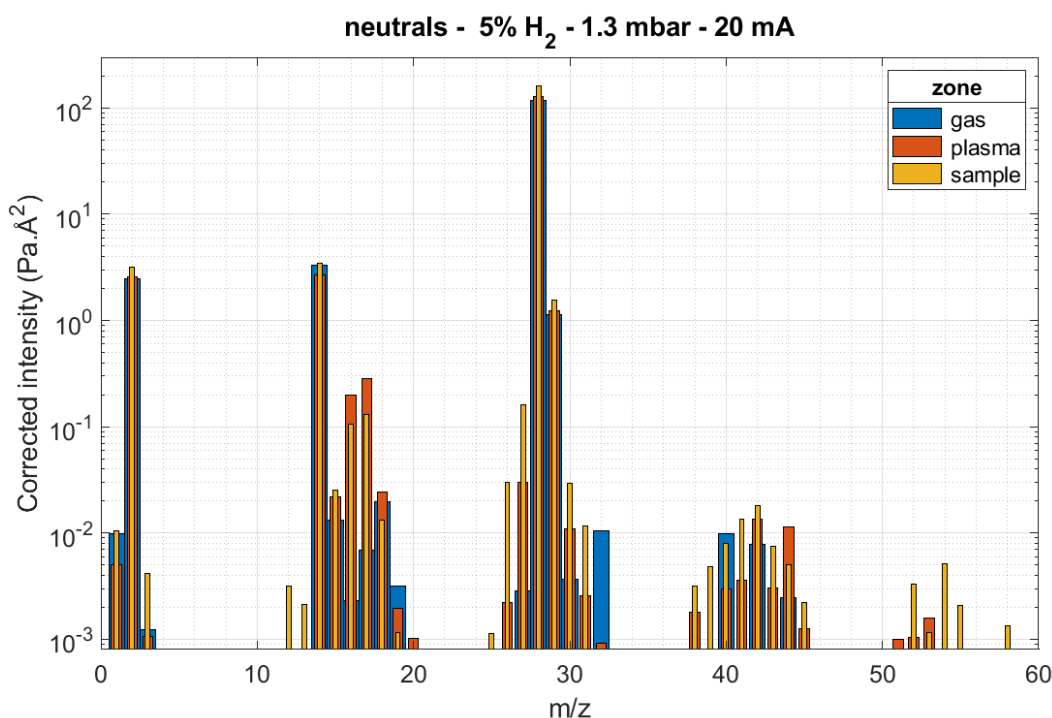
Figure III.3-3: Spectra obtained for the reference experiment (5% H_2, 1.3 mbar, 20 mA): before plasma (large blue bars), after ignition and stabilization of the plasma (medium orange bars), and after the addition of the tholins sample (thin yellow bars).

	gas	plasma	sample
formation	injected: **N_2**: m/z 14, 15, **28**, 29, 42 **H_2**: m/z 1, **2** *traces:* *H_2O: m/z 16, 17, **18** O_2: m/z 32 Ar: m/z 40 CO_2: m/z 44*	**NH_3**: m/z 16, **17** *traces:* *organics at m/z 26, 27, 30, 31, 38, 41-43 CO_2: m/z 44 (at the beginning, from O_2)*	**HCN**: m/z 26, **27** **other carbon-bearing molecules**, with peaks at m/z 26-31, 38-45, 52, 54
loss		*traces:* *O_2, Ar, H_2O (decrease with time)*	**NH_3**

Table III.3-1: Summary of the modifications of the neutral gas phase species during the experiment in reference conditions. The threshold for the 'traces' in the gas and plasma cases is set to 3x10-2 Pa.Å² on **Figure III.3-3**.

We observe a non-common impurity at **m/z 42**. It is systematically detected when nitrogen is present in the gas phase: with only gases and with plasma, with the pure N_2 bottle or the N_2-H_2 bottle, in different reactors... Besides, its intensity is very reproducible. Junk and Svec (1958) had a similar observation and investigated its origin. They found that N_3^+ was formed inside the MS, by low probability endothermic reactions. This point does not impact our results, except at m/z 42 that we will not discuss further.

The experiment presented on **Figure III.3-3** has been repeated three times with exactly the same conditions and on different weeks. Results are **highly repeatable** as shown on **Figure III.3-4.**

neutrals - 5% H$_2$ - 1.3 mbar - 20 mA - plasma + sample
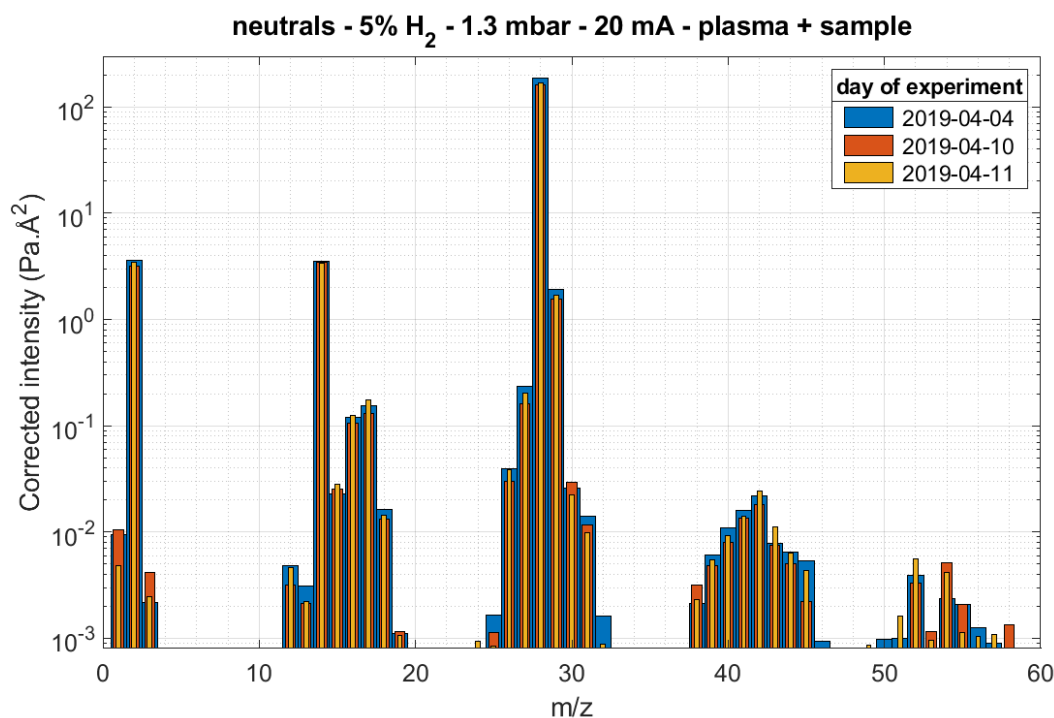
Figure III.3-4: Repeatability of the reference experiment on three different days. Situation with the sample added to the plasma. **Figure III.3-3** corresponds to day 2019-04-10.

The formation of HCN (and maybe CN) at 26 and 27 u is observed, as well as the formation of C$_2$N$_2$ at 52 u. These gas products have also been detected by Optical Emission Spectroscopy in Hong and Turban (1999) and by mass spectrometry in Hong et al. (2002) and Kurihara et al. (2006) as they exposed various (C:H) polymers to a N$_2$ plasma. Ishikawa et al. (2006) explains that in a N$_2$-H$_2$ plasma, CN and NH bonds are formed at the surface of the organic film. In particular, CN bonds submitted to ion bombardment form CN, HCN and C$_2$N$_2$.

Many other gas species are observed in our experiment, in the case of tholins exposed to a N$_2$-H$_2$ plasma. They can be due to the presence of nitrogen and various chemical structures in the tholins, contrarily to the (C:H) polymer films. **The main suspected molecule is acetonitrile CH$_3$-CN** with fragments from 38 to 41 u**.** Other molecules are suggested in **Table III.3-2**.

m/z	suggestion of attribution	m/z	suggestion of attribution
26	fragment HCN acetylene (C_2H_2) radical CN *fragment ethene* *fragment ethane*	40	fragment acetonitrile
27	**hydrogen cyanide (HCN)** *fragment ethene* *fragment ethane*	41	**acetonitrile (CH_3-CN)** *main fragment propene (C_3H_6)*
28	**N_2** *fragment ethylamine* *fragment dimethylamine* *fragment propane nitrile* *ethene (C_2H_4)* *main fragment ethane (C_2H_6)*	42	MS artefact *cyanamide (NH_2-CN)* *main fragment ethylenimine* *fragment propene*
29	N_2 isotope *methanimine (CH_2=NH)* *fragment ethane*	43	ethanimine (CH_3-CH=NH)* ethenamine (NH_2-CH=CH_2)* N-methylmethanimine (CH_2=N-CH_3)* fragment ethylenimine (cyclic-CH_2(NH)CH_2)
30	N_2 isotope main fragment methylamine (CH_3-NH_2) *main fragment ethylamine (CH_3-CH_2-NH_2)* *fragment ethane*	44	main fragment dimethylamine (CH_3-NH-CH_3) *fragment ethylamine*
31	fragment **methylamine**	45	fragment dimethylamine *fragment ethylamine*
38	fragment acetonitrile	52	**cyanogen (NC-CN)**
39	fragment acetonitrile *fragment propene* *main fragment butadiene (C_4H_6)*	54	propane nitrile (C_2H_5-CN) *fragment butadiene*

Table III.3-2: Suggestions of organic contributions of the MS peaks detected in **Figure III.3-4**. The fragmentation patterns of the molecules come from the NIST database. The ones unknown are marked with a *.

The results presented in **Figure III.3-3** and **III.3-4** were obtained with the **MS collecting head aligned with the plasma axis**, as shown in **Figure III.3-1** and **III.3-5**. In this configuration, **the plasma is only a few centimeters away from the MS**. **Then, the metallic collecting head is very close to the plasma and could induce some perturbations**.
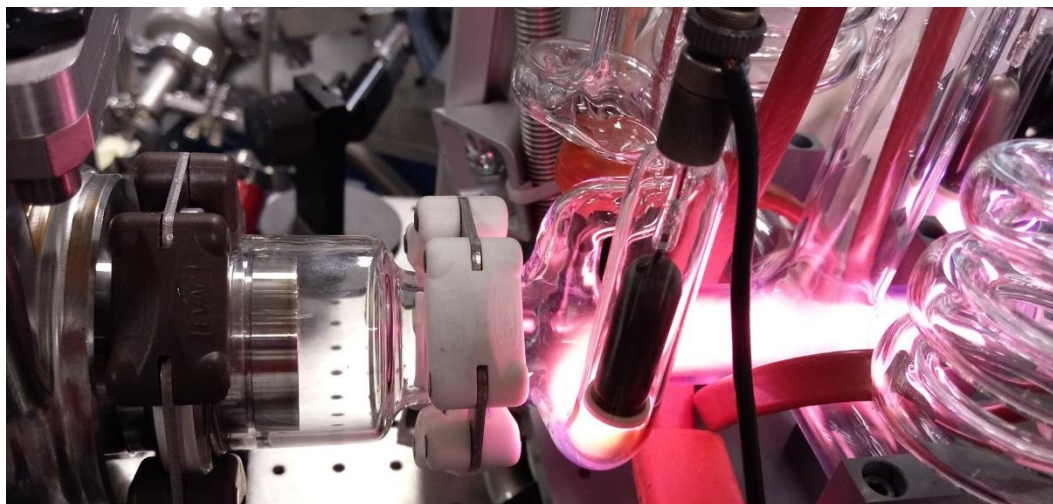
Figure III.3-5: Configuration with the MS collecting head close to the plasma (~5 cm).

To quantify this effect, two other experiments were conducted in the same reference conditions, but with the **MS collecting head further from the plasma** (at ~30 cm). It is the configuration presented on **Figure III.1-3** and **III.3-1**. The results (shown in **Figure III.3-6**) are globally identical. The main observation in the 'far' case is that ammonia is lost in greater quantity after the insertion of tholins. The **higher level of ammonia detected in the case closer to the plasma** suggests that it could be formed on the collecting head even if not directly in contact but close to the plasma. Indeed, ammonia is mainly formed by radical species that have a longer life time than excited species, and can easily reach the surface of the MS stick. We notice that in the case of a N_2-H_2 plasma without tholins (see **Section II.3.1.c**) the detection of ammonia does not depend on the distance of the MS stick to the plasma. The insertion of tholins disturbs the production of ammonia and certainly changes its production processes.

Similarly to the NH_3 modifications, peaks at **m/z 30 and 43** proportionally increase slightly in the 'close' configuration (see **Figures III.3-9/10/11**). According to **Table III.3-2**, both molecules certainly contain amines. On the opposite, **-C≡N containing species** are present in slightly higher proportions in the 'far' configuration: HCN (26-27 u), CH_3-CN (40-41 u) and C_2N_2 (52 u). In the 'close' configuration, molecules produced on the tholins have to go through 7-8 cm of plasma before reaching the MS. Contrarily, in the 'far' configuration they only have a few millimeters of plasma to cross. In this configuration, HCN, CH_3-CN and C_2N_2 are certainly less altered by the plasma in the gas phase.

Ion measurements (see **Section III.3.2**) can only be done in the 'close' configuration. Therefore, each of the two configurations ('close' and 'far') has its advantages and drawbacks: consistency with ion measurements versus ammonia surface catalysis. **To validate the results**

presented further, experiments have been performed at least once in each position. We observe globally the same trends in the two configurations with the variation of plasma parameters.
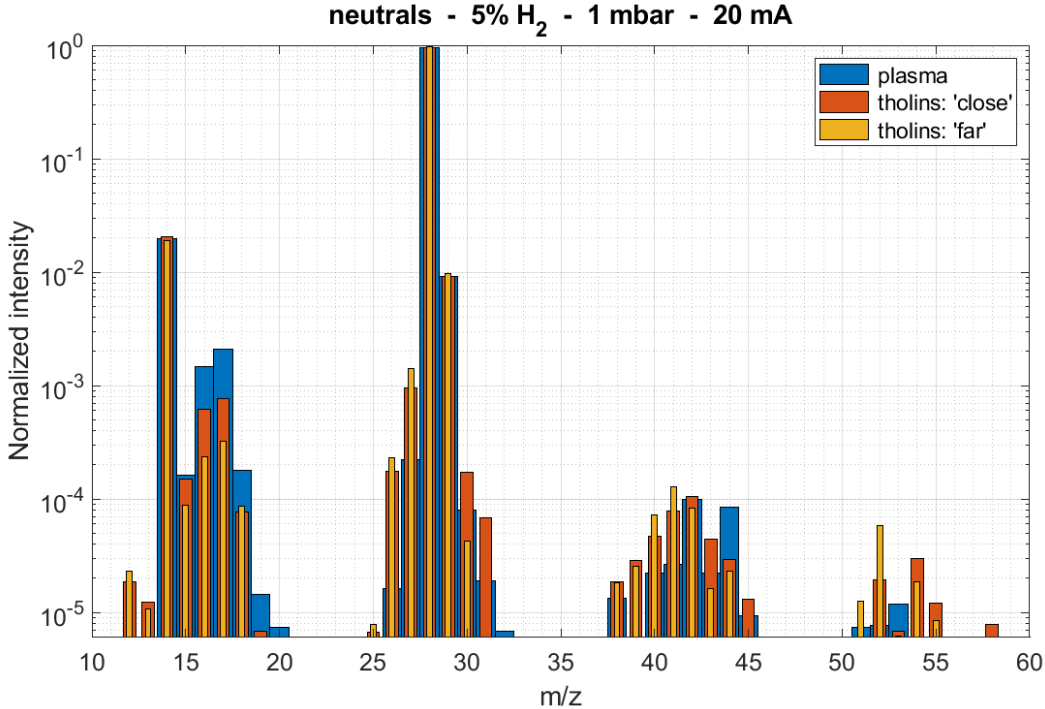
Figure III.3-6: Comparison of the spectrum acquired without tholins, identical in the configurations 'close' and 'far' (large blue bars), with the spectra acquired after the insertion of tholins in the configurations 'close' (medium orange bars), and 'far' (thin yellow bars).
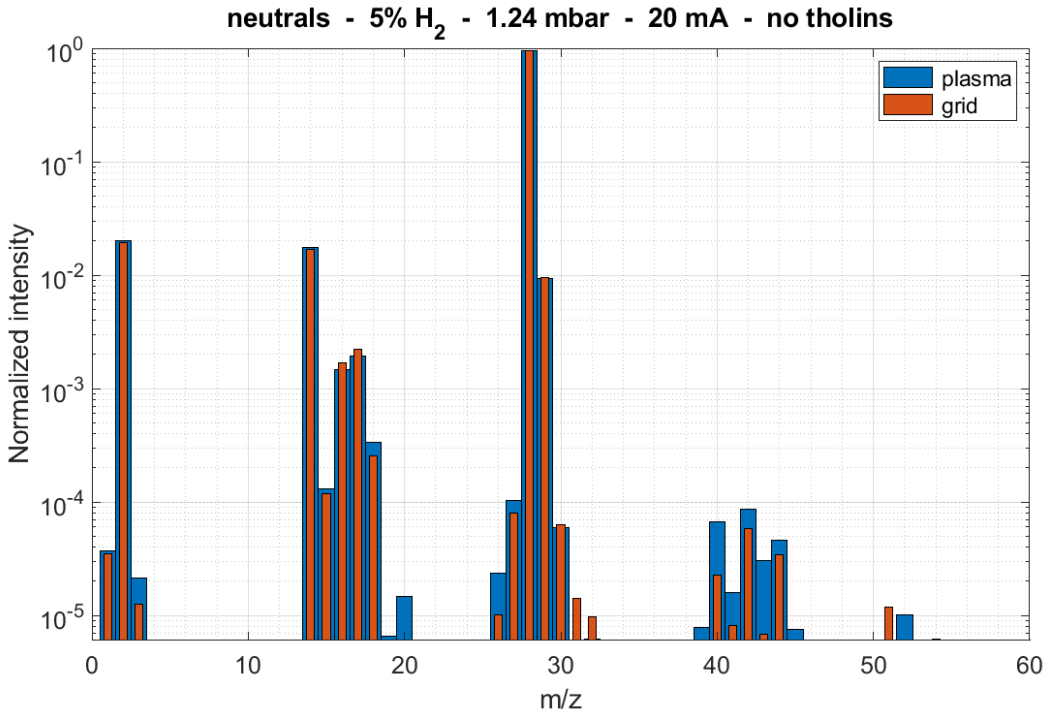
Figure III.3-7: Spectra obtained for the experiment in reference conditions in the 'close' configuration. Comparison of the spectrum acquired without tholins (large blue bars), with the spectrum acquired after the insertion of a grid without tholins (medium orange bars).

To confirm the effect of tholins on the plasma, an experiment was done without tholins on the grid. In this case, no changes have been detected with the addition of the sample, except perhaps a very slight increase of ammonia (x2), as shown in **Figure III.3-7**. The metallic grid certainly enhances the surface production of NH$_3$. In conclusion, all the effects observed previously are due to the presence of tholins.

3.1.b. Effect of the gas injected

In the previous section, we observed that the exposure of tholins to a N$_2$-H$_2$ plasma leads to the formation of new carbon-containing species. As no carbon is injected in the gas phase, it necessarily comes from the tholins. **To investigate the nature of the processes forming these new carbon-bearing molecules, we performed experiments with different gases**.

First, to examine the effect of H$_2$ and N$_2$ separately, we exposed tholins in a **pure N$_2$ plasma**. The spectra obtained are given in **Figure III.3-8**. Nearly **no modifications** are observed in the spectrum with the ignition of the plasma and the addition of the sample. In particular, traces of H$_2$O (18 u) are transformed into traces of H$_2$ (2 u) at the ignition of the plasma. In conclusion, the sole plasma species formed in a N$_2$ plasma do not affect tholins much compared to the N$_2$-H$_2$ plasma. The observations seen in the above section are thus not triggered only by plasma sputtering of pure N$_2$ plasma species. **The presence of H in the plasma is necessary to erode the tholins**, possibly through chemical reactions including H-bearing species.

In more details, **Figure III.3-8** shows a small increase at m/z 26, 27 and 52 attributed to HCN and C$_2$N$_2$. The formation of these species was also observed in Hong et al. (2002), Hong and Turban (1999) and Kurihara et al. (2006) with the exposure of (C:H) films to N$_2$ plasmas. Many works discuss the importance of the hydrogen for an enhanced film erosion (Ishikawa et al., 2006; Morikawa et al., 2003; Nagai et al., 2003, 2002; Van Laer et al., 2013). They conclude on a **synergistic effect induced by N$_2$ and H$_2$ plasma species. Nitrogen is added to the surface especially by N*, NH$_2$* and N$_2$*, then the ion bombardment leads to a release of H, forming the double and triple bonds C=C, C=N, C≡N, that finally lead to the stable products HCN and C$_2$N$_2$.** In particular, HCN requires H* and *NH$_2$ to form from -C≡N. Consequently, its production is enhanced by the presence of hydrogen in the gas phase. Otherwise, the surface is passivated by an accumulation of -C≡N bonds, explaining the lower etching rates in pure N$_2$ plasma.

For comparison, an experiment was performed in a **pure argon plasma.** Except traces of H$_2$, no new molecules were formed at the ignition of the plasma and with the addition of the tholin sample (see **Figure III.3-9**). Consequently, the processes eroding tholins require the use of hydrogen and nitrogen. **Tholins cannot just be decomposed into smaller molecules by sole ion bombardment; a combined nitrogen and hydrogen chemistry is required.** The experiment in argon also shows that **the observed effects in a N$_2$-H$_2$ plasma are not due to the increase in temperature** of a few 10s of degrees induced by the plasma discharge. Indeed, this increase is nearly identical in all cases, but no modifications are observed in pure argon.
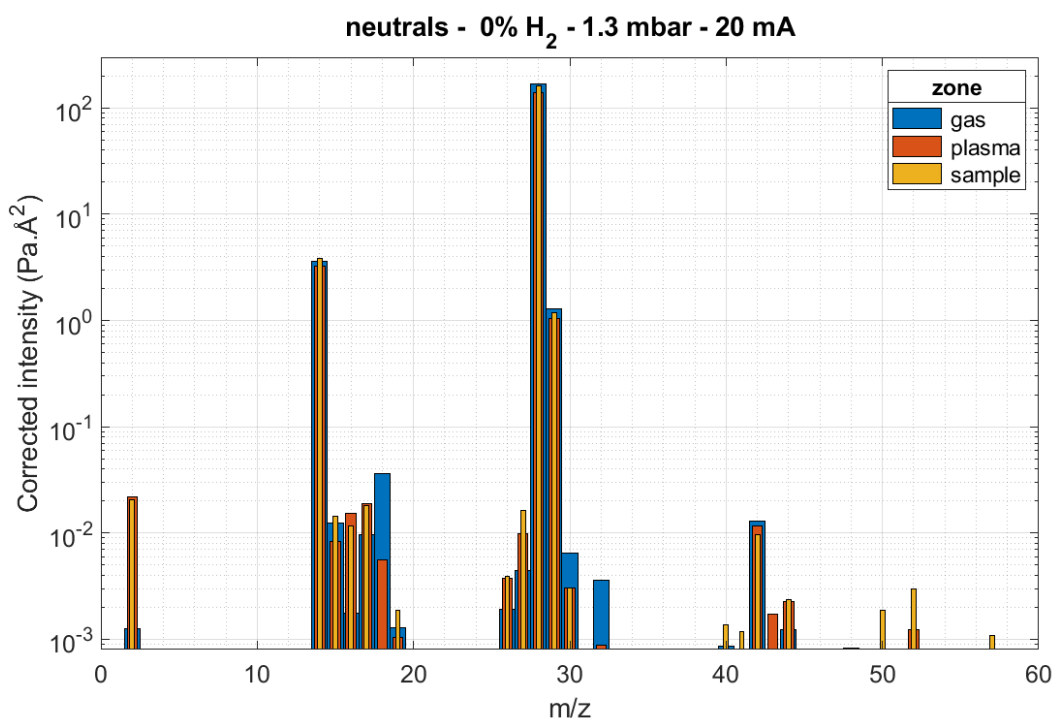
Figure III.3-8: Spectra obtained for the experiment in pure N₂ plasma: before plasma (large blue bars), after ignition and stabilization of the plasma (medium orange bars), and after the addition of the tholin sample (thin yellow bars).
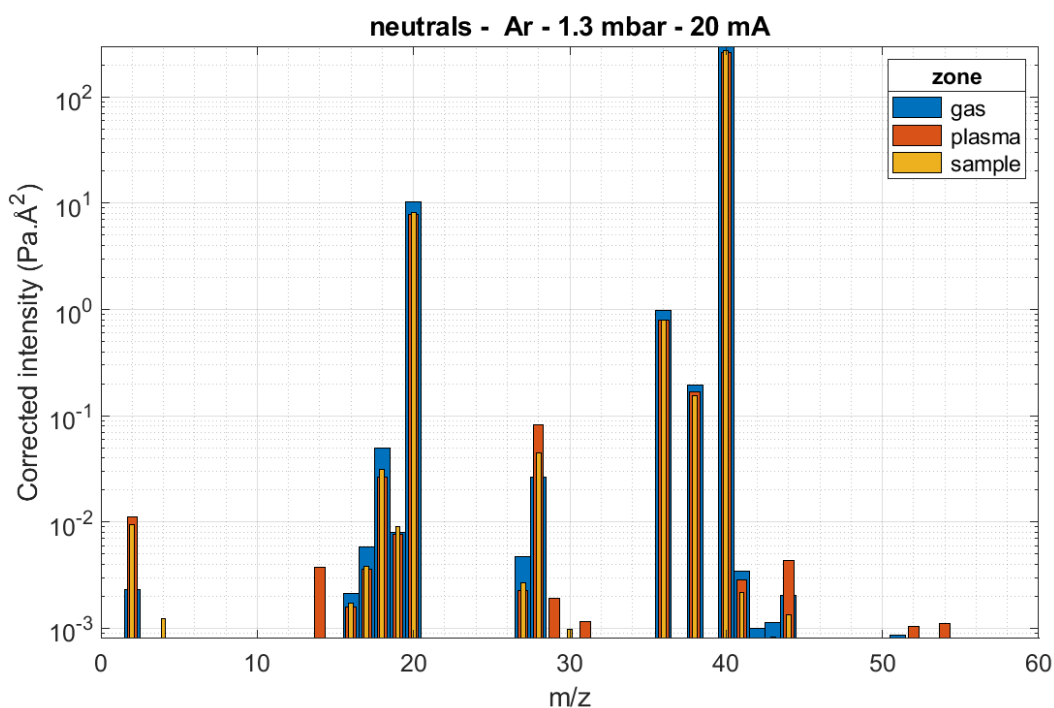
Figure III.3-9: Spectra obtained for the experiment in pure argon plasma. Argon isotopes and double ionized ions are found at m/z 18, 19, 20, 36, 38, 40. Water traces are found at m/z 17, 18. Nitrogen traces at m/z 28. Plasma leads to the formation of traces of H₂ (m/z 2), CO (m/z 28) and CO₂ (m/z 44).

3.1.c. Effect of the plasma parameters in N_2-H_2

THE QUANTITY OF H_2 INJECTED

To study more precisely the effect of the addition of H_2 in the gas phase, experiments with different amounts of H_2 (1%, 3% and 5%) were performed. To observe fine evolutions in the comparison of spectra, they are normalized over the cumulated intensities of all mass peaks. **Figure III.3-10** shows the spectra obtained when tholins are immersed into the plasma for different amounts of H_2 injected. The increasing amount of H_2 is easily observed at m/z 2.
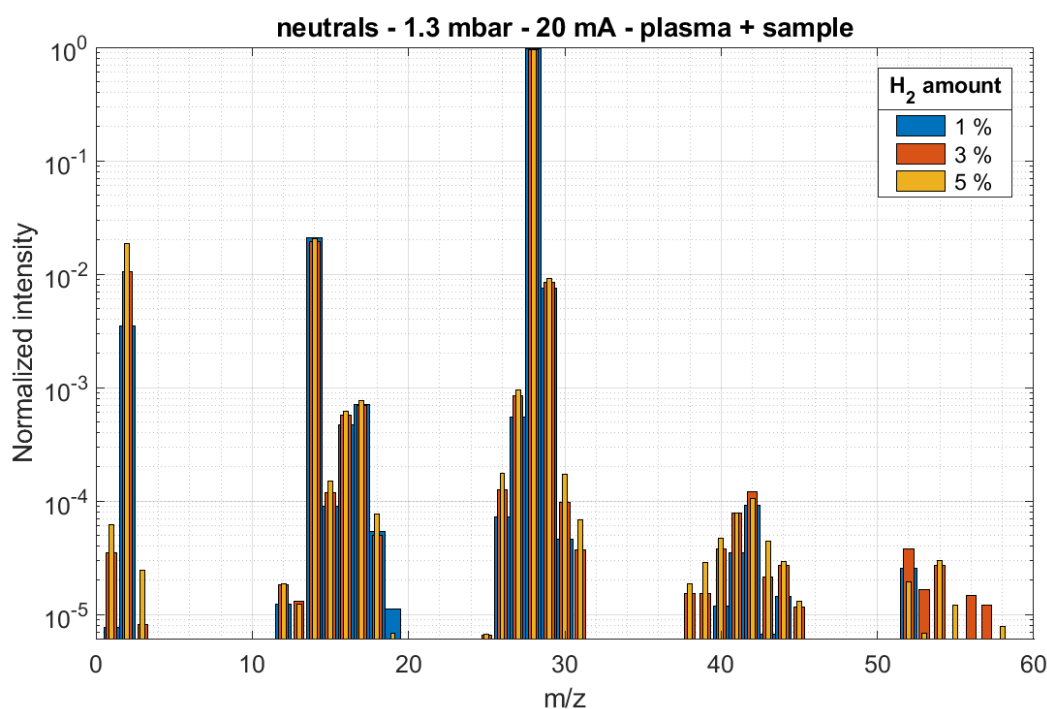
Figure III.3-10: Spectra obtained during the exposure of tholins to a N_2-H_2 plasma at different percentages of H_2. The MS is in the 'close' configuration.

We observe that the quantity of ammonia at m/z 16 and 17 is rather constant with the injected H_2 percentage, from 1 to 5%. This trend is similar to the one observed in the plasma without tholins (see **Section II.3.1.c**). On the other hand, **Figure III.3-11** shows that **many carbon-containing species at m/z 27, 26, 30, 39, 40, 41 and 43 grow quasi-linearly with the amount of H_2% injected**. The chemical pathways leading to their production depend directly on the hydrogen content in the gas phase.
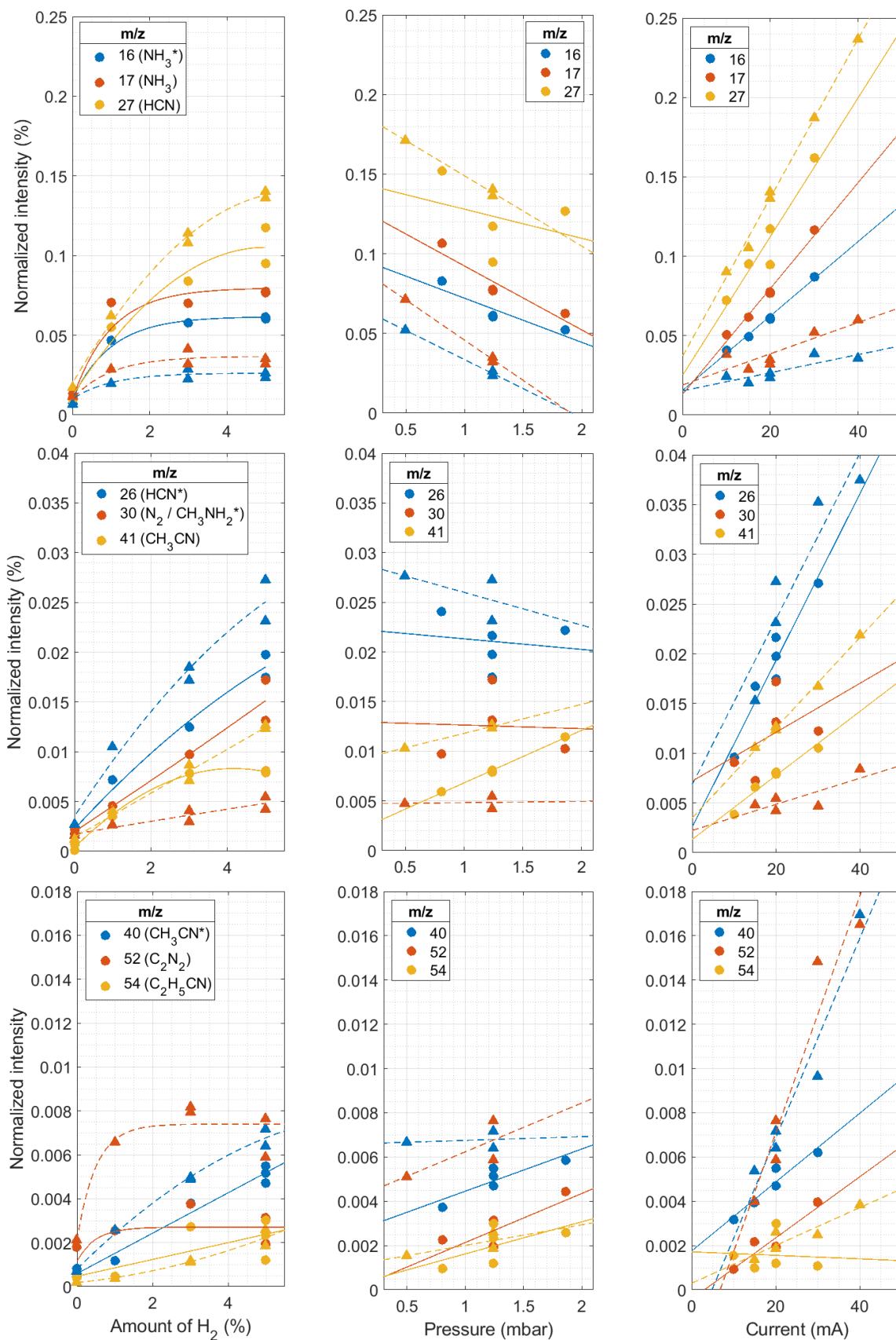
Figure III.3-11: Evolution of some masses with the H_2 amount, the pressure and the electric current, with reference conditions at 5% H_2, 1.3 mbar and 20 mA, in both the 'close' (circles) and the 'far' (triangles) configurations. The intensity is normalized to the sum of the intensities of all the masses. Suggested attributions are given in the first column. * indicates fragments.

A varying pressure has an effect on the production of the neutral species (see **Figure III.3-11**). Contrarily to experiments without tholins (see **Figure II.3-7 (b)**), the increase in pressure leads to a **decrease of the ammonia proportion** in the gas phase (at 16 and 17 u). More precisely, the ammonia partial pressure stays constant. The observations for HCN (at 27 u) are similar. On the other hand, the concentration of the carbon-containing species at 40 u, 41 u, 52 u and 54 u increase with pressure. **A higher pressure favors the formation of heavier species**.

E<small>FFECT OF THE CURRENT</small>

An increase of the electric current leads to a relative increase of many species, the main ones having peaks at m/z 16, 17, 26, 27, 38 to 41 and 52 (see **Figure III.3-11**). **A higher current enhances the chemical reactions and the formation of the new neutral species**. C_2N_2 at m/z 52 increases strongly especially in the configuration 'far'.

3.1.d. Conclusion: neutrals formed by the exposure of tholins to a N_2-H_2 plasma

The formation of the neutral products depends strongly on the plasma parameters. The same molecules are formed, but in varying quantities. This gives insights on the formation processes at stake. Results obtained in the previous section are synthesized in **Table III.3-3**.

Ammonia partial pressure is globally constant with the H_2 amount and the pressure. These two parameters are therefore not the limiting variables to the production of ammonia. Besides, ammonia is detected in higher quantity when the MS stick is close to the plasma. Ammonia is certainly formed also on its surface. The limiting parameters for the production of ammonia are the presence of surfaces and the current. This property of ammonia to form easily on metallic surfaces is discussed in Cui et al. (2009) as it could also have happened on INMS walls on Titan. **Due to this tendency to form on instrument walls or to stick on surfaces, ammonia is very difficult to quantify. Nevertheless, we show here that ammonia decreases strongly with the addition of tholins in the plasma. Ammonia or ammonia precursors are certainly destroyed by tholins or molecules formed from tholins.**

Effect of increasing: molecule (m/z)	H₂%	Pressure (in %)	Current	Distance to the MS head (in %)	Previous work on Titan
NH₃ (16, **17**)	constant	relative decrease, but partial pressure constant	linear increase	loss	observations: (Cui et al., 2009; Magee et al., 2009; Yelle et al., 2010) models: (Vuitton et al., 2019)
HCN (26, **27**)	increase	relative decrease, but partial pressure quasi constant	linear increase	increase	observation: (Waite et al., 2005) models: (Vuitton et al., 2019)
CH₃-CN (38-**41**)	linear increase	linear increase	linear increase	increase	observation: (Cui et al., 2009) tholins: (He and Smith, 2014) models: (Balucani et al., 2012; Vuitton et al., 2019)
NC-CN (**52**)	increase	increase	linear increase	increase	observations: (Cui et al., 2009; Waite et al., 2005) models: (Vuitton et al., 2019)
CH₃-NH₂ (**30**-31)	linear increase	~constant	~constant	small decrease	tholins: (He and Smith, 2014) models: (Vuitton et al., 2019)
CH₃-CH=NH CH₂=N-CH₃ NH₂-CH=CH₂ *cyclic*-CH₂(NH)CH₂ (**43**)	increase	~decrease	small increase or constant	small decrease	possible fragments of the structures proposed in (Pernot et al., 2010) model: (Balucani, 2012; Balucani et al., 2010)
C₂H₅-CN (**54**)	increase	~increase	small increase or constant	-	observation: (Magee et al., 2009) models: (Vuitton et al., 2019)

Table III.3-3: Global trends of the main products with the different plasma parameters. The last column refers to previous works done on the suggested molecules on Titan (observations, models or study of laboratory tholins).

HCN is the main product with the addition of tholins. It is likely to be **formed at the surface of tholins,** as it is the case for (C:H) polymers (see discussions above, i.e. **Section III.3.1.a**). Its formation is enhanced with increasing H_2 amount and electric current. These results are consistent, as higher H_2% and current values increase the formation of H*, in great part responsible of the formation of HCN at the surface of tholins. With increasing pressure HCN proportion decreases, while products containing the function -C≡N increase (i.e. CH_3-CN, NC-CN, NH_2-CN, C_2H_5-CN). **In conclusion, at higher pressure the formation of R-CN compounds is enhanced at the expense of the production of HCN in the gas phase**.

The majority of the other detected molecules contains carbon and nitrogen, $C_xN_yH_z$. Their formation increase with the amount of H_2 in the plasma, which confirms that their formation pathways require H*, H_2, H^+ or H-containing species. Their production is also increased with an increasing electric current. This is especially the case for CH_3-CN and C_2N_2.

3.2- Evolution of positive ions

3.2.a. General observations

During the experiment, positive ions were also measured by mass spectrometry. Ions were hardly collected in the 'far' configuration at ~30 cm from the plasma. Therefore, all measurements presented have been done **in the 'close' configuration**, at a few centimeters from the glow discharge. Collected intensities are corrected as discussed in **Section II.1.2** to obtain the normalized ion flux. Ions are collected at a few centimeters from the plasma glow, and are certainly slightly different from the ions at the center of the glow, next to the sample.

Figure III.3-12 presents the positive ion spectrum in the N_2-H_2 plasma, and its evolution with the insertion of the tholin sample. Many variations are observed, and in particular the **decrease of m/z 16, 17 and 18**, attributed mainly to the ammonia ions NH_2^+, NH_3^+ and NH_4^+. This is consistent with the decrease of ammonia discussed above. In addition, we observe the **increase** of some peaks and the apparition of new ones. It is especially the case of m/z 12, 13, 24 to 28, 36 to 41 and 52 to 54. These are **carbon-containing species**, thus formed from the interaction of the plasma with the tholins. Some attributions to these peaks are discussed in **Table III.3-4**.

An experiment done with a **grid sample without tholins** shows no variation to the N_2-H_2 plasma ion spectrum. The decrease of the ammonia ions and the apparition of the carbon-containing ions is entirely due to the presence of tholins.

The reference experiment at 5% of injected H_2, 1.3 mbar and 20 mA has been done three times, with a **good repeatability** of the observed ion peaks. **Figure III.3-13** superimposes the three spectra, to give an idea of the variability of the spectrum for given plasma parameters.
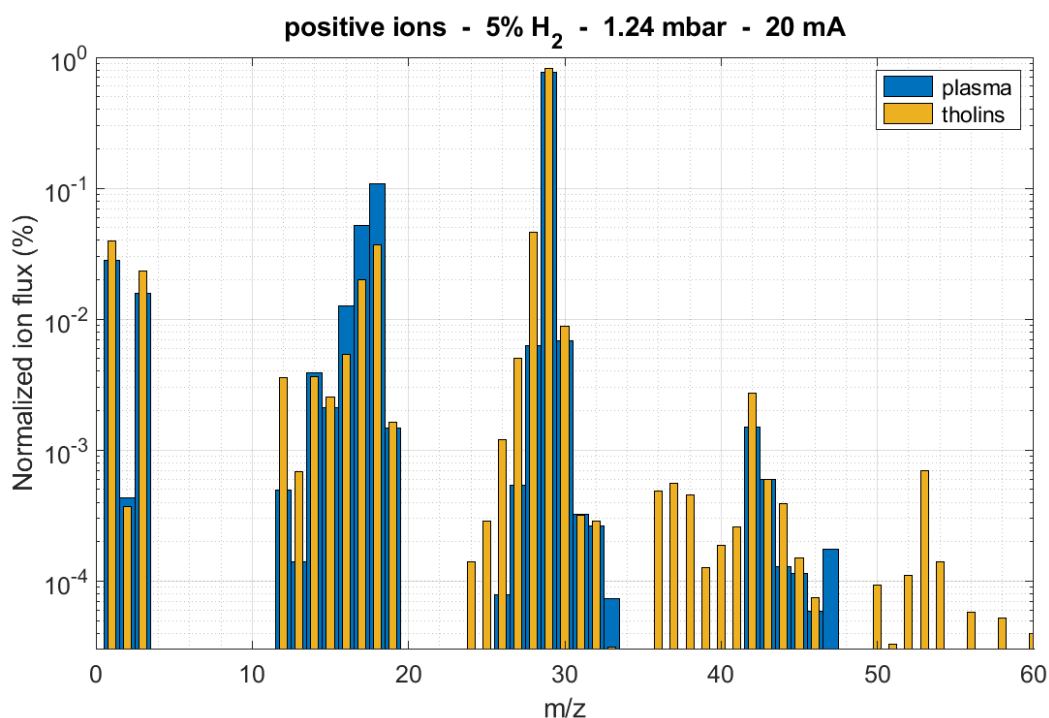
Figure III.3-12: Comparison of the positive ion spectra obtained in the reference experiment, in the N₂-H₂ plasma, and with the addition of tholins.
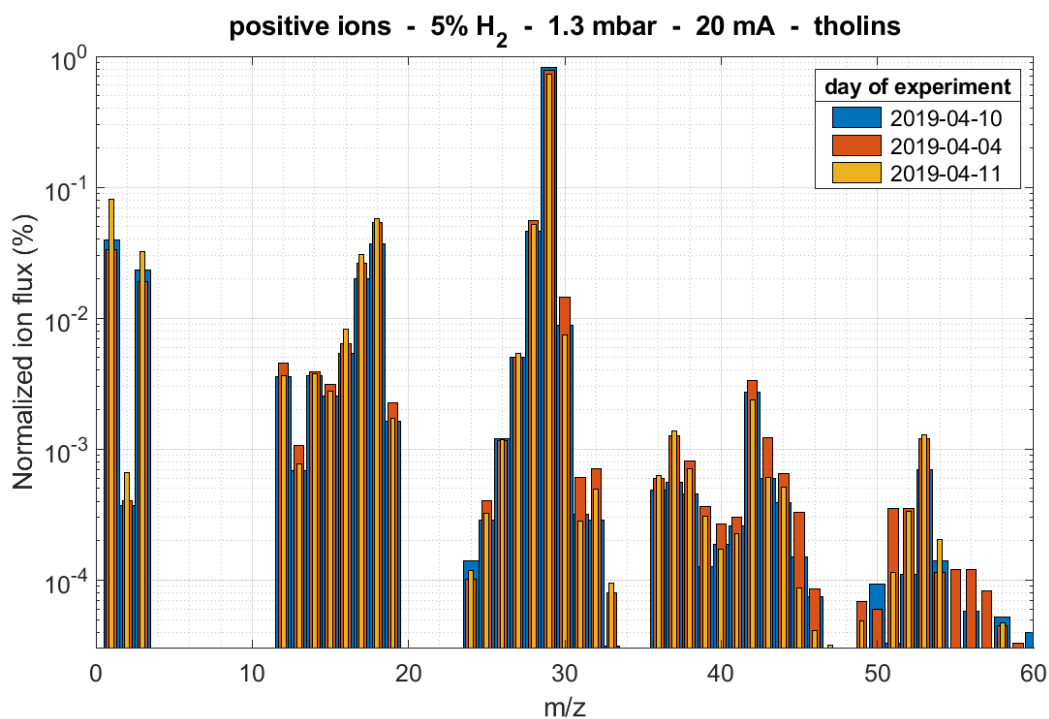
Figure III.3-13: Repeatability of the positive ion spectra obtained in the reference experiment with tholins.

3.2.b. Effect of the gas injected

Nearly no effect is observed in a pure N₂ plasma (see **Figure III.3-14 (a)**). The ignition of the plasma increases only slightly the amount of H_3^+, C^+, C_2^+, CN^+, HCN^+, $C_2N_2^+$. No variations are observed in argon plasma (see **Figure III.3-14 (b)**). These observations are consistent with the ones concerning neutrals. Therefore, **the evolutions shown in Figure III.3-12 require the presence of hydrogen and nitrogen in the gas phase. They are not due to direct decomposition by ion sputtering, similarly to the observations on the neutrals.**
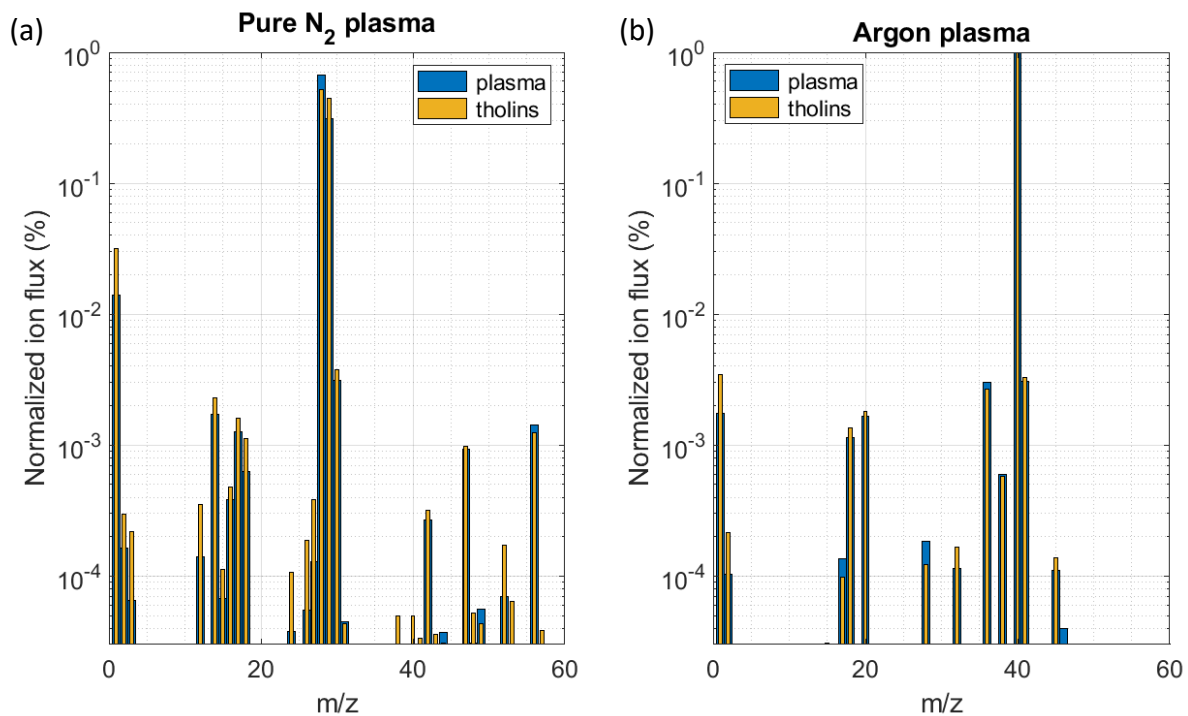
Figure III.3-14: Positive ion spectra obtained in (a) pure N_2 and (b) pure argon plasmas, and with the injection of tholins.

3.2.c. Effect of the plasma parameters in N₂-H₂

Figure III.3-15-16-17 shows the evolution of the ion spectrum with the plasma parameters. More details on the major ions are given in **Figure III.3-18**.

EFFECT OF THE INJECTED QUANTITY OF H₂

Figure III.3-15 shows the evolution of the ion spectrum in presence of tholins with the increase of the injected H₂ amount in the gas phase. We observe that **most of the ion species formed in the presence of tholins increase strongly**. This confirms the fundamental role of hydrogen in the erosion of the tholins. The heavier ions (m/z 42-43, 52-54) increase less than the lighter ones, especially m/z 3, 12-13, 15-18, 25-27 and 36-39. Ammonia ions (m/z 15-17) also increase, similarly to the case without tholins.

Effect of the pressure

Figure III.3-16 shows the evolution of the ion spectrum in presence of tholins with the increase of the pressure. This time, **the increase mainly concerns the heavier ions**: at m/z 36-39, 43, 49-53. Only a slight increase is observed at m/z 12-13 and 25-26. And similarly to the case without tholins (see **Section II.3.1.c**), H_3^+ decreases and the ammonia ions stay constant.

Effect of the current: fluorine contamination?

Figure III.3-17 shows the evolution of the ion spectrum in presence of tholins with the increase of the electric current. Similarly to the case without tholins (see **Section II.3.1.c**), it favors mainly the **formation of the ammonia ions** (m/z 16-18) and the formation of ions at m/z 19.

This peak at m/z 19 could be attributed to the enhanced desorption of protonated water. However, we suspect it comes from F^+ that could be formed at the higher current conditions by the sputtering of N_2^+ or N_2H^+ ions on the cathode (containing BaF_2) or the PTFE (polytetrafluoroethylene) junction present close to the MS collecting head (see **Figure III.3-5**). This observation can be linked to the detection of peaks at m/z 47, 66 and 85 in pure N_2 plasmas, that can be attributed to N_2F^+, $N_2F_2^+$ and $N_2F_3^+$. These three peaks are especially observed in the pure N_2 plasma case because the absence of hydrogen leads to a stronger N_2^+ sputtering on the cathode to obtain the same current. Therefore, we suspect that also in N_2-H_2 plasmas, fluorine-containing species could appear at the highest current conditions. In particular, $N_2F^+/C_2H_xF^+$ ions could explain the increase of m/z from 43 to 47 with the electric current, as well as NF^+/CH_xF^+ at 31-33 u and $NH_xF_2^+/CH_xF_2^+$ at 52 to 54 u. **For precaution, experiments at high electric current are not investigated further.**
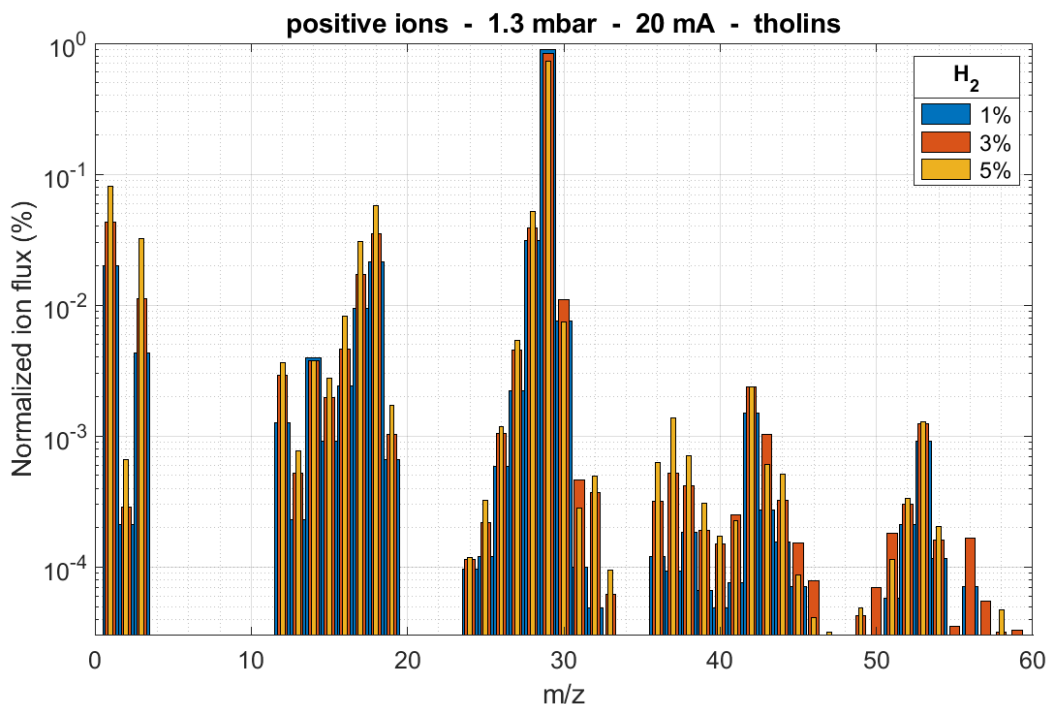
Figure III.3-15: Evolution of the positive ion spectrum in the presence of tholins with the increase of the injected H_2 amount in the gas phase.
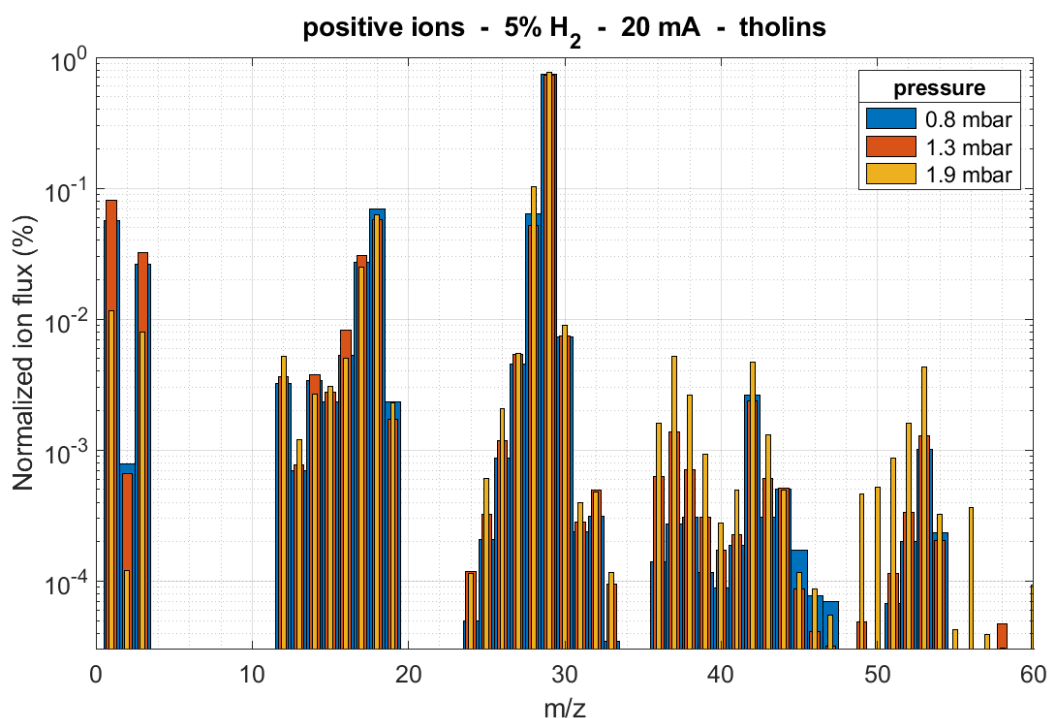
Figure III.3-16: Evolution of the positive ion spectrum in the presence of tholins with the increase of the pressure of the gas phase.
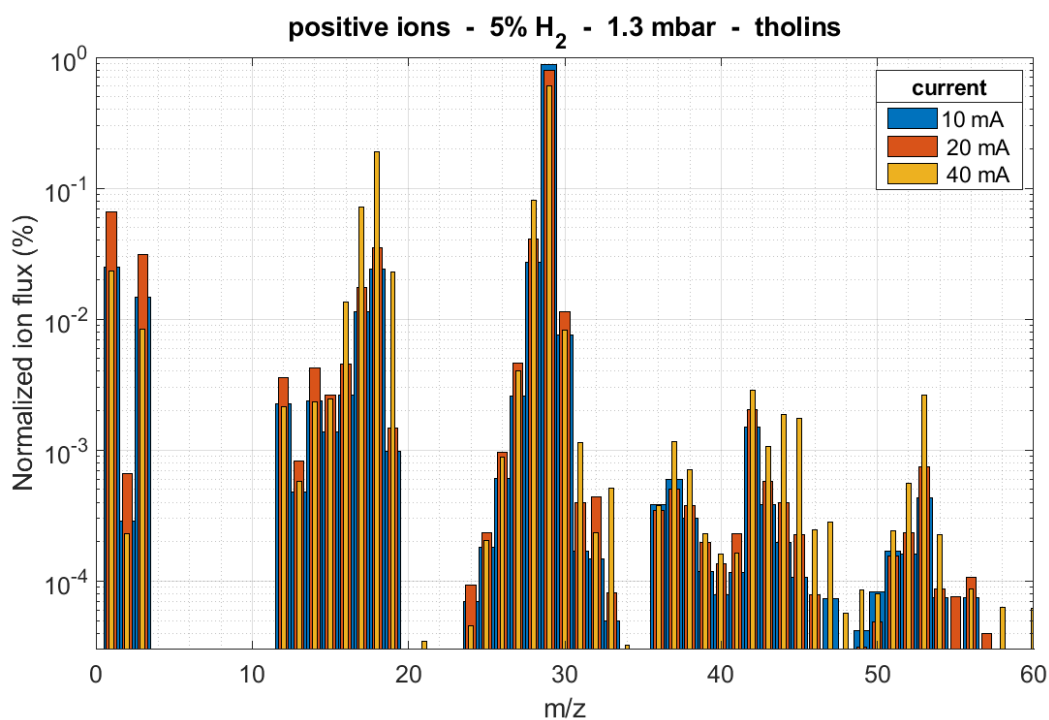
Figure III.3-17: Evolution of the positive ion spectrum in the presence of tholins with the increase of the electric current.
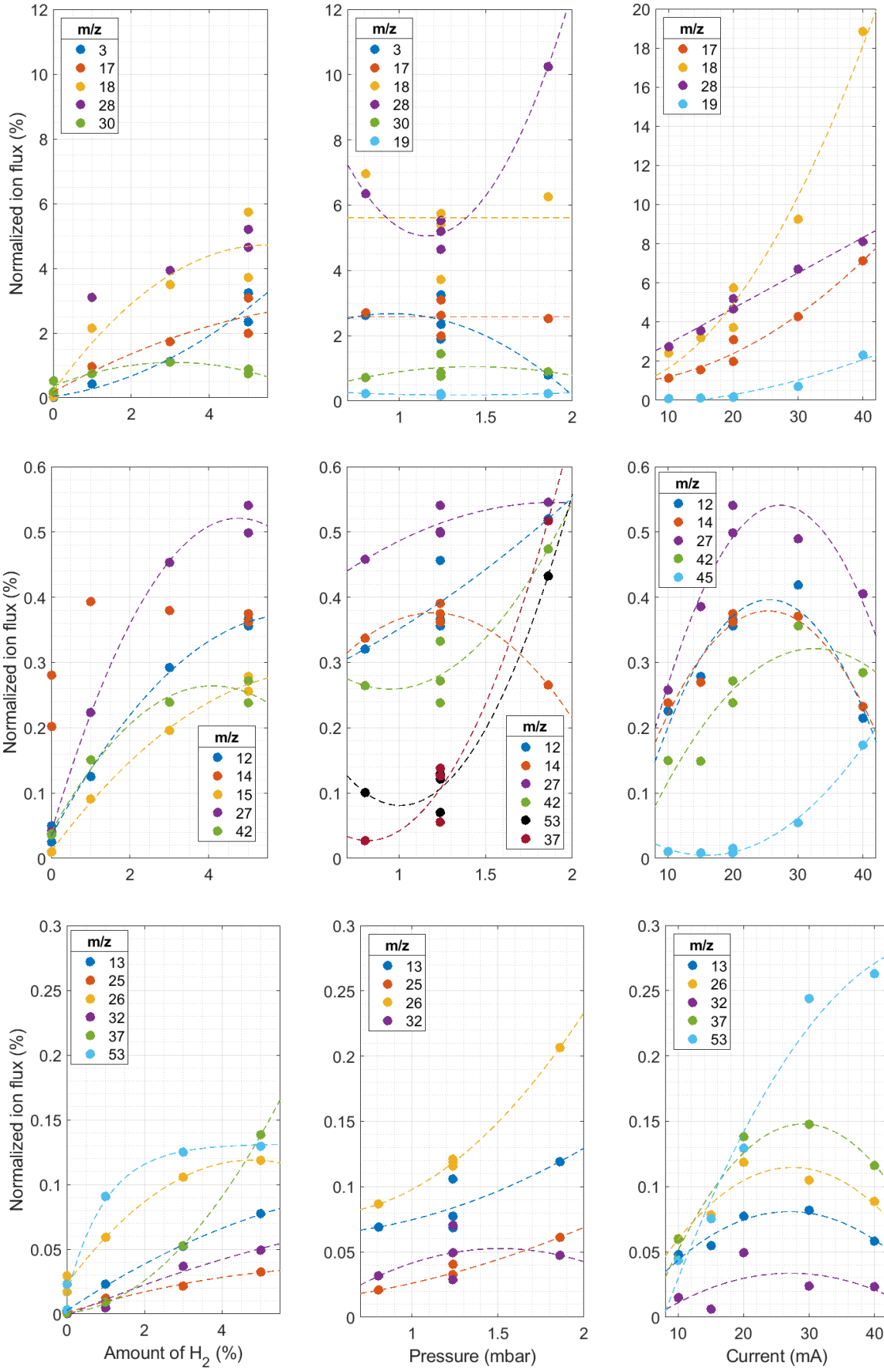
Figure III.3-18: Evolution of the main positive ions in the presence of tholins with the plasma parameters. The reference condition is at 5% H₂, 1.3 mbar and 20 mA.

Table III.3-4 collects all the observations presented above and associates possible ion attributions to each mass. These are discussed in the following paragraphs.

H$^+$, H$_2$$^+$, H$_3$$^+$

The hydrogen ions are formed in the N$_2$-H$_2$ plasma. Variations with the plasma parameters (H$_2$ %, pressure and current) are similar in the plasma alone or with tholins. Consequently, the dominant processes dictating the hydrogen ions are those of a N$_2$-H$_2$ plasma discharge (see discussion in **Section II.3.2**).

'C1 GROUP': NH$_x$$^+$ AND CH$_x$$^+$

N$^+$ and NH$_x$$^+$ ions are produced in the N$_2$-H$_2$ plasma. The addition of tholins in the plasma leads to a strong decrease of m/z 16, 17 and 18 (NH$_2$$^+$, NH$_3$$^+$ and NH$_4$$^+$). Nevertheless, these masses are still dominant, and their variations with the injected H$_2$ amount, pressure and current is similar to the ones without tholins (see **Section II.3.1**). This suggests that **the peaks at m/z 16, 17 and 18 are still mainly due to NH$_2$$^+$, NH$_3$$^+$ and NH$_4$$^+$.**

Nevertheless, new species also appear with the insertion of tholins. **m/z 12 and 13 are attributed to C$^+$ and CH$^+$.** They are strong indications of the presence of CH$_x$$^+$ ions. However, main ions as CH$_2$$^+$, CH$_4$$^+$ and CH$_5$$^+$ cannot be detected as the peaks at their respective masses are governed by N$^+$ (m/z 14), NH$_2$$^+$ (m/z 16) and NH$_3$$^+$ (m/z 17). On the other hand, as m/z 15 does not decrease with the insertion of tholins similarly to m/z 16, 17 and 18, we attribute it mainly to **CH$_3$$^+$**. Besides, its variation with plasma parameters is more similar to C$^+$ and CH$^+$ variations than those of m/z 16, 17 and NH$_4$$^+$.

The NH$_x$$^+$ ions variations are similar to those in plasma without tholins, but the variations of the CH$_x$$^+$ are different. While an increase in the hydrogen content increases the production of all the ions at m/z 12-13, 15-18, an increase of the pressure increases only the CH$_x$$^+$ ions. **CH$_x$$^+$ ions are therefore more easily extracted from tholins at higher pressure.** On the opposite, the increase of the current has mainly a strong effect on the ammonia ions. At higher currents, the production of the NH$_4$$^+$ ion is so efficient that it impacts strongly the total ion flux. This explains why the ratios of CH$_x$$^+$ decrease at higher pressure.

'C2 GROUP': N$_2$H$_x$$^+$, CNH$_x$$^+$ AND C$_2$H$_x$$^+$

The insertion of tholins in the N$_2$-H$_2$ plasma leads to a strong increase in the ions from m/z 24 to 28. On the other hand, m/z 30 to 33 do not change significantly. Besides, their evolution with plasma parameters are the same with and without tholins. This suggests that no main new species are formed from the interaction of the plasma with tholins at m/z 31 to 33. Nevertheless, peaks at m/z 29 and 30 are high, and could hide the formation of new ions.

The peaks at m/z 24 and 25 are attributed to C$_2$$^+$ and C$_2$H$^+$. This suggest the presence of others C$_2$H$_x$$^+$ ions, with x = 2 to 6. However, these ions have masses equal to other ions

certainly present in large quantities: **CN$^+$** at 26 u, **HCN$^+$** at 27 u and **HCNH$^+$** at 28 u. N$_2$H$^+$ prevents from detecting ions at m/z 29, as C$_2$H$_5^+$ or CH$_2$NH$^+$.

The peak at m/z 28 could also be attributed to N$_2^+$. Nevertheless, its variations with the plasma parameters are different from the case without tholins. It follows the variations of the peaks from m/z 24 to 27, sign that it is also created from the tholins. These carbon-containing species are produced with a higher efficiency if the injected H$_2$ amount and the pressure are increased. An increase followed by a decrease of the ion flux ratios are observed for the variations with the electric current. In conclusion, **the variations with the hydrogen amount, the pressure and the current are the same as for the CH$_x^+$ ions.**

'C3 GROUP': N$_3$H$_x^+$, N$_2$CH$_3^+$, C$_2$NH$_x^+$ AND C$_3$H$_x^+$

New ion species appear between m/z 36 and 41 with the addition of tholins to the N$_2$-H$_2$ plasma. Peaks at m/z 36, 37 and 38 are particularly important and are the sign the decomposition of the tholins in strongly unsaturated ions: **C$_3^+$, C$_3$H$^+$ and C$_3$H$_2^+$**. The last one can also be due to **C$_2$N$^+$**. The small peaks from **39 to 41 are certainly mainly due to the acetonitrile ions**, CHCN$^+$, CH$_2$CN$^+$ and CH$_3$CN$^+$, as we observed previously the presence of acetonitrile. However, these masses can correspond also to C$_3$H$_x^+$ ions and to CHCNH$^+$. **Similarly to the CH$_x^+$, C$_2$H$_x^+$ and CNH$_x^+$ ions, the ions at m/z 36 to 41 increase with the injected H$_2$ amount and the pressure**.

Peaks at masses from 42 to 46 are already present in the plasma without tholins (see **Section III.3.1**). They are certainly due to N$_3^+$ and N$_3$H$_x^+$ ions. Traces of CO$_2$, O$_2$ and carbon in the experiment can lead to small peaks at m/z 44 and 45 with CO$_2^+$ and CO$_2$H$^+$. In any case, with the insertion of tholins in the experiment, carbon-containing species may appear with masses between 42 and 46, in particular the ions linked to the neutrals observed at m/z 42 and 43 (see **Section II.3.1.c**). Acetonitrile can also lead to the formation of CH$_3$CNH$^+$ at m/z 42. However, as the variations of these peaks with the plasma parameters is identical to the variations without tholins, we cannot conclude on the possible new carbon-containing species.

'C4 GROUP': N$_4^+$, C$_2$N$_2$H$_x^+$, C$_3$NH$_x^+$ AND C$_4$H$_x^+$

The addition of tholins into a N$_2$-H$_2$ plasma also leads to a few heavier ions. The main one is at mass 53, surrounded by two smaller peaks at m/z 52 and 54. As C$_2$N$_2$ is a neutral detected in this experiment, we can legitimately expect the ions **C$_2$N$_2$H$^+$** at 53 u, C$_2$N$_2^+$ at 52 u and C$_2$N$_2$H$_2^+$ at 54 u. Besides, these peaks increase with H$_2$ amount, pressure and power, similarly to the molecule C$_2$N$_2$.

An increase in pressure reveals ions at m/z 49 and 50, attributed to C$_4$H$^+$ and C$_4$H$_2^+$/C$_3$N$^+$. In the neutral mode, the detection of C$_2$H$_5$CN suggests also the presence of related ions (C$_2$H$_x$CNH$_x^+$) at masses 53 to 56 in small quantities.

m/z	plasma N₂	plasma N₂-H₂	N₂-H₂ + tholins	↗ H₂ %	↗ pressure	attribution
2	-	+	+	↗↗	↘↘	H_2^+
3	-	++	++	↗↗↗	↘↘	H_3^+
12	-	+	**++**	↗↗	↗	C^+
13	-	-	**+**	↗↗	↗	CH^+
14	+	++	++	-	-	**N^+** - CH_2^+
15	-	+	+	↗↗	↗	NH^+ - **CH_3^+**
16	+	++	++	↗↗	-	**NH_2^+** - CH_4^+
17	+	+++	++	↗↗	-	**NH_3^+** - CH_5^+
18	+	+++	+++	↗↗	-	**NH_4^+** - H_2O^+
19	-	+	+	↗↗	-	H_3O^+
24	-	-	-	-	↗	C_2^+
25	-	-	-	↗↗	↗↗	C_2H^+
26	-	-	**+**	↗↗	↗↗	CN^+ - $C_2H_2^+$
27	-	+	**++**	↗↗	↗	HCN^+ - $C_2H_3^+$
28	+++	++	**+++**	↗	↗	N_2^+ - **$HCNH^+$** - $C_2H_4^+$
29	+++	+++	+++	↘	-	**N_2H^+** - CH_2NH^+ - $C_2H_5^+$
30	++	++	++	-	-	**$N_2H_2^+$** - **isotope N_2H^+** $CH_2NH_2^+$ - CH_3NH^+ - $C_2H_6^+$
31	-	-	-	↗↗	↗	$N_2H_3^+$ - $CH_3NH_2^+$ - NOH^+
32	-	-	-	↗↗	↗	$N_2H_4^+$ - $CH_3NH_3^+$ - NOH_2^+
33	-	-	-	↗	↗↗	$N_2H_5^+$ - NOH_3^+
36	-	-	**+**	↗↗↗	↗↗↗	C_3^+
37	-	-	**+**	↗↗↗	↗↗↗	C_3H^+
38	-	-	**+**	↗↗	↗↗↗	C_2N^+ - $C_3H_2^+$
39	-	-	-	↗↗	↗↗↗	$CHCN^+$ - $C_3H_3^+$
40	-	-	-	↗↗	↗↗	$CHCNH^+$ - CH_2CN^+ - $C_3H_4^+$
41	-	-	-	↗	↗↗	CH_3CN^+ - $C_3H_5^+$
42	+	+	++	↗	-	N_3^+ - $N_2CH_2^+$ - CH_3CNH^+ - $C_3H_6^+$
43	-	+	+	↗	↗↗	N_3H^+ - $N_2CH_3^+$ - $C_2H_3NH_2^+$ - $C_3H_7^+$
44	-	-	**+**	↗↗	-	$N_3H_2^+$ - $C_2H_5NH^+$ - $C_3H_8^+$
45	-	-	-	-	-	$N_3H_3^+$ - $C_2H_5NH_2^+$ - $C_3H_9^+$ - CO_2H^+
46	-	-	-	-	-	$N_3H_4^+$ - NO_2^+
49	-	-	-	-	↗↗	C_4H^+
50	-	-	-	-	↗↗	C_3N^+ - $C_4H_2^+$
51	-	-	-	↗	↗↗↗	HC_3N^+ - $C_4H_3^+$
52	-	-	-	↗	↗↗↗	**$C_2N_2^+$** - HC_3NH^+ - $C_4H_4^+$
53	-	-	**+**	↗	↗↗↗	**$C_2N_2H^+$** - $C_2H_3CN^+$ - $C_4H_5^+$
54	-	-	-	↗	-	CN_3^+ - **$C_2N_2H_2^+$** - $C_2H_3CNH^+$ - $C_4H_6^+$

Table III.3-4: Positive ions peaks detected in N₂ and N₂-H₂ plasmas with tholins, their evolution with plasma parameters, and their suggested attributions. '+++' is for an ion flux > 3%, '++' for [0.3 ; 3]%, '+' for [0.03 ; 0.3]% and '-' for < 0.03%. '↗↗↗' is for x6+, '↗↗' for x3, '↗' for x2. Grey boxes show trends also observed in plasma without tholins. Red '**+**' in the fourth column indicates the masses strongly increased by the insertion of tholins. The main molecules suspected at a given mass are indicated in bold in the attribution column.

Tanarro et al. (2007) **studied the ions of a H_2-N_2-CH_4 DC glow discharge.** They also observed NH_x^+, CH_x^+, $C_2H_x^+$, $HCNH^+$ and CH_3CNH^+ ions. **The formation of these ions is directly linked to the addition or the loss of a proton to/from neutral molecules**: NH_3, CH_4, C_2H_2, C_2H_4, C_2H_6, HCN and CH_3CN. In our experiment, CH_4 is not injected in the gas phase, the $C_xH_y^+$ species come from fragments of tholins. In particular, $C_xH_y^+$ with smaller values for y are present in high quantity. Tanarro et al. (2007) suggest that their non-detection of CN and C_2N_2 is due to their high content in hydrogen (95%). On the opposite, **$HCNH^+$** does not react with H_2 and N_2 and accumulate in their experiment. This can also explain the strong peak detected at m/z 28 in our experiment.

As previously discussed in **Section III.1.1.b**, **the etching of organic (C:H) films and polymers by N_2 and N_2-H_2 plasma discharges leads to the formation of new gaseous species**. The main molecules detected are CN, HCN and C_2N_2 (Hong et al., 2002; Hong and Turban, 1999; Ishikawa et al., 2006; Kurihara et al., 2006), coming from the formation of the C≡N bond at the surface of the sample (Nagai et al., 2003, 2002). Van Laer et al. (2013) modelled the erosion of the films and predicted the following ions: N_2H^+, N_2^+, H_2^+, NH^+, N^+, H^+, NH_2^+, NH_3^+, H_3^+, NH_4^+, CH_3^+, CH_4^+, HCN^+, CH_2^+, CH^+, C^+. **All those species are consistent with the observation of the erosion of tholins in THETIS. Nevertheless, heavier species are also detected here, as $C_3H_x^+$, CH_3CNH^+, $C_2N_2H^+$, which could come from fragments directly extracted from tholins.**

3.3- Suggestion of surface processes and conclusions relevant for Titan

3.3.a. The surface processes in the experiment

Here we suggest some surface processes that could appear on tholins. They are strongly inspired by the surface model described by Van Laer et al. (2013), studying (C:H) films exposed to a N_2-H_2 plasma. We extended them to the case of tholins that contains also nitrogen. **Figure III.3-19** synthesizes these processes in a schematic.

SURFACE CHEMISTRY GOVERNED BY RADICALS

A first important process is the **adsorption of neutral nitrogen on the surface**. It comes mainly from the radical N, and NH and N_2 in a lower measure. Then, it reacts with the surrounding carbon and nitrogen atoms to form double and triple bonds. Studies of (C:H) films mention essentially **C≡N bonds**. However, in the case of tholins we can also consider N=N and N≡N bonds.

Contrarily to NH, NH_2 is more likely to extract hydrogen from the tholin material to form the stable molecule **NH_3**.

Neutrals containing hydrogen, namely H, NH and H_2, also attach to the surface, and **hydrogenate** the surrounding functions, in particular the unsaturated ones. Thus, it forms $CH_{x+1(s)}$ from $CH_{x(s)}$, up to the production of the stable molecule $CH_{4(g)}$. The hydrogenation of $C{\equiv}N_{(s)}$ gives $HCN_{(s)}$. **Amines** are also formed at the surface (Ishikawa et al., 2006).

Therefore, **N, H and NH are actively used to form $HCN_{(s)}$, instead of NH_3** in the case without tholins. This could explain the decrease of ammonia in the gas phase at the insertion of the tholin sample.

Nitrogen plasma are known for their massive production **of metastable and vibrationally excited species** (Guerra et al., 2004). Such species are reactive, though less than radicals, and present in large quantities. Consequently, they can also play a quantitative part in the surface chemistry described above.

Ion sputtering to extract molecules from the tholins

The surface chemistry described above leads in particular to the formation of $HCN_{(s)}$. However, if HCN is a stable molecule, it would not desorb without supplementary energy. The sputtering by heavy nitrogen ions (N_2^+ and N_2H^+) is required to desorb HCN. Otherwise, it would form a passivation layer at the surface of the sample grains.

Ion sputtering is necessary to erode the grains. However, the surface chemistry induced by the hydrogen does the up-front work. Indeed, it forms small stable molecules from the complex organic structure of the tholins. These small molecules are then easier to desorb by ion sputtering. This explains why only few molecules and ions are observed in the gas phase with the exposure of tholins to a pure N_2 plasma.

Unlike neutral species, ions are sensitive to the electric field in the sheath surrounding the tholins. They are strongly accelerated perpendicularly towards the surface. They **bombard the surface** and physically eject small pieces not strongly attached to the main structure of tholins.

Studies on (C:H) films observe the desorption of CN, HCN and C_2N_2. In the case of tholins, we observe many more molecules and ions. They could be formed afterwards in the gas phase. Nevertheless, most of the species in the gas phase are N_2-H_2 products and could not lead to the formation of complex organic species. Therefore, we suggest that **at least part of the complex species observed are directly desorbed from tholins**. This is in particular the case of CH_3CN, C_2N_2, CH_3NH_2, the molecules suggested at m/z 43 and 54, and their corresponding ions. Besides, these molecules can be easily extracted from identified structures of tholin fragments analyzed by high-resolution mass spectrometry. In particular, He and Smith (2014) and Pernot et al. (2010) suggest amino-acetonitrile ($NC-CH_2-NH_2$) that could either give acetonitrile (CH_3CN) or methylamine (CH_3NH_2). Acetamidine ($CH_3-C(NH_2)=NH$) can lead to ethanimine ($CH_3-CH=NH$). m/z 44 could maybe also be due to $NH_2-CH=NH$ extracted from guanidine ($NH_2-C(NH_2)=NH$). Various molecules can similarly be extracted from cycles as methylimidazole and vinylimidazole.

THETIS ion spectra show the presence of **strongly unsaturated ions**, namely C^+, CH^+, C_2^+, C_2H^+, C_3^+, C_3H^+. These are probably directly extracted by the ion sputtering as secondary ions. They

can perhaps correspond to the remaining parts of a cycle or a strongly unsaturated structure that has partly reacted with radicals in the processes presented above. As they are not observed in pure N_2 plasma exposure, we suspect that the hydrogen chemistry plays a role in the formation of these ions.
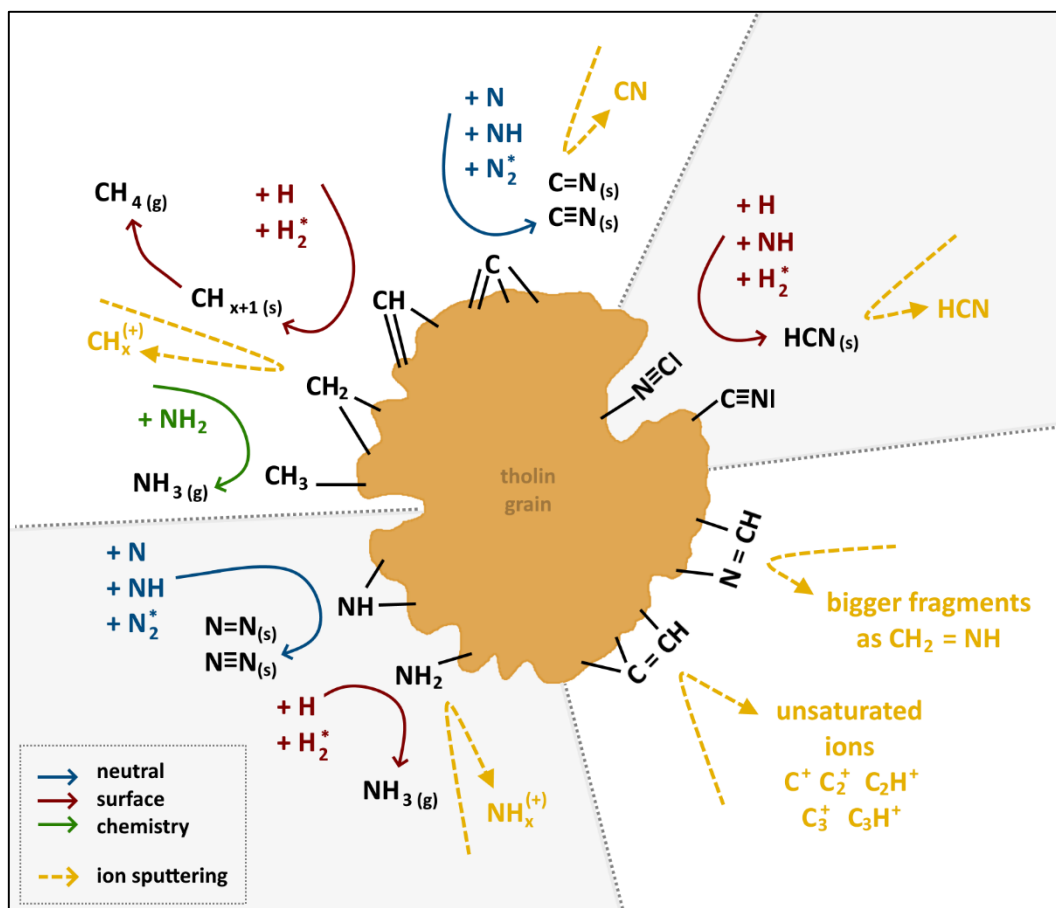
Figure III.3-19: Suggestion of surface processes on a tholin grain exposed to a N_2-H_2 plasma. The two upper parts come from Van Laer et al. (2013) and the two lower parts are suggestions inspired from THETIS observations.

EFFECT OF THE PLASMA PARAMETERS

At higher pressure, more reactive species are present, and therefore the **processes are accelerated**. However, the reduced electric field E/N is smaller, which decreases the average electron energy that could break heavy tholin fragments in the gas phase. At higher pressure the sheath is more collisional and thus ions reaching the surface are less energetic. The sputtering is consequently **less destructive**. This explains the increased proportion of carbon-containing products, and especially the strong increase of the heavier ones.

As discussed above, **H_2 plays a fundamental role** in the chemical erosion of tholins. An increase of the hydrogen content between 0 to 5% therefore increases the hydrogen-induced chemistry at the surface of the tholins. It explains the **increase of gas species produced** from tholins, and tends to form smaller species.

The processes described above are in complete agreement with the evolution of the IR absorption spectrum of tholins studied in **Section III.2**.

First, as observed by the SEM images and the absolute absorbance, the tholins on the sample are **physically eroded** and removed from the pellet. This loss is realized by the combined effects of the chemical surface alteration by the radicals, and the ion sputtering.

Secondly, the **chemical evolutions observed by IR absorption are consistent with the chemical processes happening at the surface of grains**. The bands of nitriles around 2100-2250 cm^{-1} (4.76-4.44 µm) are easily extracted in the gas phase as HCN, explaining their quickest erosion than the other bands. Besides, isonitriles (2135 cm^{-1}/4.68 µm), the most unstable nitriles are lost in the first place. The study of the IR absorption also showed the apparition of a new nitrile band at 2210 cm^{-1} (4.52 µm), which could be attributed to the new C≡N bonds forming at the surface of the tholins, with the processes presented just above. The decrease of C=N bonds (1665 cm^{-1}/6.01 µm) and of CH_3 bonds possibly linked to >CH-CN (2950 cm^{-1}/3.39 µm) are also consistent with the processes discussed above, in which C=N are transformed into C≡N bands and HCN and CH_3-CN desorbed into the gas phase.

3.3.b. Conclusions relevant for Titan

RADICALS IN TITAN'S IONOSPHERE

Radicals and excited species are also present in quantity in planetary ionospheres (Majeed et al., 2004, 1991). Nevertheless, they are complicated to measure and there had been only few detections. However, models of the upper atmosphere, especially of Titan, suggest that **radicals and excited species play an important role in the ionospheric chemistry** (Vuitton et al., 2019). Lavvas et al. (2011a) studied the formation of the main radicals and excited species in Titan ionosphere, including photoionization of H_2 and N_2. In particular, between 1000 and 1200 km, the radical H is present at 0.1%, N at 0.01%, and NH and NH_2 at a ratio of 10^{-6}.

Therefore, atomic H is present in quantity in the ionosphere. Sekine et al. (2008a, 2008b) studied the **interaction between atomic H and tholins**. They observed a strong loss of H atoms by heterogeneous processes, mainly from **hydrogenation and H_2 recombination**, and only slightly from chemical erosion. They suspect that 60 to 75% of hydrogen atoms are removed from the gas phase by these processes in the stratosphere and the mesosphere. Contrarily to the hydrogenation process that adds an H atom in the structure of the tholins, the H_2 recombination removes a H atom present in the tholins structure. Therefore, it enables also the formation of unsaturated structures. We went further with the THETIS experiment, by adding N-bearing radicals and ions to the gas phase, and found that they work in close combination with the H radicals at the surface of tholins.

Lavvas et al. (2011b) also observed the **importance of radical-including chemistry in the formation of the aerosols**. However, they only focus on **'heavy' radicals**, as C_2H, CN and HCCN. Such radicals lead to the formation of heavier species in the gas phase that ultimately adsorb on aerosols, or directly adsorb themselves on the aerosols.

As H and N radicals, as well as others N_2, H_2, N_xH_y radicals or excited species, are strongly represented in Titan's ionosphere, we suspect that the processes described in **Section III.3.3.a** could also happen up to a certain extent on Titan's ionospheric aerosols. In particular, we are able to make two suggestions.

First, the **H and N radicals could induce a chemistry at the surface of the aerosols.** N would lead to the addition of nitrogen at the surface that would evolve into double and triple bonds between N and an atom of the aerosol structure, in particular forming C≡N. It would produce new unsaturated structures at the surface of the aerosol. On the other side, H adsorption would hydrogenate some other parts of the surface. Then, aerosol structure would continuously evolve during its growth in the ionosphere.

Secondly, the **aerosols could also exchange small fragments with the surrounding gas phase**. Sputtering induced by collision with energetic species could desorb small molecules or ions from their surface. It could especially lead to HCN and R-CN gas species.

Quantitatively, the pressure in Titan's ionosphere is lower than in the THETIS experiment. However, the electron density measurements in **Section II.3.1.b** shows that the **ionization degree** is similar. This suggests a similar equilibrium between the chemistry induced by neutrals and ions. The **sheath** induced by the grains on Titan is not collisional at such low pressures. The acceleration of ions toward the surface depends mainly on the charge of the aerosols, which is likely to evolve with altitude (Shebanits et al., 2016). It would be interesting to model the energy of the incoming ions on Titan's aerosols and compare it to laboratory values. Concerning **radicals**, estimations in THETIS plasma conditions give radical mixing ratios about one order of magnitude higher than the model results on Titan (~1% for H and N, ~10^{-4} for NH and ~10^{-5} for NH_2) (V. Guerra, *private communication*). These values will have to be experimentally measured in THETIS. Nevertheless, higher radical ratios (x10) would increase the surface chemistry induced by radicals on the grains in THETIS compared to Titan.

The THETIS experiment shows the increase in the production of tholin-extracted species in the gas phase with increasing pressure and hydrogen content. Both variations are anti-correlated on Titan, with the increase of hydrogen at higher altitudes, while pressure decreases. However, in THETIS we observed heavier molecules desorbed with increasing pressure and decreasing H_2 amount. This suggest a desorption of heavier molecules at lower altitude on Titan.

COMPARISON TO INMS SPECTRUM

The ions observed in THETIS have all been detected in Titan's ionosphere by the mass spectrometer of Cassini, INMS (Magee et al., 2009; Mandt et al., 2012; Waite et al., 2007). This validates the fact that the processes going on in THETIS could also be part of the complex Titan chemistry. **Figure III.3-20** shows a comparison of a THETIS spectrum to a spectrum by INMS at 1016 km on Titan during the T40 flyby.

The chemistry happening in Titan's ionosphere is very complex. Models up to now essentially focus on the gas phase chemistry. However, a strong disagreement between model results and Cassini data on nitriles led the latest models to take into account the sticking of the polar molecules (nitriles) and of H atoms onto the aerosols. Aerosols are used as a sink of molecules/atoms. Nevertheless, **no model investigated the evolution of the chemical structure of the aerosols after the adsorption of these species. They do not either include the possibility of aerosols to give back small organic molecules in the gas phase.** A further investigation on such heterogeneous processes happening at the surface of aerosols could bring some insights, especially concerning the **HCN and CN-bearing molecules** present in Titan's ionosphere.

Besides, the main ion peak detected by INMS is attributed to HCNH$^+$. Models predict that HCNH$^+$ comes mainly from the protonation of HCN. HCNH$^+$ is an ion of fundamental importance in the complex chemistry going on in Titan's ionosphere. We observe also a strong production of HCN, and HCNH$^+$ in the THETIS experiment, with the exposure of tholins to N$_2$-H$_2$ plasma species. As both N$_2$-H$_2$ plasma species and organic aerosols are present in Titan's ionosphere, we suspect that the processes leading to the formation of CN and HCN at the surface of aerosols could also happen on Titan. HCNH$^+$ is an important species on Titan and its production is not yet well constrained (Vuitton et al., 2019; Westlake et al., 2012), therefore it is worth investigating these new heterogeneous formation processes.

Apart from HCNH$^+$, the THETIS experiment leads also to the formation of **acetonitrile, cyanogen and their protonated ions**: CH$_3$CNH$^+$ (m/z 42) and C$_2$N$_2$H$^+$ (m/z 53). These molecules / ions are also found in high quantities on Titan. This suggests that they could be bricks forming the aerosols and ejected back in the gas phase after ion sputtering.
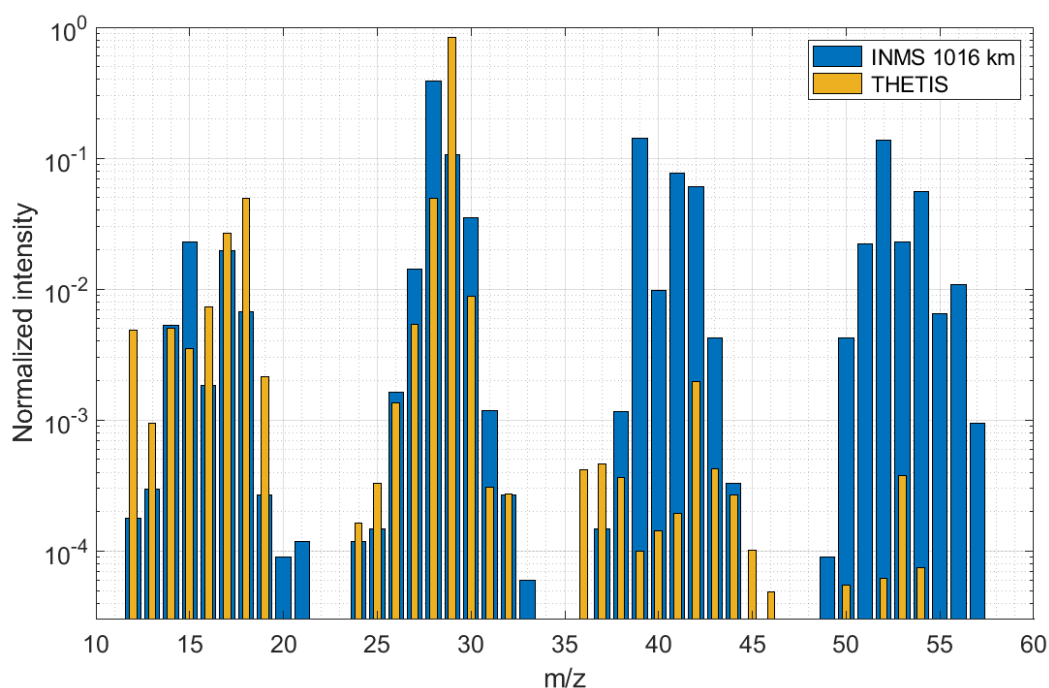

Figure III.3-20: Comparison of the THETIS ion spectrum in reference conditions (5% H$_2$, 1.3 mbar, 20 mA, tholins) to a spectrum taken by INMS in Titan's ionosphere on the T40 flyby (Magee et al., 2009).

During the production of tholins in PAMPRE, it is also possible to measure the ion mass spectrum. In this case, N_2 and CH_4 are injected in the chamber. Under ionization, CH_4 leads to the production of H and many other H-containing species. Therefore, **N_2, H_2 and aerosols are present in the gas phase, similarly to the THETIS experiment**. This time, there is **also methane**, that provides the gas phase with carbon. Besides, we know that the plasma discharges in PAMPRE and THETIS are globally similar (see **Section II.3.2**).

In a N_2-CH_4 discharge in PAMPRE, several processes are simultaneously at work: **(1) the production of new (heavy) ions** in the gas phase, enhanced by the presence of methane, **(2) the formation and growth of the aerosols** through heavy species adsorption and continuous carbon chain growth on the grain surface and **(3) the erosion of aerosols by N_2-H_2 species** as studied in THETIS.
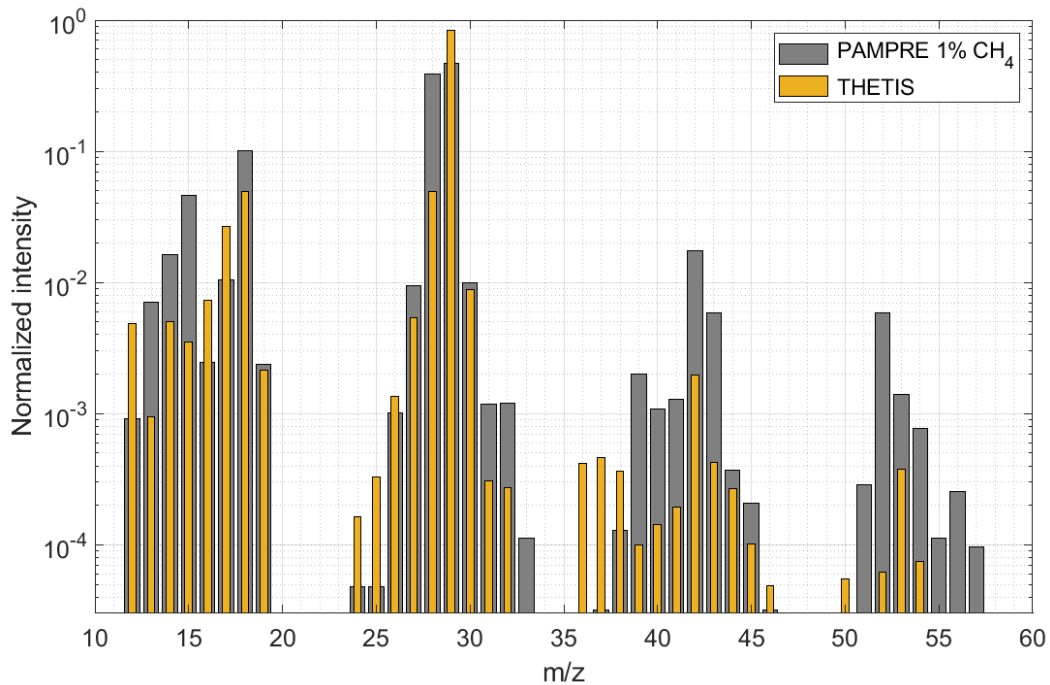
Figure III.3-21: Comparison of the THETIS ion spectrum in reference conditions (5% H_2, 1.3 mbar, 20 mA, tholins) to an ion spectrum taken in PAMPRE in a N_2-CH_4 plasma simulating Titan's atmosphere (1% CH_4, 30 W injected power, 0.9 mbar) (Dubois et al., 2020).

Figure III.3-21 compares PAMPRE and THETIS ion spectra. It enhances the parts of the PAMPRE spectrum linked to the processes (3) and (1). The process (2) does not form species visible by the gas mass spectrometer. **On THETIS, ammonia and its ions are overrepresented** compared to PAMPRE, because they are directly formed from N_2 and H_2. **HCN, CH_3-CN and C_2N_2 derived ions** are an important part of the THETIS spectrum, also present in the case of PAMPRE. Finally, **highly unsaturated ions** as C^+, C_2^+, C_2H^+, C_3^+, C_3H^+ and $C_3H_2^+$/C_2N^+ are present in higher quantity in THETIS than in PAMPRE. This suggests that their formation pathways are favored in the THETIS case, without the presence of methane. Such ions are maybe less extracted from tholins with the parallel carbon growth at work, or are quickly used by the carbon chemistry

in the gas phase. On the other side, PAMPRE has a larger diversity of ions, that are formed thanks to the methane chemistry. It is especially the case for CH^+ (13 u), CH_2^+ (14 u), CH_3^+ (15 u) and the others $C_xH_y^+$ ions.

<div style="border:1px solid #000; padding:10px;">

CONCLUSION AND PERSPECTIVES OF SECTION III

The THETIS experiment has been created to study the **interactions between tholins and N_2-H_2 plasma species**. Both the solid phase and the gas phase have been investigated, by Scanning Electron Microscopy and IR transmission spectroscopy for the grains, and by neutral and ion mass spectrometry of the gas species.

Tholins are **physically eroded** during their exposure. Chemical processes induced by radicals at the surface weakens the tholin structure and ion sputtering desorbs small molecules and highly unsaturated ions.

The **chemistry at the surface** modifies the IR absorption bands of the material. Nitriles decrease strongly compared to the other chemical bonds. Nevertheless, new CN bonds are simultaneously formed at the surface through the efficient radical-induced surface chemistry.

In the gas phase, HCN, NH_3-CN, C_2N_2 are extracted in quantity from the tholins as well as some other carbon-containing species and their derived ions. On the other hand, the production of ammonia is strongly decreased, certainly because the H, NH and N radicals are rather used for the production of HCN at the surface of tholins.

On Titan, the heterogeneous chemistry could participate to the formation of C≡N bonds in the aerosol structure, as well as the production of HCN or R-CN species in the gas phase.

To go further in the experimental investigation:

Obviously, such an investigation never ends, and the discoveries made by the THETIS experiment lead to **new questions**. I selected the most interesting ones to my opinion, that would be worth investigating in future works:

(1) According to studies on (C:H) films exposed to N_2-H_2 plasmas, HCN forms at the surface of and produces a strong desorption of HCN in the gas phase. Nevertheless, CN bonds are already present in the material structure. **What is the part of HCN with N coming from the tholins and the part coming from the injected N_2?** To easily answer this question, the THETIS experiment could be performed with the use of **isotopically marked nitrogen** in the gas phase. This works for HCN, but also for the many other species appearing in the gas phase with the insertion of tholins.

(2) Radicals seem to play a fundamental role in the erosion of tholins. What is exactly their role? **How do the radical densities vary with the insertion of tholins?** Which are the most important ones? It would be very interesting to measure them, in different conditions and at different places in the discharge. This could be realized **by actinometry and/or TALIF** (two photon absorption laser induced fluorescence). In the case without tholins it would also be

</div>

interesting to **model** the discharge to get access to the radical densities and their main formation / sink processes. Typically, in glow discharges in the working conditions of THETIS, N and H radicals are ~1% of the total neutral density, NH are ~10^{-4} and NH$_2$ ~10^{-5}. These values are about one order of magnitude higher than in Titan's ionosphere, but they are likely to change with the insertion of tholins in the discharge.

(3) **On Titan and in PAMPRE, erosion and growth processes work in parallel. Quantitatively, what is the part of each in the global formation of the aerosols?** Such an investigation can be done on PAMPRE. **Varying the gas phase composition** with more or less hydrogen compared to methane would change the balance between erosion and growth processes. Another interesting path to investigate is the **residence time of aerosols** inside the plasma. It is very complex to model, the grains being in suspension in the discharge because they are repelled from the walls by their electric charge, but also dragged down by the gas flux coming from above. They finally sediment once grown after a limit size. Then a variation of the gas flux changes this limit size, enabling the grains to stay more or less in the plasma discharge. Another strategy to shorten the residence time of tholins in the discharge is to stop the plasma after a certain duration. It then requires the use of plasma pulses. A previous work already studied the growth of grains in such various conditions, mainly based on SEM images (Hadamcik et al., 2009). However, it would be interesting to look at variations in the chemical composition and structure of the grains, by IR absorption spectroscopy and/or high resolution mass spectrometry. The presence of the aerosols in the chamber can be directly observed thanks to the diffusion of a green laser (see **Figure III.3-22**). The only point is to find a way to follow particles to retrieve how long they stay in the plasma!

Figure III.3-22: Sedimentation of tholins out of the plasma box observed by a green laser diffraction in PAMPRE. White arrows show the position of the particles, moved aside by the central void of the RF CCP discharge.

The two previous sections studied the interaction of tholins with plasma in the laboratory, focusing on the evolution of the solid material, the neutrals and the ions in the gas phase. However, what about electrons? Are they affected by the presence of the aerosols? This is the focus of the next section.

References for Chapter III

Abdu, Y.A., Hawthorne, F.C., Varela, M.E., 2018. Infrared Spectroscopy of Carbonaceous-chondrite Inclusions in the Kapoeta Meteorite: Discovery of Nanodiamonds with New Spectral Features and Astrophysical Implications. Astrophys. J. 856, L9. https://doi.org/10.3847/2041-8213/aab433

Ågren, K., Wahlund, J.-E., Garnier, P., Modolo, R., Cui, J., Galand, M., Müller-Wodarg, I., 2009. On the ionospheric structure of Titan. Planet. Space Sci. 57, 1821–1827. https://doi.org/10.1016/J.PSS.2009.04.012

Azzolina-Jury, F., Thibault-Starzyk, F., 2017. Mechanism of Low Pressure Plasma-Assisted CO2 Hydrogenation Over Ni-USY by Microsecond Time-resolved FTIR Spectroscopy. Top. Catal. 60, 1709–1721. https://doi.org/10.1007/s11244-017-0849-2

Balucani, N., 2012. Elementary reactions of N atoms with hydrocarbons: first steps towards the formation of prebiotic N-containing molecules in planetary atmospheres. Chem. Soc. Rev. 5473–5483. https://doi.org/10.1039/c2cs35113g

Balucani, N., Leonori, F., Petrucci, R., Stazi, M., Skouteris, D., Rosi, M., Casavecchia, P., 2010. Formation of nitriles and imines in the atmosphere of Titan: Combined crossed-beam and theoretical studies on the reaction dynamics of excited nitrogen atoms N(2D) with ethane. Faraday Discuss. 147, 189–216. https://doi.org/10.1039/c004748a

Balucani, N., Skouteris, D., Leonori, F., Hamberg, M., Geppert, W.D., Casavecchia, P., 2012. Combined Crossed Beam and Theoretical Studies of the N(2D) + C2H4. Reaction and Implications for Atmospheric Models of Titan. J. Phys. Chem. A 116, 10467–10479.

Bogaerts, A., Neyts, E., Gijbels, R., Van der Mullen, J., 2002. Gas Discharge Plasmas and Their Applications. Spectrochim. Acta Part B 57, 609–658.

Bonnet, J.Y., Quirico, E., Buch, A., Thissen, R., Szopa, C., Carrasco, N., Cernogora, G., Fray, N., Cottin, H., Roy, L. Le, Montagnac, G., Dartois, E., Brunetto, R., Engrand, C., Duprat, J., 2015. Formation of analogs of cometary nitrogen-rich refractory organics from thermal degradation of tholin and HCN polymer. Icarus 250, 53–63. https://doi.org/10.1016/j.icarus.2014.11.006

Carrasco, E., Tanarro, I., Herrero, V.J., Cernicharo, J., 2013. Proton transfer chains in cold plasmas of H$_2$ with small amounts of N$_2$. The prevalence of NH$_4^+$. Phys. Chem. Chem. Phys. 15, 1699–1706. https://doi.org/10.1039/c2cp43438e

Carrasco, N., Jomard, F., Vigneron, J., Etcheberry, A., Cernogora, G., 2016. Laboratory analogues simulating Titan's atmospheric aerosols: Compared chemical compositions of grains and thin films. Planet. Space Sci. 128, 52–57. https://doi.org/10.1016/j.pss.2016.05.006

Carrasco, N., Schmitz-Afonso, I., Bonnet, J.Y., Quirico, E., Thissen, R., Dutuit, O., Bagag, A., Laprévote, O., Buch, A., Giulani, A., Adandé, G., Ouni, F., Hadamcik, E., Szopa, C., Cernogora, G., 2009. Chemical characterization of titan's tholins: Solubility, morphology and molecular structure revisited. J. Phys. Chem. A 113, 11195–11203. https://doi.org/10.1021/jp904735q

Carrasco, N., Tigrine, S., Gavilan, L., Nahon, L., Gudipati, M.S., 2018. The evolution of Titan's high-altitude aerosols under ultraviolet irradiation. Nat. Astron. 2, 1. https://doi.org/10.1038/s41550-018-0439-7

Cui, J., Yelle, R. V., Vuitton, V., Waite, J.H., Kasprzak, W.T., Gell, D.A., Niemann, H.B., Müller-Wodarg, I.C.F., Borggren, N., Fletcher, G.G., Patrick, E.L., Raaen, E., Magee, B.A., 2009. Analysis of Titan's neutral upper atmosphere from Cassini Ion Neutral Mass Spectrometer measurements. Icarus 200, 581–615. https://doi.org/10.1016/j.icarus.2008.12.005

Danger, G., Orthous-Daunay, F.R., de Marcellus, P., Modica, P., Vuitton, V., Duvernay, F., Flandinet, L., Le Sergeant d'Hendecourt, L., Thissen, R., Chiavassa, T., 2013. Characterization of laboratory analogs of interstellar/cometary organic residues using very high resolution mass spectrometry. Geochim. Cosmochim. Acta 118, 184–201. https://doi.org/10.1016/j.gca.2013.05.015

Dartois, E., Muñoz Caro, G.M., Deboffle, D., Montagnac, G., d'Hendecourt, L., 2005. Ultraviolet photoproduction

of ISM dust. Astron. Astrophys. 432, 895–908. https://doi.org/10.1051/0004-6361:20042094

de Marcellus, P., Fresneau, A., Brunetto, R., Danger, G., Duvernay, F., Meinert, C., Meierhenrich, U.J., Borondics, F., Chiavassa, T., d'Hendecourt, L.L.S., 2017. Photo and thermochemical evolution of astrophysical ice analogues as a source for soluble and insoluble organic materials in Solar system minor bodies. Mon. Not. R. Astron. Soc. 464, 114–120. https://doi.org/10.1093/mnras/stw2292

Dionnet, Z., Aleon-Toppani, A., Baklouti, D., Borondics, F., Brisset, F., Djouadi, Z., Sandt, C., Brunetto, R., 2018. Organic and mineralogic heterogeneity of the Paris meteorite followed by FTIR hyperspectral imaging. Meteorit. Planet. Sci. 16, 1–16. https://doi.org/10.1111/maps.13178

Dubois, D., Carrasco, N., Jovanovic, L., Vettier, L., Gautier, T., Westlake, J., 2020. Positive ion chemistry in an N_2-CH_4 plasma discharge: Key precursors to the growth of Titan tholins. Icarus 338. https://doi.org/10.1016/j.icarus.2019.113437

Fox-Lyon, N., Oehrlein, G.S., Ning, N., Graves, D.B., 2011. Hydrogenation and surface density changes in hydrocarbon films during erosion using Ar/H2 plasmas, in: Journal of Applied Physics. American Institute of Physics, p. 104314. https://doi.org/10.1063/1.3662953

Fray, N., Bardyn, A., Cottin, H., Altwegg, K., Baklouti, D., Briois, C., Colangeli, L., Engrand, C., Fischer, H., Glasmachers, A., Grün, E., Haerendel, G., Henkel, H., Höfner, H., Hornung, K., Jessberger, E.K., Koch, A., Krüger, H., Langevin, Y., Lehto, H., Lehto, K., Le Roy, L., Merouane, S., Modica, P., Orthous-Daunay, F.R., Paquette, J., Raulin, F., Rynö, J., Schulz, R., Silén, J., Siljeström, S., Steiger, W., Stenzel, O., Stephan, T., Thirkell, L., Thomas, R., Torkar, K., Varmuza, K., Wanczek, K.P., Zaprudin, B., Kissel, J., Hilchenbach, M., 2016. High-molecular-weight organic matter in the particles of comet 67P/Churyumov-Gerasimenko. Nature 538, 72–74. https://doi.org/10.1038/nature19320

Gautier, T., Carrasco, N., Mahjoub, A., Vinatier, S., Giuliani, A., Szopa, C., Anderson, C.M., Correia, J.J., Dumas, P., Cernogora, G., 2012. Mid- and far-infrared absorption spectroscopy of Titan's aerosols analogues. Icarus 221, 320–327. https://doi.org/10.1016/j.icarus.2012.07.025

Gronoff, G., Lilensten, J., Desorgher, L., Flückiger, E., 2009. Ionization processes in the atmosphere of Titan - I. Ionization in the whole atmosphere. Astron. Astrophys. 506, 955–964. https://doi.org/10.1051/0004-6361/200912371

Guerra, V., Sá, P.A., Loureiro, J., 2004. Kinetic modeling of low-pressure nitrogen discharges and post-discharges. EPJ Appl. Phys. 28, 125–152. https://doi.org/10.1051/epjap:2004188

Hadamcik, E., Renard, J.B., Alcouffe, G., Cernogora, G., Levasseur-Regourd, A.C., Szopa, C., 2009. Laboratory light-scattering measurements with Titan's aerosols analogues produced by a dusty plasma. Planet. Space Sci. 57, 1631–1641. https://doi.org/10.1016/j.pss.2009.06.013

He, C., Smith, M.A., 2014. Identification of nitrogenous organic species in Titan aerosols analogs: Implication for prebiotic chemistry on Titan and early Earth. Icarus 238, 86–92. https://doi.org/10.1016/j.icarus.2014.05.012

He, J., Buch, A., Carrasco, N., Szopa, C., 2015. Thermal degradation of organics for pyrolysis in space: Titan's atmospheric aerosol case study. Icarus 248, 205–212. https://doi.org/10.1016/j.icarus.2014.10.010

Henderson, B.L., Gudipati, M.S., 2015. Direct detection of complex organic products in ultraviolet (Lyα) and electron-irradiated astrophysical and cometary ice analogs using two-step laser ablation and ionization mass spectrometry. Astrophys. J. 800, 66. https://doi.org/10.1088/0004-637X/800/1/66

Herd, C.D.K., Blinova, A., Simkus, D.N., Huang, Y., Tarozo, R., Alexander, C.M.O.D., Gyngard, F., Nittler, L.R., Cody, G.D., Fogel, M.L., Kebukawa, Y., Kilcoyne, A.L.D., Hilts, R.W., Slater, G.F., Glavin, D.P., Dworkin, J.P., Callahan, M.P., Elsila, J.E., De Gregorio, B.T., Stroud, R.M., 2011. Origin and evolution of prebiotic organic matter as inferred from the Tagish Lake meteorite. Science 332, 1304–1307. https://doi.org/10.1126/science.1203290

Hong, J., Truica-Marasescu, F., Martinu, L., Wertheimer, M.R., 2002. An Investigation of Plasma-Polymer Interactions by Mass Spectrometry. Plasmas Polym. 7, 245–260. https://doi.org/10.1023/A:1019938424698

Hong, J., Turban, G., 1999. Etching process of hydrogenated amorphous carbon (a-C:H) thin films in a dual ECR-r.f. nitrogen plasma. Diam. Relat. Mater. 8, 572–576. https://doi.org/10.1016/s0925-9635(98)00337-9

Imanaka, H., Khare, B.N., Elsila, J.E., Bakes, E.L.O., McKay, C.P., Cruikshank, D.P., Sugita, S., Matsui, T., Zare, R.N., 2004. Laboratory experiments of Titan tholin formed in cold plasma at various pressures: Implications for nitrogen-containing polycyclic aromatic compounds in Titan haze. Icarus 168, 344–366. https://doi.org/10.1016/j.icarus.2003.12.014

Ishikawa, K., Yamaoka, Y., Nakamura, M., Yamazaki, Y., Yamasaki, S., Ishikawa, Y., Samukawa, S., 2006. Surface reactions during etching of organic low- k films by plasmas of N2 and H2. J. Appl. Phys. 99, 083305. https://doi.org/10.1063/1.2191567

Jacob, W., Hopf, C., Schlüter, M., 2006. Chemical sputtering of carbon materials due to combined bombardment by ions and atomic hydrogen. Phys. Scr. T T124, 32–36. https://doi.org/10.1088/0031-8949/2006/T124/007

Jia, Z., Rousseau, A., 2016. Sorbent track: Quantitative monitoring of adsorbed VOCs under in-situ plasma exposure. Sci. Rep. 6. https://doi.org/10.1038/srep31888

Junk, G., Svec, H.J., 1958. The presence of N3+ and N4+ in the mass spectra of molecular nitrogen. J. Am. Chem. Soc. https://doi.org/10.1021/ja01544a085

Kim, S.J., Jung, A., Sim, C.K., Courtin, R., Bellucci, A., Sicardy, B., Song, I.O., Minh, Y.C., 2011. Retrieval and tentative indentification of the 3 μm spectral feature in Titans haze. Planet. Space Sci. 59, 699–704. https://doi.org/10.1016/j.pss.2011.02.002

Kral, M., Ogino, A., Narushima, K., Inagaki, N., Yamashita, M., Nagatsu, M., 2007. Low-Temperature Nitrogen Introduction onto Polyurethane Surface Using Surface-Wave Excited N2/H2 Plasma. Jpn. J. Appl. Phys. 46, 7470–7474. https://doi.org/10.1143/JJAP.46.7470

Kuga, M., Marty, B., Marrocchi, Y., Tissandier, L., 2015. Synthesis of refractory organic matter in the ionized gas phase of the solar nebula. Proc. Natl. Acad. Sci. U. S. A. 112, 7129–34. https://doi.org/10.1073/pnas.1502796112

Kurihara, K., Egami, A., Nakamura, M., 2005. Study of organic polymer thin-film etching by plasma beam irradiation. J. Appl. Phys. 98, 084907. https://doi.org/10.1063/1.2113410

Kurihara, K., Karahashi, K., Egami, A., Nakamura, M., 2006. Measurement of desorbed products during organic polymer thin film etching by plasma beam irradiation. J. Vac. Sci. Technol. A Vacuum, Surfaces, Film. 24, 2217–2222. https://doi.org/10.1116/1.2364000

Laurent, B., Roskosz, M., Remusat, L., Leroux, H., Vezin, H., Depecker, C., 2014. Isotopic and structural signature of experimentally irradiated organic matter. Geochim. Cosmochim. Acta 142, 522–534. https://doi.org/10.1016/j.gca.2014.07.023

Lavvas, P., Galand, M., Yelle, R. V., Heays, A.N., Lewis, B.R., Lewis, G.R., Coates, A.J., 2011a. Energy deposition and primary chemical products in Titan's upper atmosphere. Icarus 213, 233–251. https://doi.org/10.1016/j.icarus.2011.03.001

Lavvas, P., Sander, M., Kraft, M., Imanaka, H., 2011b. Surface chemistry and particle shape: Processes for the evolution of aerosols in Titan's atmosphere. Astrophys. J. 728. https://doi.org/10.1088/0004-637X/728/2/80

Lavvas, P., Yelle, R. V., Koskinen, T., Bazin, A., Vuitton, V., Vigren, E., Galand, M., Wellbrock, A., Coates, A.J., Wahlund, J.E., Crary, F.J., Snowden, D., 2013. Aerosol growth in Titan's ionosphere. Proc. Natl. Acad. Sci. U. S. A. 110, 2729–2734. https://doi.org/10.1073/pnas.1217059110

Lebonnois, S. ébastie., Bakes, E.L.O., McKay, C.P., 2003. Atomic and molecular hydrogen budget in Titan's atmosphere. Icarus 161, 474–485. https://doi.org/10.1016/S0019-1035(02)00039-8

López-Puertas, M., Dinelli, B.M., Adriani, A., Funke, B., García-Comas, M., Moriconi, M.L., D'Aversa, E., Boersma, C., Allamandola, L.J., 2013. Large abundances of polycyclic aromatic hydrocarbons in Titan's upper

atmosphere. Astrophys. J. 770, 132. https://doi.org/10.1088/0004-637X/770/2/132

Loureiro, J., Ricard, A., 1993. Electron and vibrational kinetics in an N_2-H_2 glow discharge with application to surface processes. J. Phys. D. Appl. Phys. 26, 163–176. https://doi.org/10.1088/0022-3727/26/2/001

Magee, B.A., Waite, J.H., Mandt, K.E., Westlake, J., Bell, J., Gell, D.A., 2009. INMS-derived composition of Titan's upper atmosphere: Analysis methods and model comparison. Planet. Space Sci. 57, 1895–1916. https://doi.org/10.1016/j.pss.2009.06.016

Majeed, T., McConnell, J.C., Yelle, R. V., 1991. Vibrationally excited H2 in the outer planets thermosphere: Fluorescence in the Lyman and Werner bands. Planet. Space Sci. 39, 1591–1606. https://doi.org/10.1016/0032-0633(91)90085-O

Majeed, T., Waite, J.H., Bougher, S.W., Yelle, R. V., Gladstone, G.R., McConnell, z. J.C., Bhardwaj, A., 2004. The ionospheres-thermospheres of the giant planets. Adv. Sp. Res. 33, 197–211. https://doi.org/10.1016/j.asr.2003.05.009

Mandt, K.E., Gell, D.A., Perry, M., Hunter Waite, J., Crary, F.A., Young, D., Magee, B.A., Westlake, J.H., Cravens, T., Kasprzak, W., Miller, G., Wahlund, J.E., Gren, K., Edberg, N.J.T., Heays, A.N., Lewis, B.R., Gibson, S.T., De La Haye, V., Liang, M.C., 2012. Ion densities and composition of Titan's upper atmosphere derived from the Cassini Ion Neutral Mass Spectrometer: Analysis methods and comparison of measured ion densities to photochemical model simulations. J. Geophys. Res. E Planets 117. https://doi.org/10.1029/2012JE004139

Mohammad Gholipour, A., Rahemi, N., Allahyari, S., Ghareshabani, E., 2017. Hybrid Plasma-Catalytic Oxidation of VOCs with NiMn/Montmorillonite: Plasma and Catalyst Considerations. Top. Catal. 60, 934–943. https://doi.org/10.1007/s11244-017-0758-4

Moon, C.S., Takeda, K., Sekine, M., Setsuhara, Y., Shiratani, M., Hori, M., 2010. Etching characteristics of organic low-k films interpreted by internal parameters employing a combinatorial plasma process in an inductively coupled H2/N2 plasma. J. Appl. Phys. 107. https://doi.org/10.1063/1.3415535

Morikawa, Y., Hayashi, T., Uchida, T., 2003. Etching characteristics of organic polymers in the magnetic neutral loop discharge plasma. Japanese J. Appl. Physics, Part 1 Regul. Pap. Short Notes Rev. Pap. 42, 1441–1444. https://doi.org/10.1143/jjap.42.1441

Morisson, M., Szopa, C., Carrasco, N., Buch, A., Gautier, T., 2016. Titan's organic aerosols: Molecular composition and structure of laboratory analogues inferred from pyrolysis gas chromatography mass spectrometry analysis. Icarus 277, 442–454. https://doi.org/10.1016/j.icarus.2016.05.038

Moroz, L., Baratta, G., Strazzulla, G., Starukhina, L., Dotto, E., Barucci, M.A., Arnold, G., Distefano, E., 2004. Optical alteration of complex organics induced by ion irradiation: 1. Laboratory experiments suggest unusual space weathering trend. Icarus 170, 214–228. https://doi.org/10.1016/j.icarus.2004.02.003

Mutsukura, N., Akita, K.I., 1999. Infrared absorption spectroscopy measurements of amorphous CNxfilms prepared in CH4/N2r.f. discharge. Thin Solid Films 349, 115–119. https://doi.org/10.1016/S0040-6090(99)00237-0

Nagai, H., Hiramatsu, M., Hori, M., Goto, T., 2003. Plasma induced subsurface reactions for anisotropic etching of organic low dielectric film employing N2 and H2 gas chemistry. Japanese J. Appl. Physics, Part 2 Lett. https://doi.org/10.1143/jjap.42.l212

Nagai, H., Takashima, S., Hiramatsu, M., Hori, M., Goto, T., 2002. Behavior of atomic radicals and their effects on organic low dielectric constant film etching in high density N2/H2and N2/NH3plasmas. J. Appl. Phys. 91, 2615–2621. https://doi.org/10.1063/1.1435825

Nuevo, M., Milam, S.N., Sandford, S.A., De Gregorio, B.T., Cody, G.D., Kilcoyne, A.L.D., 2011. XANES analysis of organic residues produced from the UV irradiation of astrophysical ice analogs. Adv. Sp. Res. 48, 1126–1135. https://doi.org/10.1016/j.asr.2011.05.020

Öberg, K.I., 2016. Photochemistry and Astrochemistry: Photochemical Pathways to Interstellar Complex Organic Molecules. Chem. Rev. https://doi.org/10.1021/acs.chemrev.5b00694

Pernot, P., Carrasco, N., Thissen, R., Schmitz-Afonso, I., 2010. Tholinomics—Chemical Analysis of Nitrogen-Rich Polymers. Anal. Chem. 82, 1371–1380. https://doi.org/10.1021/ac902458q

Pintassilgo, C.D., Guerra, V., 2017. Modelling of the temporal evolution of the gas temperature in N2 discharges. Plasma Sources Sci. Technol. 26. https://doi.org/10.1088/1361-6595/aa5db2

Quirico, E., Montagnac, G., Lees, V., McMillan, P.F., Szopa, C., Cernogora, G., Rouzaud, J.N., Simon, P., Bernard, J.M., Coll, P., Fray, N., Minard, R.D., Raulin, F., Reynard, B., Schmitt, B., 2008. New experimental constraints on the composition and structure of tholins. Icarus 198, 218–231. https://doi.org/10.1016/j.icarus.2008.07.012

Sciamma-O'Brien, E., Carrasco, N., Szopa, C., Buch, A., Cernogora, G., 2010. Titan's atmosphere: An optimal gas mixture for aerosol production? Icarus 209, 704–714. https://doi.org/10.1016/j.icarus.2010.04.009

Sciamma-O'Brien, E., Upton, K.T., Salama, F., 2017. The Titan Haze Simulation (THS) experiment on COSmIC. Part II. Ex-situ analysis of aerosols produced at low temperature. Icarus 289, 214–226. https://doi.org/10.1016/j.icarus.2017.02.004

Sekine, Y., Imanaka, H., Matsui, T., Khare, B.N., Bakes, E.L.O., McKay, C.P., Sugita, S., 2008a. The role of organic haze in Titan's atmospheric chemistry. I. Laboratory investigation on heterogeneous reaction of atomic hydrogen with Titan tholin. Icarus 194, 186–200. https://doi.org/10.1016/j.icarus.2007.08.031

Sekine, Y., Lebonnois, S., Imanaka, H., Matsui, T., Bakes, E.L.O., McKay, C.P., Khare, B.N., Sugita, S., 2008b. The role of organic haze in Titan's atmospheric chemistry. II. Effect of heterogeneous reaction to the hydrogen budget and chemical composition of the atmosphere. Icarus 194, 201–211. https://doi.org/10.1016/j.icarus.2007.08.030

Sharma, M.K., Saikia, B.K., Phukan, A., Ganguli, B., 2006. Plasma nitriding of austenitic stainless steel in N2 and N2-H2 dc pulsed discharge. Surf. Coatings Technol. 201, 2407–2413. https://doi.org/10.1016/j.surfcoat.2006.04.006

Shebanits, O., Wahlund, J.-E., Edberg, N.J.T., Crary, F.J., Wellbrock, A., Andrews, D.J., Vigren, E., Desai, R.T., Coates, A.J., Mandt, K.E., Waite, J.H., 2016. Ion and aerosol precursor densities in Titan's ionosphere: A multi-instrument case study. J. Geophys. Res. Sp. Phys. 121, 10,075-10,090. https://doi.org/10.1002/2016JA022980

Socrates, 2004. Infrared and Raman characteristic group frequencies, Journal of Raman Spectroscopy. https://doi.org/10.1037/pspi0000025

Sode, M., Jacob, W., Schwarz-Selinger, T., Kersten, H., 2015. Measurement and modeling of neutral, radical, and ion densities in H2-N2-Ar plasmas. J. Appl. Phys. 117, 083303. https://doi.org/10.1063/1.4913623

Tanarro, I., Herrero, V.J., Islyaikin, A.M., Méndez, I., Tabare, F.L., Tafalla, D., 2007. Ion chemistry in cold plasmas of H2 with CH4 and N2. J. Phys. Chem. A 111, 9003–9012. https://doi.org/10.1021/jp073569w

Truica-Marasescu, F., Wertheimer, M.R., 2008. Nitrogen-rich plasma-polymer films for biomedical applications. Plasma Process. Polym. 5, 44–57. https://doi.org/10.1002/ppap.200700077

Uchida, S., Takashima, S., Hori, M., Fukasawa, M., Ohshima, K., Nagahata, K., Tatsumi, T., 2008. Evaluation of property changes due to radiation, radicals, and ions on organic low-k films in H2/N2 plasma etching. Jpn. J. Appl. Phys. 47, 3621–3624. https://doi.org/10.1143/JJAP.47.3621

Van Laer, K., Tinck, S., Samara, V., de Marneffe, J.F., Bogaerts, A., 2013. Etching of low- k materials for microelectronics applications by means of a N2/H2 plasma : modeling and experimental investigation. Plasma Sources Sci. Technol. 22, 025011. https://doi.org/10.1088/0963-0252/22/2/025011

Voitsenya, V.S., Masuzaki, S., Motojima, O., Sagara, A., Jacob, W., 2006. Impact of N2+ H2 mixture plasma on carbon-containing film. Probl. At. Sci. Technol. Ser. Plasma Physics. 6, 141.

Vuitton, V., Yelle, R. V., Klippenstein, S.J., Hörst, S.M., Lavvas, P., 2019. Simulating the density of organic species in the atmosphere of Titan with a coupled ion-neutral photochemical model. Icarus 324, 120–197. https://doi.org/10.1016/j.icarus.2018.06.013

Waite, J.H., Niemann, H., Yelle, R. V., Kasprzak, W.T., Cravens, T.E., Luhmann, J.G., McNutt, R.L., Ip, W.H., Gell, D., De La Haye, V., Müller-Wordag, I., Magee, B., Borggren, N., Ledvina, S., Fletcher, G., Walter, E., Miller, R., Scherer, S., Thorpe, R., Xu, J., Block, B., Arnett, K., 2005. Ion Neutral Mass Spectrometer results from the first flyby of Titan. Science 308, 982–986. https://doi.org/10.1126/science.1110652

Waite, J.H., Young, D.T., Cravens, T.E., Coates, A.J., Crary, F.J., Magee, B., Westlake, J., 2007. Planetary science: The process of tholin formation in Titan's upper atmosphere. Science 316, 870–875. https://doi.org/10.1126/science.1139727

Wertheimer, M.R., Fozza, A.C., Holländer, A., 1999. Industrial processing of polymers by low-pressure plasmas: the role of VUV radiation. Nucl. Instruments Methods Phys. Res. Sect. B Beam Interact. with Mater. Atoms 151, 65–75. https://doi.org/10.1016/S0168-583X(99)00073-7

Westlake, J.H., Waite Jr, J.H., Mandt, K.E., Carrasco, N., Bell, J.M., Magee, B.A., Wahlund, J.-E., 2012. Titan's ionospheric composition and structure: Photochemical modeling of Cassini INMS data. J. Geophys. Res. Sp. PhysicsGR Sp. Phys. 117, 1–21. https://doi.org/10.1029/2011JE003883

Yelle, R. V., Vuitton, V., Lavvas, P., Klippenstein, S.J., Smith, M.A., Hörst, S.M., Cui, J., 2010. Formation of NH_3 and CH_2NH in Titan's upper atmosphere. Faraday Discuss. 147, 31–49. https://doi.org/10.1039/c004787m

RE-ANALYSIS OF THE CASSINI LANGMUIR PROBE DATA: ARE THE ELECTRONS DISTURBED BY THE AEROSOLS IN THE IONOSPHERE?

Contents

1- Introduction: the RPWS/LP on-board Cassini

The previous chapters studied the interaction between aerosols and plasma species thanks to laboratory simulation. They gave insights on processes going on at the surface of the aerosols. Nevertheless, it is still necessary to confirm that such interactions can actually happen on Titan. The aim of this last chapter is to get clues on the interaction between the aerosols and the ionospheric plasma on Titan.

Similarly to laboratory plasmas, the ionosphere of Titan contains radicals, excited species, ions and electrons. Radicals and excited species are difficult to study, and the main information we know about them on Titan come from chemical models. Positive and negative ions have been measured by INMS and CAPS on-board Cassini. The detection of heavy ions suggests the importance of ion chemistry in the formation of the aerosols. Then, the last species that can inform us on the modification of the plasma induced by the presence of the aerosols are the electrons.

In this chapter, I analyze the data of the Langmuir Probe on-board Cassini, from which information on the electrons can be deduced, in particular their density and their temperature.

1.1- The Cassini Langmuir Probe (LP)

1.1.a. The Radio and Plasma Wave Science (RPWS) instrument

This instrument was designed to continue and improve the first radio and plasma wave measurements in the Saturn system, done by Voyager 1 and 2 (Gurnett et al., 1981; Scarf et al., 1982). A main objective was also to measure the flux of dust and estimate the mass of the dust particles from their impacts on the spacecraft.

This instrument aimed to study radio emissions, plasma waves, thermal plasma and dust (Gurnett et al., 2004). It was formed by a suite of antennas and sensors (see **Figure IV.1-1**). Electric fields in the frequency range 1 Hz – 16 MHz were measured by three nearly-orthogonal 10-meter electric field antennas. Magnetic fields in the frequency range 1 Hz – 12 kHz were detected by three orthogonal search coil magnetic antennas. And a Langmuir Probe was used to measure electron densities and temperatures.
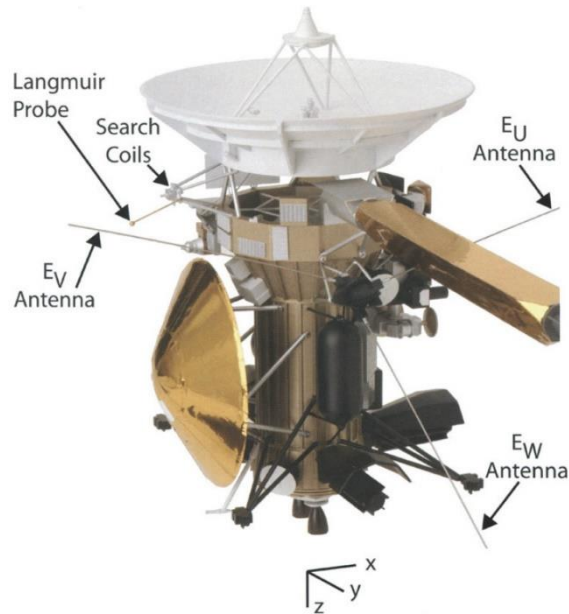
Figure IV.1-1: Antennas and sensors of the RPWS instrument on-board Cassini. (Gurnett et al., 2004)

1.1.b. Bases of the Langmuir Probe

Langmuir Probes (LP) are widely used in the plasma community, to analyze charged particles in a low pressure environment, since their introduction in 1924 by Irving Langmuir. The LP is usually a metallic stick with a plane, a cylinder or a sphere at its extremity plunged in the plasma environment. **A potential is applied to the probe and the current collected is measured.** Depending on the potential applied, the probe attracts electrons or positive ions, and therefore leads to a positive or negative current (see **Figure IV.1-2**). From sweeps of voltage from negative to positive values, the current collected gives information on the electrons and ions present in the surroundings of the probe, the densities and the temperatures.
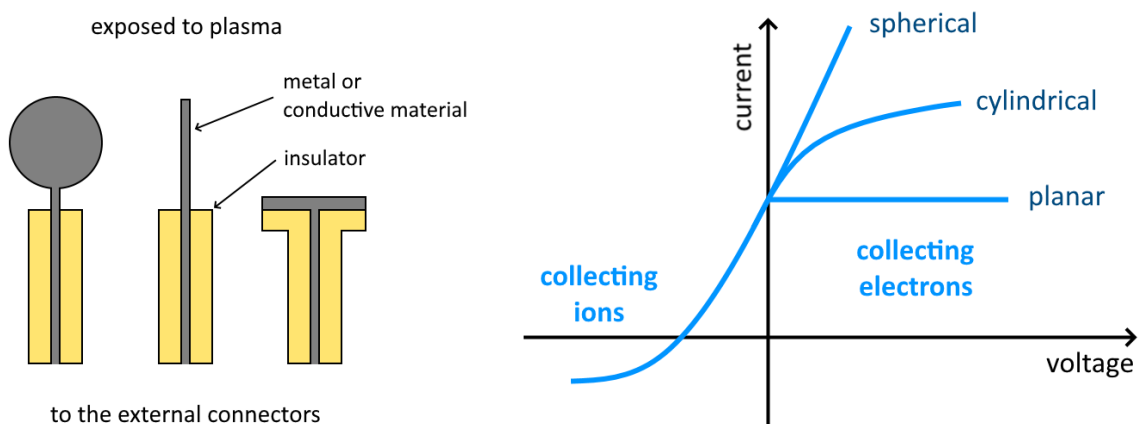

Figure IV.1-2: Scheme of typical Langmuir Probes and their corresponding 'sweeps' in the case of spherical, cylindrical and planar probes.

- 238 -

The LP on board Cassini has been built by the Swedish Institute of Space Physics. It was positioned below the radio antenna, as far as possible, at least 1.5 m, from the spacecraft to avoid any perturbation. The probe was a sphere of titanium of 5 cm in diameter (see **Figure IV.1-3**). Contrarily to previous probes designed for Earth's ionosphere that have a graphite coating, the RPWS/LP is coated with titanium nitride. This material is very reflective and limits photoelectric effects. It is also very hard and consequently enhances solid particle impact resistance and eliminates hysteresis effects that can be observed with other surface coatings (Wahlström et al., 1992). A small part of the stick in contact with the sphere is kept at the same potential as the sphere to shield it from photo- and secondary electrons. It had three operation modes (Gurnett et al., 2004): voltage sweep (used here), density (at constant voltage) and cleaning. The cleaning mode aims to remove a possible contamination on the surface. In this mode, the voltage is set to +32 V to induce sputtering of the probe with high energy electrons.

The LP gives measurements of electron density (n_e) and temperature (T_e). It can also give some information on the spacecraft potential, and on the ion mass, density and temperature (Ågren et al., 2007; Shebanits et al., 2016, 2013).

Figure IV.1-3: Engineering model of the Cassini PRWS Langmuir Probe, folded. © Swedish Institute of Space Physics.

1.1.c. Theory of the Langmuir Probe

Some notions and theories on the Langmuir Probe that were useful in the analysis of the data in **Section IV.2** are presented here.

SURFACE CHARGING

An object in a plasma is likely to gain or lose charges, and therefore it accumulates potential relatively to the plasma. It was the case for the Cassini spacecraft when plunged in the ionosphere of Titan, its potential is noted U_{SC} (spacecraft potential) (Cully et al., 2007). It was measured by the LP, and found very stable in the ionosphere (-1.5 / -0.5 V) (Ågren et al., 2007; Wahlund et al., 2005).

The spacecraft potential has a reduced effect at the distance of the LP. The floating potential of the probe is noted U_{float}. It can be measured by the LP and can be used to retrieve U_{SC} (Wahlund et al., 2009):

$$U_{SC} - U_{float} = c.U_{SC}.\exp\left(-\frac{d_{LP}}{\lambda_D}\right) \qquad (IV.1-1)$$

with d_{LP} the distance between the LP and the spacecraft main body, λ_D the Debye length of the surrounding plasma and $c \approx 5/6$, a constant empirically determined by cross-calibration with CAPS/ELS. The Debye length is a fundamental length reference in plasma studies: any shielding of a charged body by space charge in the surrounding plasma occurs in a distance on the order of λ_D. When the Debye length is larger than d_{LP}, the spacecraft acts as a potential barrier: only electrons with energies higher than $|U_{SC}|$ can go through (Shebanits, PhD thesis, 2017). In the case of Titan's ionosphere, the Debye length is ~3 cm << 1.5 m = d_{LP}. Therefore, the spacecraft potential is strongly attenuated at the position of the LP.

THE OML THEORY

The Orbital Motion Limited (OML) theory is often used to interpret LP voltage sweeps, in particular the sweeps obtained in ionospheric plasmas. The theory, first exposed by Mott-Smith and Langmuir (1926), deduces some information on the particles at the origin of the current measured by the probe. It is based on the conservation of energy and angular momentum. The particle speed distribution is supposed Maxwellian in this work. To use the OML theory, we assume that no particle comes from the probe itself. In addition, the radius of the probe (r_p = 2.5 cm) should be shorter than the Debye length in the probed region.

In the OML theory, the electron and ion currents (I_e and I_i) are described by two different equations depending on the sign of $\Psi = U_{bias} - U_1$ (Wahlund et al., 2009; Whipple, 1965). U_{bias} is the potential of the probe. U_1 is the characteristic potential of the electron/ion population in the plasma. In the case of electrons photo-detached from the spacecraft, U_1 is equal to U_{float}. The electron current I_e (resp. the ion current I_i) can be expressed as a function of $I_{e,0}$ (or $I_{i,0}$) and χ_e (resp. χ_i):

$$I_x = I_{x,0}(1-\chi_x) \qquad \begin{array}{c}\text{with x = e if } \Psi > 0, \text{ with x = i if } \Psi < 0 \\ \text{['attractive' part for electrons]}\end{array} \qquad (IV.1-2)$$

$$I_x = I_{x,0}\exp(-\chi_x) \qquad \begin{array}{c}\text{with x = e if } \Psi < 0, \text{ with x = i if } \Psi > 0 \\ \text{['repelling' part for electrons]}\end{array} \qquad (IV.1-3)$$

The two equations join in $\Psi = 0$, i.e. when $U_{bias} = U_1$. Then, the collected current $I_{x,0}$ is formulated as follow. It combines the effect of flow kinetic energy and thermal energy:

$$I_{x,0} = -A_{LP}.n_x.q_x.\sqrt{\frac{v_x^2}{16}+\frac{k_B T_x}{2\pi.m_x}} \qquad \text{with either x = e or i} \qquad (IV.1-4)$$

A_{LP} is the surface area of the probe ($4\pi.r_p{}^2$). n_x, q_x, v_x, T_x and m_x are respectively the density, the charge, the velocity, the temperature and the mass of electrons or ions. k_B is the Boltzmann constant. χ_x depends on Ψ and is expressed as:

$$\chi_x = \frac{q_x.\Psi}{\frac{m_x v_x^2}{2} + k_B T_x} \qquad\qquad (IV.1-5)$$

In the case of electrons, the flow kinetic energy term can be neglected compared to the thermal term. It is the opposite in the case of ions (positive and negative), which are heavier than electrons and transported along the ion ram flux. When $\Psi \ll 0$, the collected current is governed by positive ions while it is dominated by electrons when $\Psi > 0$.

THE SHEATH LIMITED THEORY

However, in Titan's ionosphere, the Debye length (λ_D) is similar to the radius of the probe (r_p). It is the limit of validity to use the OML theory.

$$\lambda_D = \sqrt{\frac{\epsilon_0 k_B T_e}{n_e e^2}} \sim 3\ cm \sim r_p \qquad\qquad (IV.1-6)$$

with ϵ_0 the permittivity of free space, k_B the Boltzmann constant, e, T_e and n_e the electron charge, temperature and density in Titan's ionosphere. For this computation, we took n_e = 3000 cm^{-3} and T_e = 0.05 eV.

In these conditions, a small correction can be added by using the Sheath Limited (SL) theory (Bettinger and Walker, 1965; Whipple, 1965). The idea is to add the dependence of the sheath thickness (s) with the potential and the size of the probe. It supposes a collisionless maxwellian plasma. It changes the expression of the attractive part. For electrons, it gives for $\Psi > 0$:

$$I_e = I_{e,0} \times \left[1 + \xi \times \left(1 - \exp\left(-\frac{\chi_e}{\xi} \right) \right) \right]$$
$$with \quad \xi = \left(\frac{s}{\rho} + 1 \right)^2 - 1, \qquad \rho = \frac{r_p}{\lambda_D} \qquad\qquad (IV.1-7)$$
$$and \quad s = 0.83.\sqrt{\chi}.\rho^{\frac{1}{3}}$$

The expression of the sheath thickness (s) is empirically obtained by Bettinger and Walker (1965) in the case of spherical bodies. The OML theory joins the SL theory when the sheath is very large compared to the radius of the probe.

1.1.d. Measurements with the Cassini Langmuir Probe

THE OPERATION MODE

The operation mode of the LP used in this chapter is the voltage sweep. In Titan's ionosphere, the probe voltage (U_{bias}) was shifted from +4 V to -4 V in 0.5 s, in 512 voltage steps. To give an idea of possible charging effects, the current was sampled twice between two voltage shifts. In addition, usually double-sweeps were performed, from +4 V to -4 V, and back to +4 V. The spatial resolution is limited to ~3 km due to the spacecraft motion (at ~6 km/s).

Usually for $\Psi \gg 0$, the current measured by the probe is not usable because of a saturation of the pre-amplifier. This part of the signal is not taken into account in the analyses.

THE PHOTOELECTRON CURRENT (I_{PE})

Three different currents are conventionally collected by the LP: the electron and ion currents from the surrounding plasma, and the photoelectron current. This last component is due to solar EUV photoelectron emission from the probe. This current is directly correlated with the incident EUV flux onto the probe and is strongly dependent on the shadowing of the probe (Jacobsen et al., 2009). It dominates the LP signal in the magnetosphere (Ågren et al., 2007; Wahlund et al., 2005), and its intensity decreases with altitude. It tends to vanish below ~1400 km on Titan due to the extinction of most of the more energetic solar EUV irradiation.

The photoelectron current is usually removed in the LP analyses (Jacobsen et al., 2009; Shebanits et al., 2017b; Wahlund et al., 2009). Besides, on Titan it is negligible compared to ion and electron currents, below 1200 km. On a LP sweep, the photoelectron current is added to the main electron and ion currents, as another population of electrons, with a different Maxwellian distribution, collected at the potential $U_1 = U_{float}$ (Wahlund et al., 2009). This effect has experimentally been characterized by Grard (1973). He validated the maxwellian distribution and observed a strong dependence with the material used. On Cassini, the influence of photoelectrons was minimized thanks to the outermost 10.9-cm part of the boom which was very thin (6.35 mm in diameter) (Gurnett et al., 2004).

1.2- Electrons in Titan's ionosphere

Many studies already investigated the electrons in Titan's ionosphere, in particular their density and their temperature which are used as reference for ionospheric models. Here is a summary of what we know about Titan's ionospheric electrons nowadays.

1.2.a. Electron density

ELECTRONIC STRUCTURE OF THE UPPER ATMOSPHERE OF TITAN

The Cassini spacecraft went inside the ionosphere of Titan during many flybys. The measurements of electron density all along the flyby enables to observe the layers in the upper atmosphere that are differently ionized. With this technique, Agren et al. (2007) deduced the structure of the upper atmosphere during one flyby (T5).

The ionosphere is the lower part of a flyby by the Cassini spacecraft. It is a region with a lot of electrons (~1000 cm^{-3}), which are cold (< 0.1 eV). Just above 1400-1500 km in altitude, an exo-ionosphere makes the transition between the ionosphere and the magnetosphere. The plasma of the exo-ionosphere is produced by a combination of processes coming from the underneath ionosphere ('pick-up ions') and from the above magnetosphere (magnetic forcing). It results in an average density ~> 10 cm^{-3}. In the magnetosphere, above the Induced Magnetosphere Boundaries (IMB) around 2200-2500 km, the density decreases to ~0.1 cm^{-3}. This work focuses to the ionosphere, below 1400 km altitude.

ELECTRON DENSITY IN THE IONOSPHERE

The ionosphere spreads from ~1400-1500 km to ~800-900 km. These limits vary with sun enlightenment and seasons. Between 1400 km and 1200 km electron density always increases with decreasing altitude because of a more important EUV energy deposition at these lower altitudes. Ågren et al. (2009) showed that **the electron density is mainly governed by solar photons during the day.**

On the day side, a maximum of electron density forms around 1100 km, named the electron ionospheric peak (see **Figure IV.1-4**). The electron ionospheric peak was early guessed at this position (1175 km, 2400 cm^{-3}) thanks to the Voyager 1 radio occultation experiment (Bird et al., 1997). Other ionization sources than solar EUV exist (see **Section I.2.2.b**), and combine with transport processes to form a constant electron density of ~400-700 cm^{-3} from 1200 to < 950 km on the night side.
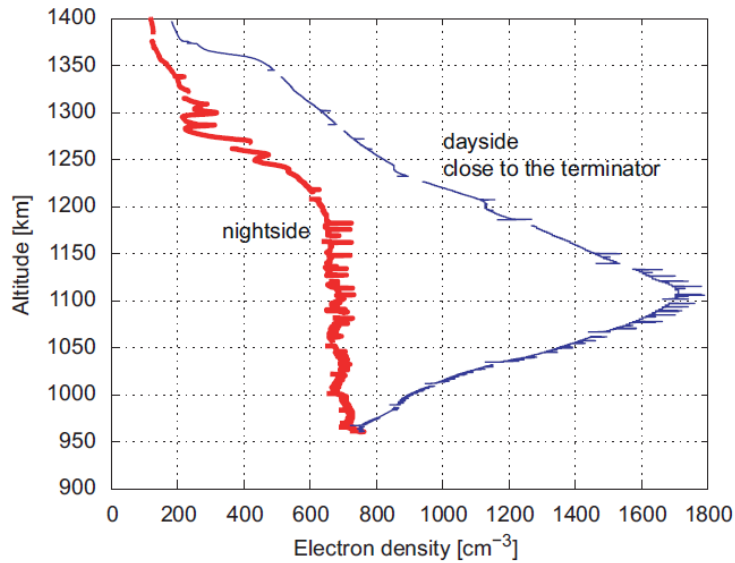
Figure IV.1-4: Electron density as a function of altitude during the T5 flyby. Inbound on dayside close to terminator and outbound on nightside. (Ågren et al., 2009)

DENSITIES BELOW 1100 KM

In the lower part of the ionosphere, below the electron ionization peak at 1100 km, positive, negative ions and dust have increasing densities, and start to influence electrons. Shebanits et al. (2016, 2013) studied the ion and aerosol precursor densities in the ionosphere of Titan. They generally increase strongly below 1100 km altitude. However, it is at the altitude from which electron density starts to decrease. Such ionospheric plasmas should be globally neutral. The fact that positive ion density exceeds the electron density below 1100 km can be explained thanks to negative ions ad negatively charged dust grains. Indeed, **dust particles in a plasma tend to attach free electrons and charge negatively** (Farrell et al., 2009; Shukla and Mamun, 2015). Therefore, in a dusty plasma the increase of the dust density or grain size leads to a decrease in the electron density. It is the case in the ionosphere of Titan below 1100 km, where negative ions become a strong negative charge carrier. Shebanits et al. (2016) used this property of dusty plasmas to deduce the presence of dust from the measurements of electron and positive ion densities (when the electron to positive ion charge density ratio is < 0.5).

In parallel, another process increases the positive ion densities below 1100 km altitude. The recombination of positive ions with free electrons is ~5-10 times quicker than the recombination with negative ions or dust (Vigren et al., 2014). We just saw that below the peak of energy deposition induced by EUV (1100 km), the electron density decreases, and negative ions become the dominant negative charge carriers. Therefore, positive ions recombine more slowly and their densities increase. It leads to an **ion-ion dusty plasma below 1100 km (with dominantly positive and negative ions), which has charge densities higher than at the electron ionization peak** (see **Figure IV.1-5**). On dayside, its peak is below 900 km. The average negative ion/dust (> 1000 u) charge is estimated between -1.5 and -2.3, increasing from 1150 to 950 km in altitude.
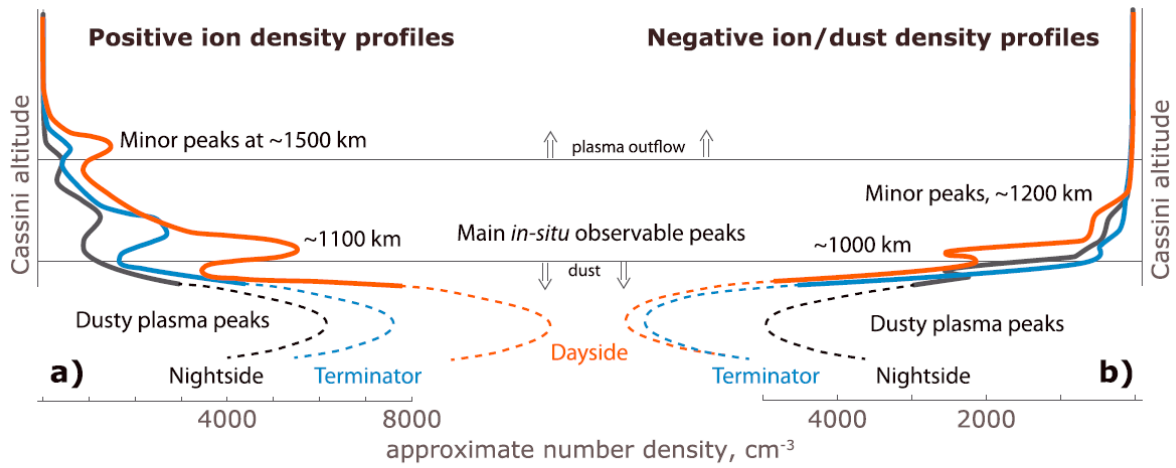
Figure IV.1-5: Scheme of positive, negative ions and dust density profiles. Based on the average density profiles from the RPWS/LP measurements. (Shebanits et al., 2017b)

1.2.b. Electron temperature

The energy of electrons in the ionosphere is associated to their temperature. Usually, 'electron-volts' are used to express the electron temperatures (T_e).

$$\widetilde{T}_e \ [eV] = \frac{k_B.T_e \ [K]}{e} \qquad\qquad (IV.1-8)$$

with k_B the Boltzmann constant and e the elementary charge. As an example, 0.1 eV corresponds to 1161 K.

Ågren et al. (2009) derived the electron temperature profiles from 17 Cassini flybys. **They observed that the electron temperature at the ionospheric peak is always confined between 0.03 and 0.06 eV (≈ 350-700 K).** There is no strong variation with the Solar Zenith Angle (SZA) contrarily to electron densities.

Later, Edberg et al. (2010) studied the electron temperature for 52 Cassini flybys. They observed a global exponential correlation between electron density and electron temperature considering altitudes up to 13 000 km. Around 1000 km altitude, they stated a temperature rather stabilized around 0.04 eV, as seen by Ågren et al. (2009) (see **Figure IV.1-6**).
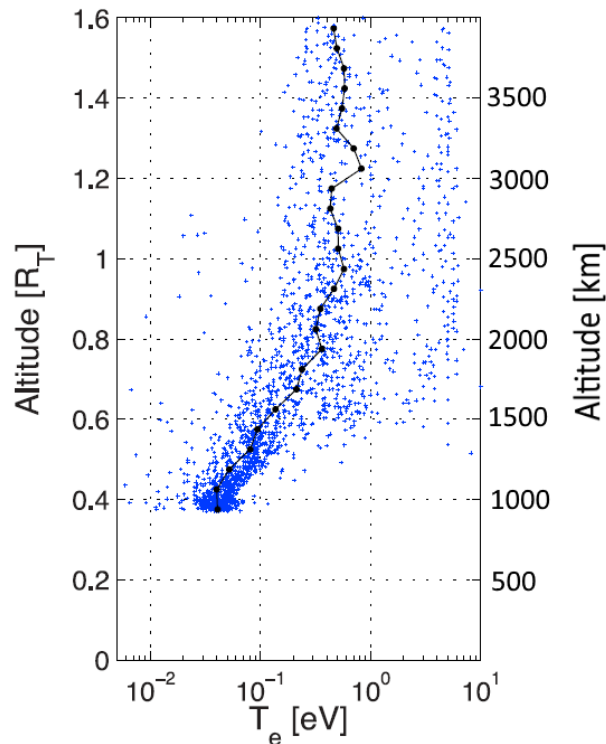
Figure IV.1-6: Electron temperature as a function of altitude. (Edberg et al., 2010)

1.2.c. Modeling of Titan's ionosphere

Several models have been developed to understand the processes at work in Titan's ionosphere (Galand et al., 2014).

Energetic suprathermal electrons of ~10 eV to ~1 MeV are detected in the ionosphere of Titan by CAPS (Coates et al., 2007) and by the Magnetospheric Imaging Instrument (MIMI) (Cravens et al., 2008). Galand et al. (2006) showed that **the ionospheric thermal electrons (< 1 eV) are heated through Coulomb collisions with these suprathermal electrons**. Thermal electrons thus have temperatures significantly higher than the temperature of neutral species of ~145-160 K (Waite et al., 2005). Galand et al. (2006) found out that this heating depends strongly on the topology used for the magnetic field lines that transport the suprathermal and secondary electrons. Nevertheless, this work did not study the ionosphere below 1200 km.

Richard et al. (2011) coupled a suprathermal electron transport model to a thermal electron and ion energetics model, with an altitude range from 800 to 1800 km. They predict a sudden drop in electron thermal temperature around 1000 km altitude, with cold electrons (< 200 K, < 0.02 eV) below 900 km. On nightside or on dayside above 1400 km, magnetospheric inputs are required to heat the electrons. **But below 1400 km on the dayside, solar radiation is sufficient to explain electron temperatures observed, except around 1000 km where measured electrons are always hotter. A significant heat source seems to be missing in the model to explain such large electron temperatures around 1000 km. It could be linked to the presence of aerosols and/or waves.**

Vigren et al. (2013) present an ionospheric model which goal is to test if electron densities can be predicted thanks to the knowledge of N_2 and CH_4 densities from INMS, electron temperature from the LP, laboratory data for ion dissociative recombination rates, a solar energy deposition model based on Galand et al. (2010) and some assumptions: they assume that the photochemistry is at equilibrium and that electrons are exclusively lost through dissociative recombination with molecular ions. On the sunlit part of the atmosphere, their model overestimates the electron densities by a factor of 2, while such models work better in the ionospheres of Venus and Mars. **They propose that other processes than dissociative recombination with molecular ions are at work in Titan's ionosphere to consume free electrons, certainly related to the presence of negative ions and dust.** On the contrary, the nightside ionosphere is reasonably well reproduced by the models (Vigren et al., 2015).

Vigren et al. (2016) and Shebanits et al. (2017a) focused their studies on the 'factor 2' problem in electron density, trying to find the missing process consuming electrons. It is directly linked to the effective recombination coefficient expected from the ion composition and the electron temperature measured. Shebanits et al. (2017a) showed that **the addition of negative ions in the model decreases the discrepancy between Cassini data and model results** for electron density. They observed significant variation trends for the rate coefficients with Solar Zenith Angle (SZA), corotational plasma direction and solar EUV flux. Such parameters could induce modifications in the photochemistry and in the ionization by energetic particles.

Mukundan and Bhardwaj (2018) observed that **reducing the electron temperature by a factor of 5 brings the electron densities predicted by the model closer to the measured values.**
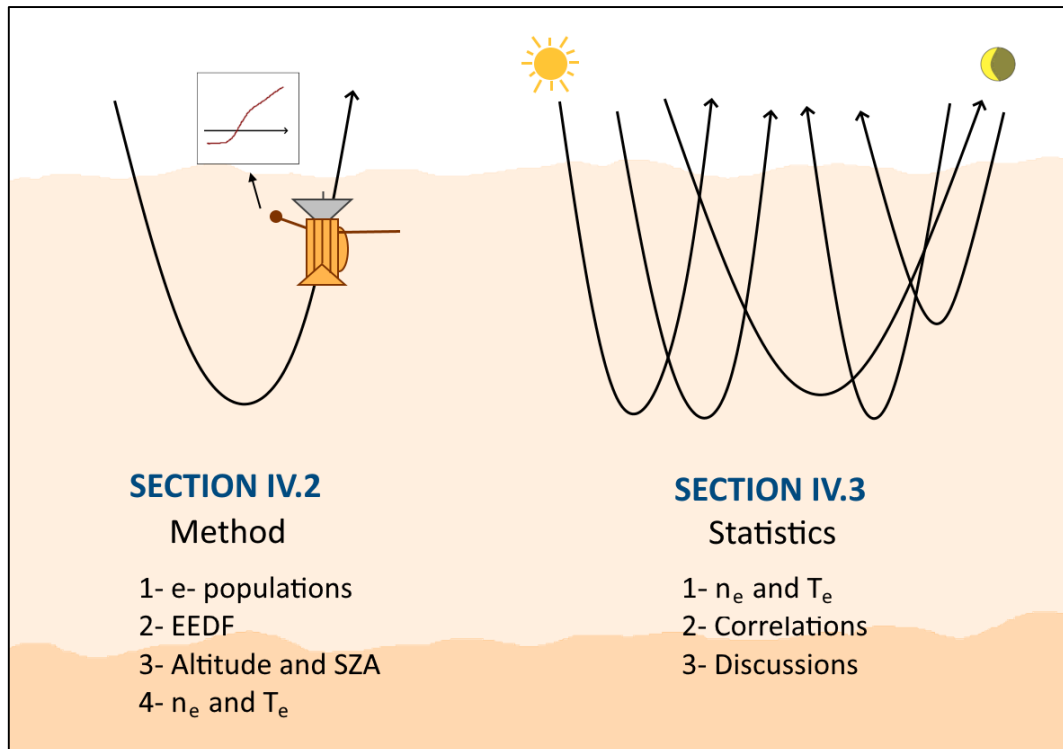
1.2.d. Objective of Chapter IV

The objective of this chapter is to investigate the interaction between aerosols and plasma in the ionosphere of Titan thanks to Cassini *in situ* data. The study is focused on the thermal electrons, measured by the Langmuir Probe.

Numerical models of the ionosphere face a 'factor 2' miscorrelation for the electron density compared to data measurements. Latest studies show a possible explanation through interactions with heavy negative ions and also maybe by a reduction of the electron temperature. The suggestion of the interaction of the electrons with heavy species is especially interesting in our aim to investigate the interaction between aerosols and plasma species in the ionosphere of Titan.

Therefore, I re-analyzed in detail the complete dataset taken by the Cassini Langmuir Probe during Titan flybys below 1300 km. A special effort was also put to retrieve the electron temperature.

Section IV.2 presents the **detailed analysis of representative examples of Langmuir Probe measurements**. It shows the necessity of using several electron populations in the analysis. The distribution of the populations with altitude and solar illumination is investigated. **Section IV.3** shows the **results from the analysis of 57 Cassini flybys** in the ionosphere. Correlations with the UV fluxes, the seasons and the ion densities are studied. Finally, suggestions for the origin of the four populations are given. In particular, one population seems linked to the presence of the aerosols.

SECTION IV.2
Method

1- e- populations
2- EEDF
3- Altitude and SZA
4- n_e and T_e

SECTION IV.3
Statistics

1- n_e and T_e
2- Correlations
3- Discussions

2- Re-analysis of the LP data: method

This section focuses on the re-analysis of the Langmuir Probe data on a few Titan flybys. It describes the analysis procedure, which I had to adapt to the special conditions of the ionosphere of Titan.

This work was done in close collaboration with Jan-Erik Wahlund and the team of the Swedish Institute of Space Physics (IRF) in Uppsala University (Sweden). It resulted in the redaction of **Paper 6** (*Re-analysis of the Cassini RPWS/LP data in Titan's ionosphere. Part 1. Detection of several electron populations*). Its content is reproduced below, and some supplementary information is added with grey boxes.

2.1- Fitting LP data: the necessity of several electron populations

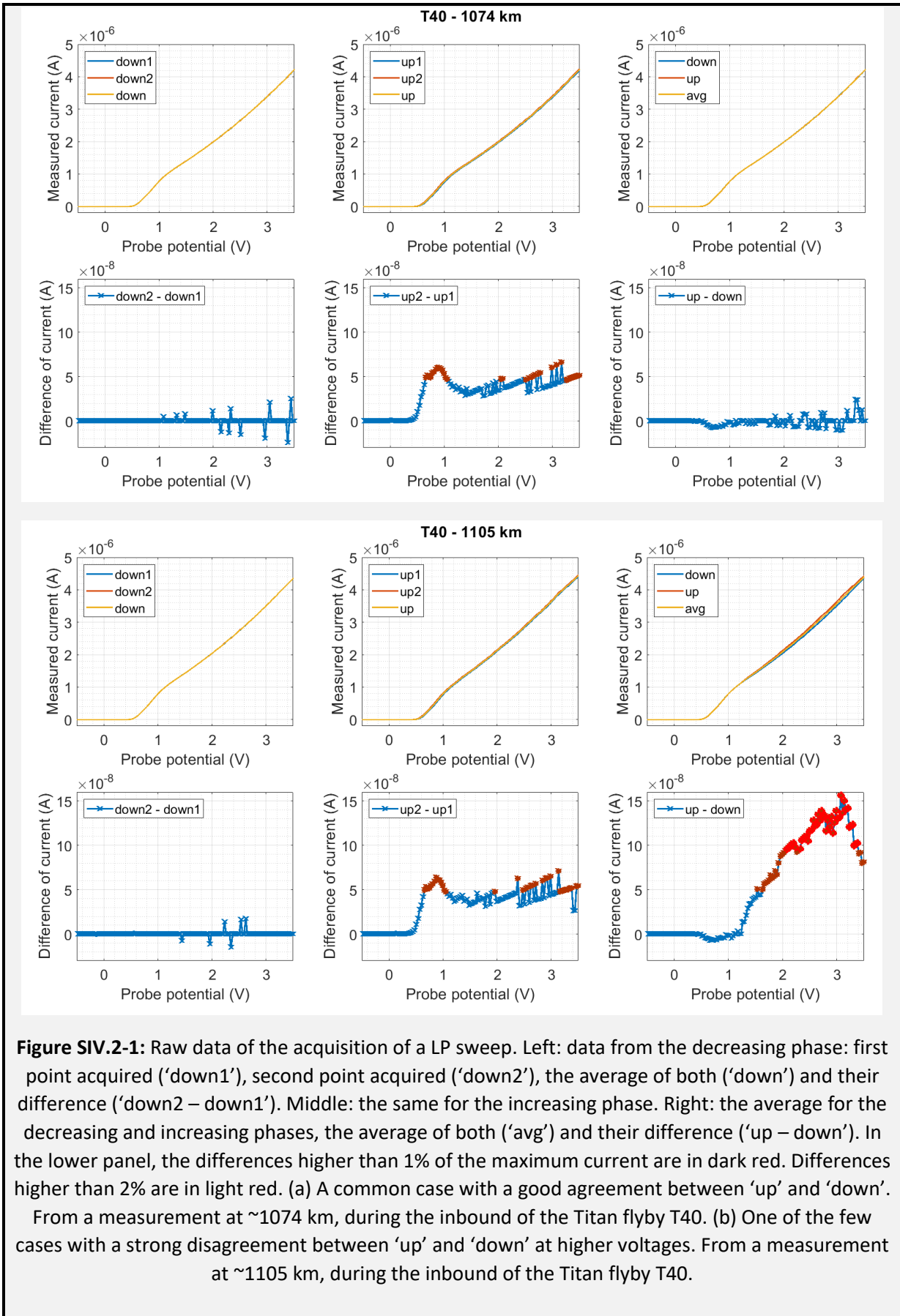### 2.1.a. Extraction of the electron current from the LP raw data

No hysteresis effects

The LP took redundant measurements. **Supplement SIV.2-1** investigates the reproducibility of the data, which appears to be very good without any strong hysteresis effects. This validates the analysis of the LP data.

SUPPLEMENT SIV.2-1: REPRODUCIBILITY AND HYSTERESIS EFFECTS

The LP took redundant measurements. At each altitude, sweeps are acquired twice: once with a decreasing potential from +4 V to -4 V ('down'), the other with an increasing potential from -4 V to +4 V ('up'). Furthermore, data points are acquired twice between two voltage shifts to give an idea of possible charging effects. Therefore, four data points are acquired at a given voltage and altitude. They are compared in **Figure SIV.2-1**.

We observe that the two data points taken at a same voltage step during the decreasing voltage phase are always very close to each other: the current stabilizes quickly after each voltage step. On the contrary, the current continues to increase between the two measurements during the increasing voltage phase: the current takes longer to stabilize, especially in the strongly varying parts of the sweep.

Figure SIV.2-1: Raw data of the acquisition of a LP sweep. Left: data from the decreasing phase: first point acquired ('down1'), second point acquired ('down2'), the average of both ('down') and their difference ('down2 – down1'). Middle: the same for the increasing phase. Right: the average for the decreasing and increasing phases, the average of both ('avg') and their difference ('up – down'). In the lower panel, the differences higher than 1% of the maximum current are in dark red. Differences higher than 2% are in light red. (a) A common case with a good agreement between 'up' and 'down'. From a measurement at ~1074 km, during the inbound of the Titan flyby T40. (b) One of the few cases with a strong disagreement between 'up' and 'down' at higher voltages. From a measurement at ~1105 km, during the inbound of the Titan flyby T40.

The differences observed between the measurements on the decreasing and increasing phases are generally low, less than 1% of the maximum current value measured during the sweep. Some rare cases can reach up to 2% difference, but they are isolated. Besides, the part of the sweep showing the higher differences is always the part at higher voltage, which corresponds to the saturation current that cannot be used in the analysis. Consequently, it does not impact the fitting of the electron current. **We finally use the average of the two points taken during the decreasing phase for the next parts.**

FIT OF THE ELECTRON AND ION PART

The electron temperature and the Electron Energy Distribution Function (EEDF) can be obtained from the part of a LP sweep (called the 'transition region') where the electron current starts to dominate the positive ion current, i.e. for Ψ being just a bit negative. **Equation IV.1-3** for a 'repelling' probe is therefore used.

In this transition region, the positive ion current is not always negligible compared to the electron current. The measured (total) current should be corrected by the positive ion part to obtain only the electron current. According to **Equation IV.1-2**, **this ion current is fitted by a linear curve and subtracted.**

SUPPLEMENT SIV.2-2: FIT OF THE ION PART

A linear fit is applied to the ion part of the sweep. It is then removed from the total current to give the electron current.
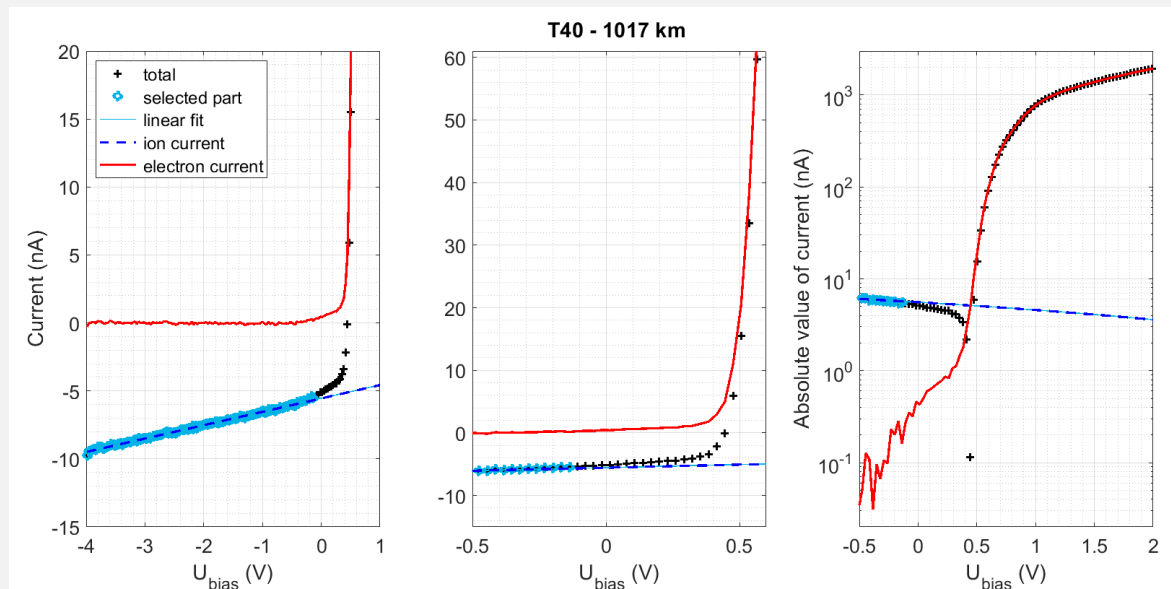

Figure SIV.2-2: How to obtain the electron current (different zooms). The data points (black dots) correspond to the sum of the electron and the positive ion current. Data points far from the apparition of the electron current (blue circles) are fitted by a line (light blue line). The negative part of this line corresponds to the ion current (dark blue dashed line). The resulting electron current is represented by the red line.

2.1.b. Examples of sweeps from Titan's ionosphere: several electron populations

According to the theory in a maxwellian thermalized plasma, the electron current can be fitted using Equations IV.1-2 and IV.1-3. Then, the plasma potential (U_p), the electron density (n_e) and the electron temperature (T_e) can be deduced from the fit. **Figure SIV.2-3** shows an example in such a case in the appendix.

Using only one electron 'population' (i.e. one combination of Equations IV.1-2 and IV.1-3) results in a poor fit of the electron current. In certain cases, a second population has to be added. It leads to two different sets of (U_p, n_e, T_e). Below 1300 km, two maxwellian populations of electrons are usually still not sufficient to correctly fit the electron current. A third, and in rare occasions a fourth, population is required. One example is shown in **Figure IV.2-1** and more are given in **Figure SIV.2-4/5**.
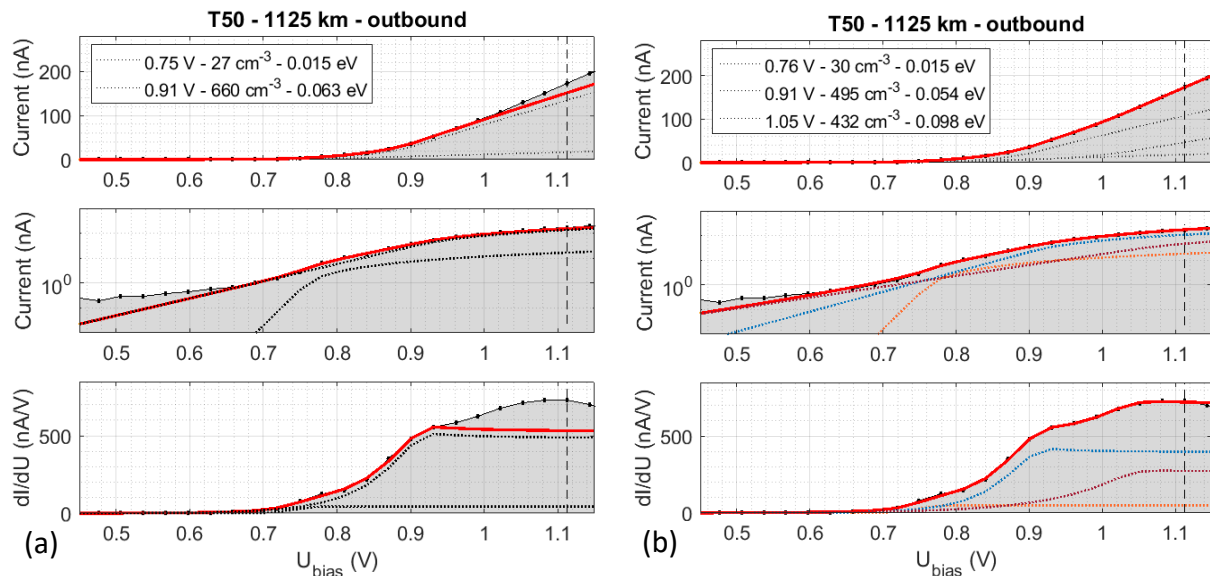

Figure IV.2-1: Fitting of the LP sweep acquired during T50 at 1125 km altitude. (a) Two electron populations are used for fitting. (b) Three electron populations are used for fitting. The part of the curve after the dashed line corresponds to the saturated part, which is not usable for fitting.

In conclusion, the analysis of LP sweeps in the ionosphere of Titan often leads to 2-4 sets of (U_p, n_e, T_e) per sweep.
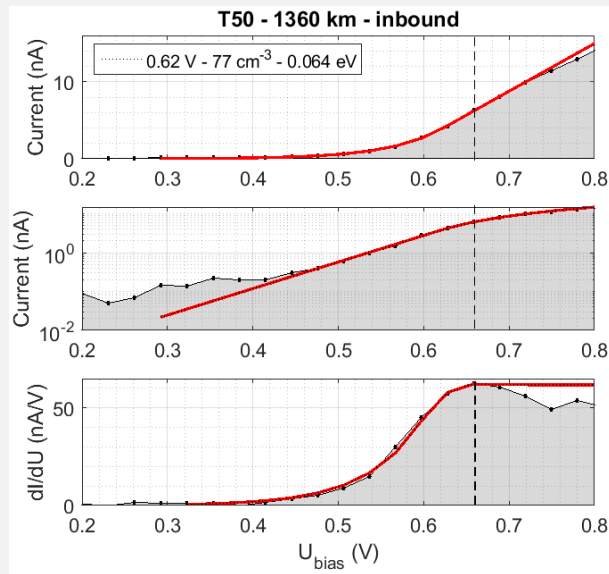
Figure SIV.2-3: Fitting of the LP sweep acquired during T50 at 1360 km altitude. One electron population is used for fitting. The part of the curve after the dashed line corresponds to the saturated part, which is not usable for fitting.
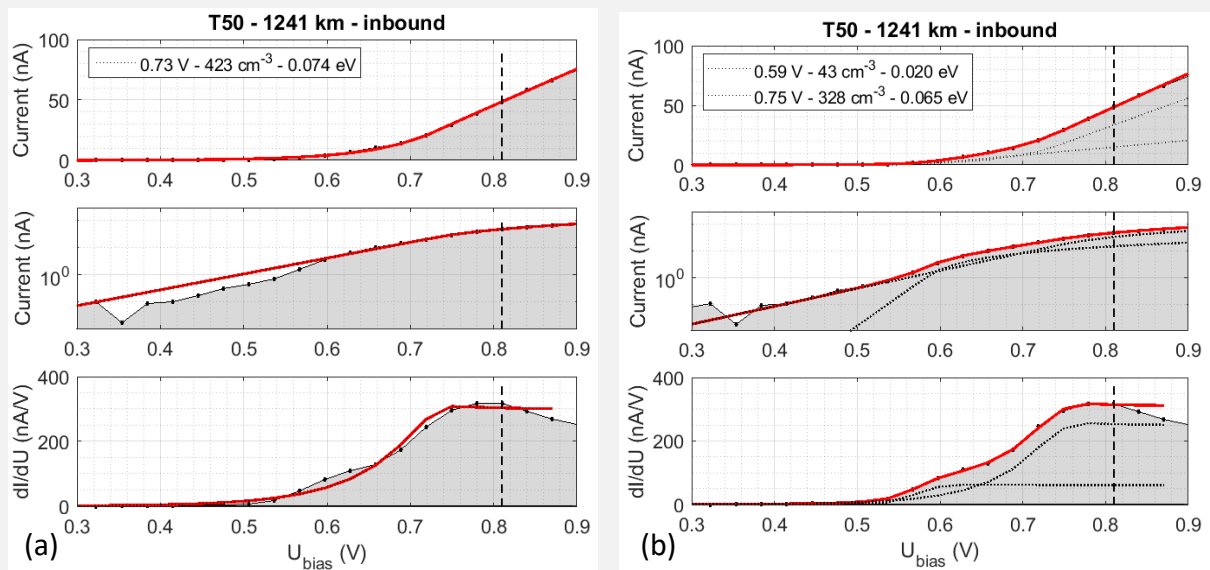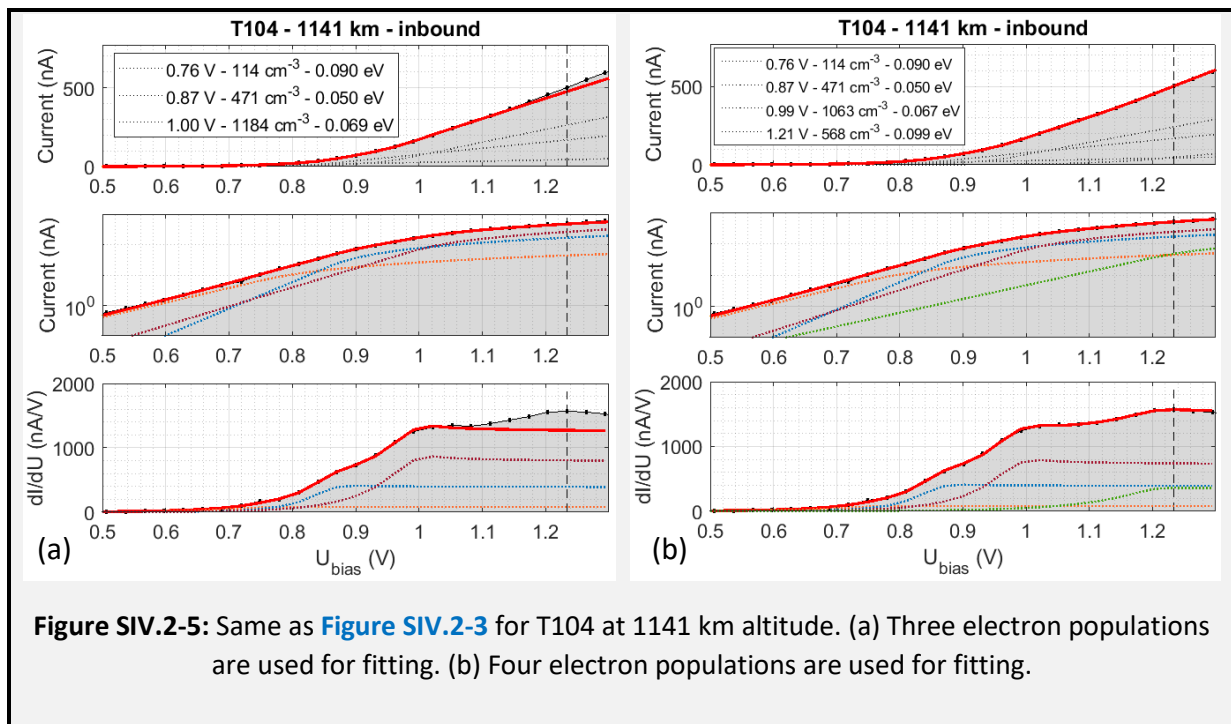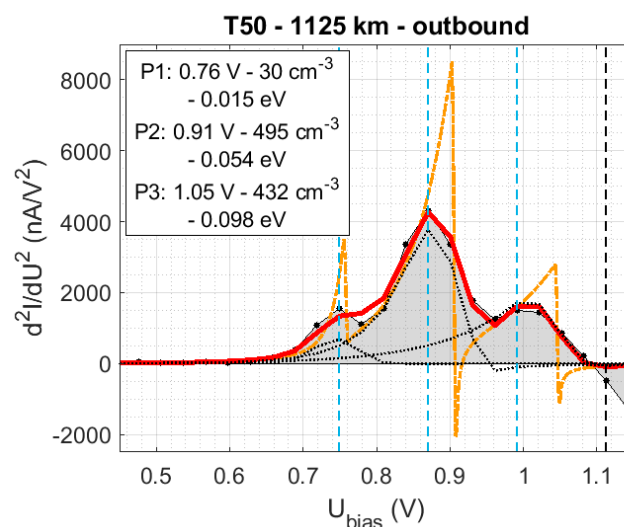

Figure SIV.2-4: Same as **Figure SIV.2-3** for T50 at 1241 km altitude. (a) One electron population is used for fitting. (b) Two electron populations are used for fitting.

Figure SIV.2-5: Same as **Figure SIV.2-3** for T104 at 1141 km altitude. (a) Three electron populations are used for fitting. (b) Four electron populations are used for fitting.

2.1.c. The second derivative of the current: a quick way to spot electron populations

The second derivative of the current is a good indicator of the presence of several electron populations. Each peak corresponds to a population, and its area is globally proportional to the electron density associated (this is explained in **Section IV.2.2.c**). **Figure IV.2-2** shows the second derivative of the current associated with the fitted sweep plotted on **Figure IV.2-1(b)**. Cases with 1, 2 and 4 populations are shown in **Supplement SIV.2-4**.

Figure IV.2-2: Second derivative of current for the sweep shown in **Figure IV.2-1**. The fitted curve obtained in **Figure IV.2-1(b)** is derived to obtain d²I/dU², at the resolution of the data points (red line) and at higher resolution (orange dot dashed line). The part of the curve after the dashed line corresponds to the saturated part.

The second derivative of the current can also be obtained from the fitted curve obtained in **Figure IV.2-1(b)**. The data points are at very low resolution, with only four to ten points per peak. Consequently, the computation of the second derivative is strongly impacted. This effect is observed in **Figure IV.2-2**, showing the second derivative of the current computed both with high resolution, and with a low resolution equal to the one of the dataset.
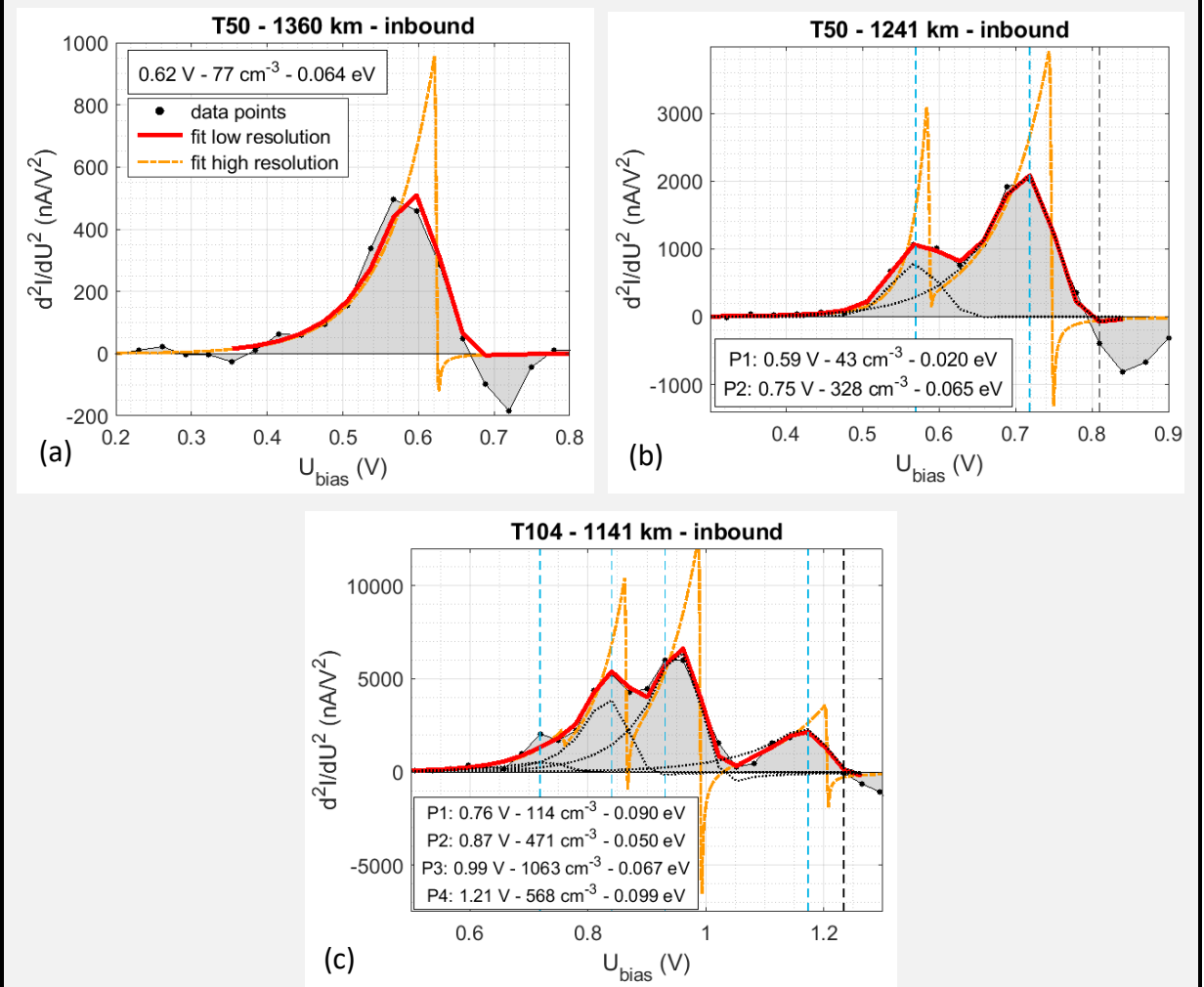

Figure SIV.2-6: Same as **Figure IV.2-2**, for the sweeps shown in **Supplement SIV.2-3**.

2.1.d. A complex case: how many populations?

In some rare cases, the U_p of two different populations are very close and it becomes difficult to fit both separately. The result on the electron density and temperature can be slightly different if only one population or two are used. With only one population, the total density is 5-10% lower, and the temperature of the main population is ~5 meV higher. **Figure IV.2-3 (a)** and **(b)** illustrate this point.
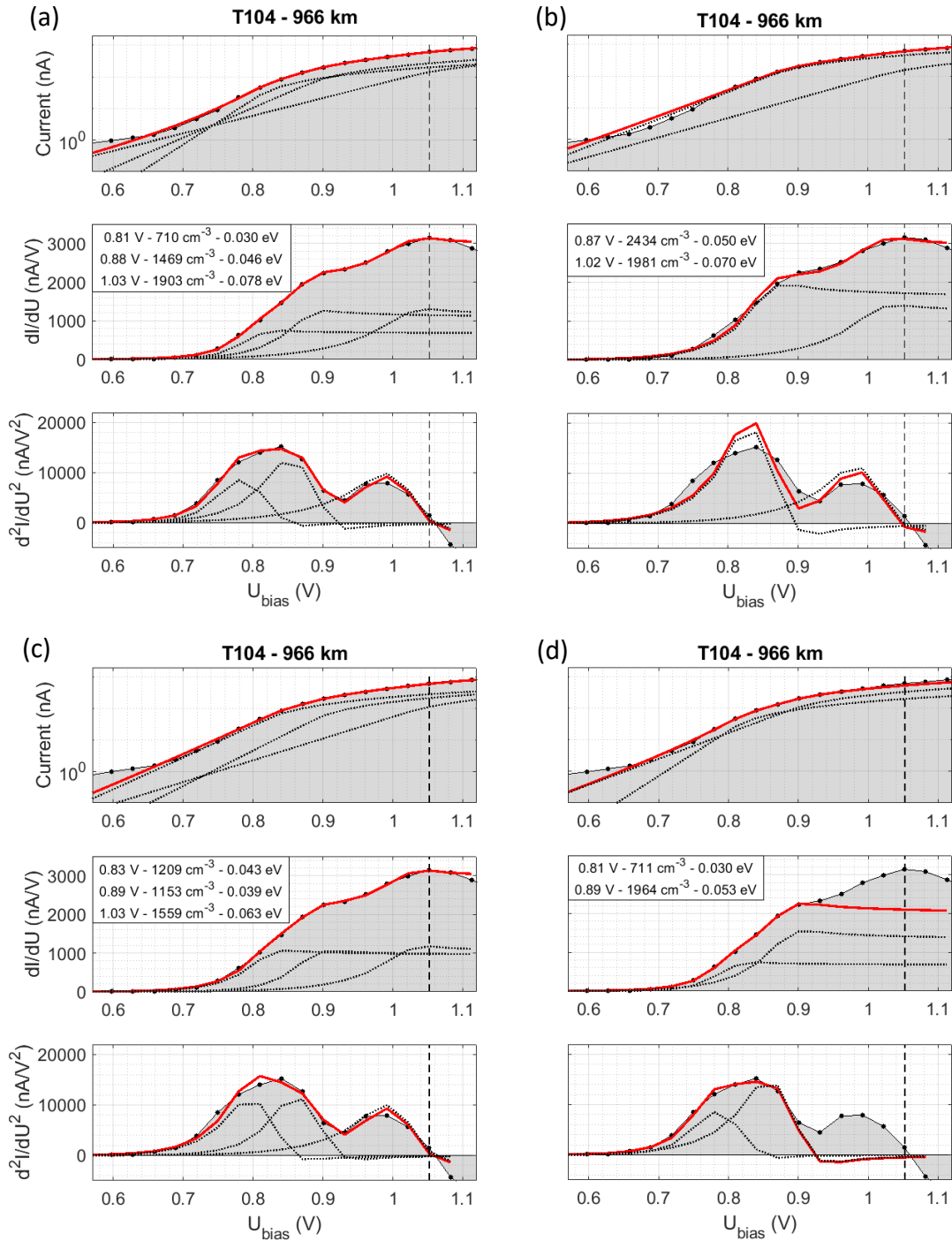

Figure IV.2-3: Example of a LP sweep difficult to fit. The first large hump comes from the fusion of two. It is fitted by: (a), (c) and (d) two populations; (b) one population. The second hump (P_{far}) is not fitted in the case of (d).

With two populations, in a few cases, several pairs of (U$_p$, n$_e$, T$_e$) give a reasonable fitting (see **Figure IV.2-3 (a)** and **(c)**). In the following analysis, we used the continuity of results from sweeps taken one after the other to choose between the several fit possibilities. In any case, it increases the uncertainty for the electron temperature. Variations on temperature of the main population can be of ~5-10 meV.

Concerning the fitting of the hump at higher U$_p$, it does not affect much the fitting of the other populations (see **Figure IV.2-3 (a)** and **(d)**). Indeed, it has a potential U$_p$ different enough from the U$_p$ of the other populations so that the humps can be fitted independently. In the worst cases, the temperature of the main population can be increased by 5-10 meV. In any case, not fitting the second hump strongly decreases the total electron density.

In conclusion, when it becomes difficult to fit with electron populations with close Up values, the uncertainty on the temperature increases compared to the simple cases. It can be +/- 5-10 meV. Not fitting the populations at a potential Up close to the potential of the main population tends to increase the temperature of the main population by 5-10 meV.

2.2- Link between d²I/dU² and the Electron Energy Distribution Function (EEDF)

EEDF in ionospheres can be computed from LP sweep data using the Druyvesteyn method (Druyvesteyn, 1930).

2.2.a. The Druyvesteyn method

The EEDF can easily be deduced from a LP measurement of the electron current (I$_e$) as a function of voltage. The Druyvesteyn method uses the second derivative of I$_e$ to compute the EEDF.

The method is described by Druyvesteyn (1930) and Lieberman and Lichtenberg (2005). It is valid for any convex probe geometry and does not depend on the probe dimension compared to Debye length, or on the ratio T$_i$/T$_e$. It can even measure non-Maxwellian distributions.

The equation for the electron velocity distribution as a function of the second derivative of the electron current is given by the equation (3) in Druyvesteyn (1930):

$$V\left(\Psi\right) = \frac{4\,m_e}{A_{LP}\,e^2} \cdot \Psi \cdot \frac{d^2 I_e}{d\Psi^2} \qquad\qquad [(m.s^{-1})^{-1}.m^{-3}] \qquad\qquad (IV.2-1)$$

Electrons with a speed between v and v+dv have energies between E and E+dE, therefore:

$$V(v).dv = EEDF(E).dE \qquad\qquad (IV.2-2)$$

The derivative of the speed with respect to energy is given by:

$$E = \frac{1}{2} m_e v^2 \quad => \quad \frac{dv}{dE} = (2 m_e E)^{-\frac{1}{2}} \qquad (IV.2-3)$$

Therefore, we obtain the EEDF by dividing the electron speed distribution by $\sqrt{2 m_e E}$, with $E(\Psi) = -e \cdot \Psi$:

$$EEDF_{Dr}(\Psi) = \frac{2\sqrt{2}}{A e^2} \sqrt{\frac{m \cdot (-\Psi)}{e}} \frac{d^2 i}{d\Psi^2} \qquad [J^{-1} . m^{-3}]$$

$$(IV.2-4)$$

$$with \; n_e = \int_0^{+\infty} EEDF_{Dr}(E(\Psi)) . dE$$

Therefore, the EEDF is proportional to the second derivative of the current, and the electron density is equal to the integral of the EEDF.

If the Druyvesteyn method is applied to the expression of the current given in **Equation IV.1-3**, it gives back the expression of an EEDF in the case of a Maxwellian speed distribution (see **Supplement SIV.2-5**):

$$EEDF_{Maxw}(E) = \frac{2}{\sqrt{\pi}} \cdot (k_B . T_e)^{-\frac{3}{2}} . n_e . \sqrt{E} . \exp\left(-\frac{E}{k_B . T_e}\right) \qquad (IV.2-5)$$

SUPPLEMENT SIV.2-5: EEDF FOR A MAXWELLIAN DISTRIBUTION

In the case of a gas at equilibrium, uniform and with isotropic densities and velocities, the velocity distribution is Maxwellian. The velocity distribution, taking into account the three directions (v_x, v_y, v_z), and normalized to 1 is expressed as:

$$f(v_x, v_y, v_z) = \left(\frac{m}{2\pi k_B T}\right)^{\frac{3}{2}} . \exp\left(-\frac{m}{2 k_B T}(v_x^2 + v_y^2 + v_z^2)\right) \qquad (SIV.2-1)$$

In terms of magnitude of the velocity ($v = \sqrt{v_x^2 + v_y^2 + v_z^2}$), the velocity distribution function $V(v)$ is the velocity distribution $f(v_x, v_y, v_z)$ in the interval [v, v+dv] whose volume is $4\pi v^2 dv$:

$$V(v) = 4\pi v^2 . \left(\frac{m}{2\pi k_B T}\right)^{\frac{3}{2}} . \exp\left(-\frac{m}{2 k_B T} v^2\right) \qquad (SIV.2-2)$$

We obtain the EEDF (normalized to 1) by dividing the velocity distribution $V(v)$ by $\sqrt{2mE}$:

$$EEDF_{Maxw}(E) = \frac{2}{\sqrt{\pi}} . (k_B . T_e)^{-\frac{3}{2}} . n_e . \sqrt{E} . \exp\left(-\frac{E}{k_B . T_e}\right) \qquad (SIV.2-3)$$

2.2.b. EEDF in the case of one population

The Druyvesteyn method (Equation IV.2-4) is applied to the simple case with one electron population presented in **Figure SIV.2-6 (a)** (T50 at 1360 km). **Figure IV.2-4** compares the EEDF obtained from the LP data points to the 'Maxwellian' EEDF computed with the fitted electron density and temperature (**Equation IV.2-5**). They do not perfectly match because of the low resolution of LP data points. Indeed, the **Druyvesteyn method uses the second derivative of the current, which is highly distorted because of the lack of data points.**

To show this effect, the Druyvesteyn method is applied to the fit of the current. The EEDF obtained using a fitting curve at high resolution superimposes perfectly with the 'Maxwellian' EEDF. On the other hand, the EEDF obtained using a fitting curve with the resolution of the LP data points matches well with the EEDF obtained from the data points.

The EEDF obtained using the Druyvesteyn method on the LP data points is therefore fairly well represented by a 'Maxwellian' EEDF if one takes the problem of low resolution into account.
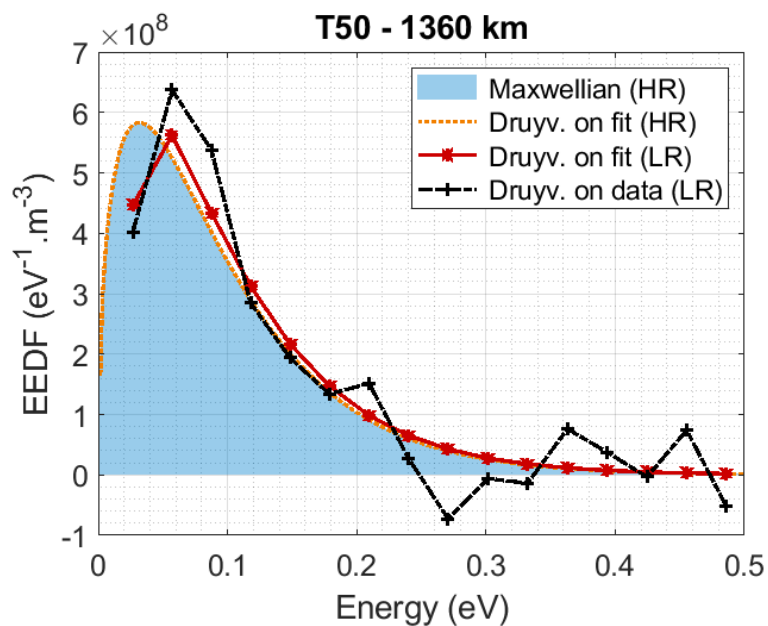

Figure IV.2-4: Example of EEDF obtained from LP data with only one population. Dotted-dashed black line: EEDF using the Druyvesteyn method data points. Red line: EEDF using the Druyvesteyn method on the fit at low resolution (LR) shown on **Figure SIV.2-6 (a)**. Dotted orange line: EEDF using the Druyvesteyn method on the fit at high resolution (HR). Blue area: 'Maxwellian' EEDF from fitted n_e and T_e.

2.2.c. Maxwellian EEDF for each population

In the case of LP data showing several populations, applying the Druyvesteyn method is less straightforward. Indeed, the method requires one plasma potential U$_p$, whereas the fitting gives as much U$_p$ as populations detected.

Figure IV.2-5 shows the case of two populations. The Druyvesteyn method is applied to the LP data points using the U$_p$ potential from **(a)** the first population and **(b)** the second population. On the **Figure IV.2-5 (b)**, the two populations appear in reverse order compared to the plot of d²I/dU², because the x-axis is reversed ($E = -e \cdot \Psi \propto -U_{\text{bias}} + U_P$).
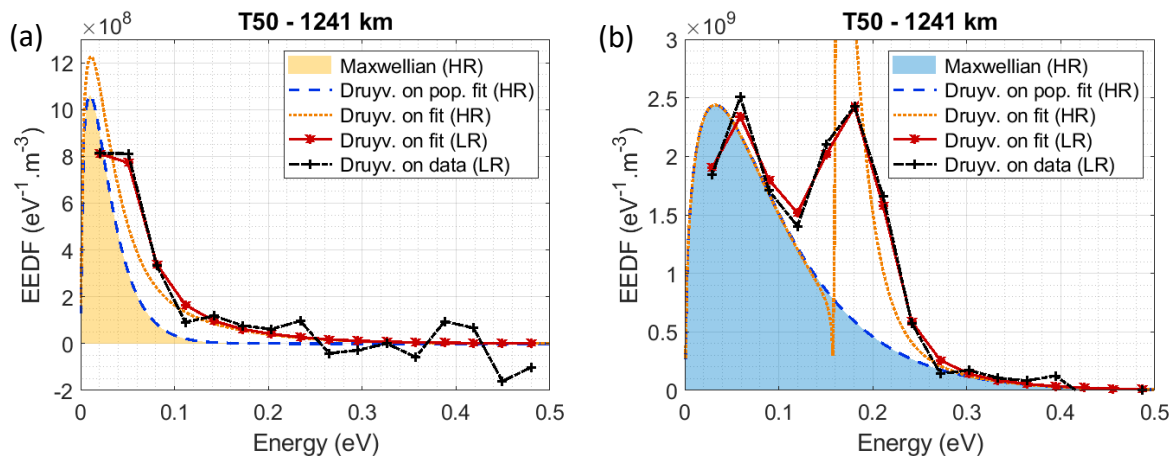

Figure IV.2-5: Example of EEDF obtained from LP data with two populations: (a) EEDF computed from (U$_p$, n$_e$, T$_e$) of population 1; (b) EEDF computed from (U$_p$, n$_e$, T$_e$) of population 2. Dotted-dashed black line: EEDF using the Druyvesteyn method data points. Red line: EEDF using the Druyvesteyn method on the fit at low resolution (LR) shown on **Figure SIV.2-6 (b)**. Dotted orange line: EEDF using the Druyvesteyn method on the fit at high resolution (HR). Dashed blue line: EEDF using the Druyvesteyn method on the fit of only one population at high resolution (HR). Colored area: 'Maxwellian' EEDF from fitted n$_e$ and T$_e$.

Figure IV.2-5 shows that in the case of several electron populations, the EEDF computed for one population with the Druyvesteyn method is disturbed by the other populations with U$_p$ close. To observe this effect, the Druyvesteyn method is applied to the fit of the LP data points with the two populations (orange line), and to the fitted current corresponding only to one population (dashed blue line). **If one takes into account both the presence of nearby populations and the effects of low resolution, the EEDF from data points can reasonably be modelled by a 'Maxwellian' EEDF.**

However, the closer the U$_p$ of different populations are, the more difficult it is to precisely fit each population and deduce the electron density and temperature. EEDF deduced from the fitted electron density and temperature can therefore show larger error bars than in the usual case.

As mentioned in **Section IV.2.2.a**, **the area under each EEDF corresponds to the electron density of each population. The position of the maximum of the EEDF is related to the electron temperature.** The case of three populations is presented in **Supplement SIV.2-6**.
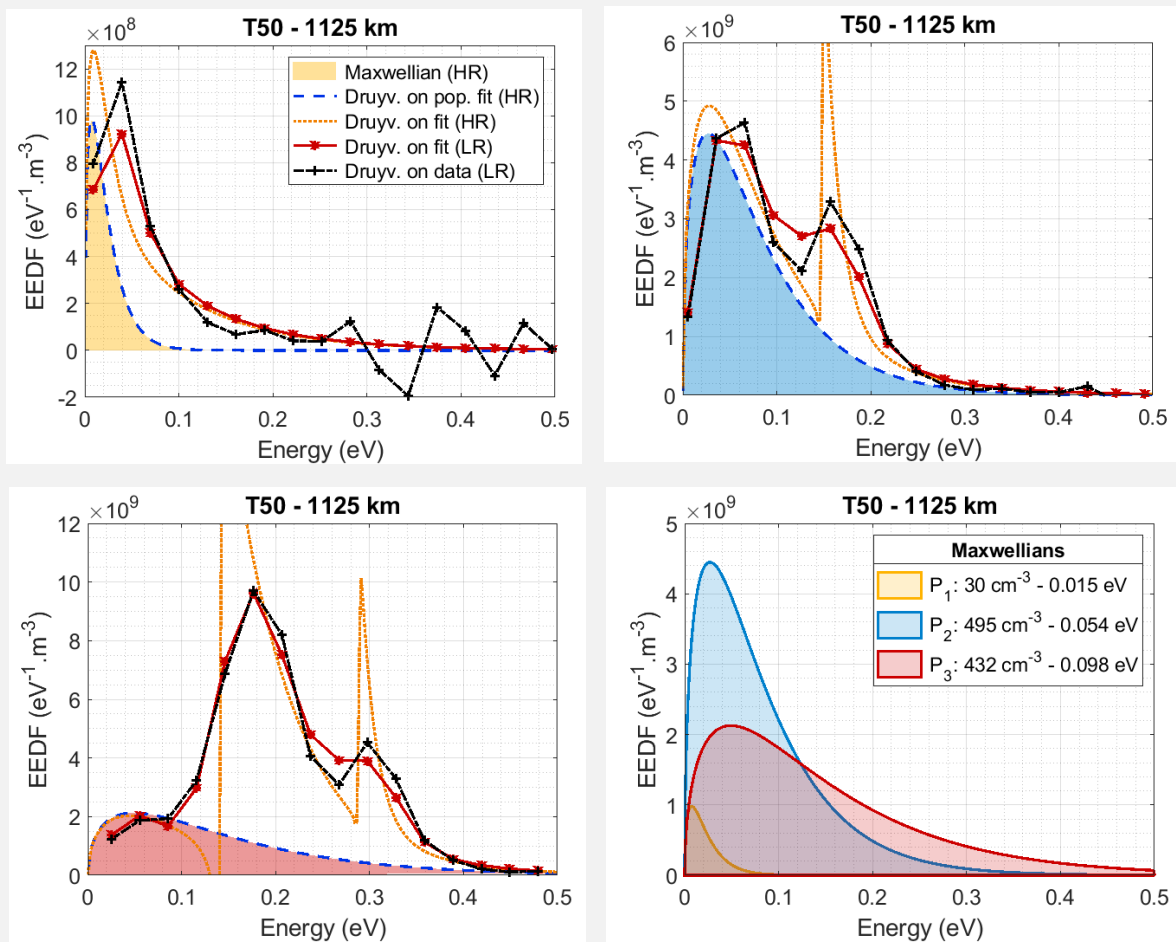
Figure SIV.2-7: Same as **Figure IV.2-5** on a case with three populations: (a,b,c) EEDF computed from (U_p, n_e, T_e) respectively from population 1, 2 and 3; (d) comparison of the 'Maxwellian' EEDF obtained for the three populations.

An example of the variability of the populations between the flybys is shown in Figure IV.2-6. It illustrates three very different cases of 'Maxwellian' EEDF obtained at ~1000 km altitude. The three cases are representative of the three flyby families presented below (in **Section IV.2.3**).

The first case (in the family F1) shows two populations (P_1 and P_2). The area (and so the electron density) of P_2 dominates P_1. The second case (F2) has one more population (P_3). The area of P_2 and P_3 are equivalent and higher than the area of P_1. We observe that P_3 EEDF is in average at higher energy than the EEDF of P_2: its electron temperature is higher. Finally, the family F3 shows also a new population (P_{far}). In most cases, P_1 becomes negligible compared to the others. P_3 dominates P_2 in density. P_{far} characteristics vary with altitude: it can be denser than the others, and it is usually hotter.
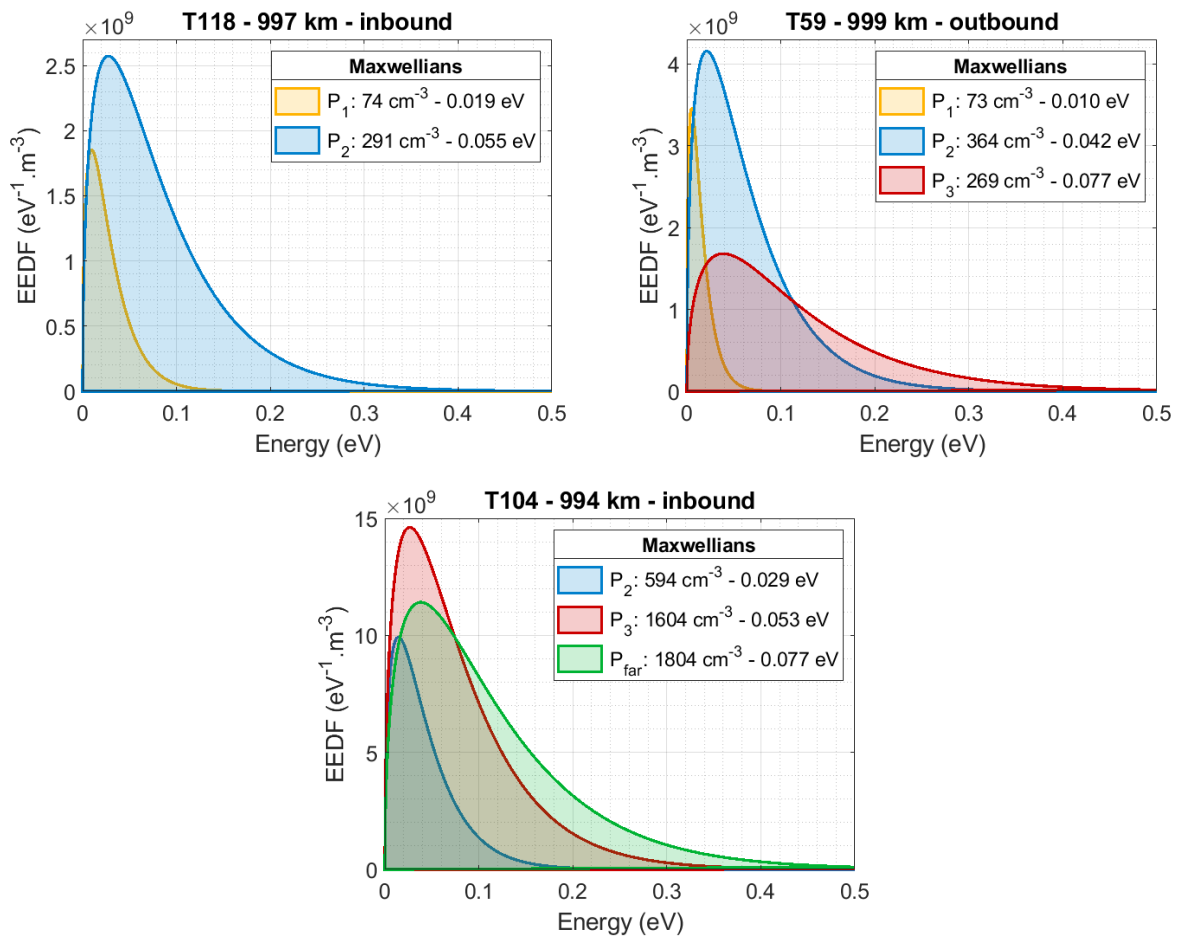
Figure IV.2-6: 'Maxwellian' EEDF obtained at ~1000 km altitude for the flybys: (a) T118 (family F1); (b) T59 (F2); (c) T104 (F3).

2.3- Evolution of the electron populations with altitude and Solar Zenith Angle

2.3.a. d²I from data points as a function of altitude: simple diagnostics of the electron population evolution

Sweeps evolve during a flyby. The number of observed humps in the second derivative of the current varies with altitude. Therefore, the number of populations detected is not the same at all altitudes for a given flyby. We focus on the part of the ionosphere below 1200 km. 57 flybys have LP measurements at these altitudes. All the altitude profiles obtained can be classified in three families. They are described in **Table IV.2-1** and examples of profiles for the three cases are shown in **Figure IV.2-7**.

Name of the flyby family	Characteristics of d²I/dU² at lower altitude	Flybys
F1	2 separated peaks	T21, T25-28, T55, **T118**, T119
F2	3 peaks	T5, T16, T46, T50, T56, T57, T58, **T59**, T65, T117, T121
F3	1 large peak (or 2 close) + 1 further, at higher U_{bias}	T17, T20, T23, T39, **T40**, T41-43, T47, T48, T51, T83-88, T91, T92, T95, T100, **T104**, T106-108, T113, T126
F1/F2	with different characteristics on inbound and outbound	T29, T30, T32, T120
F2/F3		T18, T19, T36, T49, T61, **T70**, T71

Table IV.2-1: Definition of the 3 flyby families and their corresponding flybys. The flybys studied in details in this section are indicated in bold.
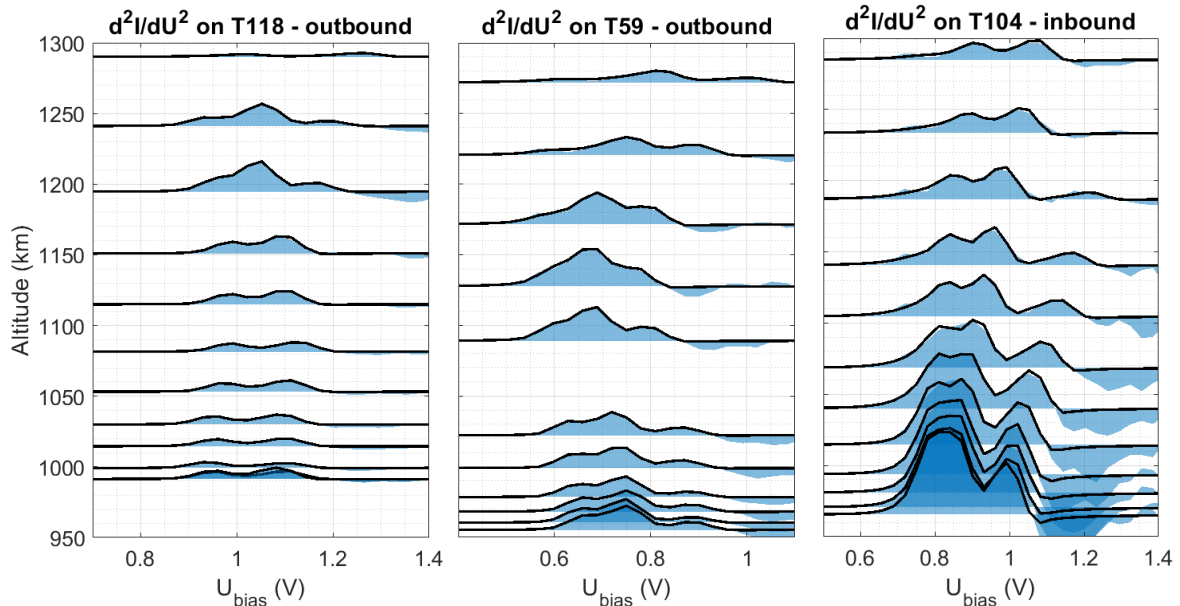

Figure IV.2-7: 'Typical' d²I/dU² profiles with altitude, represented with examples: T118 (F1), T59 (F2) and T104 (F3). LP data is in blue area, and d²I/dU² from fit is represented by a black line. The scaling of d²I/dU² is the same for all the plots.

All the profiles have similar d²I/dU² curves around 1250-1200 km, showing usually two-three contiguous humps. However, this curve evolves differently with altitude in the three cases.

At lower altitude, in all cases, there is a main hump formed either by one large peak, two or three peaks (further named P_1, P_2, P_3 for clarity). In addition, for the profiles of the family F3, a small hump detached from the main one (P_{far}), at higher voltage, is observed below ~1200 – 1150 km altitude.

In conclusion, the curves of the second derivative of the current as a function of the altitude allow to easily classify Titan flybys in three families. Each family has a different number of electron populations, with different characteristics.

2.3.b. d²I from data points as a function of altitude: strong correlation with Solar Zenith Angle (SZA)

The influence of the Solar Zenith Angle (SZA) on the repartition of the three families is shown in **Figure IV.2-8.** It plots for each analyzed flyby its family number as a function of the SZA and the altitude at closest approach.
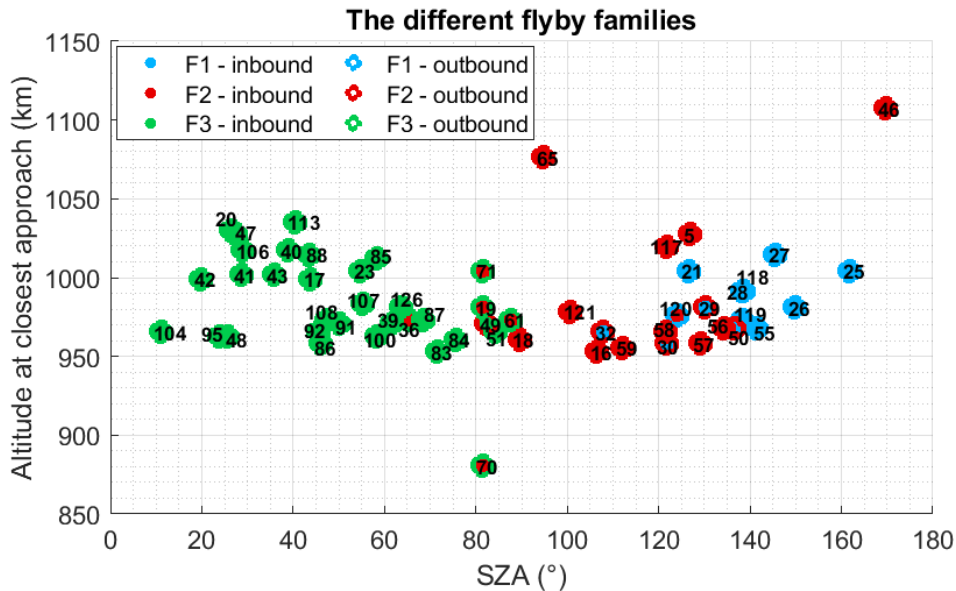

Figure IV.2-8: Flyby families as a function of Solar Zenith Angle (SZA) and altitude at closest approach. Inbound data are filled dots; outbound data are circles. The numbers of the flybys are indicated on the data points.

The flybys belonging to the family with a small detached hump (F3) are all found on dayside. In addition, no flyby from another family is observed on the dayside. **The appearance of the small peak P$_{far}$ is therefore directly linked to the solar irradiation.**

The families are strongly dependent on the SZA. F3 is on dayside, F2 on nightside next to the terminator and F1 on nightside far from the terminator. One can also observe an increase in the area of the peaks from F1 to F3 on **Figure IV.2-7**. It is linked to the increase of the electron density from nightside to dayside.

2.3.c. A different evolution of the populations with altitude on nightside and on dayside

Figure IV.2-9 shows the distribution of the electron populations with altitude and SZA in the case of 57 Cassini flybys. As observed above, the population P$_{far}$ appears always below ~1200 km altitude and for SZA < 80-90°. Such flybys belong to the family F3. On the opposite, the family F1 that does not show a P$_3$ population at lower altitude is observed only on the nightside, at high SZA (>~120°).
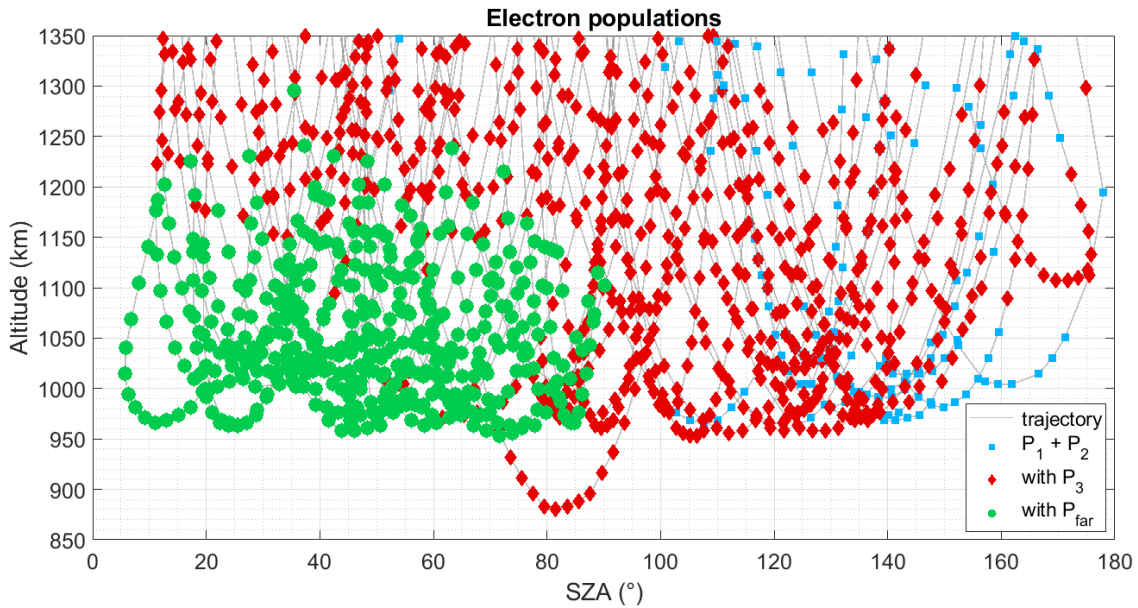
Figure IV.2-9: Detection of electron populations as a function of altitude and SZA. With 57 flybys. Blue squares represent sweeps with populations P_1 and P_2, red diamonds show the presence of P_3, and green dots are for P_{far}.

The evolution with altitude and SZA of the detected peaks of the second derivative of the current can be schematized as in **Figure IV.2-10**. Each peak is attributed to an electron population among P_1, P_2, P_3 and P_{far}.
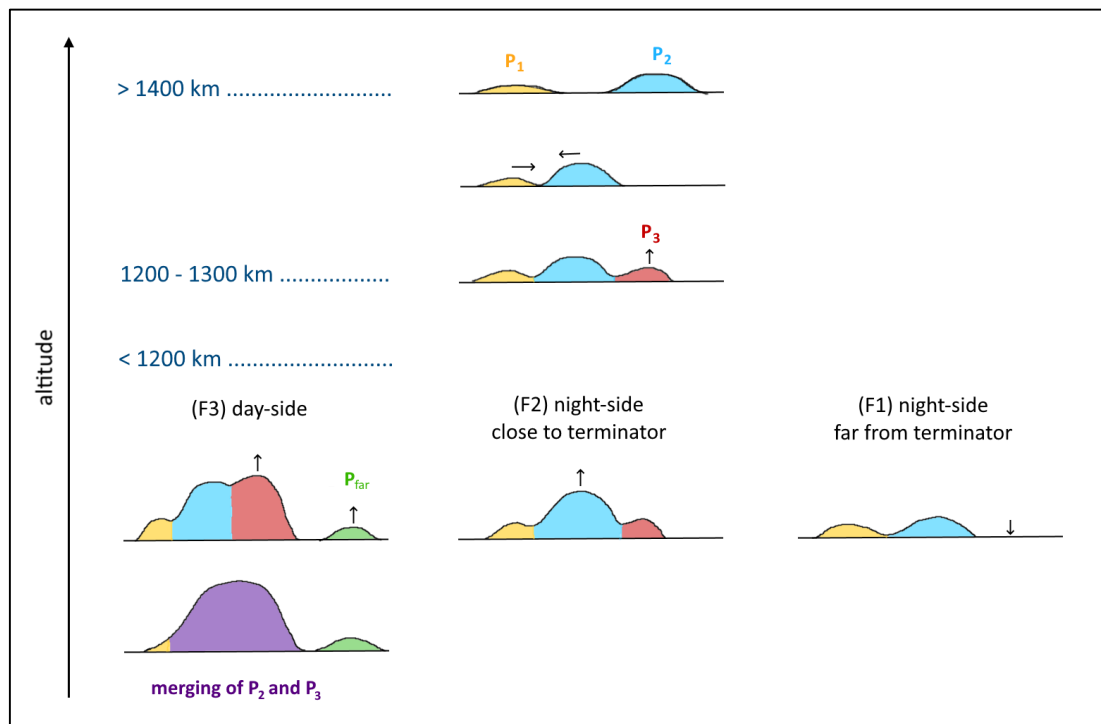

Figure IV.2-10: Summary scheme of the evolution of d²I/dU² peaks with altitude in the 3 cases: nightside far from terminator (F1), nightside close to terminator (F2) and dayside (F3). Small arrows indicate the evolution trends with decreasing altitude.

2.4- Electron densities and temperatures

As shown in Section IV.2.2.b and IV.2.2.d, the number of populations used can have an impact on the measurement of the electron temperature(s). The electron density and temperature profiles obtained for different cases are presented in this section.

2.4.a. Typical profile for the family F1: nightside far from the terminator

LP sweeps taken on the nightside far from the terminator always present two clearly distinct peaks in the second derivative of the current. They can easily be fitted separately and lead to two sets of (U_p, n_e, T_e). **Figure IV.2-11** shows typical F1 profiles (far nightside) of the electron density and temperature.
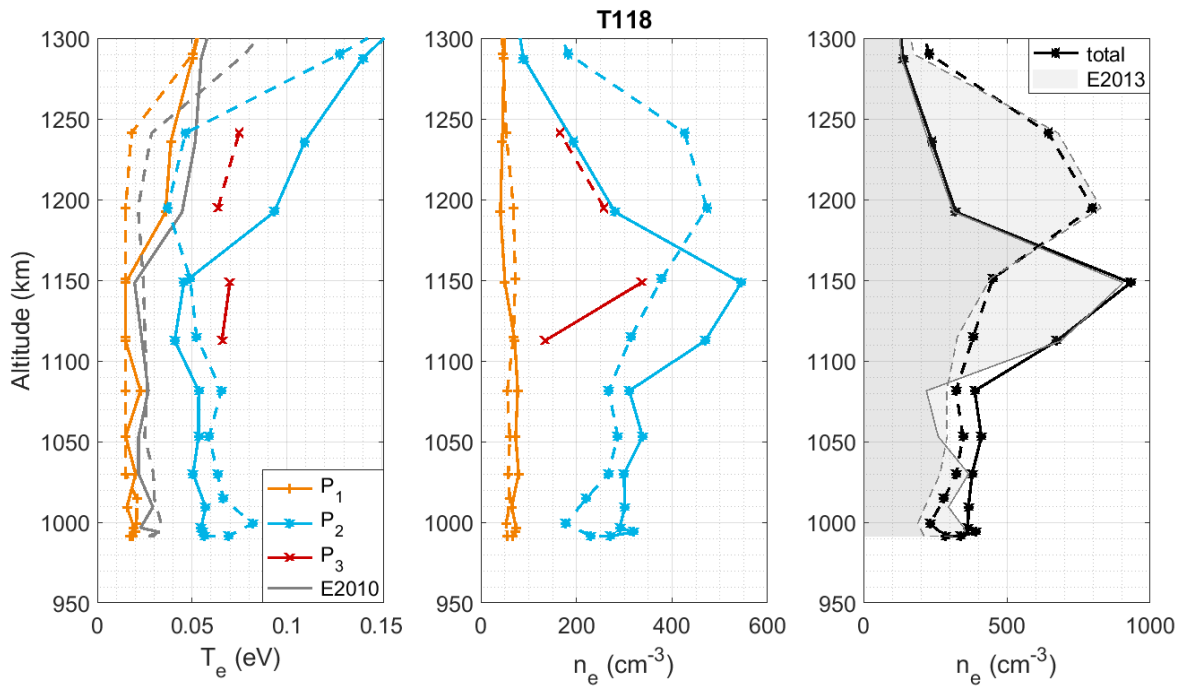
Figure IV.2-11: Electron density and temperature profiles in the case of a F1 family flyby; inbound (line) and outbound (dashed line). Results for the different populations P_1, P_2 and P_3 (colors) compared to the total density as the sum of the densities of all the populations (black). Comparison to data from Edberg et al. (2013, 2010), noted E2013 and E2010 (grey).

For flybys of the F1 family, a dominant population (P_2) can be observed, with a rather constant temperature around 40-60 meV below 1150-1250 km altitude. The density of this population peaks at an altitude varying between 1150 and 1250 km.

The population with the lowest U_p is very constant with altitude. Its density is low, less than 100 cm^{-3}. Its temperature is around 10-20 meV, at the detection limit of the probe.

The total electron density obtained is consistent with previous measurements by Edberg et al. (2013). Another method was used to precisely determine the electron density. The comparison of our fit to the density measurements by Edberg et al. (2013) serves as a validation tool.

The previous electron temperature analysis, done by Edberg et al. (2010), gives usually an electron temperature between the one found for P_1 and P_2. For instance, in the case of T118 shown in **Figure IV.2-11**, they obtained a temperature not representative of the main population of electrons (P_2). Their temperature is close to the temperature of the small population P_1. **In conclusion, using several electron populations in the fitting of the sweeps significantly improves the analysis. This process attributes a temperature for each population, and consequently, the temperature of the dominant electron population can be found without ambiguity.**

For comparison, we studied the case where the whole current curve before the saturation is fitted, but using only one population, as shown in **Figure SIV.2-3 (a).** A hot bias of ~0.01 eV is induced in the determination of the temperature of the dominant population (see **Figure IV.2-**

12). In addition, the total electron density increases by ~10% and is no more consistent with the density measured by Edberg et al. (2013). **In conclusion, even if the population P₁ is not dense, it is necessary to fit it separately from the main population P₂ to avoid a hot bias on the determination of the temperature of P₂.**
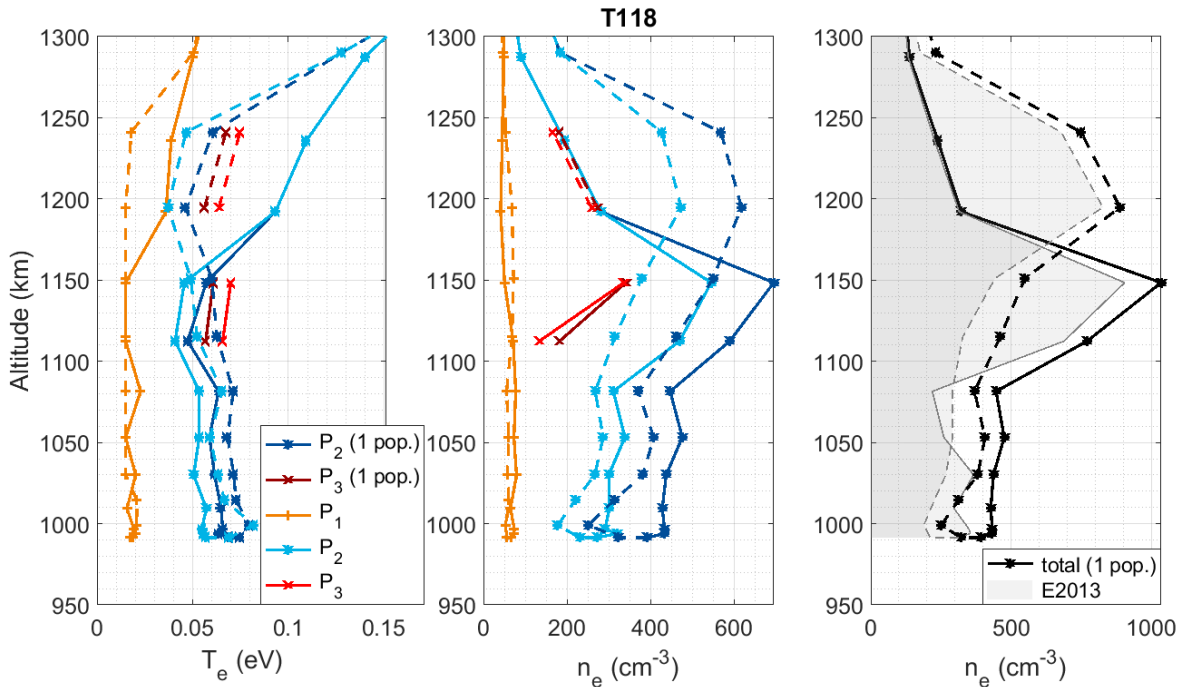

Figure IV.2-12: Same as **Figure IV.2-11**, superimposed to the T_e and n_e profiles obtained with only one population to fit P₁ and P₂ when their potentials are close enough (i.e. below 1200 km for inbound, and below 1300 km for outbound).

Therefore, F1 family profiles should be fitted with mainly two populations. We observe that P₁ is cold and not dense, and P₂ is denser with a temperature of ~40-60 meV.

In addition, **Figure IV.2-11** shows that a third population appears (P₃) at the ionospheric peak, when the total electron density exceeds 500 cm^{-3}. It has a temperature higher than the other populations, around 60-90 meV.

2.4.b. Typical profile for the family F2: nightside close to the terminator

Flybys on the nightside closer to the terminator show a third population at all altitudes (see **Figure IV.2-13**). The total electron density is globally higher than for F1 flybys (far nightside), which is expected because of the influence of photoionization on dayside (Ågren et al., 2009). The temperatures observed for the three populations are similar to the ones of F1 flybys: P₁ below 20 meV, P₂ generally between 30 and 50 meV and P₃ at 60-80 meV.

If the fit does not include the population P₃, as plotted in **Figure IV.2-1 (a)**, the temperatures obtained for P₁ and P₂ are almost unchanged (see **Figure SIV.2-9**). However, the total electron density decreases by 25%. **In conclusion, the addition of a third population does not disturb**

the fitting of the two first populations. Besides, it is necessary to include it to obtain the right electron density in total.
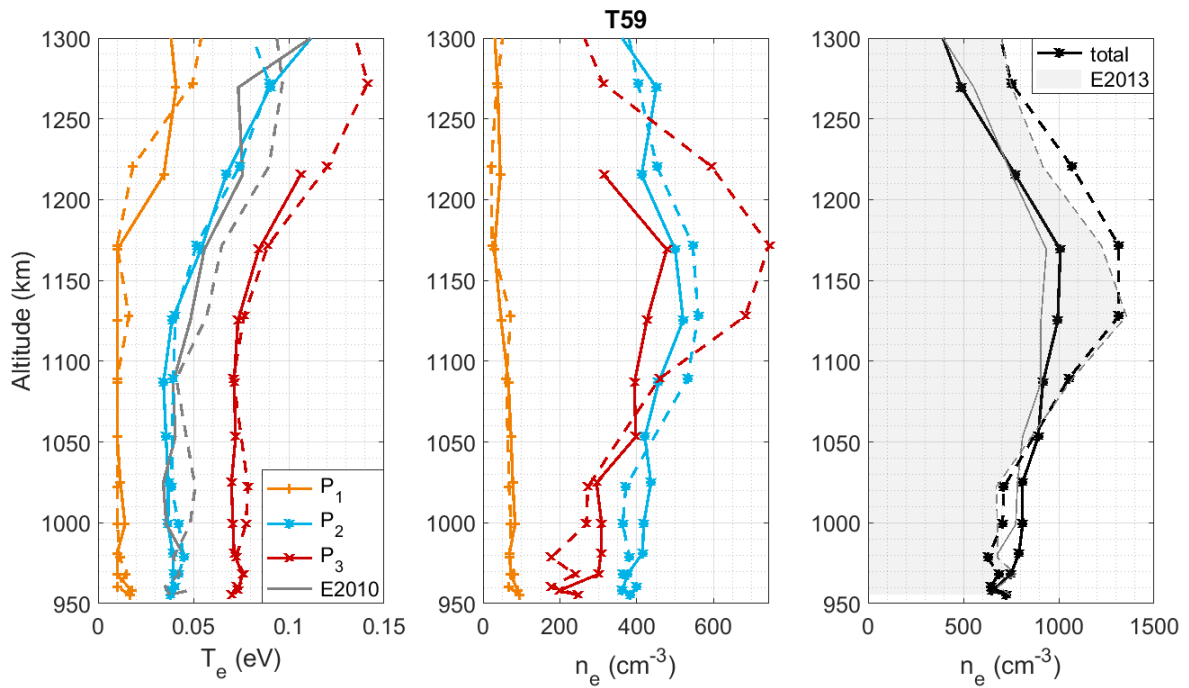
Figure IV.2-13: Same as **Figure IV.2-11**, in the case of a F2 family flyby.
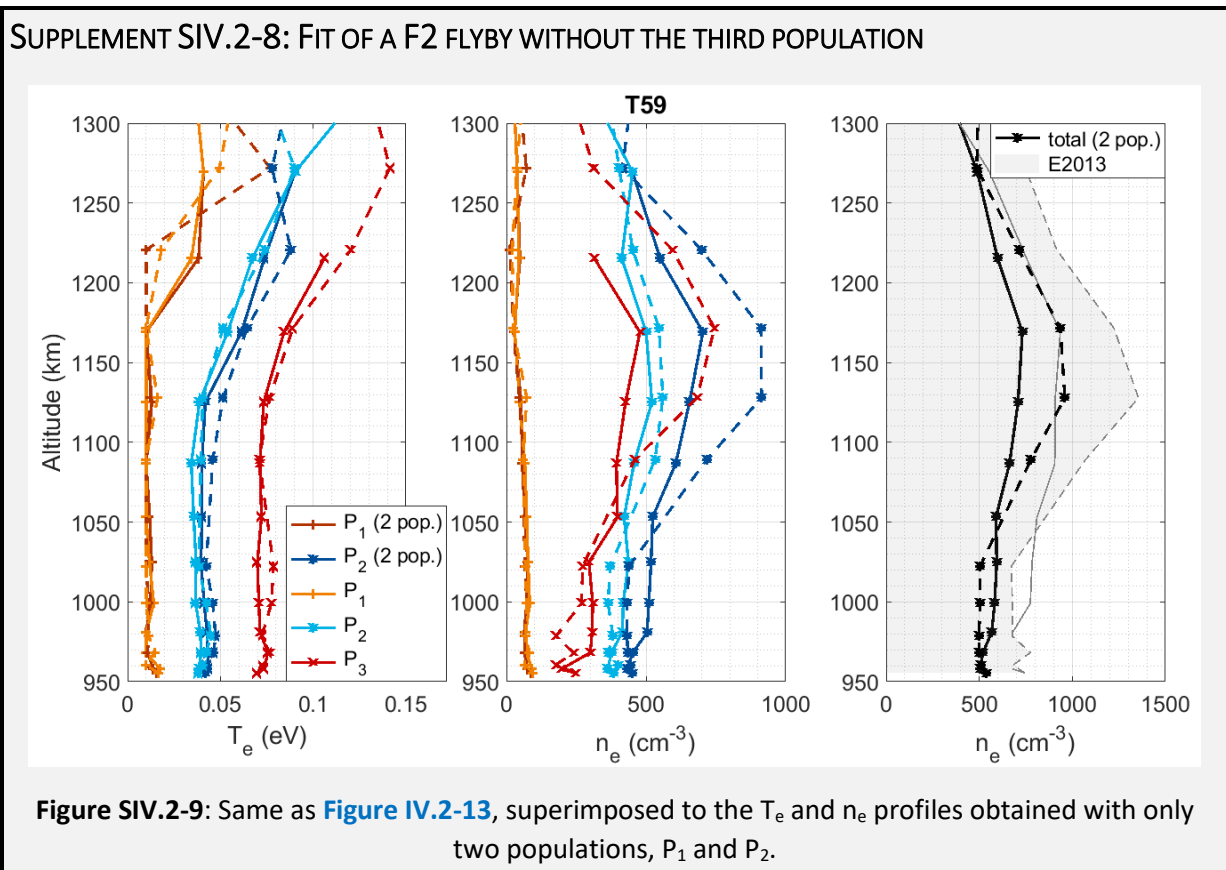

SUPPLEMENT SIV.2-8: FIT OF A F2 FLYBY WITHOUT THE THIRD POPULATION

Figure SIV.2-9: Same as **Figure IV.2-13**, superimposed to the T_e and n_e profiles obtained with only two populations, P_1 and P_2.

2.4.c. Typical profile for the family F3: dayside

On dayside, a new population (P_{far}) appears on the sweeps at a potential U_p higher than the other populations. Its temperature is generally higher than for the other populations, up to 0.1 eV. This population appears only at altitudes below ~1200-1150 km. Contrarily to the constant profiles on the nightside, the temperatures of all the populations decrease slightly with altitude, by ~0.03 eV in 200 km.

We studied the effect of taking this new population into account for the fitting (see **Supplement SIV.2-9**). We observe it does not impact the (U_p, n_e, T_e) done on the other populations. Indeed, the peak is completely separated from the others and does not affect their fitting (as shown in **Figure SIV.2-5 (a)** and **Figure SIV.2-6 (c)**). However, the total electron density then decreases by up to 30%. **The electron population P_{far} is often non-negligible and should be taken into account when present.**

In some cases, the fitting of P_2 and P_3 can be ambiguous (see **Figure IV.2-3**), especially at lower altitudes. The use of two populations is required to obtain a correct fitting. Besides, it is consistent if one compares the sweeps with sweeps at higher altitudes (see **Figure IV.2-7** for T104). The n_e and T_e profiles obtained in both cases are compared in **Supplement SIV.2-9**. The total electron density stays globally the same. The temperature of the main population is not impacted. The population P_{far} can vary, but generally stays in the range of its large error bars. **In conclusion, it seems that the fusion of P_2 and P_3 at lower altitudes in F3 flybys happens smoothly: at one point, fitting with two or three populations gives globally the same results: P_2 becomes negligible compared to P_3.**
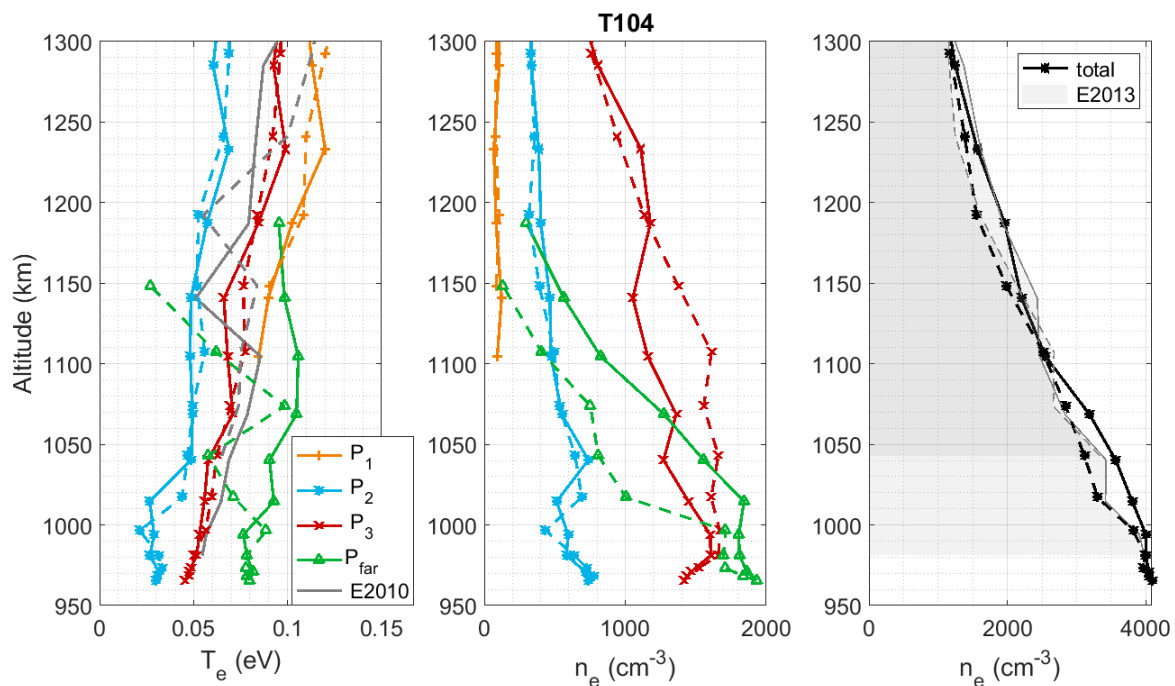
Figure IV.2-14: Same as **Figure IV.2-11**, in the case of a F3 family flyby.

Figure SIV.2-10 (a) shows that if the population P_{far} is not taken into account during the fitting, as shown on **Figure SIV.2-5 (a)**, the (U_p, n_e, T_e) resulting parameters for the other populations do not change.

Figure SIV.2-10 (b) shows that fitting F3 flybys at low altitude can sometimes be done either with 2 or 3 populations, with globally the same results. P_2 becomes negligible compared to P_3.

Figure SIV.2-10: Same as **Figure IV.2-14**, superimposed to the T_e and n_e profiles obtained: (a) without the population P_{far}; (b) with only one population to fit P_2 and P_3 when their potentials are close enough (i.e. below 1100 km). In both cases only two populations are used to fit below 1100 km.

2.4.d. Summary: typical profiles for the three flyby families

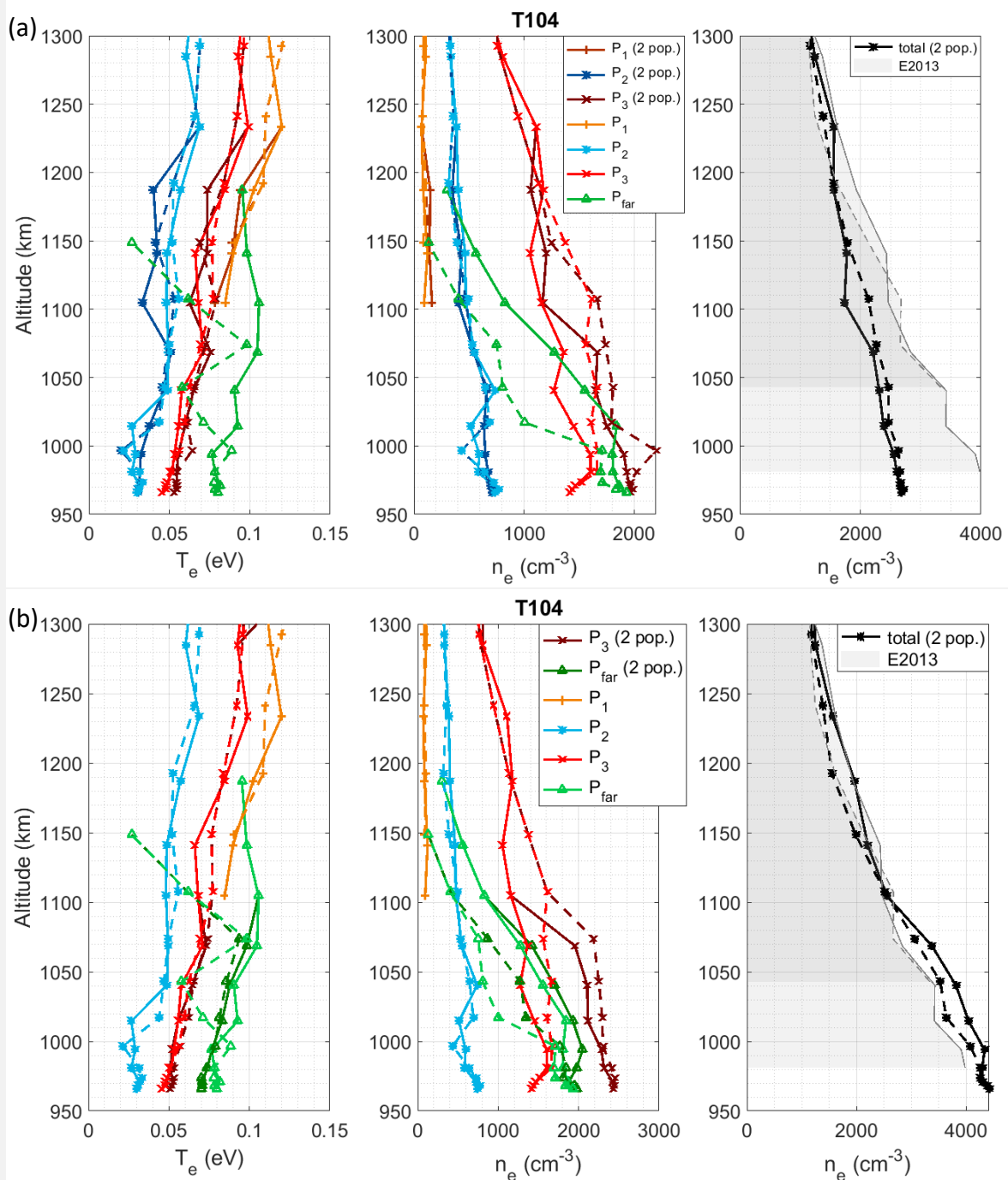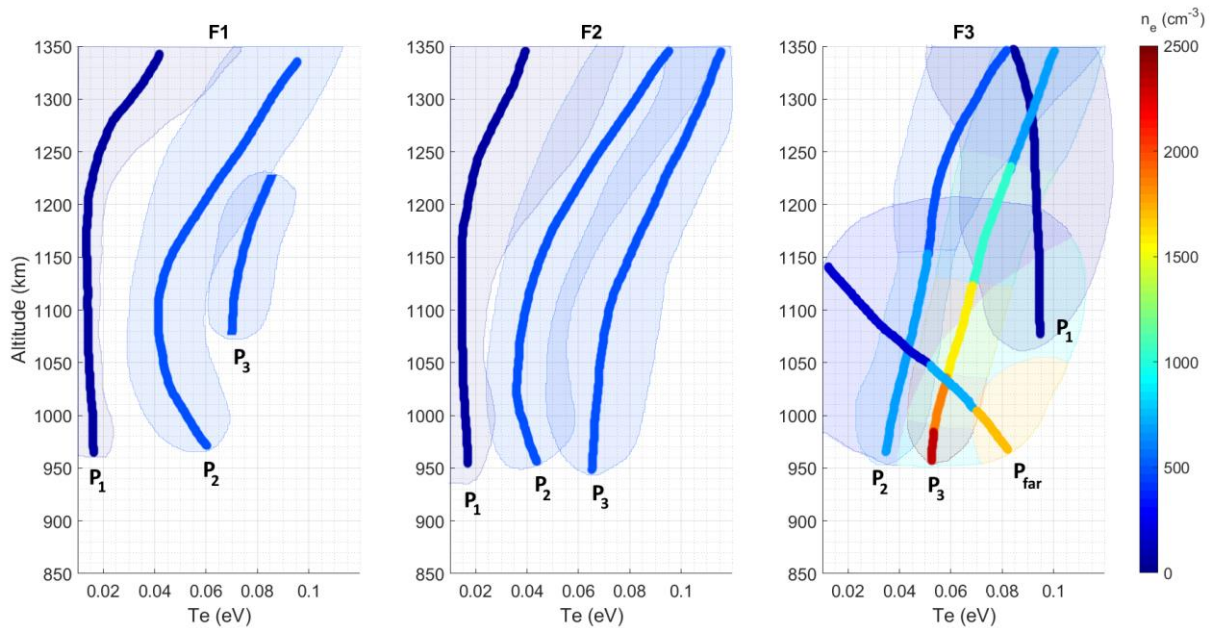**Figure IV.2-15**: Electron temperatures and densities of the four populations as a function of altitude, in the case of the three flyby families: F1 for SZA > 140°, F2 for 90° < SZA < 140° and F3 for SZA < 70°. The shaded areas include all the data points obtained on 57 flybys. The lines indicate the average values.

2.4.e. Discussion on the origin of the electron populations

The work presented above shows that the analysis of LP sweeps in the ionosphere of Titan often leads to two to four sets of (U_p, n_e, T_e). The four populations have different potentials U_p. Consequently, they should come from different sources.

However, the plasma at such altitudes is supposed to be thermalized from the model predictions (Galand et al., 2014). Suprathermal electrons from the magnetosphere and electrons coming from the photoionization of N_2 and CH_4 should thermalize through collisions, leading to only one electron population.

We discuss the possible origins for the different electrons populations observed in the data, controlling that they are not due to instrumental effects.

DETACHED ELECTRONS COMING FROM THE BOOM

One of the populations can be due to electrons detached from the boom next to the probe, after the collision of an energetic photon or particle at its surface. Such electrons are created on the surface of the boom, they are close to it and easily caught back. Therefore, it corresponds to the population with the lower potential U_p.

The population 1 observed in the LP sweeps is then possibly due to these electrons detached from the boom. Impacts with energetic ions (Ågren et al., 2007; Cravens et al., 2008) can explain the observation of population 1 also on the nightside.

PHOTO-ELECTRONS COMING FROM THE SPACECRAFT

Energetic photons and particles can also detach electrons from the surface of the spacecraft. Nevertheless, in the ionosphere the electrons are cold enough to prevent these spacecraft electrons to reach the Langmuir probe (Wang et al., 2015). Indeed, the Debye length in the ionosphere is always below 7 cm, far lower than the distance between the spacecraft and the Langmuir Probe (1.5 m). **Electrons detached from the spacecraft cannot reach the LP.**

ELECTRONS COLLECTED DIFFERENTLY ON BOTH SIDES OF THE PROBE DUE TO THE SPACECRAFT MOTION?

With energies from 0.02 to 0.08 eV in the ionosphere, the electrons of the various populations have a thermal velocity of 85 to 170 km/s. It is highly superior to the spacecraft velocity (~6 km/s). Therefore, there should be no difference in the electron collection from all around the probe. **This point cannot explain the presence of several electron populations.**

PERTURBATION OF THE COLLECTED CURRENT BY ORGANIC DEPOSIT ON THE SURFACE OF THE PROBE?

The probe goes through the ionosphere during 10-15 minutes. The complex organic chemistry happening in the ionosphere could possibly lead to the formation of a deposit on the surface of the probe. Then, depending on its covering at the surface of the probe and on its dielectric properties, the film would induce the detection of several electron components in the sweeps.

Nevertheless, this hypothesis is not likely. Indeed, no difference have been observed between two sweeps taken at the interval of a few seconds (see **Supplement SIV.2-1**). In addition, the probe is cleaned between two flybys (see **Section IV.1.1.b**), and observations during the inbound and the outbound are very similar (in the case of flybys with inbound and outbound at similar SZA).

ELECTRON POPULATIONS DUE TO A DUSTY PLASMA EFFECT?

The models do not expect several electron populations. However, they do not take precisely the presence of the aerosols into account. **We can therefore suspect dust grains to disturb electrons, and potentially form a new electron population. It is especially possible in the case of P_{far}.** Indeed, this population appears only below 1200-1150 km altitude, exactly where the dusty plasma starts (Shebanits et al., 2016). This possibility is investigated in **Section IV.3**.

3- Statistics with the complete Cassini dataset

The previous sections revealed the detection of several electron populations by the Langmuir Probe in the ionosphere of Titan. To get clues on the characteristics and the possible origins of these populations, their density and temperature profiles have been retrieved for the 57 Cassini flybys that reached the ionosphere.

This work was done in close collaboration with Jan-Erik Wahlund and the team of the Swedish Institute of Space Physics (IRF) in Uppsala University (Sweden). It resulted in the redaction of **Paper 7** (*Re-analysis of the Cassini RPWS/LP data in Titan's ionosphere. Part 2. Electron densities and temperatures*).

3.1. Electron densities and temperatures

3.1.a. Study of all the Cassini flybys in Titan's ionosphere

The Cassini spacecraft flied-by Titan on 126 occasions. As this study focuses on the effect of aerosols on the ionospheric plasma, we selected the flybys during which Cassini went below 1200 km, altitude from which the aerosols start forming.

Generally, Cassini went down to ~950/1000 km altitude. Its crossing of the ionosphere took ~15 min, during which it carried out 26 to 30 voltage sweeps.

The 57 selected flybys covered a large range of Solar Zenith Angle, latitudes and half a Titan year (see **Figure IV.3-1**).
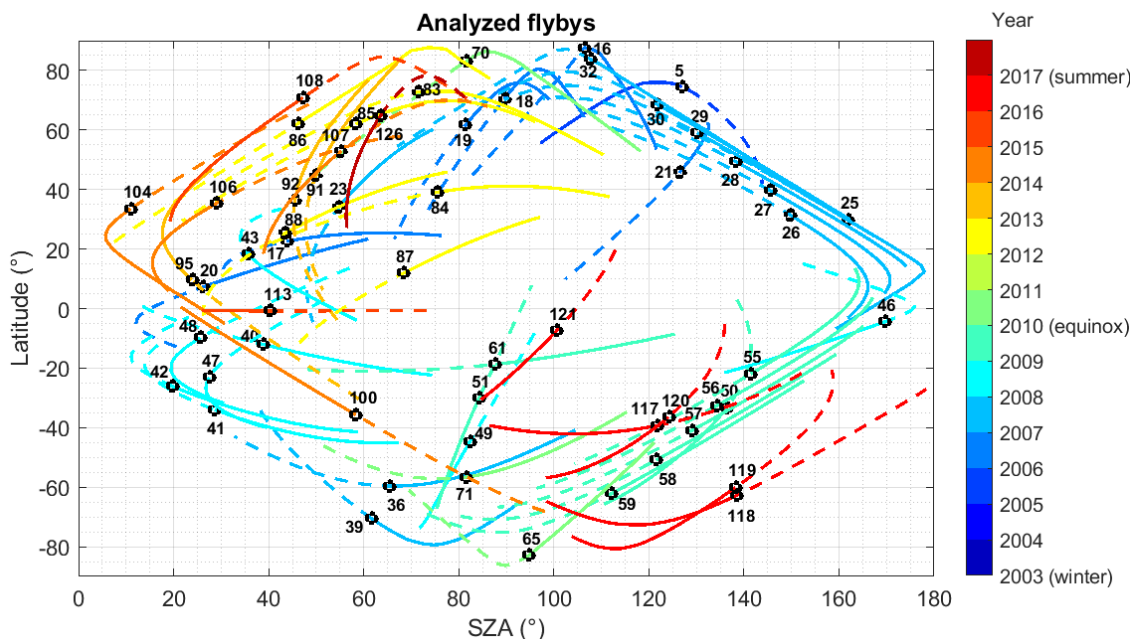

Figure IV.3-1: Trajectories of the 57 flybys analyzed: Solar Zenith Angle, latitude and year.

3.1.b. Electron densities and temperatures for the electron populations

Each of the four populations have a different behavior with altitude (see **Figure IV.3-2**). They are named P_1, P_2, P_3 and P_4 accordingly to the previous section (in which $P_4 = P_{far}$).

P_2 electrons reach temperatures mainly between 0.025 and 0.08 eV (0.12 eV at maximum). P_3 electrons are generally hotter, with a minimum at 0.04 eV. **P_2 and P_3 show in average a linear decrease in temperature with a decreasing altitude.** The slopes for the two populations are different. Estimations give -0.010 eV / 100 km for P_2 and -0.017 eV / 100 km for P_3. Therefore, the electrons of P_3 are hotter, but their temperature decreases with altitude ~70% faster than the electrons of P_2. Higher densities are globally found at lower altitudes.

P_4 electrons have the particularity to appear only below ~1250-1200 km altitude, with a large range of temperatures, between 0.01 and 0.12 eV. Higher densities are correlated with higher temperatures.

P_1 is a population at very low density (< 150 cm^{-3}). Two different behaviors are observed: the low temperature electrons (< 0.02 eV) at all altitudes, and hotter electrons (0.07 − 0.12 eV) found only above 1100 km.
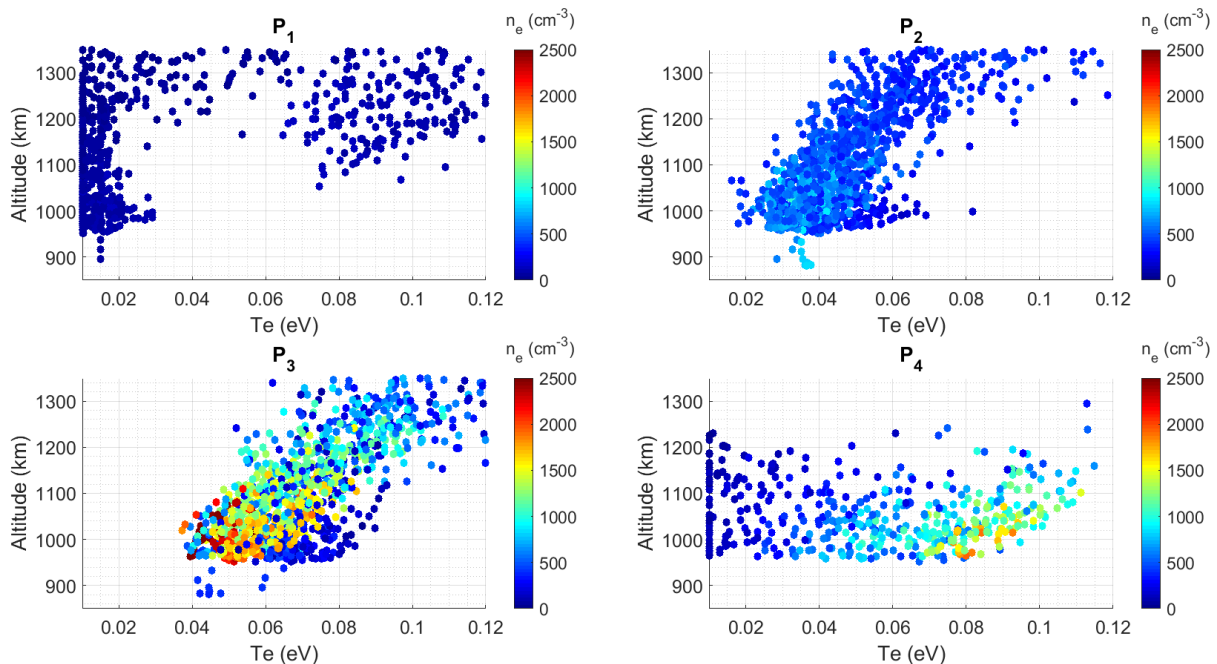

Figure IV.3-2: Electron temperature and density as a function of altitude for the four populations. Data from 57 flybys.

3.1.c. Strong dependence with Solar Zenith Angle

We observe a strong dependence of the electron populations with the Solar Zenith Angle (SZA).

In terms of electron density, the populations show very different behaviors (see **Figure IV.3-3**). P_1 electrons at low SZA are only observed at high altitudes. Their density remains low (~100 cm^{-3}) in any condition. **P_2 electron density stays globally constant around 500 cm^{-3} at all altitudes and all SZA.** Only a small shift is observed at low altitude, with higher densities on the dayside (~700 cm^{-3}) and lower densities on the nightside (~400 cm^{-3}).

The effect of SZA is stronger on P_3 and P_4. **While the density of P_3 is globally constant with altitude on the nightside (~300 cm^{-3}), it strongly increases with decreasing altitude on the day side**, with a slope of +350 cm^{-3} / -100 km (up to ~1900 cm^{-3} at 950 km). **For P_4, the maximum density reached at each altitude increases strongly with decreasing altitude and SZA.** In the case of SZA < 20°, the increase of density is about +600 cm^{-3} / -100 km.
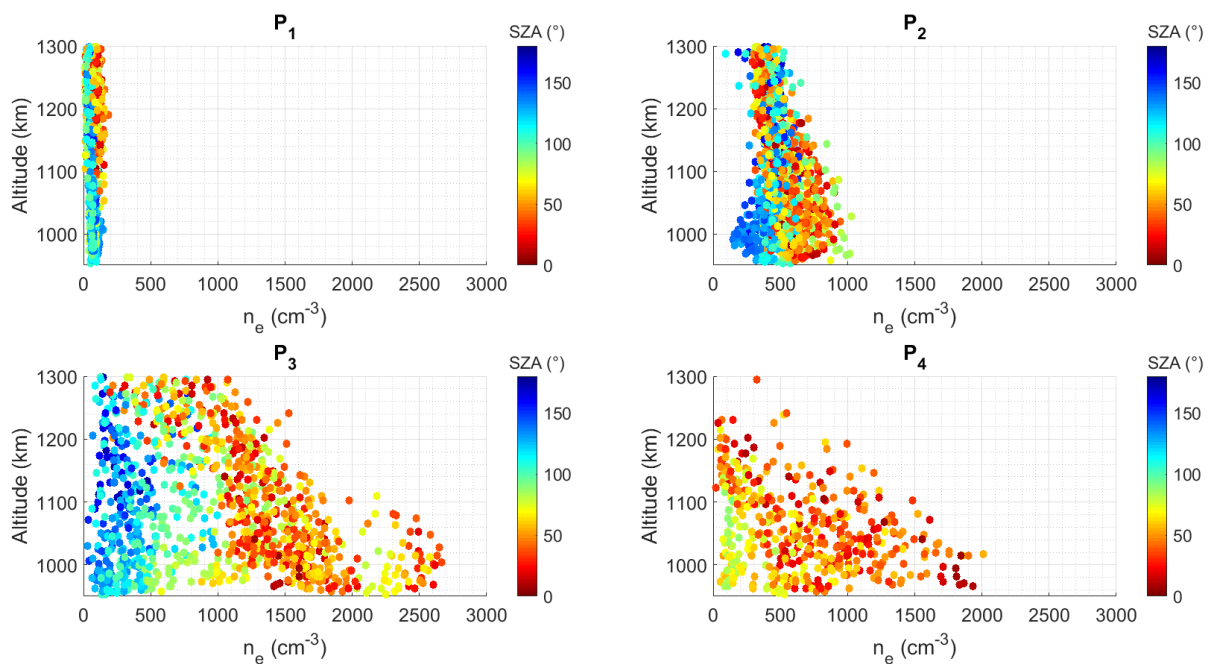
Figure IV.3-3: Electron density as a function of altitude and Solar Zenith Angle (SZA) in the case of the four populations. Data from 57 flybys.

Figure IV.3-4 shows the variation of electron temperature with SZA for each of the four populations. At higher altitudes, between 1250 and 1350 km, no strong differences are observed with SZA. However, with decreasing altitudes from 1250 to 850 km, a differentiation occurs between dayside and nightside measurements.

As seen in **Section IV.3.1.b**, we observe that the electrons of populations P_2 and P_3 get colder with decreasing altitude. **However, at a given altitude, the temperatures of P_2 and P_3 are globally constant with SZA.** This was previously observed in the case of an analysis with one single electron population by Ågren et al. (2009). Only a small difference is observed below 1050 km: electrons on nightside seems slightly hotter (+0.01-0.02 eV), for SZA > 130° in the case of P_2, and for SZA > 100° in the case of P_3.

In the case of P_4, **Figure IV.3-4** shows a sharp limit at 90° SZA: **no electrons from the P_4 family can be observed on the nightside.** Therefore, P_4 electrons appear only in sunlit regions. However, there is no relation between the electron temperature and the SZA.

As for population P_1, there is a clear separation between two blocks below 1050 and 1250 km. We observe cold electrons (< 0.03 eV) on the nightside, down to the lower altitudes reached. On the dayside, we observe hot electrons (0.07-0.12 eV). No detection is done below 1050 km. However, this can be due to the fact that the currents from P_2 and P_3 increase strongly and possibly cover the P_1 current (see **Section IV.2**).
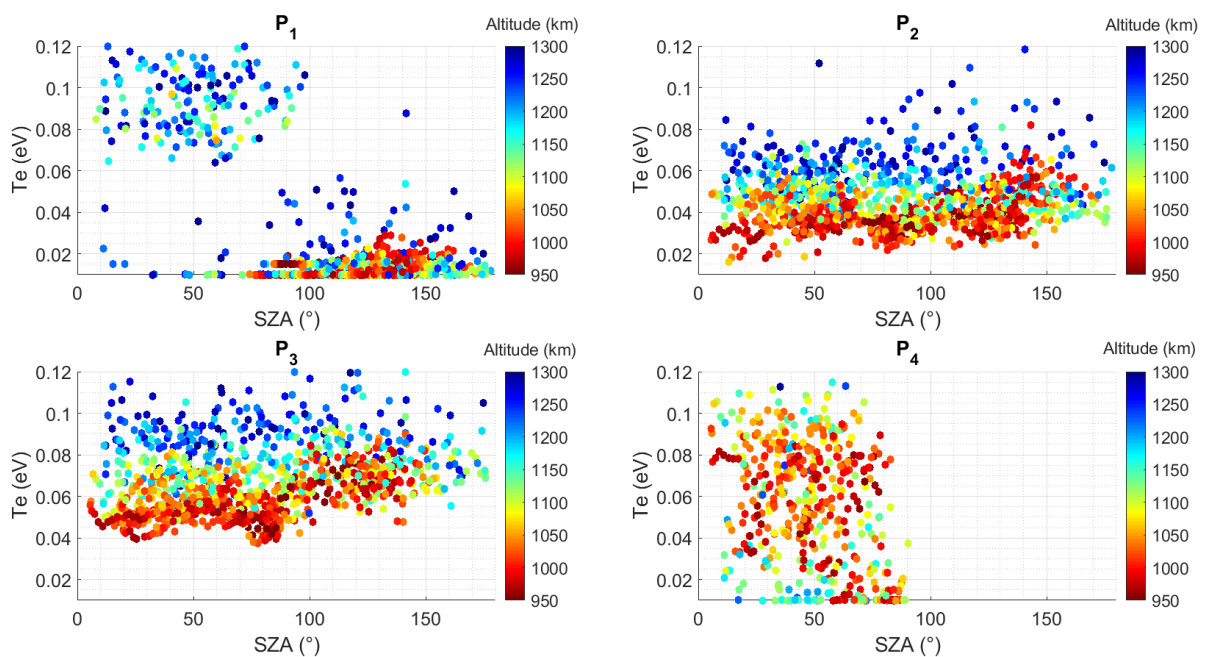

Figure IV.3-4: Electron temperature as a function of Solar Zenith Angle (SZA) and altitude, for the four populations. Data from 57 flybys.

3.1.d. Relation between electron density and temperature measurements

At a given altitude, electrons from P₂ and P₃ do not show any variation in temperature with density. For those populations, the temperature seems essentially governed by the altitude.

However, results are very different for the population P₄. **Figure IV.3-5 shows a linear trend between electron temperature and density, observed at all altitudes where P₄ electrons are detected.** The linear coefficient varies with altitude (see **Table IV.3-1**), from 0.016 eV/cm^{-3} at 1150-1250 km to 0.0067 eV/cm^{-3} below 1050 km. Below 1050 km, the slope varies also with SZA. Near the terminator (SZA > 70°) the coefficient is higher (0.011 eV/cm^{-3}).
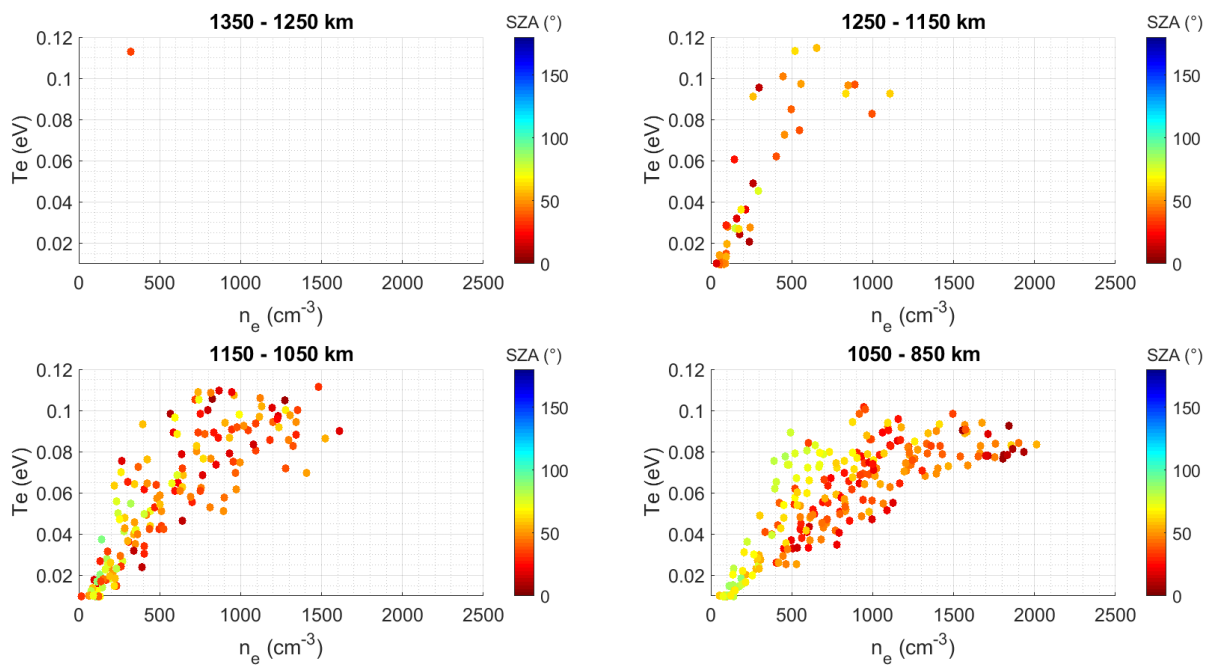
Figure IV.3-5: Electron temperature as a function of density and Solar Zenith Angle (SZA) at four different altitudes, for P₄. Data from 57 flybys.

Altitude (km)	Mean slope (eV / 100 cm^{-3})	Extrema values (eV / 100 cm^{-3})
1250 – 1150	0.016	0.011 – 0.024
1150 – 1050	0.011	0.0060 – 0.024
1050 – 850 ; SZA > 70°	0.011	0.0092 – 0.017
1050 – 850 ; SZA < 70°	0.0067	0.0045 - 0.010

Table IV.3-1: Linear coefficient between electron temperature and density in the case of P₄. From results presented in **Figure IV.3-5**.

3.2- Correlations with UV fluxes, seasons and ion densities

3.2.a. Correlation with the extreme UV fluxes?

The correlations observed with extreme ultraviolet (EUV) fluxes are strongly dependent on the population chosen.

For P_2, at given SZA and altitude ranges, the electron density and temperatures are constant with EUV. **Electrons of the population P_2 are not EUV dependent.**

P_3 electron temperature depends only on altitude. However, **Figure IV.3-6 (b)** shows that **an increase with EUV flux is observed in the P_3 electron density on the dayside at low altitude.** Below 1000 km, the increase in electron density is of +300 cm^{-3} every 0.1×10^{-4} $W.m^{-2}$.

Figure IV.3-6 (a,c) also shows the variation of the electron temperature of P_1 and of the electron density of P_4 as a function of the extreme UV flux for SZA < 70°. **P_1 electron temperature globally increases with the EUV flux** (+0.01 eV every 0.1×10^{-4} $W.m^{-2}$). In parallel, **P_4 denser cases are only observed at higher EUV fluxes.**
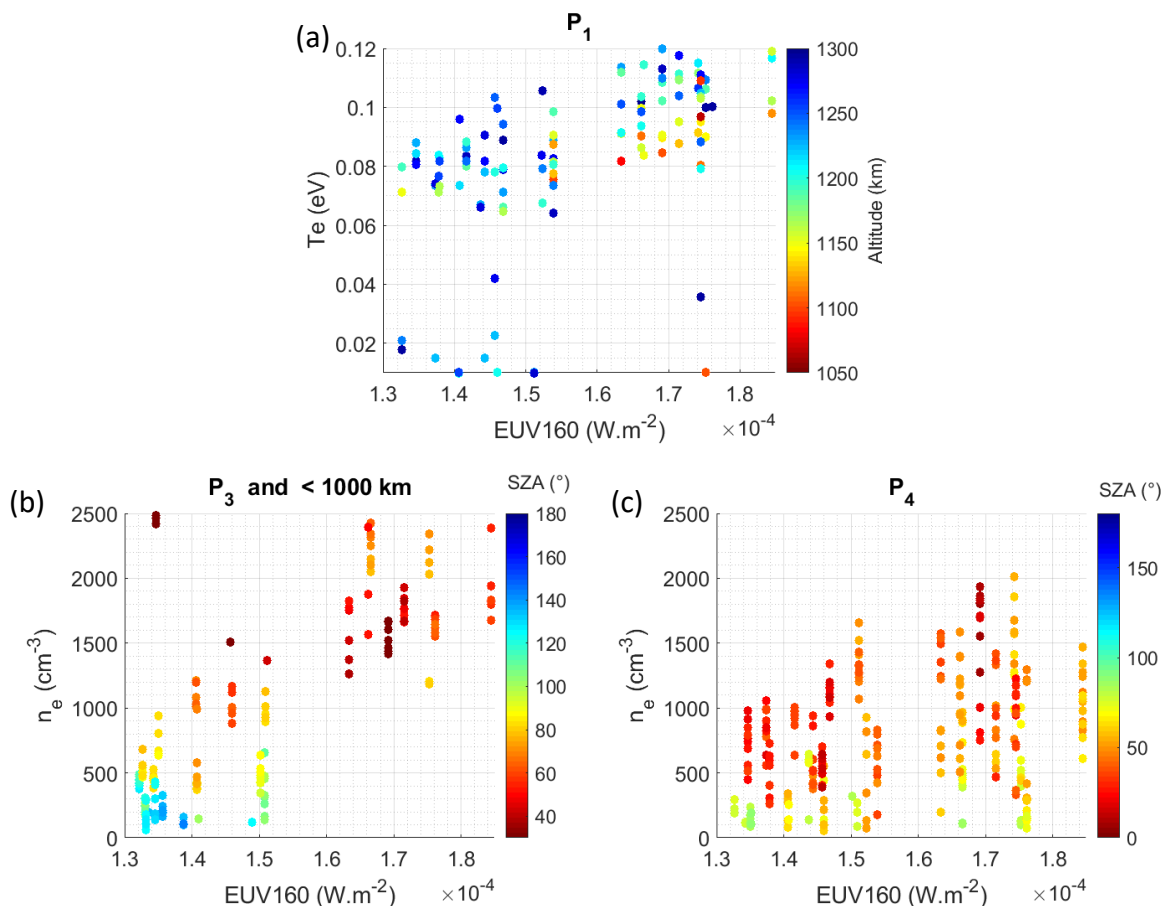

Figure IV.3-6: Electron characteristics as a function of extreme UV flux (integrated between 0.5-160.5 nm). (a) With P_1, electron temperature and altitude for SZA < 70°. (b) With P_3, electron density and SZA, below 1000 km. (c) With P_4, electron density and SZA.

3.2.b. Impact of seasons?

The Cassini mission covered two seasons in the Saturnian system, from the beginning of winter in the northern hemisphere to the summer solstice (May 2017). The Vernal equinox was in the middle of the mission (August 2009). The LP measurements spread over all the period. Therefore, a study of the evolution of electron density and temperature can be done over the seasons. The previous sections show that the SZA plays a fundamental role in the observation of the electron populations and in the values of n_e and T_e. **Figure IV.3-7** plots the orbital parameters, showing the different flyby configurations in terms of year, latitude and SZA. Particularly in the case of SZA > 70°, two blocks of data have sufficient data points to be compared: one from 2006 to 2009 in the southern hemisphere ('B1') and one from 2012 to 2015 in the northern hemisphere ('B2').
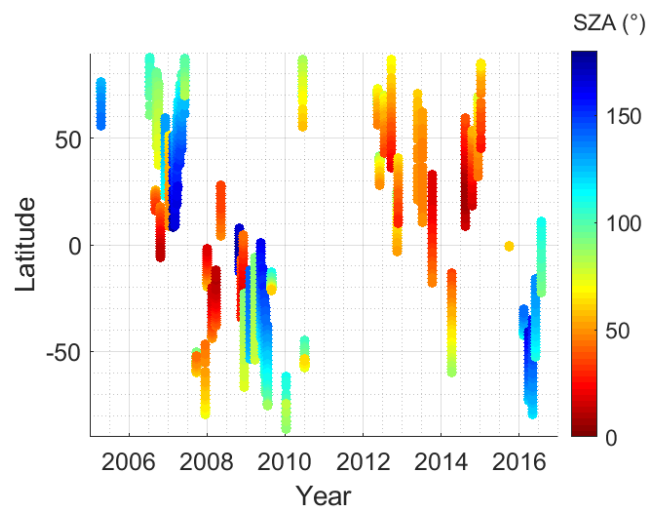

Figure IV.3-7: Orbital parameters of the 57 studied flybys in terms of year, latitude (°) and Solar Zenith Angle (°).

At a given altitude, no variations with year and latitude are observed in P_2 and P_3 electron temperatures, and in P_2 density. However, **P_3 electron density for SZA < 70° shows some variations**. **Figure IV.3-8 (b)** illustrates this effect for measurements below 1200 km altitude. Measurements in the 'B1' part are globally less dense than in the 'B2' part. **Figure IV.3-8 (a)** shows a similar pattern with the electron temperature of P_1: measurements give hotter electrons in the 'B2' part. **As for the population P_4, the effect is seen on both the electron density and temperature.** It is coherent with the observation of a linear correlation between its density and temperature (see **Section 3.1.d**).

In conclusion, on the dayside, P_3 and P_4 electrons are denser in the northern hemisphere from 2012 to 2014 (northern spring) than in the southern hemisphere from 2006 to 2008 (southern summer). Similarly, P_1 and P_4 electrons are hotter during the northern spring than during the southern summer. These observations are anti-correlated with the evolution of the Saturn-Sun distance, which was at its closest in 2003 (9 A.U.) and at its furthest in 2018 (10 A.U.).

On the other hand, **Figure IV.3-8 (a)** shows a strong correlation of the previous observations with the extreme UV flux. The formation of electrons and their heating is strongly linked to the EUV flux, as shown in **Section IV.3.2.a**. In addition, these observations are correlated with

the solar cycle that was at a minimum between 2005 and 2011 and at a maximum between 2011 and 2016. **In conclusion, the modifications of the electron temperature and density in long time scales is mainly due to the evolution of EUV fluxes with the solar cycle.**

Figure IV.3-8 (b) shows also a strong correlation with the ion density.

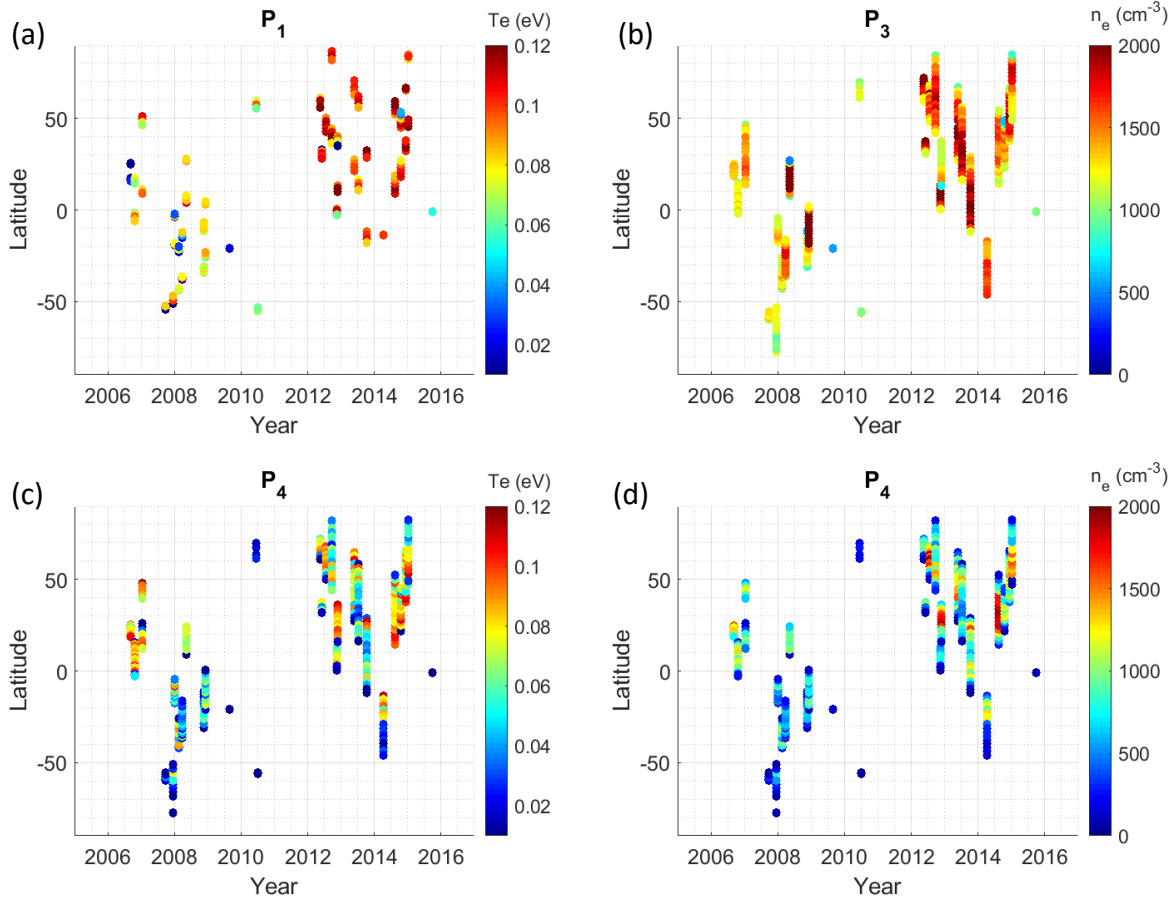**Figure IV.3-8**: Electron temperature and/or density as a function of year and latitude for SZA < 70°. (a) P_1; (b) P_3, for altitudes below 1200 km; (c,d) P_4.
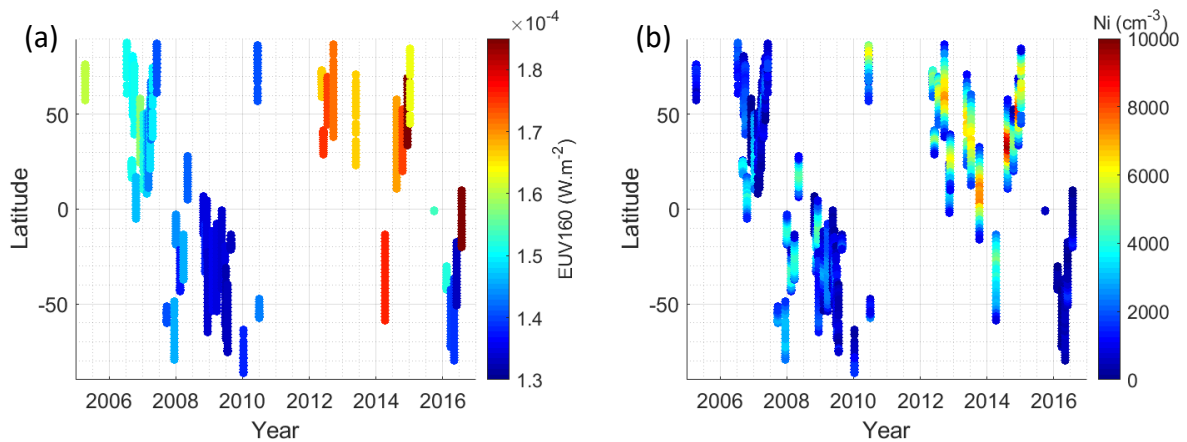

Figure IV.3-9: (a) Extreme UV flux (integrated between 0.5-160.5 nm) and (b) positive ion density (from Shebanits et al. 2016) as a function of year and latitude.

3.2.c. Correlation with ion density?

The positive and negative ion density has previously been retrieved by Shebanits et al. (2016), from the comparative study of different instruments on-board Cassini (the RWPS/LP, the Ion and Neutral Mass Spectrometer INMS, the Cassini Plasma Science Electron Spectrometer CAPS/ELS and Ions Beam Spectrometer CAPS/IBS). Higher densities are observed at lower SZA and at lower altitudes. The P_2 population density does not show any correlation with the ion density.

Contrastingly, **Figure IV.3.10** and **Table IV.3-2** show that **P_3 and P_4 electron densities are correlated to the positive (n_i+) and negative (n_i-) ion densities.** For the positive ion densities, three different domains can be distinguished. At low ion densities ($n_i+ < 2300$ cm^{-3} usually at high altitudes or on the nightside), P_3 electron density is linearly correlated to the positive ion density with a linear coefficient $n_i+/n_e(P_3)$ close to 2: there are two positive ions for one P_3 electron. Between ~2300 and ~3500 cm^{-3}, it is the turn of P_4 electron density to be linearly correlated to the positive ion density with a linear coefficient $n_i+/n_e(P_4)$ close to 2. For both cases, above respectively ~2300 and ~3500 cm^{-3}, the relations between electron densities and positive ion densities are less clear. In average, there is a linear increase with coefficients $n_i+/n_e(P_{3-4})$ close to 10. In these conditions, the positive ion electrical charge is absolutely not compensated by the electrons, P_2 being constant with n_i+.

Figure IV.3.10 (c,d) shows the **strong role of negative ions in these high ion density cases**. The negative ion distribution with P_3 and P_4 electron density is similar to the positive ion distribution, with a global linear growth with coefficients $n_i-/n_e(P_{3-4})$ around 8. This point is validated by the **Figure IV.3.10 (e)** showing a linear dependence between the positive and negative ion densities. Especially on the dayside, the linear increase is valid for $n_i+ > 3000$ cm^{-3}, with a slope $n_i+/n_i- \approx 1.1$: in these conditions, the formation of positive ions is mainly compensated by the formation of negative ions. These cases with high ion densities correspond to the lowest altitudes.

In conclusion, at higher altitudes, and lower positive ion densities, P_3 electron density increases linearly with positive ion density. For $n_i+ > $ ~2300 cm^{-3}, it is the growth of P_4 electrons which is linear with n_i+. Finally, at lower altitudes, for $n_i+ > 3500$ cm^{-3}, the formation of new positive ions is mainly compensated by negative ions, even if a slight increase of P_3 and P_4 electrons with n_i+ and n_i- is still present.

As for the electron temperatures, no dependence is observed with the ion densities. For P_2 and P_3, the temperature depends only on the altitude, and for P_4 the temperature depends on the P_4 density.
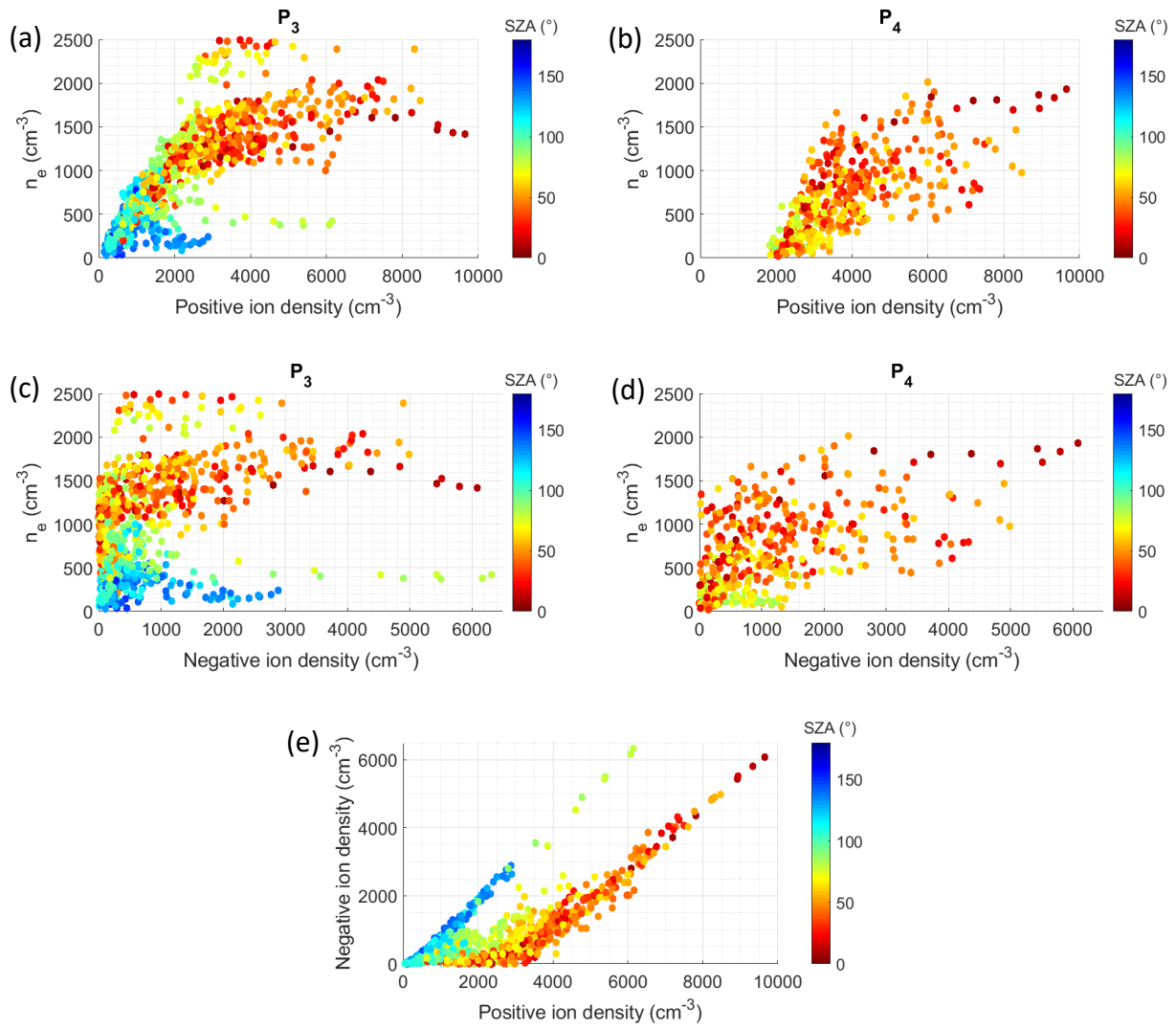
Figure IV.3.10: P$_3$ (a,c) and P$_4$ (b,d) electron densities as a function of positive and negative ion densities. (e) Negative ion density as a function of positive ion density.

Population	Zone (cm^{-3})	Slope n_i+/n_e(P$_{3-4}$)	Zone (cm^{-3})	Slope n_i+/n_e(P$_{3-4}$)	Zone (cm^{-3})	Slope n_i-/n_e(P$_{3-4}$)
P$_3$	$n_i+ < 2300$ n_e(P$_3$) < 1250	**1.8** (1.4-2.4)	$n_i+ > 2300$ n_e(P$_3$) > 1250	**11** (8-25)	n_i- > 300	**8** (6-15)
P$_4$	$n_i+ < 4000$ n_e(P$_4$) < 900	**1.9** (1-2.6)	$n_i+ > 4000$ n_e(P$_4$) > 900	**9.5** (5.5-13)	n_i- > 300	**8.5** (4.5-12)

Table IV.3-2: Linear coefficients between ion and electron densities. For electron populations P$_3$ and P$_4$, for positive and negative ions, for different conditions of density.

3.3- Discussions

The four populations show strong differences in their relation to altitude, solar irradiation and ion density. Here we discuss the possible origin of these populations in the light of the previous observations.

3.3.a. Distribution of the negative charge carriers with altitude and SZA

Figure IV.3-11 synthesizes the average distribution of negative charge carrier densities (electrons and negative ions) with altitude and SZA. It shows that above 1050 km in altitude, the negative charges essentially come from the electrons. On the other hand, below 1000 km, the negative ions play a dominant role. Besides, the number of charge per negative ion is certainly higher than 1 (Shebanits et al., 2016). In the distribution of the electrons, a strong difference appears between the dayside and the nightside. P_2 electrons dominate the nightside while P_3 electrons play the main role on the dayside.
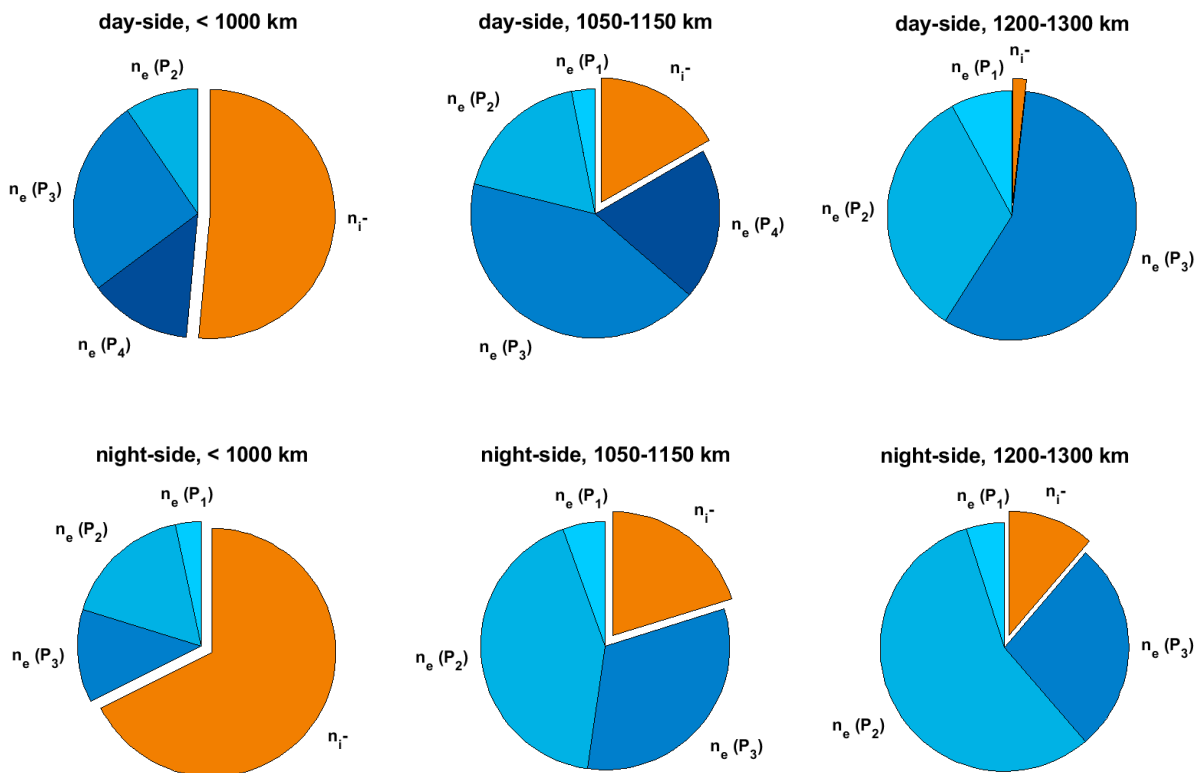

Figure IV.3-11: Average repartition of negative charge carrier densities, between the different electron populations and the negative ions. Comparison at different altitudes, on dayside (SZA < 60°) and on nightside (SZA > 100°).

3.3.b. Summary of the characteristics of the 4 populations

Table IV.3-3 summarizes the correlations observed between n_e, T_e, altitude, solar irradiation and ion density, for the 4 populations.

Popula-tion	$n_e - T_e$	altitude	SZA, EUV, seasons	ions	origin?
P_1	**-n_e: constant and low** (~80 cm^{-3}) **-T_e: 2 blocks (b1 and b2)**: b1 at ~0.1 eV and b2 at < 0.02 eV	-b1 only above 1100 km -b2 at all altitudes	-b1 always present (and only) on dayside -T_e: on dayside, hotter at higher EUV fluxes. -b2 on nightside	/	electrons detached from the probe by collision with energetic photons or particles
P_2	/	**-n_e: globally constant** (500 cm^{-3}), slight shift at lower altitudes depending on SZA (400-700 cm^{-3}) **-T_e: linear decrease with decreasing altitude** (-0.01 eV / -100 km)	**-n_e: slightly denser on dayside at low altitude** (x2). -T_e: On nightside (SZA > 130°) and at low altitude (< 1050 km), T_e increases by +0.02 eV	/	thermaliza-tion of the suprathermal electrons coming from the magneto-sphere
P_3	/	**-n_e**: constant on nightside. **Linear increase on dayside with decreasing altitude** (+350 cm^{-3} / -100 km) **-T_e: linear decrease with decreasing altitude** (-0.017 eV / -100 km)	**-n_e: denser on dayside** (x6+) -below 1000 km, denser at higher EUV fluxes. -T_e: On nightside (SZA > 130°) and at low altitude (< 1050 km), T_e increases by +0.02 eV	**-n_e: linear increase**, n_i+/n_e = 2 for n_i+ < 2000 cm^{-3}. Above, n_i+/n_e ~10.	from photo-ionization of N_2 and CH_4, and ion chemistry
P_4	**-n_e and T_e proportional** (~0.01 eV / 100 cm^{-3})	**-only below 1200-1150 km** -denser cases are only at lower altitudes	- **always present (and only) on dayside** -dense cases mainly at strong EUV	**-n_e: linear increase**, n_i+/n_e = 2 for n_i+ < 4000 cm^{-3}. Above, n_i+/n_e ~9.	from interaction of solar photons with aerosols or heavy negative ions

Table IV.3-3: Summary of the correlations between n_e, T_e, altitude, solar irradiation and ion density, for the 4 populations.

3.3.c. Suggestions on the origins of the electron populations

P_3 AND P_4: STRONG CORRELATIONS WITH THE SZA AND THE EUV FLUX

P_3 and P_4 populations show strong correlations with the Solar Zenith Angle and the EUV flux. Consequently, their origin should be linked to the solar irradiation. Both have a density increasing with decreasing altitude. More ions are formed with more solar photons and at higher pressure. Therefore, these electrons are formed from the energy deposition of solar photons in the atmosphere. **The main difference between the two populations is their temperature.** P_3 electron temperature depends essentially on the altitude: more collisions at higher pressure lead to a lower temperature. On the other hand, the temperature of the P_4 electrons depends mainly on their density: their temperature is higher when their density is higher. These points suggest a different origin for the two populations. P_3 electrons appear nearly at all altitudes, contrarily to P_4 electrons that are confined below 1150-1200 km, where negative ions and certainly dust particles are present in huge quantities. **In the light of these observations, we suggest that P_3 electrons come from the photo-ionization of neutral atmospheric molecules (mainly CH_4 and N_2) and the subsequent ion chemistry, while P_4 electrons are formed on the dust grains or heavy negative ions by interaction with the solar photons**.

P_4: EXTRACTED FROM AEROSOLS

P_4 electrons are a clue about the interaction of the plasma with the aerosols in the ionosphere of Titan. Extracted from the aerosols, their floating potential is then different from the plasma potential. This explains why the P_4 electrons are collected at a very different voltage bias of the probe than the other populations (see **Section IV.2**).

A few hypotheses can be made on the processes forming electrons from the interaction of aerosol grains with solar photons. **Photo-extraction from the bulk of the material requires strong UV photons (> 6 eV), while photo-desorption can happen with low energy photons (1-2 eV), but with lower efficiency**. In these cases, the energy of the electron formed depends on the energy of the incident photon. This can explain the linear dependence between n_e and T_e: higher and stronger solar radiations lead to more P_4 electrons, and at higher energies. Tigrine et al. (2018) studied photo-emission of electrons on analogues of Titan's aerosols under VUV irradiation. Using an extrapolation of their data points, we observe that the formation of electrons at 0.1 eV would be possible and require incoming photons of ~6 eV.

Woodard et al. (2020) studied a laboratory dusty plasma with a Langmuir Probe and also observed an unexpected electron population at a potential different from the plasma potential. They showed that the potential of the unexpected population is the same as the potential of the aerosols. Thanks to a numerical modeling they investigated its origin. In their conditions, the electron photo-emission and the secondary electron emission from the flux of charged species to the particle surface are not sufficient to explain the density of the new population. They propose another process: the **thermo-emission of electrons from the nanoparticles, enhanced by electrostatic effects**. Indeed, the aerosols are heated by the ion

bombardment, the collection of electrons and the recombination of radicals and ions at their surface. The accumulated heat cannot be transferred to the background gas because of the low pressure and the inefficient radiation of small particles. On the other hand, the charge of the aerosols decreases the barrier for electron emission. **In conclusion, the P_4 population observed on Titan could similarly be due to electron emission from the aerosols heated by the ion chemistry and the collection of the numerous electrons present on the dayside**.

P_1 AND P_2: THE BACKGROUND ELECTRONS DETECTED BY THE LP

On the other hand, P_2 electrons depend only slightly on solar illumination. Their density is globally constant with altitude and their temperature depends only on the altitude (as for P_3). For these reasons, we guess that **P_2 electrons are background thermalized electrons, present in all the ionosphere of Titan**. Their constancy with solar illumination indicates that they could mainly be suprathermal magnetospheric electrons that have been thermalized.

Finally, the **P_1 electrons** are not dense and nearly always present. Their plasma potential being the smallest of all the populations, it is a strong indication that they are **formed on the boom next to the probe**, by collision with energetic photons or particles (see **Section IV.2**).
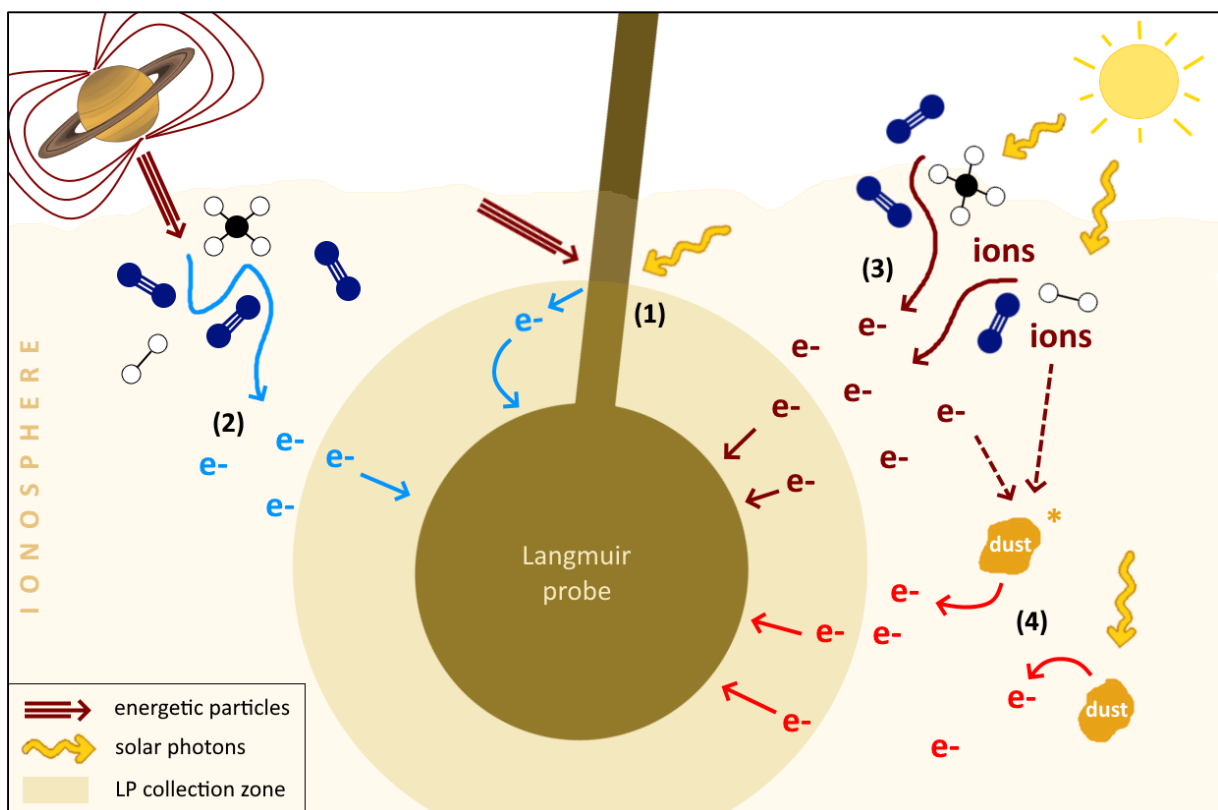

Figure IV.3-12: Schematic representing suggested origins for the 4 electron populations detected by the Langmuir Probe in Titan's ionosphere.

Conclusion of Chapter IV

In this chapter, the electron density and temperature in the ionosphere of Titan have been re-estimated by re-analysis of the Cassini Langmuir Probe data. The detailed analysis of the data revealed the presence of several electron populations, not predicted by the models. The second derivative of the electron current was found to be an efficient tool to identify the populations.

The analysis of 57 flybys during which Cassini went below 1200 km altitude enabled a statistical study of the electron populations. **Four electron populations have been identified.**

(1) A low density population, with the lower potential, is attributed to **electrons emitted from the probe**, by collision with an energetic photon or magnetospheric particle.

(2) A second population is always detected, with densities and temperatures that do not depend on the solar illumination. It is rather cold, at ~0.04 eV below 1100 km. This population can be attributed to **background thermalized electrons**, possibly originally coming from suprathermal magnetospheric electrons.

(3) The third population density is strongly correlated with the solar illumination and the EUV fluxes. Nevertheless, its temperature is rather constant below 1100 km at ~0.06-0.07 eV. This population is attributed to **electrons coming from the photoionization of N_2 and CH_4, and the subsequent ion chemistry.**

(4) Finally, a fourth population is detected in very specific conditions: only on the dayside, and below 1150-1200 km altitude. It can reach densities as high as 2000 cm^{-3} and its temperature is proportional to its density. Aerosols start forming at this altitude. **The fourth population is then strongly suspected to be linked to the presence of aerosols**. We propose two main processes, based on experimental work: the **photo-emission** of electrons from the surface of the aerosols, or the **thermo-emission** of electrons by the grains heated by the ion chemistry and the collection of electrons.

In conclusion, the presence of this fourth population could be an indicator of the presence of aerosols on the dayside. To confirm this hypothesis, the next logical step is to model the two suspected processes (the photo-detachment and/or the thermionic emission of electrons coming from the aerosols) in the conditions of the ionosphere of Titan, and compare the modeled electrons emitted from the aerosols with the fourth population detected with the Langmuir Probe data. Then, it would be very interesting to implement global ionospheric models with these new processes!

References for Chapter IV

Ågren, K., Wahlund, J.-E., Garnier, P., Modolo, R., Cui, J., Galand, M., Müller-Wodarg, I., 2009. On the ionospheric structure of Titan. Planet. Space Sci. 57, 1821–1827. https://doi.org/10.1016/J.PSS.2009.04.012

Ågren, K., Wahlund, J.E., Modolo, R., Lummerzheim, D., Galand, M., Müller-Wodarg, I., Canu, P., Kurth, W.S., Cravens, T.E., Yelle, R. V., Waite, J.H., Coates, A.J., Lewis, G.R., Young, D.T., Bertucci, C., Dougherty, M.K., 2007. On magnetospheric electron impact ionisation and dynamics in Titan's ram-side and polar ionosphere - a Cassini case study. Ann. Geophys. 25, 2359–2369. https://doi.org/10.5194/angeo-25-2359-2007

Bettinger, R.T., Walker, E.H., 1965. Relationship for Plasma Sheaths about Langmuir Probes. Phys. Fluids 748, 748–751. https://doi.org/10.1063/1.1761293

Bird, M.K., Dutta-Roy, R., Asmar, S.W., Rebold, T.A., 1997. Detection of titan's ionosphere from voyager 1 radio occultation observations. Icarus 130, 426–436. https://doi.org/10.1006/icar.1997.5831

Coates, A.J., Crary, F.J., Young, D.T., Szego, K., Arridge, C.S., Bebesi, Z., Sittler, J.C., Hartle, R.E., Hill, T.W., 2007. Ionospheric electrons in Titan's tail: Plasma structure during the Cassini T9 encounter. Geophys. Res. Lett. 34, L24S05. https://doi.org/10.1029/2007GL030919

Cravens, T.E., Robertson, I.P., Ledvina, S.A., Mitchell, D., Krimigis, S.M., Waite, J.H., 2008. Energetic ion precipitation at Titan. Geophys. Res. Lett. 35, L03103. https://doi.org/10.1029/2007GL032451

Cully, C.M., Ergun, R.E., Eriksson, A.I., 2007. Electrostatic structure around spacecraft in tenuous plasmas. J. Geophys. Res. Sp. Phys. 112, n/a-n/a. https://doi.org/10.1029/2007JA012269

Druyvesteyn, M.J., 1930. Der niedervoltbogen. Zeitschrift für Phys. 64, 781–798.

Edberg, N.J.T., Andrews, D.J., Shebanits, O., Ågren, K., Wahlund, J.E., Opgenoorth, H.J., Cravens, T.E., Girazian, Z., 2013. Solar cycle modulation of Titan's ionosphere. J. Geophys. Res. Sp. Phys. 118, 5255–5264. https://doi.org/10.1002/jgra.50463

Edberg, N.J.T., Wahlund, J.E., Ågren, K., Morooka, M.W., Modolo, R., Bertucci, C., Dougherty, M.K., 2010. Electron density and temperature measurements in the cold plasma environment of Titan: Implications for atmospheric escape. Geophys. Res. Lett. 37, L20105. https://doi.org/10.1029/2010GL044544

Farrell, W.M., Kurth, W.S., Gurnett, D.A., Johnson, R.E., Kaiser, M.L., Wahlund, J.-E., Waite, J.H., 2009. Electron density dropout near Enceladus in the context of water-vapor and water-ice. Geophys. Res. Lett. 36, L10203. https://doi.org/10.1029/2008GL037108

Galand, M., Coates, A.J., Cravens, T.E., Wahlund, J.-E., 2014. Titan's Ionosphere, in: Titan. Cambridge University Press, Cambridge, UK, pp. 296–361.

Galand, M., Yelle, R., Cui, J., Wahlund, J.-E., Vuitton, V., Wellbrock, A., Coates, A., 2010. Ionization sources in Titan's deep ionosphere. J. Geophys. Res. Sp. Phys. 115. https://doi.org/10.1029/2009JA015100

Galand, M., Yelle, R. V, Coates, A.J., Backes, H., Wahlund, J., 2006. Electron temperature of Titan's sunlit ionosphere. Geophys. Res. Lett. 33, L21101. https://doi.org/10.1029/2006GL027488

Grard, R.J.L., 1973. Properties of the satellite photoelectron sheath derived from photoemission laboratory measurements. J. Geophys. Res. 78, 2885–2906. https://doi.org/10.1029/ja078i016p02885

Gurnett, D.A., Kurth, W.S., Kirchner, D.L., Hospodarsky, G.B., Averkamp, T.F., Zarka, P., Lecacheux, A., Manning, R., Roux, A., Canu, P., Cornilleau-Wehrlin, N., Galopeau, P., Meyer, A., Boström, R., Gustafsson, G., Wahlund, J.-E., Åhlen, L., Rucker, H.O., Ladreiter, H.P., Macher, W., Woolliscroft, L.J.C., Alleyne, H., Kaiser, M.L., Desch, M.D., Farrell, W.M., Harvey, C.C., Louarn, P., Kellogg, P.J., Goetz, K., Pedersen, A., 2004. The Cassini Radio and Plasma Wave Investigation, in: The Cassini-Huygens Mission. Springer Netherlands, pp. 395–463. https://doi.org/10.1007/978-1-4020-2774-1_6

Gurnett, D.A., Kurth, W.S., Scarf, F.L., 1981. Plasma waves near Saturn: Initial results from Voyager 1. Science

212, 235–239. https://doi.org/10.1126/science.212.4491.235

Jacobsen, K.S., Wahlund, J.E., Pedersen, A., 2009. Cassini Langmuir probe measurements in the inner magnetosphere of Saturn. Planet. Space Sci. https://doi.org/10.1016/j.pss.2008.10.012

Lieberman, M.A., Lichtenberg, A.J., 2005. Principles of Plasma Discharges and Materials Processing: Second Edition, Principles of Plasma Discharges and Materials Processing: Second Edition. https://doi.org/10.1002/0471724254

Mott-Smith, H.M., Langmuir, I., 1926. The theory of collectors in gaseous discharges. Phys. Rev. 28, 727–763. https://doi.org/10.1103/PhysRev.28.727

Mukundan, V., Bhardwaj, A., 2018. Dayside ionosphere of Titan: Impact on calculated plasma densities due to variations in the model parameters. Icarus 299, 222–239. https://doi.org/10.1016/j.icarus.2017.07.022

Richard, M.S., Cravens, T.E., Robertson, I.P., Waite, J.H., Wahlund, J.-E., Crary, F.J., Coates, A.J., 2011. Energetics of Titan's ionosphere: Model comparisons with Cassini data. J. Geophys. Res. Sp. Phys. 116, A09310. https://doi.org/10.1029/2011JA016603

Scarf, F.L., Gurnett, D.A., Kurth, W.S., Poynter, R.L., 1982. Voyager 2 plasma wave observations at Saturn. Science 215, 587–594. https://doi.org/10.1126/science.215.4532.587

Shebanits, O., 2017. Titan's ionosphere and dust. Uppsala Universitet.

Shebanits, O., Vigren, E., Wahlund, J.-E., Edberg, N.J.T., Cui, J., Mandt, K.E., Waite, J.H., 2017a. Photoionization Modeling of Titan's Dayside Ionosphere. Astrophys. J. 850, L26. https://doi.org/10.3847/2041-8213/aa998d

Shebanits, O., Vigren, E., Wahlund, J.E., Holmberg, M.K.G., Morooka, M., Edberg, N.J.T., Mandt, K.E., Waite, J.H., 2017b. Titan's ionosphere: A survey of solar EUV influences. J. Geophys. Res. Sp. Phys. 122, 7491–7503. https://doi.org/10.1002/2017JA023987

Shebanits, O., Wahlund, J.-E., Edberg, N.J.T., Crary, F.J., Wellbrock, A., Andrews, D.J., Vigren, E., Desai, R.T., Coates, A.J., Mandt, K.E., Waite, J.H., 2016. Ion and aerosol precursor densities in Titan's ionosphere: A multi-instrument case study. J. Geophys. Res. Sp. Phys. 121, 10,075-10,090. https://doi.org/10.1002/2016JA022980

Shebanits, O., Wahlund, J.E., Mandt, K., Ågren, K., Edberg, N.J.T., Waite, J.H., 2013. Negative ion densities in the ionosphere of Titan-Cassini RPWS/LP results. Planet. Space Sci. 84, 153–162. https://doi.org/10.1016/j.pss.2013.05.021

Shukla, P.K., Mamun, A.A., 2015. Introduction to dusty plasma physics, Introduction to Dusty Plasma Physics. CRC Press. https://doi.org/10.1088/0741-3335/44/3/701

Tigrine, S., Carrasco, N., Bozanic, D.K., Garcia, G.A., Nahon, L., 2018. FUV Photoionization of Titan Atmospheric Aerosols. Astrophys. J. 867, 164. https://doi.org/10.3847/1538-4357/aae4d8

Vigren, E., Galand, M., Shebanits, O., Wahlund, J.E., Geppert, W.D., Lavvas, P., Vuitton, V., Yelle, R. V., 2014. Increasing positive ion number densities below the peak of ion-electron pair production in titan's ionosphere. Astrophys. J. 786. https://doi.org/10.1088/0004-637X/786/1/69

Vigren, E., Galand, M., Wellbrock, A., Coates, A.J., Cui, J., Edberg, N.J.T., Lavvas, P., Sagnières, L., Snowden, D., Vuitton, V., Wahlund, J.-E., 2016. Suprathermal electrons in Titan's sunlit ionosphere: model-observation comparisons. Astrophys. J. 826, 131. https://doi.org/10.3847/0004-637x/826/2/131

Vigren, E., Galand, M., Yelle, R. V., Cui, J., Wahlund, J.E., Ågren, K., Lavvas, P.P., Mueller-Wodarg, I.C.F., Strobel, D.F., Vuitton, V., Bazin, A., 2013. On the thermal electron balance in Titan's sunlit upper atmosphere. Icarus 223, 234–251. https://doi.org/10.1016/j.icarus.2012.12.010

Vigren, E., Galand, M., Yelle, R. V., Wellbrock, A., Coates, A.J., Snowden, D., Cui, J., Lavvas, P., Edberg, N.J.T., Shebanits, O., Wahlund, J.E., Vuitton, V., Mandt, K., 2015. Ionization balance in Titan's nightside ionosphere. Icarus 248, 539–546. https://doi.org/10.1016/j.icarus.2014.11.012

Wahlström, M.K., Johansson, E., Veszelei, E., Bennich, P., Olsson, M., Hogmark, S., 1992. Improved Langmuir probe surface coatings for the Cassini satellite. Thin Solid Films 220, 315–320. https://doi.org/10.1016/0040-6090(92)90591-X

Wahlund, J.E., André, M., Eriksson, A.I.E., Lundberg, M., Morooka, M.W., Shafiq, M., Averkamp, T.F., Gurnett, D.A., Hospodarsky, G.B., Kurth, W.S., Jacobsen, K.S., Pedersen, A., Farrell, W., Ratynskaia, S., Piskunov, N., 2009. Detection of dusty plasma near the E-ring of Saturn. Planet. Space Sci. 57, 1795–1806. https://doi.org/10.1016/j.pss.2009.03.011

Wahlund, J.E., Boström, R., Gustafsson, G., Gurnett, D.A., Kurth, W.S., Pedersen, A., Averkamp, T.F., Hospodarsky, G.B., Persoon, A.M., Canu, P., Neubauer, F.M., Dougherty, M.K., Eriksson, A.I., Morooka, M.W., Gill, R., André, M., Eliasson, L., Müller-Wodarg, I., 2005. Cassini measurements of cold plasma in the ionosphere of Titan. Science 308, 986–989. https://doi.org/10.1126/science.1109807

Waite, J.H., Niemann, H., Yelle, R. V., Kasprzak, W.T., Cravens, T.E., Luhmann, J.G., McNutt, R.L., Ip, W.H., Gell, D., De La Haye, V., Müller-Wordag, I., Magee, B., Borggren, N., Ledvina, S., Fletcher, G., Walter, E., Miller, R., Scherer, S., Thorpe, R., Xu, J., Block, B., Arnett, K., 2005. Ion Neutral Mass Spectrometer results from the first flyby of Titan. Science 308, 982–986. https://doi.org/10.1126/science.1110652

Wang, X., Hsu, H.W., Horányi, M., 2015. Identification of when a Langmuir probe is in the sheath of a spacecraft: The effects of secondary electron emission from the probe. J. Geophys. Res. Sp. Phys. 120, 2428–2437. https://doi.org/10.1002/2014JA020624

Whipple, E.C.J., 1965. The equilibrium electric potential of a body in the upper atmosphere and in the interplanetary space. PhD thesis, Georg. Washingt. Univ.

Woodard, A., Shojaei, K., Berrospe-Rodriguez, C., Nava, G., Mangolini, L., 2020. Electron emission from particles strongly affects the electron energy distribution in dusty plasmas. J. Vac. Sci. Technol. A 38, 023005. https://doi.org/10.1116/1.5134706

CONCLUSION

The climatic system of the moon Titan is governed by the intense production of organic aerosols in its upper atmosphere. Aside from the understanding of Titan, the research on the formation of such aerosols in the atmosphere and their impact on the climatic system of a planet can be applied to the early Earth. Indeed, as today on Titan, methane was present in Earth's atmosphere before the apparition of life and at its beginning.

The Cassini-Huygens mission discovered that the aerosols are formed in the ionosphere, an atmospheric layer ionized by the solar radiations and the energetic particles coming from the magnetosphere of Saturn. In addition to the usual neutral molecules N_2, CH_4 and H_2, this ionized environment contains very reactive species as radicals, ions, electrons and excited species.

In particular, the ionization and dissociation of methane induces a complex chemistry. The mass spectrometer INMS and the plasma spectrometer CAPS on-board Cassini detected heavy ions, and especially very heavy negative ions. The chemical reactions happening in the gas phase are nowadays fairly well reproduced by photochemical models (Vuitton et al., 2019).

The presence of aerosols deeply disturbs the behavior of the plasma, which is then called a 'dusty plasma' (Lavvas et al., 2013). Then the modeling of the plasma environment requires to take the aerosols into account. In addition, the presence of the organic grains in the ionosphere can also have a strong effect on the chemistry. In particular, some atmospheric compounds would tend to adsorb on them.

To go further in the understanding of the processes at stake, laboratory experiments become a wonderful asset. Such experiments started as far as 1953, and played a major role in the preparation of the Cassini mission. Nowadays, we know thanks to Cassini the importance of the ion chemistry that eventually form aerosols in the ionosphere. Laboratory experiments aim to simulate this ion chemistry. A first group of experiments studies the photo-ionization of N_2-CH_4 gas mixtures by VUV irradiation (usually at very precise wavelengths). A second strategy is to directly mimic the ionospheric plasma with a N_2-CH_4 plasma discharge. Then, it is possible to study the effects of the various plasma species (radicals, ions, electrons…).

N_2-CH_4 plasma discharges lead to the formation of solid organic material. In particular, the use of an RF CCP discharge enables the material to form in levitation, as round particles. These are then analogues of the aerosols formed on Titan; they are called 'tholins'. The analysis of these tholins give insights on their formation processes and growth mechanisms.

On Titan, the aerosols certainly stay days, weeks or longer in the ionosphere as they sediment slowly towards the lower atmospheric layers. During this time, they are in contact with the reactive species of the ionospheric plasma: radicals, excited and metastable species, ions and electrons. Up to now, the envisaged processes are very few. H atoms are

suspected to be adsorbed and/or recombined at the surface of the aerosols (Sekine et al., 2008). Electrons could also attach on the grains (Vigren et al., 2014). Finally, polar molecules such as nitriles possibly stick on the aerosols (Vuitton et al., 2019).

Therefore, aerosols are considered only as a sink for molecules that are overestimated in the chemical models. No study goes further: what chemistry happens at the surface of the grains at the arrival of a H atom, an electron or a nitrile? And what are the effects of the other reactive species? Is the chemical structure of the grains modified? Are new species outgassed? This was the starting point of my PhD studies. **My objective was to find out how the aerosols interact with the surrounding plasma in the ionosphere. To tackle this issue, I considered two very different strategies: the laboratory simulation and the analysis of Cassini data. My studies led to some (partial) answers.**

The first strategy was to reproduce the plasma-aerosols interaction in the laboratory. The general idea is to insert tholins in a plasma discharge and observe modifications on the solid grains and on the gas phase. This idea was completely new and I had to design the experimental setup and protocol.

Interactions of the aerosols with the plasma are complex. Mainly two opposite effects take place at the same time on Titan: the organic growth orchestrated by the formation of carbon chains, and the processing/evolution of the chemical structures. The first point is based on carbon-containing species while the second effect can be triggered by non-carbon-bearing species. During my PhD work I focused on the 'processing/evolution' part. I avoided the 'carbon growth' processes by using only nitrogen and hydrogen in the gas phase.

To understand the effects of a N_2-H_2 plasma on tholins, I first had to characterize the N_2-H_2 plasma. This kind of plasma has already been studied with parameters a bit different than in my case, in particular in the study of the interstellar medium and in the microelectronics industry. I characterized the N_2-H_2 plasma in two different discharges: PAMPRE and THETIS. PAMPRE is an RF CCP discharge in which the tholins are formed. The gas mixture for the tholins production is N_2-CH_4. Then, the understanding of the N_2-H_2 plasma is also a first necessary step in the modeling of the final N_2-CH_4 discharge. Electrons have been measured by a resonant cavity method. The formation of ammonia has been observed by IR spectroscopy, and the neutrals and positive ions in the discharge have been analyzed by mass spectrometry. A collaboration with a team in Portugal (IPFN) enabled to couple the experimental efforts to a numerical model of the discharge. The 2D modeling especially revealed the strong influence of the reactor walls on the discharge: they enhance the production of fast electrons by secondary emission and ammonia by surface catalysis, which then affect the ion chemistry at the center of the discharge.

Electron density, neutrals and ions have also been measured in THETIS, a DC glow discharge. The results obtained in the two reactors are very similar. In both cases, the gas mixture was N_2 with 0 to 5% of H_2, at a pressure varying between 0.5 and 4 mbar, and at low power density

(0.02-0.2 W.cm^{-3}). The addition of less than 1% H$_2$ has a strong effect on the pure N$_2$ plasma discharges. Hydrogen quenches the (higher) vibrational levels of N$_2$. This leads to the increase of the discharge electric field and consequently of the electron energy. Then, higher quantities of radical and excited species are suspected to be produced in the reactor. The addition of hydrogen also leads to the formation of new species. In particular, it is the case of H and NH$_x$ radicals that start the formation of ammonia on the walls of the discharges. The apparition of many new ions have also been observed: N$_2$H$^+$ and NH$_4$$^+$ being the major ones, and also H$_3$$^+$, NH$^+$, NH$_2$$^+$, NH$_3$$^+$, N$_3H^+$ and N$_3$H$_3$$^+$.

After having investigated the plasma species present in the N$_2$-H$_2$ plasma discharge, the next step was to insert tholins in the reactor. Then, the objective was to look closely at both the tholins and the gas species to observe potential modifications. My first task was to design a plasma reactor in which the plasma could be ignited, the sample inserted in the plasma under vacuum and various instruments coupled to study the gas phase and the tholins. This experiment is named THETIS, for THolin Evolution in Titan's Ionosphere Simulation.

In THETIS, tholins are exposed during several tens of minutes to hours to the plasma. The first important observation is that nearly nothing happens in a pure N$_2$ plasma: tholins are not eroded neither quantitatively modified by the exposure to N$_2$ plasma species. On the other hand, strong modifications are observed during the exposure to a N$_2$-H$_2$ plasma. Scanning Electron Microscopy of the samples after exposure reveals the formation of erosive structures of a few tens of nanometers on the usually round tholin grains of ~400 nm diameter. A chemical evolution of the samples is also diagnosed by *in situ* IR transmission spectroscopy. Nitriles, and especially isonitriles, are eroded more quickly than the other chemical functions. Globally, double bonds are more affected by the erosion processes than amines and CH bonds.

The study of the gas phase by mass spectrometry shows the release of many new carbon-containing neutrals and ions. HCN, NH$_3$-CN, C$_2$N$_2$ are extracted in quantity from the tholins as well as some other carbon-containing species and their derived ions. Very highly unsaturated ions are observed, such as C$^+$, C$_2$$^+$, C$_2H^+$, C$_3$$^+$, C$_3$H+ and C$_3H_2$$^+$/C$_2N^+$. On the other hand, the production of ammonia is strongly decreased.

Previous works also observed that N$_2$-H$_2$ plasmas erode efficiently organic materials. A great effort has been made to understand the etching of (C:H) films by N$_2$-H$_2$ plasma in the field of the microelectronics. Their suggested plasma processes are consistent with the observations on THETIS (Van Laer et al., 2013). In particular, N atoms and other N$_2$ excited species would adsorb on the surface and react with carbon atoms, forming at the end C≡N bonds. In the case of a pure N$_2$ plasma, these bonds passivate the surfaces. However, in the presence of hydrogen, H atoms, NH radicals and other H$_2$ excited species transform CN into the stable molecule HCN, which is eventually ejected into the gas phase by ion sputtering. On THETIS, the observations are consistent with these suggested processes. The gas phase analyses reveal the important formation of HCN, and IR spectra show the loss of nitrile bonds. In details, IR spectra also show the apparition of a new CN band at 2210 cm^{-1} (4.52 μm) that we attribute to the new CN forming at the surface of tholins. On (C:H) films, CH$_x$ gas species are also

suspected to be formed by interaction of H and H_2^* with the surface CH_x bonds. NH_3 is formed by the protonation of NH_2 radicals by hydrogen atoms from the surface. Contrarily to the case without organics in the discharge, the radical NH is used to form HCN instead of NH_3. This can explain the decrease of ammonia formed in THETIS when tholins are inserted in the plasma. In addition to C and H atoms, tholins also contain nitrogen in quantity. The various chemical functions formed with various C – N or N – N bonds at the surface of the tholins are also very likely to interact with the plasma species. Some new surface processes can be proposed on the model of the processes presented for (C:H) films. For instance, nitriles are likely to be extracted as HCN from other gas product containing C≡N. The formation of amines at the surface can be done by addition of hydrogen on tholin structures containing nitrogen thanks to H atoms or other H_2 excited species. Similarly to the formation of CN bonds, one could consider the formation of N=N and N≡N bonds.

The THETIS experiment showed that tholins interact strongly with their ionized plasma environment. Their chemical structure changes and they release new carbon-containing species in the gas phase. The major observation is the formation of nitriles at the surface and the release of HCN in the gas phase. Those two processes could be considered in the case of aerosols in Titan's ionosphere.

Concerning the perspectives of the THETIS experiment, I think of two main logical developments to go further in this experimental investigation. First, it would be very interesting to closely investigate the role of the radicals in the chemical processes happening at the surface of the tholins. Then, once the N_2-H_2 plasma interaction with tholins is fully understood, the next step is to add a small quantity of methane in the gas phase to investigate the opposite effects of the erosion by hydrogen and the carbon growth induced by methane. This experiment could be done on grains in levitation in PAMPRE.

Experimental simulations enable to guess the processes going on in Titan's ionosphere. Nevertheless, we still need to find clues that it is effectively happening there. Aerosols have not been directly studied by Cassini in the ionosphere, but the plasma has been closely investigated. My second strategy during my PhD work was then to analyze Cassini data of the ionospheric plasma in the hope to find clues on its interaction with the aerosols.

For this project I collaborated with Jan-Erik Wahlund and the team of the Swedish Institute of Space Physics (IRF) in Uppsala (Sweden) who designed the Langmuir Probe on-board Cassini. This instrument measures the low energy charged species in space plasmas. I re-analyzed its data to obtain the electron density and temperature in the ionosphere of Titan. The detailed analysis of the data revealed the presence of several electron populations, not predicted by the models. The second derivative of the electron current was found to be an efficient tool to identify the populations.

The analysis of 57 flybys during which Cassini went below 1200 km altitude enabled a statistical study of the electron populations. Four electron populations have been identified. Two are present in all conditions and are attributed to electrons coming from the nearby boom and background thermalized electrons, possibly originally coming from suprathermal

magnetospheric electrons. The third population density is strongly correlated with the solar illumination and the EUV fluxes. Nevertheless, its temperature is rather constant below 1100 km at ~0.06-0.07 eV. This population is attributed to electrons coming from the photoionization of N_2 and CH_4, and the subsequent gas phase ion chemistry. Finally, a fourth population is detected in very specific conditions: only on the dayside, and below 1150-1200 km altitude. It can reach densities as high as 2000 cm^{-3} and its temperature is proportional to its density. Aerosols start forming at this altitude. The fourth population is then strongly suspected to be linked to the presence of the aerosols. We propose two main processes, based on experimental work: the photo-emission of electrons from the surface of the aerosols, and the thermo-emission of electrons by the grains heated by the ion chemistry and the collection of electrons.

Therefore, the presence of this fourth population could be an indicator of the presence of aerosols on the dayside. To confirm this hypothesis, the next logical step is to model the two main suspected processes (the photo-emission and/or the thermo-emission of electrons from the aerosols) in the conditions of the ionosphere of Titan, and compare the modeled electrons emitted from the aerosols with the fourth population detected with the Langmuir Probe data. Then, it would be very interesting to implement global ionospheric models with these new processes!
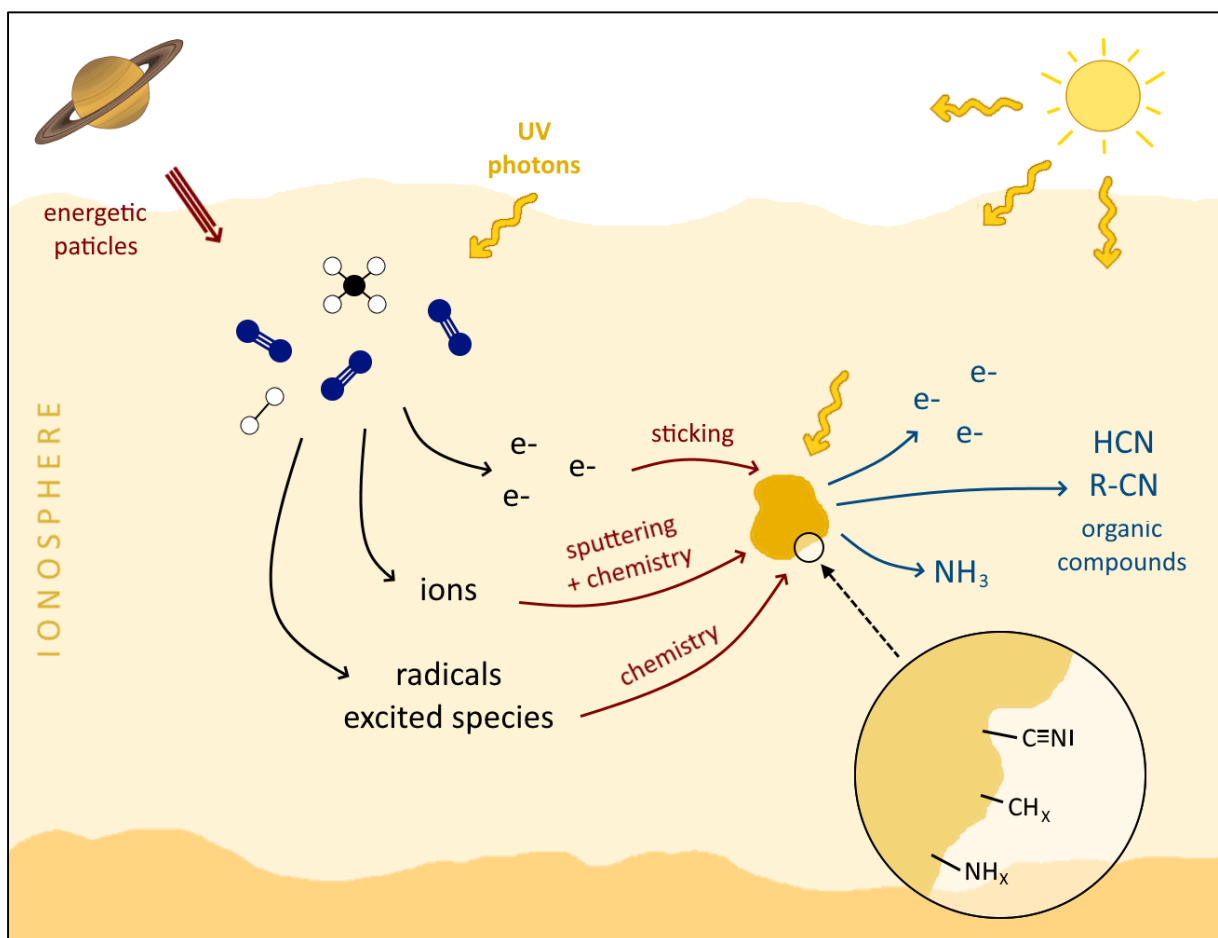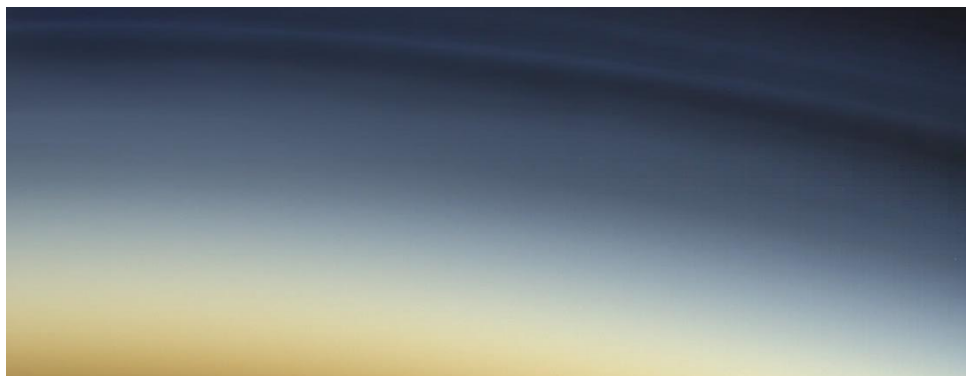
In conclusion, aerosols are certainly modified by their interaction with the reactive species of the ionospheric plasma. The other way around, they also disturb the plasma by the adsorption and/or recombination of some species, as well as by the emission of new molecules, ions and electrons in the gas phase.

After their formation/evolution in the ionosphere, the organic aerosols sediment through the lower, colder and denser, layers of the atmosphere. Then, they are likely to form aggregates and become condensation nucleus for some molecules in the gas phase. The future NASA mission Dragonfly will study the surface of Titan and in particular give insights on the morphological and chemical structure of the aerosols once deposited at the surface. It will considerably improve our understanding on the aerosols. The investigation of the evolution processes happening to the aerosols between their formation in the ionosphere and their deposition at the surface is fundamental to predict Dragonfly measurements, and interpret its results in a few years.

REFERENCES FOR THE CONCLUSION

Carrasco, E., Jiménez-Redondo, M., Tanarro, I., Herrero, V.J., 2012. Chemistry in low-pressure cold plasmas: Ions of astrophysical interest. Plasma Phys. Control. Fusion 54. https://doi.org/10.1088/0741-3335/54/12/124019

Lavvas, P., Yelle, R. V., Koskinen, T., Bazin, A., Vuitton, V., Vigren, E., Galand, M., Wellbrock, A., Coates, A.J., Wahlund, J.E., Crary, F.J., Snowden, D., 2013. Aerosol growth in Titan's ionosphere. Proc. Natl. Acad. Sci. U. S. A. 110, 2729–2734. https://doi.org/10.1073/pnas.1217059110

Sekine, Y., Imanaka, H., Matsui, T., Khare, B.N., Bakes, E.L.O., McKay, C.P., Sugita, S., 2008. The role of organic haze in Titan's atmospheric chemistry. I. Laboratory investigation on heterogeneous reaction of atomic hydrogen with Titan tholin. Icarus 194, 186–200. https://doi.org/10.1016/j.icarus.2007.08.031

Van Laer, K., Tinck, S., Samara, V., de Marneffe, J.F., Bogaerts, A., 2013. Etching of low- k materials for microelectronics applications by means of a N2/H2 plasma : modeling and experimental investigation. Plasma Sources Sci. Technol. 22, 025011. https://doi.org/10.1088/0963-0252/22/2/025011

Vigren, E., Galand, M., Shebanits, O., Wahlund, J.E., Geppert, W.D., Lavvas, P., Vuitton, V., Yelle, R. V., 2014. Increasing positive ion number densities below the peak of ion-electron pair production in titan's ionosphere. Astrophys. J. 786. https://doi.org/10.1088/0004-637X/786/1/69

Vuitton, V., Yelle, R. V., Klippenstein, S.J., Hörst, S.M., Lavvas, P., 2019. Simulating the density of organic species in the atmosphere of Titan with a coupled ion-neutral photochemical model. Icarus 324, 120–197. https://doi.org/10.1016/j.icarus.2018.06.013

INTERACTION AEROSOLS-PLASMA

DANS L'IONOSPHERE DE TITAN

Sommaire

I- Introduction

Titan est une lune de Saturne étonnante, qui présente de nombreuses similitudes avec la Terre, dont en particulier un cycle hydrologique à sa surface et une atmosphère épaisse composée principalement de diazote. **Toutefois, la grande particularité de Titan provient de ses aérosols.** Des composés organiques orangés emplissent son atmosphère sous la forme d'aérosols et sédimentent à sa surface, formant localement des dunes. L'omniprésence des aérosols orangés dans l'atmosphère et à la surface est aisément observable sur les clichés de la **Figure 1**. Les brumes d'aérosols sont particulièrement denses jusqu'à 500 km d'altitude (West et al., 2018).
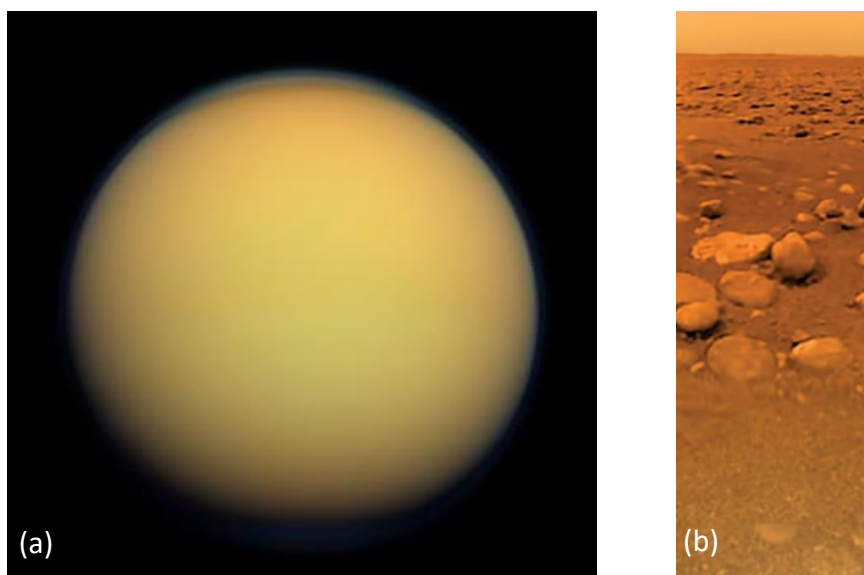

Figure 1 : (a) Titan observé par la sonde Cassini en janvier 2012. (b) Surface de Titan photographiée par la sonde Huygens en janvier 2005. Crédits : NASA/ESA

La présence d'aérosols dans l'atmosphère d'une planète impacte fortement son climat. En effet, les grains en suspension diffusent efficacement la lumière et sont des sites de nucléations favorisant la formation de nuages. Cela a pour conséquence de modifier drastiquement le budget radiatif et cela influence la dynamique atmosphérique de façon difficilement prédictible (Rannou et al., 2004).

Une intéressante particularité de Titan est que la composition de son atmosphère ressemble fortement à l'atmosphère de la Terre primitive, juste avant et aux débuts de l'apparition de la vie. En effet, l'atmosphère de Titan est composée principalement d'azote avec quelques pourcents de méthane, et du méthane était également présent dans l'atmosphère de la Terre avant l'évènement de la Grande Oxydation il y a 2,3 milliards d'années. Des travaux supposent que la Terre à cette époque possédait aussi une brume organique (Arney et al., 2016). L'étude de Titan est ainsi très intéressante pour comprendre comment de la matière organique complexe prébiotique aurait pu se former dans l'atmosphère de la Terre aux premiers instants de la vie.

Titan a été étudié par la mission Cassini-Huygens entre 2004 et 2017. La mission était composée d'un atterrisseur (Huygens) fourni par l'ESA ainsi que d'un orbiteur (Cassini) réalisé par la NASA. Huygens a traversé l'atmosphère de Titan en janvier 2005, en réalisant de nombreux diagnostiques sur l'atmosphère tout au long de la descente. De son côté, l'orbiteur Cassini a survolé Titan 126 fois, et est descendu jusqu'à 880 km d'altitude. Cette mission a conduit à de grandes découvertes, telles que la détection de dunes et de lacs d'hydrocarbures à la surface. La mission a en particulier permis une découverte fondamentale pour mes travaux de thèse : le fait que **les aérosols commencent à se former très haut dans l'atmosphère, autour de 1000-1200 km d'altitude** (Waite et al., 2007).

A cette altitude se trouve l'ionosphère, une couche de l'atmosphère ionisée comme son nom l'indique. Sur Titan, la principale source d'ionisation sont les photons solaires dans l'extrême UV qui peuvent induire jusqu'à une densité d'électrons de 3000 cm^{-3} vers 1100 km d'altitude (Ågren et al., 2009). D'autres sources d'ionisation sont aussi présentes, et dominent côté nuit, dont en particulier des électrons énergétiques en provenance de la magnétosphère de Saturne (Edberg et al., 2015). Le dépôt d'énergie de ces photons et particules énergétiques conduit à la dissociation et l'ionisation du diazote et du méthane de l'atmosphère, formant des **radicaux, des espèces excitées, des ions et des électrons libres : c'est un plasma naturel**.

La présence de ces espèces réactives formées principalement d'azote, de carbone et d'hydrogène induit une chimie organique complexe. Le spectromètre de masse INMS [*Ion Neutral Mass Spectrometer*] embarqué sur la sonde Cassini a ainsi collecté des molécules et des ions positifs de masse allant jusqu'à 100 u, sa limite de détection (Waite et al., 2007). Certains de ces composés ont pu être identifiés, notamment C_2H_2, C_2H_4, C_2H_6, CH_3C_2H, C_3H_6, C_4H_2, C_6H_6, HCN, CH_3CN, HC_3N, C_2H_5CN, C_2N_2, et NH_3 (Cui et al., 2009; Magee et al., 2009). Des indices sur la présence d'ions plus lourds que 100 u ont pu être déduits des mesures du spectromètre CAPS [*Cassini Plasma Spectrometer*] dédié à l'origine à l'étude des particules énergétiques chargées. La partie de l'instrument consacrée aux espèces positives, IBS/CAPS [*Ion Beam Spectrometer*] a permis la détection d'ion positifs de masse allant jusqu'à 350 u/q (Crary et al., 2009). Ces ions lourds deviennent même majoritaires comparé aux ions de moins de 100 u en dessous de 950 km. ELS/CAPS [*Electron Spectrometer*] a de son côté mis en évidence des ions négatifs extrêmement lourds, jusqu'à 13 800 u/q. Leur masse augmente lorsque l'altitude diminue (Coates et al., 2007, 2009). L'estimation de la taille de tels ions donne des petits aérosols, de 3.8 nm à plus de 38 nm selon leur charge (Wellbrock et al., 2013). Les mesures de CAPS révèlent la présence d'ions positifs et négatifs lourds. Toutefois, la résolution des instruments ne permet pas d'identifier chimiquement les composés.

Pour aller plus loin dans la compréhension de la chimie atmosphérique conduisant à la production d'ions complexes, plusieurs modèles de photochimie ont été mis au point. Ils ont en particulier montré qu'une chimie couplée des espèces neutres et des ions est nécessaire pour expliquer les observations. De nos jours les modèles reproduisent les densités et profils verticaux de nombreuses espèces (Vuitton et al., 2019). Ils montrent en particulier l'effet important de l'énergie déposée sur la chimie, qui varie avec l'altitude, l'ensoleillement et le cycle solaire.

La présence des aérosols dans l'ionosphère est toutefois plus complexe à modéliser. Ils interagissent électrostatiquement avec le plasma, de façon à ce que le plasma ne puisse être modélisé sans les prendre en compte. Il s'agit d'un 'plasma poudreux' (Lavvas et al., 2013; Shebanits et al., 2016). Des modèles microphysiques tentent d'expliquer la croissance des grains, par polymérisation, condensation de gaz et/ou agrégation de particules (Lavvas et al., 2011).

SIMULER L'IONOSPHERE DE TITAN EN LABORATOIRE

Une autre stratégie, complémentaire à la modélisation numérique, est la simulation en laboratoire. Reproduire la chimie de Titan expérimentalement a trois atouts majeurs : (1) le phénomène étudié est alors 'accessible', directement au laboratoire, et peut être répété ; (2) il est possible de faire varier volontairement certains paramètres pour étudier un processus en particulier ; (3) des instruments de pointe et non-spatialisables peuvent être utilisés.

De telles expériences ont commencé dès 1953 avec l'expérience de Stanley Miller et Harold Urey (Miller, 1953) dont l'objectif était de savoir si les composés organiques requis pour la vie auraient pu être produits dans l'atmosphère de la Terre primitive. Deux décennies plus tard, Carl Sagan et Bishun Khare ont réalisé de telles simulations de laboratoire dans le cadre d'atmosphères d'autres planètes, en particulier Jupiter, Saturne et Titan. Ils ont montré que l'exposition d'une atmosphère réductrice (du type N_2-CH_4) à des décharges électriques conduit à la formation d'un solide organique brun-orangé, qu'ils ont appelé 'tholins' (Sagan and Khare, 1979).

Aujourd'hui, nous savons grâce à la mission Cassini-Huygens que les aérosols de Titan sont formés à partir d'une chimie ionique complexe dans le plasma ionosphérique. De nombreuses expériences étudient ainsi la chimie d'un mélange d'azote et de méthane ionisé par un rayonnement UV, émis par une décharge dans un gaz, un laser ou un synchrotron. De telles expériences sont souvent limitées par la gamme de longueurs d'ondes accessible et l'accès aux infrastructures. **Ainsi, une autre stratégie expérimentale vise directement à reproduire le plasma ionosphérique à l'aide d'une décharge plasma dans un mélange N_2-CH_4.**

Une telle expérience a été développée au LATMOS depuis une vingtaine d'années, PAMPRE (pour Production d'Aérosols en Microgravité par Plasma REactif). Une décharge plasma radiofréquence en couplage capacitif (RF CCP) est allumée dans une chambre contenant un mélange d'azote et de méthane à 1 mbar. Un matériau solide brun-orangé se forme alors dans la décharge, tout comme pour l'expérience de C. Sagan et B. Khare. Toutefois, l'avantage d'utiliser une décharge RF CCP est que les tholins sont produits sous forme d'aérosols en lévitation électrostatique dans le plasma dans lequel ils séjournent quelques minutes (Alcouffe et al., 2010; Szopa et al., 2006). Tout comme sur Titan, les molécules et ions de la phase gaz ont pu être étudiés par spectrométrie de masse et une grande ressemblance a été observée avec les mesures de Cassini (Dubois et al., 2020, 2019b, 2019a). Après l'arrêt de la décharge plasma, les grains de tholins déposés au fond de la chambre peuvent être récoltés et analysés (voir **Figure 2**). Ce sont des grains sphériques d'environ 100 nm à 2 µm de diamètre selon les conditions expérimentales (Hadamcik et al., 2009). Ils sont composés principalement

de carbone, d'azote et d'hydrogène. La teneur en azote est particulièrement haute comparée aux composés organiques trouvés habituellement sur Terre, avec un rapport C/N ~1,5. L'analyse chimique des tholins par spectrométrie de haute résolution indique qu'ils sont constitués en partie de 'briques' élémentaires telles que C_2H_2 et HCN (Maillard et al., 2018).
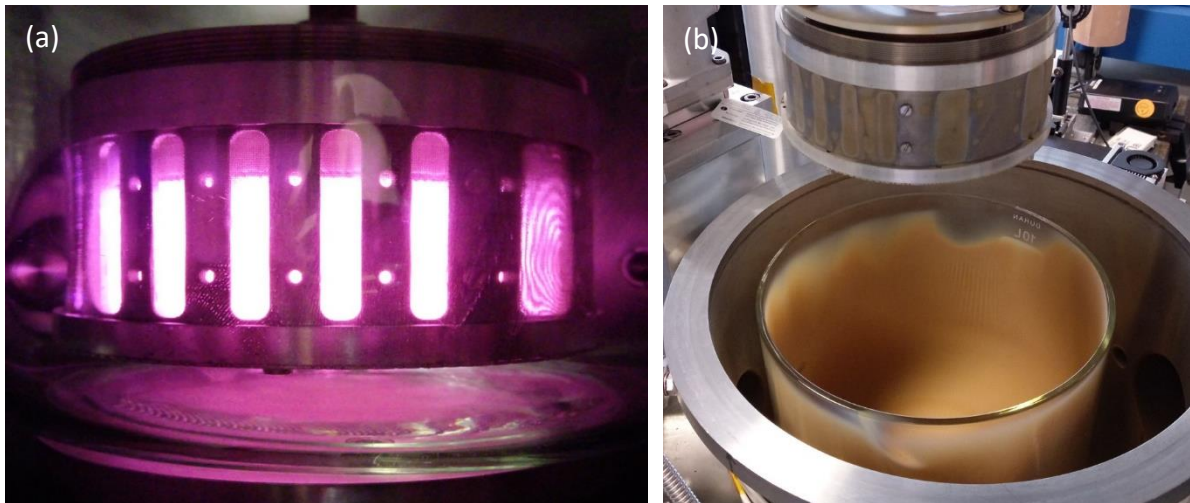

Figure 2 : (a) Décharge plasma de N_2-CH_4 dans l'expérience PAMPRE. Le plasma est confiné dans une cage métallique pour que les tholins qui sédimentent au fond de la chambre n'interagissent pas avec le plasma. (b) Dépôt de tholins au fond de la chambre après trois jours de fonctionnement.

EVOLUTION DES AEROSOLS DANS L'IONOSPHERE

Que ce soit sur Titan ou dans PAMPRE, les tholins restent un certain temps au contact du plasma dans lequel ils se sont formés (respectivement quelques jours/semaines et quelques minutes). Ils sont ainsi susceptibles d'interagir avec celui-ci. L'étude de l'évolution des tholins dans l'ionosphère de Titan est un sujet très récent, et est notamment le cœur du projet de recherche ERC-PRIMCHEM (2015-2021) au LATMOS.

Quelques travaux ont déjà étudié l'évolution des tholins sous chauffage (He et al., 2015), irradiation d'UV (Carrasco et al., 2018) et exposition à des atomes d'hydrogènes (Sekine et al., 2008). Aucun effet de la température n'a été observé sous 150°C. De très faibles modifications des liaisons chimiques ont été observées sous irradiation UV, mais des électrons photo-détachés des grains ont été mesurés. Enfin, les atomes d'hydrogène ont tendance à s'adsorber ou se recombiner en H_2 à la surface des tholins. Des modèles numériques suspectent aussi l'adsorption d'électrons (Vigren et al., 2014) et de molécules polaires tels que des nitriles (Vuitton et al., 2019) sur les grains.

Ainsi, les tholins ne sont pas inertes entre autres aux UV et aux atomes d'hydrogène. Qu'en est-il des autres espèces du plasma ? En effet, durant leur séjour dans le plasma, les aérosols sont continuellement au contact d'espèces très réactives (radicaux, espèces excitées, ions et électrons). **Cette question formule l'objectif de ma thèse : étudier l'interaction entre les aérosols et le plasma dans l'ionosphère de Titan**. Pour y apporter des réponses, j'ai suivi deux stratégies : (1) la simulation en laboratoire de l'exposition des aérosols organiques au plasma, et (2) l'étude de données plasma de la mission Cassini.

II- Etude des espèces érosives de l'ionosphère de Titan

Stratégie : simulation a l'aide d'une décharge plasma en N_2-H_2

La première partie de mon projet de thèse vise donc à reproduire en laboratoire l'interaction entre les aérosols et le plasma de l'ionosphère de Titan. L'idée de ce projet est l'insérer des tholins dans une décharge plasma et d'observer les modifications induites sur les tholins et sur le plasma. Ce projet étant tout nouveau, il a d'abord fallu concevoir le protocole et le dispositif expérimental (l'expérience THETIS est présentée en partie III).

Les interactions entre les aérosols et le plasma sont complexes. Deux principaux processus, d'effets opposés, ont lieu en parallèle sur Titan : (1) la croissance organique orchestrée par la formation de chaines carbonées, et (2) les **processus d'évolution des structures chimiques**. Le premier point ne peut être réalisé qu'à partir d'espèces contenant du carbone, à l'inverse du second qui peut avoir lieu sans espèces carbonées. Lors de ma thèse je me suis intéressée au point (2), traitant de l'évolution des tholins. Ainsi, pour restreindre tous les processus de croissance organique dans l'expérience, je n'ai utilisé que de l'azote et de l'hydrogène dans la phase gaz.

Avant de pouvoir comprendre l'effet des tholins sur le plasma de N_2-H_2, il a fallu le caractériser en l'absence des grains. Ceci est le sujet de la partie II.

La spectrometrie de masse

Le spectromètre de masse est un instrument très utile pour caractériser les espèces chimiques présentes dans un plasma. Lors de mes expériences j'ai eu accès à un spectromètre de masse quadripolaire (de Hiden Analytical, série EQP) qui m'a permis de mesurer les espèces neutres et les ions positifs présents dans la phase gaz.

La tête de prélèvement du spectromètre est positionnée proche du plasma et les espèces à mesurer entrent en passant par un trou de 100 µm, ce qui permet de conserver l'intérieur du spectromètre à très basse pression (< 5x10^{-6} mbar). Lors de l'analyse des espèces neutres, une chambre d'ionisation positionnée derrière le trou de 100 µm ionise les molécules, qui sont alors conduites dans le spectromètre par des lentilles électromagnétiques, jusqu'au détecteur compteur d'ions. Dans le cas des mesures d'ions, la chambre d'ionisation n'est pas utilisée et les ions sont directement collectés dans le plasma à l'aide d'un potentiel extracteur.

La transmission des espèces au travers des différentes zones du spectromètre de masse peut dépendre de leur nature, et en particulier de leur masse. Pour pouvoir interpréter quantitativement les spectres de masse obtenus, il a fallu calibrer l'instrument. En contrôlant chaque paramètre d'acquisition, j'ai acquis des spectres de masse de gaz injectés en quantité connue dans la chambre de PAMPRE. J'ai pu en déduire la courbe de transmission dans le spectromètre en fonction de la masse des composés. Des tests supplémentaires et l'ajout d'une petite correction m'a aussi permis d'utiliser cette courbe de transmission pour les ions.

Pour étudier les espèces présentes dans un plasma de N_2-H_2, j'ai utilisé deux décharges différentes : PAMPRE (de type RF CCP) et une décharge de type DC, qui sera utilisée pour l'expérience THETIS de la partie suivante. La comparaison des résultats de deux décharges différentes permet de valider que les observations faites ne dépendent pas d'une technique donnée, mais sont bien intrinsèques au plasma N_2-H_2. Cela permet d'extrapoler les résultats de laboratoire à ce qu'on pourrait trouver sur Titan. D'autre part, un projet initié avant ma thèse vise à modéliser la décharge plasma de N_2-CH_4 dans PAMPRE. Un premier modèle a été précédemment développé en N_2 pur (Alves et al., 2012). L'étude de la décharge en N_2-H_2 permet de franchir un pas de plus dans ce projet avec l'ajout de l'effet de l'hydrogène sur le plasma. Ce projet est réalisé en collaboration internationale avec une équipe portugaise de l'Instituto de Plasmas e Fusão Nuclear.

Nous avons d'abord expérimentalement étudié comment différents paramètres et espèces du plasma se comportent lorsque la quantité d'hydrogène, la pression et la puissance plasma changent (Chatain et al., 2020b). Notamment, les densités d'électrons ont été mesurées en utilisant la cage métallique de confinement du plasma comme une cavité résonante. La formation d'ammoniac a été mesurée par l'utilisation combinée de la spectroscopie infrarouge par absorption et de la spectrométrie de masse. Enfin, les ions positifs produits dans le plasma ont été étudiés à l'aide du spectromètre de masse.

Ces mesures nous ont ainsi permis de mettre en place un modèle numérique de la décharge plasma, prenant en compte la distribution 3D des espèces (Jiménez-Redondo, Chatain et al., 2020). Nous avons constaté que l'ajout d'hydrogène dans la décharge change considérablement le comportement du plasma, comparé au cas en N_2 pur, avec notamment l'apparition de nouveaux ions tels que N_2H^+ et NH_4^+. Les parois à l'intérieur de la décharge jouent aussi un rôle important. Elles induisent en particulier la production d'électrons secondaires énergétiques et la synthèse d'ammoniac en quantité (0.15% des gaz présents). Un schéma simplifié des processus à l'œuvre est donné en **Figure 3**.
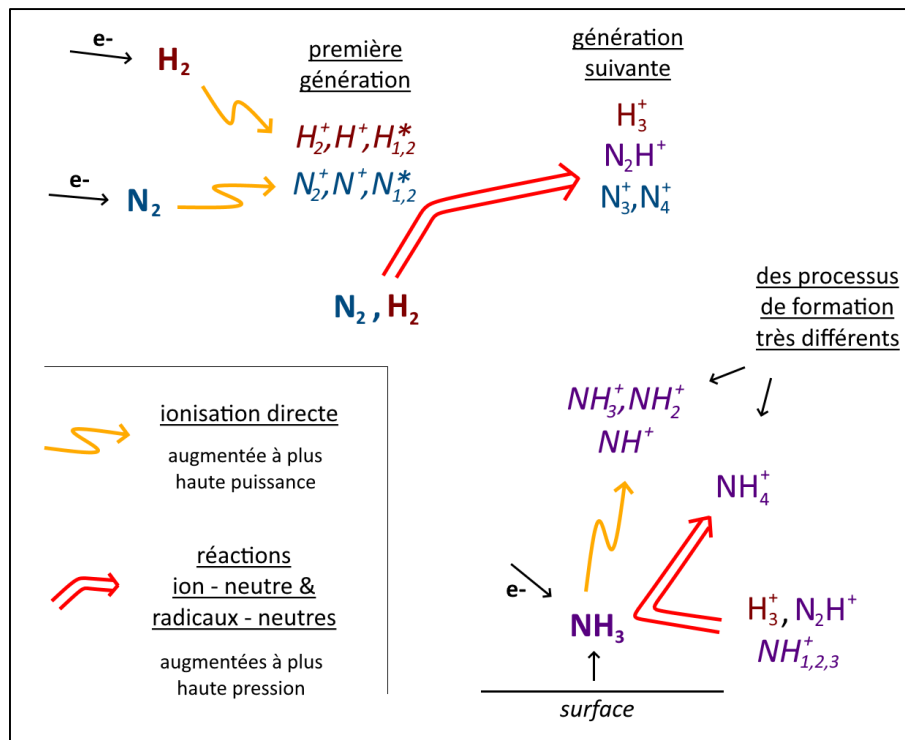
Figure 3 : Schéma simplifié des processus chimiques dans une décharge plasma en N_2-H_2.

ETUDE D'UNE DECHARGE DC

Les décharges plasma DC, aussi appelées 'glow', font partie des décharges plasma les plus simples à concevoir et étudier. Elles ont aussi l'avantage de présenter une large zone de plasma homogène. C'est ce type de décharge que nous avons donc choisi pour réaliser les expériences de la partie III.

Un flux de gaz de N_2-H_2 est injecté dans un tube en Pyrex à une pression d'environ 1 mbar, et une décharge électrique est initiée entre deux électrodes métalliques placées de part et d'autre du tube. **Tout comme dans la partie précédente, nous avons mesuré les espèces présentes en fonction de la quantité de H_2 injectée, de la pression et de la puissance plasma.** La densité des électrons a été mesurée à l'aide d'une sonde hairpin (Piejak et al., 2004) et les espèces neutres et les ions ont été analysées par spectrométrie de masse.

Ce type de décharge a déjà été étudié et modélisé dans des conditions expérimentales proches (de Souza et al., 1999; Gordiets et al., 1998; Loureiro and Ricard, 1993)**.** Nos résultats étant cohérents avec ces travaux, nous supposons que leurs résultats peuvent aussi s'appliquer à notre expérience. En particulier, ils montrent que l'ajout d'une petite quantité d'hydrogène dans une décharge plasma de N_2 crée des atomes H qui empêchent la formation des espèces excitées les plus énergétiques de N_2. Cela a des répercussions sur la valeur du champ électrique, qui augmente. La densité d'électron diminue, mais leur énergie augmente, leur permettant de dissocier plus efficacement les molécules avec lesquelles ils collisionnent. Cela conduit notamment à une production accrue d'atomes N. La **Figure 4** résume les effets observés par l'ajout d'hydrogène dans une décharge plasma de N_2.
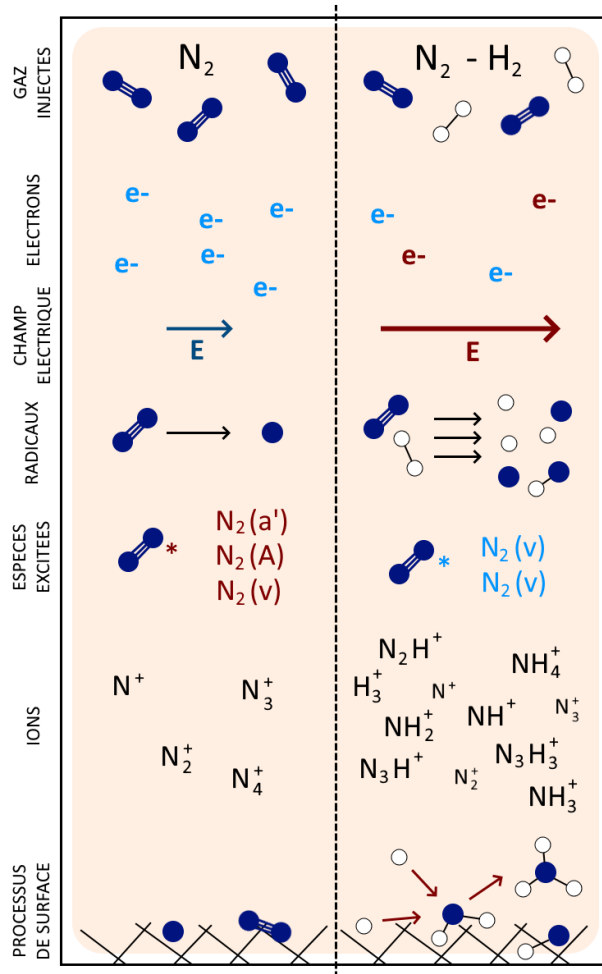
Figure 4 : Schéma des effets observés lors de l'ajout d'hydrogène dans une décharge plasma en N_2. Les espèces en bleu sont moins énergétiques que les espèces en rouge.

CONCLUSION : LES ESPECES EROSIVES DE L'IONOSPHERE DE TITAN

Les observations sur les deux types de décharges étudiées se sont révélées très similaires. La présence d'hydrogène dans le plasma composé majoritairement d'azote (>95%) entraîne la formation d'espèces très réactives dans le plasma, en particulier les atomes H et N, ainsi que les radicaux NH et NH₂, des espèces vibrationnellement excitées $N_2(v)$ et des ions comme N_2H^+, NH_4^+ ou H_3^+.

Les ions observés ont été mesurés sur Titan. Toutefois, les radicaux et les espèces excitées sont plus difficiles à détecter. Cependant, des modèles de la chimie s'y déroulant confirment la nécessité de leur présence dans l'ionosphère de Titan (Vuitton et al., 2019).

III- Erosion d'aérosols organiques dans un plasma en N_2-H_2

Après avoir caractérisé le plasma de N_2-H_2 en laboratoire, la deuxième étape du projet est d'y insérer des tholins et d'observer d'éventuelles évolutions des tholins et/ou du plasma. J'ai alors conçu un nouveau dispositif expérimental pour l'occasion, nommé THETIS [*Tholins Evolution in Titan's Ionosphere Simulation*]. Il permet d'ajouter l'échantillon de tholins sous vide après allumage du plasma, et se couple à différents instruments pour étudier *in situ* l'échantillon et le plasma (voir **Figures 5** et **6**). Les tholins sont préalablement formés dans PAMPRE, puis étalés sur une fine grille métallique servant de support pour les insérer dans le plasma. Ils sont ensuite exposés durant une quinzaine de minutes à quelques heures au plasma.
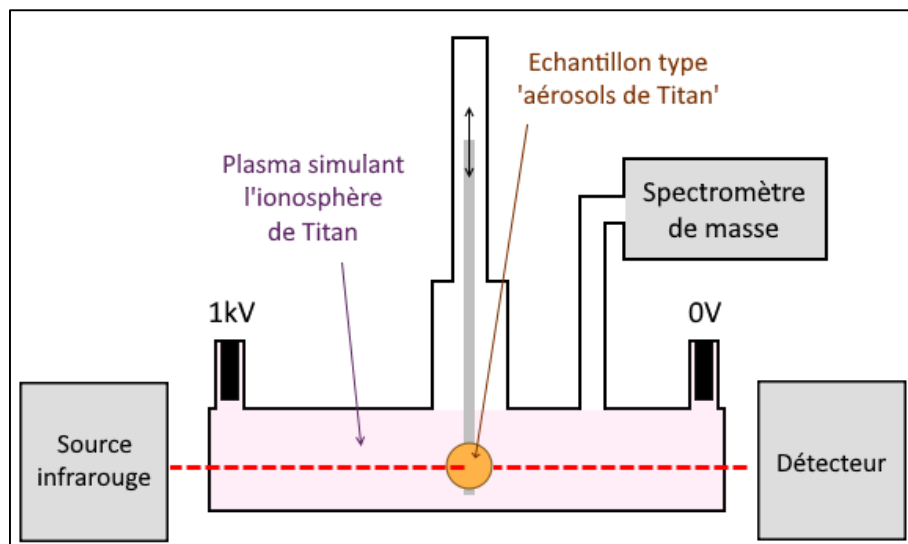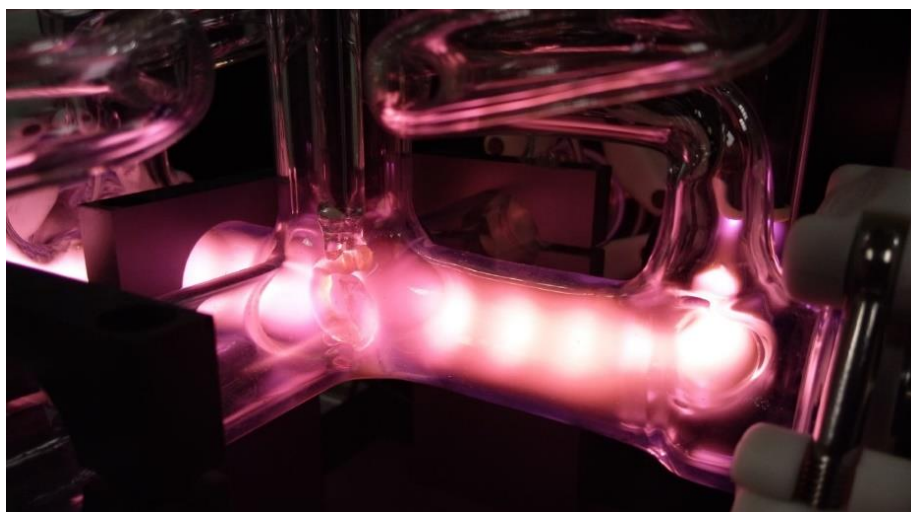

Figure 5 : Schéma de l'expérience THETIS.

Figure 6 : Photographie de l'expérience THETIS. L'échantillon est visible au centre du plasma.

Lorsque la grille de tholins est insérée dans un plasma d'azote pur, aucun effet n'est visible. A l'inverse, lorsqu'elle est insérée dans un plasma contenant 0,5 à 5% de H₂, il est possible d'observer l'érosion de la pastille à l'œil nu. Plus en détail, **des images prises au microscope électronique à balayage (MEB) montrent que les grains de tholins initialement sphériques sont creusés et présentent des marques d'érosion de quelques dizaines de nanomètres** (voir **Figure 7**).
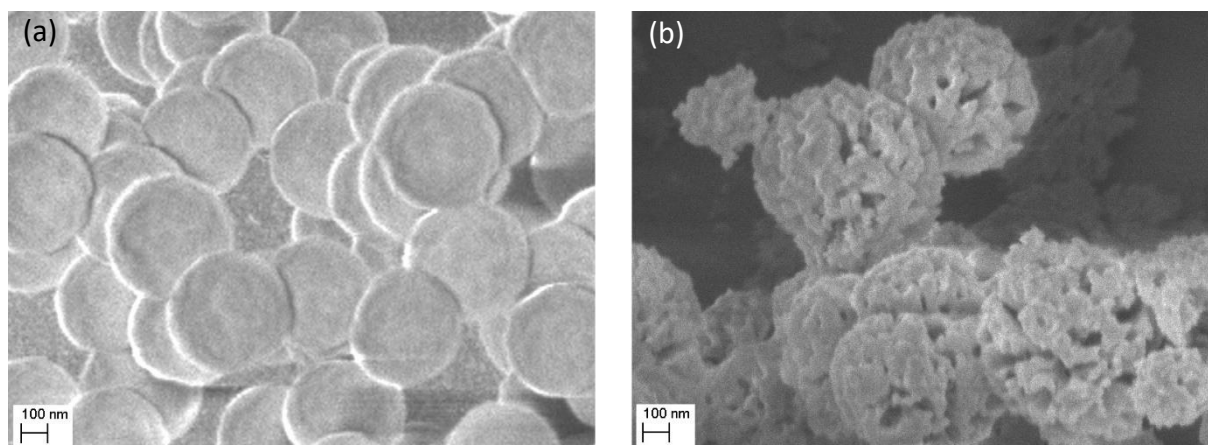

Figure 7 : Image des tholins (a) produits dans PAMPRE et (b) après exposition à un plasma de N₂-H₂.

La structure chimique des tholins a également été observée par spectroscopie d'absorption infrarouge large bande (Chatain et al., 2020a). En effet, l'absorption d'un faisceau infrarouge par les tholins nous renseigne sur les fonctions chimiques présentes. Nous avons réalisé cette mesure *in situ* tout au long de l'exposition des tholins au plasma (voir la trajectoire du faisceau infrarouge sur la **Figure 5**). **Cette technique nous a permis d'observer que les fonctions chimiques des tholins évoluent lorsqu'ils sont exposés au plasma de N₂-H₂**. En particulier, les fonctions nitriles (C≡N) diminuent fortement en comparaison des autres fonctions. Les doubles liaisons semblent aussi diminuer par rapport aux amines (NH) et aux bandes CH. Plus en détail dans les bandes des nitriles, nous observons que les isonitriles (-N≡C|) disparaissent très rapidement et qu'une autre bande de nitriles se forme (voir la **Figure 8**).
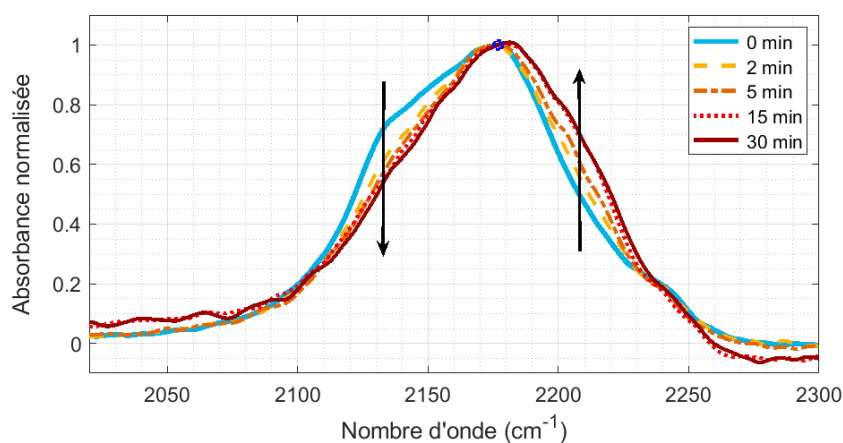

Figure 8 : Evolution des bandes nitriles des tholins lors de l'exposition à un plasma de N₂-H₂.

L'étude de la phase gaz a également révélé qu'elle est fortement modifiée par la présence des tholins (voir la **Figure 9**). La mesure des espèces neutres et des ions positifs par spectrométrie de masse montre que de nombreuses nouvelles espèces contenant du carbone apparaissent, dont en particulier du cyanure d'hydrogène HCN et des composés formés de nitriles (NH_3-CN, NC-CN). Des ions très insaturés sont aussi observés, tels que C^+, C_2^+, C_2H^+, C_3^+, C_3H^+ et $C_3H_2^+$/C_2N^+. A l'inverse, la production d'ammoniac comparée au cas sans tholins diminue.

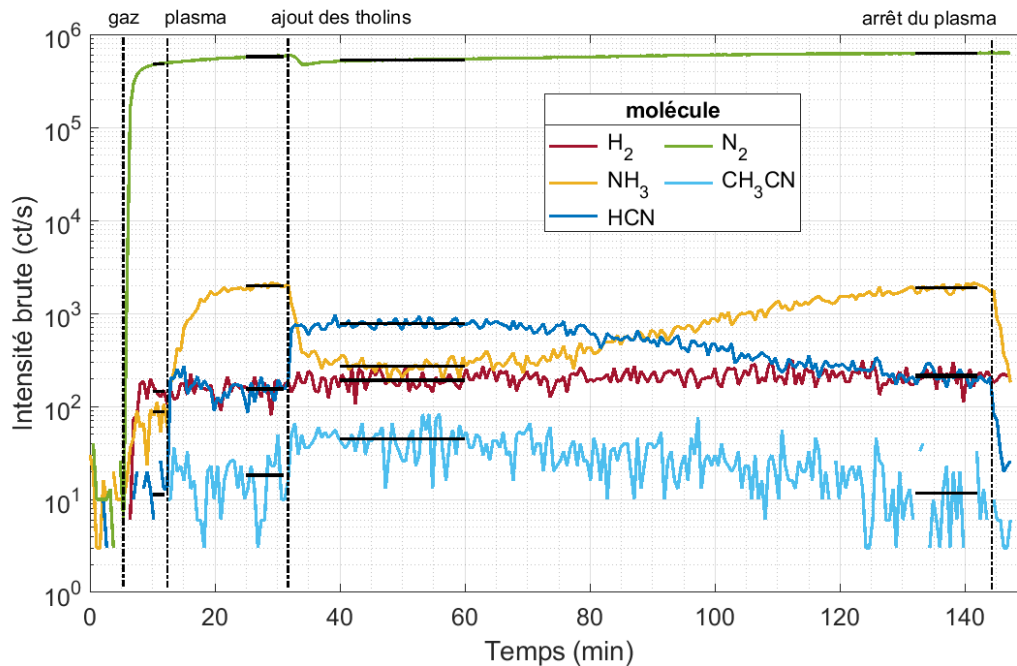**Figure 9 :** Evolution des espèces gazeuses avec l'allumage du plasma dans un mélange de gaz N_2-H_2 et après insertion des tholins.

CONCLUSION : INTERACTION ENTRE LES AEROSOLS ET LE PLASMA

Nous observons donc que les tholins interagissent avec le plasma de N_2-H_2 dans lequel ils sont insérés. Dans le domaine de la microélectronique plusieurs travaux ont étudié un processus similaire. Ils étudient des films formés de carbone et d'hydrogène exposés à des plasmas divers, et notamment en N_2-H_2. Ces films sont utilisés pour les circuits intégrés et l'exposition à des plasmas érosifs au travers de masques leur permet de réaliser des gravures fines. Van Laer et al. (2013) a mis au point un modèle des processus ayant lieu à la surface des films, dont nous pouvons nous inspirer pour expliquer les effets observés dans THETIS.

En particulier, les expériences sur les films C:H observent également la production de HCN, qu'ils expliquent de la manière suivante : des atomes N du plasma s'adsorbent à la surface des films, puis réagissent progressivement avec les atomes de carbone du film pour former une triple liaison C≡N. Ensuite, un atome H s'y greffe, formant la molécule stable HCN. Enfin, le bombardement ionique ayant lieu à la surface du film éjecte la molécule de HCN dans la phase

gaz. Ce processus a très certainement lieu aussi sur les tholins et est cohérent avec nos observations : les mesures en absorption IR montrent la formation d'une nouvelle bande de C≡N et aussi la diminution globale de tous les nitriles, et l'étude de la phase gaz révèle l'apparition de HCN. D'autres processus de surface sont proposés et illustrés sur la **Figure 10**.
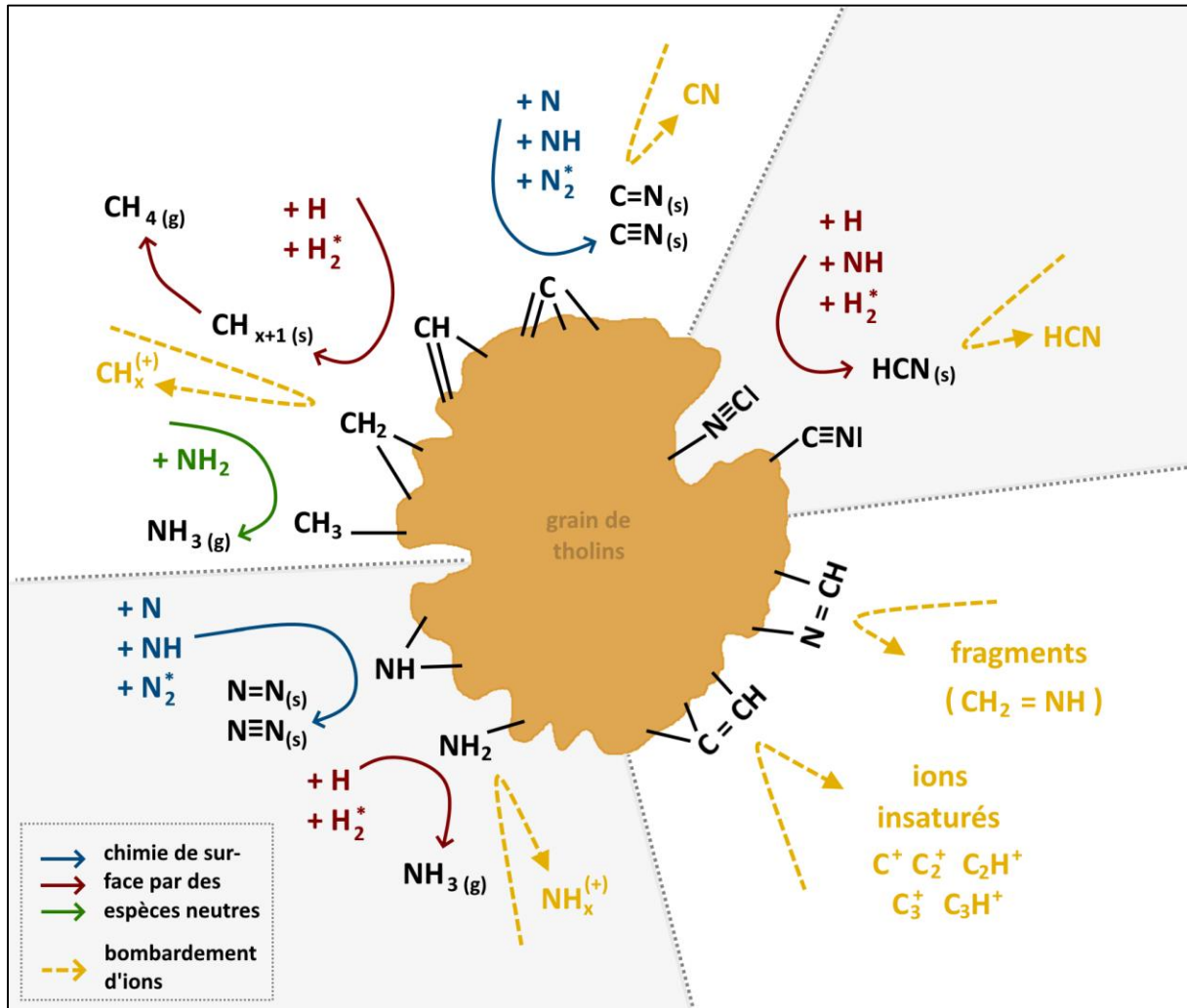

Figure 10 : Schéma représentant des suggestions de processus à l'œuvre à la surface d'un grain de tholins plongé dans un plasma de N_2-H_2.

L'expérience THETIS a mis en évidence l'interaction forte des grains de tholins avec les diverses espèces de plasma, dont en particulier les radicaux (atomes H et N, et NH). Des espèces du plasma s'adsorbent à la surface, modifient les liaisons chimiques de tholins et forment des fragments qui sont éjectés dans la phase gaz. Ces mécanismes, dont en particulier la formation de nitriles sur les aérosols et de HCN en phase gaz, pourraient également être à l'œuvre dans l'ionosphère de Titan.

IV- Des électrons perturbés par la présence des aérosols dans l'ionosphère

La simulation expérimentale étudiée dans les deux parties précédentes nous a permis de valider la possibilité d'une interaction entre les aérosols organiques et le plasma de l'ionosphère de Titan, et de suggérer des mécanismes à l'œuvre. Toutefois, il nous manque encore à trouver des indices sur Titan pour confirmer une telle interaction. Les aérosols n'ont pas été directement mesurés dans l'ionosphère par Cassini, mais le plasma quant à lui a été étudié en détails. **Lors de ma thèse je me suis ainsi intéressée à des mesures du plasma ionosphérique prises par Cassini dans l'espoir de trouver des indices de l'interaction du plasma avec les aérosols.**

Ce projet a été réalisé en collaboration internationale avec Jan-Erik Wahlund et l'équipe de l'Institut Suédois des Plasmas Spatiaux (IRF) à Uppsala. Cette équipe a conçu la sonde de Langmuir à bord de Cassini, qui permet d'étudier les espèces chargées de faible énergie, dont en particulier les électrons (Wahlund et al., 2005).

Figure 11 : (a) Position de la sonde de Langmuir sur la sonde Cassini. Crédits : NASA. (b) Sonde de Langmuir de Cassini, repliée. Crédits : IRF.

La sonde de Langmuir est une sphère en titane de 5 cm de diamètre au bout d'une tige qui la positionne à plus 1,5 m du corps du satellite (voir **Figure 11**). Cette sphère est soumise à un potentiel électrique qui est varié de façon continue entre -4 et +4 V. Le plasma autour est à un potentiel (appelé 'potentiel plasma'), généralement autour de +0.5 V. Lorsque le potentiel de la sonde est inférieur, elle attire les ions positifs, et lorsqu'il est supérieur, elle attire les électrons. **Dans ce projet je me suis intéressée aux électrons et ai essentiellement utilisé le courant mesuré par la sonde dû aux électrons.**

Généralement dans un plasma ionosphérique, les électrons sont thermalisés par des collisions avec les molécules de leur environnement (Galand et al., 2014). Dans ce cas-là, la sonde de Langmuir mesure une unique population d'électrons, représentée par une 'bosse' dans le graphe de la dérivée seconde du courant électronique en fonction du potentiel de la sonde. Toutefois, j'ai pu constater que dans l'ionosphère pour des altitudes inférieures à 1300 km, il n'y a pas une, mais 2, 3 ou même parfois 4 'bosses' (voir **Figure 12**).
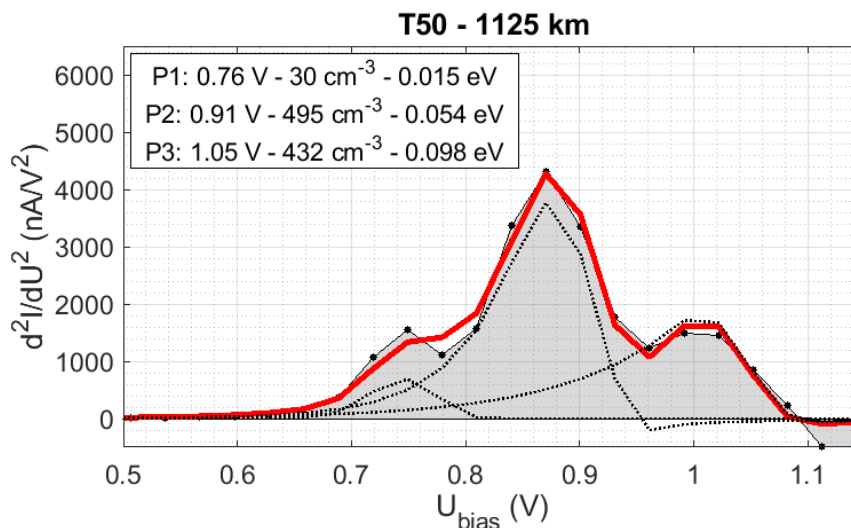

Figure 12 : Dérivée seconde du courant électronique collecté par la sonde de Langmuir de Cassini à 1125 km d'altitude lors du survol T50. Détection et modélisation de 3 populations.

A priori, la sonde de Langmuir mesure donc plus d'une population d'électrons. L'ajustement du signal à partir des équations théoriques de l'OML [*Orbital Motion Limited theory*] et de la SL [*Sheath Limited theory*] permet d'en déduire la densité et la température (= leur énergie) des électrons de chaque population (Whipple, 1965).

Lors d'un survol de Titan, la sonde Cassini traverse l'ionosphère en 15 minutes et réalise une trentaine de mesures. **Cela permet de suivre l'évolution de la densité et de la température des électrons en fonction de l'altitude**. Selon si la sonde est passée côté jour (F3), proche du terminateur (F2) ou côté nuit (F1), les profils sont différents. Ils sont présentés en **Figure 13**. Nous observons quatre populations : P_1, P_2, P_3 et P_4. P_1 et P_2 sont toujours présentes, contrairement à P_3 qui apparaît proche du terminateur et s'intensifie côté jour. La population P_4 est particulièrement intéressante : elle n'apparaît que côté jour et en dessous de 1200 km d'altitude.

La sonde a traversé 57 fois l'ionosphère de Titan, ce qui nous permet de réaliser des statistiques sur les comportements des différentes populations d'électrons. J'ai ainsi étudié les corrélations avec le flux UV, les saisons et les densités d'ions.
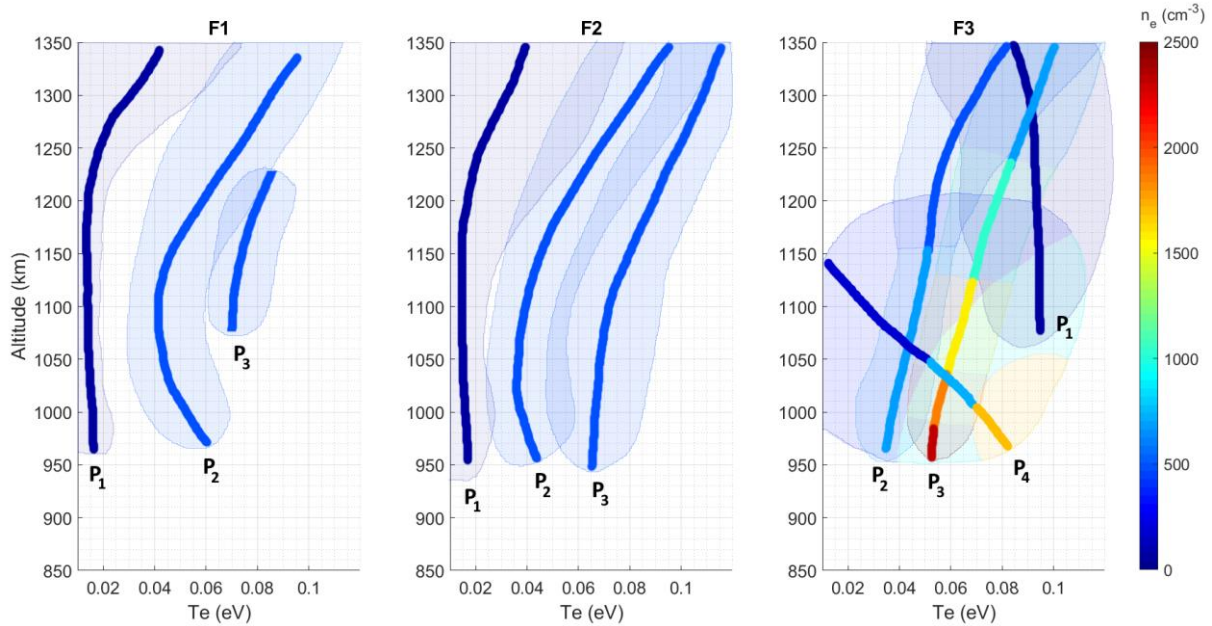
Figure 13 : Profils verticaux de la température (T_e) des électrons pour les différentes populations. Les couleurs indiquent la densité (n_e) des électrons. Les trois graphes représentent trois familles de survols : F1 côté nuit, F2 côté nuit proche du terminateur et F3 côté jour.

CONCLUSION : DES ELECTRONS EMIS PAR LES AEROSOLS

Cette étude m'a permis d'obtenir des indications sur l'origine des populations d'électrons (voir **Figure 14**).

La première population est toujours présente, en très faible quantité. C'est la première détectée par la sonde (lorsque son potentiel augmente), ce qui suggère que les électrons sont très proches de la sonde. Nous pouvons raisonnablement attribuer cette population à des **électrons émis par la tige à proximité de la sonde** après collision avec un photon solaire ou une particule énergétique provenant de la magnétosphère.

La seconde population est également toujours présente avec des densités et températures constantes (~500 cm^{-3} et 0.04 eV sous 1100 km). Elle est attribuée à des **électrons thermalisés**, provenant à l'origine de la magnétosphère.

La densité de **la troisième population** est pour sa part fortement corrélée à l'illumination solaire. Sa température est globalement constante sous 1100 km (0.06-0.07 eV). Elle est attribuée aux **électrons formés par la photo-ionisation** des molécules de l'ionosphère de Titan.

Enfin, **la quatrième population** n'est présente que côté jour et sous 1200 km, altitude à partir de laquelle les aérosols commencent à se former. Nous envisageons qu'elle soit due à des **électrons émis par les aérosols** après qu'ils aient été percutés par un photon solaire énergétique (photo-émission) ou après avoir été chauffés au-delà d'un certain seuil par la chimie environnante (émission thermo-ionique). Ces deux mécanismes ont été observés en laboratoire (Tigrine et al., 2018; Woodard et al., 2020).
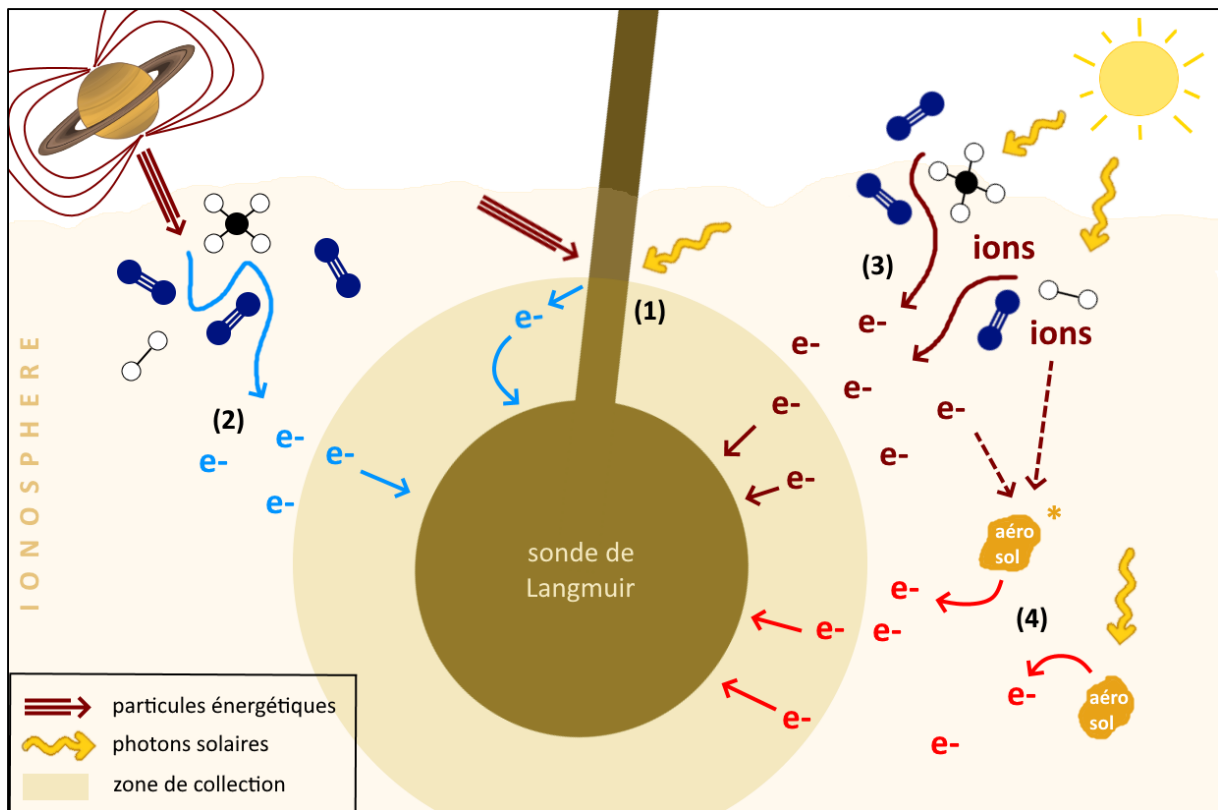
Figure 14 : Schéma proposant l'origine des 4 populations d'électrons observées par la sonde de Langmuir dans l'ionosphère de Titan.

Conclusion et perspectives

La mise en place de l'expérience THETIS et l'analyse des données de la sonde de Langmuir de Cassini dans l'ionosphère de Titan m'ont permis d'observer l'interaction entre les aérosols organiques et les espèces du plasma environnant. J'ai constaté que les grains sont eux-mêmes chimiquement modifiés par interaction avec des espèces réactives telles que les atomes H et N (radicaux). Les aérosols participent aussi à l'évolution du plasma, en adsorbant certaines espèces, et en formant de nouvelles, dont en particulier HCN, et les électrons P_4 (voir **Figure 15**). Ces travaux ont permis de déceler des mécanismes se produisant à la surface des aérosols sur Titan. La prochaine étape sera de les modéliser.

Après leur traversée de l'ionosphère, l'aventure des aérosols n'est pas terminée, ils s'agglomèrent entre eux et deviennent des noyaux de condensations des espèces gazeuses. Lorsqu'ils sédimentent à la surface, ils ont encore certainement évolué. La mission Dragonfly de la NASA prévoit d'étudier la surface de Titan dans quelques années (Lorenz et al., 2018). Elle nous donnera accès à la composition et la morphologie des aérosols une fois au sol. Toutefois, il reste encore des études à mener pour faire le lien entre les aérosols de l'ionosphère et les grains sédimentés à la surface !
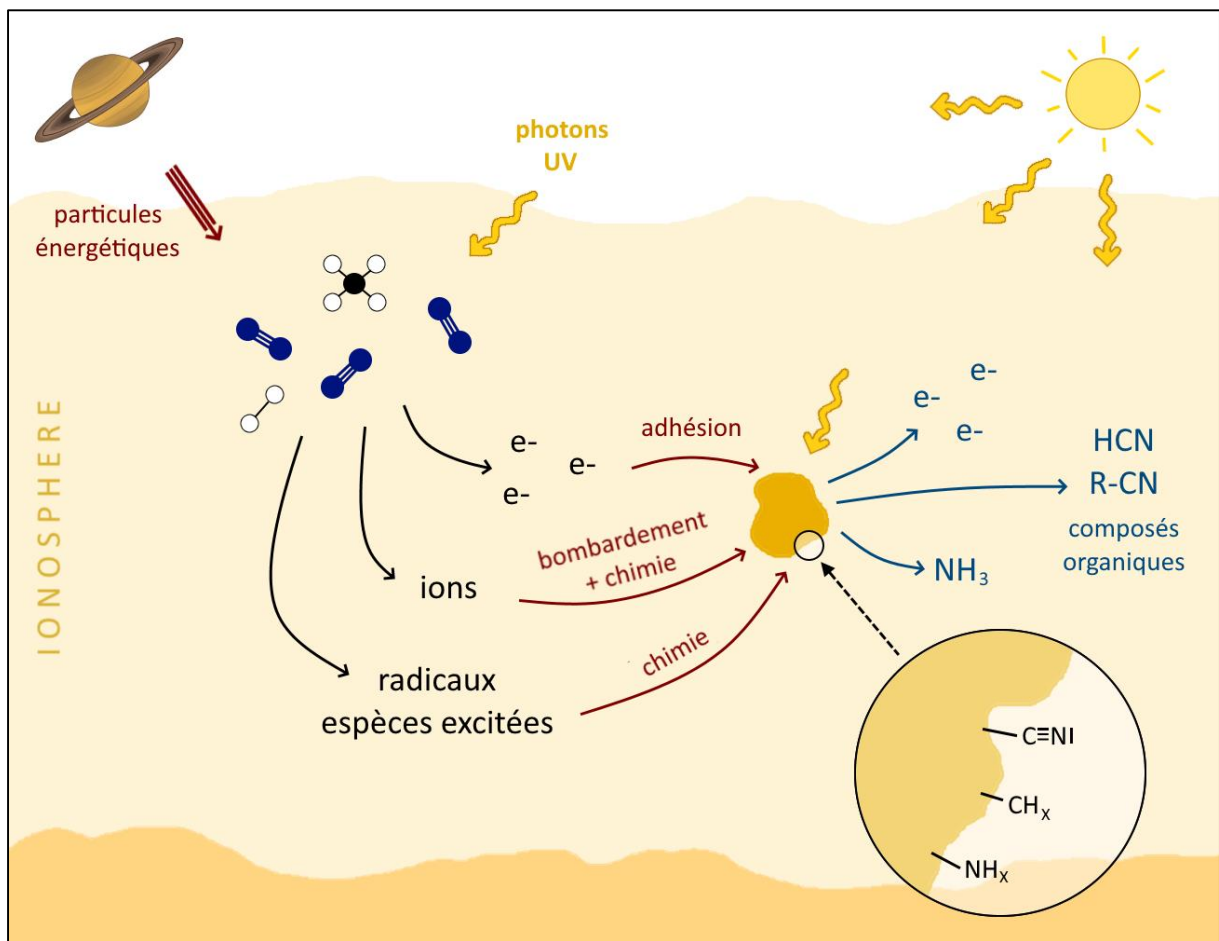
Figure 15 : Schéma bilan des interactions entre les aérosols organiques et les espèces du plasma ionosphérique de Titan discutées dans cette thèse.

REFERENCES BIBLIOGRAPHIQUES

Ågren, K., Wahlund, J.-E., Garnier, P., Modolo, R., Cui, J., Galand, M., Müller-Wodarg, I., 2009. On the ionospheric structure of Titan. Planet. Space Sci. 57, 1821–1827. https://doi.org/10.1016/J.PSS.2009.04.012

Alcouffe, G., Cavarroc, M., Cernogora, G., Ouni, F., Jolly, A., Boufendi, L., Szopa, C., 2010. Capacitively coupled plasma used to simulate Titan's atmospheric chemistry. Plasma Sources Sci. Technol. 19, 015008. https://doi.org/10.1088/0963-0252/19/1/015008

Alves, L.L., Marques, L., Pintassilgo, C.D., Wattieaux, G., Es-Sebbar, E., Berndt, J., Kovacević, E., Carrasco, N., Boufendi, L., Cernogora, G., 2012. Capacitively coupled radio-frequency discharges in nitrogen at low pressures. Plasma Sources Sci. Technol. 21, 045008. https://doi.org/10.1088/0963-0252/21/4/045008

Arney, G., Domagal-Goldman, S.D., Meadows, V.S., Wolf, E.T., Schwieterman, E., Charnay, B., Claire, M., Hébrard, E., Trainer, M.G., 2016. The Pale Orange Dot: The Spectrum and Habitability of Hazy Archean Earth. Astrobiology 16, 873–899. https://doi.org/10.1089/ast.2015.1422

Carrasco, N., Tigrine, S., Gavilan, L., Nahon, L., Gudipati, M.S., 2018. The evolution of Titan's high-altitude aerosols under ultraviolet irradiation. Nat. Astron. 2, 1. https://doi.org/10.1038/s41550-018-0439-7

Chatain, A., Carrasco, N., Ruscassier, N., Gautier, T., Vettier, L., Guaitella, O., 2020a. Interaction dust – plasma in Titan's ionosphere: an experimental simulation of aerosols erosion. Icarus 345, 113741. https://doi.org/10.1016/j.icarus.2020.113741

Chatain, A., Jiménez-Redondo, M., Vettier, L., Guaitella, O., Carrasco, N., Alvez, L.L., Marques, L., Cernogora, G., 2020b. N2-H2 capacitively coupled radio-frequency discharges at low pressure. Part I. Experimental results: effect of the H2 amount on electrons, positive ions and ammonia formation. Plasma Sources Sci. Technol. submitted.

Coates, A.J., Crary, F.J., Lewis, G.R., Young, D.T., Waite, J.J.H., Sittler, J.E.C., 2007. Discovery of heavy negative ions in Titan's ionosphere. Geophys. Res. Lett. 34, L22103. https://doi.org/10.1029/2007GL030978

Coates, A.J., Wellbrock, A., Lewis, G.R., Jones, G.H., Young, D.T., Crary, F.J., Waite, J.H., 2009. Heavy negative ions in Titan's ionosphere: Altitude and latitude dependence. Planet. Space Sci. 57, 1866–1871. https://doi.org/10.1016/j.pss.2009.05.009

Crary, F.J., Magee, B.A., Mandt, K., Waite, J.H., Westlake, J., Young, D.T., 2009. Heavy ions, temperatures and winds in Titan's ionosphere: Combined Cassini CAPS and INMS observations. Planet. Space Sci. 57, 1847–1856. https://doi.org/10.1016/j.pss.2009.09.006

Cui, J., Yelle, R. V., Vuitton, V., Waite, J.H., Kasprzak, W.T., Gell, D.A., Niemann, H.B., Müller-Wodarg, I.C.F., Borggren, N., Fletcher, G.G., Patrick, E.L., Raaen, E., Magee, B.A., 2009. Analysis of Titan's neutral upper atmosphere from Cassini Ion Neutral Mass Spectrometer measurements. Icarus 200, 581–615. https://doi.org/10.1016/j.icarus.2008.12.005

de Souza, A.R., Digiacomo, M., Muzart, J.L.R., Nahorny, J., Ricard, A., 1999. Dissociation of N2 in flowing glow discharge: Influence of H2*. Eur. Phys. J. Appl. Phys. 5, 185–189.

Dubois, D., Carrasco, N., Bourgalais, J., Vettier, L., Desai, R.T., Wellbrock, A., Coates, A.J., 2019a. Nitrogen-containing Anions and Tholin Growth in Titan's Ionosphere: Implications for Cassini CAPS-ELS Observations. Astrophys. J. 872, L31. https://doi.org/10.3847/2041-8213/ab05e5

Dubois, D., Carrasco, N., Jovanovic, L., Vettier, L., Gautier, T., Westlake, J., 2020. Positive ion chemistry in an N2-CH4 plasma discharge: Key precursors to the growth of Titan tholins. Icarus 338. https://doi.org/10.1016/j.icarus.2019.113437

Dubois, D., Carrasco, N., Petrucciani, M., Vettier, L., Tigrine, S., Pernot, P., 2019b. In situ investigation of neutrals involved in the formation of Titan tholins. Icarus 317, 182–196. https://doi.org/10.1016/j.icarus.2018.07.006

Edberg, N.J.T., Andrews, D.J., Bertucci, C., Gurnett, D.A., Holmberg, M.K.G., Jackman, C.M., Kurth, W.S., Menietti,

J.D., Opgenoorth, H.J., Shebanits, O., Vigren, E., Wahlund, J.-E., 2015. Effects of Saturn's magnetospheric dynamics on Titan's ionosphere. J. Geophys. Res. Sp. Phys. 120, 8884–8898. https://doi.org/10.1002/2015JA021373

Galand, M., Coates, A.J., Cravens, T.E., Wahlund, J.-E., 2014. Titan's Ionosphere, in: Titan. Cambridge University Press, Cambridge, UK, pp. 296–361.

Gordiets, B., Ferreira, C.M., Pinheiro, M.J., Ricard, A., 1998. Self-consistent kinetic model of low-pressure N2-H2 flowing discharges: I. Volume processes. Plasma Sources Sci. Technol. 7, 363–378. https://doi.org/10.1088/0963-0252/7/3/015

Hadamcik, E., Renard, J.B., Alcouffe, G., Cernogora, G., Levasseur-Regourd, A.C., Szopa, C., 2009. Laboratory light-scattering measurements with Titan's aerosols analogues produced by a dusty plasma. Planet. Space Sci. 57, 1631–1641. https://doi.org/10.1016/j.pss.2009.06.013

He, J., Buch, A., Carrasco, N., Szopa, C., 2015. Thermal degradation of organics for pyrolysis in space: Titan's atmospheric aerosol case study. Icarus 248, 205–212. https://doi.org/10.1016/j.icarus.2014.10.010

Jiménez-Redondo, M., Chatain, A., Vettier, L., Guaitella, O., Cernogora, G., Carrasco, N., Alvez, L.L., Marques, L., 2020. N2-H2 capacitively coupled radio-frequency discharges at low pressure. Part II. Modelling results: the relevance of plasma-surface interaction. Plasma Sources Sci. Technol. submitted.

Lavvas, P., Sander, M., Kraft, M., Imanaka, H., 2011. Surface chemistry and particle shape: Processes for the evolution of aerosols in Titan's atmosphere. Astrophys. J. 728. https://doi.org/10.1088/0004-637X/728/2/80

Lavvas, P., Yelle, R. V., Koskinen, T., Bazin, A., Vuitton, V., Vigren, E., Galand, M., Wellbrock, A., Coates, A.J., Wahlund, J.E., Crary, F.J., Snowden, D., 2013. Aerosol growth in Titan's ionosphere. Proc. Natl. Acad. Sci. U. S. A. 110, 2729–2734. https://doi.org/10.1073/pnas.1217059110

Lorenz, R.D., Turtle, E.P., Barnes, J.W., Trainer, M.G., Adams, D.S., Hibbard, K.E., Sheldon, C.Z., Zacny, K., Peplowski, P.N., Lawrence, D.J., Ravine, M.A., McGee, T.G., Sotzen, K.S., MacKenzie, S.M., Langelaan, J.W., Schmitz, S., Wolfarth, L.S., Bedini, P.D., 2018. Dragonfly: A rotorcraft lander concept for scientific exploration at titan. Johns Hopkins APL Tech. Dig. 34, 374–387.

Loureiro, J., Ricard, A., 1993. Electron and vibrational kinetics in an N2-H2 glow discharge with application to surface processes. J. Phys. D. Appl. Phys. 26, 163–176. https://doi.org/10.1088/0022-3727/26/2/001

Magee, B.A., Waite, J.H., Mandt, K.E., Westlake, J., Bell, J., Gell, D.A., 2009. INMS-derived composition of Titan's upper atmosphere: Analysis methods and model comparison. Planet. Space Sci. 57, 1895–1916. https://doi.org/10.1016/j.pss.2009.06.016

Maillard, J., Carrasco, N., Schmitz-Afonso, I., Gautier, T., Afonso, C., 2018. Comparison of soluble and insoluble organic matter in analogues of Titan's aerosols. Earth Planet. Sci. Lett. 495, 185–191. https://doi.org/10.1016/J.EPSL.2018.05.014

Miller, S.L., 1953. A production of amino acids under possible primitive earth conditions. Science 117, 528–529. https://doi.org/10.1126/science.117.3046.528

Piejak, R.B., Godyak, V.A., Garner, R., Alexandrovich, B.M., Sternberg, N., 2004. The hairpin resonator: A plasma density measuring technique revisited. J. Appl. Phys. 95, 3785–3791. https://doi.org/10.1063/1.1652247

Rannou, P., Hourdin, F., McKay, C.P., Luz, D., 2004. A coupled dynamics-microphysics model of Titan's atmosphere. Icarus 170, 443–462. https://doi.org/10.1016/j.icarus.2004.03.007

Sagan, C., Khare, B.N., 1979. Tholins: Organic chemistry of interstellar grains and gas. Nature 277, 102–107. https://doi.org/10.1038/277102a0

Sekine, Y., Imanaka, H., Matsui, T., Khare, B.N., Bakes, E.L.O., McKay, C.P., Sugita, S., 2008. The role of organic haze in Titan's atmospheric chemistry. I. Laboratory investigation on heterogeneous reaction of atomic hydrogen with Titan tholin. Icarus 194, 186–200. https://doi.org/10.1016/j.icarus.2007.08.031

Shebanits, O., Wahlund, J.-E., Edberg, N.J.T., Crary, F.J., Wellbrock, A., Andrews, D.J., Vigren, E., Desai, R.T.,

Coates, A.J., Mandt, K.E., Waite, J.H., 2016. Ion and aerosol precursor densities in Titan's ionosphere: A multi-instrument case study. J. Geophys. Res. Sp. Phys. 121, 10,075-10,090. https://doi.org/10.1002/2016JA022980

Szopa, C., Cernogora, G., Boufendi, L., Correia, J.J., Coll, P., 2006. PAMPRE: A dusty plasma experiment for Titan's tholins production and study. Planet. Space Sci. 54, 394–404. https://doi.org/10.1016/J.PSS.2005.12.012

Tigrine, S., Carrasco, N., Bozanic, D.K., Garcia, G.A., Nahon, L., 2018. FUV Photoionization of Titan Atmospheric Aerosols. Astrophys. J. 867, 164. https://doi.org/10.3847/1538-4357/aae4d8

Van Laer, K., Tinck, S., Samara, V., de Marneffe, J.F., Bogaerts, A., 2013. Etching of low- k materials for microelectronics applications by means of a N2/H2 plasma : modeling and experimental investigation. Plasma Sources Sci. Technol. 22, 025011. https://doi.org/10.1088/0963-0252/22/2/025011

Vigren, E., Galand, M., Shebanits, O., Wahlund, J.E., Geppert, W.D., Lavvas, P., Vuitton, V., Yelle, R. V., 2014. Increasing positive ion number densities below the peak of ion-electron pair production in titan's ionosphere. Astrophys. J. 786. https://doi.org/10.1088/0004-637X/786/1/69

Vuitton, V., Yelle, R. V., Klippenstein, S.J., Hörst, S.M., Lavvas, P., 2019. Simulating the density of organic species in the atmosphere of Titan with a coupled ion-neutral photochemical model. Icarus 324, 120–197. https://doi.org/10.1016/j.icarus.2018.06.013

Wahlund, J.E., Boström, R., Gustafsson, G., Gurnett, D.A., Kurth, W.S., Pedersen, A., Averkamp, T.F., Hospodarsky, G.B., Persoon, A.M., Canu, P., Neubauer, F.M., Dougherty, M.K., Eriksson, A.I., Morooka, M.W., Gill, R., André, M., Eliasson, L., Müller-Wodarg, I., 2005. Cassini measurements of cold plasma in the ionosphere of Titan. Science 308, 986–989. https://doi.org/10.1126/science.1109807

Waite, J.H., Young, D.T., Cravens, T.E., Coates, A.J., Crary, F.J., Magee, B., Westlake, J., 2007. Planetary science: The process of tholin formation in Titan's upper atmosphere. Science 316, 870–875. https://doi.org/10.1126/science.1139727

Wellbrock, A., Coates, A.J., Jones, G.H., Lewis, G.R., Waite, J.H., 2013. Cassini CAPS-ELS observations of negative ions in Titan's ionosphere: Trends of density with altitude. Geophys. Res. Lett. 40, 4481–4485. https://doi.org/10.1002/grl.50751

West, R.A., Seignovert, B., Rannou, P., Dumont, P., Turtle, E.P., Perry, J., Roy, M., Ovanessian, A., 2018. The seasonal cycle of Titan's detached haze. Nat. Astron. 2, 495–500. https://doi.org/10.1038/s41550-018-0434-z

Whipple, E.C.J., 1965. The equilibrium electric potential of a body in the upper atmosphere and in the interplanetary space. George Washington University.

Woodard, A., Shojaei, K., Berrospe-Rodriguez, C., Nava, G., Mangolini, L., 2020. Electron emission from particles strongly affects the electron energy distribution in dusty plasmas. J. Vac. Sci. Technol. A 38, 023005. https://doi.org/10.1116/1.5134706

ÉCOLE DOCTORALE
Sciences mécaniques et
énergétiques, matériaux
et géosciences (SMEMAG)

université
PARIS-SACLAY

Titre : Interaction aérosols-plasma dans l'ionosphère de Titan

Mots clés : Titan, simulation expérimentale, plasmas poudreux, chimie atmosphérique hétérogène, ionosphères, mission Cassini

Résumé : Le système climatique de la lune de Saturne Titan est gouverné par la production intense d'aérosols organiques dans sa haute atmosphère. Ce phénomène s'est aussi certainement produit sur Terre au moment de l'apparition de la vie. Ces deux points motivent fortement les recherches sur les processus de formation et d'évolution des aérosols dans l'atmosphère de Titan. Les aérosols se forment et restent plusieurs semaines dans l'ionosphère, étendue d'environ 900 à 1200 km d'altitude. Cette région de l'atmosphère est ionisée par le rayonnement solaire UV et des particules énergétiques provenant de la magnétosphère de Saturne. Des espèces plasma très réactives sont ainsi présentes : des radicaux, des espèces excitées, des ions et des électrons. Dans un tel environnement, je me suis intéressée à l'interaction entre les aérosols organiques et le plasma.

Ce phénomène est simulé en laboratoire avec une expérience développée à cet effet : des analogues des aérosols de Titan sont exposés à une décharge plasma en N_2-H_2. J'observe qu'à la fois les grains et la phase gaz évoluent. Les atomes H et N interagissent chimiquement avec les aérosols. Puis, du cyanure d'hydrogène (HCN) ainsi que d'autres molécules organiques sont éjectées en phase gaz par le bombardement ionique. Ces résultats mettent en évidence une contribution importante des processus hétérogènes dans l'ionosphère de Titan.

Ma ré-analyse des données de la sonde de Langmuir de la mission Cassini a d'autre part révélé la présence d'une population d'électrons inattendue dans l'ionosphère, sous 1200 km d'altitude et côté jour, zone dans laquelle des ions lourds ont également été détectés. Ces électrons pourraient être émis par les aérosols, après collision avec un photon et/ou après chauffage par la chimie ionique très active dans cette région.

Title: Aerosols-plasma interaction in Titan's ionosphere

Keywords: Titan, experimental simulation, dusty plasma, heterogeneous atmospheric chemistry, ionospheres, Cassini mission

Abstract: The climatic system of Saturn's moon Titan is governed by the intense production of organic aerosols in its upper atmosphere. This phenomenon also certainly happened on Earth at the beginning of life. These two points strongly motivate research on the formation and evolution processes of the aerosols in the atmosphere of Titan. The aerosols form and stay several weeks in the ionosphere, between ~900 and 1200 km of altitude. This atmospheric layer is ionized by UV solar rays and energetic particles coming from Saturn's magnetosphere, forming a plasma with very reactive species: radicals, excited species, ions and electrons. In such an environment, the main question I tackle is how the organic aerosols interact with the plasma species.

The phenomenon is simulated in the laboratory with a plasma setup developed on purpose: analogues of Titan aerosols are exposed to a N_2-H_2 plasma discharge. Both an evolution of the solid and the gas phase are observed. H and N atoms chemically interact with the aerosols. Then, hydrogen cyanide (HCN) and other organic molecules are ejected in the gas phase by ion sputtering. These results highlight an important contribution of heterogeneous processes in Titan's upper atmosphere.

My re-analysis of the Cassini Langmuir probe data revealed the presence of an unexpected electron population in the ionosphere, below 1200 km and on the day-side, where heavy ions are also detected. These electrons could be emitted by the aerosols, after collision with a photon, and/or heating by the active ion chemistry.